

AD-A191 689

COMPILATION OF REPRINTS NUMBER 64(U) OREGON STATE UNIV
CORVALLIS COLL OF OCEANOGRAPHY NOV 87 REF-85-23
N88014-76-C-8867

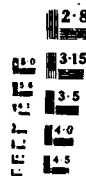
1/3

UNCLASSIFIED

F/G 8/3

ML

I



AD-A191 609

OFFICE OF NAVAL RESEARCH
COMPILATION OF REPRINTS NO. 64
November 1987

Compiled by Jeannie Rhodes, Admin. Asst., OSU Oceanography
Corvallis, OR 97331

CONTENTS

IMAGING FAULT SLIP USING TELESEISMIC WAVEFORMS ANALYSIS OF A TYPICAL
INCOMPLETE TOMOGRAPHY

William Menke

EFFECT OF HETEROGENEITIES IN "D" ON THE DECAY RATE OF P DIFF

William Menke

SEMIDIURNAL INTERNAL TIDE IN JASIN: OBSERVATIONS AND SIMULATIONS

L.M. deWitt, M.D. Levine, C.A. Paulson, and W.V. Burt

HEAT AND ENERGY BALANCES IN THE UPPER OCEAN AT 50 DEGREES N,
140 DEGREES W DURING NOVEMBER 1980 (STREX)

J.D. Paduan and R.A. deSzoeki

THE BIOLOGICAL AND ACOUSTICAL STRUCTURE OF SOUND SCATTERING LAYERS
OFF OREGON

John M. Kalish, Charles F. Greenlaw, William Pearcy and
D. Van Holliday

THE AUSTRALIAN COASTAL EXPERIMENT: A SEARCH FOR COASTAL-TRAPPED
WATERS

H.J. Freeland, F.M. Boland, J.A. Church, A.J. Clarke,
A.M.G. Forbes, A. Huyer (OSU), R.L. Smith (OSU),
R.O.R.Y. Thompson, & N.J. White

DEEP-SEA CURRENTS OFF NORTHERN CALIFORNIA

Phyllis J. Staben, and Robert L. Smith

RAPID ALTERNATING VERTICAL TEMPERATURE GRADIENTS IN THE E. CHINA SEA

Wayne V. Burt, Steve Neshyba, and Clifford L. Trump

ON THE NONLINEAR EVOLUTION OF BAROCLINIC INSTABILITY OVER TOPOGRAPHY

Roland A. deSzoeki

OBSERVATIONS OF INTERNAL GRAVITY WAVES UNDER THE ARCTIC PACK ICE

Murray D. Levine, Clayton A. Paulson, and James H. Morrison

SIMULTANEOUS SPATIAL AND TEMPORAL MEASUREMENTS OF THE INTERNAL WAVE
FIELD DURING MATE

Murray d. Levine, James D. Irish, Terry E. Ewart,
and Stephen A. Reynolds

DTIC
SELECTED
JAN 28 1988
E

This document has been approved
for public release and sale; its
distribution is unlimited.

COASTAL-TRAPPED WAVES ON THE EAST AUSTRALIAN CONTINENTAL SHELF

PART I: PROPAGATION OF MODES

John A. Church, Howard J. Freeland, and Robert L. Smith

MEASUREMENTS OF NEAR-SURFACE SHEAR IN THE OCEAN

J.G. Richman, R.A. deSzoeko, and R.E. Davis

THE AVAILABLE POTENTIAL ENERGY OF OVERTURNS AS AN INDICATOR OF MIXING
IN THE SEASONAL THERMOCLINE

Thomas M. Dillon, Melora M. Park

ON THE WIND-DRIVEN CIRCULATION OF THE SOUTH PACIFIC OCEAN

Roland A. deSzoeko

COASTAL-TRAPPED WAVES ON THE EAST AUSTRALIAN CONTINENTAL SHELF.

PART II: MODEL VERIFICATION

John A. Church, Neil J. White, Allan J. Clarke,

Howard J. Freeland, and Robert L. Smith

VERTICAL HEAT FLUXES THROUGH THE BEAUFORT SEA THERMOHALINE STAIRCASE

Laurie Padman and Thomas M. Dillon

Accession For	
NTIS GRA&I	<input checked="checked" type="checkbox"/>
DTIC TAB	<input checked="checked" type="checkbox"/>
Unannounced	<input type="checkbox"/>
Justification	
By	
Distribution/	
Availability Codes	
Dist	Avail and/or Special
A-1	



Unclassified

SECURITY CLASSIFICATION OF THIS PAGE (When Data Entered)

REPORT DOCUMENTATION PAGE		READ INSTRUCTIONS BEFORE COMPLETING FORM
1 REPORT NUMBER 85-23	2. GOVT ACCESSION NO.	3 RECIPIENT'S CATALOG NUMBER
4 TITLE (and Subtitle) IMAGING FAULT SLIP USING TELESEISMIC WAVEFORMS: ANALYSIS OF A TYPICAL INCOMPLETE TOMOGRAPHY PROBLEM		5. TYPE OF REPORT & PERIOD COVERED reprint, 1984
7 AUTHOR(s) Menke, William		6 PERFORMING ORG. REPORT NUMBER
9 PERFORMING ORGANIZATION NAME AND ADDRESS College of Oceanography Oregon State University Corvallis, OR 97331		8 CONTRACT OR GRANT NUMBER(s) N00014-84C-0218
11 CONTROLLING OFFICE NAME AND ADDRESS Office of Naval Research Ocean Science & Technology Division Arlington, VA 22217		10 PROGRAM ELEMENT, PROJECT, TASK AREA & WORK UNIT NUMBERS NR083-102
14 MONITORING AGENCY NAME & ADDRESS (if different from Controlling Office)		12 REPORT DATE 1984
		13. NUMBER OF PAGES 8
		15 SECURITY CLASS. (of this report) unclassified
		16a DECLASSIFICATION/DOWNGRADING SCHEDULE
16 DISTRIBUTION STATEMENT (of this Report) Distribution unlimited; approved for public release		
17. DISTRIBUTION STATEMENT (of the abstract entered in Block 20, if different from Report) Approved for public release; distribution unlimited		
18. SUPPLEMENTARY NOTES Reprint from Geophys. J.R. astr. Soc. (1985) 81, 197-204		
19. KEY WORDS (Continue on reverse side if necessary and identify by block number)		
20 ABSTRACT (Continue on reverse side if necessary and identify by block number) None		

DD FORM 1473

EDITION OF 1 NOV 65 IS OBSOLETE
S/N 0102-014-6601

Unclassified

SECURITY CLASSIFICATION OF THIS PAGE (When Data Entered)

Unclassified

SECURITY CLASSIFICATION OF THIS PAGE (When Data Entered)

REPORT DOCUMENTATION PAGE		READ INSTRUCTIONS BEFORE COMPLETING FORM
1. REPORT NUMBER 86-4	2. GOVT ACCESSION NO.	3. RECIPIENT'S CATALOG NUMBER
4. TITLE (and Subtitle) EFFECT OF HETEROGENEITIES IN "D" ON THE DECAY RATE OF P _{DIFF}		5. TYPE OF REPORT & PERIOD COVERED reprint
		6. PERFORMING ORG. REPORT NUMBER
7. AUTHOR(s) MENKE, WILLIAM		8. CONTRACT OR GRANT NUMBER(s) N00014-84-C-0218
9. PERFORMING ORGANIZATION NAME AND ADDRESS College of Oceanography Oregon State University Corvallis, OR 97331		10. PROGRAM ELEMENT, PROJECT, TASK AREA & WORK UNIT NUMBERS NR085-102
11. CONTROLLING OFFICE NAME AND ADDRESS Office of Naval Research Ocean Science & Technology Division Arlington, VA 22217		12. REPORT DATE 10 February 1986
		13. NUMBER OF PAGES 7
14. MONITORING AGENCY NAME & ADDRESS (if different from Controlling Office)		15. SECURITY CLASS (of this report) unclassified
		16. DECLASSIFICATION/DOWNGRADING SCHEDULE
16. DISTRIBUTION STATEMENT (of this Report) Distribution unlimited; approved for public release		
17. DISTRIBUTION STATEMENT (of the abstract entered in Block 20, if different from Report)		
18. SUPPLEMENTARY NOTES Reprint from JOURNAL OF GEOPHYSICAL RESEARCH, Vol. 91, No. B2, pages 1927-1933, February 10, 1986		
19. KEY WORDS (Continue on reverse side if necessary and identify by block number)		
20. ABSTRACT (Continue on reverse side if necessary and identify by block number) We use physical models to examine the effect of scatterers in the "D" region of the mantle on the decay rate of the P _{diff} phase in the core shadow. Scatterers are in the size range 7.5-81 km, and measurements of the decay rate are made in the period range 3-60 s. We find that the presence of scatterers in "D" can change the decay rate of P _{diff} by as much as 50%. The heterogeneity does not affect the decay rate for periods greater than about 10-20 s. At shorter periods, the decay rate can be either lower or higher than the laterally homogeneous case, depending on the scatterer geometry. We find that a layer of		

DD FORM 1 JAN 73 1473

EDITION OF 1 NOV 65 IS OBSOLETE
S/N 0102-014-6601

Unclassified

SECURITY CLASSIFICATION OF THIS PAGE (When Data Entered)

Unclassified

SECURITY CLASSIFICATION OF THIS PAGE (When Data Entered)

small (7.5 km) scatterers can decrease the decay rate, while layers of larger scatterers (41-81 km) mainly increase it. We did not identify any major effect of scatterer aspect ratio on the decay rate in the one relevant test that we performed (dikes and sills on the core-mantle boundary).

Unclassified

SECURITY CLASSIFICATION OF THIS PAGE (When Data Entered)

Unclassified

SECURITY CLASSIFICATION OF THIS PAGE (When Data Entered)

REPORT DOCUMENTATION PAGE		READ INSTRUCTIONS BEFORE COMPLETING FORM
1. REPORT NUMBER 86-5	2. GOVT ACCESSION NO.	3. RECIPIENT'S CATALOG NUMBER
4. TITLE (and Subtitle) SEMIDIURNAL INTERNAL TIDE IN JASIN: OBSERVATIONS AND SIMULATION		5. TYPE OF REPORT & PERIOD COVERED reprint
		6. PERFORMING ORG. REPORT NUMBER
7. AUTHOR(s) L.M. deWitt, M.D. Levine, C.A. Paulson, and W.V. Burt		8. CONTRACT OR GRANT NUMBER(s) N00014-76-C-0197 N00015-84-C-0218
9. PERFORMING ORGANIZATION NAME AND ADDRESS College of Oceanography Oregon State University Corvallis, OR 97331		10. PROGRAM ELEMENT, PROJECT, TASK AREA & WORK UNIT NUMBERS NR083-102
11. CONTROLLING OFFICE NAME AND ADDRESS Office of Naval Research Ocean Science & Technology Division Arlington, VA 22217		12. REPORT DATE 15 February 1986
		13. NUMBER OF PAGES 12
14. MONITORING AGENCY NAME & ADDRESS (if different from Controlling Office)		15. SECURITY CLASS. (of this report) unclassified
		16. DECLASSIFICATION/DOWNGRADING SCHEDULE
16. DISTRIBUTION STATEMENT (of this Report) Distribution unlimited; approved for public release		
17. DISTRIBUTION STATEMENT (of the abstract entered in Block 20, if different from Report)		
18. SUPPLEMENTARY NOTES Reprint from "Journal of Geophysical Research," Volume 91, No. C2, pages 2581-2592, February 15, 1986		
19. KEY WORDS (Continue on reverse side if necessary and identify by block number)		
20. ABSTRACT (Continue on reverse side if necessary and identify by block number) Temperature was observed in the upper 80 m by moored thermistor chains at three locations in Rockall Channel west of Scotland. Isotherms were interpolated, and a 1-week period of exceptionally energetic tidal oscillations was analyzed. The moored array (horizontal separations ranging from 6 to 20 km) was used as an antenna to determine the dominant horizontal wavelength and direction of propagation of the internal tide within the array. Rockall Bank, 100 km to the southeast, was identified as the source of the internal tide. The semidiurnal internal tide generated by the interaction of the surface tide with Rockall Bank was simulated by use of a model due to Prinsenber and Rattray. The model predicts generation of the internal tide at the shelf break and propagation seaward as energetic beams which lie along internal wave characteristics. Some energy is trapped near the surface in association with the pycnocline. There is substantial structure in the velocity and vertical displacement fields. Most of the		

DD FORM 1473
1 JAN 73EDITION OF 1 NOV 65 IS OBSOLETE
S/N 0102-014-6601

Unclassified

SECURITY CLASSIFICATION OF THIS PAGE (When Data Entered)

Unclassified

SECURITY CLASSIFICATION OF THIS PAGE (When Data Entered)

total energy of the internal tide is in the first vertical mode. However, at particular depths, vertical modes as high as 4 (horizontal wavelengths of 25 km) dominate. The high degree of spatial variability in the modeled internal tide illustrates the potential for error when basing a description of the tide on sparse observations. There is good agreement between the modeled vertical displacements and the 1-week period of energetic oscillations of isotherm depth observed at the moorings. In addition, there is good agreement between the model and the tidal velocity variance measured during the same week at depths ranging from 10 to 1000 m and distances ranging from 50 to 130 km from Rockall Bank. Richardson numbers associated with the vertical shear of the modeled internal tide range down to values less than 2.

Unclassified

SECURITY CLASSIFICATION OF THIS PAGE (When Data Entered)

Unclassified

SECURITY CLASSIFICATION OF THIS PAGE (When Data Entered)

REPORT DOCUMENTATION PAGE		READ INSTRUCTIONS BEFORE COMPLETING FORM
1. REPORT NUMBER 86-8	2. GOVT ACCESSION NO.	3. RECIPIENT'S CATALOG NUMBER
4. TITLE (and Subtitle) HEAT AND ENERGY BALANCES IN THE UPPER OCEAN AT 50°N, 140°W DURING NOVEMBER 1980 (STREX)		5. TYPE OF REPORT & PERIOD COVERED Reprint
		6. PERFORMING ORG. REPORT NUMBER
7. AUTHOR(s) Paduan, J.D. and deSzoek, R.A.		8. CONTRACT OR GRANT NUMBER(s) N00014-84-C-0218
9. PERFORMING ORGANIZATION NAME AND ADDRESS College of Oceanography Oregon State University Corvallis, OR 97331		10. PROGRAM ELEMENT, PROJECT, TASK AREA & WORK UNIT NUMBERS NR083-102
11. CONTROLLING OFFICE NAME AND ADDRESS Office of Naval Research Ocean Science & Technology Division Arlington, VA 22217		12. REPORT DATE Nov. 1980
		13. NUMBER OF PAGES 14
14. MONITORING AGENCY NAME & ADDRESS (if different from Controlling Office)		15. SECURITY CLASS. (of this report) unclassified
		16. DECLASSIFICATION/DOWNGRADING SCHEDULE
16. DISTRIBUTION STATEMENT (of this Report)		
17. DISTRIBUTION STATEMENT* (of the abstract entered in Block 20, if different from Report) Approved for public release; distribution unlimited		
18. SUPPLEMENTARY NOTES		
19. KEY WORDS (Continue on reverse side if necessary and identify by block number)		
20. ABSTRACT (Continue on reverse side if necessary and identify by block number) Subsurface temperature data and surface meteorological data are analyzed from thermistor chain moorings deployed near 50°N, 140°W during the Storm Transfer and Response Experiment (STREX). The upper-ocean heat and potential energy (PE) contents to 90 m are examined for an 18-day period and their changes compared to the sources and sinks of heat and turbulent kinetic energy (TKE). Heat and TKE do not balance in the vertical dimension alone. The heat content change, for example, averages -200 W m^{-2} while the net cooling at the surface, estimated from bulk formulas for latent and sensible heat fluxes and radiation measurements, averaged only -86 W m^{-2} . Advection of heat and PE, in either the vertical or horizontal, play major roles in the budgets of this area. We describe a method for using the large-scale wind stress and SST data around the site to compute the advection in the Ekman layer and close the heat (to 23%) and TKE (to 24%) budgets.		

DD FORM 1 JAN 73 1473

EDITION OF 1 NOV 68 IS OBSOLETE
S/N 0102-014-6601

Unclassified

SECURITY CLASSIFICATION OF THIS PAGE (When Data Entered)

Unclassified

SECURITY CLASSIFICATION OF THIS PAGE (When Data Entered)

Though the heat and PE contents exhibit long-term trends, there are two marked events associated with storms on 15 and 27 November 1980 that account for much of the overall cooling and PE change. The advection estimates mimic the episodic character of the heat and PE contents and are clearly important on the short, storm time scale. The relative contributions of horizontal and vertical advection are quite different for the two storms, showing that the upper-ocean response very much depends on the proximity and orientation of the storm as it moves past the observational site.

The TKE budget is complex, and some terms can only be estimated by uncertain parameterizations so that the relative importance of surface production, shear production, and advection is unclear. Still, the fact emerges that mixed layer deepening is dominated by wind-forcing even during the season of significant cooling.

Unclassified

SECURITY CLASSIFICATION OF THIS PAGE (When Data Entered)

Unclassified

SECURITY CLASSIFICATION OF THIS PAGE (When Data Entered)

REPORT DOCUMENTATION PAGE		READ INSTRUCTIONS BEFORE COMPLETING FORM
1. REPORT NUMBER 86-11	2. GOVT ACCESSION NO.	3. RECIPIENT'S CATALOG NUMBER
4. TITLE (and Subtitle) THE BIOLOGICAL AND ACOUSTICAL STRUCTURE OF SOUND SCATTERING LAYERS OFF OREGON		5. TYPE OF REPORT & PERIOD COVERED Reprint
		6. PERFORMING ORG. REPORT NUMBER
7. AUTHOR(s) John M. Kalish, Charles F. Greenlaw, William G. Pearcy and D. Van Holliday		8. CONTRACT OR GRANT NUMBER(s) N00014-79-C-0004
9. PERFORMING ORGANIZATION NAME AND ADDRESS College of Oceanography Oregon State University Corvallis, Oregon 97331		10. PROGRAM ELEMENT, PROJECT, TASK AREA & WORK UNIT NUMBERS NR083-102
11. CONTROLLING OFFICE NAME AND ADDRESS Office of Naval Research Ocean Science & Technology Division Arlington, Virginia 22217		12. REPORT DATE 1985
		13. NUMBER OF PAGES 26
14. MONITORING AGENCY NAME & ADDRESS (if different from Controlling Office)		15. SECURITY CLASS. (of this report) Unclassified
		15a. DECLASSIFICATION DOWNGRADING SCHEDULE
16. DISTRIBUTION STATEMENT (of this Report) Approved for public release; distribution unlimited		
17. DISTRIBUTION STATEMENT (of the abstract entered in Block 20, if different from Report)		
18. SUPPLEMENTARY NOTES		
19. KEY WORDS (Continue on reverse side if necessary and identify by block number)		
20. ABSTRACT (Continue on reverse side if necessary and identify by block number) Four discrete acoustical frequencies were used to determine the depths of migratory and non-migratory scattering layers. Layers were insonified with a broad-band, low frequency (1-30 kHz) acoustic source and sampled with a 100 m ² rope trawl with five opening and closing codends. The predominant fishes with gas-filled swimbladders caught in deep (188-250 m) day time layers were <i>Protomycetophum crockeri</i> and <i>P. thompsoni</i> , whereas <i>Protomycetophum</i> spp. and <i>Diaphus theta</i> were the most common species in deep		

DD FORM 1 JAN 73 1473

EDITION OF 1 NOV 65 IS OBSOLETE
S/N 0102-014-66011

Unclassified

SECURITY CLASSIFICATION OF THIS PAGE (When Data Entered)

(125-255 m) night-time layers. The common fishes with gas-filled swimbladders in shallow (0-80 m) night-time layers were *D. theta*, *Stenobranchius leucopsarus* (<35mm), *Tarletonbeania crenularis*, *Symbolophorus californiensis* and *Engraulis mordax*.

Arcer estimates of distributions of bubble radii were similar for deep day and deep night scattering layers, but a wider range of bubble sizes existed in shallow night-time layers than in deep day and deep night layers.

A model which considered species-specific parameters of morphology, physiology and behavior provided estimations of the distributions of swimbladder radii that most closely matched the acoustically estimated distributions of bubble radii. Comparisons of acoustic data and net catch data indicate that myctophids with gas-filled swimbladders may maintain swimbladder volume at a level below that required for neutral buoyancy. Furthermore, there is some evidence suggesting that large myctophids maintain a constant swimbladder volume during vertical migrations, but at volumes that result in negative buoyancy; smaller myctophids may maintain a constant swimbladder mass during vertical migration.

Unclassified

SECURITY CLASSIFICATION OF THIS PAGE (When Data Entered)

REPORT DOCUMENTATION PAGE		READ INSTRUCTIONS BEFORE COMPLETING FORM
1. REPORT NUMBER 86-15	2. GOVT ACCESSION NO.	3. RECIPIENT'S CATALOG NUMBER
4. TITLE (and Subtitle) The Australian Coastal Experiment: A Search for Coastal-trapped Waters		5. TYPE OF REPORT & PERIOD COVERED Reprint
		6. PERFORMING ORG. REPORT NUMBER
7. AUTHOR(s) H.J. Freeland, F.M. Boland, J.A. Church, A.J. Clarke, A.M.G. Forbes, A. Huyer (OSU), R.L. Smith (OSU), R.O.R.Y. Thompson, & N.J. White		8. CONTRACT OR GRANT NUMBER(s) N00014-84-C-0218
9. PERFORMING ORGANIZATION NAME AND ADDRESS College of Oceanography Oregon State University Corvallis, Oregon 97331		10. PROGRAM ELEMENT PROJECT TASK AREA & WORK UNIT NUMBERS NR083-102
11. CONTROLLING OFFICE NAME AND ADDRESS Office of Naval Research Ocean Science & Technology Division Arlington, Virginia 22217		12. REPORT DATE
		13. NUMBER OF PAGES
14. MONITORING AGENCY NAME & ADDRESS (if different from Controlling Office)		15. SECURITY CLASS. (of this report) Unclassified
		15a. DECLASSIFICATION/DOWNGRADING SCHEDULE
16. DISTRIBUTION STATEMENT (of this Report) Approved for public release; distribution unlimited		
17. DISTRIBUTION STATEMENT (of the abstract entered in Block 20, if different from Report)		
18. SUPPLEMENTARY NOTES		
19. KEY WORDS (Continue on reverse side if necessary and identify by block number)		
20. ABSTRACT (Continue on reverse side if necessary and identify by block number) The Australian Coastal Experiment (ACE) was conducted in the coastal waters of New South Wales from September 1983 to 1984. The data obtained allow a detailed examination of the dynamics of flow on the continental shelf and slope and in particular allow a description of coastal trapped wave modes propagating within the coastal waveguide. The trapped-wave signal is contaminated by energy from the East Australian current eddies approaching the continental slope. However, the data to allow a		

DD FORM 1 JAN 73 1473

EDITION OF 1 NOV 63 IS OBSOLETE
S/N 0102-014-66011

Unclassified

SECURITY CLASSIFICATION OF THIS PAGE (When Data Entered)

Unclassified

SECURITY CLASSIFICATION OF THIS PAGE (When Data Entered)

clear separation of the first three coastal trapped wave modes over the range of frequencies appropriate to the weather forcing band. Through that frequency range the phase speed is computed and an empirical dispersion relation determined for each mode. The empirical dispersion relations compare well with the theoretical relations indicating that a large fraction of the variance in current velocities on the continental shelf can be accounted for by coastal trapped wave theory.

Wind forcing of trapped waves is also considered and evidence presented that in the ACE area the motions are dominated by the propagation of free waves through the arrays.

SECURITY CLASSIFICATION OF THIS PAGE (When Data Entered)

Unclassified

SECURITY CLASSIFICATION OF THIS PAGE (When Data Entered)

REPORT DOCUMENTATION PAGE		READ INSTRUCTIONS BEFORE COMPLETING FORM
1. REPORT NUMBER 87-7	2. GOVT ACCESSION NO.	3. RECIPIENT'S CATALOG NUMBER
4. TITLE (and Subtitle) DEEP-SEA CURRENTS OFF NORTHERN CALIFORNIA		5. TYPE OF REPORT & PERIOD COVERED Reprint
		6. PERFORMING ORG. REPORT NUMBER
7. AUTHOR(s) Stabeno, Phyllis J, and Smith, Robert L.		8. CONTRACT OR GRANT NUMBER(s) N00014-84-C-0218
9. PERFORMING ORGANIZATION NAME AND ADDRESS College of Oceanography Oregon State University Corvallis, Oregon 97331		10. PROGRAM ELEMENT, PROJECT, TASK AREA & WORK UNIT NUMBERS NR083-102
11. CONTROLLING OFFICE NAME AND ADDRESS Office of Naval Research Ocean Science & Technology Division Arlington, Virginia 22217		12. REPORT DATE January 1987
		13. NUMBER OF PAGES 17
14. MONITORING AGENCY NAME & ADDRESS (if different from Controlling Office)		15. SECURITY CLASS. (of this report) Unclassified
		15a. DECLASSIFICATION/DOWNGRADING SCHEDULE
16. DISTRIBUTION STATEMENT (of this Report) Approved for public release; distribution unlimited		
17. DISTRIBUTION STATEMENT (of the abstract entered in Block 20, if different from Report)		
18. SUPPLEMENTARY NOTES		
19. KEY WORDS (Continue on reverse side if necessary and identify by block number)		
20. ABSTRACT Current meter records from 14 moorings in the deep-sea basin (3000-4500 m deep) south of the Mendocino Fracture Zone are analyzed. All moorings had current meters between 200 m and 500 m above the bottom, and some extended to within 150 m of the surface. There were high vertical correlations between measurements on the same mooring within 1500 m of the bottom and within 800 m of the surface but almost no significant correlation in the horizontal. In the basin the presence of eddies appears strongest at depths below 1200 m. Several of the records exceed 3 years in length, and one extended for 5 years. Spectral analysis of these shows that most of the kinetic energy below 3000 m is in the temporal mesoscale (periods of 31 to 120 days), while the spectral estimates in the upper 1000 m are dominated by longer time scales. Only in the deep records is there a significant southward mean flow. Neither a mean California Current nor a poleward undercurrent is apparent in the shallower data (above 1250 m). The currents in the upper 500 m nearest the continental margin are influenced by the presence of cold filaments originating near Point Arena.		

DD FORM 1473

1 JAN 73

EDITION OF 1 NOV 65 IS OBSOLETE
S/N 0102-014-66011

Unclassified

SECURITY CLASSIFICATION OF THIS PAGE (When Data Entered)

Unclassified

SECURITY CLASSIFICATION OF THIS PAGE (When Data Entered)

REPORT DOCUMENTATION PAGE		READ INSTRUCTIONS BEFORE COMPLETING FORM
1. REPORT NUMBER 87-8	2. GOVT ACCESSION NO.	3. RECIPIENT'S CATALOG NUMBER
4. TITLE (and Subtitle) RAPID ALTERNATING VERTICAL TEMPERATURE GRADIENTS IN THE EAST CHINA SEA		5. TYPE OF REPORT & PERIOD COVERED Reprint
		6. PERFORMING ORG. REPORT NUMBER
7. AUTHOR(s) Burt, Wayne V.; Neshyba, Steve;; Trump, Cliffor L.		8. CONTRACT OR GRANT NUMBER(s) N00014-C-76-0067
9. PERFORMING ORGANIZATION NAME AND ADDRESS College of Oceanography Oregon State University Corvallis, Oregon 97331		10. PROGRAM ELEMENT, PROJECT, TASK AREA & WORK UNIT NUMBERS NR083-102
11. CONTROLLING OFFICE NAME AND ADDRESS Office of Naval Research Ocean Science & Technology Division Arlington, Virginia 22217		12. REPORT DATE 1986
		13. NUMBER OF PAGES 10
14. MONITORING AGENCY NAME & ADDRESS (if different from Controlling Office)		15. SECURITY CLASS. (of this report) Unclassified
		15a. DECLASSIFICATION/DOWNGRADING SCHEDULE
16. DISTRIBUTION STATEMENT (of this Report) Approved for public release; distribution unlimited		
17. DISTRIBUTION STATEMENT (of the abstract entered in Block 20, if different from Report)		
18. SUPPLEMENTARY NOTES		
19. KEY WORDS (Continue on reverse side if necessary and identify by block number)		
20. ABSTRACT (Continue on reverse side if necessary and identify by block number) Abstract--Data from an array of current meters, thermistor chains, and meteorologically instrumented buoys deployed in the shallow water (depths of 97 to 115 m) of the East China Sea during AMT-X 75 (February 1985) show that the vertical temperature difference between the 20 and 70 m depths regularly alternated between 0.4°C and a maximum of 0.65°C. The periodicity of change was predominantly that of the semidiurnal tide (12.4 h) with some modulation of diurnal or near diurnal periodicity. The vertical gradient developed most often when currents were in a northwest direction, a direction parallel to the average northwest-southeast horizontal surface water temperature gradient when the currents reversed 180° to the southeast, the vertical gradients tended to decrease or disappear altogether. An explanation is given in terms of vertical shear in the semidiurnal tidal currents coupled with the slightly higher current speeds during the offshore phase (southeast direction) of the current ellipse.		

DD FORM 1473
1 JAN 73EDITION OF 1 NOV 63 IS OBSOLETE
S/N 0102-014-6601

Unclassified

SECURITY CLASSIFICATION OF THIS PAGE (When Data Entered)

Unclassified

SECURITY CLASSIFICATION OF THIS PAGE (When Data Entered)

REPORT DOCUMENTATION PAGE		READ INSTRUCTIONS BEFORE COMPLETING FORM
1. REPORT NUMBER 87-9	2. GOVT ACCESSION NO.	3. RECIPIENT'S CATALOG NUMBER
4. TITLE (and Subtitle) ON THE NONLINEAR EVOLUTION OF BAROCLINIC INSTABILITY OVER TOPOGRAPHY		5. TYPE OF REPORT & PERIOD COVERED Reprint
		6. PERFORMING ORG. REPORT NUMBER
7. AUTHOR(s) De Szoeki, Roland A.		8. CONTRACT OR GRANT NUMBER(s) N00014-84-C-0218
9. PERFORMING ORGANIZATION NAME AND ADDRESS College of Oceanography Oregon State University Corvallis, Oregon 97331		10. PROGRAM ELEMENT, PROJECT, TASK AREA & WORK UNIT NUMBERS NR083-102
11. CONTROLLING OFFICE NAME AND ADDRESS Office of Naval Research Ocean Science & Technology Division Arlington, Virginia 22217		12. REPORT DATE 1986
		13. NUMBER OF PAGES 21
14. MONITORING AGENCY NAME & ADDRESS (if different from Controlling Office)		15. SECURITY CLASS. (of this report) Unclassified
		15a. DECLASSIFICATION/DOWNGRADING SCHEDULE
16. DISTRIBUTION STATEMENT (of this Report) Approved for public release; distribution unlimited		
17. DISTRIBUTION STATEMENT (of the abstract entered in Block 20, if different from Report)		
18. SUPPLEMENTARY NOTES		
19. KEY WORDS (Continue on reverse side if necessary and identify by block number)		
20. ABSTRACT (Continue on reverse side if necessary and identify by block number) A theory is presented for the nonlinear evolution of fluctuations in a zonal baroclinic shear flow over topography on a β -plane. It extends an earlier linearized theory on the same subject, which showed that unstable growth was possible for hybrid modes made up of a pair of primary modes with the same frequency but different wavenumbers, each stable in the absence of topography, but made unstable by topography with wavenumber that bridges the wavenumber gap between the primary modes. The slow evolution of the amplitudes of the hybrid modes can be expressed quite generally in terms of elliptic functions that fluctuate regularly between maximum and minimum values determined in a complicated way by initial		

DD FORM 1473
1 JAN 73EDITION OF 1 NOV 65 IS OBSOLETE
S/N 0103-014-6601

Unclassified

SECURITY CLASSIFICATION OF THIS PAGE (When Data Entered)

unclassified
SECURITY CLASSIFICATION OF THIS PAGE (When Data Entered)

amplitudes and parameters characterizing the primary modes. For small initial amplitudes, the evolution can be described in terms of even simpler functions, i.e., trains of hyperbolic-secant pulses that recur with a period that depends on the logarithm of (the inverse of) the initial amplitude.

Maximum fluctuation velocities comparable to, or even larger than, mean flow velocities can be achieved for disturbances of the scale of the internal deformation radius (typically 50 km in the oceans, 1000 km in the atmosphere), topography variations 10% of total fluid depth, and parameters typical of oceans and atmosphere.

unclassified
SECURITY CLASSIFICATION OF THIS PAGE (When Data Entered)

Unclassified

SECURITY CLASSIFICATION OF THIS PAGE (When Data Entered)

REPORT DOCUMENTATION PAGE		READ INSTRUCTIONS BEFORE COMPLETING FORM
1. REPORT NUMBER 87-11	2. GOVT ACCESSION NO.	3. RECIPIENT'S CATALOG NUMBER
4. TITLE (and Subtitle) OBSERVATIONS OF INTERNAL GRAVITY WAVES UNDER THE ARCTIC PACK ICE		5. TYPE OF REPORT & PERIOD COVERED Reprint
		6. PERFORMING ORG. REPORT NUMBER
7. AUTHOR(s) Levine, Murray D.; Clayton A. Paulson, James H. Morrison		8. CONTRACT OR GRANT NUMBER(s) N00014-84-C-0218
9. PERFORMING ORGANIZATION NAME AND ADDRESS College of Oceanography Oregon State University Corvallis, Oregon 97331		10. PROGRAM ELEMENT, PROJECT, TASK AREA & WORK UNIT NUMBERS NR083-102
11. CONTROLLING OFFICE NAME AND ADDRESS Office of Naval Research Ocean Science & Technology Division Arlington, Virginia 22217		12. REPORT DATE January 1987
		13. NUMBER OF PAGES 4
14. MONITORING AGENCY NAME & ADDRESS (if different from Controlling Office)		15. SECURITY CLASS. (of this report) Unclassified
		15a. DECLASSIFICATION/DOWNGRADING SCHEDULE
16. DISTRIBUTION STATEMENT (of this Report) Approved for public release; distribution unlimited		
17. DISTRIBUTION STATEMENT (of the abstract entered in Block 20, if different from Report)		
18. SUPPLEMENTARY NOTES		
19. KEY WORDS (Continue on reverse side if necessary and identify by block number)		
20. ABSTRACT (Continue on reverse side if necessary and identify by block number) Internal gravity waves measured under the Arctic pack ice were strikingly different from measurements at lower latitudes. The total wave energy, integrated over the internal wave frequency band, was lower by a factor of 0.03-0.07, and the spectral slope at high frequency was nearly -1 in contrast to the -2 observed at lower latitudes. This result has implications for theoretical investigations of the generation, evolution, and destruction of internal waves and is also important for other processes, such as the propagation of sound, and the wave-induced turbulent diffusion of heat, plankton, and chemical tracers		

DD FORM 1 JAN 73 1473

EDITION OF 1 NOV 65 IS OBSOLETE
S/N 0102-014-66011

Unclassified

SECURITY CLASSIFICATION OF THIS PAGE (When Data Entered)

Unclassified

SECURITY CLASSIFICATION OF THIS PAGE (When Data Entered)

REPORT DOCUMENTATION PAGE		READ INSTRUCTIONS BEFORE COMPLETING FORM
1. REPORT NUMBER 87-12	2. GOVT ACCESSION NO.	3. RECIPIENT'S CATALOG NUMBER
4. TITLE (and Subtitle) SIMULTANEOUS SPATIAL AND TEMPORAL MEASUREMENTS OF THE INTERNAL WAVE FIELD DURING MATE		5. TYPE OF REPORT & PERIOD COVERED Reprint
		6. PERFORMING ORG. REPORT NUMBER
7. AUTHOR(s) Levine, Murray D.; Irish, James D.; Ewart, Terry E.; and Reynolds, Stephen A.		8. CONTRACT OR GRANT NUMBER(s) N00014-79-C-0004 N00014-84-C-0218
9. PERFORMING ORGANIZATION NAME AND ADDRESS College of Oceanography Oregon State University Corvallis, Oregon 97331		10. PROGRAM ELEMENT, PROJECT, TASK AREA & WORK UNIT NUMBERS NR083-102
11. CONTROLLING OFFICE NAME AND ADDRESS Office of Naval Research Ocean Science & Technology Division Arlington, Virginia 22217		12. REPORT DATE August 1986
		13. NUMBER OF PAGES 11
14. MONITORING AGENCY NAME & ADDRESS (if different from Controlling Office)		15. SECURITY CLASS. (of this report) Unclassified
		16a. DECLASSIFICATION/DOWNGRADING SCHEDULE
16. DISTRIBUTION STATEMENT (of this Report) Approved for public release; distribution unlimited		
17. DISTRIBUTION STATEMENT (of the abstract entered in Block 20, if different from Report)		
18. SUPPLEMENTARY NOTES		
19. KEY WORDS (Continue on reverse side if necessary and identify by block number)		
20. ABSTRACT <p>A statistical description of the deep ocean internal wave field is presented using measurements from the Midocean Acoustic Transmission Experiment, conducted near Cobb Seamount in the NE Pacific (46° 46' N, 130° 47' W) during June-July 1977. The unique feature of this experiment is the variety of data obtained simultaneously from the same location: time series of temperature and velocity, and vertical and horizontal profiles of temperature. A generalized form of the Garrett-Munk (GM) internal wave spectrum is developed and used to interpret the data. This spectral model is specified by three parameters, \bar{E}, ℓ, and p (energy level, wave number bandwidth, and frequency spectral slope, respectively). The variety of measurement types permit these three model parameters to be estimated from more than one measurement. The overall best fit values to the MATI data were $p = 2.7$ (GM use $p = 3$), $\ell = 3.1 \text{ m}^{-1} \text{ s}$ (equivalent to $J_0 = 6$, twice the GM value), and $\bar{E} = 8 \times 10^{-4} \text{ J kg}$ (within 20% of the GM level). Although significant differences were found in the values of the bandwidth (ℓ) and spectral slope (p) from those specified by Garrett-Munk, the deviations are consistent with the behavior expected in a random internal wave field.</p>		

DD FORM 1473
1 JAN 73EDITION OF 1 NOV 65 IS OBSOLETE
S/N 0102-010-6601

Unclassified

SECURITY CLASSIFICATION OF THIS PAGE (When Data Entered)

Unclassified

SECURITY CLASSIFICATION OF THIS PAGE (When Data Entered)

REPORT DOCUMENTATION PAGE		READ INSTRUCTIONS BEFORE COMPLETING FORM
1. REPORT NUMBER 87-13	2. GOVT ACCESSION NO.	3. RECIPIENT'S CATALOG NUMBER
4. TITLE (and Subtitle) COASTAL-TRAPPED WAVES ON THE EAST AUSTRALIAN CONTINENTAL SHELF PART I: PROPAGATION OF MODES		5. TYPE OF REPORT & PERIOD COVERED Reprint
		6. PERFORMING ORG. REPORT NUMBER
7. AUTHOR(s) Church, John A.; Freeland, Howard J.; Smith, Robert I.		8. CONTRACT OR GRANT NUMBER(s) N00014-84-C-0218
9. PERFORMING ORGANIZATION NAME AND ADDRESS College of Oceanography Oregon State University Corvallis, Oregon 97331		10. PROGRAM ELEMENT, PROJECT, TASK AREA & WORK UNIT NUMBERS NR083-102
11. CONTROLLING OFFICE NAME AND ADDRESS Office of Naval Research Ocean Science & Technology Division Arlington, Virginia 22217		12. REPORT DATE Nov. 1986
		13. NUMBER OF PAGES 15
14. MONITORING AGENCY NAME & ADDRESS (if different from Controlling Office)		15. SECURITY CLASS. (of this report) Unclassified
		15a. DECLASSIFICATION/DOWNGRADING SCHEDULE
16. DISTRIBUTION STATEMENT (of this Report) Approved for public release; distribution unlimited		
17. DISTRIBUTION STATEMENT (of the abstract entered in Block 20, if different from Report)		
18. SUPPLEMENTARY NOTES		
19. KEY WORDS (Continue on reverse side if necessary and identify by block number)		
20. ABSTRACT (C) The currents observed over the shelf and slope during the Australian Coastal Experiment (ACE) are used to determine the amplitudes (as functions of time) of the first three coastal-trapped wave (CTW) modes at three locations along the southeast coast of Australia. A statistical "eddy" mode is included to minimize contamination of the coastal-trapped wave currents from East Australian Current eddies. The first three CTW modes account for about 65% of the observed variance in the alongshelf currents on the shelf and slope at Cape Howe, about 40% at Stanwell Park, but only about 24% at Newcastle. Currents associated with the East Australian Current dominate the observations offshore from Newcastle. CTWs account for all but 10%, 37% and 27% of the currents observed at the most nearshore locations on the shelf at Cape Howe, Stanwell Park and Newcastle. The first two coastal-trapped wave modes propagate at close to the appropriate theoretical phase speeds, but the third coastal-trapped wave mode and the eddy mode are not coherent between the three current meter sections along the coast. Surprisingly, mode 2 carries a greater fraction of the coastal-trapped wave energy than does mode 1 at two of the sections. Modes 1 and 2 are coherent with each other at the 95% significance level. The major energy source for the CTWs is upstream (in the CTW sense) of the first line of current meters.		

DD FORM 1473
1 JAN 73EDITION OF 1 NOV 68 IS OBSOLETE
S/N 0102-014-66011

Unclassified

SECURITY CLASSIFICATION OF THIS PAGE (When Data Entered)

Unclassified

SECURITY CLASSIFICATION OF THIS PAGE (When Data Entered)

REPORT DOCUMENTATION PAGE		READ INSTRUCTIONS BEFORE COMPLETING FORM
1. REPORT NUMBER 87-16	2. GOVT ACCESSION NO.	3. RECIPIENT'S CATALOG NUMBER
4. TITLE (and Subtitle) MEASUREMENTS OF NEAR-SURFACE SHEAR IN THE OCEAN		5. TYPE OF REPORT & PERIOD COVERED Reprint
		6. PERFORMING ORG. REPORT NUMBER
7. AUTHOR(s) Richman, J.G.; de Szoeki, Roland A.; Davis, R. E.		8. CONTRACT OR GRANT NUMBER(s) N00014-79-C-0004 N00014-84-C-0218
9. PERFORMING ORGANIZATION NAME AND ADDRESS College of Oceanography Oregon State University Corvallis, Oregon 97331		10. PROGRAM ELEMENT, PROJECT, TASK AREA & WORK UNIT NUMBERS NR083-102
11. CONTROLLING OFFICE NAME AND ADDRESS Office of Naval Research Ocean Science & Technology Division Arlington, Virginia 22217		12. REPORT DATE March 1987
		13. NUMBER OF PAGES 8
14. MONITORING AGENCY NAME & ADDRESS (if different from Controlling Office)		15. SECURITY CLASS. (of this report) Unclassified
		15a. DECLASSIFICATION/DOWNGRADING SCHEDULE
16. DISTRIBUTION STATEMENT (of this Report) Approved for public release; distribution unlimited		
17. DISTRIBUTION STATEMENT (of the abstract entered in Block 20, if different from Report)		
18. SUPPLEMENTARY NOTES		
19. KEY WORDS (Continue on reverse side if necessary and identify by block number)		
20. ABSTRACT (Continue on reverse side if necessary and identify by block number) In an effort to measure current shear very near the sea surface a string of vector-measuring current meters suspended beneath a surface float was deployed 180 km off southern California at 34°N 121°30'W on November 26, 1981 and allowed to drift freely for over 6 days. This arrangement, which we call the current meter drifter (CMD), gave measurements at depths of 2.5, 5.5, 8.5, 11.5, 14.5, 25, and 63 m. During the first two days, when the winds were light (≈ 8 m/s) and variable in direction, a nearly uniform current shear was observed in the upper 15 m with a low-frequency velocity difference of 5 cm/s between the instruments at 2.5 and 14.5 m. During the last four days, when the winds were brisk (> 12 m/s) and steady in direction from the NNW, a strong downwind shear of order 10^{-2} s^{-1} was observed in the upper 10 m with a velocity difference of ~ 7 cm/s between the instruments at 2.5 and 8.5 m. During this		

DD FORM 1473
1 JAN 73EDITION OF 1 NOV 68 IS OBSOLETE
S/N 0102-014-6401

Unclassified

SECURITY CLASSIFICATION OF THIS PAGE (When Data Entered)

same period the shear below 10 m was much smaller. The average currents during the CMD drift veer to the right of the wind stress with angular displacement increasing with depth. Time series of the velocity difference between 2.5 and 5.5 m compare very well with $\theta(t)u_*\kappa^{-1}$ in (5.5/2.5), where $\theta(t)$ is the wind direction vector (of unit magnitude), $u_* = (\text{wind stress}/\rho)^{1/2}$ is the friction velocity in water, and $\kappa = 0.4$ is von Karman's constant. On the other hand, a similar comparison of the velocity difference between 5.5 and 8.5 m to $\theta(t)u_*\kappa^{-1}$ in (8.5/5.5) is much poorer with observed velocity difference being much larger, possibly due to stable stratification effects. Possible errors in the measurements have been considered and estimated as less than the observed velocity differences. Near-surface shears as large as the observed are very important in closing the momentum budget for the oceanic boundary layer.

Unclassified

SECURITY CLASSIFICATION OF THIS PAGE (When Data Entered)

REPORT DOCUMENTATION PAGE		READ INSTRUCTIONS BEFORE COMPLETING FORM
1. REPORT NUMBER 87-21	2. GOVT ACCESSION NO.	3. RECIPIENT'S CATALOG NUMBER
4. TITLE (and Subtitle) THE AVAILABLE POTENTIAL ENERGY OF OVERTURNS AS AN INDICATOR OF MIXING IN THE SEASONAL THERMOCLINE		5. TYPE OF REPORT & PERIOD COVERED Reprint
		6. PERFORMING ORG. REPORT NUMBER
7. AUTHOR(s) Dillon, Thomas M., Park, Melora M.		8. CONTRACT OR GRANT NUMBER(s) N00014-84-C-0218
9. PERFORMING ORGANIZATION NAME AND ADDRESS College of Oceanography Oregon State University Corvallis, Oregon 97331		10. PROGRAM ELEMENT PROJECT TASK AREA & WORK UNIT NUMBERS NR083-102
11. CONTROLLING OFFICE NAME AND ADDRESS Office of Naval Research Ocean Science & Technology Division Arlington, Virginia 22217		12. REPORT DATE 15 May 1987
		13. NUMBER OF PAGES 9
14. MONITORING AGENCY NAME & ADDRESS (if different from Controlling Office)		15. SECURITY CLASS. (of this report) Unclassified
		15a. DECLASSIFICATION/DOWNGRADING SCHEDULE
16. DISTRIBUTION STATEMENT (of this Report) Approved for public release; distribution unlimited		
17. DISTRIBUTION STATEMENT (of the abstract entered in Block 20, if different from Report)		
18. SUPPLEMENTARY NOTES		
19. KEY WORDS (Continue on reverse side if necessary and identify by block number)		
20. ABSTRACT (Continue on reverse side if necessary and identify by block number) Using empirical observations, it is shown that the available potential energy of fluctuations (the APEF) is proportional to the product of the Cox number C_X , the local buoyancy frequency N , and the molecular diffusivity of temperature D . The nondimensional number $C_{pe} = APEF/(ND)$ is shown to be a good predictor of the Cox number and can be used as an indicator of mixing in stratified fluids. Analysis of the APEF at ocean station P shows that turbulence in the seasonal thermocline responds to strong surface forcing.		

DD FORM 1473
1 JAN 73EDITION OF 1 NOV 65 IS OBSOLETE
S/N 0102-014-6601

Unclassified

SECURITY CLASSIFICATION OF THIS PAGE (When Data Entered)

Unclassified

SECURITY CLASSIFICATION OF THIS PAGE (When Data Entered)

REPORT DOCUMENTATION PAGE		READ INSTRUCTIONS BEFORE COMPLETING FORM
1. REPORT NUMBER 87-23	2. GOVT ACCESSION NO.	3. RECIPIENT'S CATALOG NUMBER
4. TITLE (and Subtitle) ON THE WIND- DRIVEN CIRCULATION OF THE SOUTH PACIFIC OCEAN		5. TYPE OF REPORT & PERIOD COVERED Reprint
		6. PERFORMING ORG. REPORT NUMBER
7. AUTHOR(s) deSzoeko, Roland A.		8. CONTRACT OR GRANT NUMBER(s) N00014-84-C-0218
9. PERFORMING ORGANIZATION NAME AND ADDRESS College of Oceanography Oregon State University Corvallis, Oregon 97331		10. PROGRAM ELEMENT, PROJECT, TASK AREA & WORK UNIT NUMBERS NR083-102
11. CONTROLLING OFFICE NAME AND ADDRESS Office of Naval Research Ocean Science & Technology Division Arlington, Virginia 22217		12. REPORT DATE May 1987
		13. NUMBER OF PAGES 18
14. MONITORING AGENCY NAME & ADDRESS (if different from Controlling Office)		15. SECURITY CLASS. (of this report) Unclassified
		15a. DECLASSIFICATION/DOWNGRADING SCHEDULE
16. DISTRIBUTION STATEMENT (of this Report) Approved for public release; distribution unlimited		
17. DISTRIBUTION STATEMENT (of the abstract entered in Block 20, if different from Re. art)		
18. SUPPLEMENTARY NOTES		
19. KEY WORDS (Continue on reverse side if necessary and identify by block number)		
20. ABSTRACT (Continue on reverse side if necessary and identify by block number) A layered model of the steady circulation in the South Pacific Ocean is constructed along the lines of Luyten, Pedlosky and Stommel, and driven by the mean annual wind stress distributions computed by Hellerman and Rosenstein. The results of the model agree quite well with published maps of topography of density surfaces and circulation. Best agreement is found in the deeper layers. The deepest modeled layer, of density range $26.90 < \sigma_\theta < 27.30$, which contains the core layer of the Antarctic Intermediate Water, transports northwards some 14 Sv ($1 \text{ Sv} = 10^6 \text{ m}^3 \text{ s}^{-1}$) between New Zealand and South America. Of this, about three quarters comes from the west in an intense zonal jet that rounds the southern tip of New Zealand and quickly fans out from the boundary current along those islands into the anticyclonic gyre. Some 5 Sv returns southwards in the Australian boundary current. Much of the anticyclonic gyre in the western South Pacific is taken up by a shadow zone		

DD FORM 1473

1 JAN 73

EDITION OF 1 NOV 65 IS OBSOLETE
S/N 0102-014-6601

Unclassified

SECURITY CLASSIFICATION OF THIS PAGE (When Data Entered)

unclassified

SECURITY CLASSIFICATION OF THIS PAGE (When Data Entered)

formed in the shelter of New Zealand, where the submerged layer loses direct contact with the wind driving, and where uniform potential vorticity is postulated. The modeled circulation in the shallowest layer in tropical regions is considerably weaker than the observed circulation.

Transport in the New Zealand western boundary current is determined by the necessity to achieve the same pressure in each layer at the northern end of the islands as at the southern. Similar considerations applied to the landmass of Australia and Papua-New Guinea, regarded as isolated from Southeast Asia, suggest a considerable net northward transport between Australia and South America, which can only escape through the Indonesian passages. The distribution of this transport among layers is set in the model by the input conditions at the southern boundary (where much of it must be in the deeper layers), after which it cannot change because of mass conservation within each layer (i.e., no cross-isopycnal flux is allowed). This modeling assumption is too strict and may be the reason for the prediction of shallow circulations much weaker than observed.

SECURITY CLASSIFICATION OF THIS PAGE (When Data Entered)

Unclassified

SECURITY CLASSIFICATION OF THIS PAGE (When Data Entered)

REPORT DOCUMENTATION PAGE		READ INSTRUCTIONS BEFORE COMPLETING FORM
1. REPORT NUMBER 87-25	2. GOVT ACCESSION NO.	3. RECIPIENT'S CATALOG NUMBER
4. TITLE (and Subtitle) COASTAL-TRAPPED WAVES ON THE EAST AUSTRALIAN CONTINENTAL SHELF. PART II: MODEL VERIFICATION		5. TYPE OF REPORT & PERIOD COVERED Reprint
7. AUTHOR(s) John A. Church, Neil J. White, Allan J. Clarke, Howard J. Freeland, Robert L. Smith		6. PERFORMING ORG. REPORT NUMBER
9. PERFORMING ORGANIZATION NAME AND ADDRESS College of Oceanography Oregon State University Corvallis, Oregon 97331		8. CONTRACT OR GRANT NUMBER(s) N00014-84-C-0218
11. CONTROLLING OFFICE NAME AND ADDRESS Office of Naval Research Ocean Science & Technology Division Arlington, Virginia 22217		10. PROGRAM ELEMENT, PROJECT, TASK AREA & WORK UNIT NUMBERS NR083-102
14. MONITORING AGENCY NAME & ADDRESS (if different from Controlling Office)		12. REPORT DATE Nov. 1986
		13. NUMBER OF PAGES 13
		15. SECURITY CLASS. (of this report) Unclassified
		15a. DECLASSIFICATION/DOWNGRADING SCHEDULE
16. DISTRIBUTION STATEMENT (of this Report) Approved for public release; distribution unlimited		
17. DISTRIBUTION STATEMENT (of the abstract entered in Block 20, if different from Report)		
18. SUPPLEMENTARY NOTES		
19. KEY WORDS (Continue on reverse side if necessary and identify by block number)		
20. ABSTRACT (Continue on reverse side if necessary and identify by block number) The Australian Coastal Experiment (ACE) was designed to test coastal-trapped wave (CTW) theory and the generation of coastal-trapped waves by the wind. For the ACE dataset, we use CTW theory to attempt to hindcast the observed alongshelf currents and coastal sea levels at locations remote from the upstream (in the CTW sense) boundary of the ACE region. Local (in the ACE region) wind forcing is responsible for only about a quarter of the CTW energy flux at Stanwell Park (the center of the ACE region), and the remainder enters the ACE region from the south and propagates northward through the ACE region. Including the second-mode CTW improves the correlation between the hindcast and the observed near-bottom currents on the upper slope at Stanwell Park, but the use of the third-mode CTW cannot be justified. A linear bottom drag coefficient of $r = 2.5 \times 10^{-4} \text{ m s}^{-1}$ works better than a larger drag coefficient, and simplifying the CTW equations by assuming the modes are uncoupled does not detract from the quality of the hindcasts. The hindcast and observed coastal		

DD FORM 1473
1 JAN 73EDITION OF 1 NOV 65 IS OBSOLETE
S/N 0102-014-66011

Unclassified

SECURITY CLASSIFICATION OF THIS PAGE (When Data Entered)

sea levels are correlated at greater than the 99% significance level. For the nearshore locations at Stanwell Park, the hindcast and observed alongshelf currents are correlated at greater than the 99% significance level, and the CTW model can account for about 40% of the observed variance. On the shelf at Stanwell Park, we find the hindcasts agree with the observations only if direct wind forcing within the ACE region and the correct (nonzero) upstream boundary conditions are included. However, even after attempting to remove the effects of the eddies and the East Australian Current, the CTW model is not useful for predicting the currents on the slope at Stanwell Park and on the shelf and slope at Newcastle (the northern boundary of the ACE region). The currents at these locations are dominated by the effect of the East Australian Current and its eddies.

Unclassified

Unclassified

SECURITY CLASSIFICATION OF THIS PAGE (When Data Entered)

REPORT DOCUMENTATION PAGE		READ INSTRUCTIONS BEFORE COMPLETING FORM
1. REPORT NUMBER 87-27	2. GOVT ACCESSION NO.	3. RECIPIENT'S CATALOG NUMBER
4. TITLE (and Subtitle) VERTICAL HEAT FLUXES THROUGH THE BEAUFORT SEA THERMOHALINE STAIRCASE		5. TYPE OF REPORT & PERIOD COVERED Reprint
		6. PERFORMING ORG. REPORT NUMBER
7. AUTHOR(s) Padman, Laurie; Dillon, Thomas M.		8. CONTRACT OR GRANT NUMBER(s) N00014-84-C-0218
9. PERFORMING ORGANIZATION NAME AND ADDRESS College of Oceanography Oregon State University Corvallis, Oregon 97331		10. PROGRAM ELEMENT, PROJECT, TASK AREA & WORK UNIT NUMBERS NR083-102
11. CONTROLLING OFFICE NAME AND ADDRESS Office of Naval Research Ocean Science & Technology Division Arlington, Virginia 22217		12. REPORT DATE September 1987
		13. NUMBER OF PAGES 8
14. MONITORING AGENCY NAME & ADDRESS (if different from Controlling Office)		15. SECURITY CLASS. (of this report) Unclassified
		15a. DECLASSIFICATION/DOWNGRADING SCHEDULE
16. DISTRIBUTION STATEMENT (of this Report) Approved for public release; distribution unlimited		
17. DISTRIBUTION STATEMENT (of the abstract entered in Block 20, if different from Report)		
18. SUPPLEMENTARY NOTES		
19. KEY WORDS (Continue on reverse side if necessary and identify by block number)		
20. ABSTRACT (Continue on reverse side if necessary and identify by block number) Microstructure profiles of temperature, conductivity, and velocity shear during the Arctic Internal Wave Experiment (AIWEX) in March-April 1985 in the Beaufort Sea are used to investigate the thermodynamic processes in a diffusive thermohaline staircase. The staircase occurs between depths of about 320 and 430 m, above the core of the relatively warm, salty Atlantic water, where the mean temperature and salinity are increasing with depth. Individual isothermal layers can be tracked for at least several hours, suggesting a horizontal length scale of several hundred meters or more, assuming a typical relative velocity of 0.01 m s^{-1} at this time. Over the depth range 320-430 m the mean (average over several steps) density ratio $\langle R_\rho \rangle = \beta \langle S_\rho \rangle / \alpha \langle T_\rho \rangle$ varies between 4 and 6, while the typical temperature difference between layers decreases from 0.012° to 0.004°C . The mean thickness of the layers also varies, from 1 m		

DD FORM 1 JAN 73 1473

EDITION OF 1 NOV 65 IS OBSOLETE
S/N 0102-014-6601

Unclassified

SECURITY CLASSIFICATION OF THIS PAGE (When Data Entered)

at 320 m depth to 2 m at 430 m. The relationship proposed by Kelley (1984), relating layer height to $\langle N^2 \rangle$, $\langle R_p \rangle$, and molecular properties of the fluid, overestimates the mean layer thickness by about a factor of 2. The variability of staircase characteristics suggests that oceanic staircases may rarely, if ever, be steady state, but in general be slowly evolving from previous perturbations. Heat fluxes estimated from laboratory-based flux laws, involving R_p and ΔT , are in the range $0.02 < F_H < 0.1 \text{ W m}^{-2}$, which is in agreement with the molecular heat fluxes through the maximum interfacial temperature gradients. There are no interfaces where the kinetic energy dissipation rate (averaged over 0.5 m) exceeds the lower limit for diapycnal mixing, $24.5\nu N^2$.

unclassified

Imaging fault slip using teleseismic waveforms: analysis of a typical incomplete tomography problem

William Menke *College of Oceanography, Oregon State University, Corvallis,
OR 97331, USA*

Accepted 1984 October 8; Received 1984 October 1; in original form 1984 July 6

Summary. Several important geophysical imaging problems can be cast in the form of the classic tomography problem, in which a function of two variables is reconstructed from its projection along a set of straight lines. However, geophysical imaging problems tend to be incomplete: some of the straight lines projection paths are missing from the data. A typical example is the problem of imaging the slip rate as a function of position and time along a long, thin fault plane. The far field seismic pulse shape is a projection of the fault's slip rate function. However, a complete suite of far field observations does not span the complete set of possible projection lines. Consequently, the exact slip rate function cannot be recovered from the data. At best, only a filtered version of it can be reconstructed. This filter is not completely determined by the mathematics of the problem, and can therefore be optimized to yield images of the slip rate that have good resolution.

Introduction

Tomography is the process of reconstructing images (i.e. functions of several variables) from data which are related to the images by line integrals. The simplest tomography problem occurs when the image is a 2-D function $m(x, y)$ and the line integrals are along straight lines. The data, d , are then related to the image by the so-called Radon transform:

$$d(s, \theta) = \int_{-\infty}^{\infty} m(x \cos \theta - u \sin \theta, x \sin \theta + u \cos \theta) du \quad (1)$$

where each datum is indexed according to the intercept, s , and angle, θ , of its corresponding projection line. The Radon transform is known to have a unique inverse, as long as every possible (s, θ) pair is measured (see, for example, Herman 1979, chapter 2).

In actual practice, only a finite number of (s, θ) pairs can be measured. This limitation presents no special problem as long as s and θ can be sampled evenly over the ranges for which $d(s, \theta)$ is non-zero. In this case there is a simple relationship between the sampling density and the sharpness of the reconstructed image. A much more serious problem arises when $d(s, \theta)$ can be sampled only within some limited range of s or θ . Then some information about the image is lost, regardless of how fine the sampling density might be.

This kind of incomplete tomography problem arises in geophysics for several reasons. Sometimes the incompleteness is due to poor experimental geometry. For example, the seismic velocity in the Earth can be imaged by using the travel times of seismic waves. The line integrals in the tomography problem then have the interpretation of travel-time integrals along ray-paths, which may be approximately straight lines. Since it may be impossible to place seismographs in some areas (under the oceans, deep within the Earth, etc.), some ray-paths may not be measured. Sometimes the incompleteness is more fundamental, and arises as a consequence of the physics of the problem. The problem of imaging slip on a fault is one example, which we will analyse in detail below.

Two possible actions can be taken when the data needed to construct an image are incomplete. One possible approach is to assume 'reasonable' values for the missing information (see, for example, Sezan & Stark 1984; Menke 1984a). While the addition of this so-called prior information enables one to reconstruct the image, the image may contain artefacts if the assumptions are in error. A different approach is only to try to construct a filtered version of the image, where the filter is designed to remove from the image any information that cannot be observed. This is the approach that is recommended by Backus & Gilbert (1970), who pointed out that it has the advantage of producing a unique reconstruction. However, it is often difficult to find a filter that excludes all unmeasured information while not completely scrambling the image. As shall be shown below, in some incomplete tomography problems it is possible to find filters that lead to images with reasonably good resolution.

In this paper we concentrate on the simplest incomplete tomography problem: one where some range of projection line slopes is missing from the data. As we shall see, this problem has a simple interpretation in terms of the properties of the Radon transform. Furthermore, since the ray coverage is spatially (but not azimuthally) uniform, the resolving power of the imaging procedure will not be a function of position in the image. More complicated types of incompleteness occur, but generally must be explored by purely numerical methods (see, for example, Eisler, New & Calderone 1982; Menke 1984b).

Imaging fault slip as a tomography problem

We consider the problem of determining the slip rate on a fault using far field seismic waveforms. Many authors have recognized that this inverse problem is incomplete (see, for instance, Aki & Richards 1980, chapter 14.1). Recently several authors have noted that it corresponds to a tomography problem (Spudich & Frazer 1985; Ruff 1985). The most general form of this imaging problem is 3-D; two spatial dimensions on the fault plane and time. However, we will simplify the problem to two dimensions, by assuming that the fault is long and thin. This simplification is made so that the essential ideas of the problem can be presented without the mathematical complications that arise in the planar fault problem. Nevertheless, the two problems are completely analogous and suffer the same kind of incompleteness, except, as noted below, it is somewhat worse for the planar fault case than for the linear one.

That this imaging problem is tomographic in nature can be seen from the equation relating slip rate $m(x, t)$ on the fault plane (the image) as a function of position, x and time, t to the far field (Fraunhofer approximation) pulse shape $d(\phi, \tau)$ as a function of receiver angle, ϕ and time, τ (Aki & Richards 1980, chapter 14.1).

$$d(\phi, \tau) = \int_{\text{fault plane}} m(x, \tau - r_0/c + x \cos \phi/c) dx \quad (2)$$

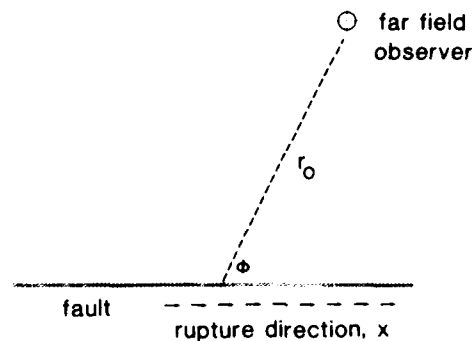


Figure 1. Geometry of the fault slip problem. Slip on the fault induces seismic waves that are observed at a distance r_0 and angle ϕ from the fault plane. The imaging problem is to reconstruct the fault slip rate as a function of position and time from far field waveform observations.

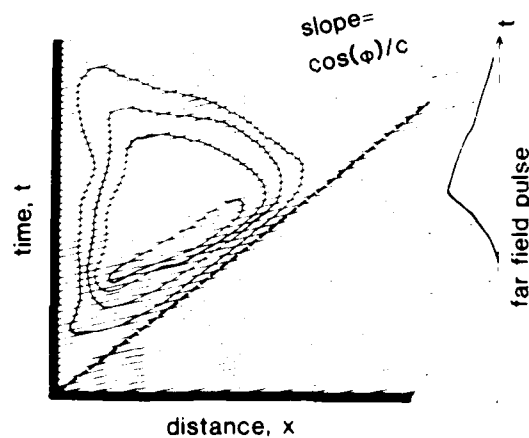


Figure 2. The slip rate on the fault is contoured as a function of distance x and time t . This function constitutes the image in the tomography problem. The far field pulse shape is the projection of the slip rate along parallel projection lines whose slope is controlled by the angle of observation ϕ and the seismic velocity c . Note that if the velocity of rupture propagation (dashed line) is slower than the propagation velocity (typical of P -wave observations), then the maximum slope of the projection lines is less than the typical trends in the image. Image reconstruction is therefore difficult.

where r_0 is the distance between the fault and observer and c is the propagation velocity in the medium (Fig. 1). The pulse shape is related to the slip rate by a line integral along a straight line, i.e. a Radon transform (Fig. 2). The intercept of the projection line is given by $t = \tau - r_0/c$ and its slope by $dt/dx = \cos(\phi)/c$. While all possible intercepts can be measured by suitable choosing of the observation time, τ , only some slopes can be measured:

$$-1/c \leq dt/dx \leq 1/c \quad (3)$$

The imaging problem is therefore incomplete. Note that in this formulation we have assumed that the pulse shape has been corrected for geometrical spreading and other propagation effects that may be encountered in a realistic earth. We have also neglected the effect of velocity gradients (especially near the fault) that can distort the integration paths in equation (2) so that they are no longer exactly straight lines. Spudich & Frazer (1985) have given some attention to this problem.

Wavenumber domain representation

The significance of the missing projection lines (those with slopes outside the range of equation 3) can be seen by the application of the projection or central slice theorem (see, for example, Herman, 1979, chapter 2). This theorem relates a 1-D Fourier transform of the Radon transform to the 2-D Fourier transform of the original function (Fig. 3).

$$\int_{-\infty}^{\infty} dt s_t(\theta) \exp(-iSk_t) = m(k_x) = S \cos \theta, k_y = S \sin \theta. \quad (4)$$

Here k_x and k_y refer to wavenumber. The limited range of slopes available through teleseismic waveform observations implies that only a sector in the $(k_x, k_y = \omega)$ plane of the slip rate is known (where we have identified k_y with temporal frequency ω , Fig. 4). Some

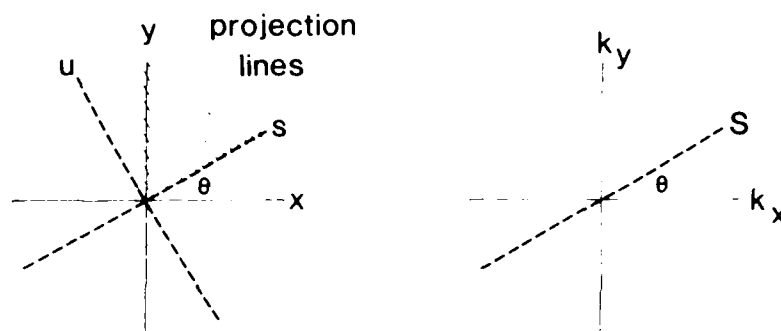


Figure 3. Left: the Radon transform of a function $m(x)$ is the collection of line integrals obtained by projecting the integrand $m(x)$ along lines parallel to the x -axis of a coordinate system that is rotated by an angle θ with respect to $x = 0$. Right: the projection theorem states that the 1-D Fourier transform of the projected function integrand is equal to the 2-D Fourier transform of $m(x)$ evaluated along a line S in wavenumber space at $k_y = \omega$.

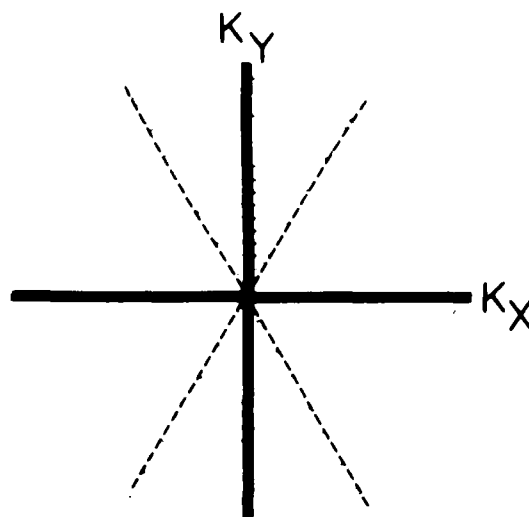


Figure 4. Due to the incompleteness of the tomography problem only wavenumbers within the shaded sectors of the (k_x, k_y) plane can be determined.

motions of the fault do not radiate energy into the far field (see Aki & Richards 1980, chapter 14.1). Note that the complete 3-D (planar fault) problem has an even large degree of incompleteness. In this problem there are two spatial coordinates on the fault plane, say (x_1, x_2) and therefore two spatial wavenumbers (k_{x1}, k_{x2}) . The transform of the slip function can be measured only in a small cone in the $(k_{x1}, k_{x2}, k_y = \omega)$ volume centred on the $k_y = \omega$ axis. The 3-D problem must therefore be approached with more caution than the 2-D one.

Incompleteness and fan filtering

In order to invert the $(k_x, k_y = \omega)$ representation of the slip rate to the (x, t) domain, one must deal with the sectors of the (k_x, k_y) plane which lack data. One way to handle these areas is to invert a filtered version of the image $F(k_x, k_y)m(k_x, k_y)$ where F is a filter which is zero in the sectors that lack data. The recovered image can then be interpreted as a convolution of the true image and an (x, t) domain filter. If this filter is reasonably spiky, then the recovered image will be a good approximation to the true one. (This procedure is analogous to the 1-D problem of choosing appropriate window functions when estimating the spectra of time series.) The simplest filter is the so-called fan filter, which takes on the value of unity in the sectors that have data, and is zero everywhere else. Unfortunately, this filter has very poor properties in the (x, t) domain, as can be seen by computing its (x, t) representation.

$$\begin{aligned} F_{\text{fan}}(x, t) &= \int_{-\infty}^{\infty} \int_{-\infty}^{\infty} F_{\text{fan}}(k_x, k_y) \exp(ik_x x + ik_y t) dk_x dk_y \\ &= 4 \int_0^{\tan(\theta)} \int_0^{\tan(\theta)/\cos(\theta)} \cos(k_x x) \cos(k_y t) dk_x dk_y \\ &= 4 \tan(\theta) \\ &= t^2 \tan(\theta) - x^2 \end{aligned} \quad (5)$$

where the sector with data are bounded by the angle θ . $F_{\text{fan}}(x, t)$ has two lines of singularities, extending from the origin in the $(\pm 2 - \theta)$ direction (i.e. it has large sidelobes), and is therefore a very poor filter. The recovered image will be a very distorted version of the true image.

Designing an optimum filter

The problem of poor resolution can be circumvented, at least to a degree, by choosing a better filter than F_{fan} . This filter must still be zero outside the observed sectors of the (k_x, k_y) plane, but takes values different than unity within the observed sector. Some of the poor properties of F_{fan} stem from the sharp change from unity to zero at the boundary of the observed region. By properly tapering the filter, we can substantially reduce the sidelobes. Unfortunately, this tapering has the effect of throwing away some of the information that was collected. The image will tend to have fewer artefacts than the fan filtered image, but be somewhat more blurred.

We assume that the optimum filter, say F_{opt} , is zero outside the known sectors and is a real function within the observed sectors. We also assume it possesses mirror symmetry about the k_x and k_y axes. The optimum filter is the one which satisfies these constraints and which minimizes some measure of the spread of the resolution. We minimize the

variance of its width in the (x, t) plane, since the resulting filter tends to have small side-lobes:

$$\text{minimize: } \int_{-\infty}^{+\infty} \int_{-\infty}^{+\infty} (x^2 + c^2 t^2) F_{\text{opt}}^2(x, t) dx dt. \quad (6)$$

Note that we have chosen the time-distance scaling factor to be the propagation velocity, c . The observable sector of the $(k_x, k_y = \omega)$ plane subtends an angle of 45° . Finally, we note that in order to complete the specification of the problem we must add some normalization. Two reasonable choices are that optimum filter have unit area or unit energy:

$$\int_{-\infty}^{+\infty} \int_{-\infty}^{+\infty} F_{\text{opt}}(x, t) dx dt = 1 \quad (7a)$$

or

$$\int_{-\infty}^{+\infty} \int_{-\infty}^{+\infty} F_{\text{opt}}^2(x, t) dx dt = 1. \quad (7b)$$

There are a variety of ways to implement this optimization problem. If one uses the normalization defined by equation (7b), one can generalize the approach that Papoulis (1983) has used for 1-D filters. This procedure involves using the calculus of variations to find an Euler-Lagrange equation for F_{opt} . Parseval's theorem can be used to show that equations (6) and (7b) are equivalent to:

$$\begin{aligned} &\text{minimize: } \iint_R [(\partial F / \partial k_x)^2 + c^2 (\partial F / \partial \omega)^2] dk_x d\omega \\ &\text{subject to: } \iint_R F^2(k_x, \omega) dk_x d\omega = 1 \end{aligned} \quad (8)$$

where the region R is that part of the $(k_x, k_y = \omega)$ plane in which F_{opt} can be non-zero. In realistic experiments the region R will have finite area, since the limited sampling interval of the seismometers will limit the data to a disc centred on the origin of the $(k_x, k_y = \omega)$ plane. The Euler-Lagrange equation is then the Helmholtz equation:

$$\frac{\partial^2 F}{\partial^2 k_x} + c^2 \frac{\partial^2 F}{\partial^2 \omega} + \lambda F = 0 \quad (9)$$

where λ is a Lagrange multiplier. This equation is to be solved with the boundary condition that $F = 0$ on the boundary of R . While there are an infinity of 'modes' that satisfy this equation, the desired one is the lowest order mode. It has the least amount of fluctuation over R .

The Euler-Lagrange approach assumes that the data are known continuously over the region R . In practice, they will be known only at discrete points within R , since the seismic waves from the fault are sampled at discrete times. While the optimum filter solving equation (9) can easily be discretized and then applied to the data, another approach is also possible, in which the filter is assumed to be discrete from the very start of the derivation. By substituting the finite Fourier transform representation, $F(x_p, t_q) = \sum_j^N \sum_k^M a_{jk} \exp(2\pi i j p / N + 2\pi i k q / M)$ into equations (6) and (7), and then minimizing (i.e. differentiating) equation (6) with respect to the finite number of coefficients a_{jk} , we obtain a matrix equation for the a_{jk} . This alternate approach to determining F_{opt} is particularly useful if the seismographs observing the rupturing fault are poorly distributed, leading to large gaps in the coverage of

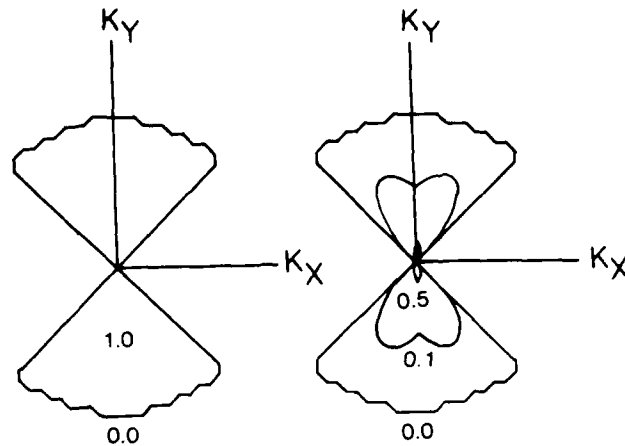


Figure 5. Left: the wavenumber representation of the discretized fan filter, which is zero everywhere outside the two opposing sectors of the (k_x, k_y) plane. The filter is also zero outside a disc centred on the origin, reflecting the finite sampling rate of the recording of the original waveforms. Right: the wavenumber representation of the optimized filter. Note that it has been tapered significantly when compared to the fan filter.

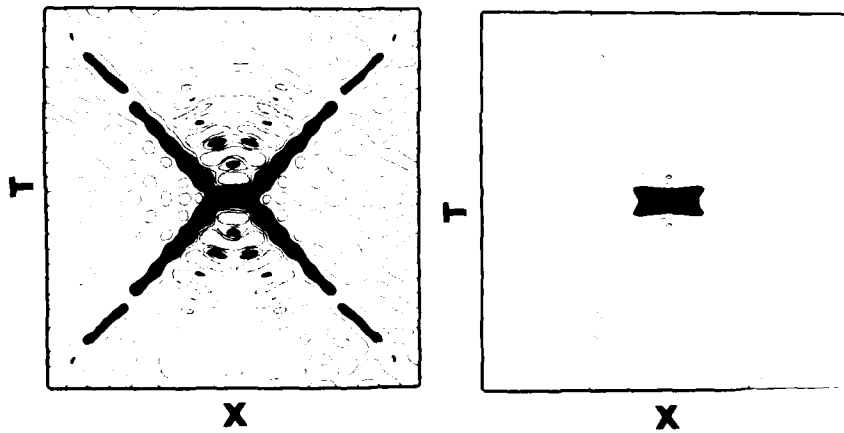


Figure 6. Contour plots of the (x, t) representation of the fan (left) and optimum (right) filters of Fig. 5. Large positive and negative are shaded solid and stippled, respectively. Note that the fan filter has much larger sidelobes than the optimum filter. While not apparent from this figure, the central peak of the optimum filter is about four times wider than the central peak of the fan filter. The sharpness of the filter has been reduced in order to minimize its sidelobes.

the $(k_x, k_y = \omega)$. These missing points can simply be left out of the finite Fourier transform, which in effect changes the shape of R to accommodate the data gaps.

We have computed the optimal filter for the fault slip problem, using the second approach and normalization (7a). We constrain the filter to be zero outside some disc centred on the origin of the $(k_x, k_y = \omega)$ plane, thus modelling the fact that the pulse shapes are recorded at a finite sampling interval in time. The resulting filter is very tapered compared to the fan filter (Fig. 5). In the (x, t) domain, however, the optimum filter has only very small sidelobes, compared to pronounced ridges for the fan filter (Fig. 6).

Conclusions

If one uses all the information that is collected in an incomplete tomography problem, then the recovered image has undergone the least amount of filtering compared to the true image. However, this filtering may have a large distorting effect on the image, and may be equivalent to convolving the true image with a function possessing large sidelobes. The solution is to find a filter that weights the available data unevenly, with the goal of reducing the sidelobes. The price paid is that the recovered image will be rather blurred. When this process is applied to the problem of imaging fault slip rate using teleseismic waveform data, the width of the central peak in the filter $F_{\text{opt}}(x, t)$ increases by a factor of about 4 compared to the evenly weighting fan filter $F_{\text{fan}}(x, t)$, but the undesirable sidelobes are almost completely removed.

Acknowledgments

This research was supported by the Office of Naval Research under contract N00014-84C-0218 and the National Science Foundation under grant EAR-831904. I thank L. N. Frazer for helpful discussions.

References

- Aki, K. & Richards, P. G., 1980, *Quantitative Seismology: Theory and Methods*, W. H. Freeman, San Francisco.
- Backus, G. & Gilbert, F., 1970, Uniqueness in the inversion of inaccurate gross Earth data, *Phil. Trans. R. Soc. A*, **226**, 123-192.
- Eisler, L. J., New, R. & Calderone, D., 1982, Resolution and variance in acoustic tomography, *J. acoust. Soc. Am.*, **72**, 1965-1977.
- Herman, G. T. (ed.), 1979, *Image Reconstruction from Projections*, Topics in Applied Physics 32, Springer-Verlag, New York.
- Menke, W., 1984a, *Geophysical Data Analysis: Discrete Inverse Theory*, Academic Press, New York.
- Menke, W., 1984b, The resolving power of cross-borehole tomography, *Geophys. Res. Lett.*, **11**, 105-108.
- Papoulis, A., 1983, Minimum-bias windows for high-resolution spectral estimates, *IEEE Trans. Inform. Theory* **29**.
- Ruff, L. R., 1985, Tomographic imaging of the earthquake rupture process, *Geophys. Res. Lett.*, in press.
- Sezan, M. T. & Stark, H., 1984, Tomographic image reconstruction from incomplete view data by convex projection and direct Fourier inversion, *IEEE Trans. Medical Imaging* **MI-3**, 91-97.
- Spudich, P. & Frazer, L. N., 1985, Use of ray theory to calculate high-frequency radiation from earthquake sources having spatially variable rupture velocity and stress drop, *Bull. seism. Soc. Am.*, in press.

EFFECT OF HETEROGENEITIES IN D" ON THE DECAY RATE OF P_{diff}

William Menke

College of Oceanography, Oregon State University, Corvallis

Abstract. We use physical models to examine the effect of scatterers in the D" region of the mantle on the decay rate of the P_{diff} phase in the core shadow. Scatterers are in the size range 7.5-81 km, and measurements of the decay rate are made in the period range 3-60 s. We find that the presence of scatterers in D" can change the decay rate of P_{diff} by as much as 50%. The heterogeneity does not affect the decay rate for periods greater than about 10-20 s. At shorter periods, the decay rate can be either lower or higher than the laterally homogeneous case, depending on the scatterer geometry. We find that a layer of small (7.5 km) scatterers can decrease the decay rate, while layers of larger scatterers (41-81 km) mainly increase it. We did not identify any major effect of scatterer aspect ratio on the decay rate in the one relevant test that we performed (dikes and sills on the core-mantle boundary).

Introduction

The structure of the lowermost 200 km of the mantle (often called the D" region) is of interest not only to seismologists studying the earth's seismic structure but also to the wider geophysical community because of its bearing on the thermal evolution of the earth. If the whole mantle is convecting and if the earth's core is a sufficiently important source of heat, simple thermodynamic considerations predict that its laterally averaged temperature gradient would be approximately adiabatic, except for two thin boundary layers, one at the top of the mantle (that is, the lithosphere) and one at the bottom. Seismological evidence supports the existence of some type of anomalous structure in the lowermost mantle, although there is as yet uncertainty as to its nature and to whether it can be explained by a temperature anomaly (that is, a thermal boundary layer) or whether some compositional change must be invoked.

Not only is there uncertainty about the laterally averaged structure of D", but there is also substantial evidence that the structure is laterally heterogeneous. Lateral heterogeneity is consistent with the thermal boundary layer interpretation, since zones of upwelling and downwelling, and other dynamically supported structures are to be expected in a convecting system. However, very little is at present known about the scale lengths and velocity contrasts of these heterogeneities.

The decay rate of the core-diffracted compressional wave P_{diff} is sensitive to the structure of D". Several authors have used observed decay rate data to derive estimates of the velocity structure in D", and in particular the velocity gradient just above the core-mantle boundary, by fitting these data to theoretical estimates [e.g., Doornbos and Mondt, 1979b; Mula, 1981; Ruff and Helmberger, 1982; Doornbos 1983; Schlittenhardt et al., 1985]. Since the theoretical predictions are based on a laterally homogeneous earth, the velocity estimates may be biased if significant lateral heterogeneity is present.

The way in which these hypothetical mantle heterogeneities affect the decay rate of P_{diff} is difficult to analyze theoretically. Simple estimates based on the Born approximation predict that heterogeneities will have little effect [Doornbos and Mondt, 1979a], but since the Born approximation is valid only for very weak, single scattering, these predictions cannot be taken as definitive. Analysis of the effect of multiple scattering based on the work of Biot [1968] indicates that this mechanism can lead to significant changes in wave propagation near boundaries. We evaluate this possibility and perform a sequence of model experiments that exactly account for the scattering interactions that occur in a laterally heterogeneous, two-dimensional, idealized earth. The purpose of these experiments is to gauge the severity of the influence of the scatterers on the decay rate of the diffraction when these scatterers are near the core-mantle boundary. While the model decay rates cannot be directly compared to

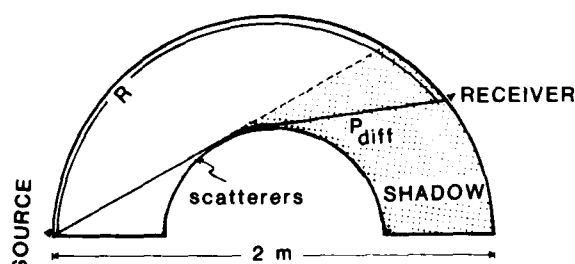


Fig. 1. Schematic diagram of model earth, which consists of a thin aluminum plate that represents a homogeneous mantle. The effect of a layer of scatterers just above the core-mantle interface on the decay rate of the core-diffracted compressional wave P_{diff} is studied. Ultrasonic sources and receivers are used to produce and detect the waves. The surface Rayleigh wave R is used as a calibration, since its amplitude is independent of range and unaffected by the presence of scatterers in the lower mantle.

Copyright 1986 by the American Geophysical Union.

Paper number 5B5654.
0148-0227/86/005B-5654\$05.00

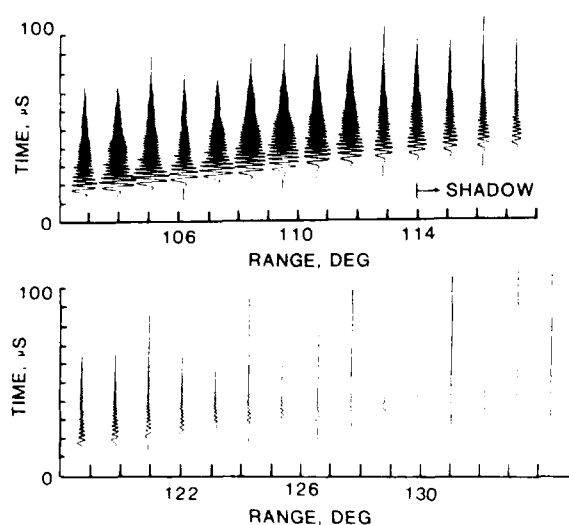


Fig. 2. Typical record section showing the decay of the core-diffracted compressional wave P_{diff} as a function of range. Because the propagation is occurring in a thin plate, the wave's velocity is dispersive. The P_{diff} phase is therefore quite ringy, an effect which is unaesthetic but which does not affect the measurement of decay rate. Note the loss of amplitude, particularly at high frequencies, which increases with distance into the shadow.

similar measurements for the real earth, they provide estimates of the order of the effect and suggest kinds of features to look for in the real data.

Experimental Design

We model the mantle as a two-dimensional medium with curved upper and lower edges. This mantle is homogeneous, except for certain areas into which we introduce scatterers. No attempt is made to model the core; the lower boundary is a free surface. However, since P_{diff} involves grazing incidence interactions with the core, very little energy is transmitted into the core, and this approximation is not

unreasonable. A thin metal plate is used as an analogue to the mantle, since at wavelengths long compared to the plate thickness, compressional waves propagate through the plate as if it were two-dimensional. The compressional waves have frequencies in the 0.05-1.0 MHz range and wavelengths of several centimeters. A plate 2 m in diameter (Figure 1) can, therefore, model what would correspond to periods of between 3 and 60 s in the earth (Table 1). This is the band in which many observations of P_{diff} are made. The model P waves are in fact the lowest-order compressional mode of a thin plate and have phase velocities that are dispersive. Seismograms therefore contain dispersed wave trains rather than sharp pulses (Figure 2). While the dispersion is unaesthetic, it does not affect measurement of the decay rate of the diffraction (Figure 3).

We generate and receive the waves using piezoelectric transducers (Panametrics Model V101 source and Model V110 receiver), and record them with a digital oscilloscope (Analogic Model D6000/630) with an effective dynamic range of about 12 bits. The digital seismograms are collected for both the P_{diff} phase and the lowest-mode Rayleigh wave. The Rayleigh mode's energy is confined to the upper, laterally homogeneous part of the mantle and therefore provides an internal standard that permits very precise (1.0%) measurements of relative amplitude. Spectral analysis is then performed on the digital seismograms to produce plots of the decay rate of P_{diff} as a function of period. The decay curve for a homogeneous mantle with no core is a smooth monotonically decreasing function of period and is reasonably close in character to the decay curve for a homogeneous mantle with a solid brass core (Figure 4). The technology of model experiments is described further by other authors [e.g., Oliver et al., 1954; Dainty and Toksoz, 1975; Menke and Richards, 1983].

Scatterer Geometries

We examine three classes of scatterers near the core-mantle boundary (Figure 5).

A thick layer of small circular voids. Here we place a 128-km-thick layer just above the

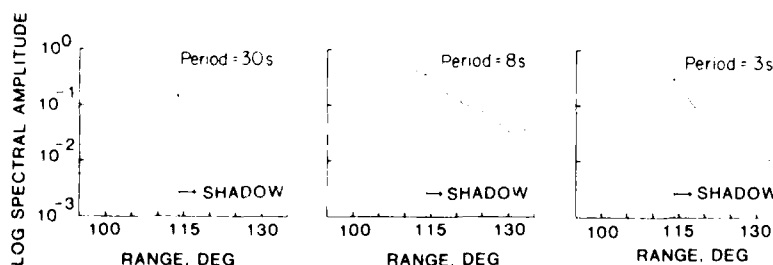


Fig. 3. The spectral amplitude of the P_{diff} waves of Figure 2 is plotted as a function of range, for three selected periods, T . Note that the amplitude decays exponentially with distance into the shadow at a rate that decreases with period. The decay rates were measured by fitting a straight line to the data between ranges of 114° and 125° . The leveling off that occurs at ranges greater than 127° is due to interference by another seismic phase.

TABLE 1. Scaling Factors Used in Modeling

	Actual Units	Scaled Units
General		
Diameter	1000 mm	6371 km
Aluminum	5.47 km/s	13.64 km/s
Brass	3.93 km/s	9.33 km/s
Observable wavelengths	6-60 mm	38-380 km
Observable periods	1-20 microseconds	3-60 s
Distance to shadow	114°	114°
Wavelengths in path	20-300	20-300
Thick layer of small circular scatterers		
Diameter of scatterers	1.18 mm	7.5 km
Thickness of scattering layer	20 mm	128 km
Maximum concentration of scatterers	0.054 mm^{-2}	0.00136 km^{-2}
Homogeneous layer		
Thickness	11 mm	70 km
Thin layer of large circular scatterers		
Height above core	12.7 mm	81 km
Mean distance between scatterers	57 mm	365 km
Diameter of scatterers		
	6.25 mm	41 km
	9.53 mm	61 km
	12.7 mm	81 km
Dikes and sills		
Short dimension	3.5 mm	22 km
Long dimension	9.0 mm	57 km

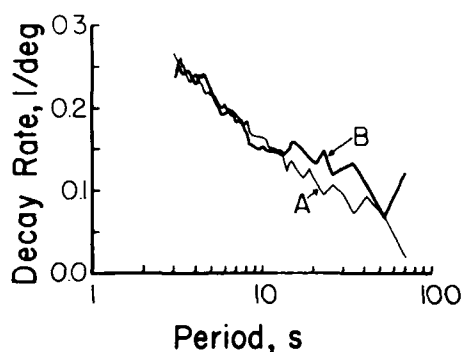


Fig. 4. The decay rate as a function of period for (curve A) the homogeneous mantle with no core, and (curve B) the homogeneous mantle with a solid brass core (compressional velocity ratio of 13.64 : 9.33, compared to 13.64 : 8.1 in the real earth). Note that the decay rate of the diffraction is not strongly dependent upon the properties of the core.

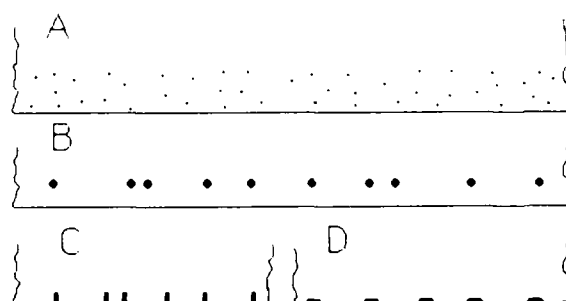


Fig. 5. Classes of heterogeneities placed at the core mantle boundary. (a) A 128 km thick layer of small (7.5 km) voids, (b) A layer of large (41-81 km) circular void or slow velocity inclusions, (c) Slow velocity dikes on the core-mantle boundary, (d) Slow velocity sills on the core-mantle boundary.

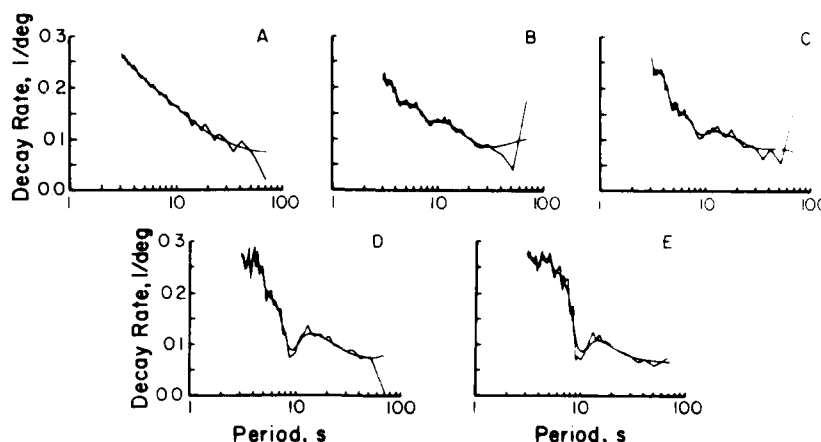


Fig. 6. The decay rate of P_{diff} as a function of period for earth models that contain a thick layer of small circular scattering voids. (a) In the absence of scatterers, the decay rate monotonically decreases with period. (b-e) As the concentration of scatterers is increased in steps of $3.4 \times 10^{-3} \text{ km}^{-2}$, the decay rate changes. The presence of scatterers leads to a much more complicated behavior than the nonscattering case. The smooth curves are three-point running averages of the data and are used in subsequent figures.

core-mantle boundary. The layer contains a random (white) distribution of circular voids, each 7.5 km in diameter. Of course, any individual scatterer in the real earth is not as strong as one of these model scatterers, but the overall effect of the layer of scatterers can be made similar by adjusting the number of

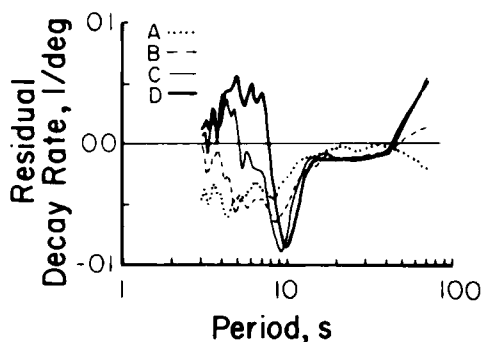


Fig. 7. Residual decay rates as a function of period for earth models that contain a thick layer of small circular scattering voids. The residuals are computed relative to the smoothed homogeneous earth data (Figure 5a). The concentration of scatterers is increased in steps of $3.4 \times 10^{-3} \text{ km}^{-2}$ for curves A through D. Note that the residuals are small at long periods, indicating that these long wavelengths are not influenced by the layer of scatterers. At shorter periods the residuals can be either strongly positive or strongly negative, depending upon the concentration of scatterers. The strong minimum that occurs at a period of about 10 s is due to a resonance in the scattering layer. At the very longest wavelengths, the layer of scatterers emulates a homogeneous, slow-velocity layer.

scatterers. We perform a set of five measurements in which the number of scatterers per unit area is slowly increased.

A thin layer of large scatterers. We place a row of larger scatterers 80 km above the core-mantle boundary. The scatterers have diameters that range from 41-81 km, and their spacing, while random, averages 364 km. Two types of scatterers are examined, voids, and scatterers filled with a material (brass) that is about 30% slower than the velocity of the surrounding mantle.

Sills and dikes. We place a row of sills and dikes just above the core-mantle boundary.

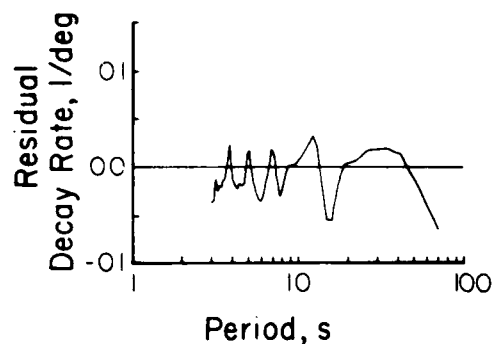


Fig. 8. Residual decay rates for a homogeneous, slow-layer (compressional velocity 9.33 km/s) thickness of 70 km. The sequence of minima and maxima in the decay rate is caused by resonances in the layer. The longest-period minimum corresponds to a wavelength of twice the layer thickness. Note that this pattern differs qualitatively from the one observed for the layer of scatterers: the scattering case has only a single, long-period minimum (Figure 7).

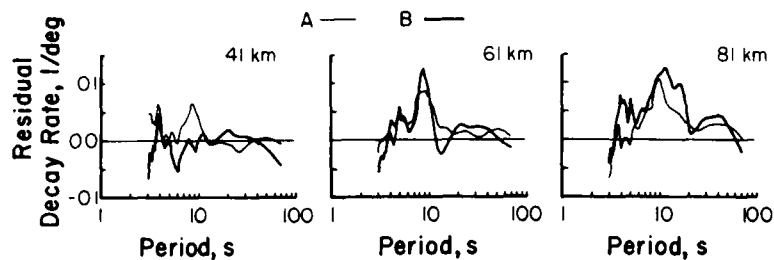


Fig. 9. Residual decay rates for a thin layer of large circular scatterers. The left, middle, and right plots are for scatterer diameters of 41, 61, and 81 km, respectively. In each plot, curve A is for circular voids, and curve B is for circular solid inclusions (with a compressional velocity 30% below the surrounding mantle).

These scatterers measure 57 by 22 km and have an average horizontal spacing of 364 km. The scatterers are made of a material (brass) that is about 30% slower than the surrounding mantle. Two orientations of the scatterers are examined, one with the long dimension vertical (dikes) and the other with it horizontal (sills). These cases can be combined with one from the thin layer of large scatterers to yield a sequence of scatterers, all with the same velocity contrast and mass but with a sequence of aspect ratios: vertical dikes, circular inclusions, and horizontal sills.

Results

A thick layer of small circular voids. The decay rate for the model with no scatterers smoothly increases with frequency (Figure 6a). When a layer of randomly distributed scatterers is placed just above the core-mantle interface, the decay rate is reduced compared to the no scatterer case, except at the very lowest frequencies, where it is unchanged (Figures 6b and 7, Curve A). The very lowest frequencies, corresponding to wavelengths 5-10 times the layer thickness and 50-100 times the scatterer diameter, apparently are completely unaffected by the scatterers. On the other hand, the

decay rate of the higher frequencies is reduced by about 20%.

This pattern changes somewhat as the number of scatterers is increased. The lowest frequencies are still completely unaffected by the scatterers. The decay rate of the intermediate frequencies remains less than the homogeneous case, and a pronounced minimum develops at a period of about 10 s. This minimum is associated with a resonance within the layer of scatterers. The layer of scatterers acts like a homogeneous, slow-velocity layer at these relatively long periods. The decay rate of the shortest periods now becomes faster than the homogeneous case. The period bounding these two regimes increases as the number of scatterers is increased.

Although the layer of scatterers acts like a homogeneous, slow-velocity layer at longer periods, its behavior at shorter periods is distinctly different. To demonstrate this difference, we have measured P_{diff} in a model earth consisting of a homogeneous aluminum mantle with a thin brass layer (thickness of 11 mm, or 70 km in the real earth) at the core-mantle interface. This layer is slower

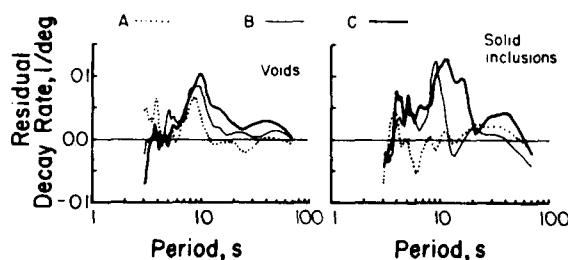


Fig. 10. Residual decay rates for a thin layer of large circular scatterers. These are the same data as in Figure 8, now rearranged to emphasize the change in decay rate associated with changing the diameter of the scatterers from 41 to 61 to 81 km (curves A-C, respectively). Circular voids are plotted to the left; circular solid inclusions are plotted to the right.

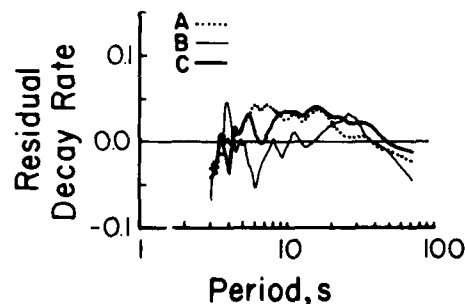


Fig. 11. Residual decay rates for (curve A) horizontal sills, (curve B) circular solid inclusions, and (curve C) vertical dikes. These three scatterer types vary only in their shape. Each has the same mass and material properties. Note that the pattern of residuals for dikes and sills is broadly similar, suggesting that scatterer orientation may not strongly influence the decay rate.

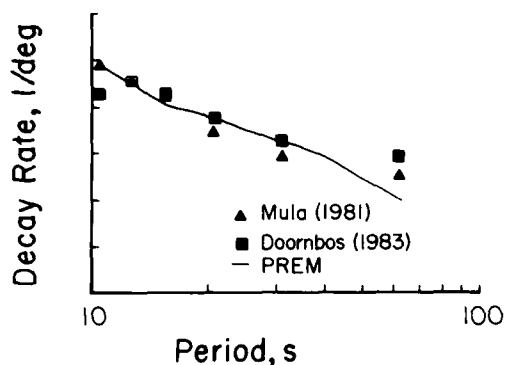


Fig. 12. Observed decay rate as a function of period, as observed by Mula [1981] (triangles) and Doornbos [1983] (squares). The solid line is a prediction of laterally homogeneous model, PREM.

than the surrounding mantle (compressional velocity of 9.33 km/s compared to 13.64). The decay rate (Figure 8) shows a sequence strong minima associated with the effect of multiple reverberations in the layer, which are not observed in the case of the layer of scatterers. The decay curve oscillates about the decay curve for the homogeneous mantle, in contrast to the scatterer case where it systematically departs from it at the shorter periods. These differences may be useful in discriminating between laterally homogeneous and randomly varying structures near the core-mantle boundary.

A thin layer of large scatterers. Like the layer of small circular voids, the layer of large voids has little effect on the decay rate at the longest periods (>20 s) (Figures 9 and 10, Curve A). Unlike the layer of small voids, there is a decay rate maximum at intermediate periods (~ 10 s) where the scatterer diameter is about a half wavelength. This maximum increases in period and amplitude as the diameter of the scatterers is increased (Figure 10, Curve A). While the small scatterers decrease the decay rate at some frequencies, the large scatterers seem mainly to increase it. They seem to be scattering energy out of the diffraction and thus increasing its decay rate. Large, solid, slow-velocity (9.33 km/s) inclusions (Figure 10, Curve B) have an effect on the decay rate that is grossly similar to the effect of the voids, except for the smallest diameter tested, where the maximum is not evident and a distinct minimum occurs. This case may represent a case intermediate between the small scatterers of the previous section, where resonances in the average layer caused a minimum in the decay rate and the large scatterers where scattering acts only to increase the decay rate. At shorter periods the decay rate is faster than for the homogeneous mantle. In the elastic inclusion case there is some hint of short-period (~ 3.5 and 5 s) maxima, which may be associated with short period resonances in the inclusions.

Scatterers of different aspect ratios. The

decay rate curves for dikes and sills just above the core-mantle boundary are remarkably similar to one another (Figure 11).

The decay rate is higher than the homogeneous case for intermediate periods (5-30 s) and lower than the homogeneous case for periods greater than 30 s or less than 5 s. These two curves differ markedly from the curve for the circular inclusions. The difference is probably due to the difference in depth of the scatterers rather than to difference in their shape. The sills and dikes are located just above the core-mantle boundary, and the circular inclusions are about 81 km above it.

Conclusions

There is considerable evidence that the D" region of the mantle contains significant lateral heterogeneity. Analysis of diverse data sets, including core phases such as PKP and PKIKP [e.g., Sacks and Snoke, 1977; Haddon and Cleary, 1974], diffracted waves [Ruff and Lettvin, 1984] and mantle P waves [Clayton and Cramer, 1983] all provide some evidence for heterogeneity. However, there is not yet agreement regarding the velocity contrast or scale lengths of these heterogeneities, which is in part due to the fact that the different techniques have different resolving powers and have been applied to different portions of the core-mantle boundary.

Our model data demonstrate that lowermost mantle heterogeneities have a significant effect on the decay rate of diffracted waves, an effect that is at some periods distinct from the effect of laterally homogeneous structure. Variations in the decay rate of up to 50% are observed. Available data for the real earth consist of measurements of the decay rate in the 10-60 s period range [Mula, 1981; Doornbos, 1983] and at about 1 s [Ruff and Helmburger, 1982; Ruff and Lettvin, 1984]. The 10-60 s data (Figure 12) are very smooth and can be fit fairly well by a laterally homogeneous earth. This result is in agreement with our model experiments, which show little variation in the longest-period decay rates between models with different amounts of lateral heterogeneity. On the other hand, the shorter period data of Ruff and Lettvin [1984] reveal significant differences in the position of the edge of the shadow zone and decay rate for different patches on the core-mantle boundary. At these shorter periods our model shows that the decay rate curves are very complex, containing minima and maxima associated with strong excitation of, or scattering from, the diffraction. However, Ruff and Lettvin's [1984] data are relatively narrow band, so that the detailed way in which decay rate varies with frequency is not yet known. These limitations stress the importance of making broad band observations of P_{diff} , and of measuring its decay rate for periods shorter than 10 s.

Acknowledgments. I thank R. A. W. Haddon for a helpful critique of the manuscript and Paula Pitts for drafting the figures. This research was supported by the National Science Foundation under grant EAR-8319104 and the

Office of Naval research under grant
N00014-84C-0218.

References

- Biot, M. A., Generalized boundary condition for multiple scatter in acoustic reflection, J. Acoust. Soc. Am., **44**, 1616-1622, 1968.
- Clayton, R. W., and R. P. Cramer, A tomographic analysis of mantle heterogeneities from body wave travel times, Eos Trans. AGU, **64**, 776, 1983.
- Dainty, A. M., and M. N. Toksz, Elastic wave propagation in highly scattering media--A diffusive approach, Geophysics, **43**, 375-388, 1975.
- Doornbos, D. J., Present seismic evidence for a boundary layer at the top of the mantle, J. Geophys. Res., **88**, 3498-3505, 1983.
- Doornbos, D. J., and J. C. Mondt, Attenuation of P and S waves diffracted around the core, Geophys. J. R. Astron. Soc., **57**, 353-379, 1979a.
- Doornbos, D. J., and J. C. Mondt, P and S waves diffracted around the core and the velocity structure at the base of the mantle, Geophys. J. R. Astron. Soc., **57**, 381-395, 1979b.
- Haddon, R. A. W., and J. R. Cleary, Evidence for scattering of seismic PKP waves near the mantle--Core boundary, Phys. Earth Planet. Interiors, **18**, 211-234, 1974.
- Menke, W., and P. G. Richards, The horizontal propagation of P waves through scattering media: Analog model results relevant to long range P_n propagation, Bull. Seismol. Soc. Am., **73**, 125-142, 1983.
- Mula, A. H. G., Amplitudes of diffracted long-period P and S waves and the velocities and Q structure at the base of the mantle, J. Geophys. Res., **86**, 4999-5011, 1981.
- Oliver, J. A., F. Press, and M. Ewing, Two-dimensional model seismology, Geophysics, **14**, 202-219, 1954.
- Ruff, L., J., and D. V. Helmburger, The structure of the lowermost mantle determined by short period P wave amplitudes, Geophys. J. R. Astron. Soc., **68**, 95-119, 1982.
- Ruff, L., and E. Lettvin, Short period P wave amplitudes and the variability of the core shadow zone, Eos Trans. AGU, **65**, 999, 1984.
- Sacks, J. S., and J. A. Snoke, Heterogeneous velocity structures at the base of the mantle, J. Geophys., **43**, 505, 1977.
- Schlittenhardt, J., J. Schweitzer, and G. Muller, Evidence against a discontinuity at the top of D", Geophys. J. R. Astron. Soc., **81**, 295-306, 1985.

W. Menke, Geophysics Group, College of
Oceanography, Oregon State University,
Corvallis, OR 97331.

(Received May 21, 1985;
revised October 8, 1985;
accepted October 11, 1985.)

Semidiurnal Internal Tide in JASIN: Observations and Simulation

L. M. DEWITT, M. D. LEVINE, C. A. PAULSON, AND W. V. BURT

College of Oceanography, Oregon State University, Corvallis

Temperature was observed in the upper 80 m by moored thermistor chains at three locations in Rockall Channel west of Scotland. Isotherms were interpolated, and a 1-week period of exceptionally energetic tidal oscillations was analyzed. The moored array (horizontal separations ranging from 6 to 20 km) was used as an antenna to determine the dominant horizontal wavelength and direction of propagation of the internal tide within the array. Rockall Bank, 100 km to the southeast, was identified as the source of the internal tide. The semidiurnal internal tide generated by the interaction of the surface tide with Rockall Bank was simulated by use of a model due to Prinsenberg and Rattray. The model predicts generation of the internal tide at the shelf break and propagation seaward as energetic beams which lie along internal wave characteristics. Some energy is trapped near the surface in association with the pycnocline. There is substantial structure in the velocity and vertical displacement fields. Most of the total energy of the internal tide is in the first vertical mode. However, at particular depths, vertical modes as high as 4 (horizontal wavelengths of 25 km) dominate. The high degree of spatial variability in the modeled internal tide illustrates the potential for error when basing a description of the tide on sparse observations. There is good agreement between the modeled vertical displacements and the 1-week period of energetic oscillations of isotherm depth observed at the moorings. In addition, there is good agreement between the model and the tidal velocity variance measured during the same week at depths ranging from 10 to 1000 m and distances ranging from 50 to 130 km from Rockall Bank. Richardson numbers associated with the vertical shear of the modeled internal tide range down to values less than 2.

1. INTRODUCTION

It is now generally accepted that the internal tide is generated by the interaction of the surface tide with bottom topography [e.g., Hendershott, 1981]. However, observations of the internal tide in deep water have seldom been unequivocally identified with generation at a particular topographic feature. Regal and Wunsch [1973] found that the internal tide south of Cape Cod was intensified and coherent near the surface. They attributed the intensification to generation on the continental slope about 60 km away and subsequent propagation of energy along internal wave characteristics which approached the surface at the point of observation. Hendry [1977] analyzed moored measurements of temperature and velocity in the western North Atlantic and concluded that the Blake Escarpment 700 km away was a major generation area for the observed internal tide. There have also been measurements on the continental slope [Torgrimson and Hickey, 1979] which demonstrate generation on the slope and propagation along characteristics.

Theoretical models of the generation of the internal tide over topography have grown in sophistication over the past 2½ decades. The earliest models describe generation in a two-layer fluid [e.g., Rattray, 1960]. The limitations of a two-layer fluid were overcome by Rattray *et al.* [1969], who investigated generation on a step continental shelf in an ocean having constant buoyancy frequency N . This work was continued by Prinsenberg *et al.* [1974] for the case of a sloping continental shelf and further extended for variable N by Prinsenberg and Rattray [1975]. Baines [1973, 1974] has developed a model for generation of the internal tide in an ocean with nearly arbitrary bottom topography and density stratification. The models predict strong generation of the internal tide at the shelf break where the bottom slope is greater than or equal to the slope of the local internal wave characteristic. The internal tide generated at the shelf break propagates seaward along

characteristics as energetic beams. Comprehensive reviews of the theories and observations of the internal tide have been given by Wunsch [1975] and Hendershott [1981].

In this paper we analyze observations of the internal tide and compare them to a model. The analysis is concentrated on a 1-week period of exceptionally energetic oscillations observed west of Scotland during the Joint Air-Sea Interaction (JASIN) experiment. The topographic source of the observed internal tide is identified, and the generation and propagation from this source are simulated with a model due to Prinsenberg and Rattray [1975]. The model has a step shelf and depth-dependent buoyancy frequency. Predicted vertical displacements and tidal velocity variances are compared with observations. The spatial variability of the internal tide is described, and its contribution to shear-induced mixing is evaluated.

2. OBSERVATIONS

As part of the JASIN experiment [Pollard *et al.*, 1983], observations of temperature were taken from late July to early September 1978 by use of thermistor chains moored in Rockall Channel about 300 km west of Scotland. Thermistor chains, manufactured by Aanderaa, were attached to surface moorings at four locations, B1, B2, B3, and B4, shown in Figure 1. Moorings B1, B2, and B3 were part of the Fixed Intensive Array (FIA), a cluster of many moorings within a 6-km square (Figure 1). Measurements at B3 were unreliable and have been excluded. Thermistors were distributed throughout the upper 81.5 m of the water column at each mooring and sampled at 10-min intervals. The observations analyzed in this paper come primarily from thermistors 5 m apart at depths ranging from 36.5 to 81.5 m. This range of depths encompasses the maximum in the buoyancy frequency (Figure 2). Isotherms were linearly interpolated between adjacent temperature measurements.

Temperature observations were also taken during JASIN with a towed thermistor chain [Baumann *et al.*, 1980]. The chain was towed at a speed of 3 m s around a 15-km square which contained the FIA moorings (Figure 1). The chain had thermistors installed at 2-m intervals from approximately 20

Copyright 1986 by the American Geophysical Union.

Paper number 5C0843.
0148-0227/86/005C-0843\$05.00

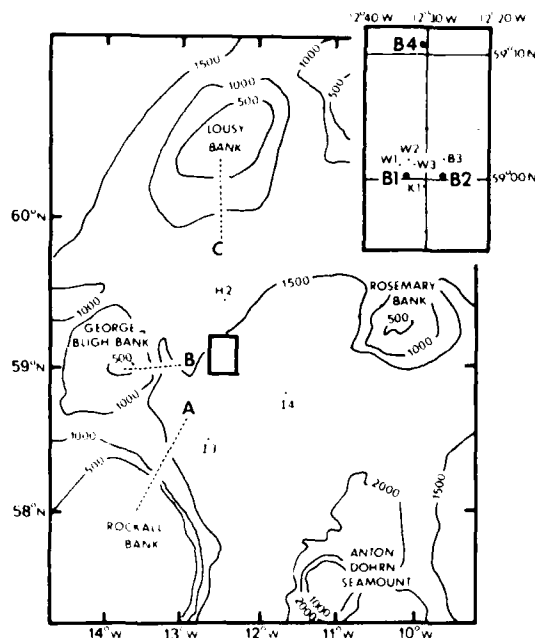


Fig. 1. Location of the B moorings in relation to topography and other moorings. The cluster of moorings centered on 59°N, 12°30'W (see inset) is called the Fixed Intensive Array (FIA). The dotted line in the inset is the track of the towed thermistor chain. Bottom slope along the dashed lines labeled A, B, and C is shown in Figure 8.

to 70 m depth. Pressure was measured at three locations on the chain. The temperature observations were averaged over sequential 30-s intervals to filter the effects of ship motion. Isotherm depths were linearly interpolated.

The time series of isotherm depths from the B moorings were divided into segments of 1024 points (nearly 1 week; see Table 1), and spectra were computed. Spectra of isotherm displacement at a mean depth of 50 m are shown in Figure 3. The spectral level at mooring B4 is higher on average than the level at B1 or B2, but levels are similar at the frequency of the semidiurnal tide (0.0805 cph). The tidal peak is the most prominent feature in the spectra and is larger than the spectral estimate at the inertial frequency (0.0714–0.0716 cph) by a

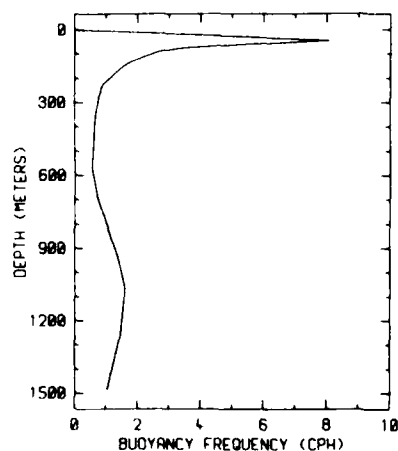


Fig. 2. Mean buoyancy frequency profile. The profile is a smoothed representation of a profile calculated by Pennington and Briscoe [1979] from conductivity, temperature, and depth casts during the experiment.

TABLE 1. Time Periods Used for Spectral Analysis.

Segment	Start		End	
	Date	Time, UT	Date	Time, UT
1	Aug. 1	1220	Aug. 8	1450
2	Aug. 8	1500	Aug. 15	1730
2	Aug. 15	1740	Aug. 22	2010
4	Aug. 22	2020	Aug. 29	2250
5	Aug. 29	2300	Sept. 6	0130

factor of 4 or more at all three moorings. At frequencies higher than the semidiurnal tide the spectra decrease with a slope of about ω^{-1} except for a small peak at twice the semidiurnal frequency. A general discussion of internal waves observed during JASIN is given by Levine *et al.* [1983].

The spectral levels and coherences in the semidiurnal tidal band calculated over nearly week-long segments during the experiment are shown in Figure 4. For each segment, three raw spectral estimates were averaged in the frequency band extending from 0.0732 to 0.0908 cph. The temporal variation of variance in the tidal band (Figure 4a) was similar at moorings B1 and B2. The variance at all moorings was the greatest during segment 4. High horizontal coherence was observed between moorings B1 and B2 during segment 4 at all depths, and coherence decreased as the variance fell during segment 5 (Figure 4b). The maximum variance at mooring B4 was larger than at the other two moorings, but coherence at the larger horizontal separations (B1-B4 and B2-B4) fell slightly during segment 4. The high variance in the tidal band during segment 4 was also accompanied by very high vertical coherence for all vertical separations at all three moorings. Figure 4c illustrates this for mooring B2. Note that the low coherence during segment 3 is not necessarily representative of moorings B1 and B4 but that the high coherences during segment 4 occurred to the same extent at all three moorings.

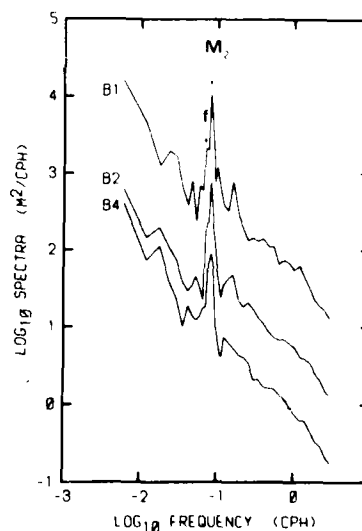


Fig. 3. Isotherm displacement spectra for isotherms with a mean depth of 50 m. The ordinate scale applies to the spectrum from mooring B2. Spectra from moorings B1 and B4 are offset by one decade upward and downward, respectively. The spectra are ensemble averaged over four or five segments. No band averaging was performed at frequencies below 0.115 cph; smoothing was performed above 0.115 cph by band averaging into 15 nonoverlapping bands per decade. Light lines are 95% confidence intervals.

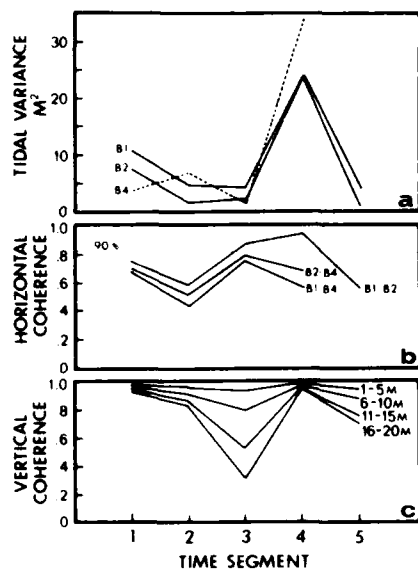


Fig. 4. (a) Temporal variation in the semidiurnal tidal band of the variance of isotherm displacement at about 50 m depth. (b) Horizontal coherence between isotherms at each mooring. (c) Vertical coherence at mooring B2 for isotherms which have various vertical separations, regardless of actual mean depth. All coherences in Figure 4c are significantly different than zero at the 90% level. Time segments are defined in Table 1.

In the section that follows we analyze segment 4, the 1-week period during which the tidal variance observed at the B moorings was exceptionally high.

3. DIRECTIONAL WAVE SPECTRA

The horizontal array of moorings, B1, B2, and B4 (Figure 1), was used as an antenna to determine the dominant horizontal wavelength and direction of propagation of the internal tide during segment 4. The technique used to estimate the wave number spectrum is called the beam-forming method [Capon, 1969]. This method is easy to implement, and the resolution in wave number space is as good as in more sophisticated methods, provided the observed wavelengths are of the order of the largest sensor separation [Davis and Regier, 1977]. The applicability of the beam-forming method to the

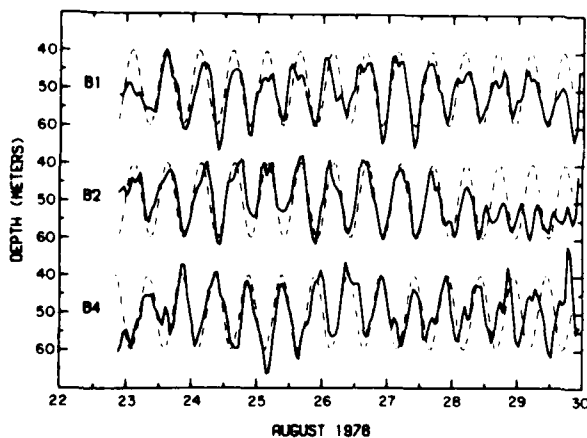


Fig. 5. Time series of 2-hour moving averages of isotherm depth with a mean of 50 m during segment 4 (solid curve). The modeled plane wave (equation (3)) is shown as a dashed curve. The isotherms are 10.8°C at B1, 10.6°C at B2, and 10.0°C at B4.

TABLE 2. Observed and Modeled Phase Differences at Semidiurnal Frequency at About 50 m Depth During Segment 4.

Mooring Pair	Separation, km	Observed Phase Difference, deg	Modeled Phase Difference, deg
B1-B2	5.8	-25	-22
B1-B4	19.2	166	-167
B2-B4	19.7	-141	-145

Modeled phase differences are from Prinsenberg and Rattray [1975].

scales encountered in this study is demonstrated by examination of Figure 5. Time series of 2-hour moving averages of isotherm depth at about 50 m calculated once an hour during segment 4 are shown for all three moorings. The internal tide at mooring B4 is about 180° out of phase with observations at mooring B1, and the phase difference between observations at moorings B1 and B2 is always small (Table 2). These phase differences suggest that the internal tide during segment 4 was traveling in a direction close to north to south, with a wavelength approximately twice the largest sensor separation, or about 40 km.

The estimate of the wave number spectrum by the beam-forming method at horizontal wave number k and frequency ω_0 is given by [Capon, 1969]

$$S(k, \omega_0) = \frac{1}{M^2} \sum_{p,q=1}^M \frac{f_{pq}(\omega_0)}{[f_{pp}(\omega_0)f_{qq}(\omega_0)]^{1/2}} \exp[i2\pi k \cdot (x_p - x_q)] \quad (1)$$

where f_{pq} is the cross spectrum at frequency ω_0 between observations at sensors p and q . M is the number of sensors in the array, and x_p is the location of the p th sensor. The wave number window for this estimator, called the beam pattern (Figure 6) of the array, depends only on sensor separations and is given by

$$B(k) = \frac{1}{M^2} \sum_{p,q=1}^M \exp[i2\pi k \cdot (x_p - x_q)] \quad (2)$$

Instead of using a conventional estimator of the cross spectrum f_{pq} , we follow the example of Hendry [1977] and use the "raw" Fourier coefficients at tidal frequency, that is

$$f_{pq} = \hat{\zeta}(x_p) \hat{\zeta}^*(x_q)$$

where $\hat{\zeta}(x_p)$ is the Fourier transform of vertical displacement at location x_p . This is a modification of the beam-forming method in that one assumes that the internal tide can be modeled as a deterministic rather than a random process. It can then be shown that for any noncolinear array of three points the wave number spectrum (1) will be exactly the beam pattern (2) reproduced with its center at k_0 , where k_0 is the average wave number of the tide.

The calculated wave number spectrum at tidal frequency for segment 4 is shown in Figure 6. The most probable wave solutions occur at peaks in the wave number spectrum; a peak at wave number (k_x, k_y) represents a wave of wavelength $[1/(k_x^2 + k_y^2)]^{1/2}$ traveling in a direction defined by a vector drawn from the peak toward the origin. For example, the peak closest to the origin in the southwest quadrant of the wave number spectrum (Figure 6) is interpreted as a wave with an average wavelength of 36 km traveling in the direction of the arrow, about 25° to the east of north. The uncertainty in this estimate is indicated by the broadness of the peak in the beam pattern. The peak in the northwest quadrant that is closest to

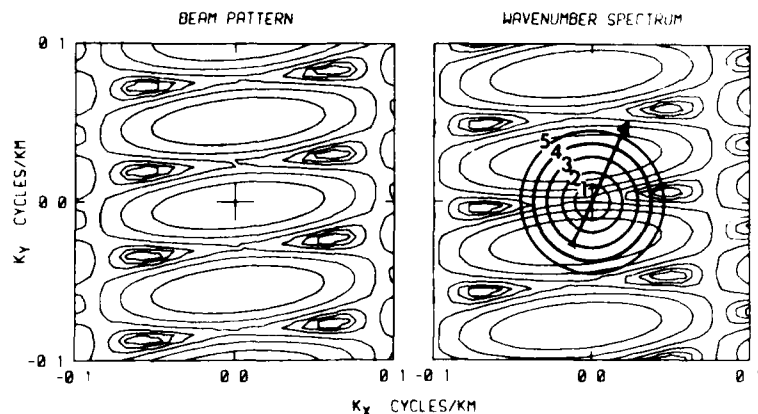


Fig. 6. Beam pattern and wave number spectrum at tidal frequency during segment 4. The peaks in these figures are the large ovals, and the troughs are smaller teardrop-shaped regions. Contouring is in 3-dB intervals down from the peaks. Circles in the wave number spectrum represent wave numbers of the first five internal wave modes, and the arrow is the direction of propagation indicated by the peak closest to the origin in the lower left-hand quadrant.

the origin also represents a wave with a wavelength near 36 km but traveling toward the southeast, about 155° to the east of north. These two peaks closest to the origin are the most likely solutions. All peaks farther from the origin are interpreted as aliases of the main peaks. These aliases occur because there may be integral multiples of waves between the moorings in addition to the fractional waves associated with the peaks closest to the origin. The wavelengths associated with the aliased peaks are short, 12 km or less. The true spectral density at these wavelengths is likely to be less than the density at longer wavelengths, because we expect that the longer waves will be more energetic at the point of generation and that they will be less easily dissipated. Hence locally at a depth of 50 m, the vertical displacement ξ during this time can be reasonably represented as a plane wave of the form

$$\xi = A \cos [2\pi(k_x x + k_y y + \omega_0 t) + \phi] \quad (3)$$

where (k_x, k_y) are determined from the beam-forming analysis and ϕ is the absolute phase. Values of (k_x, k_y) at all peaks in

the wave number spectrum (Figure 6) give the same solution for ξ at the three moorings. Comparison of this representation with the data for $A = 10$ m, $\omega_0 = 1.122$ cph (average of M_2 and S_2) is shown in Figure 5. The agreement is good in both amplitude and phase except for the last few days at B2 and B4.

One may determine which of the two peaks closest to the origin (Figure 6) is the most likely solution from the location of possible topographic internal wave generators. If the arrow drawn from the peak in the southeast quadrant of the wave number spectrum is superimposed on the topography in Figure 1, it points directly from Rockall Bank toward the FIA. Weigand *et al.* [1969] showed that internal waves propagate normal to bathymetric contours regardless of the angle of incidence of the barotropic wave. This is consistent with generation at Rockall Bank. An arrow drawn in the direction indicated by the peak in the northwest quadrant of the wave number spectrum does not lead directly from any topographic feature.

The local spatial variation of isotherm depth provides another means of distinguishing between the two most likely solutions given by the wave number spectrum (Figure 6). Isotherms were constructed from observations by a thermistor chain towed around the moorings (dotted line, Figure 1) for two time periods during segment 4 [see Baumann *et al.*, 1980]. Isotherm depths from a pair of repeated east-to-west transects on August 25 are shown in Figures 7a and 7b; a similar pair of isotherm profiles from a north-to-south track on August 27 are shown in Figures 7c and 7d. The isotherms were smoothed to eliminate small-wavelength oscillations. The plane wave solution (3) derived from the wave number spectrum is compared with the observed horizontal profiles of isotherm depth (Figure 7). The predicted displacements for the two plane waves with about 36-km wavelengths, one propagating from the northwest and one from the southwest, are plotted. For the east-to-west tracks the observations agree with a wave propagating from Rockall Bank better than with a wave from the northwest. The time interval between repeated tracks is about 6 hours or about one-half the tidal period, and the tracks nearly coincide with the times of maximum (Figure 7a) and minimum (Figure 7b) tidal displacement. The agreement of observed displacement with the plane wave propagating from Rockall Bank is also better for the north-to-south tracks, although for the first track (Figure 7c) there is not much to distinguish between the two solutions. Most of the 16 transects that were compared in this manner indicated either a

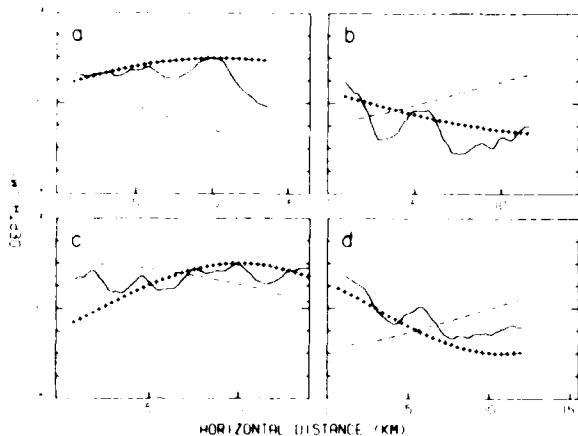


Fig. 7. Comparison between isotherm depth from the towed thermistor chain (see Figure 1 for tow track) and plane wave solutions (3) from the two directions indicated by the two peaks in the wave number spectrum (Figure 6). Solid curves are the observed horizontal profiles of isotherm depth for (a and b) two time periods (August 25, 1620–1740 and 2145–2245 UT) of east-to-west tracks and (c and d) two time periods (August 27, 1332–1452 and 1902–2022 UT) of north-to-south tracks. Plus signs represent the model plane wave solutions for an internal wave propagating from Rockall Bank. Dashed curves represent the plane wave solutions from a direction 25° to the west of north. Start times for the model are the same as for Figure 5.

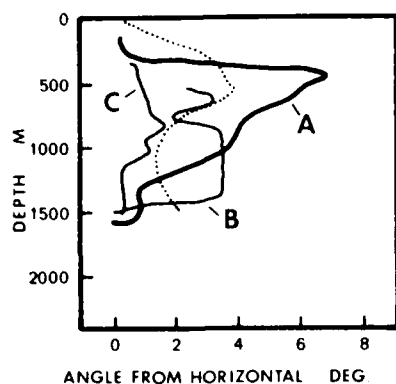


Fig. 8. Slopes of the topography corresponding to section lines in Figure 1 (solid curves) and of the tidal characteristics (dotted curve) calculated from the mean buoyancy frequency profile (Figure 2).

better fit to the wave from Rockall Bank or not enough difference in the two solutions to choose a better fit. Hence the data from the towed thermistor chain support the conclusion that the tide can be described locally as a plane wave propagating from the southwest.

4. GENERATION MODEL AND COMPARISON WITH OBSERVATIONS

While the internal tide may appear as a plane wave on small spatial scales, on larger scales we expect that the correlated modes generated by interaction of the barotropic tide with topography will produce a modulated, beamlike pattern. Topographic features were examined to determine their effectiveness as generators. The internal tide propagates along characteristics with slope given by

$$\frac{dz}{dx} = \left(\frac{\omega^2 - f^2}{N^2 - \omega^2} \right)^{1/2} \quad (4)$$

The most effective generator is one with slope equal to or greater than the slope of the characteristic [Baines, 1974]. Slopes of three topographic features near the mooring array are shown in Figure 8, and the corresponding section lines are drawn in Figure 1. Also shown is the slope of the tidal characteristic calculated from (4) by use of the JASIN mean buoyancy profile (Figure 2). The slope of Rockall Bank (profile A) is approximately equal to or steeper than the slope of the characteristic over depths ranging from 350 m to 1400 m, which indicates that it may be an effective generator. Lousy Bank to the north of the array (profile C) has one of the least steep slopes in the area and is therefore not an effective generator. George Bligh Bank, located directly to the west (profile B), and the remaining topographic features, located to the east of the moored array (Figure 1), have slopes favorable for the generation of an internal tide, but the wave number spectrum indicates a low probability that the observed internal tide propagated from the west or east during segment 4.

The internal tide generated by Rockall Bank was calculated by use of a model due to *Prinsenbergh and Ratray* [1975]. The model consists of a steplike shelf (region I) of depth H_1 and width L , and a deep ocean (region II) of depth H_2 (Figure 9). The solution in each region is the sum of a surface standing wave (barotropic tide) and a set of progressive internal waves propagating away from the shelf break. Internal waves traveling up the shelf can be reflected at the coast but are not expected to return as far as the shelf break [Prinsenbergh *et al.*, 1974]. The N profile is taken to be a function of depth only, and the internal waves in each region are represented as a sum of horizontally propagating, vertically standing modes. The vertical wave functions ϕ_n and horizontal wave numbers κ_n corresponding to mode n are determined by solving the boundary value problem

$$\frac{d^2\phi}{dz^2} + k^2 \left(\frac{N^2 - \omega^2}{\omega^2 - f^2} \right) \phi = 0 \quad (5)$$

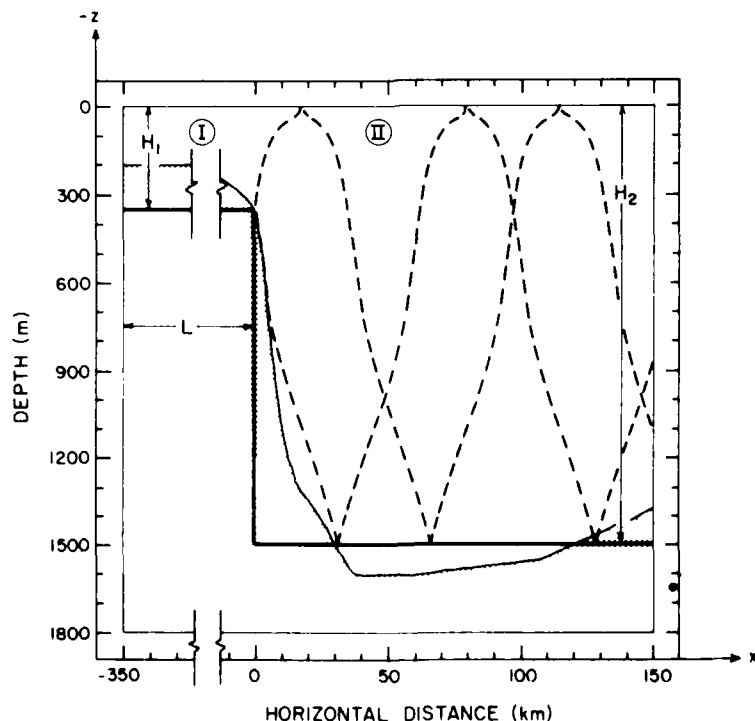


Fig. 9. Model topography (heavy solid line), Rockall Bank (light solid line), and internal wave characteristics (dashed curves) calculated from (4) in the deep ocean (region II).

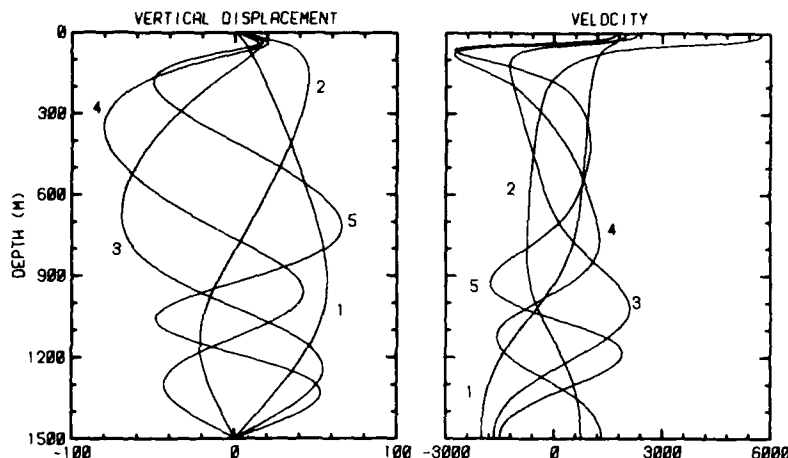


Fig. 10. First five internal wave modes calculated from (5) at a frequency of 1 12.2 cph. The velocity modes are the derivative of the vertical displacement modes divided by the wave number (Table 3). Units on the abscissa are nondimensional.

with $\phi = 0$ at the surface and bottom. The first five modes for vertical displacement and velocity in region II are shown in Figure 10, and wavelengths, wave numbers, and phase speeds are given in Table 3. The vertical displacement in regions I and II is then given by [Prinsenber and Ratray, 1975, equations 12 and 13]

$$\eta^I = \left\{ A_0^I \left(1 - \frac{z}{H_1} \right) \cos \kappa_0^I (x + L) + \sum_{n=1}^5 A_n^I \exp(-i\kappa_n^I x) \phi_n^I(z) \right\} e^{-i\omega t} \quad (6a)$$

$$\eta^{II} = \left\{ A_0^{II} \left(1 - \frac{z}{H_2} \right) \cos \kappa_0^{II} (x + x_0) + \sum_{n=1}^5 A_n^{II} \exp(i\kappa_n^{II} x) \phi_n^{II}(z) \right\} e^{-i\omega t} \quad (6b)$$

where A_0 and κ_0 are the amplitudes and wave numbers of the barotropic tide and A_n is the amplitude of mode n . The parameter x_0 shifts the phase of the barotropic wave in region II to match the horizontal and vertical velocities of the barotropic wave in region I at the shelf break. Relationships between the barotropic and baroclinic amplitudes are obtained by matching the total vertical displacement and horizontal velocity above the shelf break. These relationships are coupled matrix equations containing sums over an infinite number of modes but can be solved approximately for A_n^I and A_n^{II} in terms of A_0^I by using a finite number of modes. The higher modes mainly contribute fine structure to the solutions and in general have smaller amplitudes than the lower modes. In particular, for the case of constant N the contribution of the n th mode is proportional to $(1/n) \sin(n\pi H_1/H_2)$ [Ratray et al., 1969]. The amplitude thus decreases roughly proportionally to mode number but has zeros at integer values of nH_1/H_2 .

TABLE 3. Wave Numbers, Wavelengths, and Phase Speeds of the First Five Internal Wave Modes at 1 12.2 cph

Mode	Wave Number, rad m	Wavelength, km	Phase Speed, cm s
1	7.45×10^{-4}	84.4	192
2	1.24×10^{-4}	50.6	115
3	1.86×10^{-4}	33.7	76.7
4	2.53×10^{-4}	24.8	56.5
5	3.14×10^{-4}	20.0	45.6

H_2 . For realistic stratification the mode shapes are no longer sinusoidal, and the relative contribution of each mode is more complicated than but qualitatively similar to the case of constant N . The model of the internal tide generated at Rockall Bank was obtained by increasing the number of modes in the sums (6a) and (6b) until the solution for the amplitudes of the first 10 modes was not significantly changed by the addition of more modes. Thirty modes were used. This approach was validated by comparing the simulation for constant N with the exact solution.

One expects internal waves generated at Rockall Bank to propagate away from the shelf break along internal wave characteristics, forming beams of internal wave energy. The position of the beams and the amplitude of the internal tide are determined by the stratification, the frequency and amplitude of the barotropic tide, and the dimensions of the topography. If the shelf depth is small, reflection from the surface occurs near the shelf break, and the two beams emanating from the break combine into a single beam [e.g., Ratray et al., 1969]. In the present analysis, Rockall Bank is approximated by a steplike shelf with constant depth on each side. The actual topography is compared to this approximation in Figure 9. A sharp discontinuity in depth eliminates the generation from internal waves along the slope between the shelf break and the ocean floor. The effect of the weak generation along the slope is a broadening of the beams [Prinsenber and Ratray, 1975]. The depth at which Rockall Bank becomes steeper than the slope of the internal wave characteristics, about 350 m, was used as the shelf depth H_1 . The depth of the shelf determines the tangent point of the characteristics to the topography, affecting the horizontal position of the beams. The shelf width controls the phase of the barotropic standing wave in region I over the shelf break and sets the amplitude of the baroclinic tide relative to the barotropic, while leaving the details of the solution relatively unaffected. A standing wave over a shelf may not be the best representation of the barotropic tide, because there is no true coast, although Rockall Island surfaces about 50 km to the south of the shelf break. Rather than a detailed modeling of the local modification of the barotropic tide by the surrounding topography, the model shelf width was treated as a free parameter. The need to adjust the shelf width is an artifact of approximating the topography of Rockall Bank by a step shelf. Given a surface tide with an amplitude of about 1 m in deep water [Cartwright et al.,

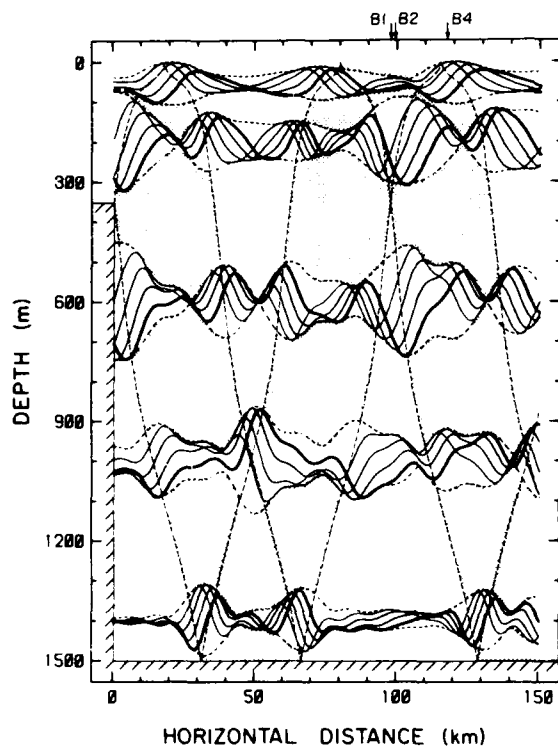


Fig. 11. Vertical displacement as a function of horizontal distance from Rockall Bank calculated from (6) using the model of *Prinsenbergh and Rattray* [1975] with a frequency of 1 12.2 cph, a shelf depth of 350 m, and a shelf width of 350 km. Superimposed are internal wave characteristics calculated from (4). The envelope of vertical displacement (dashed curves) is shown at depths of 50, 200, 600, 1000, and 1400 m together with vertical displacement at four times separated by one-eighth the tidal period. A vertical displacement of 1 m is represented by 5 m on the ordinate.

1980], a shelf width of 350 km was chosen to yield modeled amplitudes in agreement with the observed internal tide displacements at the B moorings.

The stratification and the frequency of the barotropic tide affect the width and horizontal position of the beam by controlling the slope of the characteristics given by (4). In the present analysis we choose a frequency of 1 12.2 cph (average of M_2 and S_2), in agreement with the data (Figure 5). The dominant components of the barotropic tide are M_2 and S_2 , and the amplitude of S_2 is 38% of M_2 [Cartwright et al., 1980]. The N profile (Figure 2) is taken to be horizontally uniform. Horizontal variation of N can affect the position of the characteristics [Torgrimson and Hickey, 1979]. However, the effect of the horizontal variation of N could not be assessed, because N was not well sampled in the vicinity of Rockall Bank during JASIN.

The spatial variability in vertical displacement associated with the modeled internal tide is illustrated in Figure 11. On the large scale, regions of high vertical displacement tend to follow the characteristics to form beams of internal wave energy. Maximum values of vertical displacement exceed 25 m in the beams. The internal tide at the depth of the B moorings (50 m) has wavelengths of about 40 km. However, at 1000 m the dominant horizontal wavelengths are 70 km and longer.

The modeled horizontal velocity field is shown in Figure 12. There is large spatial variation with amplitudes ranging from zero to 25 cm/s. Velocity contours tend to be parallel to the internal wave characteristics, and the highest velocities are

found in the beams, near the surface, and near the bottom where the beams cross and reflect. The beamlike structure becomes more tenuous with increasing distance from the source. The high-velocity region around 50 m depth is associated with the pycnocline and the peak in mode 2 (Figure 10). The phase of the horizontal velocity is shown in Figure 12b. Lines of constant phase tend to parallel the beams, and phase changes most rapidly perpendicular to the beams. Amphidromes occur at locations of vanishing velocity amplitude.

The vertical structure of the modeled internal tide is further illustrated in Figure 13, which shows the horizontal wave number composition of vertical displacement (Figure 13b) and horizontal velocity (Figure 13a) at various depths. The contribution from each of the modes is a strong function of depth, varying over an order of magnitude or more at wavelengths corresponding to each of the first 10 modes. At a given depth, mode 1 is not always dominant. At depths of 200 and 1400 m the dominant contributions to the variance of vertical displacement are from mode 4. The dominant contribution to the tidal velocity variance at a depth of 1000 m comes from mode 3. Even when the first mode is dominant, there are often significant contributions from mode 2, 3, or 4.

The modeled vertical displacement associated with the internal tide is compared with observed isotherm displacement at the B moorings in Figure 14. The start time for the model, which fixes the absolute phase of the tide, was chosen to fit the data. Even with the large horizontal and vertical variability predicted by the model, the relative phases at the three moorings are in good agreement during segment 4 (Table 2), although the observed amplitude of vertical displacement at moorings B1 and B2 is slightly higher than the modeled amplitude.

The modeled vertical displacement can also be compared to observed horizontal profiles of isotherm depth from the towed thermistor chain (Figure 7). Using the same start time and depth as in Figure 14, vertical displacement was calculated for each of the 16 tow transects for a tide propagating 25° to the east of north. Two pairs of transects are shown in Figure 15, with Figure 15c included as a worst case. Most of the model transects are in reasonable agreement in average depth with the tows, considering that the higher wave number oscillations evident in some of the tow tracks may not be associated with the tide. The model also assumes that there is no along-shelf variation and that wave crests are always parallel to the shelf. Curvature of the wave crests is not taken into account.

The large spatial variability evident in the modeled velocity field was also seen in the velocity measured in the JASIN area. The amplitude of the component of the tidal velocity perpendicular to Rockall Bank measured from the W and I moorings [Tarbell et al., 1979] during segment 4 is compared to the velocity amplitudes predicted by the model in Figure 12a. The measured and modeled amplitudes are tabulated in Table 4. The differences between the amplitudes are less than 2 cm/s at nine out of the 11 locations. Even though the differences are usually small, measured amplitudes exceed modeled amplitudes at all except two locations. The measured amplitudes may be overestimates because of the presence of energy from other sources in the tidal frequency band. Some of the measurements were at locations where the model predicts strong gradients in amplitude (Figure 12a). Relatively minor shifts in position of strong gradients by processes neglected in the model would cause differences between the measurements and the model. Given the uncertainties in the measurements and the complexity of the velocity field generated by an idealized model, the agreement between observations and theory is good.

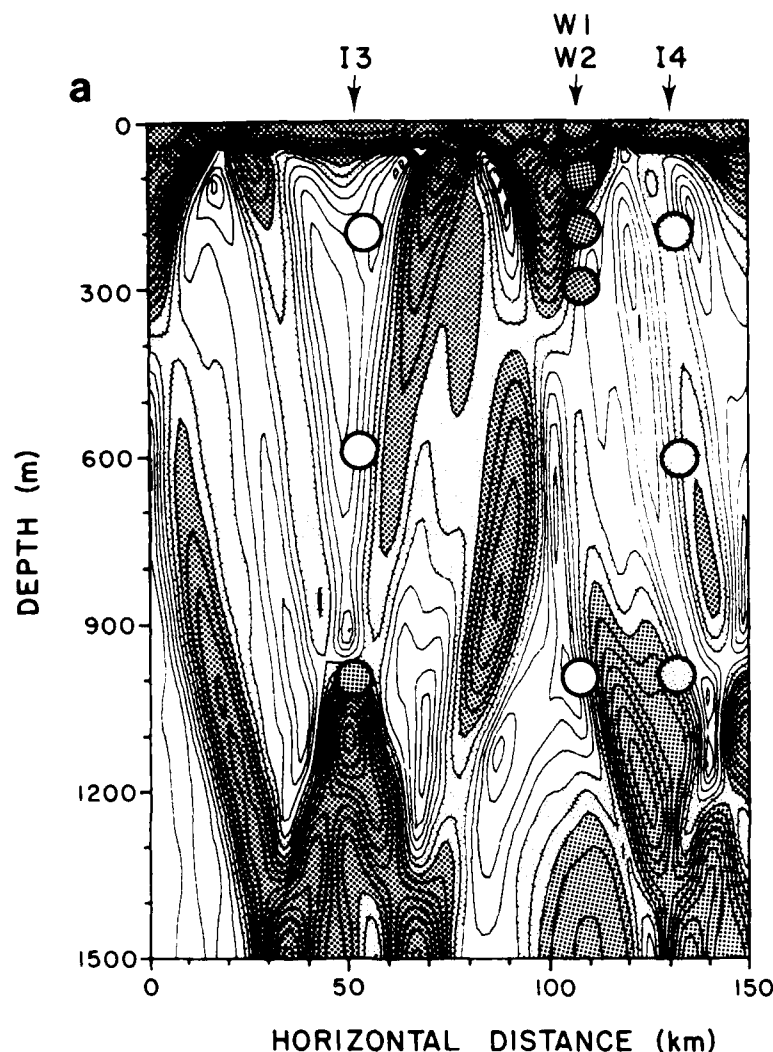


Fig. 12. (a) The amplitude of horizontal velocity (baroclinic plus barotropic) and (b) phase of horizontal velocity generated by interaction of the barotropic tide with Rockall Bank (model of *Prinsenberq and Ratray* [1975]) as a function of horizontal distance from Rockall Bank. The amplitude of horizontal velocity perpendicular to Rockall Bank at tidal frequency from current meters at moorings I3, W1, W2, and I4 during segment 4 is superimposed (circles) on contours of the model velocity. Model parameters are given in connection with Figure 11. Contour intervals are 1 cm s. Areas of no shading are regions where velocities are less than 5 cm s, of medium shading 5–7 cm s, and of dark shading greater than 7 cm s. The shading at each instrument is on the same scale and indicates the amount of energy in the tidal band (Table 4).

5. DISCUSSION

The analysis (section 3) of the energetic oscillations of isotherm displacement observed at the B moorings showed that the internal tide had a horizontal wavelength of 36 km at a depth of 50 m within the moored array. This wavelength may be compared with the wavelengths associated with the vertical mode solutions (6) for horizontally propagating free waves. The wave numbers, wavelengths, and phase speeds of the first five vertical modes at tidal frequency are given in Table 3, and circles have been drawn on the wave number spectrum (Figure 6) to represent the wave number of each mode. The mode 3 circle nearly intersects the center of each of the two peaks in the wave number spectrum which are closest to the origin. Hence within the FIA at a depth of 50 m the vertical displacement appears to have the wavelength of a mode 3 plane wave. This result may not be valid in other regions because of the beamlike nature of the internal tide (Figure 11).

The modeled spatial variability of semidiurnal tidal amplitude and wavelength (Figures 11 and 12) illustrates the potential for error when describing the internal tide based on sparse measurements. We observed a wavelength characteristic of mode 3 at a depth of 50 m within the B moored array. This wavelength is consistent with the model at the B moorings (Figure 14 and Table 2), but it is impossible to generalize to other depths and locations because of the spatial variability expected on the basis of the model (Figures 11 and 12). At 50 m depth, mode 2 is dominant in the model (Figure 13), but the dominant wavelength measured in a particular region may not be characteristic of mode 2, e.g., within the B array. If the B moorings had been located 50 km closer to Rockall Bank, the model predicts that the measured horizontal wavelength would have been much longer than 36 km (Figure 11). Although mode 1 is dominant in the aggregate, modes as high as 4 may dominate at a particular depth (Figure 13).

Independent estimates of the horizontal wavelength of the

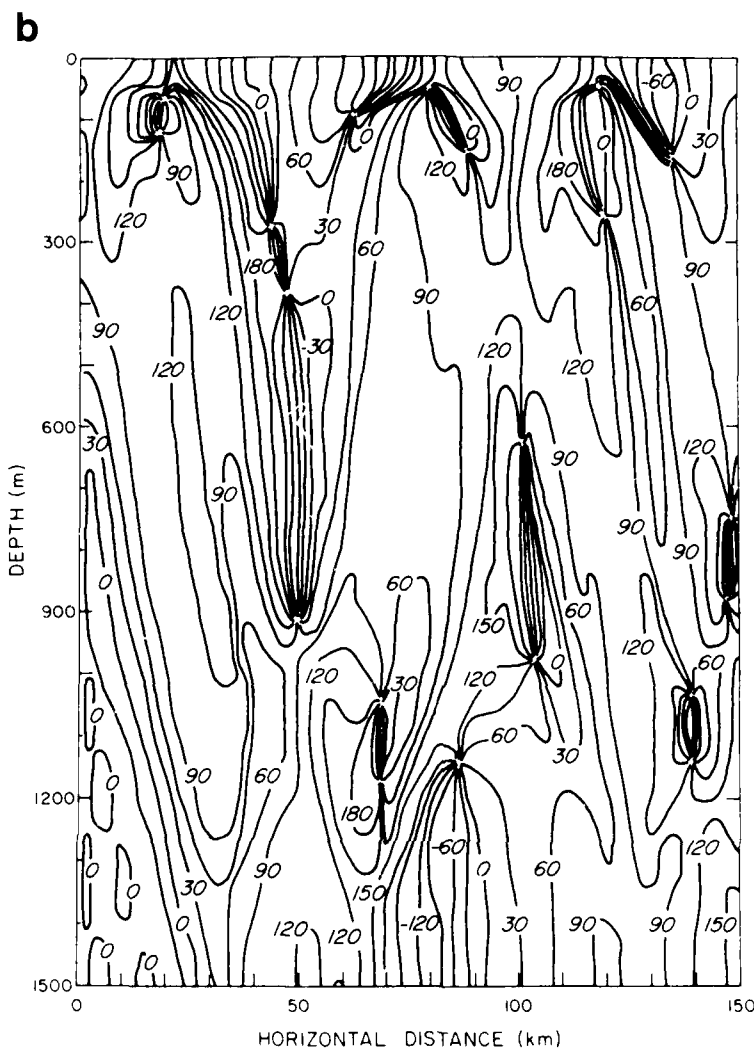


Fig. 12. (continued)

internal tide were made during JASIN by Pollard [1983b]. These observations were made 1 week after segment 4, 10–40 km west of the FIA at depths of 14–42 m from a drifting spar buoy. Pollard reported that the internal tide had a horizontal wavelength of 25–30 km, corresponding to mode 3 or 4, consistent with analysis of the B moorings.

The inconsistencies in previous descriptions of the internal tide may have been caused by the attempt to generalize from sparse measurements. In the deep ocean far from large topographic features, such as continental shelves, the internal tide is traditionally thought to be composed of a few surviving low modes which have become uncorrelated. Using this assumption in the analysis of data from Mid-Ocean Dynamics Experiment (MODE), Hendry [1977] found most energy in mode 1. He identified Blake Plateau 700 km to the west as the source of the 160-km wavelength tide. In contrast, mid-ocean observations in the Pacific from the Pole experiment (35°N, 155°W) [Simpson and Paulson, 1979] and the Mixed Layer Experiment (MILE) (50°N, 145°W) [Davis et al., 1981] indicate that modes higher than 1 were probably present, because 10-m vertical displacements were found in the upper 100 m at semidiurnal frequency. If the vertical structure were entirely mode 1, this would imply a maximum amplitude at middepth of at

least 40 m, which may be unrealistically large. From measurements of horizontal coherence in the mid-Pacific by Barnett and Bernstein [1975], Simpson and Paulson [1979] estimate a horizontal wavelength of 35 km, corresponding to a wave of order mode 3. One explanation for the differences among these midocean determinations of the structure of the internal tide may be differences in sampling. Hendry [1977] may not have found significant energy in modes higher than 1, because he lacked data in the upper 400 m where higher modes may dominate. The spatial complexity of the modeled internal tide (Figures 11 and 12) illustrates the difficulty of determining the characteristics of the tide from sparse measurements.

The sampling problem is further compounded by temporal variability. Large temporal variation in the internal tide was observed at the B moorings (Figure 4). Ketzler [1983] also found significant variation in the amplitude of the semidiurnal tide on time scales of a week during JASIN. The observations consisted of horizontal velocity measured from July 18 to August 28 at six depths at the K1 mooring (Figure 1) in the FIA. The depths ranged from 70 to 980 m. The variation observed at 70 m depth is qualitatively similar to the variation in the variance of vertical displacement shown in Figure 4. In particular, there was an increase by a factor of 3 in the ampli-

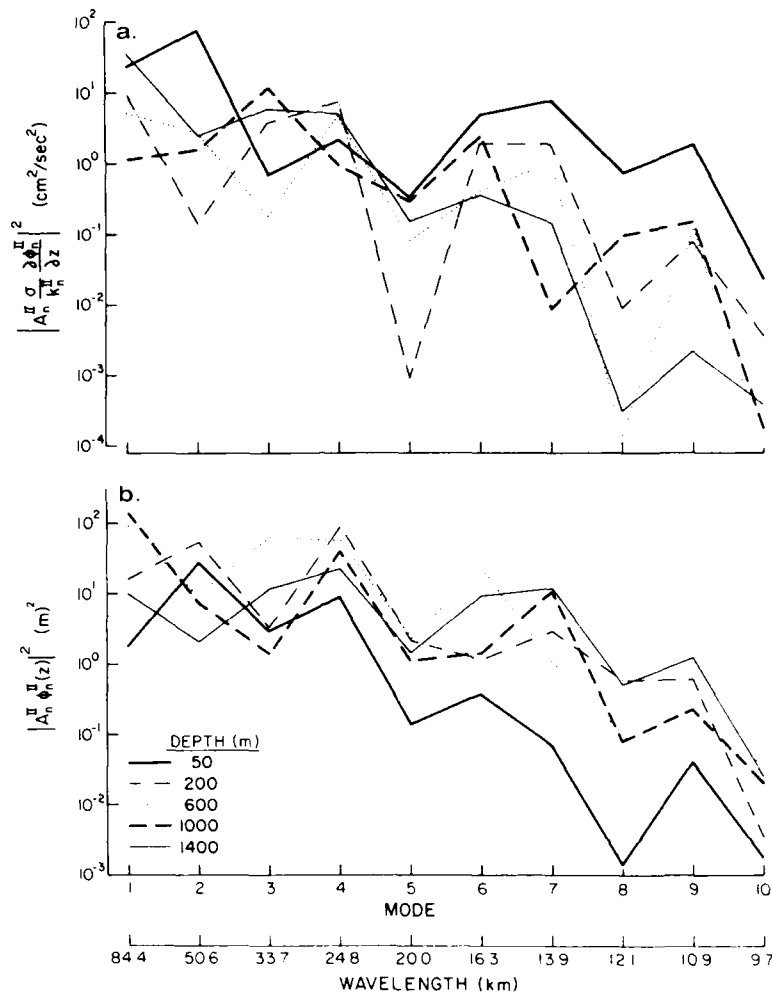


Fig. 13. Modal composition of (a) horizontal velocity and (b) vertical displacement for the first 10 internal wave modes in the deep ocean from the model of *Prinsenberg and Ratnay* [1975] (see Figure 11 for model parameters).

tude of the semidiurnal tide at 70 m during the week (August 22–29) when the variance of vertical displacement was also high (Figure 4). The vertical variation of semidiurnal tidal amplitude during this week was qualitatively similar to the

modeled vertical variation (Figure 12) at the location of the K1 mooring (Figure 1). The observed amplitude was a maximum near the surface (10 cm s at 70 m) and decreased to low values (2–4 cm s) at depths of 480 m and below. These amplitudes and their variation compare favorably with the measured and modeled amplitudes (Table 4 and Figure 12) at the W1 and W2 moorings, which were less than 5 km away from K1 (Figure 1). The results of Ketzler's analysis are consistent with ours and provide additional support for the model.

The 1-week period of tidal oscillations which we analyzed appears to be unusually energetic (Figure 4). In his review paper, *Wunsch* [1975] remarks "... the most common observation is that the internal tides tend to come and go, i.e., they appear to be intermittent." There are several possible causes of intermittency. The generation process may be affected by variations in the magnitude of the surface tide and fluctuations of density and velocity in the region of generation [Baines, 1982]. Once generated, the high-energy beams may be refracted, reflected, or trapped by fluctuations of density and velocity along the paths of propagation [e.g., *Moore*, 1975]. In JASIN the 1-week energetic period nearly coincides with a maximum in the surface tide [Cartwright et al., 1980]. However, the amplitude of the surface tide changes slowly and by no more than 30% during the 5 weeks of observations. It is more likely that the intermittency is caused by shifting of the beams of internal wave energy due to fluctuations in density and velocity.

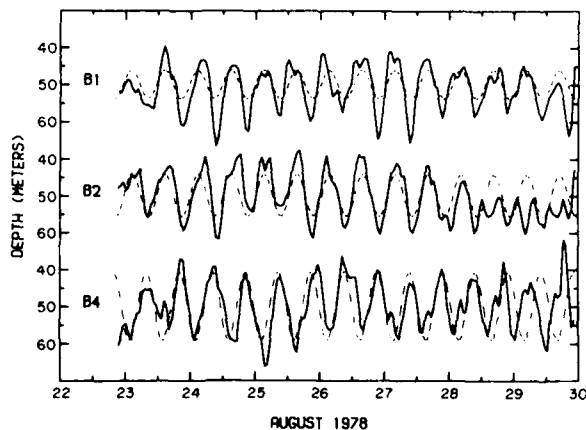


Fig. 14. Time series of 2-hour moving averages of isotherm depth with a mean of 50 m during segment 4 (solid curve). The modeled plane wave [Prinsenberg and Ratnay, 1975] is shown as a dashed curve. (See Figure 11 for model parameters.) The isotherms are 10.8°C at B1, 10.6°C at B2, and 10.0°C at B4.

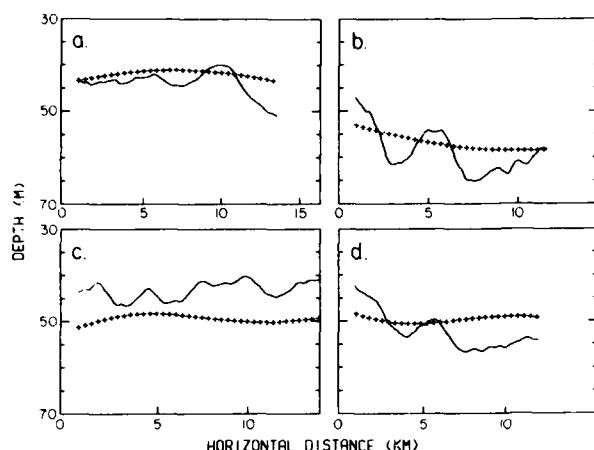


Fig. 15. Comparison between tow tracks (80 min) in duration shown in Figure 1 and the model solution [Prinsenber and Rattray, 1975]. Solid curves are the observed horizontal profiles for (a and b) two time periods (August 25, 1620–1740 and 2145–2245 UT) of east-to-west tracks and (c and d) two time periods (August 27, 1332–1452 and 1902–2022 UT) of north-to-south tracks. Plus signs represent the model solution for an internal wave generated at Rockall Bank and propagating toward 25° to the east of north. Start times for the model are the same as for Figure 14.

ty associated with mesoscale eddies (described by Pollard [1983a]) in the JASIN area.

The temporal variation of the tidal velocity amplitude at the K1 mooring [Ketzler [1983], described above] is consistent with a horizontal shifting of beams of internal wave energy. During the 1-week period analyzed here the tidal velocity amplitude at 70, 170, and 270 m depth at K1 was high, a factor of 2–3 times higher than during the first month of observation. The amplitude at 980 m during the same week, however, was low, 4–8 times lower than during the previous weeks. From Figure 12a, if the beam reached the surface after its first reflection just slightly closer to Rockall Bank, then the pattern of high and low velocities measured with depth at the FIA would be entirely different. The shallow sensors would be located in a region of low velocity, and the deeper ones in a region of higher velocities. This may have been the case during the last few weeks in July at K1.

There is indirect evidence that changes in the magnitude of the internal tide during JASIN may have been associated with changes in the eddy field. The velocity near the thermistor chain moorings changed direction (northwest to southwest) from August 20 to 22 [Weller and Halpern, 1983], just before the onset of the large-amplitude tidal oscillations. This nearly simultaneous occurrence may have been fortuitous. There is probably not enough information to determine a cause and effect relationship. In any case, an investigation of the effects

of the eddy field on the internal tide is beyond the scope of this paper.

Little is known about the role of the internal tide in mixing the interior [Hendershott, 1981], although Baines [1974] suggests that mixing driven by tidal shear is easily achieved. The model predicts large velocity shear in the beams and near the surface (Figure 12a) which may contribute to mixing. A measure of the potential for overturning is the Richardson number $N^2/(\partial u/\partial z)^2$, where u is the horizontal velocity of the internal tide. Contours of a minimum Richardson number over a tidal cycle are shown in Figure 16. The contours tend to parallel internal wave characteristics, with lower Richardson numbers occurring along the beams which emanate from the shelf break. The greatest potential for the internal tide to contribute to mixing exists near the surface where Richardson numbers less than 2 are found. Even though a Richardson number of 2 is not subcritical, the addition of shear from other sources or fine structure in the vertical density profile could cause mixing. The model neglects nonlinear processes which could also contribute to mixing.

6. SUMMARY

We have presented the results of an investigation of the internal tide. The investigation included an analysis of observations in the Rockall Channel during the JASIN experiment, simulation of the generation and propagation of the internal tide by use of a model [Prinsenber and Rattray, 1975], and comparison of the model with observations.

The internal tide was exceptionally energetic in the upper 80 m during the 1-week period chosen for analysis (Figure 4). Analysis of vertical displacement of isotherms observed by an array of three moored thermistor chains (Figure 1) and a towed thermistor chain showed that the internal tide at a depth of 50 m within the array propagated from the direction of Rockall Bank, about 100 km away. Because of its location and favorable topography (Figure 8), Rockall Bank was identified as the source of the observed internal tide.

The internal tide generated by the interaction of the barotropic tide with Rockall Bank was simulated by use of a model due to Prinsenber and Rattray [1975], which has a step shelf and a depth-dependent buoyancy frequency. The modeled internal tide exhibits a large degree of spatial variability (Figures 11, 12, and 13) which is associated with beams propagating from the shelf break along internal wave characteristics (Figure 9). Tidal energy is also concentrated near the surface, in association with the seasonal pycnocline. In the aggregate most of the modeled tidal energy is in the first mode, but at particular depths, modes as high as 4 (wavelengths of 25 km) contain most of the energy (Figure 13). The spatial variability in the modeled amplitudes and wavelengths illustrates the potential for error when drawing conclusions about the structure of the internal tide from sparse observa-

TABLE 4. Amplitude of Horizontal Tidal Velocity Perpendicular to Rockall Bank Measured at Current Meters Shown in Figure 1

Mooring	Distance From Rockall Bank, km	Depth, m					
		10	100	200	300	600	1000
I3	52			4.2 (2.4)		3.1 (2.6)	9.5 (9.3)
W1	107		8.5 (14.0)	7.5 (6.0)	7.2 (4.6)		4.5 (3.2)
W2	109	17.8 (16.5)					
I4	130			6.5 (4.8)		6.1 (4.9)	5.7 (7.6)

Amplitudes are in centimeters per second. Data from moorings I3, W1, and W2 are averaged over a 7-day period from August 22 to 29 (segment 4) and from mooring I4 over a 54-day period starting from August 22. Amplitudes in parentheses are from the model (Figure 11).

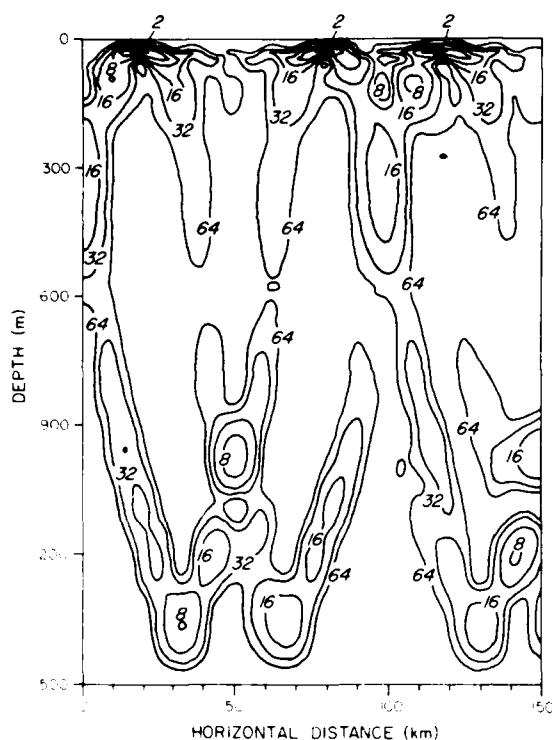


Fig. 16 Minimum Richardson number ($N^2 / (g' / z)^2$) over a tidal cycle calculated from the velocity field.

tions. Calculation of the field of a minimum Richardson number associated with the model (Figure 16) shows that the internal tide can contribute to mixing near the surface where beams of tidal energy are reflected.

There is good agreement between the modeled internal tide and the 1-week period of energetic displacements observed at the B moorings 100 km from Rockall Bank (Figure 14). In addition, tidal velocity variance measured during the same week at depths ranging from 10 to 1000 m also agrees with the model (Figure 12a and Table 4). We conclude that a relatively simple theory [Prinsenberg and Rattray, 1975] can, under some conditions, successfully simulate the internal tide at distances up to 100 km from the point of generation.

Acknowledgments. This research was supported by the Office of Naval Research under contracts N00014-76-C-0197 and N00014-84-C-0218. We are grateful to W. J. Gould, M. G. Briscoe, and R. A. Weller for providing observations of currents. Useful comments on an early draft were provided by S. A. Thorpe.

REFERENCES

- Baines, P. G., The generation of internal tides by flat-bump topography, *Deep Sea Res.*, **20**, 179–205, 1973.
- Baines, P. G., The generation of internal tides over steep continental slopes, *Philos. Trans. R. Soc. London, Ser. A*, **277**, 27–58, 1974.
- Baines, P. G., On internal tide generation models, *Deep Sea Res.*, **29**, 307–338, 1982.
- Barnett, T. P., and R. L. Bernstein, Horizontal scales of midocean internal tides, *J. Geophys. Res.*, **80**, 1962–1964, 1975.
- Bennett, R. J., C. A. Paulson, and J. Wagner, Towed thermistor chain observations in JASIN, *Data Rep. 80, Ref. 80-14*, 202 pp., School of Oceanogr., Oreg. State Univ., Corvallis, 1980.
- Capon, J., High-resolution frequency-wavenumber spectrum analysis, *Proc. ILLF*, **57**, 1408–1418, 1969.
- Cartwright, D. E., A. C. Edden, R. Spencer, and J. M. Vassie, The tides of the northeast Atlantic Ocean, *Philos. Trans. R. Soc. London, Ser. A*, **298**, 87–139, 1980.
- Davis, R. E., and L. A. Regier, Methods for estimating directional wave spectra from multi-element arrays, *J. Mar. Res.*, **35**, 453–477, 1977.
- Davis, R. E., R. deSzoeke, D. Halpern, and P. Niiler, Variability in the upper ocean during MILE, I. The heat and momentum balances, *Deep Sea Res., Part A*, **28**, 1427–1451, 1981.
- Hendershott, M. C., Long waves and ocean tides, in *Evolution of Physical Oceanography*, edited by B. A. Warren and C. Wunsch, pp. 292–341, MIT Press, Cambridge, Mass., 1981.
- Hendry, R. M., Observations of the semidiurnal internal tide in the western North Atlantic Ocean, *Philos. Trans. R. Soc. London, Ser. A*, **286**, 1–24, 1977.
- Ketzler, C., Zur Kinematik der Gezeiten im Rockall-Gebiet, *Rep. 112*, 70 pp., Inst. für Meereskunde, Univ. Kiel, Federal Republic of Germany, 1983.
- Levine, M. D., C. A. Paulson, M. G. Briscoe, R. A. Weller, and H. Peters, Internal waves in JASIN, *Philos. Trans. R. Soc. London, Ser. A*, **308**, 389–405, 1983.
- Moore, C. N. K., Several effects of a baroclinic current on the cross-stream propagation of inertial waves, *Geophys. Astrophys. Fluid Dyn.*, **6**, 245–275, 1975.
- Pennington, N., and M. G. Briscoe, Atlantis-II (Cruise 102) preliminary CTD data from JASIN 1978, *Tech. Rep. W.H.O.I.-79-42*, 225 pp., Woods Hole Oceanogr. Inst., Woods Hole, Mass., 1979.
- Pollard, R. T., Mesoscale (50–100 km) circulations revealed by inverse and classical analysis of the JASIN hydrographic data, *J. Phys. Oceanogr.*, **13**, 377–394, 1983a.
- Pollard, R. T., Observations of the upper ocean: Wind-driven momentum budget, *Philos. Trans. R. Soc. London, Ser. A*, **380**, 407–425, 1983b.
- Pollard, R. T., F. H. Guymer, and P. K. Taylor, Summary of the JASIN 1978 field experiment, *Philos. Trans. R. Soc. London, Ser. A*, **380**, 221–230, 1983.
- Prinsenberg, S. J., and M. Rattray, Jr., Effects of continental slope and variable Brunt-Vaisala frequency on the coastal generation of internal tides, *Deep Sea Res.*, **22**, 251–263, 1975.
- Prinsenberg, S. J., W. L. Wilmot, and M. Rattray, Jr., Generation and dissipation of coastal internal tides, *Deep Sea Res.*, **21**, 263–281, 1974.
- Rattray, M., Jr., On the coastal generation of internal tides, *Tellus*, **12**, 54–62, 1960.
- Rattray, M., Jr., J. Dworski, and P. Koval, Generation of long internal waves at the continental slope, *Deep Sea Res.*, **16**, 179–195, 1969.
- Regal, R., and C. Wunsch, M_2 tidal currents in the western North Atlantic, *Deep Sea Res.*, **20**, 493–508, 1973.
- Simpson, J. J., and C. A. Paulson, Observations of upper ocean temperature and salinity structure during the POLE experiment, *J. Phys. Oceanogr.*, **9**, 869–884, 1979.
- Tarbell, S., M. G. Briscoe, and R. A. Weller, A compilation of moored current meter and wind recorder data, vol. XVIII (JASIN 1978, moorings 651–653), *Tech. Rep. W.H.O.I.-79-64*, 201 pp., Woods Hole Oceanogr. Inst., Woods Hole, Mass., 1979.
- Forgrimson, G. M., and B. M. Hickey, Barotropic and baroclinic tides over the continental slope and shelf off Oregon, *J. Phys. Oceanogr.*, **9**, 945–961, 1979.
- Weigand, J. G., H. Farmer, S. Prinsenberg, and M. Rattray, Jr., Effects of friction and surface tide angle of incidence on the coastal generation of internal tides, *J. Mar. Res.*, **27**, 241–259, 1969.
- Weller, R. A., and D. Halpern, The velocity structure of the upper ocean in the presence of surface forcing and mesoscale oceanic eddies, *Philos. Trans. R. Soc. London, Ser. A*, **308**, 327–340, 1983.
- Wunsch, C., Internal tides in the ocean, *Rev. Geophys.*, **13**, 167–182, 1975.
- W. V. Burt, L. M. deWitt, M. D. Levine, and C. A. Paulson, College of Oceanography, Oregon State University, Corvallis, OR 97331.

(Received July 29, 1985;
accepted August 20, 1985.)

Heat and Energy Balances in the Upper Ocean at 50°N, 140°W during November 1980 (STREX)

J. D. PADUAN AND R. A. DESZOEKE

College of Oceanography, Oregon State University, Corvallis, OR 97331

(Manuscript received 15 March 1985, in final form 16 July 1985)

ABSTRACT

Subsurface temperature data and surface meteorological data are analyzed from thermistor chain moorings deployed near 50°N, 140°W during the Storm Transfer and Response Experiment (STREX). The upper-ocean heat and potential energy (PE) contents to 90 m are examined for an 18-day period and their changes compared to the sources and sinks of heat and turbulent kinetic energy (TKE). Heat and TKE do not balance in the vertical dimension alone. The heat content change, for example, averages -200 W m^{-2} while the net cooling at the surface, estimated from bulk formulas for latent and sensible heat fluxes and radiation measurements, averaged only -86 W m^{-2} . Advection of heat and PE, in either the vertical or horizontal, play major roles in the budgets of this area. We describe a method for using the large-scale wind stress and SST data around the site to compute the advection in the Ekman layer and close the heat (to 23%) and TKE (to 24%) budgets.

Though the heat and PE contents exhibit long-term trends, there are two marked events associated with storms on 15 and 27 November 1980 that account for much of the overall cooling and PE change. The advection estimates mimic the episodic character of the heat and PE contents and are clearly important on the short, storm time scale. The relative contributions of horizontal and vertical advection are quite different for the two storms, showing that the upper-ocean response very much depends on the proximity and orientation of the storm as it moves past the observational site.

The TKE budget is complex, and some terms can only be estimated by uncertain parameterizations so that the relative importance of surface production, shear production, and advection is unclear. Still, the fact emerges that mixed layer deepening is dominated by wind-forcing even during the season of significant cooling.

1. Introduction

In this paper we attempt to close the budgets of heat and turbulent kinetic energy for the upper ocean at the site, near 50°N, 140°W, of thermistor chain moorings deployed as part of the Storm Transfer and Response Experiment (STREX) in the North Pacific during November 1980. The turbulent kinetic energy balance can be used to relate changes of potential energy of the water column to sources (wind stirring, convection) and sinks (dissipation) of kinetic energy. The nature of these relations is at the heart of mixed layer dynamics.

The sources of data are as follows:

(i) Thermistor chain time series of temperature at many depths between the surface and 143 m and used to calculate heat and potential energy changes of the water column;

(ii) High quality surface meteorological data from a surface buoy and from two research vessels operating in the area, used to estimate components of heat flux, radiation, surface wind stress, and production of kinetic energy by wind stirring and convection;

(iii) Lesser quality surface meteorological data, mainly of sea level pressure and air and sea temperature, obtained from a network of ships of opportunity

and other platforms and used to estimate surface temperature gradients and the horizontal distribution of surface wind stress. More details on the data sources and processing are given in Section 2.

Tully and Giovando (1963) and Tabata (1965) examined the average annual heat budget of the upper ocean at Ocean Weather Station P, very near the site of the present experiment, and concluded that over an average year there should be a net heat gain of 32 W m^{-2} resulting, mainly, from the winter months when only 50% of the observed heat loss is accounted for by the surface heat flux. Since secular warming of the water column is not observed and the apparent net heating is less than 20% of the maximum flux estimates, this disparity is arguably within the experimental certainty of the heat transfer estimates. It is also, however, qualitatively consistent with the idea of equatorward export of heat by wind drift in the surface layer. In the past, emphasis has been placed on one-dimensional models that neglect the influence of advection processes. Camp and Elsberry (1978) concluded that both vertical and horizontal advection of heat could be neglected for most of the weather ship data that they investigated. Denman and Miyake (1973) and Davis *et al.* (1981a) discounted the importance of horizontal advection in

the summer heat budget near Station P, and other investigators (Gill and Niiler, 1973; Emery, 1976; Stevenson and Niiler, 1983) concluded that it plays a minor role in the seasonal changes of heat content in the northeastern Pacific Ocean.

Kraus and Turner (1967) produced a theory of the ocean mixed layer based on the heat balance and certain parameterizations of the source and sink terms in the turbulent kinetic energy budget. Denman and Miyake (1973) applied this theory to an analysis of a month-long series of bathythermograph profiles at Station P and obtained what they considered agreement, although this has been criticized (Thompson, 1976).

Elsberry and Camp (1978) give evidence showing that the seasonal changes in mixed layer temperatures and thicknesses are mostly the result of episodic storms. Price *et al.* (1978) achieved success in modeling data from the Gulf of Mexico on the response of the mixed layer, on the several-day time-scale, to a hurricane; they assumed heat and momentum balance and a critical bulk Richardson number for the inertial oscillations in the mixed layer, following Pollard *et al.* (1973). In a simple laboratory experiment on turbulent convection, Deardorff *et al.* (1969) used the assumption of heat balance to relate entrainment of a boundary layer heated from below to the driving heat flux. Moore and Long (1971) and Kato and Phillips (1969) used similar tactics to relate entrainment to surface shear stress. Davis *et al.* (1981a,b) also verified, although working with field data during late summer from a mooring near Station P, a kind of one-dimensional heat balance—modified by vertical advection of cold water from below—before comparing changes in potential energy to parameterizations of wind stirring. Niiler and Kraus (1977) reviewed theories of the bulk mixed layer and showed how they all, including *ad hoc* critical Richardson number models, amounted in physical terms to statements about the turbulent kinetic energy balance.

In Section 3 we examine the heat balance during the deployment of our thermistor chain array in late autumn. We estimate the effect of advection in this balance and argue that it makes a very important contribution that comes in episodes associated with storms. In Section 4, analogously, we examine the turbulent kinetic energy balance from our data set, again paying close attention to the effect of advection.

2. The experiment

The Storm Transfer and Response Experiment (STREX) was a joint meteorological-oceanographic experiment carried out in the northeastern Pacific Ocean during November and December 1980 in order to examine the response of the atmospheric and oceanic boundary layers to the passage of storms (Fleagle *et al.*, 1982). In this study we have drawn on data acquired

and analyses carried out as part of STREX. We shall briefly summarize these here.

a. Thermistor chain moorings

Four surface moorings were deployed by the NOAA ship *Oceanographer* near 50°N, 140°W. Figure 1 shows the location and configuration of the mooring array. We refer to the moorings by the letter codes A, B, C, and D as shown in the figure. Each mooring consisted of a 2.4 m toroid surface float anchored tautly in about 4600 m of water. As the figure indicates, three of the moorings, A, B, and C, supported two subsurface thermistor chains with thermistors every 10 m between 10 and 110 m, and every 3 m between 113 and 143 m. The thermistor chains contained Aanderaa model TR-1 recorders that recorded temperature internally on magnetic tape every 1200 s. Mooring D supported only a shallow chain between 10 and 110 m with thermistors every 10 m, but it was also equipped with meteorological instruments that measured air temperature and vector-averaged wind velocity 3.4 m above the surface and sea surface temperature (Reynolds, 1982). The data were subsampled every 1200 s to match with the subsurface temperatures. Figure 1 shows the time span of the data return for each component of the mooring instruments. For example, mooring B supported the longest shallow temperature chain record extending for approximately 19 days over Julian days 315 to 333 (10–28 November).

Figure 2 shows the time series from the shallow thermistor chain at mooring B. This was the data set we chose to compute the heat content and potential energy time series, described in Sections 3 and 4, because it contains the longest continuous records and it best covers the two major storm events of the experiment. The curves in Fig. 2 have been offset in the vertical so that the upper trace is the temperature of the 10 m thermistor, the next one down is the 20 m thermistor, etc. Above 60 m there is a definite cooling trend over the 18 days shown in the figure, but the temperatures are nearly isothermal at any given time. Beneath this well-mixed layer is the seasonal thermocline between 60 and 90 m. The thermocline shows up in the time series as the region of high frequency and high amplitude variability attributed to internal waves within a region of large temperature gradient. A small temperature change with depth below the thermocline produced the low amplitude variability that can be seen in the deeper (90–110 m) time series.

Two relatively abrupt cooling events are visible in Fig. 2. The first one occurred on day 320 (15 November). On that date, the mixed layer thickened to overtake the 60 m thermistor as evidenced by the slight decrease in mean temperature and the cessation of the high frequency variability in the 60 m trace. A similar event occurred on day 332 (27 November). Again the

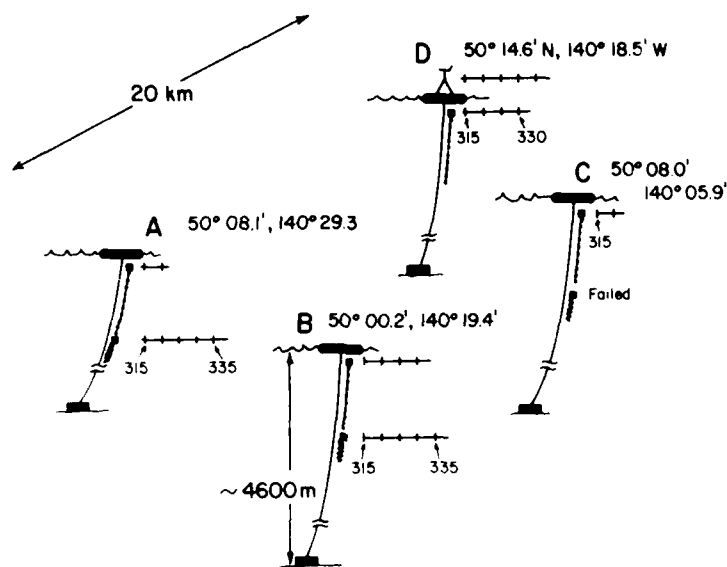


FIG. 1. Schematic representation of STREX mooring array. Subsurface thermistor chains extended between 10 and 110 m, and between 113 and 143 m. Mooring D meteorological platform measured air temperature and wind velocity 3.4 m above the surface. Time lines indicate length of data return with tick marks every five days at 0000 GMT and labeled in Julian days.

thermocline deepened on the order of 10 m, while the mixed layer temperature fell by almost 0.5°C within several hours. These short time, mixed-layer deepening events can also be seen in Fig. 3 where we have plotted the mixed layer depth, h , defined as the depth at which the temperature was 0.2°C lower than the surface value. The figure shows h after having been smoothed with a

12.4 hour running average filter to remove tides and higher frequencies. Large increases in the magnitude of h on days 320 and 332 are clearly visible. Figure 3 also shows the 10 m temperature which was assumed to be identical to the temperature at the surface and, for comparison, the air temperature at mooring D. The surface temperature function mimics that of the mixed

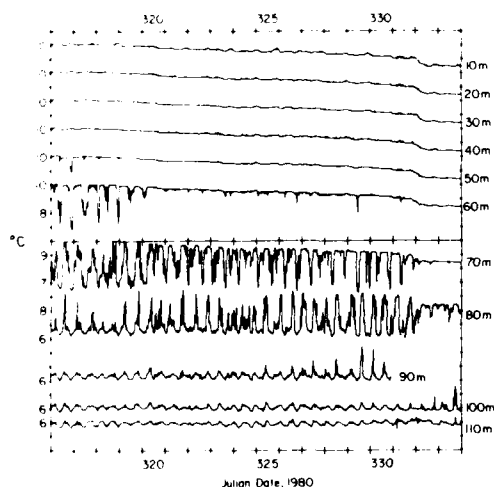


FIG. 2. Offset temperature time series from the shallow thermistor chain at mooring B. Note the cooling trend in the well-mixed layer above 60 m and the two rapid cooling and deepening events on Julian days 320 and 332.

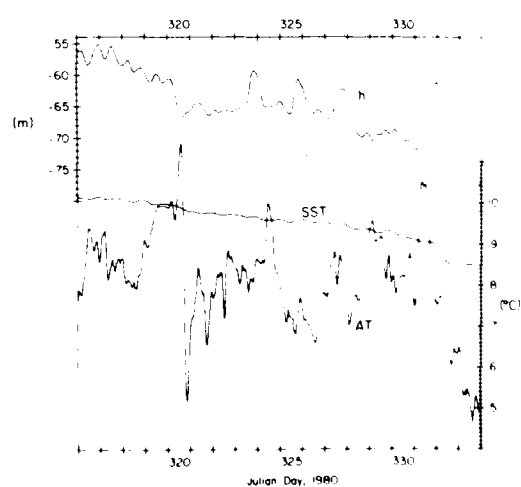


FIG. 3. Mixed-layer depth, h , and sea surface temperature, SST, from mooring B, and air temperature, AT, from mooring D. The mixed-layer depth is defined by a 0.2°C temperature change and the sea surface temperature was measured at a depth of 10 m.

layer depth with noticeably large decreases on days 320 and 332. The air temperature was almost always lower than the sea surface temperature, indicating that sensible heat flux accounted for part of the observed cooling trend and that the air just above the water surface was always unstably stratified.

b. Surface meteorology

The experiment was carried out with the aid of two vessels: the Canadian weather ship CCGS *Vancouver* stationed at Ocean Weather Station P (50°N, 145°W) and the NOAA ship *Oceanographer*, which operated in the vicinity of the surface moorings. Both ships made measurements of standard surface meteorological parameters including wind velocity, air pressure, and air, wet bulb, dew point and sea surface temperatures. In addition, measurements of the longwave and shortwave radiation fluxes were made from both ships (Gautier and Katsaros, 1984; Anonymous, 1981; Katsaros and Lind, 1985) and CTD casts were taken from the *Oceanographer* (Toole *et al.*, 1980).

Duplicate meteorological measurements from the two ships and mooring D allowed comparison and verification of some of the surface data. Air temperature measurements from both ships and the mooring agreed very well with no obvious biases. The same was true for comparisons of the mooring sea surface temperature with those from the *Vancouver*. The *Oceanographer*, however, reported surface temperature, measured at engine-room intake, that was nearly 0.5°C higher than at the surface buoy. This difference is attributed to the well-known positive bias of engine-room intake temperatures above true surface sea temperatures (Saur, 1963). Reynolds (1982) compared wind velocities from *Oceanographer* and mooring D and found that they agree quite well.

We used the air-sea temperature difference and the wind speed at mooring D to calculate the surface wind stress shown in Fig. 4. The wind speeds were adjusted to 10 m, and the stress was calculated using the bulk aerodynamic formulae of Large and Pond (1981). Several strong wind events are evident in the time series, especially the two storms on days 320 and 332 when wind stress magnitudes reached 0.9 and 1.3 Pa, respectively.

We used the meteorological data from mooring D and the ships to calculate the surface fluxes of sensible and latent heat from bulk formulae (Large and Pond, 1982). Figure 5 shows the computed heat fluxes together with estimates of the radiation flux component. Humidity data from *Vancouver* was used during *Oceanographer's* absence from the site, days 326 to 334. The net radiation fluxes shown in the figure are the daily averages of the sum of shortwave incoming, shortwave outgoing, longwave incoming, and longwave outgoing fluxes. The data comes from measurements taken on the *Oceanographer* when available (Katsaros

and Lind, 1985) and on the *Vancouver* otherwise (Anonymous, 1981). Over the period from day 316 through 333, the net surface heat flux averaged -86 W m^{-2} . The latent heat flux alone averaged -49 W m^{-2} ; this is twice as large as the net radiation flux, longwave plus shortwave (-26 W m^{-2}), and far larger than the sensible heat flux (-11 W m^{-2}). The latent heat flux contains isolated periods of large positive values due to warm, saturated air moving into the area and warming the ocean through condensation.

It is interesting to note the contrast between the storms on days 320 and 332 in terms of their associated heat fluxes. The day-320 storm produced an obvious feature in the heat flux curves of Fig. 5. The day-332 storm, however, created no outstanding features in the heat flux curves even though this storm coincided with the most outstanding changes in the sea surface temperature and mixed layer depth and had the strongest winds. Figure 6a, b shows the surface pressure analyses for the two days (Reed and Mullen, 1981). There are obvious differences between the two storm systems. The day-320 storm was a diffuse elongated low pressure system with a strong north-south frontal structure, while the day-332 storm was more nearly radially symmetric and very intense. The spatial scales of the two storms were similar. The effects they had at the experiment site were, however, quite different. The peak winds for day 320 were southerly, but for day 332 they were westerly. Other contrasts between the way the two storms affected the ocean at the moorings will emerge as we examine the heat and energy budgets in the following sections.

c. Surface analysis of wind stress and sea surface temperature

The large-scale wind stress field during STREX was computed using planetary boundary layer models (Brown and Liu, 1982) applied to the available synoptic data. We used data interpolated to a 100 km grid surrounding the STREX region (Lindsay and Brown, personal communication, 1983).

Sea surface temperatures on a similar grid, derived from 3-day averaged analyses by the Canadian Weather Service, were used to prepare the maps in Fig. 7a-f. The contour maps exhibit, individually, the WSW to ENE slope of surface isotherms in the region and, collectively as a time series, the cooling trend over the STREX period. This data was used to estimate horizontal temperature gradients needed to calculate the advective contributions to the local heat and energy budgets at the thermistor chain mooring site (Sections 3 and 4).

3. The heat budget

In this section we investigate the heat budget of the upper ocean during STREX. We shall see that the heat content decrease measured at the thermistor chains is

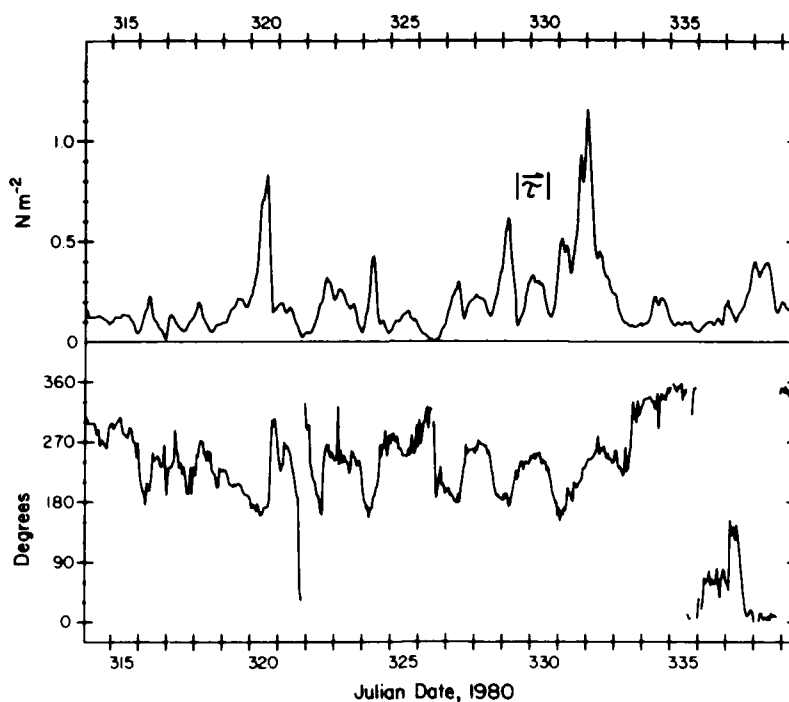


FIG. 4. Wind stress (upper panel) and direction from which the wind blew (lower panel) at mooring D.

more than twice as large as the total surface heat loss. We attempt to reconcile this imbalance by estimating the advective contributions to the budget. This attempt is reasonably successful. It turns out that there are two advective events in the STREX data record that account for the heat content-surface exchange imbalance.

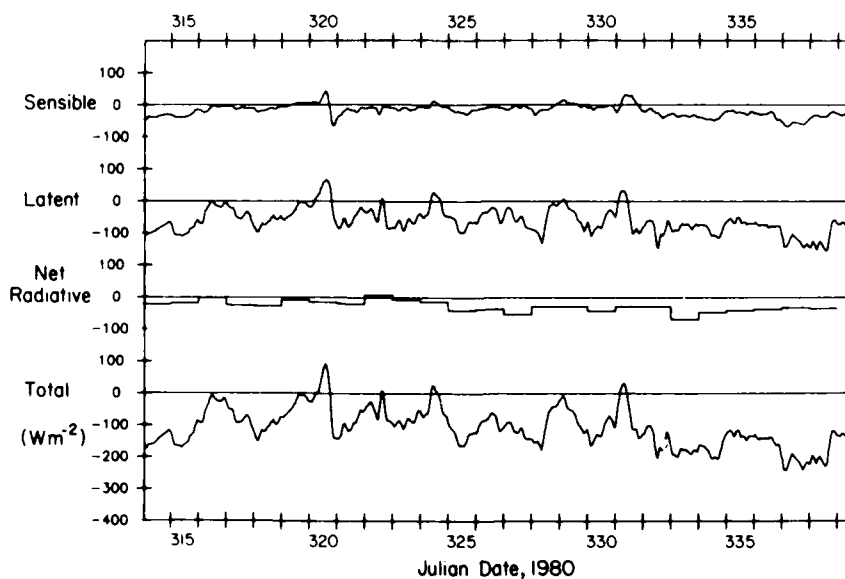


FIG. 5. Surface fluxes of sensible and latent heat at mooring D smoothed with a 12.4 hour filter, daily averages of the net radiative heat flux onboard the *Oceanographer* and *Vancouver* (days 326 to 334), and the algebraic total of all three components. Note the sharp frontal structure indicated by the sensible and latent heat flux curves on day 320.

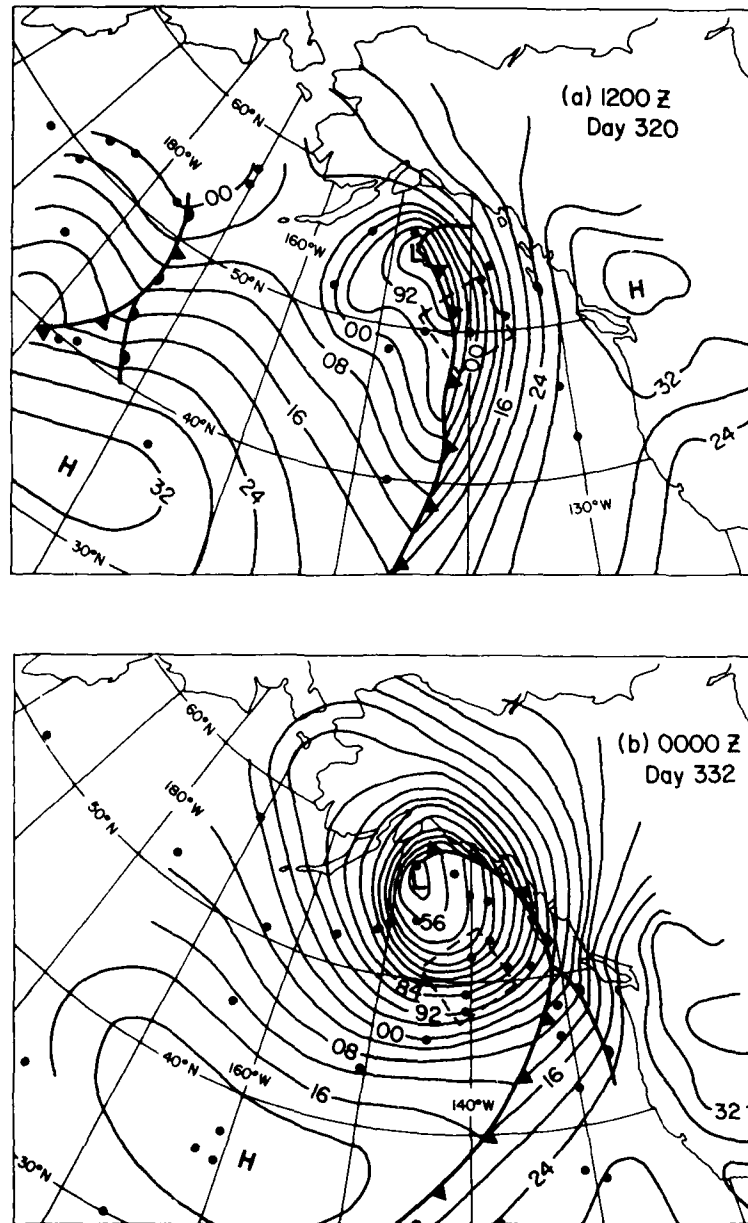


FIG. 6. Surface pressure isobars for (a) 1200 GMT on day 320 and (b) 0000 GMT on day 332 (Reed and Mullen, 1981). Dots indicate locations of data reports used to construct the pressure fields including the two ships involved with STREX, ships of opportunity, and five stationary NDBO buoys. The experiment site is approximately 50°N, 140°W. The dashed box indicates the area used to calculate average wind stress curl with this data.

The establishment of an approximate heat balance is a prerequisite for estimating potential energy changes and relating them to turbulent kinetic energy production changes in Section 4.

The heat content between the surface and fixed depth D is defined by

$$H(t, D) = \rho_0 c \int_D^0 T dz \quad (3.1)$$

where ρ_0 and c are average seawater density and heat capacity at constant pressure, respectively. The heat balance of the water column is given by

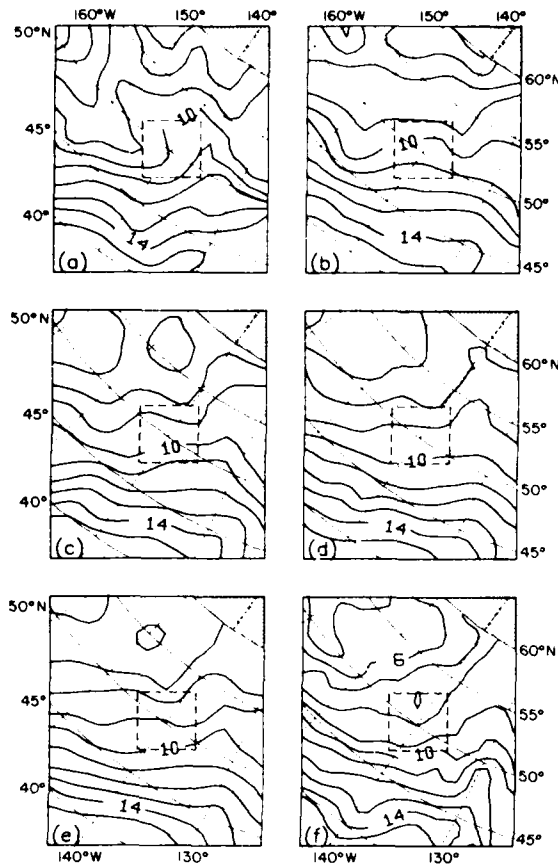


FIG. 7. Sea surface temperature isotherms from the large-scale grid for days (a) 316–318, (b) 319–321, (c) 322–325, (d) 326–328, (e) 329–332, and (f) 333. The 6, 10, and 14 degree contours are labeled and the spacing is 1°C . The dashed box indicates the area used to calculate horizontal temperature gradients.

$$\partial_t H = A + Q_0 \quad (3.2)$$

where

$$A = -\nabla \cdot \rho_0 c \int_D T u dz + \rho_0 c T \rho w|_D \quad (3.3)$$

is the vertically integrated divergence of heat advection and

$$Q_0 = -\rho_0 c \overline{wT}(0) - q(0) \quad (3.4)$$

is the total heat flux just below the water surface, composed of sensible heat plus radiant flux $q(0)$. Our notation follows that of Davis *et al.* (1981a), which may be consulted for the derivation of (3.2). It has been assumed that $w(0) = 0$ and that D is sufficiently deep so that the turbulent and radiative fluxes vanish there. We examined the heat balance for $D = 90$ m, a depth well below the mixed layer and within that part of the upper water column covered by our instruments.

One of the three components in the heat balance, the total surface flux, Q_0 , was described in Section 2

and is shown in Fig. 5. The heat content, H , was calculated from the thermistor chain records using a trapezoidal integration of the discrete temperature measurements. The changes in heat content we observed averaged -200 W m^{-2} for the period from Julian day 316 to 333. This is twice as large as the cooling at the surface described in Section 2, although it is consistent with Tabata's (1965) findings of an average 70 W m^{-2} deficit in surface cooling for this season between 1956 and 1961. This discrepancy in the one-dimensional balance puts a premium on estimating the other component in the heat budget, namely advection.

Advection has traditionally been the most elusive part of the heat budget. To our knowledge, no synoptic measurements of temperature and velocity with depth have ever been made that would allow direct calculation of A in (3.3). We are forced to estimate the advective contribution indirectly. Various methods have been employed in the past ranging from a neglect of A on the basis of historical current and temperature data (Denman and Miyake, 1973) to approximating the vertical contribution only, and neglecting horizontal effects, based on spatial measurements of $|\nabla T|$ (Davis *et al.*, 1981a). Each of the arguments for the neglect of advection or some part of it is based on averaged gradients and velocities appropriate to seasonal time scale changes in mixed layer properties. Though these arguments appear valid *ex post facto* from success of the closures of the heat budget achieved by making them, our data indicate that the situation is quite different during the fall stormy season at midlatitudes. We find that storms can produce pulses in the advection terms on time scales of several days that can be significant in the heat budget averaged over several weeks.

The advective contribution consists of two parts: horizontal advection by surface geostrophic currents that are nearly horizontally nondivergent, and advection by directly wind-driven surface currents that can be composed of both a nondivergent part giving rise to horizontal transport and a divergent part giving rise to vertical transport. Thomson (1971) showed that geostrophic currents in this region are, on the average, in the east-northeast direction at 1 cm s^{-1} and are nearly parallel to the surface temperature isotherms. Although the CTD surveys conducted during STREX were not sufficiently dense in time or space to give good estimates of geostrophic current, the data that exists confirm Thomson's estimate of 1 cm s^{-1} for surface currents relative to 1500 db. These currents tend to be aligned across the temperature gradient and hence are ineffective in transporting heat.

Tabata (1965) calculated the average temperature change at Station P for 1956–61 due to geostrophic transports and found it to be 0.26°C per month. He found the geostrophic advection to be higher during summer than winter. He also found the wind-forced Ekman contribution to advection to be largest during winter. On this basis, we shall neglect the advection of

heat due to geostrophic currents for the 18-day winter period of STREX.

We propose to estimate surface Ekman transport by

$$\int_{-h}^0 \mathbf{u}_e dz = -\mathbf{z} \times \left(\frac{\boldsymbol{\tau}_0}{\rho_0 f} \right) \quad (3.5)$$

where \mathbf{u}_e is the surface Ekman velocity, $\boldsymbol{\tau}_0$ is the surface wind stress, and h is the mixed layer depth; horizontal stress at the base of the mixed layer has been assumed to be negligible. If the Ekman transport is divergent, it leads to an upwelling velocity at the mixed layer base.

$$w_{-h} = \mathbf{z} \cdot \text{curl} \left(\frac{\boldsymbol{\tau}_0}{\rho_0 f} \right) \quad (3.6)$$

Accelerations are neglected in deriving (3.5) and (3.6). Their inclusion leads to inertial oscillations about the longer period Ekman velocity fields. One may show (see the Appendix) that averaging the time-dependent inertial solutions over a pendulum-day yields Eqs. (3.5) and (3.6) again, where \mathbf{u}_e , w_{-h} , $\boldsymbol{\tau}_0$ are now pendulum-day average quantities. Hence the use of the "steady" equations (3.5), (3.6), to estimate Ekman currents, even for synoptic wind events, is well justified.

By identifying $\int T u dz = \bar{T} \int \mathbf{u}_e dz$ where \bar{T} is the vertically-averaged temperature of the surface layer, and $w_{-h} = w_{-D}$, Eq. (3.3) can be written

$$A = A_V + A_H \quad (3.7a)$$

where

$$A_V = c(T_D - \bar{T}) \mathbf{z} \cdot \text{curl}(\boldsymbol{\tau}_0/f) \quad (3.7b)$$

$$A_H = c \mathbf{z} \cdot \boldsymbol{\tau}_0/f \times \nabla \bar{T} \quad (3.7c)$$

Were there no horizontal temperature gradient, the nonzero term A_V would represent the export of heat due to upwelling of cold water. On the other hand, were the mixed layer motion nondivergent, the term A_H would represent advection of heat by horizontal flow across the temperature gradient. The terms in (3.7) were calculated using the wind stress and temperature fields described in Section 2. Temperature gradient $\nabla \bar{T}$ was approximated by ∇T_0 where $T_0(x, y, t)$ was the sea surface temperature obtained from the large-scale grid (Fig. 7a-f). Even though the data coverage for the large-scale analyses was sparse (see the data points in Fig. 6a, b), the SST gradients were robust enough to produce consistent pictures on the scale of a few hundred kilometers. In contrast to this, the 20 km separation between thermistor chain moorings at the experiment site was not enough to reliably determine the SST gradients beyond instrument noise levels.

The total advective contribution was calculated according to (3.7a) (after rearranging terms), and the vertical component according to (3.7b). The horizontal component was calculated by difference, i.e., $A_H = A - A_V$. The required horizontal vector fields then appear only in the form of curls. These were evaluated from

the large-scale data by application of Stokes' circulation theorem

$$\iint_S \mathbf{z} \cdot \text{curl}(\boldsymbol{\tau}_0/f) dS = \oint_c (\boldsymbol{\tau}_0/f) \cdot d\mathbf{c} \quad (3.8)$$

where S is some suitable averaging area and c is its perimeter. The right side of (3.8) is evaluated from an obvious finite-grid rule of integration. We chose S to be a 600 km square (i.e., 6×6 grid points centered on the mooring site). We experimented with smaller grids (4×4 , 2×2), but this larger one seemed a sensible compromise between the ideal of $S \rightarrow 0$ and having a large enough number of points on the circumference of S to effect some averaging of atmospheric mesoscale noise. Large *et al.* (1985) suggest that the synoptic scale in this area is a few hundred kilometers, based on data from drifting thermistor chains, so it is likely that our large averaging square underestimates curl at a point. The size of the averaging square is indicated in Fig. 6a, b and 7a-f by the dashed box.

Figure 8a shows the time series of heat advection components: horizontal (dot-dashed), vertical (dotted), and their sum (dashed). Figure 8b shows the heat content of the upper 90 m at thermistor chain mooring B (solid line), the cumulative surface heat flux, $\int' Q_0 dt$ (upper dashed line), cumulative advection, $\int' A dt$ (lower dashed line), and their sum (dot-dashed line). The starting value of each quantity on the ordinate is arbitrary; the curves agree if their slopes match. Table 1 gives a summary of daily-averaged surface heat flux, advection, and heat content change for the STREX period. The most striking features in Fig. 8a is the advective peaks associated with the storms on days 320 and 332. Except for these two days, the total advection is small and changes sign often, producing a negligible contribution to the overall budget. But with the inclusion of these tremendous peaks, the mean advection over 18 days is -68 W m^{-1} which, when combined with the average heat flux at the surface, balances the mean changes in heat content to within 23% (see Table 1). The average advection is 80% of the average of the total surface flux: this is almost entirely due to the contribution from two individual days! Figure 8b shows the roughly equal importance of advection and surface flux in the heat balance over 18 days, and the episodic character of advection, coming in two marked events, in contrast with the fairly steady surface heat flux. Only the episodes of advection can account for the episodic heat content changes.

Comparison of Fig. 8a with the synoptic analyses of Fig. 6 gives some insight into the nature of the advection itself. The advective partitioning between vertical and horizontal components is different for the two storms. The day-320 peak is made up of nearly all vertical advection, that is, Ekman suction of cold water from below $z = -D$. The day-332 peak, however, is composed of approximately equal amounts of Ekman

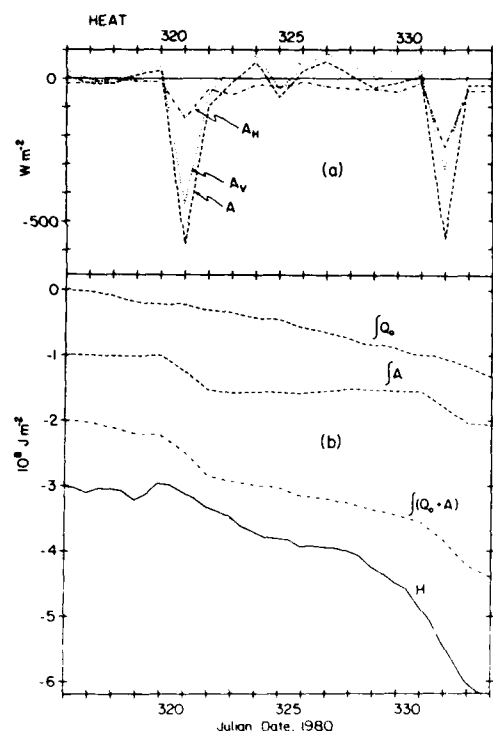


FIG. 8. (a) Daily estimates of the vertical, A_v , and horizontal, A_h , advection of heat and their algebraic sum, A , and (b) the time history of the cumulative surface heat flux, $\int Q_0 dt$, cumulative heat advection, $\int A dt$, their algebraic sum, $\int (Q_0 + A) dt$, and the daily averaged vertical integral of heat content to 90 m, H . The cumulative and vertically integrated curves in panel (b) are relative to an arbitrary reference level; it is the slopes of these curves that are important. Note the large advective peaks on days 320 and 332 and how they are responsible for making the estimated total cumulative curve more closely match the observed vertically integrated heat content.

suction and horizontal advection due to net horizontal movement of surface water across isotherms. The different advective characters of the two storms is reflected in their synoptic structure relative to the experiment site. Peak winds for the day-320 storm were southerly shifting abruptly to northerly with the passage of the front (Fig. 4). This produced a net Ekman transport to the east and then west, nearly parallel to the surface isotherms (Fig. 7b), and therefore contributed little to the horizontal advection. In contrast, the day-332 peak winds were southwesterly and produced a net Ekman transport parallel to the mean oceanic temperature gradient (Fig. 7e) and so made a large contribution to the horizontal advection of heat. This contrast shows that the horizontal advection at a particular location depends on having cross-isotherm Ekman transport produced by along-isotherm wind. This condition is sensitive to the structure of a storm and the proximity of its passage (see Fig. 6a, b) so that points separated by only a few hundred kilometers may experience quite different advection.

Vertical advection, too, makes an important contribution to the heat budget. It depends on a surface wind pattern favorable to producing upwelling. Despite several peaks in the wind stress magnitude in Fig. 4, Fig. 8a shows only two events that had local wind stress curl large enough to produce significant upwelling.

Large *et al.* (1986) suggest a rule of thumb for uncertainty of 10 W m^{-2} per component of the surface heat flux, which gives an additive uncertainty of 30 W m^{-2} for the net surface flux, Q_0 . This error grows for the cumulative surface heat flux; after ten days the error amounts to about $0.25 \times 10^8 \text{ J m}^{-2}$ (25% of one division in Fig. 8b) and after 18 days to nearly $0.50 \times 10^8 \text{ J m}^{-2}$ (50% of one division in Fig. 8b). The discrepancy in the heat budget is within this uncertainty.

Large *et al.* (1986) also investigated the advective contributions to the heat budget with drifting thermistor chain buoys in an area 500 km southwest of our moorings. They inferred water movements from the buoy tracks and relative velocities from the shape of the subsurface thermistor and pressure sensor chains. Their conclusions contrast with ours. They find that horizontal advection in the mixed layer was not a significant part of the heat budget for their region. Their buoys, however, tended to drift along the surface isotherms, thereby diminishing the effect of horizontal advection. Also, they form their balance estimates over a long time period so that they do not discern episodic synoptic events. They also make the point that vertical advection from below about 120 m, within the permanent halocline, would bring up water that is too salty to be cancelled by the $0.005 \times 10^{-3}/\text{month}$ dilution attributed to the mean excess of precipitation over evaporation. This means that the upwelling water

TABLE 1. Daily average surface heat flux, Q_0 , and change in heat content, dH/dt , and the 0000 GMT estimate of heat advection, A . The units are W m^{-2} .

Julian day	Q_0	A	dH/dt
316	-35.8	7.7	-99.2
317	-77.2	-19.7	49.6
318	-109.4	-18.8	-181.8
319	-36.4	13.4	214.9
320	-8.6	28.7	-132.3
321	-97.4	-582.6	-231.5
322	-49.5	-99.5	-165.3
323	-85.3	-14.1	-264.5
324	-36.3	56.7	-148.8
325	-129.6	67.5	-148.8
326	-89.2	26.4	-16.5
327	-113.1	59.8	-49.6
328	-99.4	10.3	-264.5
329	-68.6	-32.5	-281.1
330	-120.2	-16.0	-396.8
331	-60.8	9.9	-628.3
332	-141.4	-565.6	-677.9
333	-184.2	-25.7	-165.3
18-day means:	-85.7	-68.3	-199.3

below the mixed layer and above the halocline must be moving along nearly horizontal trajectories as it is entrained.

4. Turbulent kinetic energy

When the sea surface is cooled or agitated by the wind, turbulent kinetic energy is produced by fluctuating buoyancy forces working with vertical motions or by turbulent stress working on the sheared motion. The part of this turbulent kinetic energy that is not dissipated is available for increasing the potential energy of the surface layer by entraining dense water from below and, in effect, raising its center of mass by mixing it into the surface water. The production terms of turbulent kinetic energy, and its dissipation, are difficult to measure with accuracy. Instead, parameterizations of these terms, supported by theoretical and dimensional arguments relating them to bulk parameters that characterize the inputs, are relied on (Kraus and Turner, 1967; Niiler and Kraus, 1977). Often the parameterizations can be checked in laboratory experiments (e.g., Turner and Kraus, 1967; Kato and Phillips, 1969; Moore and Long, 1971; Kantha *et al.*, 1977; Deardorff *et al.*, 1969) in which changes in potential energy are compared to the proposed dependence on the bulk parameters and used to estimate unknown coefficients.

In principle, this can be done also with suitable field experiments. The difficulty with this approach lies in the impossibility, contrasted with the laboratory, of control of external conditions: oceanic variability and complexity on all scales lead to statistically imprecise estimates of the desired terms. Also, some important contributing terms, especially advection, that are absent in controlled laboratory experiments can only be estimated indirectly as we have already seen with the heat balance. The advantage of the field experiments is their obvious direct relevance to mixed layer dynamics: unlike laboratory experiments, they are conducted at the appropriate Reynolds and Peclet numbers and are not susceptible to "infection" by secondary circulations as in the all too finite laboratory vessels.

Davis *et al.* (1981b) expounded the theory of the turbulent kinetic energy (TKE) balance necessary for relating rate of change of potential energy of the upper ocean water column to kinetic energy generation and dissipation and their parameterizations. We need not repeat this here, except to emphasize that the rate of turbulent working of buoyant fluctuations against gravity, or buoyancy flux $g\overline{\rho'w'}$, is estimated from the vertically integrated heat balance and assumption of a stable T - S relationship; hence the establishment of an at least approximate heat budget is a necessary requirement for the strategy to succeed.

The potential energy of the water column above $z = -D$, given by

$$P(t, D) = g \int_D^0 (z + D) \rho_e dz, \quad (4.1)$$

where $\rho_e = \rho - \rho_0$ is the excess density above a reference density, is related to sources and sinks by

$$\partial_t P = B + A_p + G_0 + S - E, \quad (4.2)$$

where

$$B = \frac{\alpha g}{c} \left[-Q_0 D + \int_D^0 q(z) dz \right], \quad (4.3)$$

$$A_p = -g \nabla \cdot \int_D^0 \rho_e \mathbf{u}(z + D) dz + g \int_D^0 \rho_e w dz, \quad (4.4)$$

$$G_0 = -w' [p' + \rho_0 (\mathbf{u}' \cdot \mathbf{u}' + w'^2)/2]_0, \quad (4.5)$$

$$S = - \int_D^0 \rho \overline{\mathbf{u}' w'} \cdot \partial_z \mathbf{u} dz, \quad (4.6)$$

$$E = \int_D^0 \rho \epsilon dz. \quad (4.7)$$

Term B in (4.2) represents the effect on potential energy of surface heating or cooling and penetrative radiation: when cooling ($Q_0 < 0$), a part of $(\alpha g/c)Q_0 D$ is the energy supplied by convection. This term is readily calculated from the net surface heat flux, Q_0 , described in Section 2 and from $q(z)$ parameterized by

$$q(z) = q(0) \{ [0.77 \exp(z/1.5)] + [1 - 0.77 \exp(z/14.0)] \}, \quad (4.8)$$

for z in meters, measured negatively downwards (Paulson and Simpson, 1977). The term A_p represents the advection of potential energy. The term G_0 is the surface flux of turbulent kinetic energy, which is held to be proportional to $\rho_0 u_*^3$, where u_* is the surface friction velocity $|\tau_0/\rho_0|^{1/2}$ (Kraus and Turner, 1967; Davis *et al.*, 1981b). Term S is the shear production integrated vertically. Lacking current profile measurements, we are unable to estimate it directly. We proceed by provisionally neglecting it; but we shall return to this point later.

As noted, convective production due to surface cooling is already a part of B . For a homogeneous mixed layer this production term amounts to

$$C = \frac{\alpha g}{4c} h(|Q_0| - Q_0). \quad (4.9)$$

Term E is the vertical integral of kinetic energy dissipation. We hold that it acts to suppress a fixed fraction of the energy produced by the dominant turbulent kinetic energy production mechanisms. Hence it is proportional to C or G_0 in (4.2), whichever is dominant, and the potential energy evolution is given by

$$\partial_t P = B + A_p + G_0^* - m_c C \quad (4.10)$$

where

$$G_0^* = m_0 \rho_0 u_*^3. \quad (4.11)$$

The measurements reported by Davis *et al.* (1981b)

suggest $m_0 = 0.5$, while Deardorff *et al.*'s (1969) laboratory measurements give $m_c = 0.83$.

Advection A_p is calculated in a fashion analogous to the corresponding term in the heat balance. We assume that horizontal velocity is uniform in the mixed layer, of depth h , and given by the Ekman formula (3.5); horizontal velocity is neglected below the mixed layer. The corresponding vertical velocity grows linearly from zero at the surface to the base of the mixed layer where it is given by (3.6). Beyond the base it remains approximately constant. These assumptions of slab-like mixed layer velocity are more stringent than were required for the heat balance, where only the vertical integral of horizontal velocity mattered, because temperature is so nearly uniform in the mixed layer. The quantity A_p can be separated into horizontal and vertical components A_{pH} , A_{pV} , analogous to the heat advection terms [Eq. (3.7)] except for an additional dependence on the mixed layer depth that enters because of the factor z in (4.1). We shall save space by not writing them down here.

The quantities in the potential energy balance are correctly written in terms of density $\rho(T, S)$. To determine this salinity is required as well as temperature. This is not available from the thermistor chains. However, CTD profiles taken during November and December 1980, in the vicinity of the experiment location from the *Oceanographer* exhibit a quite stable and tight relationship between temperature and salinity above 90 m depth. Figure 9 shows the envelope for the T - S curves from 32 CTD casts taken between Julian days 311 and 337. Above 6.5°C (90 m) salinity is well represented by a linear function of temperature. A best fit line through the T - S envelope in this region was used to represent that function. This was then used to infer density from the thermistor chain temperature time series.

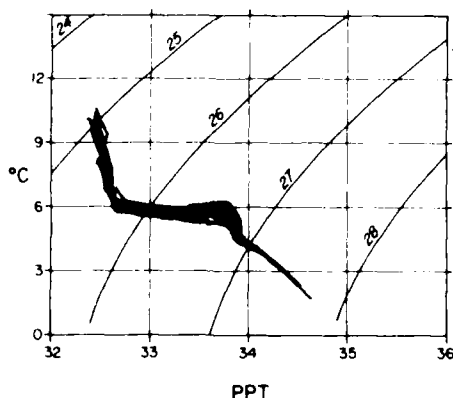


FIG. 9. T - S relations from 32 CTD casts taken onboard the *Oceanographer* between Julian days 311 and 337. The linear relation between S and T above 6.5°C (~ 90 m) was used to predict S from T for this temperature (depth) range.

TABLE 2. Daily average surface production G_0^* , net buoyancy flux B' , and change in PE, dP/dt , and the 0000 GMT estimate of PE advection, A_p . The units are mW/m^2 .

Julian day	G_0^*	A_p	B'	dP/dt
316	0.6	0.1	0.2	2.4
317	0.7	0.5	1.7	-0.4
318	0.9	0.3	2.3	3.0
319	1.3	0.0	0.8	4.6
320	4.6	0.2	0.4	11.1
321	1.2	7.2	1.9	3.5
322	1.7	1.5	1.6	3.7
323	2.3	0.9	1.8	5.8
324	1.2	0.4	1.3	2.1
325	0.8	1.1	3.8	2.8
326	0.5	0.1	2.2	4.1
327	1.5	0.2	2.0	5.9
328	1.1	0.4	2.5	5.7
329	2.9	0.8	1.7	7.7
330	1.6	0.8	2.4	13.9
331	6.9	0.1	1.1	12.7
332	7.3	9.3	2.6	32.4
333	0.6	0.6	3.7	5.8
18-day means:	2.1	1.3	2.0	7.1

Each of the terms on both sides of (4.10) can be computed from the STREX data and compared. Table 2 gives a summary of the daily-averaged values of G_0^* , B' (the net buoyancy production, $=B - m_c C$), potential energy advection, A_p , and the change in P . Figure 10a shows the time series of the advection estimates. The features are very similar to the heat advection estimates in Fig. 8a; the advection is small except on two occasions associated with storms on days 320 and 332. The day-320 event is a result of mostly vertical advection, while the day-332 event is composed of nearly equal amounts of vertical and horizontal advection. Note that though heat and turbulent mechanical energy terms have the same units, the latter is five orders of magnitude smaller than the former.

Figure 10b shows the potential energy of the upper 90 m at the thermistor chain (solid line), the cumulative surface production of TKE [$\int_0^t G_0^* dt$ (using $m_0 = 0.5$)], the cumulative advection ($\int_0^t A_p dt$), and the cumulative net buoyancy production [$\int_0^t B' dt$ (using $m_c = 0.83$)]. The last term is the difference between the total cumulative buoyancy production (upper dotted line) and the dissipation, taken to be proportional to that production, (lower dotted line). The beginning positions on the ordinate of traces on this figure are arbitrary; the curves have been offset in the vertical for clarity. A successful closure of the TKE budget is obtained when the slope of the total cumulative production curve (dot-dashed) matches that of the vertically integrated potential energy curve. This figure shows a reasonable closure of the TKE budget over 18 days, particularly for the periods prior to the day-320 storm and after the day-332 storm. The storms create large, episodic increases in the vertically integrated potential energy that are not totally reproduced by the estimated pro-

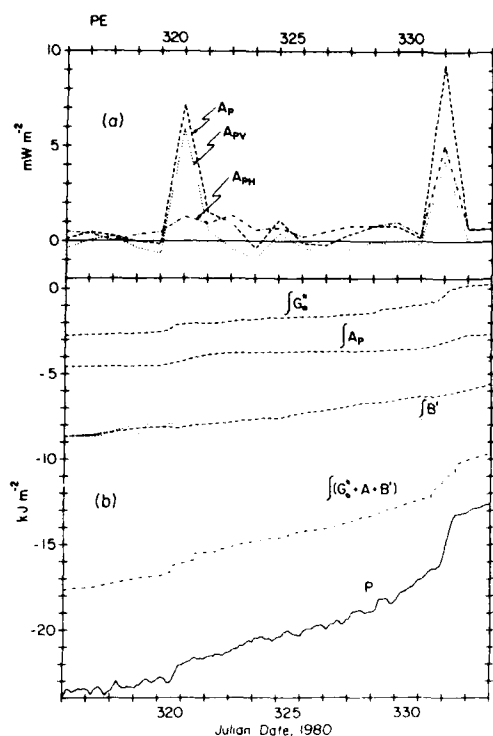


FIG. 10. (a) Daily estimates of the vertical, A_{pv} , and horizontal, A_{ph} , advection of potential energy and their algebraic sum, A_p , and (b) the time history of the cumulative surface wind stirring, $\int G_s^* dt$, cumulative potential energy advection, $\int A_p dt$, cumulative buoyancy production, $\int B' dt$, —composed of the production due to surface cooling and penetrating radiation (upper dotted line) minus the dissipation proportional to that production (lower dotted line)—their algebraic sum, $\int (G_s^* + A_p + B') dt$, and the vertical integral of potential energy to 90 m, P . The cumulative and vertically integrated curves in panel (b) are relative to an arbitrary reference level; it is changes in these curves that are important. Note how peaks in advection and wind stirring combine to produce the jumps in the estimated total cumulative curve which mimic the jumps in P on days 320 and 332.

duction terms, particularly for the day-332 storm where only one half of the increase observed in the density record is accounted for by the TKE production terms included in the budget. The figure also shows the difference between the three production terms. Both the surface wind stirring and advection terms exhibit impulsive jumps associated with the two storms but the buoyancy flux term—composed mainly of the net surface cooling—is a fairly steady function. Advection and wind stirring are, in some combination, necessary to reproduce the episodic increases observed in the vertically integrated potential energy associated with the two storms. However, the advection terms cannot be estimated with sufficient accuracy to attempt improved estimates of either m_0 or m_1 . From the viewpoint of modeling, it is still remarkable that potential energy

changes may be no less due to advection than to turbulent production of TKE.

An uncertainty in the excess density can be estimated from uncertainties in the thermistor temperatures and in the salinity derived from the best-fit linear T - S relationship above 90 m. The spread in the T - S diagram of Fig. 9 suggests an uncertainty of about 0.08×10^{-3} in inferring salinity from temperature. This, together with the thermistor errors, leads to an uncertainty of 0.07 kg m^{-3} for the excess density, and about $2.80 \times 10^3 \text{ J m}^{-2}$ (2.8 divisions in Fig. 10b) for the vertically integrated potential energy. The discrepancy in the TKE budget is within this uncertainty. The closure of the TKE budget is poorest for the time periods associated with the two major storms, particularly the second, day-332, storm. Ignoring the potential energy uncertainties, the buoyancy flux term B' is a very steady, nonepisodic component of the budget and as such is not a good candidate to explain the excess in the observed vertically integrated potential energy jumps over the predicted increases. The discrepancies are more likely the result of underestimating either the advection or the wind stirring terms, or both, because each of these terms exhibits episodic increases during the storm periods.

There is one important, additional component of the TKE budget that could explain the discrepancies in the balance. It is the neglected shear production term (4.8). Sheared currents in the water column contribute to the TKE of the layer, particularly inertial currents with shear concentrated at the base of the mixed layer. Shear production would be episodic in character and very likely associated with storms. D'Asaro (1985) examined and modeled the inertial current structure from expendable current profiler drops taken from the *Oceanographer* during STREX, paying close attention to the day-320 storm. That storm acted to change the current shear at the mixed layer base by 30 cm s^{-1} , but the preexisting currents were such that the overall shear was actually reduced. Hence, shear production of TKE was not a factor in the day-320 storm. Current profiles were not available for the day-332 storm, so it is not possible to assess what role shear production played in the TKE budget during that period. The poor closure of TKE on that day may indicate an overlooked energy source such as shear production.

5. Summary

In this paper, we outlined and demonstrated a method for incorporating large-scale wind stress data and estimates of sea surface temperature gradients into the local budgets of upper-ocean heat and TKE through advection terms. We obtained a reasonable balance for the heat and TKE budgets of the upper 90 m of the water column at the site of thermistor chain moorings in the northeast Pacific Ocean. The rate of change of heat content averaged -200 W m^{-2} over 18 days, while

the net surface heat flux averaged -86 W m^{-2} . We were able to form estimates of the large-scale advection that we found to be significant during two strong storms. The 18-day average advection was -68 W m^{-2} , which contributes to balance the budget within 23%. Our findings confirm Tabata's (1965) observations about the winter heat balance at Station P.

The changes observed in the vertically integrated heat content and potential energy are very episodic. For the heat budget this episodic character can only be explained by advection. The turbulent kinetic energy budget contains source terms from the vertical buoyancy flux, the wind stirring at the surface, and current-shear production. The last two of these are episodic in character. Our data show that advection and wind stirring are necessary to account for the episodic changes in the vertically integrated potential energy associated with the storms. The role of shear production is uncertain. D'Asaro (1985) determined that the current structure before day-320 was such that the storm on that day acted to decrease the current shear so that shear production was not a factor for that storm. No data exist to determine the role of shear production for the second, day-332, storm.

The calculations described here illustrate the importance of advection to understanding the response of the upper ocean to atmospheric forcing. The advection estimates we have made are quite rudimentary; they could be improved by better estimates of surface wind distribution on synoptic and mesoscales, and better estimates of temperature gradients. The potential energy storage estimates could be greatly improved by time series measurements of salinity (conductivity) as well as temperature. Salinity effects on density can be significant, and should be monitored, and the budget of salt could be independently checked.

Acknowledgments. We are grateful to the scientists and technicians of O.S.U. Buoy Group, the Pacific Marine Environmental Laboratory (NOAA), and the crew of the R. V. *Oceanographer* for assistance with the preparation, deployment, and recovery of the thermistor chains. Drs. M. Reynolds, K. Katsaros, and R. Brown, to whom we are grateful, provided the surface time series from mooring D, the shortwave radiation data, and the analyzed surface stress fields, respectively. Dr. J. Richman provided helpful discussion. The research was supported by grants from the Division of Ocean Sciences, National Science Foundation, and the Office of Naval Research under Contract N00014-84-C-0218.

APPENDIX

The Quasi-steady Ekman Approximation

Consider the time-dependent momentum and mass conservation equations for a slab layer of thickness h driven by a wind stress $\tau(x, t)$:

$$\partial_t Q + i f Q = \rho_0^{-1} (\tau^x + i \tau^y), \quad (\text{A1})$$

$$w_{-h} = \text{Re}(\partial_x - i \partial_y) Q, \quad (\text{A2})$$

where

$$Q = hu + i hv. \quad (\text{A3})$$

The general solutions of (A1), (A2) are easily written (Phillips, 1966):

$$Q = \rho_0^{-1} \int_0^t [\tau^x(t') + i \tau^y(t')] e^{i f (t-t')} dt', \quad (\text{A4})$$

$$w_{-h} = \rho_0^{-1} \text{Re} \int_0^t (\partial_x - i \partial_y) [\tau^x(t') + i \tau^y(t')] e^{i f (t-t')} dt'. \quad (\text{A5})$$

If these expressions are averaged over n pendulum days between times $t - 2\pi n/f$ and t , we obtain:

$$\overline{hu} + i \overline{hv} = \overline{Q} = (i f \rho_0)^{-1} (\overline{\tau^x} + i \overline{\tau^y}) - (-1)^n (i f \rho_0)^{-1} \times \int_0^t \tilde{\phi}(\omega) e^{-i \omega (t - n\pi/f)} \text{sinc}[(\omega - f)n\pi/f] \frac{d\omega}{2\pi}, \quad (\text{A6})$$

$$\overline{w_{-h}} = \mathbf{z} \cdot \nabla X \left(\frac{\tau_0}{\rho_0 f} \right) - \text{Re}(-1)^n (i f \rho_0)^{-1} \times \int_0^t \tilde{\psi}(\omega) e^{-i \omega (t - n\pi/f)} \text{sinc}[(\omega - f)n\pi/f] \frac{d\omega}{2\pi}, \quad (\text{A7})$$

where $\tilde{\phi}(\omega)$ is the direct Fourier transform of $\tau^x(t) + i \tau^y(t)$,

$$\tau^x + i \tau^y = \int_0^t \tilde{\phi}(\omega) e^{-i \omega t} \frac{d\omega}{2\pi}, \quad (\text{A8})$$

$$\tilde{\psi}(\omega) = (\partial_x - i \partial_y) \tilde{\phi}(\omega). \quad (\text{A9})$$

The first terms on the right of (A6), (A7) are the usual "steady" forms for the Ekman transport and divergence, although here they are replaced by time-averaged quantities. The remaining time-dependent contributions consist of fluctuations driven by a frequency band of the rotary wind of width f/n centered on the (clockwise) inertial frequency f ; this is the effect of the $\text{sinc}[(\omega - f)n\pi/f]$ spectral window. These can be reduced by increasing n , which reduces the bandwidth of admitted wind-driven near-inertial fluctuations. They are in any case small if subinertial variance of the wind dominates near-inertial variance.

REFERENCES

- Anonymous, 1981: Radiation summary. Atmospheric Environment Service, Toronto, Canada.
- Brown, R. A., and W. T. Liu, 1982: An operational large-scale planetary boundary layer model. *J. Appl. Meteor.*, **21**, 261-269.
- Camp, N. T., and R. L. Elsberry, 1978: Oceanic thermal response to strong atmospheric forcing. Part II: The role of one-dimensional processes. *J. Phys. Oceanogr.*, **8**, 215-224.
- D'Asaro, E. A., 1985: Upper ocean temperature structure, inertial currents, and Richardson numbers observed during strong meteorological forcing. *J. Phys. Oceanogr.*, **15**, 943-962.

- Davis, R. E., R. A. deSzoeke, D. R. Halpern and P. P. Niiler, 1981a: Variability in the upper ocean during MILE. Part I: The heat and momentum balances. *Deep-Sea Res.*, **28**, 1427-1451.
- , —, and P. P. Niiler, 1981b: Variability in the upper ocean during MILE. Part II: Modeling the mixed layer response. *Deep-Sea Res.*, **28**, 1453-1475.
- Deardorff, J. W., G. E. Willis and D. K. Lilly, 1969: Laboratory investigation of non-steady penetrative convection. *J. Fluid Mech.*, **35**, 7-31.
- Denman, K. L., and M. Miyake, 1973: Upper layer modification at Ocean Station Papa: Observations and simulation. *J. Phys. Oceanogr.*, **3**, 185-196.
- Elsberry, R. L., and N. T. Camp, 1978: Oceanic thermal response to strong atmospheric forcing. Part I: Characteristics of forcing events. *J. Phys. Oceanogr.*, **8**, 206-214.
- Emery, W. J., 1976: The role of vertical motion in the heat budget of the upper northeastern Pacific Ocean. *J. Phys. Oceanogr.*, **6**, 299-305.
- Fleagle, R. G., M. Miyake, J. F. Garrett and G. A. McBean, 1982: Storm transfer and response experiment. *Bull. Amer. Meteor. Soc.*, **63**, 6-14.
- Gautier, C., and K. B. Katsaros, 1984: Insolation during STREX. Part I: Comparisons between surface measurements and satellite estimates. *J. Geophys. Res.*, **89**, 11 779-11 788.
- Gill, A. E., and P. P. Niiler, 1973: The theory of the seasonal variability in the ocean. *Deep-Sea Res.*, **20**, 141-177.
- Kantha, L. H., O. M. Phillips and R. S. Azad, 1977: On turbulent entrainment at a stable density interface. *J. Fluid Mech.*, **79**, 753-768.
- Kato, H., and O. M. Phillips, 1969: On the penetration of a turbulent layer into stratified fluid. *J. Fluid Mech.*, **37**, 643-655.
- Katsaros, K. B., and R. Lind, 1985: Radiation measurements and model results from R.V. *Oceanographer* during STREX, 1980. *J. Geophys. Res.* (in press).
- Kraus, F. B., and J. S. Turner, 1967: A one-dimensional model of the seasonal thermocline. II. The general theory and its consequences. *Tellus*, **19**, 98-106.
- Large, W. G., and S. Pond, 1981: Open ocean momentum flux measurements in moderate to strong winds. *J. Phys. Oceanogr.*, **11**, 324-336.
- , —, and —, 1982: Sensible and latent heat flux measurements over the ocean. *J. Phys. Oceanogr.*, **12**, 464-482.
- , J. C. McWilliams and P. P. Niiler, 1986: Drifting buoy observations of the upper ocean's thermal response during STREX. Submitted to *J. Phys. Oceanogr.*
- Moore, M. J., and R. R. Long, 1971: An experimental investigation of turbulent stratified shearing flow. *J. Fluid Mech.*, **49**, 635-655.
- Niiler, P. P., and E. B. Kraus, 1977: One-dimensional models of the upper ocean. *Modeling and Prediction of the Upper Layers of the Ocean*, E. B. Kraus, Ed., Pergamon, 143-172.
- Paulson, C. A., and J. J. Simpson, 1977: Irradiance measurements in the upper ocean. *J. Phys. Oceanogr.*, **7**, 952-956.
- Phillips, O. M., 1966: *Dynamics of the Upper Ocean*. Cambridge University Press, 261 pp.
- Pollard, R. T., R. B. Rhines and R. O. R. Y. Thompson, 1973: The deepening of the wind mixed layer. *Geophys. Fluid Dyn.*, **3**, 381-404.
- Price, J. F., C. N. K. Mooers and J. C. Van Leer, 1978: Observations and simulation of storm-induced mixed layer deepening. *J. Phys. Oceanogr.*, **8**, 582-599.
- Reed, R. J., and S. L. Mullen, 1981: *Storm Transfer and Response Experiment Meteorological Atlas*. STREX Data Center, University of Washington, 87 pp.
- Reynolds, R. M., 1982: Comparison of surface meteorological observations from ship and toroid buoy in the North Pacific during STREX. *J. Appl. Meteor.*, **12**, 1032-1037.
- Saur, J. F. T., 1963: A study of the quality of sea water temperatures reported in logs of ships weather observations. *J. Appl. Meteor.*, **2**, 418-425.
- Stevenson, J. W., and P. P. Niiler, 1983: Upper ocean heat budget during the Hawaii-to-Tahiti Shuttle Experiment. *J. Phys. Oceanogr.*, **13**, 1894-1907.
- Tabata, S., 1965: Variability of oceanographic conditions at Ocean Station "P" in the Northeast Pacific Ocean. *Trans. Roy. Soc. Can., Ser. 4*, **3**, 367-418.
- Thompson, R. O. R. Y., 1976: Climatological numerical models of the surface mixed layer of the ocean. *J. Phys. Oceanogr.*, **6**, 496-503.
- Thomson, R. E., 1971: Theoretical studies of the circulation of the subarctic Pacific region and the generation of Kelvin type waves by atmospheric disturbances. Ph.D. thesis, University of British Columbia, 245 pp.
- Toole, J. M., L. J. Mangum and S. P. Hayes, 1980: Preliminary data report: STREX CTD/02. STREX Data Center, University of Washington, 200 pp.
- Tully, J. P., and L. F. Giovando, 1963: Seasonal temperature structure in the eastern subarctic Pacific Ocean. *Roy. Soc. Can., Spec. Publ.*, No. 5, M. J. Dunbar, Ed., 10-36.
- Turner, J. S., and E. B. Kraus, 1967: A one-dimensional model of the seasonal thermocline. I. A laboratory experiment and its interpretation. *Tellus*, **19**, 88-97.

The biological and acoustical structure of sound scattering layers off Oregon

JOHN M. KAUFEL,^{*} CHARLES E. GREENLAW,[†] WILLIAM G. PEARCY[‡] and
D. VAN HOUTHUYSE[§]

(Received 18 March 1985, in revised form 2 December 1985; accepted 5 December 1985)

Abstract Four discrete acoustical frequencies were used to determine the depths of migratory and non-migratory scattering layers. Layers were insonified with a broad-band, low frequency (1–30 kHz) acoustic source and sampled with a 100 m² rope trawl with five opening and closing codends.

The predominant fishes with gas-filled swimbladders caught in deep (188–250 m) day time layers were *Protomyctophum crockeri* and *P. thompsoni*, whereas *Protomyctophum* spp. and *Diaphus theta* were the most common species in deep (125–225 m) night-time layers. The common fishes with gas-filled swimbladders in shallow (0–80 m) night-time layers were *D. theta*, *Stenobrachius leucopsarus* (<35 mm), *Tarletonbeania crenularis*, *Symbiolophorus californiensis* and *Engraulis mordax*.

Arceer estimates of distributions of bubble radii were similar for deep day and deep night scattering layers, but a wider range of bubble sizes existed in shallow night-time layers than in deep day and deep night layers.

A model which considered species-specific parameters of morphology, physiology and behavior provided estimations of the distributions of swimbladder radii that most closely matched the acoustically estimated distributions of bubble radii. Comparisons of acoustic data and net catch data indicate that myctophids with gas-filled swimbladders may maintain swimbladder volume at a level below that required for neutral buoyancy. Furthermore, there is some evidence suggesting that large myctophids maintain a constant swimbladder volume during vertical migrations, but at volumes that result in negative buoyancy; smaller myctophids may maintain a constant swimbladder mass during vertical migration.

INTRODUCTION

The composition of sound scattering layers in many geographical regions has been documented utilizing both acoustical and biological sampling methods. Many studies have estimated the depths of sonic scattering layers (SSL's) by means of single frequency echosounders and sampled SSL's using opening and closing nets (FOXTON, 1963; EBELING *et al.*, 1971; PICKWELL *et al.*, 1971; KLECKNER and GIBBS, 1972; BADCOCK and MERRITT, 1976; PEARCY *et al.*, 1977; FRIED *et al.*, 1977; SAMOTOJO, 1982 and others).

Few studies have employed multiple-frequency sound scattering techniques in con-

^{*} College of Oceanography, Oregon State University, Corvallis, OR 97331, U.S.A. Present address to which correspondence should be sent: Department of Zoology, University of Tasmania, G.P.O. Box 252C, Hobart, Tasmania 7001, Australia.

[†] Tracor, Inc., Philomath, OR 97307, U.S.A.

[‡] College of Oceanography, Oregon State University, Corvallis, OR 97331, U.S.A.

[§] Tracor, Inc., San Diego, CA 92123, U.S.A.

junction with biological sampling. Utilizing an explosive acoustic source HOLLIDAY (1972) found that the low-frequency structure of the echoes from single-species schools could be correlated with resonant scattering from swimbladders. Partial collection of the targets (northern anchovy schools) made it possible to predict scattering spectra based on models of sound scattering from swimbladder fishes. Later studies by BATZLER *et al.* (1973), BATZLER *et al.* (1975) and LOVE (1975, 1977) attempted to predict sound scattering intensities based on trawl collections and models of sound scattering.

HOLLIDAY (1977), JOHNSON (1977) and GREENLAW and JOHNSON (1983) presented solutions to the opposite problem, involving the prediction of sound scattering layer composition based on multiple-frequency acoustic data. JOHNSON (1977) found some agreement between the abundance of fishes with swimbladders and abundance from fish catch data. HOLLIDAY (1976, 1978, 1980) found good agreement between relative abundance with size estimated acoustically and from net collections.

Biological studies of scattering layers off Oregon indicate that at least five species of myctophids with gas-filled swimbladders commonly occur in the upper mesopelagic zone (PEARCY and LAURS, 1966; PEARCY and MESEAR, 1971; PEARCY *et al.*, 1977). KLECKNER and GIBBS (1972) noted the importance of understanding species composition in acoustic studies of scattering layers because of species-specific differences in swimbladder size and shape. Studies by KANWISHER and EBELING (1957), MARSHALL (1960), CAPEN (1967), ZAHURANEC and PUGH (1971), BUTLER and PEARCY (1972), KLECKNER and GIBBS (1972), BROOKS (1976, 1977), JOHNSON (1979) and NEIGHBORS and NAFAKITIS (1982) have considered the relationship between fish species and swimbladder size of midwater fishes. These studies acknowledge the importance of swimbladder size in acoustical studies and, concomitantly, buoyancy regulation for understanding acoustical observations. Therefore, a thorough understanding of scattering layers based on acoustical studies requires knowledge of species composition and buoyancy regulation in the midwater environment.

In this paper we present data from multiple-frequency acoustical measurements and concurrent trawl samples and describe correlations between the acoustical and biological structure of migratory and non-migratory sound scattering layers off Oregon.

METHODS

Data were collected from the F.V. *Pat San Marie* from 10 to 19 September 1981 in an area between 44°25'N and 44°41'N and between 125°49'W and 126°05'W, approximately 100 km west of Newport, Oregon. Water depths were approximately 2800 m.

Two acoustical sampling techniques were used on this cruise. (1) An arcer (HOLLIDAY, 1978, 1980) served as a broad-band (1–30 kHz) acoustic source. The arcer consisted of three components: a bank of storage capacitors (60 kJ capacity) which was charged to approximately 7500 V through a step-up transformer, an air-gap switch or control section which fired the arcer, and an electrode assembly. Arcer electrodes and an omnidirectional hydrophone were lowered to a specific depth above the scattering layer. The arcer and hydrophone cables were separated by 15 m on the ship. Based on the experimental geometry and sample durations, insonified volumes were calculated to be ellipsoidal shells of approximately 19,000 m³ effective volume. Firing of the arcer was controlled on board the ship. Echoes were displayed in real time and only those echoes which displayed high signal-to-noise ratios were analyzed. Echoes were recorded as

voltage vs time on a digital computer. For acoustic data collections all ship power was turned off and acoustic equipment was powered by two 110 V diesel generators placed on deck to reduce ship's radiated noise. However, platform-associated noise, specifically wave slap on the ship's hull and vibration from the generators, was still a significant problem at low frequencies.

(2) Two transducers mounted in an Endeco V-Fin and suspended from a boom to a depth of 3–5 m were used to obtain quantitative data on scattering strength vs depth at four discrete frequencies (15, 20, 25 and 30 kHz). Discrete frequency data were collected before and after each arcer cast and during net tows.

Biological collections were made with a rope trawl, mouth area of about 100 m², equipped with a Multiple Plankton Sampler (MPS) with five opening and closing codend nets [see PEARCY *et al.* (1977) for a description of the MPS]. The trawl was lined with 19 mm stretch mesh; MPS nets were 6 mm mesh with 0.505 mm Nitex codend nets. The depth of the trawl was monitored either by an Institute of Oceanographic Sciences (IOS) acoustical net monitoring system (BAKER *et al.*, 1973) or a Furuno netsonde. Net tows were made in full daylight or during the night to avoid the dawn and dusk periods of most active vertical migration. Daytime tows were positioned near the migratory sound scattering layer which was centered at a depth of 235 m. Shallow (0–80 m) and deep (125–255 m) night-time tows sampled migratory and non-migratory scattering layers, respectively. Towing speed was 1.5–2.0 kn (2.8–3.7 km h⁻¹). Volumes filtered were estimated by multiplying the distance traveled by the ship (based on LORAN-C fixes) times the mouth area of the trawl. A total of 33 collections were made from 8 tows (Table 1).

Collections were frozen or preserved in 10% buffered Formalin and seawater. Micronekton were sorted into major groups (fishes, squid, shrimp and euphausiids). Fishes were transferred to 20% and then 50% isopropyl alcohol and identified, counted and measured (standard length).

Data analysis

Algorithms for estimating the biological composition of scattering layers based on acoustic data are discussed in HOLLIDAY (1977), JOHNSON (1977) and GREENSLAW and JOHNSON (1983). Estimates of the size and abundance of gas bubbles, presumably swimbladders of fishes, were obtained from the arcer data by inversion of the following set of equations (GREENSLAW and JOHNSON, 1983).

$$I_T(t, f) = I_0(t) \int_0^{\infty} R(f, a) N_c(a) da,$$

where I_T is the scattered intensity at a time t after transmission and frequency f , $R(f, a)$ is a coefficient for a scatterer of size a and $N_c(a)$ represents the number of scatterers of size a in the insonified volume. In cases where the number of scatterers is not large enough to assume a continuous distribution of sizes or where the size distribution is discontinuous we can apply the summation

$$I_T(t, f) = I_0(t) \sum_{i=1}^s N_d(a_i) R(f, a_i),$$

where s represents the number of size classes. Applying this equation to each of the

Table 1. Summary of acoustical and net data used in this study.

Arceer cast	Date (1981)	Time (hr)	Depth (m)	Trawl number	Date (1981)	Time (hr) Nets 1-5	1	2	3	4	5	Total volume inferred (10 ³ m ³)
1	15 Sept	2254-2325	34	2485	14 Sept	1440-1500	0-130	135-172	170-225	225-232	232-310	10.61
2	16 Sept	1029-1040	175	2486	14 Sept	2237-0107	0-50	48-50	50-75	75-80	80-86	8.61
3	16 Sept	1600-1618	235	2487	15 Sept	1852-1823	0-195	195-230	208-225	200-215	215-220	7.87
4	16 Sept	1731-1905	160	2488	16 Sept	0012-0042	0-50	50-80	80-80	80	48-80	9.49
5	16 Sept	1938-2010	97	2489	16 Sept	1151-1151	0-165	165-188	188-230	230	235-230	13.86
6	16 Sept	2059-2120	235									
7	16 Sept	2219	40	2490	16 Sept	2353-0013	0-50	50-240	240-255	250-268	275-290	14.42
8	17 Sept	1012-1117	277									
9	17 Sept	1302-1317	144									
10	17 Sept	1856-1930	123	2491	17 Sept	1448-1808	0-55	55	55-170	185-250	240-255	12.03
				2492	17 Sept	2113-0033	0-250	170-135	125-280	280	280-285	13.46

Volume inferred is for nets 2-5, except for trawl 2490 where volume is for nets 1-5.

Nets used for deep daytime comparisons (*m* = 10).

Nets used for shallow night time comparisons (*m* = 9).

Nets used for deep night time comparisons (*m* = 6).

Arceer data collected during a vertical migration.

frequencies sampled we obtain a set of equations

$$I(f_1) = N(a_1)R(f_1, a_1) + N(a_2)R(f_1, a_2) + \dots + N(a_3)R(f_1, a_3)$$

$$I(f_2) = N(a_1)R(f_2, a_1) + N(a_2)R(f_2, a_2) + \dots + N(a_3)R(f_2, a_3)$$

$$I(f_T) = N(a_1)R(f_T, a_1) + N(a_2)R(f_T, a_2) + \dots + N(a_3)R(f_T, a_3).$$

The abundance of different sizes of gas-filled swimbladder radii can be estimated from the solution of this set of equations. A constrained least-squares algorithm (NNLS; LAWSON and HANSEN, 1974) was applied to the acrcr data. The coefficients $R(f, a_i)$, in this case for fishes with gas-filled swimbladders, were estimated using the model of ANDREIVA (1964) as modified by WESTON (1967).

Initial estimates for the volumes of gas-filled swimbladders of fishes captured with the 100 m midwater trawl were obtained from a neutral buoyancy model. Subsequent variations of this model are considered in the results section.

RESULTS

Biology

The average biomass of all micronekton caught in the deep (125–255 m) night-time net tows was almost nine times that caught in deep (188–250 m) daytime tows, and micronekton biomass captured in shallow (0–80 m) night-time tows was almost 50% greater than that in deep night-time tows (Table 2). Much of the biomass was attributable

Table 2. Biomass index. Mean biomass per tow of micronekton caught in the deep trawl (125–255 m) during day and night tows.

	Deep day (n = 10)	Deep night (n = 6)	Shallow night (n = 9)
Non-fish			
Shrimp	0.713 (0.465)	0.978 (0.864)	0.318 (0.322)
Squid	0.060 (0.038)	3.61 (2.48)	1.99 (1.92)
Euphausiids	1.52 (1.47)	0.184 (0.068)	19.87 (28.88)
Misc. plankton	0.094 (0.088)	1.98 (1.88)	0.178 (0.197)
Total	2.387 (1.27)	6.719 (4.73)	22.380 (29.0)
Fish			
With gas-filled swimbladders			
<i>Stenobrachius leucopsarus</i>	0.001 (0.001)	0.01 (0.001)	0.220 (0.188)
<i>Protonyxotophium thompsoni</i> and <i>P. crockeri</i>	0.081 (0.066)	0.189 (0.103)	0.003 (0.006)
<i>Symphotyonus californiensis</i>	0.017 (0.036)	0.032 (0.048)	2.98 (4.63)
<i>Leptocottus armatus</i>	0.001 (0.018)	0.073 (0.052)	1.28 (1.87)
<i>Diaphus theta</i>	0.005 (0.008)	0.604 (0.236)	2.46 (2.89)
<i>Engraulis mordax</i>	0	0	2.87 (8.61)
Total	0.078 (0.063)	0.809 (0.311)	9.78 (13.7)
Without gas-filled swimbladders	0.085 (0.084)	18.9 (11.4)	1.87 (0.808)
Total fish	0.160 (0.127)	16.7 (11.7)	11.6 (14.0)
Total biomass	2.78 (1.30)	23.8 (16.3)	34.0 (36.0)

Numbers in parentheses are 1 S.D.

to *Euphausia pacifica* (deep daytime and shallow night-time) and myctophid fishes (deep night-time). Biomass estimates of euphausiids (approximately 2 cm in total length) and small fishes are underestimates of true biomass because of escape through the net mesh of the trawl. However, large relative differences in biomass between net collections indicate real variations. In the deep daytime scattering layer, fishes with and without gas-filled swimbladders contributed equally to the total biomass. The large difference between deep daytime and deep night-time biomass estimates was due to the evening ascent of fishes without gas-filled swimbladders (primarily *Stenobrachius leucopsarus* >35 mm) into the deep night-time depth range. Myctophids with gas-filled swimbladders dominated the shallow night-time collections (Table 2).

Based on our examinations of fresh specimens at sea and frozen specimens in the laboratory, six species of myctophids generally had thin-walled (an indicator of a deflated gas-filled swimbladder) and/or gas-filled swimbladders, and were, therefore, assumed to be the predominant low-frequency sound scatterers. These were *S. leucopsarus* (<35 mm), *Protomyctophum crockeri*, *P. thompsoni*, *Symbolophorus californiensis*, *Tarletonbeania crenularis* and *Diaphus theta* (Table 3). The northern anchovy (*Engraulis mordax*), which has a gas-filled swimbladder, was present in two shallow night-time net collections. Other fishes with gas-filled swimbladders occurred in insignificant numbers and are not considered in the analysis.

BUTLER and PEARCY (1972) reported both thin-walled, gas-filled swimbladders and small, reduced swimbladders in large *D. theta* and *T. crenularis*. NEIGHBORS and NAFAKITIS (1982) did not find gas in any of the large *D. theta* they examined. All of the 33 fresh *D. theta* (36–73 mm SL) and 7 of 9 fresh *T. crenularis* (34–81 mm) examined for this study had thin-walled or gas-filled swimbladders. For subsequent calculations all *D. theta* and *T. crenularis* were assumed to possess gas-filled swimbladders.

Physonect siphonophores may make a significant contribution to resonant sound scattering at low frequencies (BARHAM, 1963; PICKWELL *et al.*, 1964), but it was difficult to determine the abundance of these animals since they fragment and may be extruded through the meshes of the net. We found very few floats from physonect siphonophores in the samples. Floats collected were smaller than 6 by 2 mm and only the codend mesh of the MPS was small enough to retain them.

Acoustics

Volume scattering strength profiles at four discrete frequencies (15, 20, 25 and 30 kHz) provide evidence for depth and frequency-dependent sound scattering (Fig. 1). Differences in volume scattering strength between day and night profiles are evident at all depths. A daytime vertical profile (Fig. 1A) was characterized by a distinct scattering layer at 235 m and reduced scattering at shallower depths. Volume scattering strength at depths of <75 m could not be determined accurately with the towed acoustic array because of surface reverberation. Volume scattering during the night (Fig. 1B) was more uniform with depth; however, peak volume scattering occurred at 235 m as in the daytime profile.

Biomass estimates of all micronekton from net collections made within the main scattering layer indicate that night-time biomass (Table 2) is almost 9 times higher than daytime biomass. Based on biomass collected in nets, the night-time volume scattering at 235 m should be approximately 10 dB higher than daytime scattering at this depth, rather than the observed 5 dB lower volume scattering (Figs 1A and B). This

Table 3. Mean abundance (No. 1000 m⁻²) of fishes with gas-filled swimbladders grouped by length (mm)

[illegible]

* Numbers in parentheses are 1-S (1)

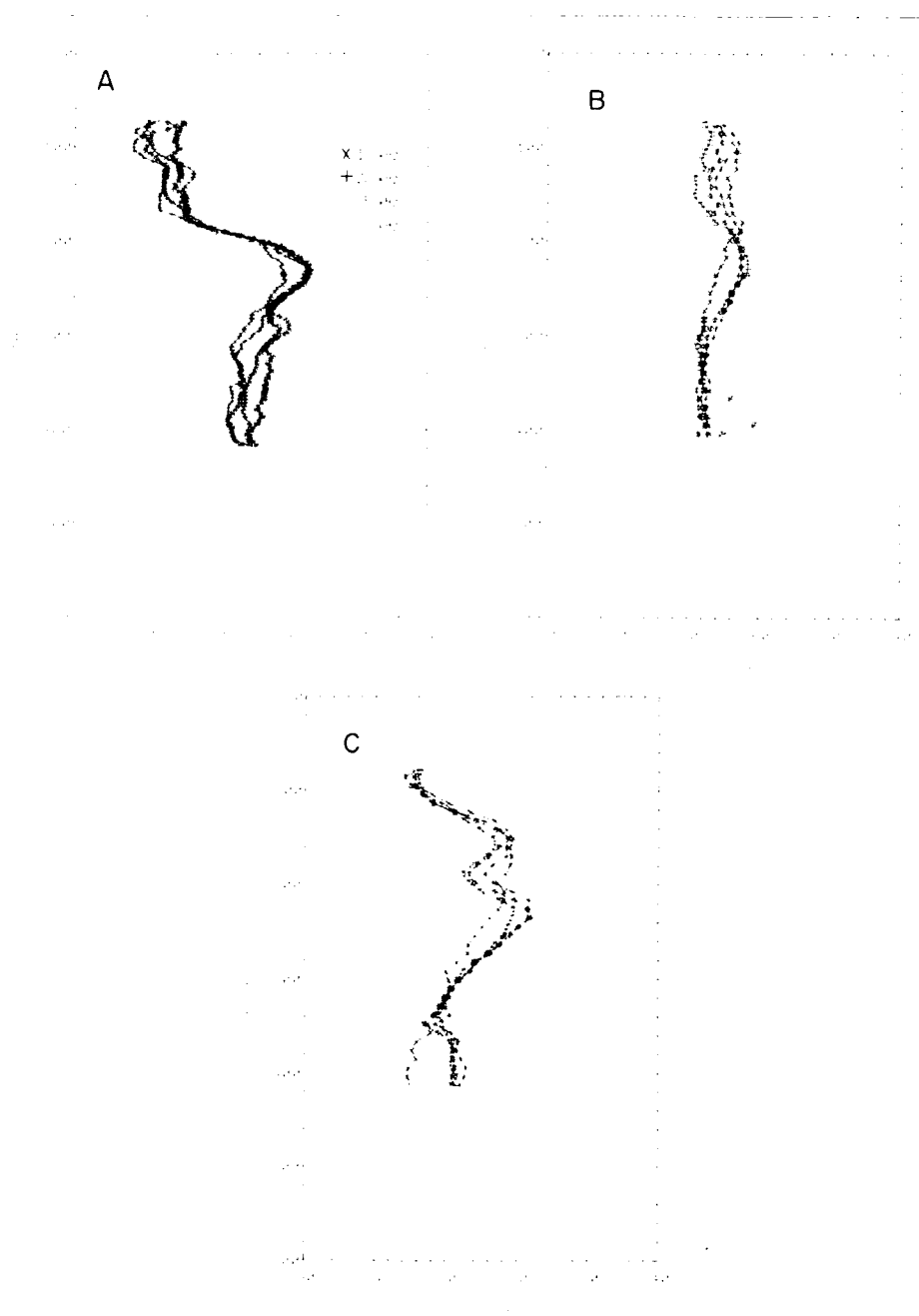


Fig. 1. Plots of depth vs volume scattering strength during different times of day and at four frequencies: (A) daytime (1600 h), (B) night-time (2130 h), (C) early evening (ascent period) (2000 h). Horizontal lines indicate depths of arcercasts taken at times close to that of the discrete frequency measurements.

discrepancy in biomass estimates between acoustic and net collections may be a result of more effective avoidance of the trawl during the daytime, changes in the orientation and scattering characteristics of the species present, or changes in species composition during the day and night.

Frequency-dependent variations in backscattering at a particular depth permit estimates of the size of resonant bubbles. Peak volume scattering at the lowest (15 kHz) or highest (30 kHz) discrete frequency makes it possible to estimate the minimum and

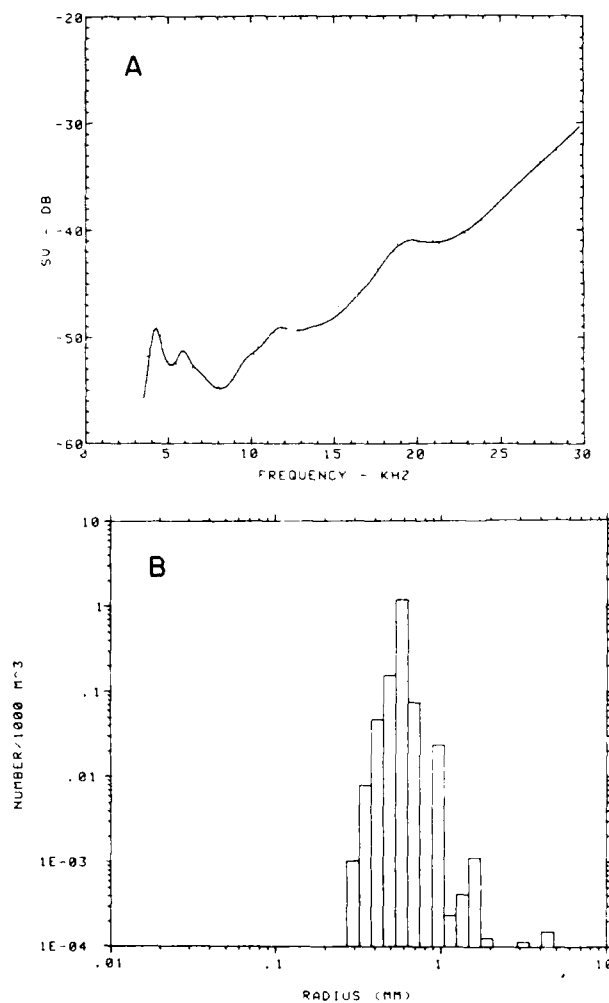


Fig. 2. Data from a deep daytime (235 m, 1600-1618 h) arcser cast. (A) Scattering spectrum. Points are mean volume scattering strengths determined from multiple firings of the arcser. Curves are based on the calculation of the scattering spectrum from the acoustical abundance estimates of bubble radii. (B) Acoustically estimated abundance of bubble radii. The total estimated number of gas bubbles was 1.5/1000 m^3 .

maximum resonant bubble size, respectively, assuming that peak scattering is caused by bubbles. Peak scattering at the intermediate discrete frequencies (20 and 25 kHz) provides an estimate of the true resonant bubble size. Using a resonance frequency relationship (Weston, 1967) it is estimated that the predominant resonant bubbles at 235 m are smaller than 0.8 mm in radius during both the day and night. Discrete frequency data collected during an evening ascent of the scattering layer (Fig. 1C) indicated that resonant bubbles at 235 m were between 0.5 and 1.0 mm.

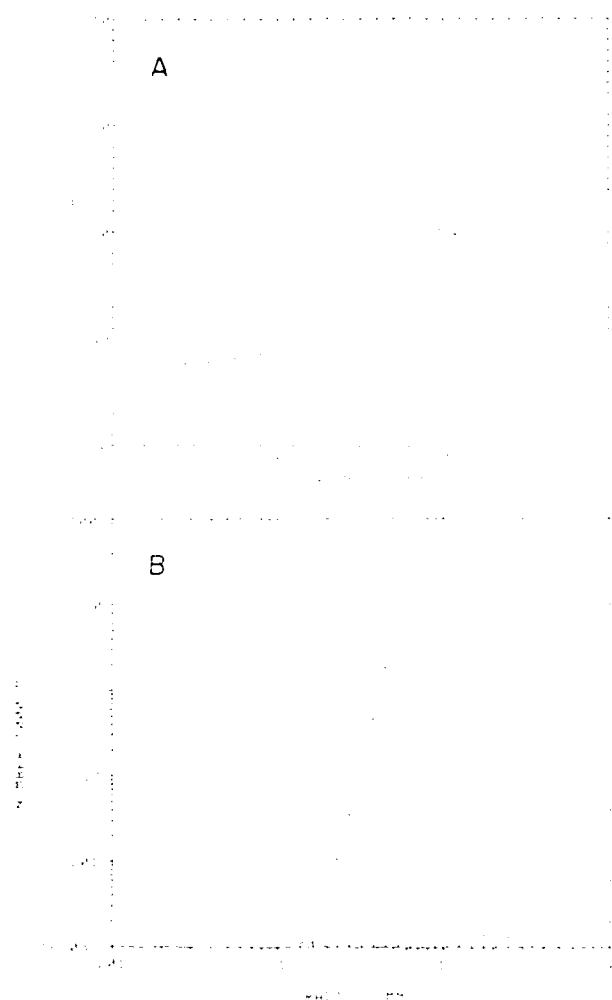


Fig. 3. Data from a deep night time (235 m, 2059-2120 hr) ascent. (A) Scattering spectrum. Points are mean volume scattering strengths determined from multiple trings of the ascent. Curves are based on the calculation of the scattering spectrum from the acoustical abundance estimates of bubble radii. (B) Acoustically estimated abundance of bubble radii. The total number of gas bubbles was 214 000/m.

Acoustic scattering strength spectra and estimated abundance of bubble radii required to produce these spectra are shown in Figs 2–5. The curves are based on the calculation of the scattering spectra from the acoustical abundance estimates of bubble radii. The total estimated numbers of gas bubbles were 1.5 and 21 per 1000 m³ for deep daytime (Fig. 2B) and deep night-time (Fig. 3B) layers, respectively. The number of bubbles in shallow night-time spectra were 23 and 980 per 1000 m³ at 34 and 40 m, respectively (Figs 4B and 5B). These abundance estimates are high when compared with values obtained from net collections off Oregon (Pryor *et al.*, 1977, this paper).

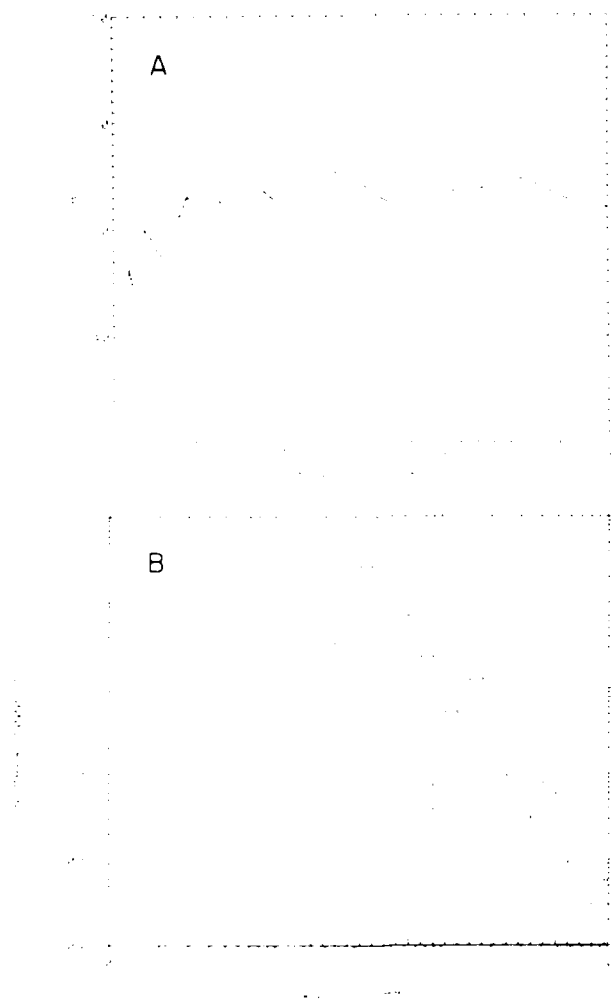


Figure 4. Deep daytime scattering strength spectrum of 40 m depth layer. A: Scattering spectrum. B: Bubble radius required to produce the spectrum from multiple plumes of the layer. Curve is an average of 10 measurements. Scatter spectrum from the acoustic abundance estimates is shown in Fig. 3A. Acoustic abundance estimates are 980 per 1000 m³. The net number of bubbles is 23 per 1000 m³ (Pryor *et al.*, 1977).

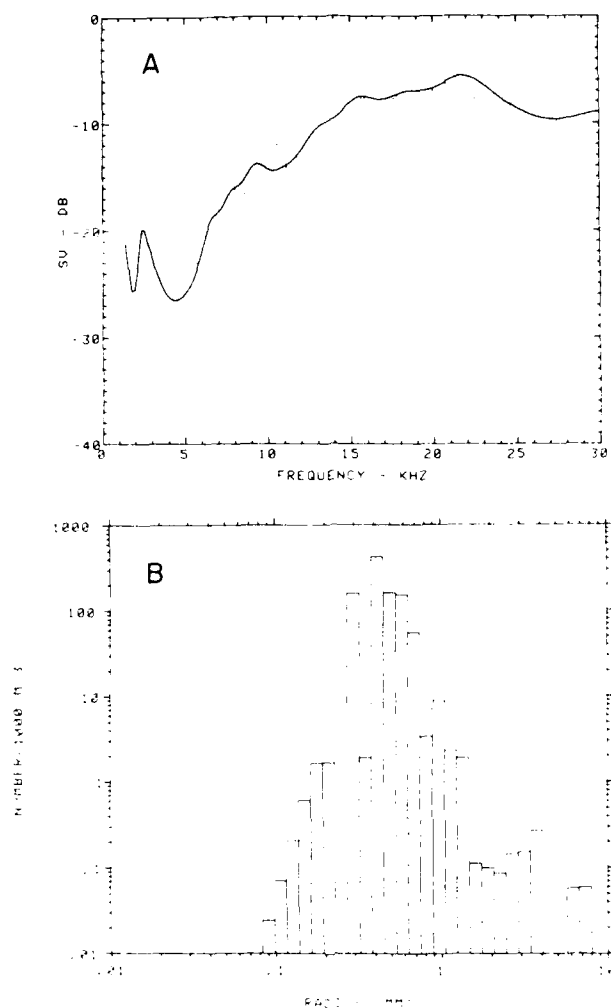


Fig. 7. Data from a shallow night-time (40 m, 2219 h) arcet cast. (A) Scattering spectrum. Plots are mean volume scattering strengths determined from multiple firings of the arcet. Curves are based on the calculation of the scattering spectrum from the acoustical abundance estimates of bubble radii. (B) Acoustically estimated abundance of bubble radii. The total number of gas bubbles was 980/1000 m³.

Scattering spectra at night-time depths of <50 m indicated the presence of a wide range of bubble sizes with a peak swimbladder abundance at a radius between approximately 0.25 and 0.41 mm at 34 and 40 m, respectively (Figs 4B and 5B). The range of bubble sizes was narrower at depths of 200–250 m in both the daytime and the night-time with the peak abundance at 0.60 mm radius (Figs 2B and 3B). Greater numbers of small bubbles were present in surface waters at night than in deeper waters during either daytime or night-time.

A log-log plot of the peak resonance frequency against the scattering layer depth plus 10 m, makes it possible to detect systematic changes in swimbladder inflation with depth during the migration period (Fig. 7). By selecting the lowest frequency where a peak in scattering occurred at each depth, we assumed that a single assemblage of fishes was being followed in the course of a vertical migration, thereby making possible the detection of any systematic changes in swimbladder inflation with depth. The nature of the points plotted on Fig. 7 can be illustrated by looking at the data sets used to determine these points. The point at 50 m corresponds to a frequency of 2.35 kHz. This point was obtained from the scattering spectrum taken at 40 m (Fig. 5A). The point at 245 m (Fig. 7) relates to the low frequency peak scattering occurring at a frequency of 4.3 kHz at 235 m (Fig. 2A). In both cases the frequency was the lowest peak frequency at that particular depth. However, at 44 m the lowest frequency of peak scattering (1.0 kHz

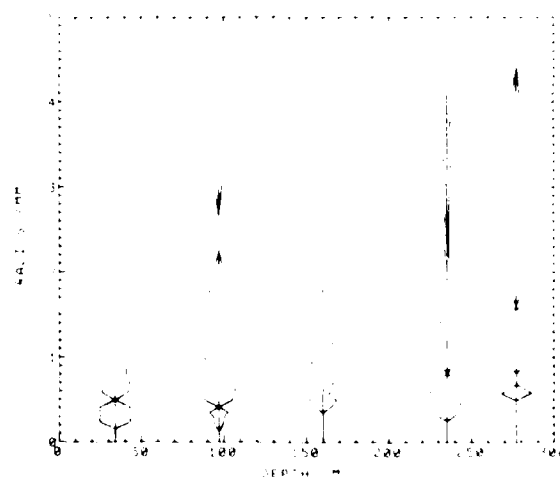


Fig. 6. Acoustically estimated abundance of different bubble radii at five different depths. Acoustical measurements were made during an evening ascent period. The width of the kite diagrams is an indicator of the abundance of a particular radius of bubble on a log scale.

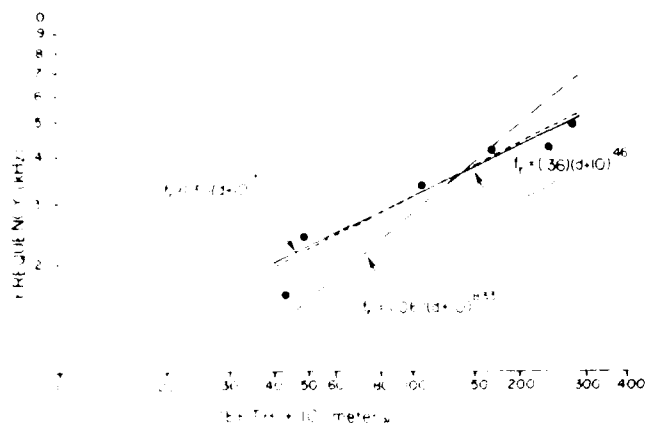


Fig. 7. Relationship between the frequency of the lowest peak used for determining swimbladder size and maintained depth of migratory animals. Data were obtained from two different depths of migrations. Points plotted were regression coefficients for the two regression lines presented. Lowest frequencies where a peak in the spectrum is present at a particular depth. These low frequency peaks represent resonance scattering, whereas the other scatter points are due to nonresonant scattering. The data points at 30, 40, and 50 m depth are regression coefficients for the two regression lines. The data points at 100, 150, 200, 300, and 400 m depth are regression coefficients for the regression line that forms a straight line. The regression coefficient for the regression line that forms a straight line is not presented because it is not significantly different from zero.

in Fig. 4A was not used because this low frequency peak is attributed to anchovies which were captured in the shallow night net collections. We attributed the second lowest frequency of peak scattering (1.5 kHz) to migratory fishes with gas filled swimbladders and this was the point that was used in Fig. 7. The remaining lowest frequencies where a peak is visible were 3.2, 4.2 and 5.0 kHz at 100, 150 and 200 m, respectively. Following scattering peaks at the higher frequencies is an increase in the amount of increased nonresonant scattering and noise.

The least squares estimate of the straight line ($f_L = 0.001d + 0.11$, $r^2 = 0.96$) in Fig. 7 is not significantly different from the line of the form $f_L = kd(d + 10)^{0.44}$ which suggests that sound scattering at the lowest frequencies was due to migratory animals that maintained a *constant volume at a constant depth*. This conclusion is based on the relationship for resonance frequency of a gas bubble of fixed size, where resonance frequency is proportional to the square root of pressure. This analysis, which considers scattering at the frequency of the lowest peak, does not provide data on regulation of intermediate and small size swimbladders.

Histograms of the average abundance of swimbladder sizes of trawl caught fishes (Fig. 8) indicate that the numbers of swimbladders were greatest in surface waters at night and lowest in deep waters during the day (Table 3). These trends were similar to those for acoustic data. However, the acoustically measured abundances were much greater than those determined by the trawl collections. This was probably because only *acoustic data* which showed good signal to noise ratios were analyzed.

The range of swimbladder sizes estimated from the net collections and the neutral buoyancy model is similar to that estimated from the *acoustic distributions* for the deep night time and deep daytime data. The discrepancy in the maximum swimbladder radius

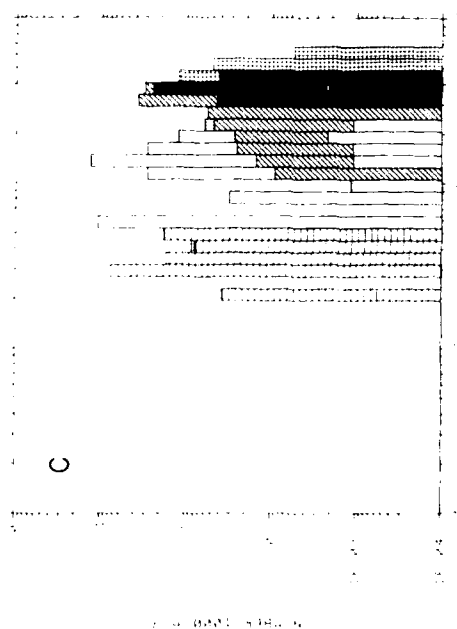
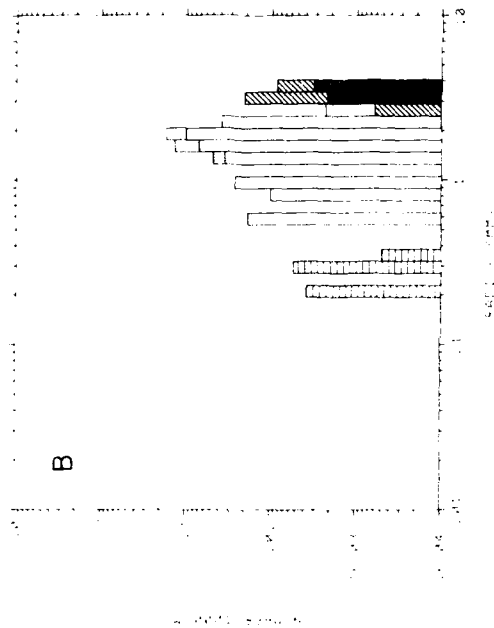
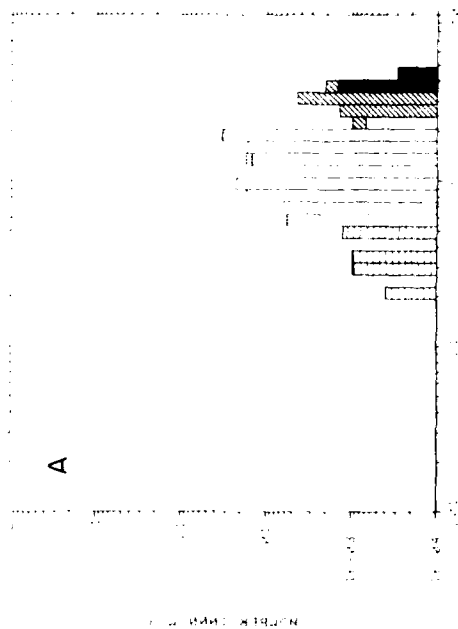


Fig. 5. The mean abundance of swimbladder radii of fishes caught in the 100 m rope trawl during different times of day and at different depths. Swimbladder radii were estimated using the neutral buoyancy model for each species and size of fish. The value of α is one for all species. (A) Deep daytime (188-250 m) (n = 40); (B) deep night-time (25-280 m) (n = 6); (C) shallow night-time (0-80 m) (n = 9). ■ *Symphodus medietatis*; ▨ *Tallichthys quadricornis*; ▩ *Stenobrama lineatus*; ▪ *Prionocyttus crockeri*; and P. thompsoni; □ *Diaplus thomasi*; ▤ *Juganthis monda*.

between the shallow night-time net catches and the shallow night-time arcer data sets may be the result of net avoidance by larger swimbladder fishes in surface waters during the night.

Because it is unlikely that all midwater fishes in the net collections were neutrally buoyant at all times, alternative models were considered for estimating the sizes of gas-filled swimbladders. Bubble radii distributions obtained from the neutral buoyancy assumption were adjusted by multiplying the radii by coefficients (α) ranging from 0.1 to 1.35. These distributions were correlated with the acoustically estimated bubble radii to determine the values of alpha that resulted in the best match of acoustical and biological data at similar depths and times of day. At a depth of 200–250 m, swimbladders filled to 3.9% (S.D. = 0.02) and 22.5% (S.D. = 1.4) of the volume required for neutral buoyancy gave the best fit for daytime and night-time periods, respectively. Correlations between shallow night-time arcer data and swimbladder distributions derived from shallow night-time trawl collections indicate that swimbladders were filled to 8.4% (S.D. = 0.6) and 13.4% (S.D. = 1.5) of the volume required for neutral buoyancy at 34 and 40 m, respectively. These results suggest that swimbladders were usually inflated to only a fraction of the volume required for neutral buoyancy.

The neutral buoyancy model, both with and without coefficients, assumes that all species regulate swimbladder volume in a similar manner. However, species-specific differences in body and swimbladder morphology, lipid and water contents, and migratory behavior suggest that similar rules regarding swimbladder inflation may not apply to all migratory midwater fishes with gas-filled swimbladders. Therefore, the abundance of swimbladder sizes from shallow night, deep night and deep daytime net collections was estimated taking into consideration the factors listed in Table 4 pertinent to buoyancy and vertical distribution.

Because *Protomyctophum* spp. are basically non-migratory we assumed that they maintain their swimbladders at a volume near that required for neutral buoyancy, and require minimal regulation to maintain neutral buoyancy. The remaining four species with gas-filled swimbladders all undertake diel vertical migrations into the upper 50 m at night (PEARCY *et al.*, 1977). However, buoyancy control mechanisms may be somewhat different among these fishes.

NEIGHBORS and NAFPAKITIS (1982) found that *T. crenularis* and *Protomyctophum* spp. both have low lipid and water contents and therefore are negatively buoyant exclusive of the swimbladder. However, *Protomyctophum* spp. is non-migratory, whereas *T. crenularis* undergoes vertical migration. The relatively narrow body, narrow caudal peduncle and large pectoral fins of *T. crenularis* are indicative of a fast swimming, active fish (BONE, 1973). These factors led us to conclude that *T. crenularis* probably depends on hydrodynamic lift to maintain neutral buoyancy.

The remaining three myctophids with gas-filled swimbladders, *S. leucopsarus* (<35 mm), *S. californiensis* and *D. theta* have high lipid and low water contents (BUTLER and PEARCY, 1972; NEIGHBORS and NAFPAKITIS, 1983). *Stenobranchius leucopsarus* larger than 35 mm achieve neutral buoyancy through the deposition of wax esters (NEVENZEL *et al.*, 1969; BUTLER and PEARCY, 1972). However, in small *S. leucopsarus* the swimbladder probably helps achieve hydrostatic equilibrium. The swimbladder probably serves a similar hydrostatic function in both *S. californiensis* and *D. theta*. *Stenobranchius leucopsarus* and *Triphoturus mexicanus* were both observed hanging motionless at day depths in the water column (BARHAM, 1977). These fish have lipid contents, water contents and

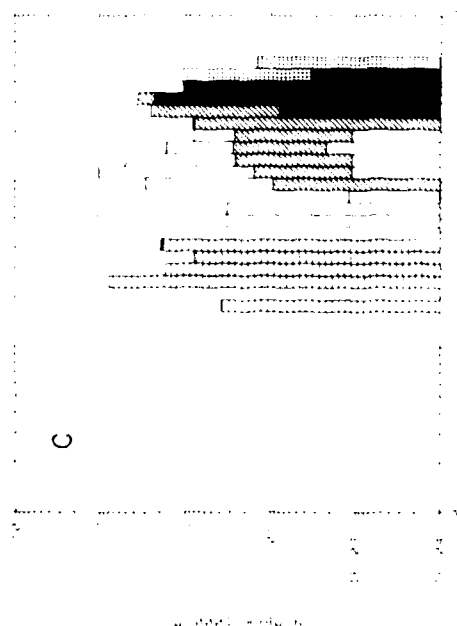
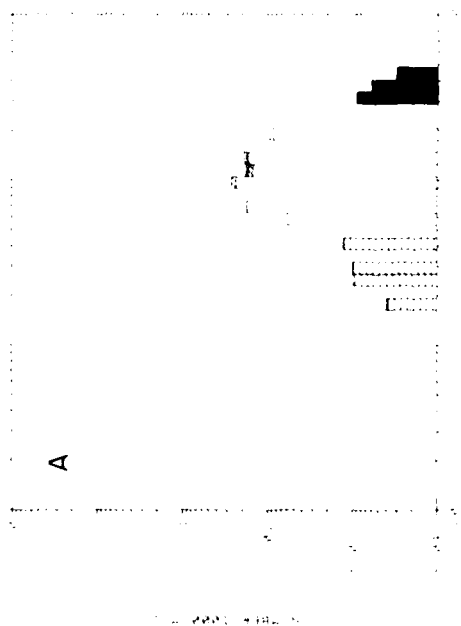


TABLE 1. The mean abundance of symbiodokter tadpoles caught in the two replicates during different times of day and at different depths. The Symbiodokter tadpoles were estimated using fractions of the neutral buoyancy model (see text) for *Tachytreutae centurionis* in (A) and (B) and were corrected for all other species in (C), (B) and (C) (A). (D), (F) tadpoles, 88, 80, 60, 100, 80 and 60 respectively (225, 250 m) (D), (F) tadpoles, 88, 80, 60, 100, 80 and 60 respectively (225, 250 m).

Table 4. Behavioral characteristics of *Daphnia magna* and *Daphnia pulex*.

	Swimbladder characteristics	Specific gravity	Lipid content	Water content	Relative size of pectoral fin	Migratory behavior	Night time depth of maximum abundance (m)	Daytime depth of maximum abundance (m)	α value for steep daytime model	Constant mass (M) or constant volume (V) migrator	References
	<i>Daphnia magna</i> Pinnules filled with air at all times	0.98-1.01	High	Low	Short	Migratory	0-100	300-500	0.0001-0.001	V	1, 2, 3, 4, 5, 6, 7, 8, 9, 10, 11, 12, 13, 14, 15, 16, 17, 18, 19, 20, 21, 22, 23, 24, 25, 26, 27, 28, 29, 30, 31, 32, 33, 34, 35, 36, 37, 38, 39, 40, 41, 42, 43, 44, 45, 46, 47, 48, 49, 50, 51, 52, 53, 54, 55, 56, 57, 58, 59, 60, 61, 62, 63, 64, 65, 66, 67, 68, 69, 70, 71, 72, 73, 74, 75, 76, 77, 78, 79, 80, 81, 82, 83, 84, 85, 86, 87, 88, 89, 90, 91, 92, 93, 94, 95, 96, 97, 98, 99, 100
	<i>Daphnia pulex</i> Pinnules filled with air at all times	0.98-1.01	High	Low	Short	Migratory	0-100	300-500	0.0001-0.001	V	1, 2, 3, 4, 5, 6, 7, 8, 9, 10, 11, 12, 13, 14, 15, 16, 17, 18, 19, 20, 21, 22, 23, 24, 25, 26, 27, 28, 29, 30, 31, 32, 33, 34, 35, 36, 37, 38, 39, 40, 41, 42, 43, 44, 45, 46, 47, 48, 49, 50, 51, 52, 53, 54, 55, 56, 57, 58, 59, 60, 61, 62, 63, 64, 65, 66, 67, 68, 69, 70, 71, 72, 73, 74, 75, 76, 77, 78, 79, 80, 81, 82, 83, 84, 85, 86, 87, 88, 89, 90, 91, 92, 93, 94, 95, 96, 97, 98, 99, 100

α value for steep daytime model

Constant mass (M) or constant volume (V) migrator

References

1. B. Lick and P. V. Arnsperg, *Journal of Theoretical Biology*, **10**, 1-10 (1977)

body morphologies similar to those of *D. theta* and *S. californiensis*. Therefore, we conclude that they are almost neutrally buoyant and maintain their swimbladders at a constant volume during vertical migration.

The swimbladders of all species, with the exception of *I. crenularis* in the deep collections, were modeled as being inflated to 0.9 times the radius of the bubble required to maintain neutral buoyancy (72% of the neutral buoyancy volume) (Fig. 9). We chose swimbladder volumes below the neutral buoyancy volume to allow for potentially rapid upward movements during feeding or predator evasion without loss of control due to positive buoyancy. Assuming constant mass, fishes with swimbladders inflated to 72% of the neutral buoyancy volume at depths of 235 m would be neutrally buoyant at 164 m, and those at 40 m would be neutrally buoyant at 24 m. We assumed that swimbladders of *I. crenularis* were inflated to 0.35 times the radius of the bubble required to maintain neutral buoyancy (4% of the neutral buoyancy volume), hence a fish at 235 m would be neutrally buoyant at the surface if it made a constant mass migration.

Histograms of abundance of various sizes of swimbladders based on net collections and the above model have ranges in the deep daytime and night-time tows (Figs 9A and B) similar to those of the acoustic estimates (Figs 2B and 3B). However, abundance peaks for both deep daytime and deep night time data occur at 0.58 mm for acoustic data and between 0.97 and 1.6 mm for the modeled net catch data. Peak abundance occurs at a swimbladder radius of 1.6 mm for the modeled net catch data from deep night-time collections. The abundance peaks from modeled net data for both the deep day and deep night catches are attributable to *Prionomyxophium* spp. which are assumed to be near neutral buoyancy ($\rho = 0.9$). The largest acoustically estimated swimbladders in the deep daytime (Fig. 2B) and deep night time (Fig. 3B) measurements are attributed to *S. californiensis* and account for the largest modeled swimbladder sizes in Figs 9A and B. *Neurolammina pacifica* smaller than 38 mm SL account for swimbladders smaller than 0.7 mm in the deep day and deep night models. Both *D. theta* and *I. crenularis* have relatively large size ranges in deep day and deep night tows (Table 3) and, concomitantly, they have a wide range of estimated swimbladder sizes in the models.

The modeled distribution of swimbladders based on shallow night-time data (Fig. 9C) shows a range of swimbladder radii similar to that in the deep day and deep night data. However, the greater abundance of fishes with swimbladders and the lack of a distinct abundance peak distinguish the shallow night time net data from other net collections. Swimbladders of radius smaller than 0.5 mm are attributed to *S. leucopsaris* in the model, and *D. theta* and *I. crenularis* show a wide range of swimbladder sizes. *Ingraulis mordax* and *S. californiensis*, based on the model, have the largest swimbladders of the fishes collected in the shallow night time nets. The northern anchovies were collected in two of ten shallow night time nets, where they comprised 10% of the catch of fishes with gas filled swimbladders and were represented by swimbladder radii of 3.8–5.3 mm in Fig. 9C. The maximum acoustically estimated swimbladder sizes agree with the swimbladder sizes measured for northern anchovy by HORTONBY (1972, 1976, 1980).

DISCUSSION

Potential differences in acoustical and net collection data include the range of estimated bubble sizes, the total number of bubbles detected or collected and the abundance of bubbles of a particular size class. The range of estimated bubble sizes was

similar as measured by the two methods. The total number of bubbles was greater in the acoustical measurements than in the net collections, although the relative numbers were similar at different depths and times of day using both techniques. The most significant differences between acoustical and net collection measurements were in the relative number of bubbles of a particular size class.

Differences in acoustical and biological measurements result from: (1) differences in the depths sampled with the arcer and with the trawl, and (2) measurement or collection of different targets at similar depths.

Errors in comparisons of acoustical and biological data can result from discrepancies between the depths sampled with the arcer and with the trawl. If biological collections are made at a depth different from that of the arcer data, the size of the fishes in the net collections may be different from the size of the fishes in the insonified water volume. Our data show that acoustical estimates of swimbladder abundances and size distributions from two shallow night-time arcer casts at 34 and 40 m were appreciably different (Figs 4B and 5B). The radius abundance peak was smaller at 34 m than at 40 m. This is probably due to differences in the sizes of fishes (*D. theta* and *S. leucopsarus*) at these two depths, with the smaller animals migrating to a shallower night-time depth than larger animals. This supports conclusions of WILLIS and PEARCY (1980) regarding vertical size segregation in certain species of myctophids.

Differences in the number of bubbles of particular size detected acoustically and with nets may result from the measurement or collection of different organisms at a similar depth. Acoustical data and net collection data were not obtained concurrently and there was some spatial and temporal separation between the collection of the two data sets (Table 1). CLARKE (1973) and PEARCY *et al.* (1979) found that not all individuals of a population of myctophids migrate to shallower night-time depths each diel period. Studies of sound scattering layers off Oregon (PEARCY *et al.*, 1977; WILLIS and PEARCY, 1980) clearly demonstrate both inter- and intraspecific differences in the extent of vertical migrations. Migrations of individuals must overlap to some degree, resulting in consolidation and mixing of scattering layer constituents.

It is generally assumed that midwater fishes with swimbladders are neutrally buoyant at some point in their vertical range (MARSHALL, 1960; ALEXANDER, 1972; VENT and PICKWELL, 1977). However, results of this study suggest that some myctophids may not achieve neutral buoyancy with gas-filled swimbladders. For example, *Protomyctophum* spp. which are collected from depths of >200 m do not float in seawater and they do not have everted stomachs or enlarged swimbladders. Possibly swimbladders rupture during ascent, gases are removed from the swimbladder by physiological mechanisms or the swimbladders are not inflated to the neutral buoyancy volume at depth. Microscopic examination of fresh specimens at sea, however, revealed no obviously ruptured swimbladders, although this does not discount the possibility of losses via gas diffusion or small leaks. Morphological and physiological studies (MARSHALL, 1960, 1972; ALEXANDER, 1971, 1972; BUTLER and PEARCY, 1972) indicated that myctophids do not possess the capability to release swimbladder gases rapidly during a forced ascent, although they can probably resorb gases rapidly enough to migrate vertically without becoming positively buoyant (MARSHALL, 1960). Furthermore, death of fishes during trawling would significantly reduce or end further resorption (but not diffusion) of swimbladder gases.

BONE (1973) concluded that several species of myctophids, including *T. crenularis*, are

negatively buoyant even though they possess functional swimbladders. He also showed that the pectoral fins of *Protomyctophum* spp., *T. crenularis* and *S. californiensis* are relatively long when compared with other myctophids (Table 4). These relatively long pectoral fins may be used to generate hydrodynamic lift to maintain equilibrium, thereby reducing the need for buoyancy generated by a gas-filled swimbladder.

Correlations between the abundance distribution of bubble radii as derived both acoustically and from the neutral buoyancy model suggest that swimbladders were filled to volumes below that required to maintain neutral buoyancy both at daytime and night-time depths. These correlations are most applicable to the more abundant fishes with medium sized swimbladders. Initial interpretation of scattering spectra indicated that an abundance peak at a bubble radius of 0.6 mm in both deep daytime and deep night-time arcer casts (Figs 2B and 3B) was attributable to non-migratory *P. thompsoni* and *P. crockeri* (Figs 8A and B). The peak bubble sizes of both the acoustic data and the modeled net data coincide if we assume that the swimbladders of *Protomyctophum* spp. were inflated to approximately 15% of the volume required to maintain neutral buoyancy ($\alpha = 0.53$).

Results suggest that the myctophids with medium sized swimbladders migrated with their swimbladders at a constant mass. Correlations between deep daytime net and arcer data indicate that swimbladders were filled to 3.9% ($\alpha = 0.34$) of the volume required for neutral buoyancy at depths of 200–250 m. A constant mass migration by these fishes to 40 m would result in expansion of their swimbladders to 18.3% ($\alpha = 0.57$) of the volume required for neutral buoyancy. Further migration to within 1 m of the surface would expand their swimbladders to 83.3% ($\alpha = 0.94$) of the neutral buoyancy volume. Based on correlations between data from the shallow night-time arcer and net data, we estimate that swimbladders were filled to 13.4% ($\alpha = 0.51$) of the neutral buoyancy volume at 40 m. Constant mass migration to a depth of 1 m would expand these swimbladders to 60.9% ($\alpha = 0.85$) of the neutral buoyancy volume, slightly less than the predicted swimbladder size of fishes migrating from 225 to 1 m. Furthermore, correlations with deep night-time arcer data showed that swimbladders were slightly larger (22.5% of the neutral buoyancy volume, $\alpha = 0.61$) than in deep daytime correlations. This may result because fishes not vertically migrating on a particular evening may pump up their swimbladders so that they are closer to neutral buoyancy. Also, it may be due to fishes with swimbladders migrating from deeper depths to about 235 m.

Analysis of acoustic and biological data indicate that the swimbladders of some myctophid fishes off Oregon may be inflated to a volume less than is required to maintain neutral buoyancy. Furthermore, these fishes may not achieve hydrostatic equilibrium at any point in their depth ranges. These results infer that some myctophids of the upper mesopelagic zone regulate swimbladder gases such that they are always slightly negatively buoyant.

Several strategies are suggested for vertical migrations by myctophids. Based on acoustical evidence we conclude that some of the larger myctophids migrated with the swimbladder maintained at a constant volume. Correlations between acoustical and biological data sets indicates that medium sized fishes migrated with swimbladders maintain at a constant mass. Swimbladder regulation in the smaller myctophids was not considered because these fishes were not sampled in the deeper collections.

Acknowledgements—We would like to thank the crew of the F.V. *Pat San Marie*, Marc Willis and Rick Brodeur for assistance at sea. This study was funded by the Office of Naval Research under contract N00014-79-C-0004.

REFERENCES

- ALEXANDER R. (1971) Swimbladder gas secretions and energy expenditure in vertically migrating fishes. In: *Proceedings of an international symposium on biological sound scattering in the ocean*, G. B. FAROJHAR, editor, Maury Center for Ocean Science, pp. 74-81.
- ALEXANDER R. (1972) The energetics of vertical migration by fishes. In: *The effects of pressure on organisms*, M. A. SLEIGH and A. G. MACDONALD, editors, Academic Press, New York, pp. 273-294.
- ANDRIEVA I. B. (1964) Scattering of sound by air bladders of fish in deep sound-scattering layers. *Soviet Physics-Acoustics*, **10**, 17-20.
- BADDOCK J. and N. R. MERRILL (1976) Midwater fishes in the eastern North Atlantic. I. Vertical distribution and associated biology in 30°N-23°W, with developmental notes on certain myctophids. *Progress in Oceanography*, **7**, 3-58.
- BAKER A. DE C., M. R. CLARKE and M. J. HARRIS (1973) The N.E.O. combination net (RM11 + 8) and further developments of rectangular midwater trawls. *Journal of the Marine Biological Association of the United Kingdom*, **53**, 167-184.
- BARHAM E. G. (1963) Siphonophores and the deep scattering layer. *Science*, **140**, 826-828.
- BARHAM E. G. (1971) Deep-sea fishes: lethargy and vertical orientation. In: *Proceedings of an international symposium on biological sound scattering in the ocean*, G. B. FAROJHAR, editor, Maury Center for Ocean Science, pp. 100-116.
- BAIZER W. E., W. A. FRIEDL and J. W. REISE (1973) Can acoustic volume scattering be predicted from net haul data? *Journal of the Acoustical Society of America*, **54**, 290.
- BAIZER W. E., J. W. REISE and W. A. FRIEDL (1975) Acoustic volume scattering: its dependence on frequency and biological scatterers. Naval Undersea Center, Technical Paper 442, 25 pp.
- BOST Q. (1973) A note on the buoyancy of some lantern-fishes (Myctophoidae). *Journal of the Marine Biological Association of the United Kingdom*, **53**, 619-633.
- BROOKS A. L. (1976) Swimbladder allometry of selected midwater fish species. Naval Undersea Science Center Technical Report 4983, 44 pp.
- BROOKS A. L. (1977) A study of the swimbladders of selected mesopelagic fish species. In: *Oceanic sound scattering prediction*, N. R. ANDERSEN and B. J. ZAHURANEK, editors, Plenum Press, New York, pp. 565-590.
- BUTLER J. L. and W. G. PEARCY (1972) Swimbladder morphology and specific gravity of myctophids off Oregon. *Journal of the Fisheries Research Board of Canada*, **29**, 1145-1150.
- CAPEN R. L. (1967) Swimbladder morphology of some mesopelagic fishes in relation to sound scattering. U.S. Navy Electronics Laboratory Research Report, 29 pp.
- CLARKE I. A. (1973) Some aspects of the ecology of lanternfishes (Myctophidae) in the Pacific Ocean near Hawaii. *United States Fishery Bulletin*, **71**, 404-434.
- FRIEDL W. A., G. M. CAHILL, R. M. IBARRA, F. A. DEWITT, JR and D. W. BROWN (1971) Pelagic communities and sound scattering off Santa Barbara, California. In: *Proceedings of an international symposium on biological sound scattering in the ocean*, G. B. FAROJHAR, editor, Maury Center for Ocean Science, pp. 1-19.
- FULTON P. (1963) An automatic opening-closing device for large plankton nets and midwater trawls. *Journal of the Marine Biological Association of the United Kingdom*, **43**, 295-308.
- FRIEDL W. A., G. V. PICKWELL and R. J. VEST (1977) The MINOX program: an example of a multidisciplinary oceanic investigation. In: *Oceanic sound scattering prediction*, N. R. ANDERSEN and G. B. FAROJHAR, editors, Plenum Press, New York, pp. 591-618.
- GREENSAW C. E. and R. K. JOHNSON (1983) Multiple-frequency acoustical estimation. *Biological Oceanography*, **2**, 227-252.
- HOLLIDAY D. V. (1972) Resonance structure in echoes from schooled pelagic fish. *Journal of the Acoustical Society of America*, **51**, 1322-1332.
- HOLLIDAY D. V. (1976) Technical report on exploratory development in the application of swimbladder resonance techniques to marine surveys. Tracor Document 1-76-SD-1101-0.
- HOLLIDAY D. V. (1977) Extracting bio-physical information from the acoustic signatures of marine organisms. In: *Oceanic sound scattering prediction*, N. R. ANDERSEN and B. J. ZAHURANEK, editors, Plenum Press, New York, pp. 619-624.
- HOLLIDAY D. V. (1978) MORDAX II/III/IV. Tracor Document 1-78-SD-0023-4-U, 2260 pp.
- HOLLIDAY D. V. (1980) Use of acoustic frequency diversity for marine biological measurements. In: *Advanced concepts in ocean measurements for marine biology*, E. P. DIERKE, E. J. VERNBERG and D. Z. MIRKIN, editors, University of South Carolina Press, pp. 423-460.
- JOHNSON R. K. (1977) Acoustic estimation of scattering-layer composition. *Journal of the Acoustical Society of America*, **61**, 1636-1639.
- JOHNSON R. K. (1979) Gas bubble sizes for selected myctophids. *School of Oceanography*, Oregon State University, Reference 79-6, 18 pp.

- KANWISHER, L. and A. EHLING (1957) Composition of the gas in bathypelagic fishes. *Deep-Sea Research*, **4**, 211-217.
- KIECKHEFER, R. C. and R. H. GIBBS, JR. (1972) Swimbladder structure of Mediterranean midwater fishes and a method of comparing swimbladder data with profiles. In *Mediterranean biological studies*, Final Report, Vol. 1, Smithsonian Institution, pp. 230-281.
- LAWSON, C. T. and R. J. HANSON (1974) *Solving least squares problems*. Prentice-Hall, Englewood Cliffs, New Jersey, 340 pp.
- LOVE, R. H. (1975) Predictions of volume scattering strength from biological trawl data. *Journal of the Acoustical Society of America*, **57**, 300-306.
- LOVE, R. H. (1977) Progress in the correlation of volume scattering strengths to biological data. In *Oceanic sound scattering prediction*, N. R. ANDERSEN and B. J. ZAHARANKO, editors. Plenum Press, New York, pp. 631-646.
- MARSHALL, N. B. (1960) Swimbladder structure of deep sea fishes in relation to their systematics and biology. *Discovery Reports*, **31**, 1-222.
- MARSHALL, N. B. (1972) Swimbladder organization and depth ranges of deep sea teleosts. *Science*, **176**, 269-272.
- NEIGHBORS, M. A. and B. G. NALPAKTELIS (1982) Lipid compositions, water contents, swimbladder morphologies, and buoyancies of nineteen species of midwater fishes (8 myctophids and 11 mesopelagials). *Marine Biology*, **66**, 207-215.
- NEVINZEL, J. C., W. RODECKER, J. S. ROBINSON, and M. KAYAMA (1969) The lipids of some conopline fishes (family Myctophidae). *Comparative Biochemistry and Physiology*, **3**, 25-36.
- PEARCY, W. G. and R. M. EATERS (1966) Vertical migration and distribution of mesopelagic fishes off Oregon. *Deep-Sea Research*, **13**, 153-165.
- PEARCY, W. G. and R. S. MUSELARK (1973) Scattering layers and vertical distribution of oceanic organisms off Oregon. In *Proceedings of an international symposium on biological oceanography*, vol. 1, ed. G. B. FAROE-HAR, editor. Marine Center for Ocean Science, pp. 381-394.
- PEARCY, W. G., L. E. KRYGIER, R. MUSELARK and E. RAMSEY (1977) Vertical distribution and migration of oceanic micronekton off Oregon. *Deep-Sea Research*, **24**, 223-245.
- PEARCY, W. G., H. A. FORK and W. PEDERSEN (1979) Comparison of the diurnal habits of a migratory, non-migratory *Stenobrachius leucopsyllus* (Myctophidae). *Marine Biology*, **51**, 1-8.
- PICKWELL, G. V., E. G. BARTHAM and J. W. WESTON (1964) Carbon monoxide production by a deep-sea siphonophore. *Science*, **144**, 860-862.
- PICKWELL, G. V., R. J. VENT, E. G. BARTHAM, W. F. BAYLECK and L. E. DAVIS (1975) Biological oceanic scattering off southern California, Baja California, and Guadalupe Island. In *Proceedings of an international symposium on biological oceanography*, vol. 1, ed. G. B. Faroe-Har, editor. Marine Center for Ocean Science, pp. 490-507.
- SAMICHO, D. D. (1982) Zooplankton and micronekton abundance in acoustic scattering layers off the New Scotland slope. *Canadian Journal of Fisheries and Aquatic Sciences*, **39**, 760-771.
- VENT, R. J. and G. V. PICKWELL (1977) Acoustic volume scattering measurements with related biological and chemical observations in the northeastern tropical Pacific. In *Oceanic sound scattering prediction*, N. R. ANDERSEN and B. J. ZAHARANKO, editors. Plenum Press, New York, pp. 697-779.
- WESTON, D. F. (1967) Sound propagation in the presence of bladder fish. In *Underwater acoustics*, Vol. 1, A. M. AUBERT, editor. Plenum Press, New York, pp. 85-88.
- WILDS, J. M. and W. G. PEARCY (1980) Spatial and temporal variations in the population structure of three lanternfishes (Myctophidae) off Oregon, U.S.A. *Marine Biology*, **57**, 181-191.
- ZAHARANKO, B. J. and W. T. PRUITT (1971) Biological results from scattering layer investigations in the Norwegian Sea. In *Proceedings of an international symposium on biological oceanography*, vol. 1, ed. G. B. Faroe-Har, editor. Marine Center for Ocean Science, pp. 360-378.

The Australian Coastal Experiment: A Search for Coastal-Trapped Waves

H. J. FREELAND*, E. M. BOLAND, J. A. CHURCH, A. J. CLARKE**, A. M. G. FORBES, A. HUYER¹,
R. L. SMITH¹, R. O. R. Y. THOMPSON¹ AND N. J. WHITE

(CSIRO Division of Oceanography, Hobart, Tasmania 7001, Australia)

(Manuscript received 8 July 1985, in final form 13 January 1986)

ABSTRACT

The Australian Coastal Experiment (ACE) was conducted in the coastal waters of New South Wales from September 1983 to March 1984. The data obtained allow a detailed examination of the dynamics of flow on the continental shelf and slope and in particular allow a description of coastal trapped wave modes propagating within the coastal waveguide.

The trapped wave signal is contaminated by energy from the East Australia current eddies approaching the continental slope. However, the data do allow a clear separation of the first three coastal trapped wave modes over the range of frequencies appropriate to the weather forcing band. Through that frequency range the phase speed is computed and an empirical dispersion relation determined for each mode. The empirical dispersion relations compare well with the theoretical relations indicating that a large fraction of the variance in current velocities on the continental shelf can be accounted for by coastal trapped wave theory.

Wind forcing of trapped waves is also considered and evidence presented that in the ACE area the motions are dominated by the propagation of free waves through the arrays.

1. Introduction

Hamon (1962, 1966) showed that the low frequency part of sea-level variations along the eastern coast of Australia was substantially nonisostatic. Furthermore, the adjusted sea-level time series at different sites (adjusted to remove the isostatic response to atmospheric pressure fluctuations) showed a definite tendency to propagate phase northwards. Robinson (1964) suggested that the nonisostatic part of sea-level and its propagation northwards were due to the existence of a type of barotropic topographic Rossby wave trapped in a continental shelf and slope waveguide. Adams and Buchwald (1969) showed that the wind stress, rather than atmospheric pressure, was the dominant generator of shelf waves. Gill and Schumann (1974) showed that the pressure amplitude of each long shelf-wave mode satisfied a simple forced, first-order wave equation. Clarke (1977) showed that this latter result was applicable not only to barotropic continental shelf waves (CSWs) which depend only on the topography but also to the generalized type of wave motion, including the

effects of stratification, known as "coastal trapped waves" (CTWs).

It was shown by Brink and Allen (1978) and Brink (1982) that the forced first-order wave equations for the infinite set of wave modes are coupled by friction. Recently, Clarke and Van Gorder (1986) reexamined the frictional long-wave problem and suggested a means for calculating the response of a coastal oceanic region to a general wind-stress field.

A review article by Mysak (1980) listed numerous observations of sea-level and longshore current perturbations which show apparent pattern propagation speeds roughly compatible with the speeds predicted by CTW theory. Details aside, it does appear that current fluctuations do occur on most of the continental shelves of the world which can be interpreted to be some sort of topographic Rossby wave. CTWs have been ascribed an important role in causing or suppressing upwelling (Crépon and Richez, 1983) and with widespread effects on fisheries and weather (O'Brien et al., 1981). Despite their reputed importance, there has been little systematic field effort to verify that the dynamics of the perturbations are those appropriate to forced coastal trapped wave theory. All of the previous experimental studies of CTWs have had to use data collected primarily to study other phenomena such as tides or upwelling. Because of this Mysak (1980) wrote that "there is a pressing need for a CSW-designed field experiment, which has never been carried out in the past." It was specifically to respond to this "pressing need" that the Australian Coastal Experiment, or ACE,

The paper was compiled by the first author with contributions from the co-authors. The co-authors are listed in alphabetical order.

* Institute of Ocean Sciences, Sidney, B.C. V8L 4B2, Canada.

** Dept. of Oceanography, Florida State University, Tallahassee, FL 32306.

¹ College of Oceanography, Oregon State University, Corvallis, OR 97331.

• P.O. Box 24, Lindisfarne, Tasmania 7015, Australia.

was designed and carried out off the coast of New South Wales (eastern Australia) between Cape Howe and Newcastle (see Fig. 1) during the period September 1983 to March 1984.

To carry out this experiment we needed a coast that 1) was accessible, 2) had fluctuations in sea level and velocity at a detectable level, 3) was free of complicating and obfuscating factors such as fronts, large topographic changes or rapid changes in stratification, and 4) was long enough for propagation to be evident. The experiment should not be carried out in a region dominated by large mean flows, so that the evolution of waves can be linear, and it was considered desirable that waves be at least partially generated within the study area. With these limitations and constraints, the New South Wales coast seemed to be a reasonable candidate.

A unique aspect of this experiment is that prior to the recovery of the experimental array, a paper was published by Clarke and Thompson (1984) that made specific predictions about the behavior of currents in

the ACE area. The predictions were based on a frictionless theory which we will summarize here.

The usual quasi-geostrophic equations of motion for a stratified Boussinesq ocean are written down and separable solutions sought of the form

$$p(x, y, z, t) = \sum_{n=1}^{\infty} F_n(x, z) \phi_n(y, t). \quad (1)$$

The functions $F_n(x, z)$ are the CTW eigenfunctions, depend on the offshore coordinate (x) and depth (z), and are solutions of an eigenvalue problem

$$F_{xx} + \left(\frac{f^2}{N^2} F_z \right)_z = 0 \quad (2)$$

with appropriate boundary conditions. In (2) N and f are the Brunt-Väisälä frequency and the Coriolis parameter, respectively. The eigenvalues for this problem are the long-wave phase speeds and emerge through the boundary conditions.

The functions $\phi_n(y, t)$ which describe the longshore evolution of the coastal trapped waves and the time variability satisfy a forced first-order wave equation

$$-\frac{1}{c_n} \frac{\partial \phi_n}{\partial t} + \frac{\partial \phi_n}{\partial y} = B_n \tau(y, t) \quad (3)$$

where c_n are the eigenvalues of the equation for $F_n(x, z)$, y is the longshore coordinate, τ is the longshore component of wind-stress, and the numbers B_n are coupling coefficients between the wind-stress and the modal eigenfunctions F_n . Using Eq. (3) the longshore evolution of currents in a coastal waveguide can be described if the initial current distribution can be expanded in a sum using the eigenfunctions F_n .

This is in principle a straightforward operation. If we write the longshore component of velocity at a particular line of moorings as $v(x, y, z, t)$ then we can expand velocities as

$$v(x, y, z, t) = \sum_{n=1}^{\infty} G_n(x, z) \phi_n(y, t) \quad (4)$$

and derive the relationship between $F(x, z)$ and $G(x, z)$ as

$$G_n(x, z) = \frac{1}{f} \frac{\partial F_n}{\partial x} \quad (5)$$

For the ACE region, Clarke and Thompson (1984) found that the observations of Hamon (1960) satisfied the boundary condition $\phi_n(0, t) = 0$, since he found that the ocean was nearly isostatic at Eden (see Fig. 1). This suggests that the ACE area would be dominated by coastal trapped waves, i.e., that signals should largely be generated within the experimental region by local wind forcing.

CTWs that enter the southern region of the experiment contribute little to the observed variability. Clarke and Thompson (1984) present a detailed discussion of the method for the distribution of the

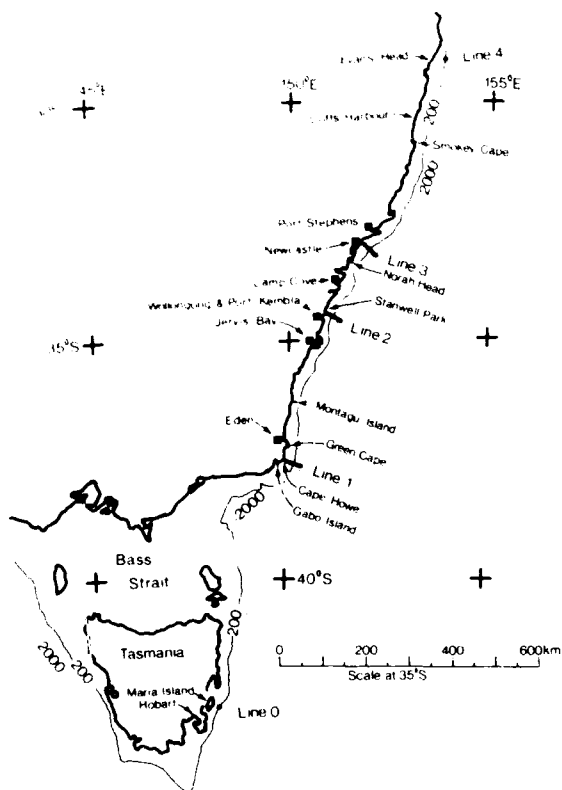


FIG. 1. Map of southeastern Australia showing the general area of the Australian Coastal Experiment, the principal landmarks referred to in the text, and a few depth contours. Tide gauge locations are marked by the symbol ■ and current meter moorings by the symbol ●.

AD-A191 689

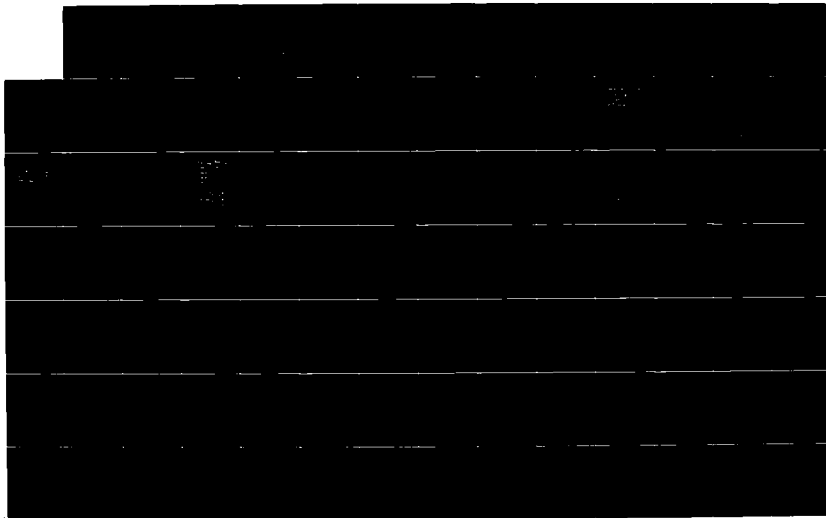
COMPILATION OF REPRINTS NUMBER 64(U) OREGON STATE UNIV
CORVALLIS COLLEGE OF OCEANOGRAPHY NOV 87 REF-88-23

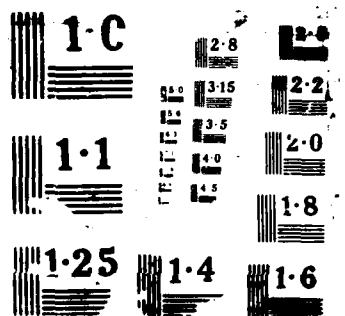
2/3

UNCLASSIFIED

F/G 8/3

HL





make specific predictions about the behavior of currents:

1) Outside the surface and bottom Ekman layers, the low-frequency fluctuating wind-driven currents should be nearly alongshore and satisfy $v = (1/\rho_0) p_x / f$.

2) The alongshore current amplitude should decrease monotonically from the coast. For 1 dyn cm^{-2} longshore wind-stress amplitude, typical longshore current amplitudes at lines 2 and 3 (see Fig. 1) should be $10\text{--}20 \text{ cm s}^{-1}$. Significant longshore current amplitudes should be confined to the shelf and upper slope.

3) Longshore currents and adjusted sea levels should propagate northward along the coast at $4\text{--}5 \text{ m s}^{-1}$. Upward phase propagation should also be observed.

4) For the lower frequencies of the "weather" frequency band ($2\pi/\text{few days}$ – $2\pi/\text{few weeks}$) longshore current and adjusted sea-level amplitudes should increase northward from line 1 ($y = 0$).

5) The wind-driven current and sea-level fluctuations should be small at the Cape Howe, or line 1, section. This prediction results from an analysis of Hamon's (1966) data.

In this paper we will attempt a synthesis of the principal results from ACE that pertain to the propagation of coastal trapped waves. In doing this we will also draw on some results from more specific papers by Church et al. (1986), Church et al. (personal communication, 1986) and Forbes (personal communication, 1985).

In section 2 of this paper we will describe the deployment of equipment in the ACE experimental array, and comment on the data return and instrument failures. In section 3 we will describe some elementary observations of the general behavior of the current fluctuations, and we will empirically establish the likelihood of free waves. In section 4 we will decompose the current fluctuations into three coastal-trapped wave modes and 1 eddy mode at each of the three principal lines of moorings. The evolution of the modes from one line to another will allow us to compute empirical dispersion relations for the dynamical modes. In the final section we will discuss the implications of the previous analysis regarding the predictability of coastal current systems and discuss the possible origins of the energy fluxes observed.

2. The experiment

ACE was conducted off the east coast of New South Wales (Figs. 1, 2) for a six-month period between September 1983 and March 1984. The experiment included an array of current meters with three main lines with five moorings each, repeated CTD and XBT surveys, meteorological measurements from moored buoys and coastal stations, sea level measurements at coastal tide gauges, and bottom pressure measurements at a few sites. Several other types of data were also acquired as part of ACE but none of these will be explicitly discussed in this paper: satellite infrared images

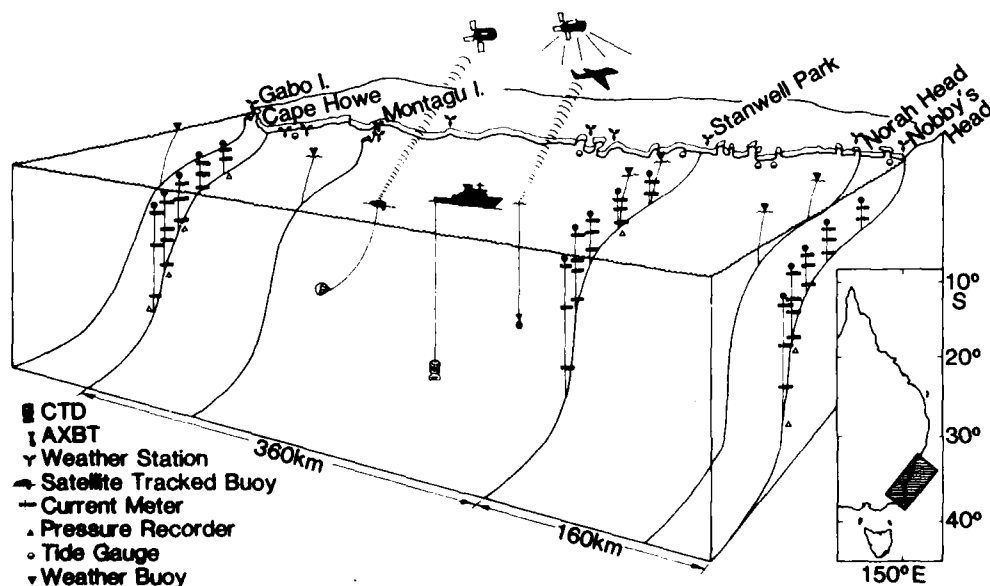


FIG. 2. A perspective view of the instrument array deployed in the intensive ACE area along the New South Wales coastline.

for determining the location of East Australia Current (EAC) eddies and meanders; AXBT profiles acquired by the Royal Australian Air Force; and satellite-tracked drifter buoys drogued at 200 m that were seeded into the EAC eddies and used to keep track of their movement (Wells and Cresswell, 1985).

a. The moored array

The current meter array consisted of three lines of moorings (Figs. 1 and 2) off Cape Howe in the south (line 1), Stanwell Park near Sydney (line 2), and Newcastle in the north (line 3). Two additional moorings were deployed, one off Evan's Head near Coff's Harbour at 29°S (line 4) and one off Maria Island off the east coast of Tasmania at 42°S (line 0). Each of the three principal lines was arranged perpendicular to the local coastline, was nominally identical with each other, and consisted of 15 Aanderaa current meters on 5 moorings (Table 1). Some of the moorings also carried Applied Microsystems tide gauges. Since we will want to refer to specific moorings in the array we have adopted a simple code: a mooring referred to as 23 will be on Line 2, and be the third mooring out from the coast. We identify individual current meters by adding a slash to the mooring designation and appending the depth of the specific current meter, e.g., 34/1000 is the current meter at 1000 m depth on Line 3, fourth mooring from the coast. A prefix letter "f" indicates a time series that has been low-pass filtered (<0.6 cpd) to remove tides and other high frequency signals, and the inclusion of the letter "p" indicates a bottom pressure record, e.g., fp11 is the low-pass filtered pressure record from the bottom of mooring 11.

Data from the current meter array have been summarized by Freeland et al. (1985). The current meter arrays returned about 70% of total possible data. Some moorings were lost due to commercial fishing and others from unexpectedly large currents (a meander in the EAC) hitting the northern line of moorings late in the experiment. These large currents (with a maximum speed of 168 cm s^{-1} at current meter 34/450) caused large vertical excursions of the tops of two moorings and caused four steel-sphere buoys to implode. Backup buoyancy farther down ensured that some useful data

were recorded from these moorings even after the implosions.

b. CTD surveys

A total of 602 CTD stations were completed on six different cruises, one each month from September 1983 through February 1984 (data report in preparation). Most of these were acquired along the principal mooring lines and have been used in this paper to define the Brunt-Väisälä frequency profile in order to compute local shapes of the CTW eigenfunctions from Eq. (2). The CTD surveys were also used to keep track of the positions of the EAC eddies which had been known to occur in this region (Nilsson and Cresswell, 1981). The CTD surveys showed that eddies occurred very near the continental slope in late September and again in January and February. The eddies are interesting in their own right and will be described elsewhere, but in this paper they are treated as an undesirable source of noise.

c. Meteorological data

A number of Metspar meteorological buoys were deployed to measure the oceanic wind field, but for a variety of reasons the buoys did not report large amounts of data. Good quality wind data were obtained from a number of shore-based meteorological stations by the Australian Bureau of Meteorology. Some of these stations show evidence of topographic steering and could not be considered to represent the marine wind field; however, other stations compared well with the short time-series obtained from the Metspar buoys (Forbes, 1985). Figure 3 shows the time series of filtered alongshore wind speed measured at two Metspar buoys and at the shore-based stations closest to these stations. The Metspar time series are shown dotted overlaying the shore-based time series; the time series are clearly well correlated. The speed series correlate at $r = 0.76$ and 0.75 at Stanwell Park and Norah Head, respectively. Similar time series for wind stress yield correlations of 0.67 and 0.66 . On the basis of this comparison, we decided to use data from seven shore-based wind stations: Gabo Island, Green Cape, Montagu Island, Wollongong (Port Kembla), Norah Head, Smokey Cape and Coff's Harbour (Fig. 1).

d. Bottom pressure and coastal sea level data

Bottom pressure was measured on Line 1 using Applied Microsystems pressure gauges moored on the bottom near moorings 11 and 13; both returned 100% data of excellent quality. Another bottom pressure gauge was moored at the bottom of mooring 31, but the data from this gauge may have been contaminated by mooring motion. Sea level data from coastal tide gauges at Eden, Jervis Bay, Port Kembla, Camp Cove in Sydney Harbour and Port Stephens (Fig. 1) were

TABLE 1. The depths of current meters and total water depths for the nominal arrays deployed on lines 1, 2 and 3. For lines 0 and 4 only mooring number 2 was deployed.

Mooring	Water depth (m)	Instrument depths (m)
1	140	75, 125
2	200	75, 125, 190
3	500	125, 190, 450
4	1200	190, 450, 650, 1000
5	2000	450, 1000, 1900

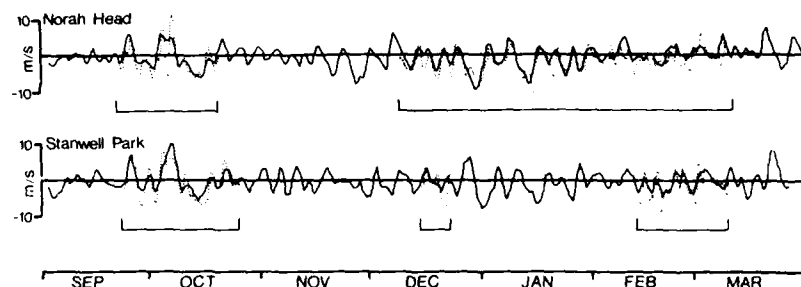


FIG. 3. The longshore component of wind speed measured at two METDATA buoys (dotted lines) plotted against time and superimposed on equivalent plots from nearby coastal wind stations.

obtained from the Maritime Services Board, Public Works Department of New South Wales. These data were adjusted for the "inverted barometer effect" using atmospheric pressure observations from nearby meteorological stations. A data report on the total pressure measurement array is in preparation.

3. Results

a. The velocity field

In Fig. 4 we show plots of current velocity vectors at two sites on each of the three principal lines and one series from the Maria Island, line 0, mooring. It is clear that there is some similarity among longshore current components between adjacent lines, particularly at the inshore locations. The currents between adjacent lines show greatest similarity when the more southerly currents are lagged somewhat in time. This implies northward propagation of current signals as expected.

The inshore currents shown on Fig. 4 clearly show considerable energy at periods appropriate to weather forcing. The same signals are also visible in the currents at sites offshore, but there is a distinct bias towards lower frequencies at those sites. This is probably due to the presence of EAC eddies in the ACE region.

Rather more startling are the general energy levels. The expectation of much lower energy levels at line 1, compared with the other two lines, is not supported by the observations. Also, though the energy levels offshore are lower than those over the shelf, the difference is not impressive; clearly there are signals in these time series besides the CTW activity.

For each current meter site the longshore component of velocity was Fourier transformed in 25 day blocks. In Fig. 5 we have contoured the variance along each line in the (x, z ; on-offshore and depth) plane for three periods, 25, 12½ and 6¼ days. In the magnitude of the variances, the three lines are remarkably similar, except for line 3 at a period of 25 days. In that case line 3 appears to have very much more energy than either of the other two lines. Only for two of the nine plots shown in the prediction, number 2, of Clarke and Thompson (1984) satisfied, that amplitudes should decrease

monotonically from inshore to offshore. Prediction 5, that wind-driven currents be small at line 1 fares no better; at a period of 6¼ days the distribution of variance, and actual magnitudes, are extremely similar at lines 1 and 3, and variances are substantially lower at line 2. The most notable difference between lines 1 and

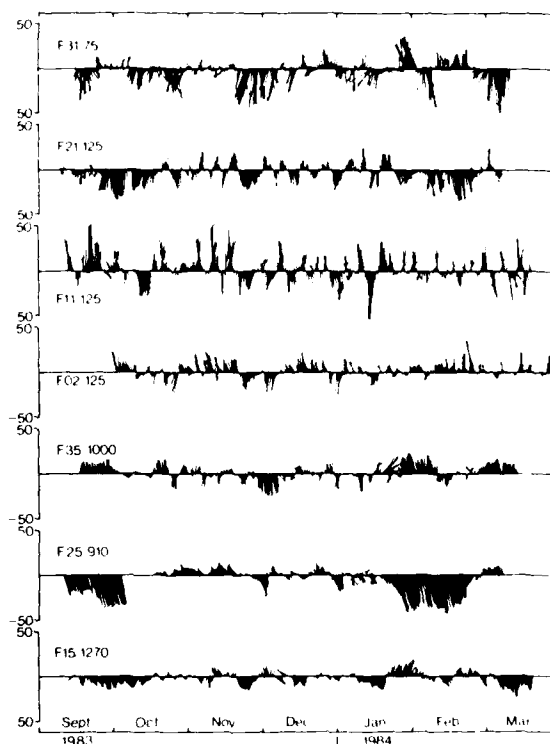


FIG. 4. Current vectors measured at two locations on each of the three principal lines of moorings, one site shallow and one site deep and one from the single mooring off Maria Island. The currents have been low-pass filtered using a Lanczos cosine filter having a half-power point of 40 h and subsampled at 12 h intervals. The currents plotted here are rotated so that the principal axis of variance is directed up and down the page. Very closely this corresponds to the longshore direction, with the direction NNE up the page.

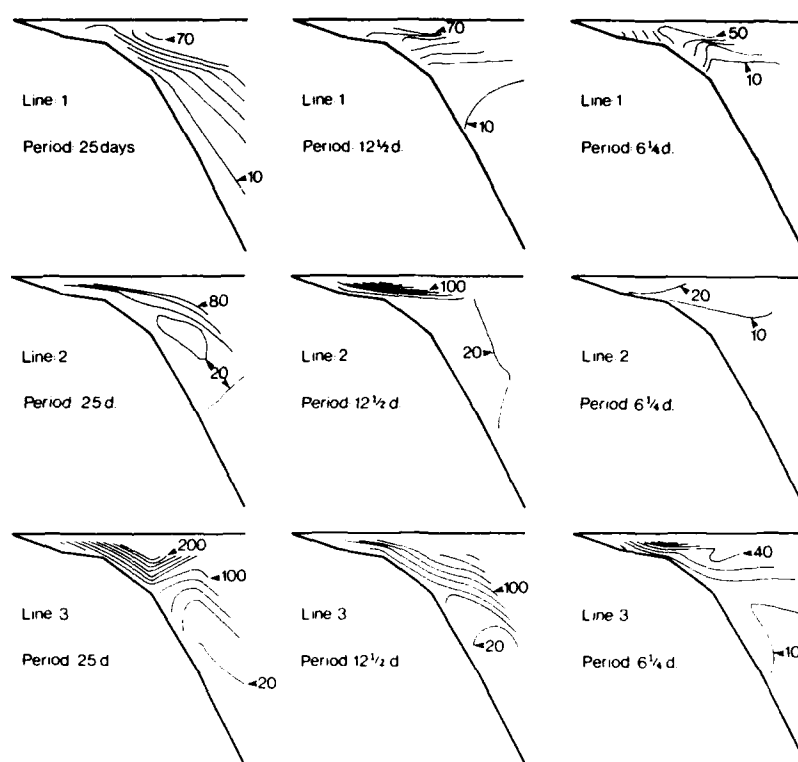


FIG. 5. Variance distribution along each of the three principal mooring lines at three frequencies in $(\text{cm s}^{-1})^2$.

3 at $6\frac{1}{4}$ days is the shift of the position of maximum variance from close inshore at line 1 to the shelf edge at line 3. At periods of $12\frac{1}{2}$ days and 25 days the general pattern of variance distribution is very similar at each of the three lines, magnitudes are similar at lines 1 and 2, but substantially greater at line 3. Clearly, compared with the other two lines, it is not at all obvious that line 1 is quiescent and it appears that we must reject this prediction of Clarke and Thompson also.

b. Sea-level observations

We consider the sea level and bottom pressure observations from two points of view: 1) Are they consistent with Clarke and Thompson's prediction 5 and Hamon's (1966) sea level data? 2) Is there evidence of northward propagation in the subsurface pressure (adjusted sea level) signal?

Clarke and Thompson based their prediction 5 (that wind-driven sea level and current fluctuations should be small at Line 1) on "the analysis by Hamon (1966) that sea levels at Hobart are isostatic and at Eden very nearly so" (Clarke and Thompson, 1984, p. 340). Correlation and regression coefficients between pairs of ACE sea level and atmospheric pressure observations (Table 2) are in substantial agreement with Hamon's

where both exist, except that the ACE regression coefficients have much larger error bars. This difference arises because we estimate the integral time scale (Lumley and Panofsky, 1964) to be about 5 days (see Fig. 6), while Hamon apparently assumed each daily value represented an independent sample, i.e., Hamon overestimated the number of degrees of freedom by as much as a factor of five, and hence significantly underestimated his errors. It appears then that the ACE sea level data are in substantial agreement with Hamon's, yet the ACE current measurements contra-

TABLE 2. Sea level adjustment statistics. Correlation and regression coefficients between measured sea-level and local atmospheric pressure. Error bars are 95% confidence intervals.

Site	Regression coefficient (cm/mb)	Correlation coefficient	Duration of data (days)
fp11	-1.03 ± 0.31	-0.74	189 ¹
Eden	-1.29 ± 0.43	-0.70	205
Jervis Bay	0.58 ± 0.51	-0.42	143
Port Kembla	0.35 ± 0.83	0.18	119
Camp Cove	0.65 ± 0.48	0.40	204 ²
fp31	-1.02 ± 0.67	0.47	176
Port Stephens	0.61 ± 0.50	-0.37	204 ¹

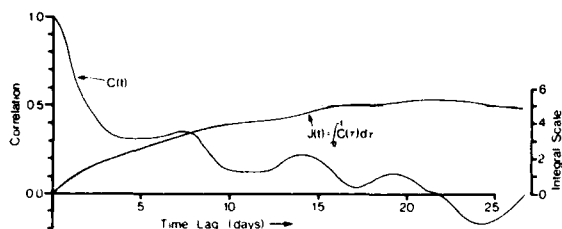


FIG. 6. The autocovariance function $C(t)$ and its integral $J(t)$ for the Eden tide gauge time series. The raw data were filtered to remove tides and other high frequency information and then subsampled at 0.5 day intervals. The function $J(t)$ approaches an asymptote, as t becomes large, which we identify as being close to a period of 5 days.

dict the prediction based on them. How does this discrepancy arise?

Consider the sea level, h_w , at a particular location. It may be decomposed into an isostatic portion, h_i , another signal of interest (e.g., the CTW signal), h_0 , and noise, ϵ_0 , i.e., $h_w = h_i + h_0 + \epsilon_0$. By definition, the isostatic portion, h_i , is proportional to the changing atmospheric pressure, p_a : $h_i = b_0 p_a$, where $b_0 = -0.99$ cm mb $^{-1}$. Then, $h_w = b_0 p_a + h_0 + \epsilon_0$. For the coastal tide gauge stations, h_w was measured directly; for the bottom pressure gauges it was estimated as $(p_b - p_a)$. The linear correlation (r^2) and regression (b) coefficients (Table 1) were calculated between h_w and p_a using the simple regression model, $h_w = a + b p_a + \epsilon_1$. Note that the noise ϵ_1 in this regression equation implicitly includes any signals, h_0 , which are either out of phase or incoherent with the atmospheric pressure. To interpret results from this regression model, we must consider both the correlation and regression coefficients. If r^2 is near 1, then ϵ_1 is small and h_0 is small, i.e., there are no other interesting signals that are out of phase with the pressure; if r^2 is near 1, and $b = -1$, we can infer that CTW signals in the sea level must be small (but note that higher mode CTWs, which have little surface expression, may still be present). This seems to be the case at Hobart, where Hamon found r^2 to be 0.87 and b to be -1.07 ± 0.11 ; even treating these error bars as overly optimistic, we would conclude that at Hobart $r^2 = 1$ and $b = -1$, i.e., that the shelf-wave signal must be weak or absent at Hobart. This result is also supported by the ACE current observations: current fluctuations off Maria Island (Fig. 1), near Hobart, are relatively small compared to those farther north (Fig. 4).

If the correlation coefficient r^2 of the regression model is significantly smaller than one (but still greater than zero), then ϵ_1 is not small and probably includes some interesting signals, h_0 , which may be either incoherent with the atmospheric pressure or simply out of phase with it. If $r^2 < 1$ and $b = -1$, then we have a local isostatic response in the presence of other interesting signals, such as CTWs. This appears to be the case at Eden, where Hamon found $r^2 = 0.26$ and $b = -0.71 \pm 0.23$ in 1957, and $r^2 = 0.56$ and $b = -0.87$

± 0.20 in 1960; ACE results show $r^2 = 0.49$ and $b = -1.29 \pm 0.43$ at the coastal tide gauge, and $r^2 = 0.56$ and $b = -1.03 \pm 0.31$ at mooring 11. Correcting for the over-optimism in Hamon's error bars, we clearly cannot reject the hypothesis that $r^2 < 1$ and $b = -1$ at Eden. Thus, Clarke and Thompson (1984) should not have ruled out the possibility of CTW signals at Eden.

An important part of Hamon's observations dealt with the apparent propagation of phase of the adjusted sea level northwards along the east Australian coast. Using the ACE adjusted sea level ($h = h_w - h_i$) or subsurface pressure data to compute lagged cross-correlation functions, we found that observations at more northerly stations typically lag those at southerly ones. A contour plot (Fig. 7) of the lagged correlations of each station against Eden shows a distinct tendency for phase to propagate northwards. A linear regression of the time lag at the maximum of each cross-correlation function (small squares in Fig. 7) against longshore displacement indicates a "best fit" phase speed of 3.34 m s $^{-1}$, which is slightly lower than that of Clarke and Thompson. We conclude then that we probably do have CTW-like signals propagating through the ACE area that warrant more detailed analysis.

c. The wind field

Wind measurements with good exposure were available at seven sites: Gabo Island, Green Cape, Montagu Island, Wollongong, Norah Head, Smokey Cape and Coff's Harbour, listed from south to north. The largest

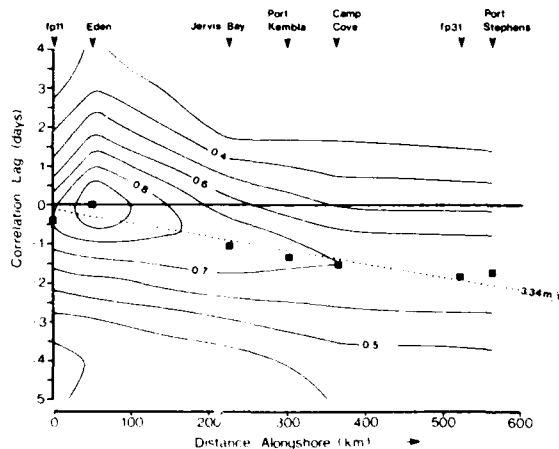


FIG. 7. Contours of equal correlation plotted in a plane of time lag, in days, and distance north of Cape Howe. All time series are correlated against Eden as the reference site. The square symbols indicate the positions for specific displacements of the local maxima in the cross-correlation functions. The dotted line is a least-squares fit through those points indicating the probable northward pattern propagation rate of 3.34 m s $^{-1}$.

separation between any adjacent pair of these sites was only 250 km (between Norah Head and Smokey Cape). Figure 8 shows a plot of wind stress vectors for the ACE experimental period from three locations in the ACE area. Two important properties of the wind field are apparent from this figure. First, the variance in the wind stress field decays rapidly with distance north from Cape Howe. Second, the variability in wind stresses measured at widely separated positions is very similar. Coherence calculations indicate that though the amplitudes of fluctuations do decay northwards the shape remains remarkably invariant. They also indicate that the phase of the longshore wind stress field propagates northwards nondispersively. Specifically in the range of periods 3 to 20 days the phase difference between Montagu Island and Smokey Cape is 0.69 days (± 0.15) and coherence is well above the 95% confidence interval. The longshore separation of these two stations is about 680 km implying a northward phase speed of 11.4 m s^{-1} . Between Montagu Island and Norah Head the phase difference is 0.38 days (± 0.02) implying (for $x = 350 \text{ km}$) a phase speed of 10.7 m s^{-1} . These values for the wind stress phase speed are very close to the value of 11.5 m s^{-1} used by Clarke and Thompson (1984) in their model of the response of the ACE area.

We conclude, therefore, that the wind systems are propagating phase northwards much more rapidly than oceanographic signals. The wind stress phase speed, about 11 m s^{-1} , is well separated from the speed at which sea-level signals are propagating, about 3.5 m s^{-1} . The properties of the ACE wind field will be discussed at greater length by Forbes (personal communication, 1985).

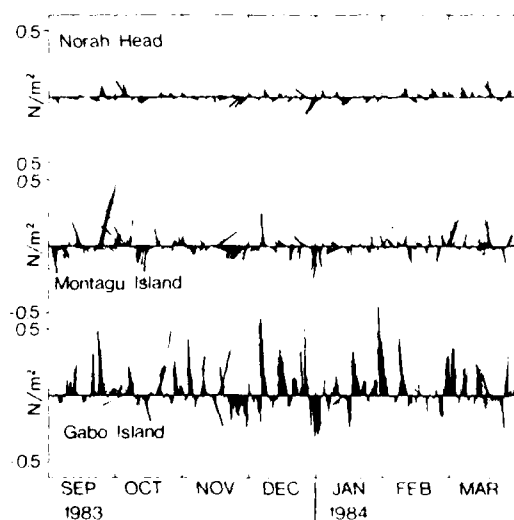


FIG. 8. Wind stress vectors at three coastal stations extending from Gabo Island, near line 1 to Norah Head near line 3. The vectors are rotated so that the principal axis is up and down the diagram. The direction of the principal axis is very nearly in the longshore direction.

d. A transfer function calculation

Contrary to our expectations shelf wave activity is large at the southern end of the experiment. This is consistent with the present observations of sea-level and also with Hamon's observations. The implication is that large amplitude CTWs are entering the southern end of the experimental region and may be propagating through the entire array. Presumably the CTWs experience some modification as they pass through the array, however, we now have to consider the possibility that the free waves may dominate, whereas it was originally expected that the forced waves would dominate. Based on the expectation that the forced waves would dominate, predictions 3 and 4 of Clarke and Thompson (1984) were made. The expected phase speed of $4\text{--}5 \text{ m s}^{-1}$ is based on a particular distribution of amplitude among the dominant modes that need not occur if the dominant waves are not forced locally. The expectation of upward phase propagation at the more northerly lines is similarly the result of analyzing the pure forced problem, as is the prediction that amplitudes should increase northwards. In the total absence of forcing one would expect a slow decline in amplitude due to dissipation by bottom friction or scattering into other wave modes.

Having found that the forced shelf wave seems to be less important than expected, it is appropriate to try to quantify the relative importance of free propagation and forcing. Let us represent the longshore component of current at the northern site then as

$$\hat{U}_n(t) = \sum_{i=0}^N a_i U_s(t - i\Delta t) + \sum_{i=0}^M b_i \tau(t - i\Delta t) \quad (6)$$

where \hat{U}_n and \hat{U}_s represent time series of alongshore component of current at the northern and southern sites respectively, the symbol $\hat{}$ represents an estimate, $\tau(t)$ is the wind stress observed at an intermediate location, Δt is the sampling interval (12 hours in all results to be quoted here) and a_i and b_i are weights to be determined. We then constrain the system (6) to find the combination of weights a_i and b_i that represent \hat{U}_n in the best (least-square sense) way. Various models can be tried by varying the lengths of the filters, i.e., varying N and M above, or by arbitrarily setting one set of weights identically equal to zero and so trying a fit using only the a_i or only the b_i type of weights. The method of solution is simple in principle, but not so in practice. By way of illustration let us consider the simple case of $b_i = 0$ for all i , (the extension including the b_i will be obvious).

Formally the problem reduces to the standard least-squares problem of minimizing E where

$$E = \left[\hat{U}_n(t) - \sum_{i=0}^N a_i U_s(t - i\Delta t) \right]^2 \quad (7)$$

and the overbar indicates an average over time. The solution can be expressed in matrix form:

$$\mathbf{x} = \mathbf{C}\mathbf{y} \quad (8)$$

where the vector $\mathbf{x} = \{x_i\}$ and $\mathbf{y} = \{y_i\}$ and the elements are of the form $x_i = \overline{V_n V_s(t - i\Delta t)}$ and $y_i = a_i$. The matrix \mathbf{C} is a symmetric, positive definite matrix with elements $C_{ij} = \overline{V_s(t - i\Delta t) V_s(t - j\Delta t)}$. Formally we express the solution of this problem as $\mathbf{y} = \mathbf{C}^{-1}\mathbf{x}$. However, the matrix \mathbf{C} generally has a large condition number (ratio of largest to smallest eigenvalue) and so the inverse can be unstable. We proceed, therefore, to solve the problem by singular value decomposition (described in detail in appendix A).

Now let us consider some specific examples of this kind of transfer-function calculation. In the following we will look at the transformation of longshore current components from lines 1 to 2 by representing $V_n(t)$ and $V_s(t)$ in Eq. (6) by f21/125 and f11/125, respectively.

Model 1: Pure current transformation: $N = 5$, $b_i = 0$ for all i . \mathbf{C} is a 6×6 matrix and the solution is stable at y_4 (see Appendix); the best fit of V_s on V_n accounts for 45.5% of the variance in V_n , i.e., the "predicted" currents correlate with V_n at $r = 0.67$. The weight distribution shows a clear maximum indicating that V_n lags behind V_s . A parabolic fit around the maximum suggests a best estimate of the lag of about 1 day.

Model 2: Pure current transformation: $N = 12$, $b_i = 0$ for all i . \mathbf{C} is a 13×13 matrix and the last stable solution is y_{10} ; the best fit of V_s on V_n accounts for 51% of the variance, with a correlation coefficient of 0.7. The list of weights extends to greater lags than for model 1 and indicates two peaks at lags of 1.03 and 3.5 days. This suggests that two signals propagate from line 1 to line 2 at speeds of 3.9 and 1.2 m s^{-1} . However, it is interesting to note that increasing the length of the transfer function from six weights to 13 weights results in increasing the amount of variance accounted for in the model by only a few percent. In that sense model 2 seems rather inefficient.

Model 3: Current transformation and winds: $N = M = 5$. This is essentially model 1 modified to include winds. The winds are renormalized so that they have the same variance as the current time series and so that the a_i and b_i all remain dimensionless. \mathbf{C} is a 12×12 matrix and the last stable solution is y_7 . For this model winds at Montagu Island were used for several reasons: the site is roughly half-way between lines 1 and 2; it is the best exposed of all our wind stations and is likely to be a good representation of the marine wind field; the instrumentation used to record winds was of a relatively high quality. The distribution of weights produced surprising results: the values of a_i were almost exactly the same as in model 1 and accounted for 45.4% of the output variance; the b_i coefficients accounted for only another 4.8% of the output variance. The total

variance accounted for is, of course, larger than that in model 1 because we have increased the information content of the fit, but the increase is not dramatic. We now account for 51.2% of the variance in $V_n(t)$, a larger amount than in models 1 or 2. For this model the best fit to $V_n(t)$ correlates with $V_n(t)$ at $r = 0.70$.

The significant result from these calculations is the clear indication that the CTW signal appears to propagate from line 1 to 2 with little modification by the winds. The addition of winds barely increases our ability to forecast the modification of currents from one line to another. Using variance accounted for as a measure, we are almost 10 times as successful at forecasting the output currents using input currents compared with using winds. We repeated the calculations for model 3 using different wind stations to find which wind station performed best, in the sense of accounting for as much of the total output variance as possible. The best result was obtained from Wollongong (the point on shore closest to line 2) which accounted for 8.6% of the output variance while the a_i terms accounted for 40.1%. Wollongong Head would not be the site of preference for describing the transformation of currents from line 1 to line 2 since it lies very close to line 2; an intermediate site like Montagu Island would be preferred. We conclude then that winds are not of great importance in describing the modification of the currents from one site to another and we should pursue the analysis of the currents into free shelf-wave modes.

4. A modal description of the velocity field

a. The mode shapes

Figure 9 shows a plot of the shapes of the first three CTW eigenfunctions computed separately for the longshore component of velocity at each of the three principal lines of moorings. The eigenfunctions are the solutions $G_n(x, z)$ of Eq. (5), computed simultaneously with the eigenvalues c_n which correspond to the phase speed of each wave. In the long-wave limit the waves are nondispersive and so phase and group velocities are identical. The wave speeds are also entered on Fig. 9. The values of $N^2(z)$ used in Eq. (2) to compute the modes displayed in the figure were calculated from CTD casts along each line of moorings averaged over the entire duration of ACE, i.e., the detailed distribution of $N^2(z)$ varies from one line to another. The bottom topography also varies. These differences do not appear to have a large effect on the structure of the eigenfunctions but do cause significant variation in the wave speeds. (Variation about the mean is about 20%, 13% and 12% for modes 1, 2 and 3, respectively.)

In all nine cases shown in Fig. 9 the largest modal amplitude occurs close inshore and both modes 2 and 3 have nodal lines not far from the shelf edge. Qualitatively the modal shapes are very similar from one line to another. Given these simple observations it is

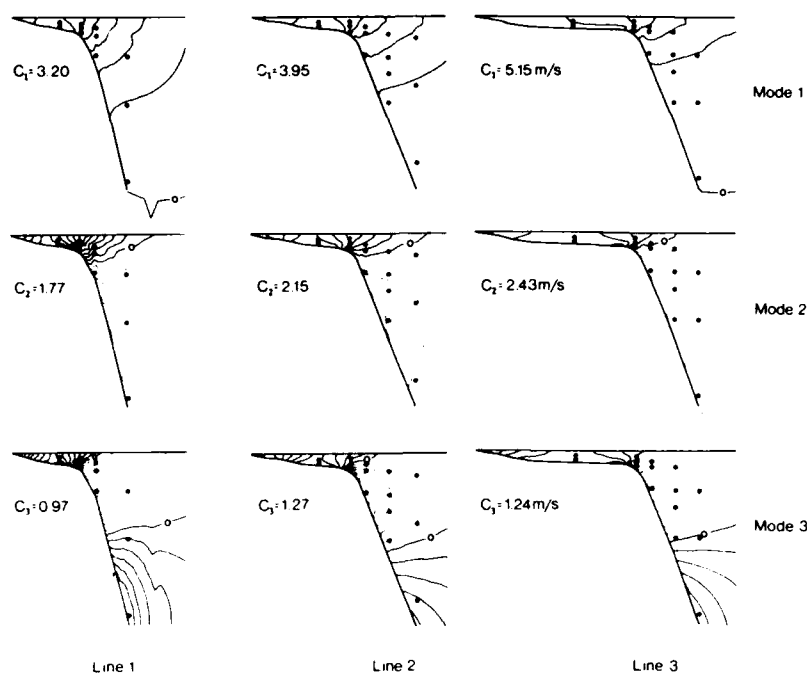


FIG. 9. The first three theoretical CTW mode shapes at each of the 3 principal lines of moorings and the phase speeds associated with each mode. The small dots represent the actual sites where current meter data were acquired on each of the principal lines. The contours are not labeled since the modes can be renormalized without affecting the least-squares computation of modal amplitudes.

difficult to see how any plausible superposition of these modes could yield the variance distributions shown in Fig. 5 which show the largest amplitudes typically at the shelf edge and in some cases seaward of the shelf edge. The conclusion to be drawn is that we are seeing contamination of the shelf-wave signal by the presence of energy from the EAC and its eddy field. Satellite photographs verified that large eddies shed from the current were indeed passing through the ACE region during parts of the experiment. Given the obvious mismatch between the distribution of variance in the experimental array and the shape of the eigenfunctions it is important to examine ways in which the wave field might be decontaminated from the eddy field.

Two methods suggest themselves. The first is to identify periods at each line that are obviously contaminated by eddy activity and excise those parts from the overall record. This approach suffers from a number of problems. It is often not clear when a current meter record is influenced by an EAC eddy; the excising of parts of the data base will inevitably remove part of the CTW signature itself; and the excising operation will inevitably involve some rather subjective judgments. A more objective approach, that removes the eddy activity while leaving the individual time series otherwise intact would be preferred. This turns out to be possible by defining a fourth mode, which we called

an eddy mode, that described the shape of the eddy field.

Examination of detailed EAC events, those that were unambiguously associated with eddies because of the presence of corroborating evidence, clearly showed that these large current events were largely restricted to the continental slope region. In contrast, the CTW modes (Fig. 9) all have their largest signals on the continental shelf. Since current meters fm5/1000 on each line ($m = 1, 2, 3$) contain predominantly eddy signals, we assumed that in any particular line the signal at any current meter that is correlated with the currents at fm5/1000 is the eddy part of the total signal at that site and so could be removed. Let us write the longshore component of velocity at fm5/1000 as $U_m(t)$, i.e., the "eddy" component of velocity at that site. Then along the line m find the value of $a(x, z)$ that minimizes a mean-square error E where

$$E = \overline{[U(x, z, t) - aV_m(t)]^2}$$

and the overbar indicates a time average. The values of $a(x, z)$ define then the shape of an eddy mode. Figure 10 shows a plot of the eddy mode computed along line 3. This was chosen as the best line to define an eddy mode since we had good reason to believe that the eddy field was most intense there, and only at line 3 do we have a substantial quantity of data available at

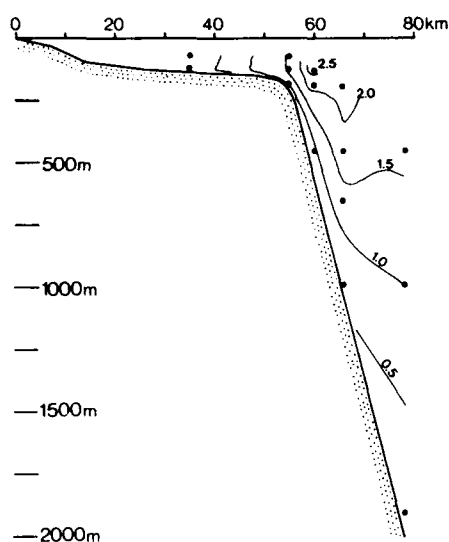


FIG. 10. The "eddy mode" defined as the regression coefficient at each current meter site along line 3 with f35/1000. This mode was used in the subsequent data reduction to absorb signals due to the EAC eddy field.

every site along the line. At both lines 1 and 2, data are missing for almost the entire deployment period at one mooring site each.

The mode shown in Fig. 10 is quite different from the coastal trapped wave modes shown in Fig. 9. In the former the most intense velocities occur seaward of the shelf edge, as one might intuitively expect from an oceanic eddy moving towards the shore. In contrast, at the sites f31/75 and f31/125 the modal amplitudes are extremely small, and this justifies the use of the inshore moorings for exploration for longshore phase propagation. It thus seems reasonable to use the mode shown in Fig. 10 to absorb some of the eddy energy and so optimize our chances of extracting amplitudes of the CTW modes.

b. The modal decomposition

For each mooring line we will expand the observations into three wave modes and one eddy mode. Let $U_j(t)$ be the longshore component of velocity at site (current meter) number j . We break the time series $U_j(t)$ into seven time blocks of 24 days and compute the Fourier transform of the time series for each block. This yields, at each site and for each time block, a series of complex numbers $\hat{U}_j(\omega)$ where ω is 2π divided by T , the period of the Fourier component being examined. For each frequency we define a complex residual \hat{E}_j where:

$$\hat{E}_j = \hat{U}_j - \hat{a}_1 G_{1j} - \hat{a}_2 G_{2j} - \dots - \hat{a}_m G_{mj}$$

and minimize E where

$$E = \sum_{j=1}^N \hat{E}_j \hat{E}_j^*.$$

In the above, $m = 4$ is the total number of modes being examined and N is the number of observations \hat{U}_j . The values G_{ij} are the values of the i th velocity mode at instrument number j , and \hat{a}_i is the complex amplitude of the i th mode. Throughout this section any complex number will be indicated by use of the caret symbol, and its complex conjugate will be denoted by an asterisk. The solution for the complex amplitudes is given by the solution of the complex matrix equation:

$$\begin{bmatrix} \sum G_{1j} \hat{U}_j^* \\ \sum G_{2j} \hat{U}_j^* \\ \vdots \\ \sum G_{mj} \hat{U}_j^* \end{bmatrix} = \begin{bmatrix} \sum G_{1i} G_{1j} & \sum G_{1i} G_{2j} & \dots & \sum G_{1i} G_{mj} \\ \sum G_{2i} G_{1j} & \sum G_{2i} G_{2j} & \dots & \sum G_{2i} G_{mj} \\ \vdots & \vdots & \ddots & \vdots \\ \sum G_{mi} G_{1j} & \sum G_{mi} G_{2j} & \dots & \sum G_{mi} G_{mj} \end{bmatrix} \begin{bmatrix} \hat{a}_1^* \\ \hat{a}_2^* \\ \vdots \\ \hat{a}_m^* \end{bmatrix} \quad (9)$$

which we write in the vector form $\hat{\mathbf{b}} = \mathbf{C} \hat{\mathbf{a}}$. As before, the inverse of the real symmetric matrix \mathbf{C} exists, however, the matrix \mathbf{C} is badly conditioned and we chose to extract the solution by singular value decomposition, see appendices A and B. In the following analysis we will use a single set of the CTW eigenfunctions computed for the Stanwell Park line of moorings, line 2, and will use the first three of the dynamical modes. In addition we will use the eddy mode as defined above at line 3 but only after renormalization so that its sum of squares does not dominate over the dynamical modes. A single set of modes is used here since we want, as a first approach at least, to examine the simplest problem of the evolution of the amplitude of a simple set of wave modes in the alongshore direction. We chose line 2 to define the dynamical modes because it is the intermediate site. We chose line 3 to define the eddy mode because we expected it to have the largest amplitude there and, furthermore, only at line 3 do long time series exist at all current meter sites so allowing the mode to be defined at all cross-shelf locations.

c. The dispersion relation

From the four time series determined independently at each of the three lines we can examine one mode at a time and look at the coherence and phase between

any pair of lines. With three lines to analyze we find four different alongshore displacements, specifically these are $\Delta y = 0$ km (for lines 1-1, 2-2 and 3-3) $\Delta y = 160$ km (for lines 2-3) $\Delta y = 360$ km (for lines 1-2) and $\Delta y = 520$ km (for lines 1-3). The phase differences are not all independent, since propagation from line 1 to 2 and from 2 to 3 implies propagation from 1 to 3 provided that the coherences are large. Accepting all of the positive longshore displacements therefore introduces some degree of redundancy among the various phase differences. In order to form an unbiased estimate of longshore propagation rate we decided to include *all* of the redundancy in the system and include estimates of the phase differences for negative displacements. A simple pattern then occurs since a phase difference of $\Delta\theta$ between lines i to j implies $-\Delta\theta$ between lines j to i .

Figure 11 shows the phase differences observed plotted against displacement alongshore for three frequencies and for the three dynamical modes. The points entered with *negative* displacements are shown with open symbols as these are wholly redundant. For the fourth (eddy) mode few significant coherences were observed, however, when phases were picked off for the fourth mode regardless of the coherence level a random scattering of phases was observed with no obvious sense of organization. At a period of 8 days a tight sequence of phase differences emerges for all possible combinations of lines for mode 1. The phase differences suggest a northward propagation speed of

around 5 m s^{-1} ; the entered value of 4.35 m s^{-1} is derived from the principal axis of the phase differences against displacement. In all other cases, phase speeds indicated on Fig. 11 are derived from a principal axis calculation. Also at 8 days, we see that modes 2 and 3 show a definite tendency for northward phase propagation though the scatter of points about the fitted line is large for mode 2. The fits do indicate that mode 2 propagates slower than mode 1 and that mode 3 propagates slower than mode 2. A striking result of this analysis is that though the speeds for a given mode will be seen to vary quite sharply with frequency in no case do we find that the phase speed for mode 3 exceeds that for mode 2 nor that for mode 2 exceeds the phase speed for mode 1.

At a 6 day period (Fig. 11b) the fastest mode, mode 1, shows a large scatter of phase observations about the fitted line, mode 2 shows a tight collection of points and mode 3 a wide scatter. The phase speeds indicated for modes 2 and 3 are very close and, given the wide scatter in the distribution of points for the mode 3 plot, the difference in phase speed is not significant. That we still observe $C_2 > C_3$ must be considered fortuitous.

For mode 1 at a period of 4 days (Fig. 11a) we see that though coherence was large enough to estimate phase differences between lines 1 and 2 and between lines 1 and 3, it was too low between lines 2 and 3, the closest pair of lines! The coherences corresponding to the other phase estimates for mode 1 are relatively low but do suggest that a propagating signal exists despite

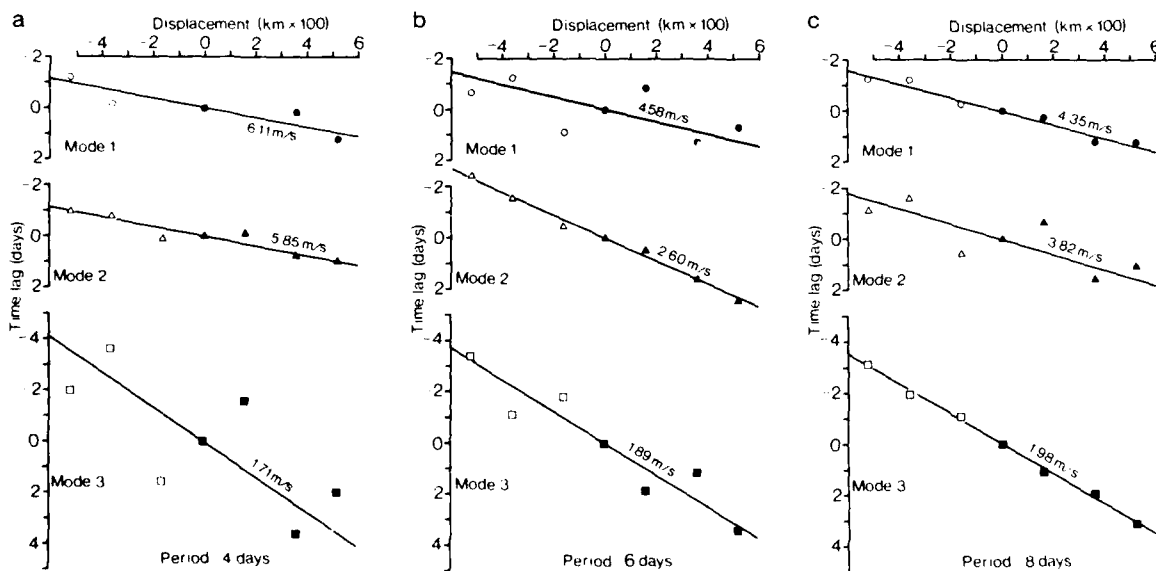


FIG. 11. Phase difference of complex amplitudes for the three dynamical modes at three different frequencies plotted against displacement alongshore. Where an expected entry is missing, the coherence was too low to provide a stable phase estimate. The open symbols represent points that are wholly redundant. The solid symbols carry some degree of redundancy since for large coherences wave propagation from line 1 to 2 and from line 2 to 3 implies propagation from 1 to 3. For small coherence values this is not true and all points with positive displacements become independent. The solid lines indicate the phase speed estimated by the major axis of the principal ellipse through the entered points.

the scatter among the phases. There is rather less scatter in the phase differences for mode 2. Once again mode 2 is slightly, but not significantly, slower than the observed speed for mode 1 and the ordering with $C_1 > C_2$ must be considered fortuitous.

The phase observations are all, of course, cyclic over 360° , or in Fig. 11a, cyclic over a time delay of 4 days and, thus, each phase estimate has an inherent ambiguity of (in the case of Fig. 11a) 4 days. The particular choice of points shown in Fig. 11a was adopted for two reasons. First, we do have physical reasons for expecting northward phase propagation, and second, any other reasonable alternative produces a very wide scatter of phase differences, almost circular, that barely allows a preferred sense of propagation to be estimated. However, for this particular case there is clearly some subjectivity in the interpretation of the phase diagram. The problem of subjectivity gets worse at shorter periods and so we decided that phase diagrams for periods less than 4 days should not be used. The subjectivity problem arose on only two occasions for results that will be quoted here, in both cases for mode 3, at periods of 4 and 4.8 days.

Table 3 shows a list of the observed phase speeds (m s^{-1}) for each of the three dynamical modes. Also listed are the estimated wavenumbers computed as $k_i = \omega/C_i$ where k_i and C_i are the estimated wavenumber and phase speed for mode i . From this table we can produce the dispersion diagrams shown in Figs. 12a, b and c. On Fig. 12 we enter for each mode separately the estimated wavenumber plotted against the frequency of the spectral line under examination. The error bars shown for each point entered represent the frequency bandwidth. The frequencies examined are low enough that the long wave approximation is good: at a period of 4 days $(\omega/f)^2 \approx 0.04$. On each of the plots in Fig. 12 the solid line is the expected dispersion relation based on the long-wave approximation for coastal trapped waves. Specifically, a mean theoretical phase speed has been estimated for the entire ACT array using the phase speeds listed on Fig. 9 and for any individual mode computing the harmonic mean:

$$C_i^{-1} = \frac{1}{L} \int_0^L C_i^{-1} dy.$$

The dashed lines show the average dispersion relation defined by the empirical observations. The shaded area on the right hand side of each plot designates an area where the length of the array exceeds the wavelength of any fitted wave. This is effectively (but not quite) a Nyquist wavelength for the array and we cannot reliably estimate any wavenumbers in that region. In fact, as was discussed earlier, some degree of subjectivity arises before we enter that region and the two points at periods of 4 and 4.8 days for mode 3 (Fig. 12c) should be interpreted with some caution.

Figure 12a shows a plot of frequency versus wavenumber for mode 1 at six frequencies. All but one of the points lie above the theoretical long-wave speed of 3.78 m s^{-1} ; an increase in the theoretical wave speed of 1 m s^{-1} would produce a good fit. However, with the exception of one point, at a period of 4.8 days, the experimental dispersion relation is approximately linear as is expected theoretically.

Figure 12b shows the dispersion characteristics for mode 2 at the same six frequencies as in Fig. 12a, and with the exception of a single outlier, the empirical dispersion relation is once again a good approximation of a straight line. Also, as in Fig. 12a, the experimental dispersion points are at systematically higher phase speeds than theory predicts with only one point below the theoretical curve. An increase of only 0.5 m s^{-1} in the theoretical speed would produce good agreement.

Figure 12c shows the same plot for mode 3. Once again the experimental data show a bias towards wave speeds higher than theory predicts. An increase of 0.5 m s^{-1} would, as in Fig. 12b, produce good agreement. The scatter about linearity appears to be rather greater for mode 3 than for the first two modes, but that is probably not an unexpected result. Indeed, in hindsight it seems quite remarkable that we have been able to make a reasonably convincing fit to three wave modes.

Figure 13 displays the variance in each mode plotted against frequency for each of the three principal lines of current meters. We define the variance of mode i as $\sigma_i^2 = \hat{a}_i \hat{a}_i^*$ where \hat{a}_i is the complex amplitude derived from Eq. (9). The variance is averaged over time and defined separately at each line. Since each mode, the three dynamical modes and the empirical eddy mode, is normalized differently, only limited comparisons between modes can be made on this plot. On Fig. 13 we see that the spectra of each mode are generally red, i.e., there is generally more energy at lower frequencies than higher. (Note that these plots are linear in frequency and energy and so are variance conserving plots.) However, at line 1 we see that the spectra peak at a period of 8 days for each of the three dynamical modes. The fourth mode for each line shows the most pronounced red spectra. Rather surprisingly it appears that the second line carries less variance, in the dynamical

TABLE 3. Phase speeds estimated at discrete periods for each of the three wave modes, and the associated wavenumber estimates. The phase speeds were estimated from the direction of the major axis of the principal ellipse of the various phase differences plotted against displacement.

Period (days)	Phase speeds (m s^{-1})			Wave numbers ($\text{m}^{-1} \times 10^3$)		
	C_1	C_2	C_3	k_1	k_2	k_3
24	4.77	2.47	0.96	0.064	0.123	0.376
12	3.30	1.77	1.11	0.184	0.342	0.546
8	4.35	3.82	1.98	0.209	0.238	0.459
6	4.58	2.60	1.84	0.265	0.467	0.641
4.8	10.82	2.33	1.34	0.140	0.651	1.127
4	6.11	5.85	1.71	0.298	0.311	1.065

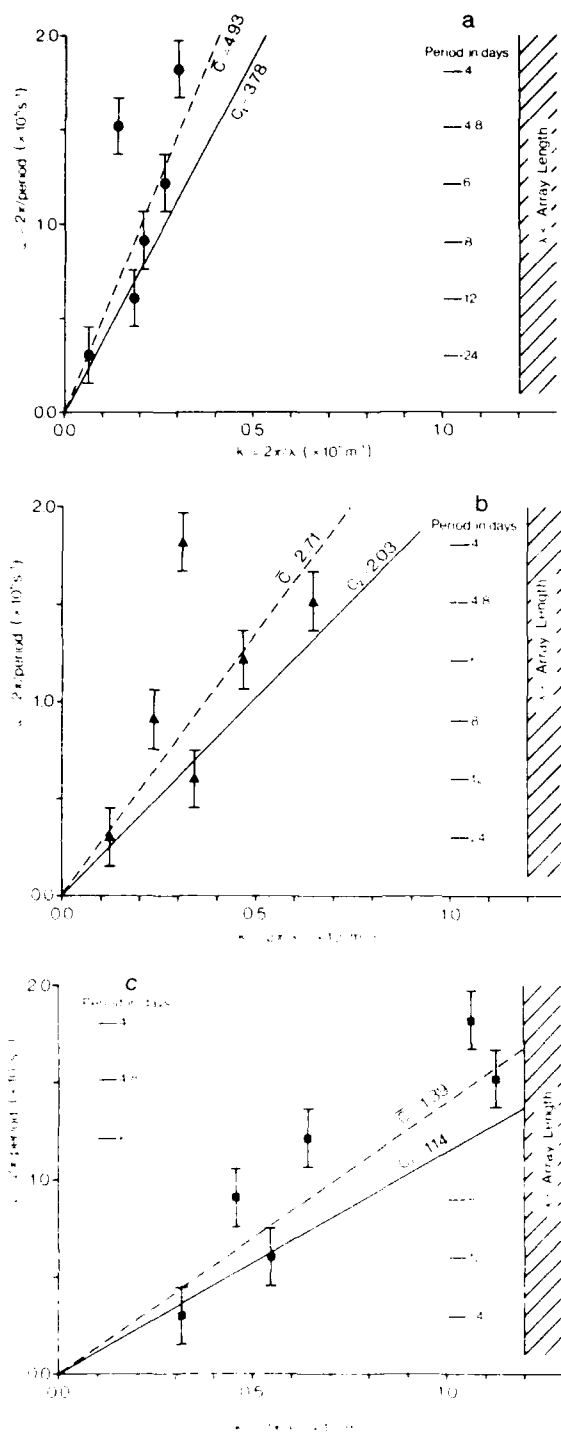


FIG. 12. Empirical dispersion relation for (a) mode 1, (b) mode 2, and (c) mode 3. The bold line shows the expected free wave speed and the dashed line the mean phase speed of the observations, defined as $C = [(\sum C_i^2)^{-1}]^{-1/2}$, i.e., the harmonic mean of the individual phase speed estimates.

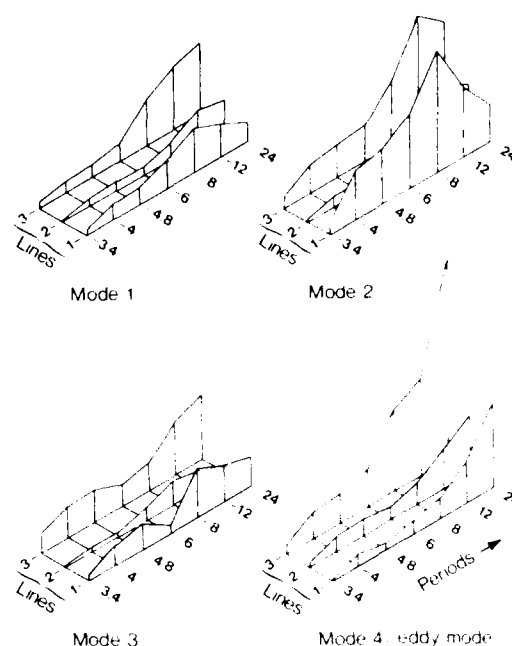


FIG. 13. Energy spectra for each of the modes extracted plotted for comparison between each line.

ical modes, than does line 1, whereas lines 1 and 3 are very similar in their energy levels. Since some moorings on line 3 were damaged by eddies it should come as no surprise to see, in Fig. 13, that the energy levels in mode 4 are very much greater at line 3 than at either of the other two lines.

In summary, Fig. 12 indicates that the dispersion characteristics computed from the ACE moored array are a reasonable approximation to the theoretical dispersion curves for the first three coastal trapped wave modes. In each case the theoretically predicted wave speed is systematically less than the experimentally determined wave speeds by 0.5 to 1 m s^{-1} , or about 25% of the theoretical wave speeds. These results suggest that after the extraneous eddy signal is removed from the data the physics of coastal trapped waves is a good descriptor of the motions on the continental shelf. However, some of the coherences used in constructing the phase plots of Fig. 11, are fairly low, indicating that a simple model of linear phase propagation at a constant speed may not necessarily account for a large fraction of the total variance at any frequency. Furthermore, Fig. 11 also shows a substantial amount of scatter of the time lags about the linear phase propagation speed indicating that still more variance is not accounted for by a simple coastal trapped wave model. In order to explore to what extent the theory of trapped waves can account for the variability observed at any one location a different approach is needed.

d. Analysis in the time domain

The expansion of current observations into modal amplitudes as described in an earlier section can be executed at individual times, rather than for Fourier coefficients, producing explicit time series of amplitudes for each mode. For the three dynamical modes the evolution alongshore can then be compared with the predictions of forced CTW theory. The methods used are described by Clarke and Van Gorder (1986). Since a detailed description of the specific procedures used and the results obtained will be described elsewhere (J. A. Church, 1986), we will restrict ourselves here to an overview of some of the results pertinent to a synthesis of the Australian Coastal Experiment.

We represent pressure as a sum of modes as in Eq. (1) where the functions $F_n(x, z)$ are solutions of an eigenvalue problem, Eq. (2). The amplitudes of the modes are described by a set of forced wave equations that are coupled by frictional coefficients

$$-\frac{1}{c_i} \frac{\partial \phi_i}{\partial t} + \frac{\partial \phi_i}{\partial y} - a_{ij} \phi_j = B_i \tau^1(y, t) + \sum_{j=1}^4 a_{ij} \phi_j, \quad (10)$$

As before the longshore velocities are expanded in a series [Eq. (4)] with on-offshore modes related to the eigenfunctions of Eq. (2) by the geostrophic relation, Eq. (5). These equations then can be used (J. A. Church, 1985) to expand the velocities observed at line 1 in the 3 local dynamical and one local eddy mode so producing the amplitudes ϕ_1 , ϕ_2 and ϕ_3 at one value of the alongshore coordinate y , say, at $y = 0$. Equation (10) then can be used to forecast the values of ϕ_1 , ϕ_2 and ϕ_3 at the two northerly lines and compare the predictions with observations.

The eddy mode cannot, of course, be described by Eq. (10), so in making a comparison between the predictions from theory and observations it is important to compare only the inherently predictable parts of the current field. From the observed currents at any particular line we define two new fields that differ slightly from each other. After analysis into the four modes we define the reconstructed currents (V_R) as the sum of the first three (dynamical) modes, i.e., the CTW part of the signal. The de-eddied currents V_d are defined as the observed currents minus the eddy signal. Specifically, at any line we compute ϕ_i by minimizing E where

$$E = [V(x, z, t) - \sum_{i=1}^4 G_i(x, z) \phi_i(t)]^2$$

then

$$V_R(x, z, t) = \sum_{i=1}^3 G_i(x, z) \phi_i(t)$$

$$V_d(x, z, t) = V(x, z, t) - G_4(x, z) \phi_4(t)$$

These time series are not identical. Both attempt in

some sense to represent the dynamical signal but V_d includes the velocity signal that is not fitted by the least-squares procedure. Over line 1 the gross correlation coefficient between V_d and V_R is about 0.9. This represents how well the least-squares procedure is working. Since the decomposition is good only to a correlation level of about 0.9 we cannot expect a forecast to do as well.

Table 4 summarizes the results of using the modal amplitudes that result from an analysis of line 1 and Eq. (10) to forecast the modal amplitudes at line 2. The "observed variances" are of the reconstructed currents at line 2 (i.e., the CTW part of the current field) and the "predicted variances" result from the modal amplitudes forecast by Eq. (10). The energy levels have been predicted accurately: the predicted and observed variances averaged over line 2 are 36.7 and 41.6 $\text{cm}^2 \text{s}^{-2}$, respectively. These are much closer to each other than to the equivalent figure for line 1, 90.7 $\text{cm}^2 \text{s}^{-2}$.

The correlation coefficients listed in Table 4 indicate that comparison between predicted and observed current fields is significant at high confidence levels. At the inshore sites the correlations are significantly different from zero at the 99.99% confidence level. (As before we assume 1 degree of freedom is accumulated every 5 days.) A stronger null hypothesis would be the equivalent of the meteorological persistence forecast, i.e., that conditions do not change along the shelf. Using the reconstructed velocities, defined earlier, the correlation coefficient between f11/75 and f21/75 is 0.25; the equivalent correlation in Table 4 is 0.62, very much higher. Furthermore, a system with population correlation of 0.25 and 36 degrees of freedom has an upper 95% confidence level of 0.48, less than the 0.62 observed which differs from the population at the 99.8% level.

TABLE 4. Variances at line 2 forecast from an analysis of line 1 and the dynamics of CTWs (the predicted variance), and the reconstructed (observed) variance for comparison. The correlation coefficients between the two fields is also listed. Variances are in $\text{cm}^2 \text{s}^{-2}$.

Meter	Observed variance	Predicted variance	Correlation
f21/75	119.4	100.2	0.62
f21/125	136.6	115.0	0.62
f22/60	67.4	53.9	0.61
f22/110	72.0	56.6	0.61
f22/175	64.3	50.8	0.55
f23/125	37.3	31.1	0.50
f23/190	32.5	30.6	0.36
f23/450	25.5	32.5	0.00
f24/205	13.8	14.6	0.23
f24/465	11.8	14.9	0.01
f24/650	9.4	11.3	0.24
f24/1000	7.4	6.4	0.51
f25/250	7.1	8.3	0.10
f25/800	3.3	3.3	0.42
f25/1700	16.7	21.2	0.97

Earlier in this paper we examined a general relationship between currents separated by distance along-shore and extracted empirical relationships of the form

$$\hat{V}_n(t) = \sum_{i=1}^N a_i V_n(t - i\Delta t) + \sum_{i=1}^M b_i \tau(t - i\Delta t).$$

The best model yielded an estimate \hat{V}_n that correlated with V_n at the level $r = 0.71$.

The linear predictor (6) is essentially the optimal linear predictor and yields an estimate \hat{V}_n that correlates with V_n at $r = 0.71$; it does do better than the dynamical model but not very much better. The optimal predictor must, by definition, perform better than any other linear predictor including a linear dynamical theory but it is satisfying that the dynamical models do almost as well. Finally we note that the dynamical correlation for inshore currents of 0.62 carries 95% bounds of 0.45 and 0.77, and so is not different from the optimal linear estimator at the 95% confidence level.

5. Discussion

In the free wave analysis we have demonstrated that waves pass through the experimental array and exhibit dispersion characteristics that are strongly indicative of coastal trapped waves. One of the more significant observations from this section is that the empirical dispersion relation suggests that the waves propagate rather faster than theory would lead us to expect. The discrepancy is too large, and of the wrong sign, to be accounted for by mean field advection. We suggest that it might be accounted for by contamination of the free wave by the presence of a relatively small forced wave.

Clarke and Thompson (1984) looked at a pure forced wave problem and found the ocean response to wind forcing, for only one mode, to be of the form

$$p(x, y, z, t) = AF_1(x, z) \cos\left[\frac{1}{2}(l + \omega/c_1)t - \omega t\right] \times \sin[(l - \omega/c_1)y/2]. \quad (11)$$

In Eq. (11) $F_1(x, z)$ is the shape of the first CTW mode (pressure field), c_1 is the longshore phase speed and l is the longshore wavenumber of the wind forcing. Thus patterns propagate along the coast at a speed c_{pat} defined by

$$c_{\text{pat}} = \frac{\omega}{\frac{1}{2}(l + \omega/c_1)} \\ c_{\text{pat}}^{-1} = \frac{1}{2}(c_w^{-1} + c_1^{-1}). \quad (12)$$

The pattern speed is the harmonic mean of the free wave speed and the speed of propagation of wind systems in the longshore direction. Since in our case c_w and c_1 are both northwards, at 11 and 3.78 m s⁻¹, respectively, the pattern speed is greater than, but in the same direction as, the free wave speed.

The forced wave pattern speed computed from (12) is 5.63 m s⁻¹ and is greater than the free wave speed and greater than the observed pattern speed, see Fig. (12a). Furthermore, we know from the analysis of section (3d) that we are dealing with neither forced nor free waves. In that section we estimated the ratio of velocity variance in the forced wave/variance in the free wave to be about 0.1. This implies a ratio of signal amplitudes of about $\sqrt{0.1} = 0.3$. Thus it seems reasonable to expect that the resulting pattern speed will be intermediate between the free and forced wave speeds, as actually observed.

However, detailed analysis shows a strong dependence on the phase relationship between the free and forced wave components. The actual pattern speed predicted for ACE can even be less than the free wave speed depending on the initial phase difference at line 1. A simple relationship that conforms fairly well to observations can result if the initial phase difference is near zero. Some evidence exists, see later discussion, that a significant part of the free wave energy is generated in Bass Strait, so it may be reasonable to expect the free and forced waves to be almost in phase at Eden.

The analysis of the forced waves in the time domain indicates quite clearly that we do have predictive skill in the sense that we can use the dynamics of forced topographic waves to forecast future conditions some distance along the coastline. However, the amount of variance accounted for in the forecast is not impressive. The correlation coefficients inshore reach highs of 0.62 indicating that we can account for only about 40% of the observed variance with a trapped wave model. Though this does not sound impressive, the best statistical predictor between line 1 and line 2 inshore currents, performs only marginally better and accounts for about 50% of the variance. We conclude that not all of the energy in the weather forcing band is described by coastal trapped waves.

We now turn to the question of the source of the CTW energy observed in ACE. Clarke and Thompson (1984) assumed there would be negligible CTW energy at Cape Howe (line 1) and that wind forcing in the region northward from there could generate CTWs to be observed at lines 2 and 3, as has been pointed out. CTW energy is already large at line 1 and the CTW energy at line 2 is largely the propagation of CTWs northward from Cape Howe as free waves. The expectation of Clarke and Thompson (1984) and the assumption in designing ACE being wrong, we are forced to consider possible sources of the CTW energy at Cape Howe. The bathymetry and meteorological conditions off southern and southeastern Australia allow for several (speculative) possibilities for generating CTWs that are observable at Cape Howe.

One, of course, is that the CTWs have come a very long way. The winds in the Great Australian Bight are strong and the existence of CTWs there has been discussed by Krause and Radok (1976). The possibility

that CTWs could be generated in the Great Australian Bight, travel in the continental-margin waveguide that bends south, and then north, around Tasmania, exists. (This would assume the shallow (<100 m) but wide aperture caused by Bass Strait would not affect the long CTWs and that the wave energy is not dissipated in that distance.) However, this possibility is not supported by the current meter observations. Although there is significant coherence (at the 95% confidence level) between the alongshore component of the current off Maria Island (f02/125) and off Cape Howe (f11/125), the phase difference is negligible. Furthermore, the variance in the coherent band is nearly an order of magnitude less off Maria Island than off Cape Howe. Currents off Maria Island and Cape Howe show some coherence with the Gabo Island wind. All this suggests that forcing of CTWs by winds off southeastern Australia is more plausible than propagation around Tasmania from the Great Australian Bight. We can pursue this possibility by estimating the energy flux at line 1 and comparing it with the rate of working by the Gabo Island wind stress.

Let us first estimate the CTW flux at Cape Howe. The analysis of Clarke and Battisti (1983) shows that the energy flux through a vertical plane perpendicular to the coast is

$$\mathcal{F} = -\frac{\rho_0}{2f} \sum_i \sum_j \overline{\phi_i \phi_j} \int_0^{\infty} F_i F_j \frac{\partial h}{\partial x} \Big|_{z=0} dx$$

where the overbar indicates a time average. Using the orthogonality property of the eigenfunctions:

$$\int_0^{\infty} F_i F_j \frac{\partial h}{\partial x} \Big|_{z=0} dx = \delta_{ij} \lambda_i,$$

this becomes

$$\mathcal{F} = -\frac{\rho_0}{2f} \sum_i \overline{\phi_i^2} \lambda_i.$$

Using the modal amplitudes calculated for Cape Howe in section 4d, we get

$$\mathcal{F} = 1.8 \times 10^8 \text{ W.}$$

The three dynamical modes used respectively contribute 30.5%, 49% and 20.5% to this total.

We can estimate the energy generated by the wind between the western end of Bass Strait and Cape Howe by following the argument of Gill and Clarke (1974): Bass Strait has an average depth of about 60 m and is about 250 km wide. The barotropic radius of deformation is small ($\sqrt{gh}/f \approx 260$ km), so the Strait is about one Rossby radius wide. For a Kelvin wave the fraction of the total wave energy between the coastline and 1 Rossby radius is $(1 - e^{-2}) \approx 0.86$. As a first approximation, let us assume that Bass Strait is 410 km long, infinitely wide and of constant depth (60 m), and that no energy enters the western end of Bass Strait.

By an analysis along the lines of Gill and Clarke (1974), it is possible to work out an analytic solution for the wind forced motion and hence estimate an energy flux of

$$\mathcal{F} = 3.0 \times 10^8 \text{ W.}$$

Reducing this by 8% to allow for friction and a further 14% because Bass Strait is not infinitely wide, we can estimate

$$\mathcal{F} = 2.4 \times 10^8 \text{ W.}$$

This is greater than the energy found at Cape Howe and, in view of the high coherence and the small phase lead of the winds at Gabo Island with respect to the currents at Cape Howe, it seems that wind forcing over Bass Strait is a possible source of the energy at Cape Howe.

Could the wind stress over the ocean east of Bass Strait be sufficient to generate CTWs of the magnitude observed? Results to be presented later (J. A. Church et al., personal communication) indicate that a substantial flux of energy is possible. Solving the CTW equation (1) for the 150 km of shelf between the eastern end of Bass Strait and Cape Howe, assuming coupling coefficients appropriate for Cape Howe, and assuming that $\phi_i(t) = 0$, for all i and t , 150 km to the west, the resulting flux at Cape Howe would be

$$\mathcal{F} = 3.4 \times 10^7 \text{ W}$$

with the three dynamical modes contributing, respectively, 46%, 46% and 8% to this total. This flux is about one-fifth of the measured flux at Cape Howe but the correlation between the "predicted" and observed current at the inshore sites is surprisingly high: it is 0.68 at meter f11/125. The correlations drop away very quickly as we move offshore (the predicted currents are much less than the measured currents) but in view of the simplistic approach taken and the short fetch (150 km, compared to the 410 km fetch in the previous estimate), this model does surprisingly well.

In view of these calculations, there would seem to be sufficient sources of energy to the south and west of Cape Howe to explain the observed CTW energy flux off Cape Howe.

Acknowledgments. The participation of R. L. Smith and A. Huyer in ACE was supported by the U.S. Office of Naval Research, and that of A. J. Clarke by the National Science Foundation Grant OCE-8300029.

The participants from North America, A. J. Clarke, H. J. Freeland, A. Huyer and R. L. Smith would like to thank the C.S.I.R.O. for their hospitality during the data analysis phase of the experiment. Finally, we would like to thank Dr. Phyllis Stabeno for helpful discussions and comments on this paper and Netta Delacretaz for her patience while typing the many drafts.

APPENDIX A

Singular Value Decomposition

In several places in this paper it was necessary to solve a least-squares problem, equation (7), for example. Formally, least-squares problems always reduce to the problem of finding a vector \mathbf{y} when a vector \mathbf{x} and a covariance matrix \mathbf{C} are known, and when \mathbf{x} , \mathbf{C} and \mathbf{y} are related by

$$\mathbf{x} = \mathbf{C}\mathbf{y}. \quad (\text{A1})$$

In the transfer function calculations of section (3d) the vector $\mathbf{x} = \{x_i\}$ is of the form $x_i = V_{in}(t)U_{is}(t - i\Delta t)$, and $\mathbf{y} = \{y_i\}$ where $y_i = a_i$. The covariance matrix $\mathbf{C} = \{C_{ij}\}$ is of the form $C_{ij} = V_{in}(t - i\Delta t)V_{is}(t - j\Delta t)$. Formally we write the solution \mathbf{y} to problem (A1) as $\mathbf{y} = \mathbf{C}^{-1}\mathbf{x}$. However, for the problems of interest in this paper \mathbf{C} generally has a large condition number (ratio of largest to smallest eigenvalue) and so the inverse can be unstable. In such a case the solution \mathbf{y} varies greatly with small variations in the data. We proceed, therefore, to solve the problem by singular value decomposition.

Let the N eigenvalues and eigenvectors of the $N \times N$ matrix \mathbf{C} be λ_i and \mathbf{e}_i , respectively. Since \mathbf{C} is a covariance matrix (i.e., symmetric and having elements satisfying the Schwartz inequality $|C_{ij}|/(C_{ii}C_{jj}) \leq 1$) the eigenvalues are all real and positive. If N_0 eigenvalues are exactly zero then the rank of \mathbf{C} is $N - N_0$. In practice, since we are dealing with noisy data, any eigenvalue that lies within the sampling noise level is effectively zero.

Let us expand the vectors \mathbf{x} and \mathbf{y} in terms of the eigenvectors, viz.

$$\mathbf{x} = \sum_{i=1}^N \alpha_i \mathbf{e}_i \quad \text{and} \quad \mathbf{y} = \sum_{i=1}^N \beta_i \mathbf{e}_i. \quad (\text{A2})$$

The coefficients α_i are easily determined using the orthogonality property of the eigenvectors

$$\mathbf{x} \cdot \mathbf{e}_j = \sum_{i=1}^N \alpha_i \mathbf{e}_i \cdot \mathbf{e}_j = \alpha_j. \quad (\text{A3})$$

We can then determine the coefficients β_i in terms of the α_i expansion (A2) in Eq. (A1) and remembering that $\mathbf{C}\mathbf{e}_i = \lambda_i \mathbf{e}_i$:

$$\begin{aligned} \mathbf{x} &= \sum_{i=1}^N \alpha_i \mathbf{e}_i = \mathbf{C}\mathbf{y} = \mathbf{C} \sum_{i=1}^N \beta_i \mathbf{e}_i \\ &= \sum_{i=1}^N \beta_i (\mathbf{C}\mathbf{e}_i) = \sum_{i=1}^N \beta_i \lambda_i \mathbf{e}_i. \end{aligned}$$

Hence, we find in general that $\beta_i = \alpha_i/\lambda_i$ and, using (A3) and (A2), express the general solution to (A1) as,

$$\mathbf{y} = \sum_{i=1}^N \left(\frac{\mathbf{x} \cdot \mathbf{e}_i}{\lambda_i} \right) \mathbf{e}_i. \quad (\text{A4})$$

Assuming that the eigenvalues are ordered so that $\lambda_1 > \lambda_2 > \dots > \lambda_N$ let us write an approximate solution \mathbf{y}_R for \mathbf{y} as

$$\mathbf{y}_R = \sum_{i=1}^R \left(\frac{\mathbf{x} \cdot \mathbf{e}_i}{\lambda_i} \right) \mathbf{e}_i$$

where R is an assumed rank of \mathbf{C} , $R \leq N$. Specifically R is chosen so that any eigenvalues that lie within the noise level are neglected.

APPENDIX B

Estimation of Modal Amplitudes

The amplitudes \hat{a} of the three dynamical and one empirical modes discussed in section (4b) are found by the solution of a complex matrix equation (9). The solution is found, as in appendix A, by singular value decomposition of the covariance matrix \mathbf{C} . A complication, however, is that the matrix \mathbf{C} varies from one line to another due to data loss from various instruments at different times. Hence, even on one line the contributions to \mathbf{C} vary with time. The variations in \mathbf{C} are, however, relatively small.

The modal covariance matrix for the nominal distribution of current meters is

$$\mathbf{C} = \begin{bmatrix} 0.273 & -0.294 & -0.138 & 0.402 \\ -0.294 & 0.470 & 0.318 & -0.261 \\ -0.138 & 0.318 & 0.404 & 0.055 \\ 0.402 & -0.261 & 0.055 & 1.000 \end{bmatrix}.$$

The eigenvalues of \mathbf{C} are (1.353, 0.707, 0.069 and 0.017) and these eigenvalues contribute, respectively, (63%, 33%, 3.2% and 0.8%) to the trace of \mathbf{C} . As the matrix \mathbf{C} changes slightly, with instrument failure, etc., the eigenvalues take other discrete values near each of the values listed for the nominal array. Since the matrix \mathbf{C} is varied by fairly small amounts, i.e., the sampling array is not changed dramatically, instead of finding four eigenvalues distributed as above, we find four groups of eigenvalues centered near 63%, 33%, etc. We will call these groups type-a, b, c and type-d eigenvalues respectively. The covariance matrix \mathbf{C} changes by sufficiently small amounts that the smallest a-type eigenvalue is never smaller than the largest b-type, and so on; i.e., the four groups are all well separated and do not overlap.

The variance averaged over all current meters deployed throughout the ACE array is $208 \text{ cm}^2 \text{ s}^{-2}$. The resolution of an Aanderaa current meter is about 1.5 cm s^{-1} , and if we use this value as an estimate of the noise level in our current meter array we find the ratio $100\% \times (\text{noise level})^2 / \text{mean variance}$ to be about 1%. So with this primitive argument we see that the smallest eigenvalue of the covariance matrix is too small; it lies below the effective noise level of the system, and should be neglected. Specifically then, we will compute the vector $\hat{\mathbf{a}}$ by singular value decomposition [see appendix

A) and reject contributions from any eigenvalue that constitutes less than some critical percentage of the trace of the matrix \mathbf{C} . Hence, from Eq. (9) we can find the set of four modal amplitudes, complex numbers denoting amplitude and phase, for each block of time at one line of moorings and then repeat the expansion at each of the other two lines of moorings. Thus we find four short time series of modal amplitudes (using 24 day long blocks we get seven distinct observations of the modal amplitudes during the ACE period)] at each line, and we can examine the coherences between each line for each mode and search for phase propagation.

First, consider the modal separation for the 3 main lines at a period of 12 days, the second harmonic of the block length of 24 days. The value $E = \sum \hat{E}_i \hat{E}_i^*$ is the so-called reduced variance ($\Delta\sigma^2$) the amount of variance not accounted for by the best modal fit. Let us compute this as a fraction of the signal variance $\sigma_0^2 = \sum \hat{I}_i \hat{I}_i^*$, and average $\Delta\sigma^2$ and σ_0^2 over the seven time blocks and the three lines. We also define the model variance $\sigma_m^2 = \sum \hat{a}_i \hat{a}_i^*$, and average that also over the seven time blocks and three lines. Let us assume that in the process of computing the complex modal amplitudes \hat{a}_i we accept contributions from the covariance matrix \mathbf{C} corresponding to all eigenvalues exceeding a cutoff value λ_0 , and examine the variation

of the normalized residual variance ($\Delta\sigma^2/\sigma_0^2$) and the model variance (σ_m^2/σ_{m0}^2) where $\sigma_{m0}^2 = \sigma_m^2$ at λ_0 . Figure 14 shows a plot of the normalized reduced variance and the model variance as a function of the eigenvalue cutoff λ_0 . Along the abscissa short lines indicate where actual eigenvalues of the slowly varying matrix \mathbf{C} occur. These are, as discussed earlier, separated into four distinct groups. Figure 14 shows that if the cutoff is set at, say, 8% so that contributions from the a-type and b-type eigenvalues are accepted, and none from the c- and d-type, then the best fit modal amplitudes account for all but 26% of the total variance. If we set the cutoff at 1.5%, so that we include contributions from a-, b- and all c-type eigenvalues, then the model fit is improved, but only marginally, accounting for only another 2% of the observed variance. Meanwhile the variance in the best fit modal amplitudes increases by about 10%. If we now set the cutoff at any value less than 0.5%, so that all eigenvalues are used, all but the last 19% of the observed variance is accounted for. This is not a dramatic improvement, and is achieved at the cost of increasing the variance in the modal amplitudes by about a factor of 6. This rapid increase in the variance in the model represents a type of instability as discussed in appendix A. Between cutoff values of 2% and 2.2% there is a substantial drop in the average model variance and an associated sharp rise in the re-

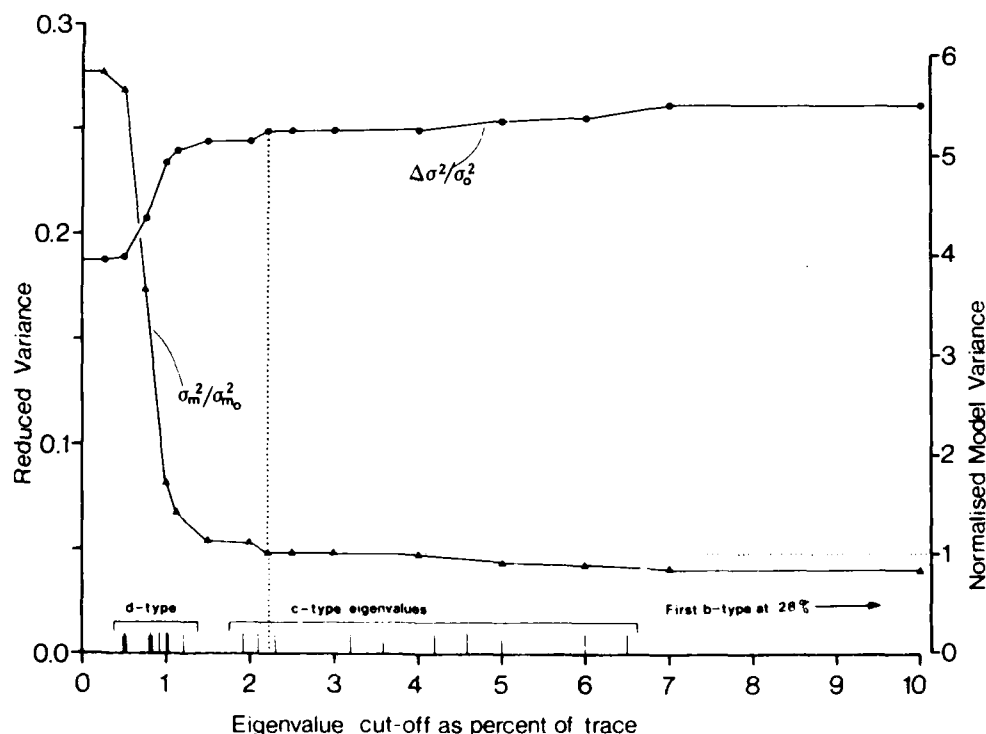


FIG. 14. Response of the least-squares fit model to the inclusion of various eigenvalues in a singular value decomposition.

sidual variance, marked on Fig. 14 by the dotted line. This sharp change occurs as a result of the loss from the array of one instrument on line 2 and affects only one time block. Seen individually it represents a rather severe instability though the averaging involved in Fig. 14 tends to disguise its severity.

Based on the rough guide outlined above, using the noise level of the instruments, we look then to place our eigenvalue cutoff near the boundary between the d- and e-type eigenvalues. The detailed behavior of the model variance and the residual variance plots suggests that the appropriate cutoff value is 2.2% and that value was used in the subsequent analysis.

REFERENCES

- Adams, J. K., and V. T. Buchwald, 1969. The generation of continental shelf waves. *J. Fluid Mech.*, **35**, 815-826.
- Brink, K. H., 1982. The effect of bottom friction on low-frequency coastal trapped waves. *J. Phys. Oceanogr.*, **12**, 127-133.
- , and J. S. Allen, 1978. On the effect of bottom friction on barotropic motion over the continental shelf. *J. Phys. Oceanogr.*, **8**, 919-922.
- Church, J. A., H. J. Freeland and R. I. Smith, 1986. Coastal-trapped waves on the East Australian continental shelf. Part I. Propagation of modes. *J. Phys. Oceanogr.*, **16** (in press).
- Clarke, A. J., 1977. Observations and numerical evidence for wind-forced coastal trapped long waves. *J. Phys. Oceanogr.*, **7**, 231-247.
- , and D. S. Battisti, 1983. Identification of the fortnightly wave observed off the northern coast of the Gulf of Guinea. *J. Phys. Oceanogr.*, **13**, 2192-2200.
- , and R. O. R. Y. Thompson, 1984. Large-scale wind-driven ocean response in the Australian Coastal Experiment region. *J. Phys. Oceanogr.*, **14**, 338-352.
- , and S. Van Gorder, 1986. A method for estimating wind driven shelf and slope water flow. *J. Phys. Oceanogr.*, **16**, 1011-1026.
- Crépon, M., and C. Richez, 1983. Upwelling, and Kelvin waves generated by transient atmospheric fronts. *Coastal Oceanography*, H. Gade, A. Edwards and H. Svendsen, Eds., Plenum, 175-203.
- Forbes, A. M. G., 1985. Meteorological data from the Australian Coastal Experiment—A data report. CSIRO Marine Laboratories Rep. No. 170, 1985, Hobart, Tasmania.
- Freeland, H. J., J. A. Church, R. I. Smith and F. M. Boland, 1985. Current meter data from the Australian Coastal Experiment—A data report. CSIRO Marine Laboratories Rep. No. 169, 1985, Hobart, Tasmania.
- Gill, A. E., and A. J. Clarke, 1974. Wind-induced upwelling, coastal currents and sea level changes. *Deep Sea Res.*, **21**, 325-348.
- , and E. H. Schumann, 1974. The generation of long shelf waves by the wind. *J. Phys. Oceanogr.*, **4**, 83-90.
- Hamon, B. A., 1962. The spectrum of mean sea level at Sydney, Coff's Harbour, and Lord Howe Island. *J. Geophys. Res.*, **67**, 5147-5155. (Correction, 1963. *J. Geophys. Res.*, **68**(15), 4635.)
- , 1966. Continental shelf waves and the effects of atmospheric pressure and wind stress on sea level. *J. Geophys. Res.*, **71**, 2883-2893.
- Krause, G., and R. Radok, 1977. Long waves on the southern ocean. *Waves on Water of Variable Depth*, No. 64. *Lecture Notes on Physics*. Australian Academy of Sciences and Springer-Verlag, 235 pp.
- Lumley, J. L., and H. A. Panofsky, 1964. The structure of atmospheric turbulence. Wiley-Interscience, 239 pp.
- Mysak, P. A., 1980. Recent advances in shelf wave dynamics. *Rev. Geophys. Space Phys.*, **18**, 211-241.
- Nilson, C. S., and G. R. Cresswell, 1981. The formation and evolution of East Australia Current warm core eddies. *Progress in Oceanography*, Vol. 9, Pergamon, 133-183.
- O'Brien, J. J., A. Busalacchi and J. Kindle, 1981. Ocean models of El Niño. *Resource Management and Environmental Uncertainty, Lessons from Coastal Upwelling Fisheries*, M. H. Glantz and J. D. Thompson, Eds., Wiley-Interscience, 1-9, 212.
- Robinson, A. R., 1964. Continental shelf waves and the response of the sea level to weather systems. *J. Geophys. Res.*, **69**, 367-368.
- Wells, G., and G. R. Cresswell, 1986. A CSIRO data report on drifting buoys in the ACE period. CSIRO Marine Laboratories Rep. No. 180, 1985, Hobart, Tasmania.

Deep-Sea Currents off Northern California

PHYLLIS J. STABENO AND ROBERT L. SMITH

College of Oceanography, Oregon State University, Corvallis

Current meter records from 14 moorings in the deep-sea basin (3000-4500 m deep) south of the Mendocino Fracture Zone are analyzed. All moorings had current meters between 200 m and 500 m above the bottom, and some extended to within 150 m of the surface. There were high vertical correlations between measurements on the same mooring within 1500 m of the bottom and within 800 m of the surface but almost no significant correlation in the horizontal. In the basin the presence of eddies appears strongest at depths below 1200 m. Several of the records exceed 3 years in length, and one extended for 5 years. Spectral analysis of these shows that most of the kinetic energy below 3000 m is in the temporal mesoscale (periods of 31 to 120 days), while the spectral estimates in the upper 1000 m are dominated by longer time scales. Only in the deep records is there a significant southward mean flow. Neither a mean California Current nor a poleward undercurrent is apparent in the shallower data (above 1250 m). The currents in the upper 500 m nearest the continental margin are influenced by the presence of cold filaments originating near Point Arena.

1. INTRODUCTION

Repeated measurements of the currents over the continental shelf off the west coast of North America have provided a basic description of the flow field on the shelf [Freeland *et al.*, 1984; Strub *et al.*, 1986; Winant *et al.*, 1986]. In contrast, current measurements in the deep sea adjacent to the continental margin are considerably rarer. One exception is in the relatively flat basin 100 to 400 km off the northern California coast between the Mendocino Fracture Zone (40°N) and the latitude of San Francisco (38°N). In this region (Figure 1), 14 current meter moorings were deployed in water deeper than 3400 m at various times from 1979 through 1985, as part of two experiments: the Low-Level Water Ocean Disposal program (LLWOD) [Heath *et al.*, 1984] and the Ocean Prediction Through Observation, Modelling and Analysis program (OPTOMA) [Moore and Robinson, 1984]. The individual records are long (5 to 13 months); all 14 moorings obtained measurements within 500 m of the bottom, eight, near 1200 m, and five within 400 m of the surface.

Five years of data, August 1979 to September 1984, were obtained at one location (the W-9 site in Figure 1), where six moorings were deployed consecutively. During the first three years there were current measurements at 1250, 3000, 3800, and 4200 m, and during the last 2 years there were also measurements at 150 and 600 m. This resulted in a record over 5 years in length at 3800 m, nearly 3 years (although not concurrent) at 1250, 3000, and 4200 m, and almost 2 years at 150 m. The length of these records is comparable to similar measurements in the deep western North Pacific [Imawaki and Takano, 1982].

For over a year, starting in September 1981, the main LLWOD horizontal array of five moorings, each with current meters at 3000 and 3800 m depth, and 40 m above the bottom, was in place (W-5, 6, 7, 8, and 9 in Figure 1). As part of OPTOMA, a smaller horizontal array of three moorings (M-1, 2, and 3 in Figure 1) was deployed in September 1984 and recovered in July 1985. Each M mooring had five current meters, nominally at 150, 350, 800, and 1250 m below the

surface and at 200 m above the bottom. The details, including statistical parameters, location, depth, and record length, of the resulting time series are listed in Table 1.

The purpose of this paper is to present a summary and synthesis of the current measurements made from moorings in the deep ocean adjacent to northern California, with emphasis on the mean currents and the low-frequency variability (below 0.1 cpd). Previous knowledge of the subsurface currents in this region was inferred mainly from hydrographic observations [Willie, 1966; Chelton, 1984], although satellite-tracked drifters have provided a few direct measurements of the surface current [McVally *et al.*, 1983; R. E. Thomson and J. E. Papadakis, unpublished manuscript, 1986]. This is a region where the California Current should be apparent [Hickey, 1979], and it is directly offshore from the Coastal Ocean Dynamics Experiment, in which the continental shelf was heavily instrumented with current meters in 1981 and 1982 [Winant *et al.*, 1986]. It is also a region where cold "filaments," extending seaward from the continental shelf, are frequently observed in infrared satellite images [Bernstein *et al.*, 1977; Kelly, 1985; Kosro and Huyer, 1986].

Since we are most interested in the low-frequency variability of currents, the time series are low-pass filtered (half-amplitude at 40 hours and half-power at 46.6 hours). The records that are formed using two or more moorings are first bridged, if the gap is less than 3 days, and then the complete series is low-pass filtered. An analysis of diurnal and semidiurnal tidal currents in some of the records is given by Noble *et al.* [1986a].

2. THE DEEP-SEA FLOW

The most extensive current measurements are at depths between 3000 m and the bottom. Flow at these depths is blocked from the north by the Mendocino Fracture Zone, which extends from the coast to about 135°W, and to the east by the continental margin. The sill depth along the escarpment is less than 2800 m until west of the longitude of W-5, the mooring furthest from the coast. Data from the mooring deployments shown in Figure 1 (September 1981 to September 1982: W-5, 6, 7, 8, and 9 and September 1984 to July 1985: M-1, 2, and 3) provide a picture of the deep flow over much of the region (Figure 2). Most of the measurements shown in Figure 2 were made near 3800 m, and all were between 200 and 500 m above the bottom. The statistical parameters are calculated using the

Copyright 1987 by the American Geophysical Union.

Paper number 6C0596.
0148-0227/87/006C-0596\$05.00

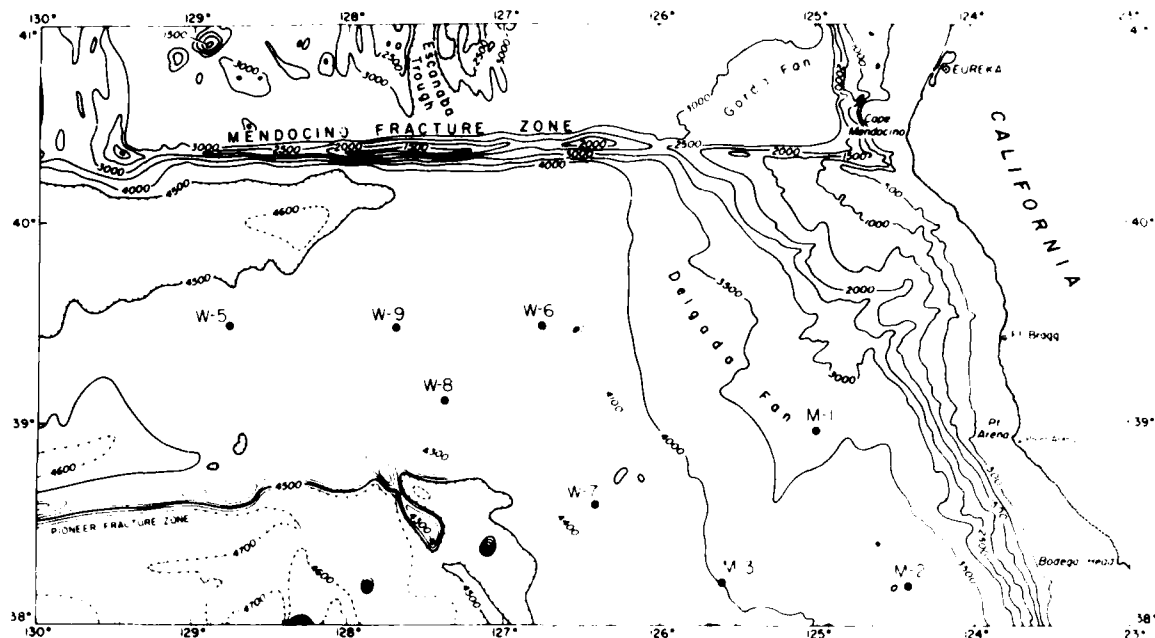


Fig. 1. Bottom topography and the location of the current meter moorings for LLWOD (W moorings) and OPTOMA (M moorings) programs. The five LLWOD moorings shown were in place from September 1981 until September 1982 and the three OPTOMA moorings from September 1984 until July 1985. The W-9 mooring was part of a 5-year sequence of moorings at the same location (W-1, 2, 4, 9, 10, and 11).

entire record (Table 1). Except for W-8 (6 months) and M-3 (5 months), each record is at least 9 months in length.

The total length of the principal (major) axes in Figure 2 represents one standard deviation. Except at the furthest offshore location, W-5, the mean velocities are less than one standard deviation. Nevertheless, there is a suggestion of a flow pattern influenced by the large-scale bathymetry. The deep water south of the Mendocino Escarpment can only enter or leave through sector W-SW-S-SE. The quasi-synoptic measurements seaward of the 4000-m isobath suggest just that: eastward flow into the basin that turns southward within the basin.

Although W-7 and M-3 are from different years, there is a similarity in the eccentricity and orientation of their principal axes, and both appear to be parallel to the local bathymetry. The remaining two OPTOMA moorings (M-1 and M-2) are closer to the coast and show markedly reduced means and variance, suggesting a "boundary" effect due to the proximity of the continental slope.

The measurements at 3800 m, shown in Figure 2, are representative of the flow in the bottom 1500 m of the basin, seaward of the 4000-m isobath. On each W mooring, current measurements are available from above (at 3000 m) and below (at 40 m above the bottom) those at 3800 m; the depth of the deepest instrument varied between 4180 and 4370 m. Examination of the current records at each W mooring shows that the currents at the three deepest instruments are very similar and highly rotary in nature. Because of the rotary behavior of the low-frequency current fluctuations, the use of complex correlation coefficients [Kundu, 1976] is necessary. These corre-

lation coefficients (listed in Table 2) were calculated and show very high correlations (well above 99.9% significance level) between the currents measured at 3000- and 3800-m depths and 40 m above the bottom. On each of the OPTOMA moorings there was only one deep instrument (200 m above the bottom), and their records are not correlated with the currents at 1200 m, the depth of the next deepest instrument.

The ellipses and mean velocities shown in Figure 2 do not fully reveal the strong eddylike behavior that dominates the deep basin. This behavior is evident in the vector time series plots of the records (Figures 3a and 3b). Strong rotary behavior can be seen in several of the records, most notably W-6 and W-9. Only at W-5 does a mean current stand out from the mesoscale eddies that dominate elsewhere in the basin. The mean current at W-5 is northeastward (the W-5 vectors in Figure 3a have been rotated 45°). If the mean velocity is removed, however, the residual currents at W-5 are very similar to those elsewhere in the basin. The vector time series at M-3 is not unlike that at the W-moorings. The currents at M-1 and M-2, which are nearer to the continental margin, are significantly weaker, in both the mean and variance, and have shorter time scales than the currents measured at the W moorings and at M-3.

Rotary spectral analysis (Figures 4a and 4b) confirms the impressions gained from vector time series (Figures 3a and 3b). The deep currents at W-5, W-6, and W-9 have significant rotary behavior at lower frequencies, with most of the energy at W-5 and W-9 clockwise and at W-6 anticlockwise. The rotary behavior is strongest at W-9 at periods of 8 to 60 days. The currents at W-7 are more rectilinear, and the evidence for

TABLE 1 The Statistics From Each Record, Including the Mean Meridional Velocity (v), the Mean Zonal Velocity (u), Mean Temperature (T), and Their Standard Deviations (σ)

Mooring	Latitude	Longitude	Depth, m	Start Time	End Time	Length, days	Time Scale, days	u , cm s ⁻¹	σ_u , cm s ⁻¹	v , cm s ⁻¹	σ_v , cm s ⁻¹	T , °C	σ_T , °C
W-1	39°27.6'N	127°41.2'W	3050	Aug. 14, 1979	June 25, 1980	316	6.7	-0.22	2.14	1.56	2.52	1.62	0.011
			3850	Aug. 14, 1979	June 25, 1980	316	8.3	0.02	2.04	-1.51	1.84	1.49	0.007
			4260	Aug. 14, 1979	June 25, 1980	316	8.3	-0.09	1.83	-1.38	2.22	1.51	0.003
W-2	39°27.1'N	127°40.0'W	1255	June 28, 1980	March 8, 1981	254	7.9	-0.85	2.87	0.19	2.14	2.99	0.058
			3000	June 28, 1980	March 8, 1981	254	8.2	-0.06	1.49	-0.11	1.45	1.61	0.010
			3800	June 28, 1980	March 8, 1981	254	11.8	0.35	1.27	-0.24	1.24	1.49	0.003
			4200	June 28, 1980	March 8, 1981	254	5.7	0.31	0.83	-0.08	0.92		
W-3	39°07.1'N	127°25.1'W	2910	June 27, 1980	March 13, 1981	260	9.6	-0.50	1.63	-1.60	1.63	1.64	0.014
			3800	June 27, 1980	March 13, 1981	260	7.7	0.66	1.71	-1.73	1.84	1.50	0.007
			4200	June 27, 1980	March 13, 1981	260	6.9	-0.39	1.87	-2.13	1.93	1.51	0.001
W-4	39°27.1'N	127°42.6'W	1250	March 15, 1981	July 26, 1981	133	5.2	-0.81	3.04	-1.27	2.47		
			3000	March 15, 1981	Aug. 28, 1981	166	5.6	-0.22	1.69	-2.10	1.51	1.61	0.008
			3800	March 15, 1981	Aug. 28, 1981	166	6.4	0.28	1.68	-2.04	1.79	1.50	0.005
W-5	39°28.4'N	128°46.5'W	4200	March 15, 1981	Aug. 28, 1981	166	6.3	0.32	1.81	-2.26	1.78	1.52	0.002
			2970	Aug. 30, 1981	Sept. 18, 1982	385	4.9	1.74	1.35	0.96	1.17	1.62	0.008
			3770	Aug. 30, 1981	Sept. 18, 1982	385	9.3	3.34	1.64	1.39	1.08	1.50	0.005
W-6	39°28.5'N	126°45.7'W	4200	Aug. 30, 1981	Sept. 18, 1982	385	9.3	3.95	1.79	1.86	1.16	1.52	0.002
			2930	Sept. 5, 1981	Sept. 21, 1982	382	10.7	-0.83	2.53	-0.87	2.54	1.63	0.016
			3750	Sept. 5, 1981	July 9, 1982	308	7.1	-1.15	3.57	-1.75	3.50	1.50	0.012
W-7	38°35.0'N	126°24.8'N	4140	Sept. 5, 1981	Sept. 21, 1982	382	7.3	-1.09	3.66	-1.33	3.79	1.52	0.004
			2950	Sept. 3, 1981	Sept. 22, 1982	385	14.3	0.42	2.14	-0.38	2.02	1.64	0.015
			3740	Sept. 3, 1981	Sept. 22, 1982	385	13.9	1.02	2.39	0.79	2.87	1.52	0.013
W-8	39°05.5'N	127°23.0'W	4260	Sept. 3, 1981	Sept. 22, 1982	385	12.6	1.50	2.78	-0.74	3.39	1.53	0.005
			3000	Sept. 4, 1981	Sept. 21, 1982	383	13.1	-0.72	2.74	-2.89	3.87	1.63	0.013
			3820	Sept. 4, 1981	March 13, 1982	191	14.9	-0.84	2.65	-3.17	4.60		
W-9	39°27.7'N	127°41.8'W	4330	Sept. 4, 1981	Oct. 22, 1981	48	5.1	-2.30	2.71	-5.61	4.64		
			1210	Sept. 1, 1981	Sept. 19, 1982	384	18.0	0.60	3.19	0.33	2.90	3.06	0.076
			2980	Sept. 1, 1981	April 28, 1982	240	9.0	0.43	2.34	-0.24	2.18	1.62	0.005
W-10	39°28.4'N	127°40.9'W	3770	Sept. 1, 1981	Sept. 19, 1982	384	13.8	0.77	1.64	-0.34	1.56	1.50	0.004
			4160	Sept. 1, 1981	Sept. 19, 1982	384	11.3	0.72	1.61	0.35	1.67	1.50	0.004
			150	Sept. 23, 1982	Sept. 1, 1983	344	18.9	-0.50	4.43	0.22	6.75	8.46	0.580
W-11	39°29.6'N	127°41.1'W	600	Sept. 23, 1982	Sept. 1, 1983	344	22.8	-0.34	2.15	-0.40	2.93	4.80	0.122
			615	Sept. 23, 1982	Sept. 1, 1983	343	22.8	-0.26	1.77	-0.39	2.65	4.64	0.117
			1250	Sept. 23, 1982	Sept. 1, 1983	344	11.4	-0.90	2.40	-0.83	3.20	3.25	0.067
W-12	39°29.6'N	127°41.1'W	3000	Sept. 23, 1982	Sept. 1, 1983	344	10.3	-0.28	2.77	-0.78	2.98	1.62	0.008
			3800	Sept. 23, 1982	Sept. 1, 1983	344	8.8	-0.03	1.99	-0.96	2.43	1.49	0.006
			200	Sept. 5, 1983	June 15, 1984	285	26.2	1.38	2.95	3.59	6.39	7.42	0.187
M-1	38°56.7'N	124°59.8'W	600	Sept. 5, 1983	Dec. 27, 1983	114	14.4	2.28	3.01	1.04	5.24	4.45	0.040
			1250	Sept. 5, 1983	Aug. 15, 1984	346	10.5	-0.47	4.37	1.58	3.96	2.92	0.072
			3800	Sept. 5, 1983	Sept. 26, 1984	388	8.9	0.27	2.45	-0.72	2.73	1.49	0.011
M-2	38°11.6'N	124°24.7'W	4200	Sept. 5, 1983	Sept. 26, 1984	388	8.6	0.43	2.05	-0.41	2.38	1.50	0.002
			175	Sept. 27, 1984	July 15, 1985	292	9.5	-2.63	4.83	-2.27	6.66	8.53	0.443
			375	Sept. 27, 1984	July 15, 1985	292	14.5	-1.03	2.56	-1.05	3.08	6.32	0.238
M-3	38°12.5'N	125°35.1'W	1220	Sept. 27, 1984	Feb. 11, 1985	138	8.0	0.83	1.25	0.16	1.12	3.11	0.033
			3250	Sept. 27, 1984	July 1, 1985	278	3.4	0.31	1.28	0.43	1.48	1.58	0.006
			145	Oct. 3, 1984	July 12, 1985	283	13.7	-1.43	3.94	1.22	8.77	8.47	0.445
M-4	38°12.5'N	125°35.1'W	340	Sept. 28, 1984	July 12, 1985	288	18.1	-0.96	2.69	1.65	5.35	6.29	0.332
			800	Sept. 28, 1984	July 12, 1985	288	19.0	-0.53	1.87	1.21	2.60	4.25	0.100
			1190	Sept. 28, 1984	July 12, 1985	288	17.4	-0.07	1.50	0.70	1.73	3.67	0.049
M-5	38°12.5'N	125°35.1'W	3560	Sept. 28, 1984	July 12, 1985	288	3.0	0.02	0.87	-0.36	1.06	1.55	0.006
			350	Sept. 28, 1984	July 14, 1985	290	18.3	-3.58	4.62	-0.67	4.28	6.33	0.371
			800	Sept. 28, 1984	July 14, 1985	290	20.4	-2.40	3.45	-0.16	2.31	4.26	0.122
M-6	38°12.5'N	125°35.1'W	1185	Sept. 28, 1984	July 14, 1985	290	20.1	-1.68	2.66	-0.83	2.48	3.25	0.078
			3810	Sept. 28, 1984	March 8, 1985	162	4.9	-0.18	2.21	0.26	3.23	1.51	0.011

The integral time scales are calculated using $(\Delta t/2) \sum_{n=0}^N C_n C_n^*$, where C_n is the lagged biased correlation coefficient and $N+1$ the number of points in the series.

eddies is less. Although the current at M-2 has more energy in the clockwise spectra than at M-1, the energy levels at the two locations are similar. The shapes of the spectra of the currents at M-1 and M-2 differ from those found in the basin and at M-3. It is not so much that there is a peak of energy at 10

days but rather that there is less energy at longer periods at the M-1 and M-2 moorings than at the moorings further off shore. The spectra from the moorings in deeper water show a general increase of energy with decreasing frequency. At the lowest frequencies the energy levels at the deeper moorings are

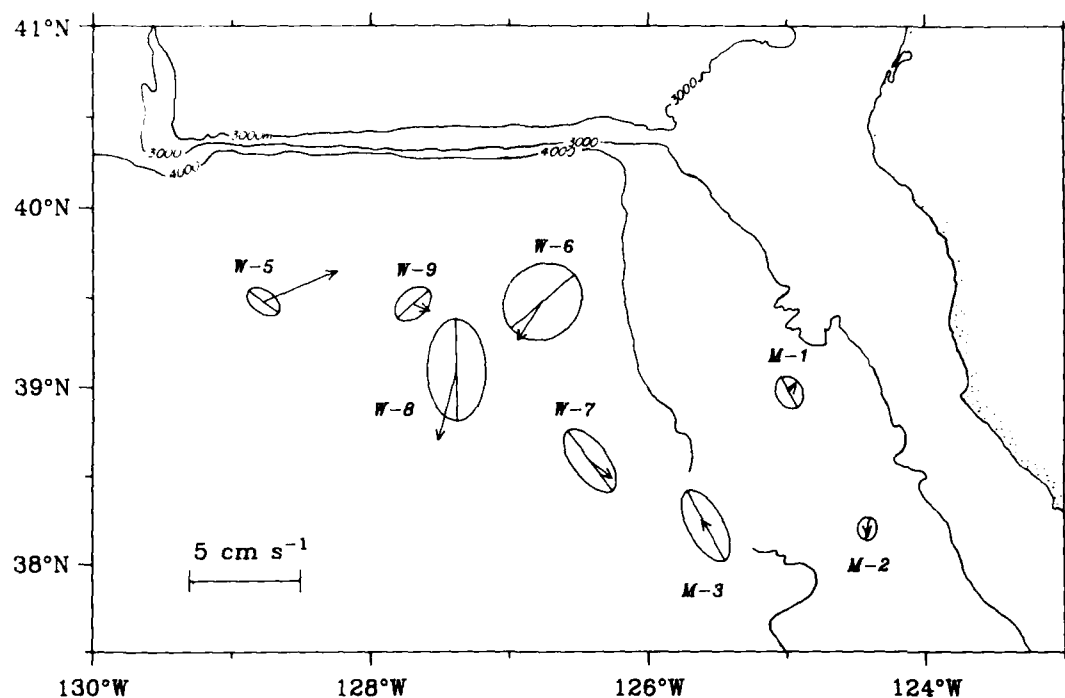


Fig. 2. The standard deviation ellipses and vector mean velocities of the currents at 3800 m for LLWOD and at 200 m above the bottom for OPTOMA. The length of the major axis is one standard deviation.

at least an order of magnitude higher than those found at M-1 and M-2, although at a period of 10 days the energy level is similar at M-1 and W-6, and at M-2 and W-7. The entire spectrum from M-3 is similar in shape and magnitude to those from W-7 and W-8, its nearest offshore neighbors.

Although the vector time series presented in Figure 3 have a "generic" similarity, they are not obviously correlated. Complex correlations were computed between the quasi-synoptic records at 3800 m and are presented in Table 3. There are no significant correlations at the 99% level. This is not totally unexpected, since the baroclinic Rossby radius of deformation in this region is approximately 25 km and the moorings are separated by at least 50 km. The highest correlations among the LLWOD array were found between W-8 and W-9 and between W-5 and W-8. The current record at 3800 m at W-8 is only half the mooring deployment length, owing to failure of the current meter, but the record at 3000 m lasted for the entire period. Since the deep currents at W-8 are very highly correlated in the vertical (Table 2) the horizontal correlations were recomputed using the longer 3000-m record at W-8. It was then found that correlations between W-8 and W-9 and between W-8 and W-5, were significant at the 99% level (listed in Table 3). In both cases the currents at W-8 lag the current measured at the neighboring instrument by several days, in the sense consistent with the mean flow. An examination of the rotary spectral coherence, however, shows no bands of high horizontal coherence between W moorings. The most significant correlations among all the horizontal pairs were between M-1 and M-2. This pair is correlated at well above the 99.9% level. The rotary spectral coherence shows two bands of high coherence, one from 7 to 15 days and the other

centered at 35 days; the coherences are strongest in the clockwise but also significant in the anticlockwise direction. The scalar coherence between the meridional components is also significant in the 7- to 15-day band with negligible phase difference, and at 35 days where the phase difference is nearly 180°.

3. TEMPORAL VARIABILITY

As mentioned in the introduction, the mooring site W-9 was instrumented for 5 years with six sequential moorings (W-1, 2, 4, 9, 10, and 11), producing continuous time series records

TABLE 2. Vertical Complex Correlations

Moorings	Depths, m	Length, days	Correlation	Rotation (+ ACW), deg	99% Significance Level
W-5	3000 vs. 3800	384	0.78	-1	0.23
W-5	3000 vs. 4200	384	0.73	0	0.24
W-5	3800 vs. 4200	384	0.89	0	0.28
W-6	3000 vs. 3800	308	0.88	5	0.29
W-6	3000 vs. 4200	308	0.84	0	0.28
W-6	3800 vs. 4200	308	0.99	-5	0.27
W-7	3000 vs. 3800	384	0.91	5	0.35
W-7	3000 vs. 4200	384	0.84	5	0.34
W-7	3800 vs. 4200	384	0.97	0	0.34
W-8	3000 vs. 3800	190	0.93	-5	0.49
W-8	3000 vs. 4200	45	0.83	0	0.59
W-8	3800 vs. 4200	45	0.99	1	0.59
W-9	3000 vs. 3800	238	0.78	3	0.38
W-9	3000 vs. 4200	238	0.75	-2	0.37
W-9	3800 vs. 4200	238	0.95	0	0.41

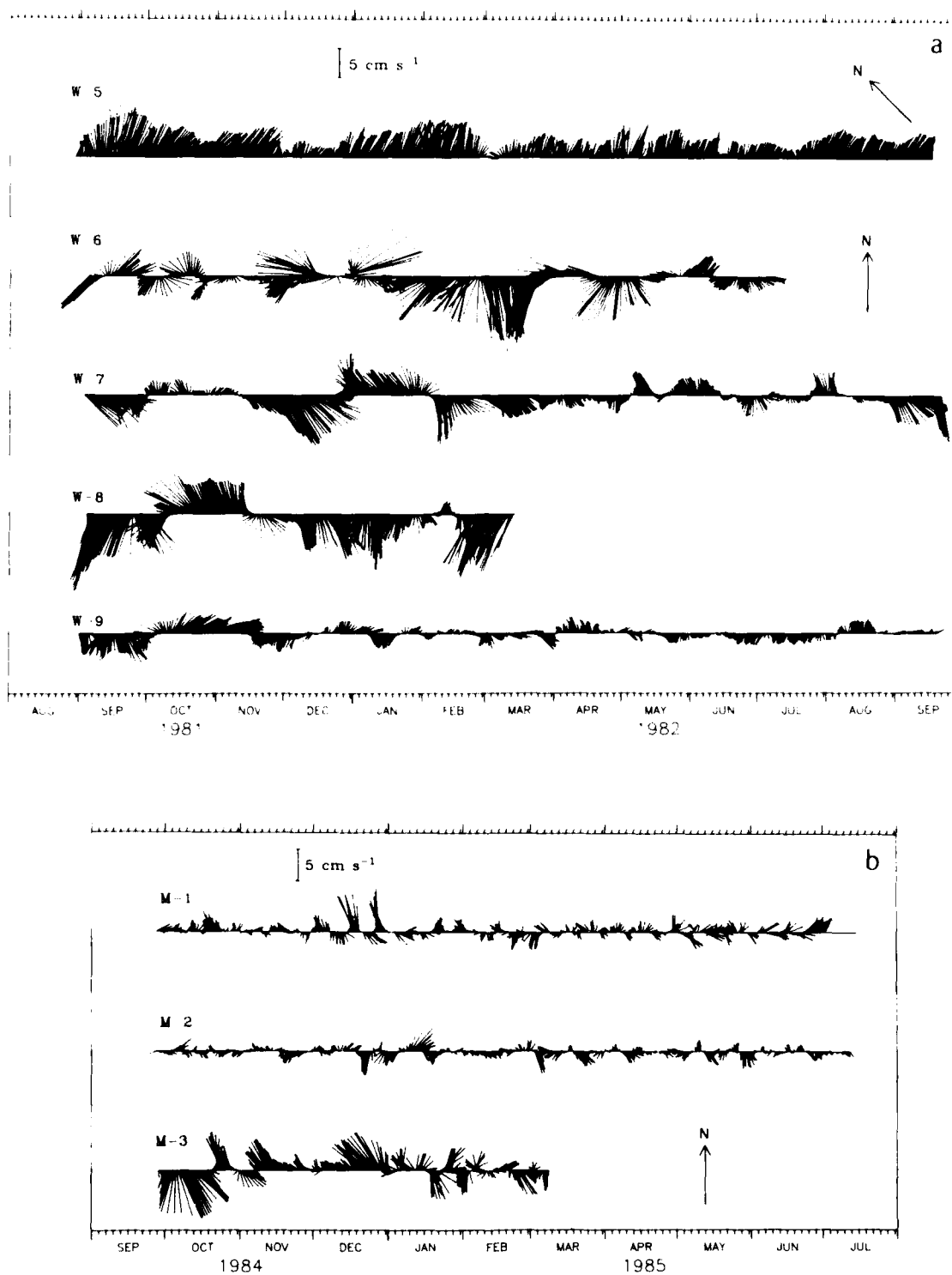


Fig. 3. (a) The 12-hourly low-passed current vectors at 3800 m at the five LLWOD mooring sites shown in Figure 1. (b) The 12-hourly low-passed current vectors at 200 m above the bottom at the three OPTOMA sites. The vectors at W-5 have been rotated 45° .

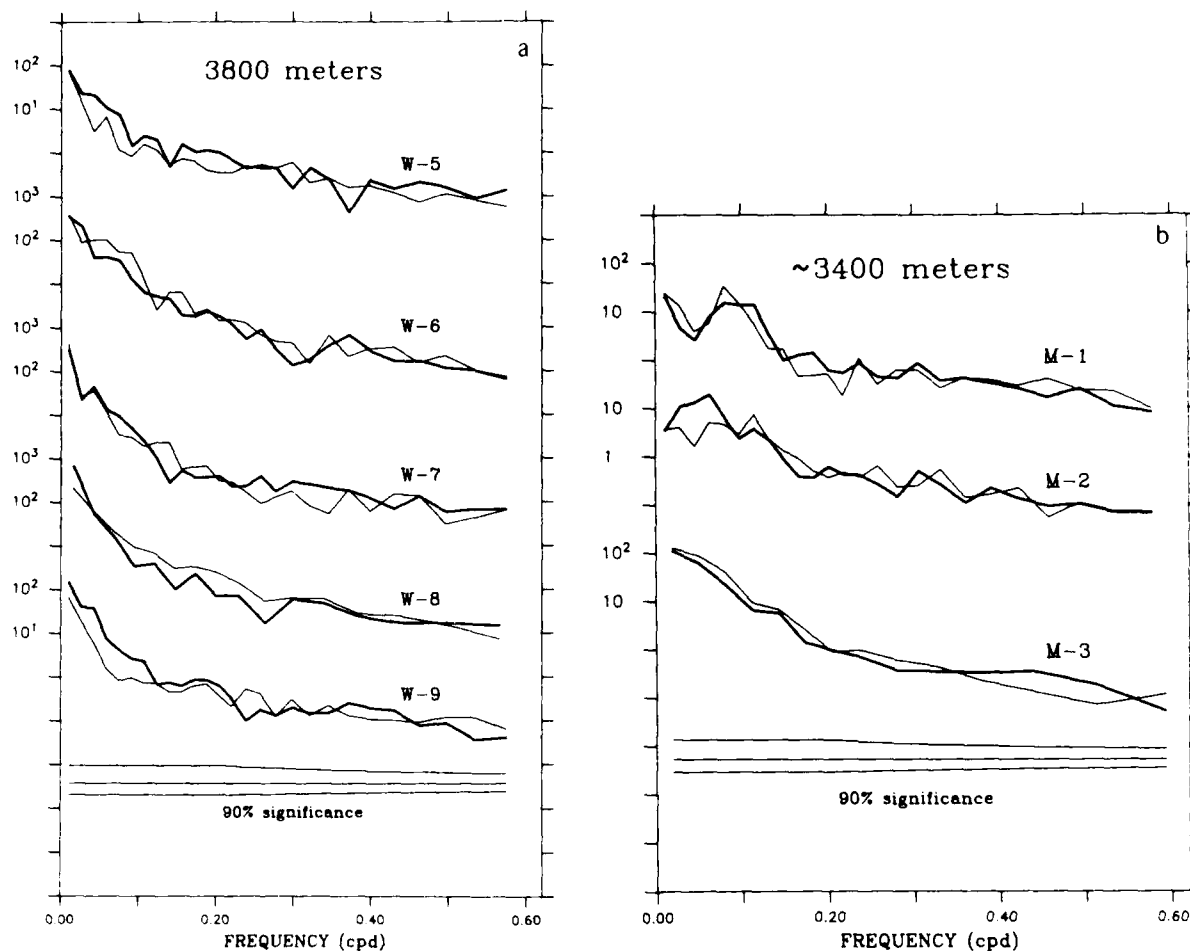


Fig. 4. Rotary spectral energies for (a) the five vector time series shown in Figure 3a and (b) the three vector time series shown in Figure 3b. The heavy line is clockwise and the lighter line anticlockwise. Also shown is the 90% confidence interval.

varying from 2 years (at 150 m) to 5 years (at 3800 m) in length. The availability of current records that span several years provides the opportunity not only to examine the low-frequency variability (less than 10^{-2} cpd) but also the observe

TABLE 3. Horizontal Complex Correlations

Moorings	Separation, km	Length, days	Correlation	Rotation, deg	Lag, days	99% Significance Level
<i>At 3800 m</i>						
W-9-W-5	92	378	0.15	10	-3	0.31
W-9-W-6	80	308	0.23	-15	-4	0.29
W-9-W-7	148	378	0.26	70	2	0.37
W-9-W-8	50	188	0.44	-55	4.5	0.45
W-8-W-5	127	188	0.38	137	1	0.42
W-8-W-6	68	188	0.13	120	-4	0.34
W-8-W-7	101	188	0.12	-28	0	0.50
W-7-W-5	227	378	0.20	145	0	0.32
W-7-W-6	104	308	0.27	-70	-2	0.30
W-6-W-5	172	308	0.18	70	0	0.27
<i>Instrument at W-8 at 3000 m</i>						
W-8-W-5	127	378	0.32	124	-0.75	0.29
W-9-W-8	50	378	0.32	-60	5	0.32
<i>OPTOMA Within 200 m of the Bottom</i>						
M-1-M-2	100	284	0.33	-134	5	0.18
M-1-M-3	100	161	0.18	30	3	0.27
M-2-M-3	100	161	0.19	120	8	0.27

how representative a given year is. The vector means and ellipses (Figure 5) are shown both for the composite of all the data at a given depth and for each mooring period. Since each mooring was at nearly the same position, this allows an examination of the temporal variability from mooring period to mooring period. The actual depths vary by less than 50 m from the nominal depths given in Figure 5. As in Figure 2, the mean velocities are less than the standard deviation, except at W-4, which was deployed for only 5 months during the spring and summer of 1981. During each deployment period, the statistics of the three deeper current meters are very similar but differ considerably from those at 1250 m. For these deeper instruments, the variations of the currents with deployment are greater than the variations with depth for a given deployment. During each period there is a southward component of

TABLE 4. Complex Correlations Between Currents at W-9

Depths, m	Length, years	Correlation	Rotation, deg	99% Significance Level
3800 vs. 1250	2.9	0.44	-1	0.18
3800 vs. 3000	3.4	0.80	-3	0.16
3800 vs. 4200	3.1	0.88	-2	0.16

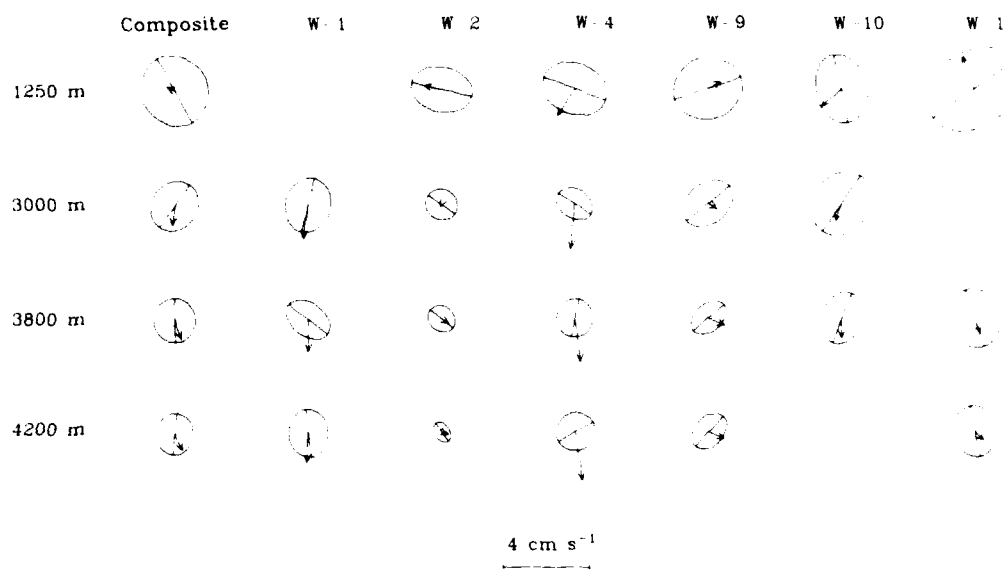


Fig. 5. The standard deviation ellipses of the currents from the six sequential moorings that form the 5-year time series at the W-9 site. The composite is the average for the complete data record at that depth; there is at least 4 years of data in each composite. The length of the major axis is one standard deviation.

the velocity at 3000, 3800, and 4200 m. At 1250 m the temporal variations of the mean current and of the orientation, size, and shape of the ellipses are even greater than at the deeper instruments. At least 4 years of data are used in the calculation of each composite standard deviation ellipse and mean velocity. The composite statistics at the three deeper instru-

ments are very similar, with the ellipses almost circular (implying the flow variability to be almost isotropic) and a small southward mean current. Even though the mean southward velocity is small, it is significantly (99%) different from zero at the three deeper instruments. (The standard test of the hypothesis $H_0: \mu = 0$ against the alternative $H_1: \mu < 0$ for a normally

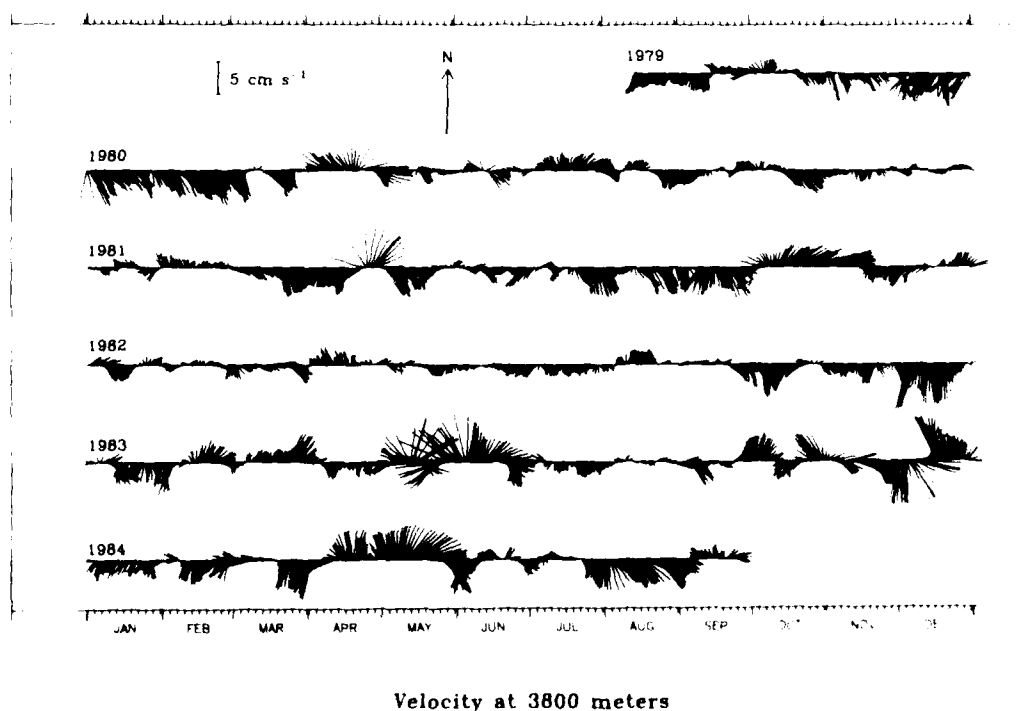


Fig. 6. The 5-year time series of velocity at 3800 m at the W-9 site. The low-passed time series of the 12-hourly velocity vectors was obtained by joining the records from the six moorings that spanned the period.

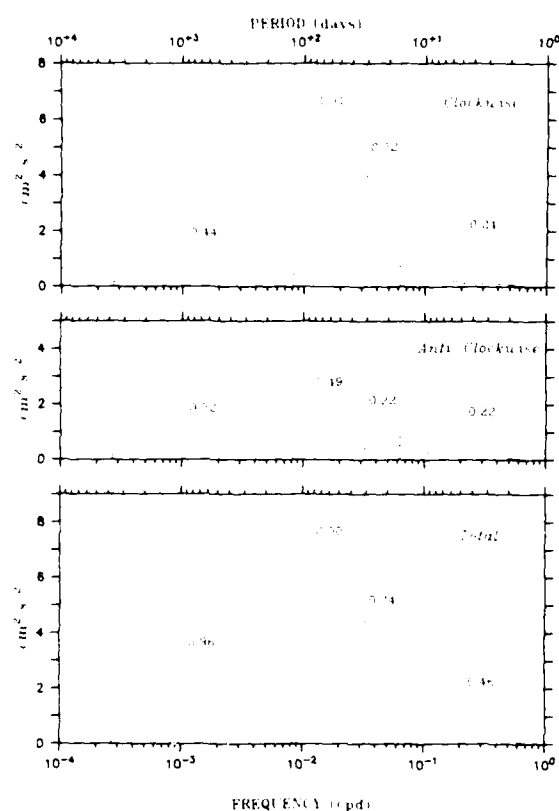


Fig. 7. The energy-preserving rotary spectral density for the 3800-m velocity time-series shown in Figure 6. They have been divided into four main bands, as listed in text, with the energy in each band shown.

distributed series was used. The number of independent estimates is taken as the length of the record divided by the integral time scale of the series.) At 1250 m the ellipse is also nearly circular, but the long-term mean does not differ significantly from zero. The mooring period that encompasses El Niño of 1982-1983 (W-10) does not stand out as being unusual at these depths.

Rotary correlation coefficients were calculated between the currents at 3800 m and those at 1250, 3000, and 4200 m using the longest possible records and are listed in Table 4. Approximately 3 years of data were used in each calculation, and they

confirm the high vertical correlations between currents within 1500 m of the bottom. The persistence of the high correlations over several years shows that this is a consistent feature of the deep flow in the region. The maximum correlation between the currents at 3800 and 3000 m (or 4200 m) is at zero lag and with negligible rotation of the velocity vectors with depth. The correlation between currents at 1250 and 3800 m is considerably less (0.44 versus 0.88) than among the deeper currents but is still significant at the 99% level. The maximum correlation between the currents at 1250 and 3800 m is at 0.5 day lag, but the coefficient at this lag is the same (to two significant digits) as that at zero lag. The only other depth at which there is more than 1 year of data is at 150 m; analysis of this 2-year record shows that the currents at 3800 and 150 m were uncorrelated (at 90% level).

4. ANALYSIS OF THE VERY LONG TIME SERIES

An examination of the 5 years of 12-hourly velocity vectors at 3800 m (Figure 6) shows a generally southward velocity with periods of highly rotary behavior at irregular intervals. Almost all are clockwise and appear as interruptions of the generally steady southward flow. One of the few anticlockwise occurrences happens in November and December of 1983. Each event lasts from a couple of weeks to a couple of months. Because of the highly rotary behavior of the currents during much of the record, it was analyzed using rotary spectra techniques.

The 3800-m record is almost twice the length of the current record discussed by Imawaki and Takano [1982] for the western North Pacific. To compare the 5-year record shown here with their results, the rotary spectra are presented in an energy-preserving manner (Figure 7). This analysis overestimates the energy in the lowest frequency band by less than 5%. As expected from the examination of the time series, the band from about 20 to 100 days contains significantly more clockwise energy than anticlockwise; however, the energy at longer periods is more evenly partitioned between clockwise and anticlockwise. The component spectra (not shown) have more energy in the meridional flow than the zonal. Following Imawaki and Takano, the spectrum has been divided into four bands: periods greater than 120 days (annual scale); periods between 120 and 31 days (temporal mesoscale as defined by Schmitz [1978]); periods between 31 and 16 days (monthly scales); and periods between 1.5 and 16 days (synoptic weather scale). For clockwise rotation, most of the energy is in the

TABLE 5. Estimates of Kinetic Energy (and Percentage of Total) for Four Frequency Bands at Different Depths at the W-9 Site and at a Site in the Western North Pacific.

Period (T), days	Imawaki & Takano, 4000-5000 m	5-Year Record	3-Year Record		
		3800 m	3800 m	1250 m	150 m
$T > 120$	1.6 (24%)	0.96 (23%)	1.21 (25%)	5.37 (44%)	22.3 (71%)
$120 > T > 31$	4.4 (65%)	2.00 (48%)	2.31 (48%)	4.63 (38%)	6.4 (20%)
$31 > T > 16$	0.6 (9%)	0.74 (18%)	0.85 (18%)	1.37 (11%)	1.0 (3%)
$16 > T > 1.4$	0.2 (3%)	0.46 (11%)	0.44 (9%)	0.85 (7%)	1.8 (6%)

From Imawaki and Takano [1982]. Estimates at the 150-m level are from the 630-day record.

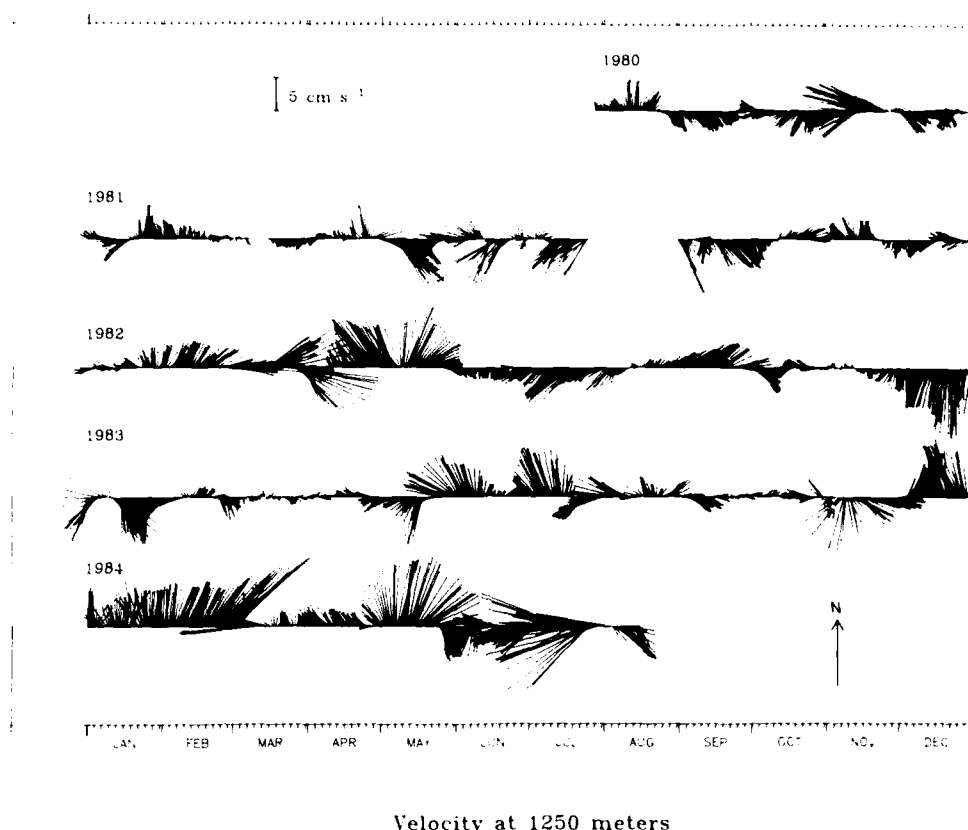


Fig. 8. The low-passed time series of the 12-hourly velocity vectors for the currents at 1250 m.

temporal mesoscale band, while for anticlockwise the energy is almost constant across the four bands. The total kinetic energy is shown and can be compared with the results of Imawaki and Takano, which are listed in Table 5. The total kinetic energy in the four spectral bands is also listed for: the 3 years of 1250-m currents, the 3 years of the 3800-m currents which are simultaneous with the 1250-m record, and the 2 years at 150 m. These will be discussed later in this section. In general, the energy levels are higher in the western North Pacific than in the eastern North Pacific off California. A greater percentage of the energy in the deep eastern North Pacific is in higher frequency bands ($T < 31$ days) than in the western North Pacific, and less than half the energy is in the temporal mesoscale band compared to almost two thirds of the energy in the western North Pacific record.

Velocity vectors for 4 years of data (with a 45-day gap at the end of the first year) at 1250 m are presented in Figure 8. It has been noted (section 3) that the currents at 1250 m are significantly correlated with those at 3800 m, so it is expected that there are apparent similarities between the currents at these two depths. The most notable similarities are the behavior of the currents at the end of 1982 and 1983, and the eddies seen in April and May 1981 and in May 1984. Differences are also apparent: at 1250 m there was a strong eddy present in January of 1983 which is barely discernible at 3800 m; during the first several months of 1984 the strong steady northward

current at 1250 m contrasts with the generally southward but variable current at 3800 m.

Rotary spectra for the three 3-year continuous record at 1250 m are presented (Figure 9) in the same energy-preserving manner as for the 3800-m record. Rotary spectra for the 3 years at 3800 m that are simultaneous with the time period of the 1250-m record are not shown, because they are virtually the same as the 5-year record. This can be seen in Table 5, where the energy levels in each frequency band of the 5-year record and the shorter 3-year record are almost identical. As at 3800 m, more energy is found in clockwise rotation than anticlockwise, but the difference is not as large as observed at the deeper instrument. Table 5 shows that there is also a shift of energy to the red at 1250 m. At 3800 m, almost half the energy is in the temporal mesoscale, twice as much as in the annual band, while at 1250 m only 38% is in the temporal mesoscale and over 44% in the annual band. These are similar to results found by Schmitz [1978] near the thermocline, where the temporal mesoscale was masked by lower-frequency energy.

The stippled areas (Figure 9) indicate the frequencies where the currents at 1250 m are strongly coherent (greater than 95% significance level) with those at 3800 m. These frequency bands of significant coherence are very robust and persist regardless of the sampling period used or the statistical techniques that are applied. It is interesting that the highest coher-

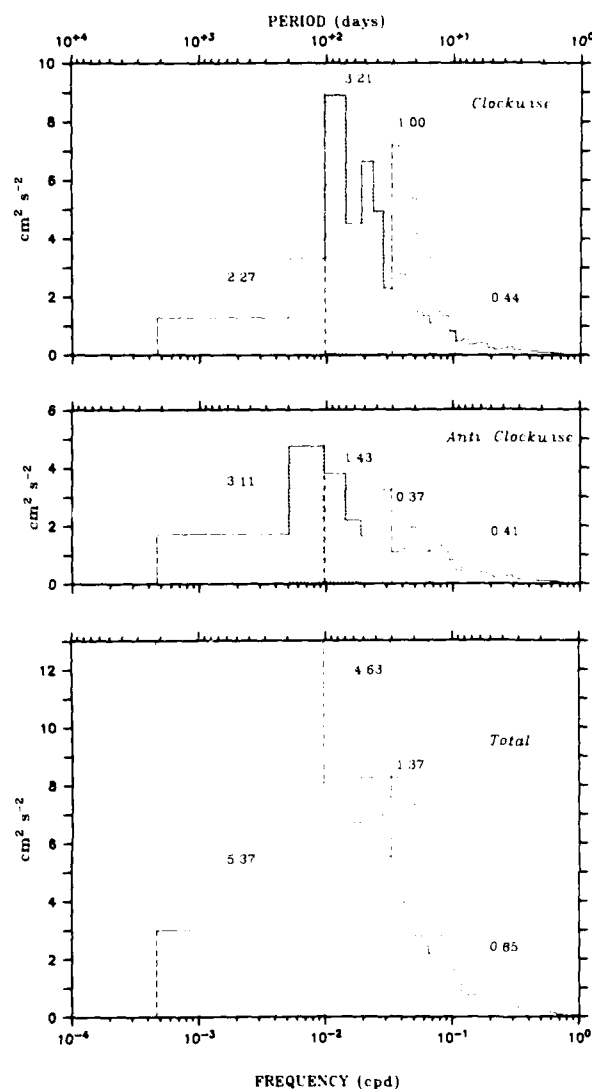


Fig. 9. The energy-preserving rotary spectral density for the currents at 1250 m. The stippled areas are those frequencies where the currents at 1250 and 3800 m are coherent (95% significance level).

ences at the lowest frequencies are in the anticlockwise band, while at shorter periods (40–50 days) the high coherences are in the more energetic clockwise rotations. The coherences between the currents at 3000 and 3800 m and between those at 3800 and 4200 m were also examined. The highest coherences between 3000 and 3800 m were found for clockwise rotation, where all periods longer than 10 days were coherent (95% significance), while for anticlockwise rotation the coherent band is limited to periods longer than 25 days. The high coherences between currents at 3800 and 4200 m extend to even shorter periods to include those longer than 5 days in the clockwise and 15 days in the anticlockwise.

Also listed in Table 5 is the total kinetic energy of the currents at 150 m in the four bands previously defined. This

record is only 630 days long but shows the general trend of the energy shifting toward the red with decreasing depth. At 150 m there is a loss of the rotary signature that was very strong at 3800 m and still evident, although weakened, at 1200 m.

5. VERTICAL STRUCTURE

Five of the moorings (W-10, W-11, M-1, M-2, and M-3) extended to within 400 m of the surface and provided time series of the currents at depths where the California Current is expected to be observed. Moorings W-10 and W-11 were continuations of the W-9 mooring in Figure 2. For the five moorings, ellipses and mean currents are shown (Figure 10). The length of the records is chosen so that each record from a particular mooring has the same start and end dates. The length of each OPTOMA record is 278 days, W-10 is 344 days, and W-11 is 285 days. (The W-11 statistics differ slightly from those shown in Figure 3, since a shorter time period is used here). A southward flowing California Current is not apparent in the mean of the shallower current records, although the deeper currents have a southward mean flow that is significantly different from zero. The energetic low-frequency variability is readily apparent in the vector time series plots (Figure 11) of W-10 and M-2, the two moorings with the most complete vertical resolution of the currents.

In general, the currents are stronger near the surface. The magnitudes of the standard deviation ellipses at M-2 decay almost linearly with depth, while, at W-10, the sizes of the ellipses become nearly constant at 600 m and do not decrease below this level. The ellipses from the shallower instruments at all the moorings are very eccentric with a tendency for north-south orientation, while the mean velocities are variable and not significantly different from zero.

Moorings W-10 and W-11 were in the same geographic location during two different years. The variations of the deep currents from mooring period to mooring period were discussed in section 3. The currents within 600 m of the surface are also highly variable from year to year. The shape and orientation of the ellipses at 150 and 600 m (W-10) are similar, although the magnitudes differ considerably (Figure 10). Qualitatively, the currents (Figure 11a) at 150 and 600 m appear very similar, while the currents at 1250 m appear to be a transition from the shallow to the deep currents. It is also evident that the small, intense eddies present below 1250 m are almost nonexistent in the two shallow records.

Evidence for the presence of subsurface eddies is not limited to the current meter records. During August 1981 a series of conductivity temperature depth (CTD) casts were done along 39°20'N from 129°W to 126°W. A depression of the deep isotherms by 100 m was attributed to the presence of a cyclonic eddy [Heath *et al.*, 1984]. The eddy was at least 50 km in diameter and was strongest at 3800 m. This is similar to the behavior of eddies found in the current measurements. They are lenslike, i.e., confined in the horizontal and vertical.

The nominal depths for the OPTOMA instruments are given in Figure 10; the actual depths vary by less than 50 m for the four upper current meters, and the deepest instrument is 200 m above the bottom. At each mooring the statistics of the two shallowest instruments are very similar, while the statistics from the deepest instrument differ markedly from the

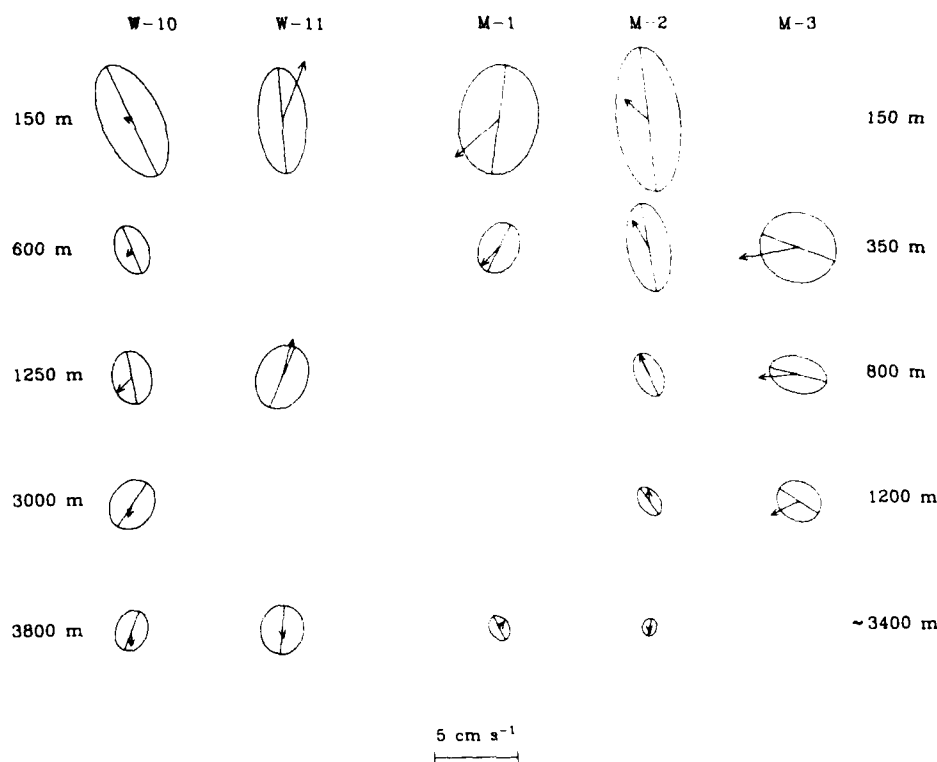


Fig. 10. The vector means and standard deviation ellipse for the three OPTOMA moorings and the two LLWOD moorings with the most complete vertical resolution. The length of the major axis is one standard deviation. Nominal depths at the left are for W-10 and W-11; those at the right are for the M moorings.

others. Figure 11b shows the current vectors for M-2. Here the four shallowest records (at and above 1200 m) are very similar, with the strength of the current decreasing with depth. There appears to be little rotary behavior in the four upper records. The current at the deepest instrument is not only much weaker but has a shorter time scale than the shallower currents.

Rotary spectra for the M-2 currents are shown (Figure 12b). The heavy line denotes the clockwise rotation. As expected from examining Figure 11, there is not any significant rotary behavior in the four shallower records, but the current at 3560 m does have significant clockwise rotation at the lower frequencies. At each depth (excluding the deepest) there is an increase of energy toward low frequencies. The magnitude at the lowest frequencies decreases with depth. These can be compared to the spectra from the year-long records for W-10 (Figure 12a). The strong rotary behavior of the deep currents is evident even in these shorter records. The energy levels are very similar at the shallowest instruments on W-10 (150 m) and M-2 (145 m). The spectra at M-2 at 1200 m are very similar to the anticlockwise spectrum at W-10 at 1250 m, but the spectra at the deepest currents differ at the two moorings, with the lowest-frequency energy levels much less at M-2 than at W-10, as noted in section 2.

To further investigate the relationships between currents at different levels in the moorings, we compute the rotary correlations between the currents for the two moorings sites with the best vertical resolution. A list of correlations between the current meter records at W-10 is given in Table 6. As expected from visual examination of the records, the currents at 150 and 600 m are highly correlated, as are those at 3000 and 3800 m. The currents at 1250 m are significantly correlated with those above and below, but there is virtually no correlation between currents at or above 600 m with those at and below 3000 m. Listed in Table 7 are the correlations between the currents at each depth at the M-2 mooring. The four shallow records are significantly correlated with each other. The currents at 3560 m are not significantly correlated with any of the currents above 1200 m.

To examine the vertical structure, empirical orthogonal functions (EOF) of the covariance matrices for W-10 and M-2 are calculated following Kundu and Allen [1976]. The results are shown in Figure 13 and Table 8. Most of the energy for both M-2 (90%) and W-10 (66%) is in the first mode. The second mode at both moorings contains over 60% of the remaining variance and has a zero crossing above 600 m. This results in over 90% of the total variance being explained by the first two modes and over 68% of the variance at each

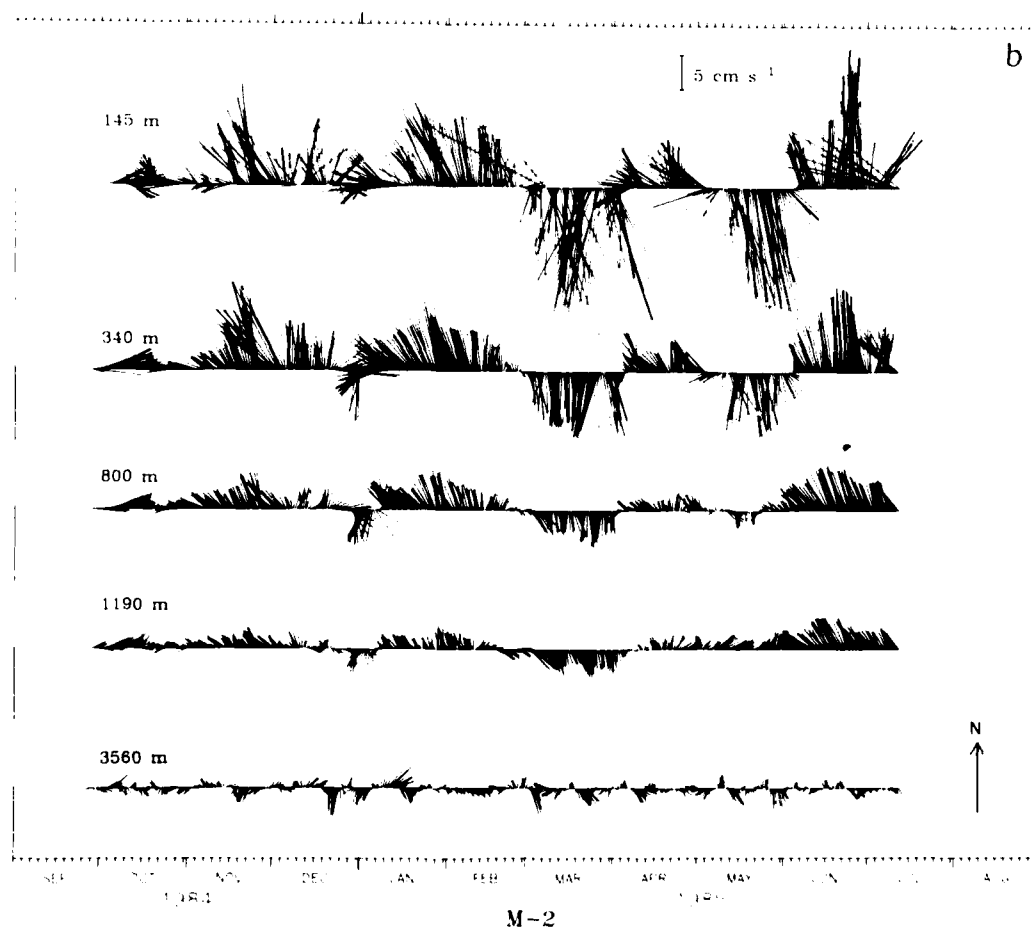
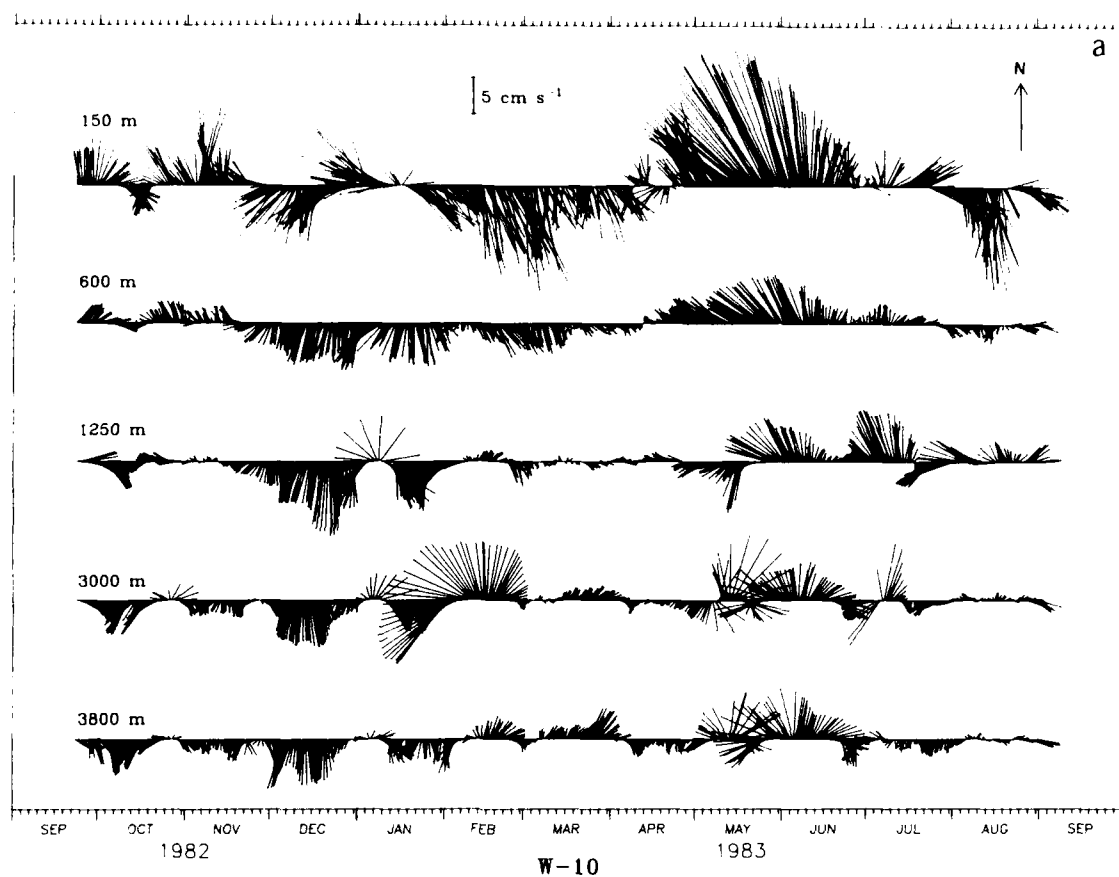


Fig. 11. The low-passed 12-hourly velocity vector time series from (a) W-10 and (b) M-2.

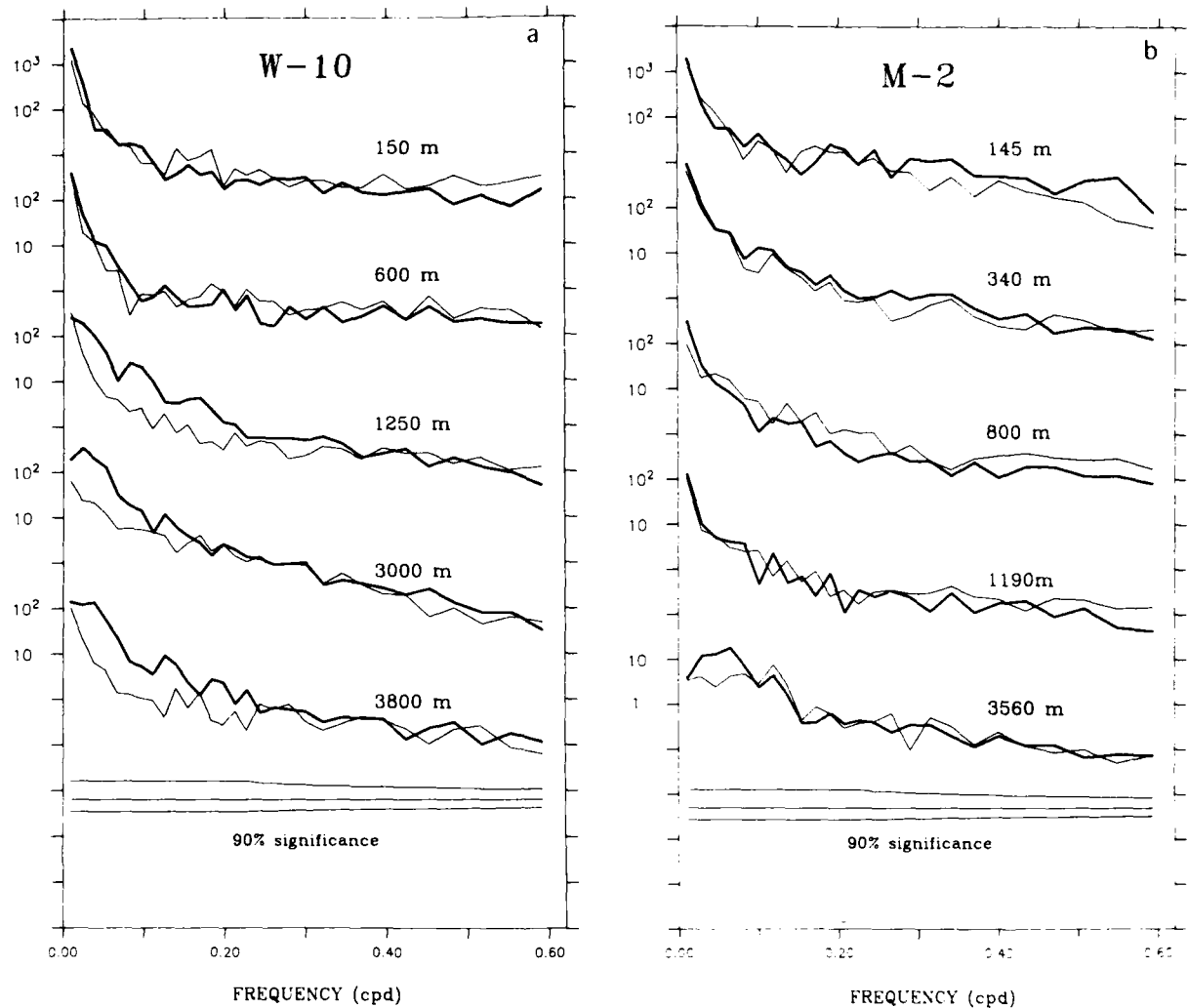


Fig. 12. Rotary spectral density of the currents shown (a) in Figure 11a and (b) in Figure 11b. The heavy line is the clockwise rotation and the lighter line anticlockwise.

depth being explained by a combination of the first and second modes (except the deepest instrument at M-2). At each mooring, the structures of both modes differ considerably from the mean velocities, which are also shown.

A statistical test for significance of EOF modes is given by Overland and Preisendorfer [1982]. Their results are for scalar EOFs and are not applicable to the complex EOFs that are used here. Following their development, the 99% significance levels for complex EOFs were calculated using 10 series, and each series consisted of 60 independent values. At both moorings the percentage of variance for which the first mode accounts is well above 33%, which is the 99% significance level. The second modes would fall below the 99% significance level (38%) if calculated from the percentage of the total energy. They are significant, however, if compared to the percentage of the remaining variance for which the second mode accounts (28%), after the variance in the first mode is removed.

At mooring W-10, the first mode is most highly correlated with the currents in the upper water column. The second

mode is more highly correlated with the deeper currents. In fact, the second mode appears to be related to the eddies found below 1200 m. The strength of these eddies is the main reason that the percent of variance explained by the second mode is so much greater at W-10 than at M-2. The strength of the February 1983 eddy, which is most energetic at 3000 m, results in only 7% of the variance at 3000 m being explained by the first mode (Table 8). If the time periods of the strong eddies are deleted from the record, then both a greater percentage of total variance and a greater percentage of the variance at each of the deeper instruments (at 3000 m it increases to over 20% from 7%) are explained by the first mode.

Unlike mooring W-10, M-2 does not experience strong eddies, and, because of this, the first mode accounts for over 90% of the total variance and almost all the variance of the two shallowest current records. The second mode accounts for most of the variance at 800 and 1190 m. The current at 3560 m is not correlated with either of the first two modes. It is not surprising that less than 8% of the variance of the current at

TABLE 6. Complex Correlations Among Currents Records From Different Depths of Mooring W-10

	150 m			600 m			1250 m			3000 m		
	Correlation	Rotation, deg	Lag, days	Correlation	Rotation, deg	Lag, days	Correlation	Rotation, deg	Lag, days	Correlation	Rotation, deg	Lag, days
600 m	0.44*											
	0.81†	13										
	0.81‡	13	0.25§									
1250 m	0.34*			0.37*								
	0.37†	29		0.59†	12							
	0.44‡	50	8.75§	0.61‡	17	2.5§						
3000 m	0.34*			0.37*			0.30*					
	0.07†	-4		0.21†	5		0.50†	-1				
	0.08‡	30	9.0§	0.23‡	7	2.0§	0.50‡	5	0.75§			
3800 m	0.34*			0.35*			0.30*			0.30*		
	0.26†	19		0.37†	7		0.53†	1		0.78†	5	
	0.26‡	40	8.0§	0.37‡	11	1.25§	0.54‡	4	0.50§	0.78§	3	0.25§

*99% significance level.

†At zero lag.

‡Maximum (within ± 10 days lag).

§Row leads column for positive lag.

3560 m is explained by the first two modes, since the deep currents are not correlated with any shallower measurements on the M moorings.

The empirical modes can be compared with the dynamical mode shapes obtained by solving the standard eigenvalue problem with a flat bottom [Kundu *et al.*, 1975]. The Brunt-Vaisala frequency, $N(z)$, which is a necessary input to the computation of the dynamical modes, was obtained from CTD casts that were done during September 1983 for W-10 and during July 1985 for M-2. Both the CTD casts were within 10 km of their respective moorings. Several other CTD casts made during different seasons within 100 km of the mooring were used to test the sensitivity of the modes to seasonal

changes. The first mode was not affected by these changes. The second mode's general structure remained the same, but the zero crossing varied in depth by 100 m depending on the N^2 profile used.

The first and second normalized dynamical modes and the empirical orthogonal functions are plotted (Figures 14a and 14b). The amplitudes of the EOF modes were obtained from the EOF vectors (shown in Figure 13) by using the length of each vector projected onto the 150-m vector (x axis). The shapes of the first empirical mode and dynamical mode are very similar at W-10 and at M-2. Both the dynamical and empirical functions for the second mode have a zero crossing above 500 m, with a maximum amplitude between 700 and

TABLE 7. Complex Correlations Among Currents Records From Different Depths of Mooring M-2

	145 m			340 m			800 m			1190 m		
	Correlation	Rotation, deg	Lag, days	Correlation	Rotation, deg	Lag, days	Correlation	Rotation, deg	Lag, days	Correlation	Rotation, deg	Lag, days
340 m	0.43*											
	0.90†	1										
	0.90‡	1	0.00§									
800 m	0.42*			0.46*								
	0.71†	8		0.84†	7							
	0.71‡	9	0.50§	0.84‡	7	0.25§						
1190 m	0.41*			0.45*			0.36*					
	0.57†	30		0.70†	22		0.83†	7				
	0.59‡	35	3.50§	0.71‡	24	1.25§	0.83‡	7	0.00§			
3360 m	0.25*			0.27*			0.27*			0.27*		
	0.10†	14		0.17†	45		0.20†	-30		0.20†	-27	
	0.13‡	10	-9.0§	0.18‡	-45	0.50§	0.20‡	-30	0.50§	0.21‡	-26	0.50§

*99% significance level.

†At zero lag.

‡Maximum (within ± 10 days lag).

§Row leads column for positive lag.

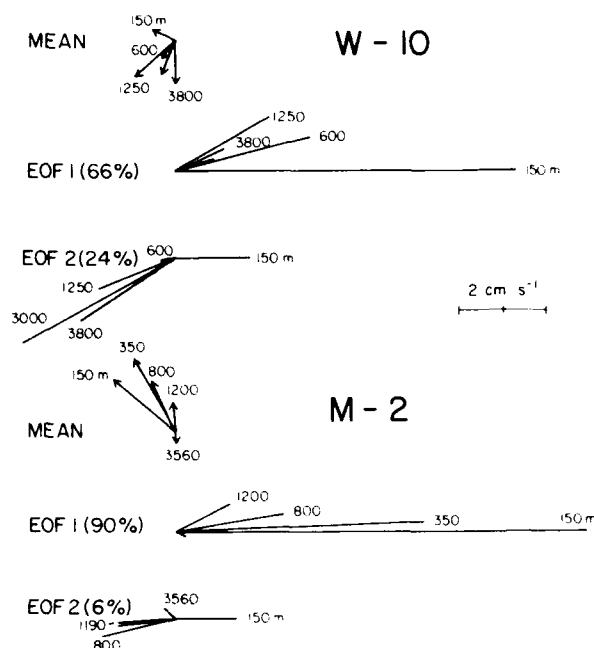


Fig. 13. The two most energetic velocity (complex) empirical orthogonal modes at (a) W-10 and (b) M-2. The vectors are relative to the shallowest, which is along the x axis. Also shown are the mean velocities relative to north, which is along the y axis. The percentage of total energy in each mode is indicated.

800 m. At W-10 the second empirical mode has a much larger magnitude than the dynamical mode at 3000 and 3800 m owing to the strength of the transient eddies.

6. CONCLUSIONS

The region offshore of the continental margin of northern California is an area of low mean current even though it is within the California Current. The currents in the upper ocean

are highly variable, with no significant mean meridional flow but with a large rms amplitude of the order of 10 cm s^{-1} . The mean current is dominated by eddies in the region and also influenced by the "squirts" or "cold filaments" that may originate in the vicinity of Point Arena and Cape Mendocino and extend as far offshore as mooring W-9 (300 km). The behavior of the currents in the 1500 m above the bottom varies significantly from that of the currents in the upper 700 m. At each mooring site in the basin there is high vertical coherence between the currents in the bottom 1500 m, where there is weak but significant southward flow. The measurements suggest the random occurrence of many intense, probably small-scale (diameters of the order of 50 km), lenslike eddies. They may be formed at the Mendocino escarpment and transported southward.

The behavior of the currents shoreward of the 4000-m depth contour differs from that of the currents in the deeper basin. The near-surface currents are clearly in the region of strong squirts and jets. In fact, during the spring that the M moorings were in place a prominent jet originated near Point Arena, passed between M-1 and M-2, and extended westward beyond M-3. In Figure 1 it can be seen that these OPTOMA moorings form a nearly equilateral triangle with sides of approximately 100 km, with M-1 northwest of M-2. During the time the cold filament was apparent in satellite IR images, there was a convergence of the current (in the upper 400 m) between M-1 and M-2 with offshore flow at the mooring furthest west, M-3. The upper currents (above 400 m) in the region near the continental margin are clearly influenced by the structure of the jets that occur there. The behavior of the deep currents shoreward of the 4000-m isobath also differs markedly from those seaward. At M-1 and M-2 the time series of the deep currents appear as if band passed, with much of the very low frequency energy filtered from the currents. This may, in part, be caused by the proximity of the slope, which is approximately one Rossby radius away.

An obvious question remains: What is the source of the high variability? Although the mean current at all depths measured is small (0.1 cm s^{-1}), the eddylike variability is strong, and subtidal currents greater than 10 cm s^{-1} are commonly sustained for weeks. Noble *et al.* [1986b] found some weak evidence for wind forcing at subtidal periods, shorter than 10 days, using relatively short records. In subsets of the basin currents data, they found evidence that the currents, with periods of several days, have characteristics similar to those predicted by stochastic models for wind-forced flow in the open ocean. This does not seem to be the case for the variability on the more energetic temporal mesoscale and annual bands. We have calculated the complex correlation coefficients between the winds at two National Data Buoy Office (NDBO) buoys, B-02 (latitude 42.30°N) and B-14 (latitude 39.12°N), and the currents measured at W-10. There was no significant correlation between the winds at either of the two buoys and the currents at 150 m. An examination of coherence between a 3.4 year record of the currents at 3800 m and wind stress at B-02 shows no bands of high coherence on periods longer than a week. A thorough analysis of the relationship between the currents and the winds remains to be done, including a test of the Sverdrup balance using the wind stress curl derived from synoptic wind fields, as was done by Valer and Kohlinsky [1988]. We are pursuing this with colleagues.

TABLE 8. Percent of Variance Explained at Each Depth by the First Two Complex Empirical Orthogonal Functions, at the W-10 and M-2 Moorings.

	Mode 1	Mode 2
W-10		
150 m	94	5
600 m	79	0
1250 m	42	26
3000 m	7	84
3800 m	20	59
M-2		
145 m	98	2
340 m	92	5
800 m	63	29
1190 m	43	17
3560 m	2	6

- Freeland, H. J., W. R. Crawford, and R. E. Thomson. Currents along the Pacific coast of Canada. *Atmos. Ocean*, 22, 151-172, 1984.
- Heath, G. R., D. K. Rea, G. Ness, R. D. Pillsbury, T. M. Beasley, and C. Lopez. Oceanographic studies supporting the assessment of deep-sea disposal of defueled decommissioned nuclear submarines. *Environ. Geol. Water Sci.*, 6(4), 189-199, 1984.
- Hickey, B. M. The California current system—hypothesis and facts. *Progr. Oceanogr.*, 5, 864-886, 1979.
- Imawaki, S., and K. Takano. Low-frequency eddy kinetic energy spectrum in the deep western North Pacific. *Science*, 216, 1407-1408, 1982.
- Kelly, K. A. The influence of winds and topography on the sea surface temperature patterns over the northern California slope. *J. Geophys. Res.*, 90, 11783-11798, 1985.
- Kosro, P. M., and A. Huyer. CTD and velocity surveys of seaward jets off northern California, July 1981 and 1982. *J. Geophys. Res.*, 91, 7680-7690, 1986.
- Kundu, P. K. A note on the Ekman veering observed near the ocean bottom. *J. Phys. Oceanogr.*, 6, 238-242, 1976.
- Kundu, P. K., and J. S. Allen. Some three-dimensional characteristics of low-frequency current fluctuations near the Oregon coast. *J. Phys. Oceanogr.*, 6, 181-199, 1976.
- Kundu, P. K., J. S. Allen, and R. L. Smith. Modal decomposition of the velocity field near the Oregon coast. *J. Phys. Oceanogr.*, 5, 683-704, 1975.
- McNally, G. J., W. C. Patzert, A. D. Kirwan, and A. C. Vastano. The near-surface circulation of the north Pacific using satellite tracked drifting buoys. *J. Geophys. Res.*, 88, 7505-7518, 1983.
- Moore, C. N. K., and A. R. Robinson. Turbulent jets and eddies in the California Current and inferred cross-shore transports. *Science*, 223, 51-53, 1984.
- Niler, P. P., and C. J. Koblinsky. A local time-dependent Sverdrup balance in the eastern North Pacific ocean. *Science*, 229, 754-756, 1985.
- Noble, M., L. K. Rosenfeld, R. L. Smith, J. V. Gardner, and R. C. Beardsley. Tidal currents seaward of the northern California continental shelf. *J. Geophys. Res.*, in press, 1986a.
- Noble, M., R. C. Beardsley, J. V. Gardner, and R. L. Smith. Observations of subtidal currents over the northern California continental slope and adjacent basin: Some evidence for local wind forcing. *J. Geophys. Res.*, in press, 1986b.
- Overland, J. E., and R. W. Preisendorfer. A significance test for principle components applied to a cyclone climatology. *Mon. Weather Rev.*, 110(1), 1-4, 1982.
- Schmitz, W. J. Observations of the vertical distribution of low frequency kinetic energy in the western North Atlantic. *J. Mar. Res.*, 36(2), 295-310, 1978.
- Strub, P. T., J. S. Allen, A. Huyer, R. L. Smith, and R. C. Beardsley. Seasonal cycles of currents, temperature, winds and sea level over the Northwest Pacific continental shelf: 35°N to 48°N. *J. Geophys. Res.*, in press, 1986.
- Winant, C. D., R. C. Beardsley, and R. E. Davis. Moored wind, temperature and current observations made during CODE-1 and CODE-2 over the northern California continental shelf and upper slope. *J. Geophys. Res.*, in press, 1986.
- Wyllie, J. G. Geostrophic flow of the California Current at the surface and at 200 m. *Calif. Coop. Oceanic Fish. Invest. Atlas*, 4, 1966.

R. L. Smith and P. J. Stabeno, College of Oceanography, Oregon State University, Corvallis, OR 97331

(Received July 22, 1986,
accepted August 26, 1986.)

Rapid alternating vertical temperature gradients in the East China Sea

WAYNE V. BURT,* STEVE NESHYBA* and CHELFORD L. TRUMP†

(Received 28 September 1982; in revised form 20 May 1985; accepted 16 July 1985)

Abstract Data from an array of current meters, thermistor chains, and meteorologically instrumented buoys deployed in the shallow water (depths of 97 to 115 m) of the East China Sea during AMTEX-75 (February 1985) show that the vertical temperature difference between the 20 and 70 m depths regularly alternated between $\sim 0^\circ\text{C}$ and a maximum of 0.65°C . The periodicity of change was predominantly that of the semidiurnal tide, 12.4 h, with some modulation at diurnal or near diurnal periodicity. The vertical gradient developed most often when currents were in a northwest direction, a direction parallel to the average northwest-southeast horizontal surface water temperature gradient; when the currents reversed 180° to the southeast, the vertical gradients tended to decrease or disappear altogether. An explanation is given in terms of vertical shear in the semidiurnal tidal currents coupled with the slightly higher current speeds during the offshore phase (southeast direction) of the current ellipse.

INTRODUCTION

The Air Mass Transformation Experiment (AMTEX-75) was one of the subprograms of the Global Atmospheric Research Program (GARP). Its main purpose was to study how the wintertime cold continental air mass is modified as it sweeps out over the East China Sea and the very warm Kuroshio Current (MITSUYA, 1977a; LENCROW and AGEE, 1974, 1976). As part of this experiment, Oregon State University anchored buoys and current meters (CM) on the continental shelf northwest of Okinawa in the waters of the East China Sea (Fig. 1). The buoys were equipped with meteorological sensors and thermistor chains (TC).

A large data base was acquired and various results have already been published. [For a listing see MITSUYA (1977a, b, 1978, 1979).] The Oregon State University data was used as a basis for the following papers. TRUMP (1976) summarized the overall analyses of the atmospheric and ocean data from the buoys. BURT and AGEE (1977) described the synoptic and the mesoscale cellular convection cells found in both buoy and satellite-derived data. TRUMP and BURT (1981) analyzed the current meter data, including current roses, rotary spectra and large-scale features. TRUMP *et al.* (1982) examined the effects of the mesoscale atmospheric convection cells upon the mesoscale structure of the underlying and shallow water column. ISHIDA *et al.* (1984) wrote on the effects of mesoscale convective cells on the surface wind field over the ocean.

This paper analyzes the unexpected variations in the vertical temperature gradient of the shallow water column, as measured with thermistor chains. The phenomenon is seen

* College of Oceanography, Oregon State University, Corvallis, OR 97331, U.S.A.

† Marine Technology Division, Naval Research Laboratory, Washington, D.C. 20375, U.S.A.

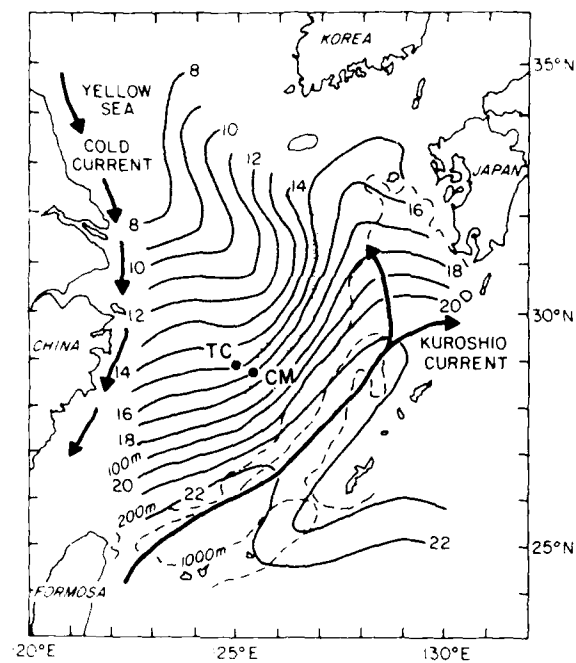


Fig. 1 The mean water surface temperature for February in the East China Sea and adjacent areas. The chart is based on data for the years 1953 to 1987 inclusive (from Gynnio, 1973). Oregon State University buoy locations are marked: TC, thermistor chain; CM, current meter.

THERMISTOR CHAIN AT AMTEX 75 STN 1

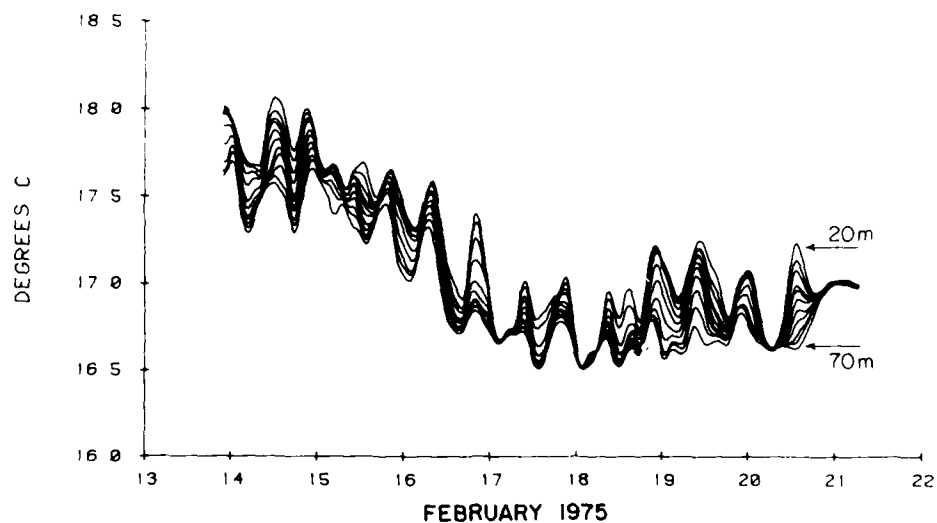


Fig. 2 Low pass filtered (3 h) thermistor chain data from AMTEX-75 Sta. 1

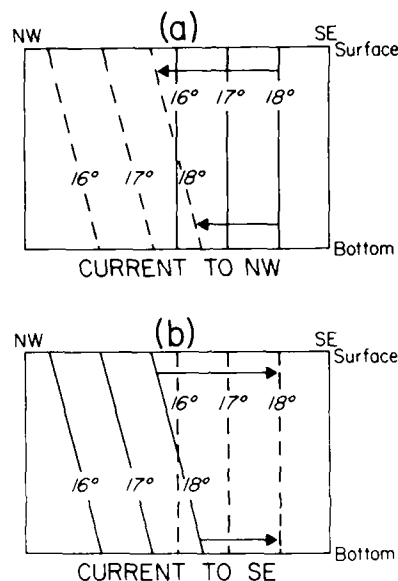


Fig. 3. Mechanism by which vertical shear in tidal currents develops vertical temperature gradients when the current is toward the northwest (a), and tends to erase the gradients when the current is towards the southeast (b) in the East China Sea near AMTEX-75 Sta. 1. The solid lines in (a) show the vertical temperature distribution when the tidal current has reached its maximum excursion toward the southeast; dashed lines show the vertical temperature distribution when the tide has reached its maximum excursion towards the northwest; (b) shows the reverse situation.

in the time series of temperature difference between the 20 and 70 m levels (Fig. 2) which at times alternates between zero or nearly zero and about 0.65 °C with a semidiurnal. Alternating setup and disappearance of thermal stratification to depths of 70 m with such rapidity is unusual. We believe that the variability can be explained by the alternating onshelf-offshelf transport of warmer Kuroshio water and cooler East China Sea water by a combination of mean and tidal currents (Fig. 3). Offshore transport results in destabilizing the water column by an overflow at the mooring of the cooler shelf waters of the East China Sea, hence the vertical thermal gradient setup prior onshelf transport of warmer water is destroyed by vertical mixing.

DATA SOURCES

Each of the three buoy-mounted thermistor chains deployed in AMTEX-75 showed the thermal stratification variability. The chain data used here is from buoy No. 1 which was anchored at about 28°52.2'N, 125°00.4'E (Fig. 1). Water depth was 97 m and the shelf floor was quite flat. The thermistor chain was manufactured by Aanderaa of Bergen, Norway, and provided a resolution of ± 0.01 °C; it was supported by a 20 m long spar buoy. Water temperatures were recorded at 5 m intervals between 20 and 70 m every 10 min from 13 to 24 February 1975.

Currents were measured at the 20 m depth level at three locations during AMTEX-75 (TRUMP and BURL, 1981). The data used here are from a current meter deployed near buoy 7 which was anchored at about $28^{\circ}38.8'$, $125^{\circ}27.2'E$, some 50 km southeast of buoy 1. Currents in this vicinity are dominated by semidiurnal tidal components superimposed upon a slow drift toward the northeast; there is also some evidence of currents with diurnal periods in the rotary spectra of the AMTEX-75 current data (TRUMP and BURL, 1981).

Eighteen STD casts (Salinity, Temperature, Depth) were made near the current meter location on 16 to 18 February from the Japanese R.V. *Tokaidaiiku Maru II*. These data are published only at standard depths and only at resolutions of $0.1^{\circ}C$ and 0.05% (NIXON and NIXON, 1976). Among the 18 casts, the temperature difference between 20 and 75 m varies from 0 to $0.7^{\circ}C$; this range of vertical temperature differences is consistent with the range of 20 to 70 m temperature differences we obtained with our thermistor chain (see the lower curve on Fig. 5) and provides useful corroboration of the variability of the vertical thermal gradient. Reported salinity values are too crude in resolution to yield useful vertical density gradients except at depths between 75 m and the bottom.

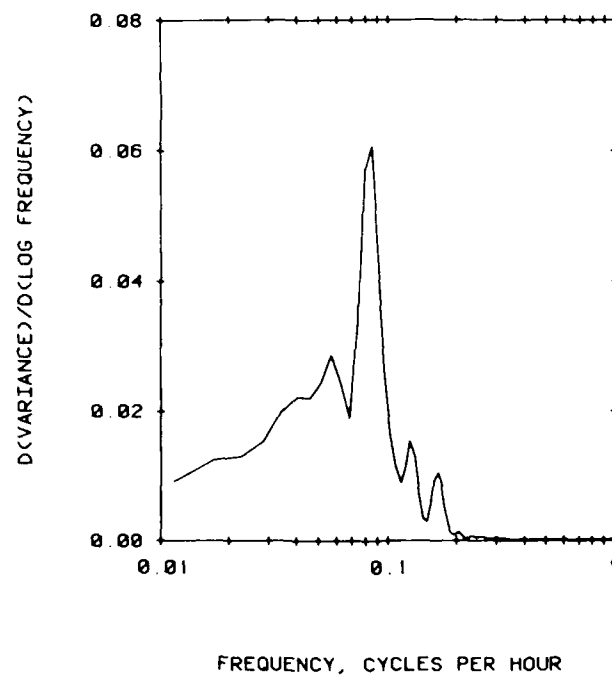


Fig. 4. Frequency times spectral density vs frequency for the difference between the temperatures at 20 and 70 m for AMTEX-75 Sta. 1. The dominant peak is for the semidiurnal M₂ tidal frequency.

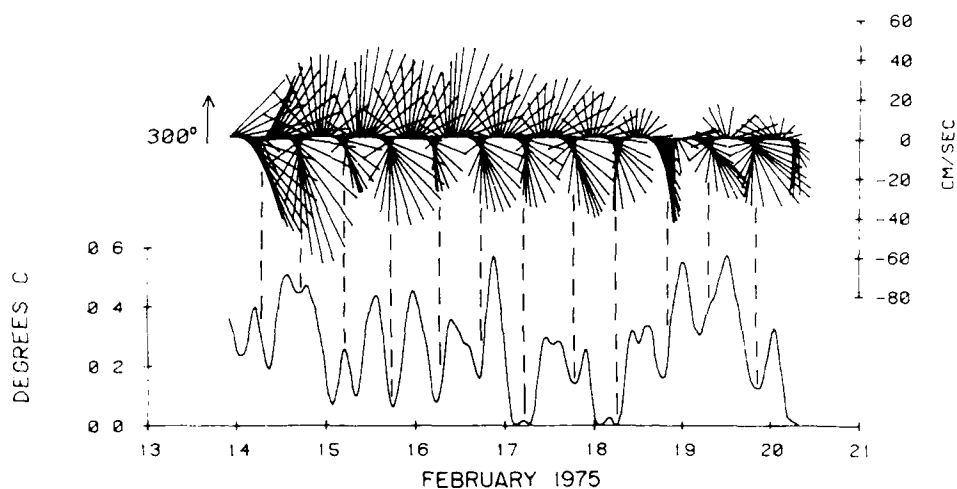


Fig. 5. Upper graph: stick diagram of current direction and speed. These data are half-hourly values obtained after the raw current series were filtered to remove variance at periods < 3 h. Note that the half-hourly vectors have been rotated so that a vector pointing straight up represents a current in the direction 300° (northwest by west). The sticks point in the direction in which the current is flowing. Lower graph: low pass filtered (3 h) temperature difference between the depths of 20 and 70 m for AMTEX-75 Sta. 1.

RESULTS

Figure 2 shows the thermistor chain data (for the period between 14 and 20 February) after it was filtered with a low-pass symmetric tapered-cosine filter to remove fluctuations at periods < 3 h. The semidiurnal tide frequency M_2 is immediately apparent and is relatively persistent.

The dominant peak in the spectrum of the temperature difference between depths of 20 and 70 m occurs at 0.08 cph which is the semidiurnal tide frequency (Fig. 4).

A superposition of the ΔT_{20-70} with a stick chart of currents oriented to 300° that were measured at the current meter site illustrates well that the times of occurrence of minimum values of ΔT_{20-70} coincide with the times when the currents were toward southeast by east (vectors pointing straight down on the stick chart, as shown in Fig. 5 with dashed lines). The squared coherence between the ΔT_{20-70} series and the current toward 120° (southeast by east) is 0.88 with a significance level of 99% and a phase separation of about 180° (175°), the latter an expected result for a strong negative correlation.

DISCUSSION

It is clear in Fig. 5 that the current structure changes considerably at about noon on 18 February. A progressive vector diagram (PVD) of this current meter record (TRUMP and BURR, 1981; see Fig. 3, CM7) also shows that from 14 to 18 February the mean flow was

5.3 cm s^{-1} toward 40° (between north-northeast and northeast). The correlation between ΔT_{20-70} minima and the southeast current direction is quite strong during this period.

During the period 18 to 21 February, the PVD showed both weakened rotary components and a shift of mean flow to the east by south (100°) at an increased mean speed of 14.3 cm s^{-1} . The ΔT_{20-70} series in Fig. 5 still shows a correlation between its minima and current vectors directed to the southeast, but the minima are less intense, i.e. do not reach the zero values after noon on 18 and 19 February, which would indicate that vertical mixing did not reach a depth of 70 m. TRUMP and BURL (1981) suggest that this sustained radical shift in the direction of the mean flow beginning on 18 February was due to a meander or eddy in the mean flow.

TIDE CURRENT-INDUCED SETUP DESTRUCTION OF VERTICAL TEMPERATURE GRADIENT

Given the strong average horizontal temperature gradient being negative to the northwest over this area of the East China Sea (Fig. 1), the presence of strong rotary tidal currents over this shallow sea suggests that vertical temperature gradients at a fixed site would alternate between maxima and minima due to vertical shear induced by bottom friction. If the vertical gradient is reduced below a critical level, then turbulent mixing fed by the shear can be sufficient to mix the entire column. In this case the vertical temperature gradient will tend to vanish, as in Fig. 5, during periods when flow is directed to the southeast. The conditions for such a vertical mixing process are enhanced if the tide current rose is highly elliptical and oriented parallel to the horizontal temperature gradient direction; this is the case for tide currents in our measurement area (Fig. 7; TRUMP and BURL, 1981).

The suggested mechanism is illustrated in Fig. 3. Given an initial condition of an isothermal, isopycnal water column, as in (a), vertical shear induced by bottom friction during down-gradient flow (to the northwest in the East China Sea) would carry warmer water over cooler, deeper water. An STD cast or thermistor chain record at the finish of flood tide would yield the stable thermal stratification seen in our records (Fig. 2).

During the reverse flow (to the southeast in the East China Sea), the condition of isothermal water column would be reinstated (Fig. 3b). However, if the reverse southeast flow is more intense than the down-gradient, northwest flow, then the condition at the finish of reverse flow is one of possible negative vertical temperature gradient and hence renewed vertical mixing by which the initial condition is reinforced.

Such non-symmetry does exist in the ellipticity of current roses from the AMTEX-75 current meter records. For the flow record of current meter Sta. 7 (Fig. 5), the current rose shown in Fig. 6 indicates that flow in the southeast direction exceeds the northwest flow by about 20%. These data support our hypothesis of the tidal current-induced setup and destruction of vertical temperature gradient in the mid-shelf area of the East China Sea.

Our current meter data also showed evidence of occasional strong transient eddies or meanders which could bring about changes in the horizontal temperature gradient (TRUMP and BURL, 1981). If the horizontal temperature gradient was temporarily reversed, then the relationship between vertical temperature gradients and tide currents would also be reversed. A study of the water surface temperature measured by the Japanese ship *Keifu Maru* at a fixed station near our thermistor chain showed a surface

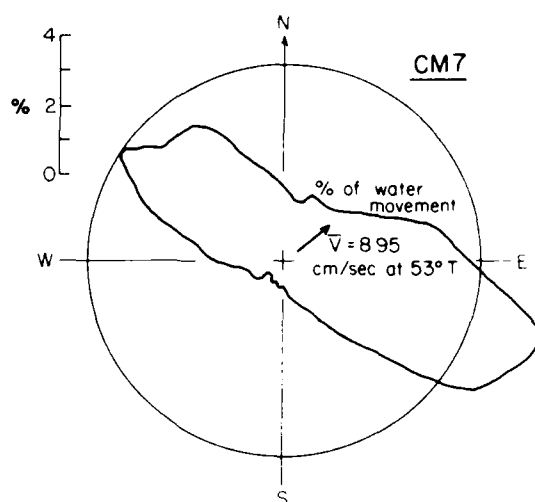


Fig. 6. Current rose for AMTEX-75 current meter Sta. 7. Percentage of total water movement is given for each 10° compass interval. Mean current velocity also shown.

temperature range of over 4°C during the period the chain was deployed. From a plot of all of the water surface temperatures measured from research ships and fishing vessels during AMTEX, we find the general trend was for temperature to decrease to the northwest in the manner shown in Fig. 1. However, there were times when the horizontal gradient was reversed due to transient eddies or meanders in the northeasterly drift.

VERTICAL SHEAR

Was the current shear between the depths of 20 and 70 m of sufficient magnitude to produce the recorded water temperature differences at those depths? Ideally, one should have a record of the currents at the above depths during the time period when the water temperatures were being recorded. Unfortunately no such record exists.

Oceanographers from the University of Tokyo deployed two current meters during AMTEX-75 at depths of 80 and 103 m at a location where the water depth was 110 m. Many of the CTD casts that were made within the OSU buoy array showed a change in the water type at depths between 75 and 100 m. The near-bottom water was usually slightly cooler and less saline than the water above 75 m, indicating a different flow and mixing regime near the bottom. Thus the University of Tokyo current meter data could not be used to make a reliable estimate of the shear in the water column above a depth of 70 m.

Oceanographers from Tohoku University (Sendai, Japan) measured currents at a location northeast of the OSU buoy array, in water of about the same depth and distance from the shelf break (Tokuda *et al.*, 1975). A special trip was made to Sendai to obtain their data and discuss oceanographic conditions with the group that had made the observations. The only data that were made available are shown in Fig. 7a. Figure 7b shows the currents at depths of 20 and 40 m with the same scale. At the start of the

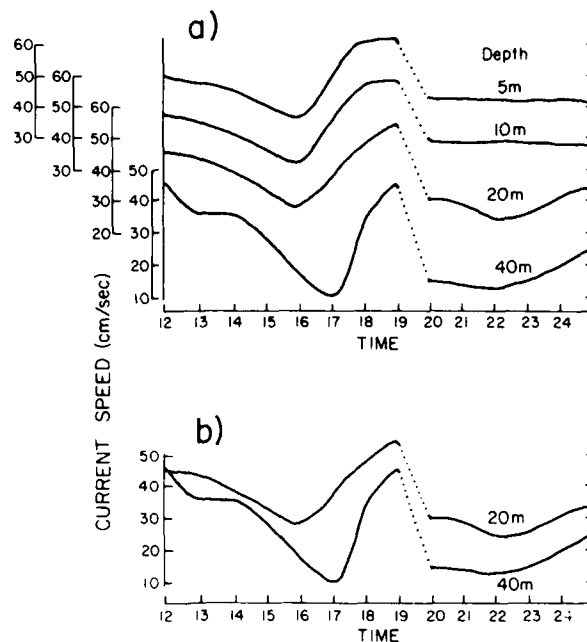


Fig. 7. Data from current meter measurements that were made by the Tohoku University on 25 and 26 February during AMTEX-75. The current meters were deployed at 29.30°N, 127.12°E. The top diagrams show the data from all four current meters with vertical speed scales offset by 10 cm s^{-1} . The bottom graph shows the currents at depths of 20 and 40 m to the same vertical (speed) scale.

record at noon on 26 February the current speed was the same at 20 and 40 m. For the rest of the time the current speed at 20 m was an average of about 10 cm s^{-1} faster than the current at 40 m. If this shear is extrapolated down to 70 m the difference in speed between the depths of 20 and 70 m would have been approximately 25 cm s^{-1} . In half a semidiurnal tidal cycle (22356 s) the difference in the movement of the water at 20 and 70 m would have been 5.4 km. The average horizontal gradient in temperature was 6°C in 60 nmi or 0.06°C km^{-1} . If the shear were perpendicular to the horizontal temperature the resulting temperature difference between the water at the two depths would have been 0.35°C after half a semidiurnal tidal cycle. This is the right order of magnitude when compared to the vertical temperature gradients found in the thermistor chain data.

CONCLUSIONS

In the East China Sea in the vicinity of 29°N, 125°E, in waters of 100 m depth, the water column appears alternately to be thermally stratified with a temperature difference, between depths of 20 and 70 m, of about 0.65°C, and neutrally stratified with isothermal structure to some depth below a depth of 20 m and sometimes to depths below a depth of 70 m. The phenomenon is unusual in that it occurs some 200 km from the nearest coast, almost 200 km from the shelf break, and over flat continental shelf

topography. These alternating states of vertical thermal structure occur with a periodicity of the semidiurnal tide, 12.4 h.

The phenomenon occurs in an area of strong horizontal thermal gradient, about 1°C per 16 km, oriented from southeast to northwest and approximately perpendicular to both the bathymetry of the shelf break and to the main stream of the Kuroshio current which here flows southwest-northeast along the slope of the Okinawa Trough (Fig. 1). At the latitude of the buoy array warm high salinity water flows northeast on approximately the outer two thirds of the shelf while relatively cold low salinity water flows southwestward on the inside of the shelf (Fig. 8; NINO and EMERY, 1961). Maximum mean current speeds exceed 40 cm s^{-1} (maximum current speeds exceed 70 cm s^{-1}); in terms of percent water movement within 10° sectors, the rose shows that southeast movement exceeds northwest movement by some 20%.

The combination of strong cross-shelf semidiurnal tide currents and strong cross-shelf horizontal thermal gradient suggests a vertical mixing mechanism induced by differential flow speeds. The mechanism creates an overflow of warm water during the onshelf portion of the tide cycle; vertical sensing of the temperature field during this phase yields a thermally stratified water column. During the more intense offshelf flow phase of the tide, cold surface shelf water overflows warmer, deeper water, creating the vertical instability and subsequent vertical mixing; temperature profiles taken during this phase show isothermal conditions to the bottom or near bottom. The mechanism is consistent with our thermistor chain data, the STD profiles taken in the vicinity, the local tide current ellipse, and the mean circulation over the East China Sea.

The occurrence of tide current-induced vertical mixing nearly to the bottom in 100 m depth shallow seas has important implications:

1. Studies of shelf or shallow seas must be carefully planned to avoid placing reliance upon serial, single sampling along cruise tracks. The alternating states of thermal stratification and vertical mixing in our data render implausible the construction of self-consistent area charts of physical parameters measured in serial profiles during AMTEX-75.

2. Biological studies, particularly of planktonic forms, chlorophyll distribution or species diversity, are likely to be impacted by the alternating mixing conditions. For example, vertical mixing is thought to be an essential element in the transfer of resting spores of some phytoplankton from the bottom up to the photic zone.

3. Periodic, tide-induced vertical mixing events of the type reported here may be a significant mechanism for the dissipation of kinetic energy in eddies associated with along-slope currents often found at shelf breaks, as well as for cross-shelf mixing of water parameters. There is a net flux of cold water in an offshore direction in the area of the buoy array.

4. Air-sea interaction is also impacted. In our data, the tide-induced vertical mixing events preceded the most intense cold air outbreak over the East China Sea during AMTEX-75, and thus set up conditions for more rapid and deeper modification of the water column as a consequence of intense surface heat and vapor fluxes during the outbreak.

Acknowledgements—The authors wish to thank Prof. Y. Mitsuta of Kyoto University, Mr K. Komatsuzaki of the Japanese Meteorological Research Institute, Dean M. Iwashita of Tokai University, and the captain and crew of the *Tokaidagakumaru Nisic* for assistance in preparation for and during AMTEX-75. They also wish to thank Joseph Bottero for his assistance in data processing, Asa Robinson who was responsible for handling the

equipment and our secretary Pam Wegner. This research was supported by the Office of Naval Research through Contract N00014-76-C-0067 under Project NR 083-102 and the Global Atmospheric Research Program of the National Science Foundation under Grant BA 28004.

REFERENCES

- BURT W. V. and L. M. AGEE (1977) Buoy and satellite observations of mesoscale cellular convection during AMTEX-75. *Boundary-Layer Meteorology*, **12**, 3-24.
- GAMBO K. (1973) "Kuroshio" and flow patterns over the AMTEX area. In: *AMTEX: Air Mass Transformation Experiments a report of the Management Committee of AMTEX*, pp. 8-13.
- ISHIDA H., W. V. BURT and Y. MISETA (1964) The effects of mesoscale convection on the surface wind field over the ocean. *Boundary-Layer Meteorology*, **29**, 75-84.
- LENSCHOW D. H. and L. M. AGEE (1974) The air mass transformation experiment (AMTEX). Preliminary results from 1974 and plans for 1975. *Bulletin of the American Meteorological Society*, **55**, 1228-1235.
- LENSCHOW D. H. and L. M. AGEE (1976) Preliminary results from the air mass transformation experiment (AMTEX). *Bulletin of the American Meteorological Society*, **57**, 1346-1355.
- MISETA Y. (1977a) Collected scientific papers of AMTEX. Japanese National Committee for GARP, Vol. 1, 298 pp.
- MISETA Y. (1977b) Collected scientific papers of AMTEX. Japanese National Committee for GARP, Vol. 2, 270 pp.
- MISETA Y. (1978) Collected scientific paper of AMTEX. Japanese National Committee for GARP, Vol. 3, 181 pp.
- MISETA Y. (1979) Collected scientific papers of AMTEX. Japanese National Committee for GARP, Vol. 4, 249 pp.
- NIINO H. and K. O. FAIRRY (1961) Sediments of shallow portions of East China and South China Sea. *Geological Society of America Bulletin*, **72**, 731-762.
- NINOMIYA K. and Y. NAGAYAMA (1976) AMTEX Data Report. Japanese Meteorological Society and the Tokyo University, Vol. 3, 298 pp.
- NIJHUI H. (1972) Beginning of the Kuroshio. In: *Kuroshio*, H. STOMMER and H. YOSHIDA, editors, University of Washington Press, 517 pp.
- TOKUDA M., M. ISHII, K. OKUDA, M. HODATE, S. KOBAYASHI and Y. TOKA (1978) Observations of upper ocean in Kuroshio boundary region in East China Sea. Abstract, Oceanographical Society, autumn meeting.
- FRIMM C. L. (1976) Effects of mesoscale atmospheric convection cells on the waters of the East China Sea. PhD thesis, Oregon State University, 124 pp.
- FRIMM C. L. and W. V. BURT (1981) Wintertime current meter measurements from the East China Sea. *Journal of Physical Oceanography*, **11**, 1300-1306.
- FRIMM C. L., S. F. NESTOROV and W. V. BURT (1982) Effects of mesoscale atmospheric convection cells on the waters of the East China Sea. *Boundary-Layer Meteorology*, **24**, 15-34.

APPENDIX

Oceanography was only a very small part of the AMTEX-75 experiment.

It should be emphasized at this point that almost all of the overall thrust of the experiment was meteorological in nature and that very little oceanographic data were gathered. The AMTEX Committee published over 2000 large pages of meteorological data and only 30 pages of oceanographic data. Of the more than 125 published papers, theses and abstracts resulting from the experiment only some of the GSU papers listed above and very few others were oceanographic in nature. Our part of the experiment was not designed to study the thermal structure of the water. We deployed the thermistor chains and current meters simply because we had the equipment, and the buoys were going to be anchored anyway. When we discovered the rather unique time varying thermal structure, the experiment was over and it was too late to systematically gather the ancillary data which could be used to construct a model. However, we believe that the temperature data is sufficiently unique and interesting to be published so that anyone doing oceanographic research in that area could use it to help design a more thorough study of the variance in the thermal structure.

ON THE NONLINEAR EVOLUTION OF BAROCLINIC INSTABILITY OVER TOPOGRAPHY

ROLAND A. DE SZOEKE

College of Oceanography, Oregon State University, Corvallis, OR 97331 (U.S.A.)

(Received August 5, 1985; revised July 14, 1986; accepted August 5, 1986)

ABSTRACT

De Szoeke, R.A., 1986. On the nonlinear evolution of baroclinic instability over topography. *Dyn. Atmos. Oceans*, 10: 221–241.

A theory is presented for the nonlinear evolution of fluctuations in a zonal baroclinic shear flow over topography on a β -plane. It extends an earlier linearized theory on the same subject, which showed that unstable growth was possible for hybrid modes made up of a pair of primary modes with the same frequency but different wavenumbers, each stable in the absence of topography, but made unstable by topography with wavenumber that bridges the wavenumber gap between the primary modes. The slow evolution of the amplitudes of the hybrid modes can be expressed quite generally in terms of elliptic functions that fluctuate regularly between maximum and minimum values determined in a complicated way by initial amplitudes and parameters characterizing the primary modes. For small initial amplitudes, the evolution can be described in terms of even simpler functions, i.e., trains of hyperbolic-secant pulses that recur with a period that depends on the logarithm of (the inverse of) the initial amplitude.

Maximum fluctuation velocities comparable to, or even larger than, mean flow velocities can be achieved for disturbances of the scale of the internal deformation radius (typically 50 km in the oceans, 1000 km in the atmosphere), topography variations 10% of total fluid depth, and parameters typical of oceans and atmosphere.

1. INTRODUCTION

The effects of topography on steady and transient motions in rotating flows have been a subject of study for over 60 years, dating from Taylor's (1923) classic experiment showing the attachment of columns of water to an obstacle towed across a rotating tank. The presence of topography on all scales and the adjustment of flow to avoid it is a patent physical feature of the ocean and atmosphere. Both atmosphere and ocean are warmed near the equator and cooled near the poles (though in different ways). The resulting nonuniformity of temperature (density) on level surfaces suggests the possi-

bility of a gravitational instability if light and dense water parcels on a level surface are interchanged. Hide and Mason (1975) called such a process 'sloping convection', but the older term is baroclinic instability, coined by Charney (1947) for a mechanism discovered by him and Eady (1949). The mechanism is governed by the balance of potential vorticity in transient motions, a balance which can be subtly affected by the vortex stretching due to topography. The effects of constant-slope bottom topography on baroclinic instability were studied by Blumsack and Gierasch (1972). De Szoeke (1975) considered the effects of cross-stream topography, consisting of constant slope plus sinusoidal components, on baroclinic instability. He found that certain kinds of hybrid instability could be set up by combining plane-wave modes of the same frequency but different wavenumber, where the wavenumber difference is bridged by a Fourier component of the bottom topography. De Szoeke (1983) was able to extend this result to wavy topography of arbitrary orientation.

These theories have all been linear. They produce estimates of growth rates valid for fluctuating disturbances that are initially small. Pedlosky (1970) and Drazin (1970) developed theories for the nonlinear development of such disturbances to finite amplitude, though their theories depend on the basic shear flow being only marginally supercritical with respect to baroclinic instability. Charney and Devore (1979) and Hart (1979) considered barotropic flows being modified by having to give up energy to resonant stationary fluctuations through form drag associated with topography: they term this mechanism 'form drag instability'. Charney and Straus (1980) extended the analysis to baroclinic flow (in two layers). These studies identify the form drag instability as the mechanism for transition between multiple equilibrium states. The form drag instability is different in nature from the topographically modified baroclinic instability of de Szoeke (1983).

In this paper we develop a nonlinear version of de Szoeke's (1983) instability theory. The method of analysis is similar to Pedlosky's (1970, 1979) nonlinear treatment in spirit, although the details are quite different. We represent the baroclinic structure of the atmosphere or oceans in the time-honored simplest possible way, with two immiscible layers. We write down (in section 2) the quasigeostrophic potential vorticity equations for those layers, and represent the flow solutions as a sum of mean zonal flow and perturbation, the latter consisting of a sum of two neutrally stable modes of the same frequency, but different wavenumbers, that are solutions of the linearized problem without topography. Allowing for the development of mode amplitudes on a long time-scale, we iterate the solution to take account of the effects of topography and nonlinear advection. In this way we obtain a set of coupled nonlinear ordinary differential equations with respect to the long time variable for the complex mode amplitudes. The

interesting case is when topography possesses a Fourier component bridging the wavenumber gap between the two modes. In section 3 we discuss the solution of these equations. We find the existence of two exact invariants or integrals of the motion; this simplifies the mathematical problem to a single equation for a mode amplitude-squared, the solution to which can be written in terms of elliptic functions. Although this sounds very like the outcome of Pedlosky's (1970) theory and there are, in fact, subtle correspondences, the situation is quite different.

The expression of the general solution in terms of elliptic functions is a bit opaque. Instead, some approximations are exploited to give solutions in terms of simple functions (section 4). The solutions for the mode amplitudes have the form of repetitive vacillations. When the initial mode amplitudes are small, a maximum mode amplitude is predicted which depends on the wavenumbers and frequency of the mode, and the topography amplitude, but is otherwise independent of the initial conditions. Typical amplitudes that might be achieved in atmosphere or ocean are computed and discussed in section 5.

2. THEORY

The quasigeostrophic equations of motion governing the behavior of potential vorticity in two layers of equal undisturbed depth H_1 and differing density on a rotating β -plane are (Pedlosky, 1979, p. 393)

$$\left\{ \partial_t + J(\hat{\psi}_n, \cdot) \right\} \left\{ \nabla^2 \hat{\psi}_n + (-1)^n r_0^{-2} (\hat{\psi}_1 - \hat{\psi}_2) + \beta y + \delta_{n2} \eta_B \right\} = 0 \quad (n = 1, 2) \quad (2.1)$$

where $\hat{\psi}_n$ are the streamfunctions in the two layers, velocities are given by

$$\mathbf{u}_n = \hat{\mathbf{z}} \times \nabla \hat{\psi}_n \quad (2.2)$$

and

$$r_0 = (g \Delta \rho H_1 / \rho_0 f^2)^{1/2} \quad (2.3)$$

is the Rossby radius of deformation. The effect of topographic vortex stretching is taken into account through the term

$$\eta_B = \frac{f_0}{H_1} h_B \quad (2.4)$$

in the lower layer potential vorticity, where $h_B(x, y)$ is topographic elevation of the bottom.

Consider motion consisting of a steady zonal flow in the upper layer with a superimposed perturbation

$$\hat{\psi}_n = -\delta_n U_1 y + \psi_n \quad (2.5)$$

Scale the variables in the equations according to

$$(x, y) = r_0(x', y'), \quad t = \frac{r_0}{U_1} t' \quad (2.6a, b)$$

$$U_1 = U_1 U_1', \quad \psi_n = r_0 U_1 \psi_n', \quad \beta = r_0^{-2} U_1 \beta' \quad (2.6b, c, d)$$

$$\eta_B = f_0 \frac{\Delta h}{H_1} \eta_B' \quad (2.6e)$$

where Δh is a scale for topographic relief. (In (2.6b) we could set $U_1' = 1$. However, it is instructive to carry the symbol through the analysis as a place marker for the mean flow.) Substitute into (2.1). After dropping primes on the scaled variables, this gives

$$(\partial_t + U_1 \partial_x) q_1 + (\beta + U_1) \psi_{1x} = -J(\psi_1, q_1) \quad (2.7a)$$

$$\partial_t q_2 + (\beta - U_1) \psi_{2x} = -J(\psi_2, q_2 + \epsilon \eta_B) \quad (2.7b)$$

where

$$q_n = \nabla^2 \psi_n + (-1)^n (\psi_1 - \psi_2) \quad (2.8)$$

and

$$\epsilon = (\Delta h / H_1) / (U_1 / f_0 r_0) \quad (2.9)$$

is the ratio of topographic aspect to Rossby number.

Neglect of the nonlinear and topographic terms on the right of (2.7) gives a system of equations that permit plane-wave solutions which can be baroclinically unstable under circumstances discussed by Pedlosky (1979). The effect of various kinds of topography has been considered by many authors. Blumsack and Gierasch (1972) considered uniform linear slope; de Szoeke (1975) considered uniform linear slope plus sinusoidal cross-stream components. De Szoeke (1983) studied the effect of arbitrary topography, considered as a sum of Fourier wavenumber components, on linearized baroclinic instability. Pedlosky (1970, 1979) and Drazin (1970) examined the nonlinear equilibration of growing baroclinic oscillations near marginal stability by taking account of the nonlinear terms on the right of (2.7). Lorenz's (1963) model of atmospheric circulation consists of a set of equations obtained by representing ψ_n by a Fourier series of spatial components truncated after a relatively small number of terms. This model includes simple oscillatory topography representing the global structure of

the continents, and is driven by an idealization of the meridional heating distribution. Charney and Straus (1980) used a form of Lorenz's (1963) model to produce a theory of multiple equilibria, involving nonlinear interactions between flow components and topography, to explain the phenomenon of atmospheric blocking.

In this paper, we consider the nonlinear equilibrations of the kinds of topographic baroclinic instability discovered by de Szoeke (1983). This earlier work considered topography as an extension of Eady's (1949) continuous model with linear shear and linear stratification, but no β -effect. We have chosen to work with the layered model because it is not essentially simpler than Eady's model, while the inclusion of effects of Earth's curvature (β -effect) is quite easy. Both the Eady and layered models filter critical-layer instabilities and furnish short-wave cutoffs for the baroclinic instabilities. On the other hand, models like Charney's (1947), with continuous shear and nonzero meridional potential vorticity gradient, permit instabilities at almost all wavelengths.

2.1. The linear solution

By neglecting topography and nonlinear effects in (2.7), plane-wave solutions of the form

$$\psi_n = a_n \exp\{ik_x x - i\omega t\} \quad (2.10)$$

may be found. These must satisfy

$$\frac{a_1}{a_2} = \frac{\omega - k_y U_1}{(\omega - k_y U_1)(k^2 + 1) + k_y(\beta + U_1)} = \frac{\omega(k^2 + 1) + k_y(\beta - U_1)}{\omega} \equiv \mu(k^2) \quad (2.11)$$

The second of these equalities gives a dispersion relation whose solution is

$$\frac{\omega}{k_y} = 1/2 U_1 - \frac{\beta(k^2 + 1)}{k^2(k^2 + 2)} \pm \frac{[\beta^2 + U_1^2 k^4 (1/4 k^4 - 1)]^{1/2}}{k^2(k^2 + 2)} \equiv c(k^2) \quad (2.12)$$

For $|\beta/U_1| < 1$, unstable solutions (i.e., complex ω with $\text{Im } \omega > 0$) are possible in the wavenumber range given by

$$2 - 2[1 - (\beta/U_1)^2]^{1/2} < k^4 < 2 + 2[1 - (\beta/U_1)^2]^{1/2}$$

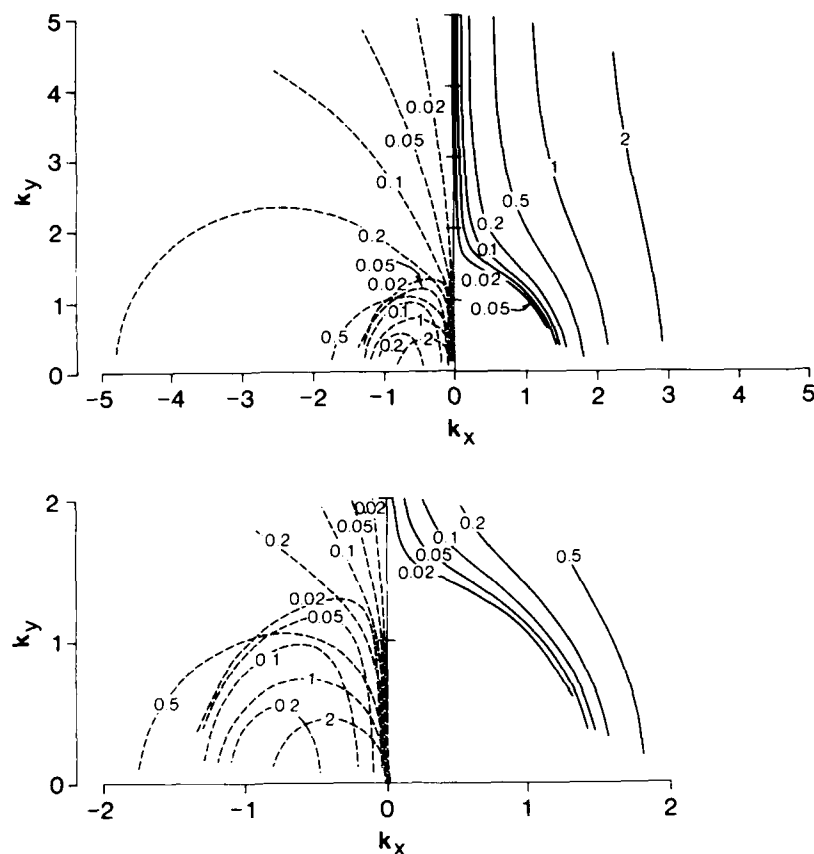


Fig. 1. Constant-frequency lines on the wavenumber plane for $\beta/U_1 = 2$. Solid lines denote $\lambda > 0$ [eq. 2.32]; dashed, $\lambda < 0$.

This is the range of classical baroclinic instability, discussed fully by Pedlosky (1979). Of more interest for our present purposes are the wavenumber ranges of neutral stability ($Im \omega = 0$). Figures 1–5 show loci of constant (real) ω on the wavenumber plane for $\beta/U_1 = 2, 0.9, 0, -0.5, -2$, respectively. For large wavenumber, $k \rightarrow \infty$, phase speed c tends to 1 or 0, while the amplitude ratio μ tends to ∞ or 0, respectively. The former corresponds to waves confined to and advected by the upper layer, while the latter corresponds to waves in the lower layer. For this reason, de Szoeke (1983) termed the two branches of the Eady model the ‘top-intensified mode’ and the ‘bottom-intensified mode’. These are the only branches that occur for $\beta = 0$ (Fig. 3). However, for $\beta \neq 0$ the terminology is inadequate or

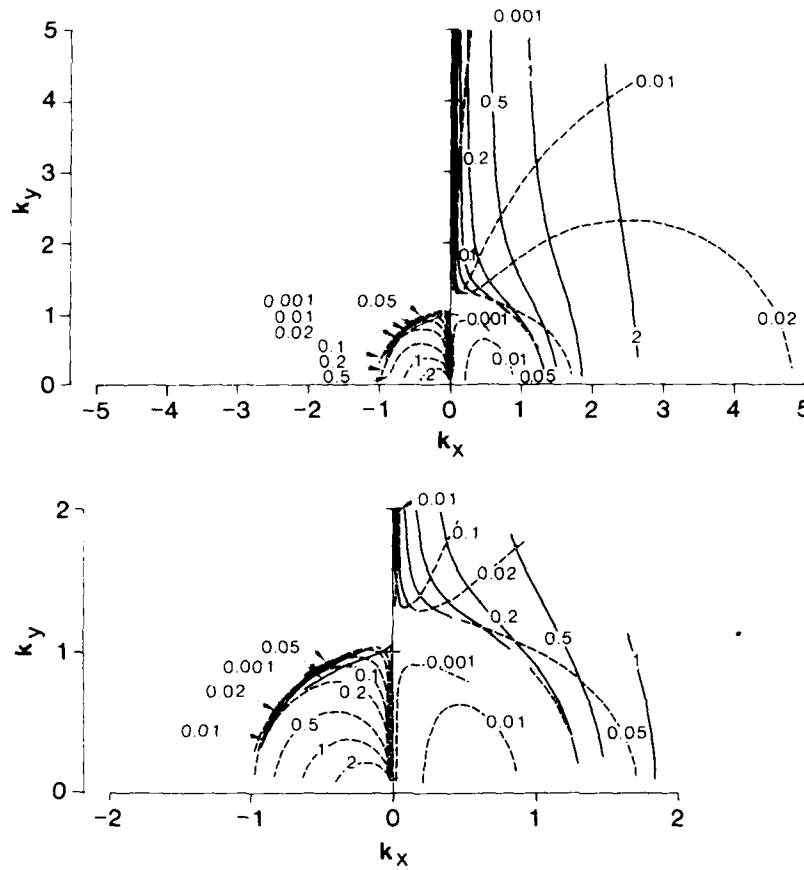


Fig. 2. Like Fig. 1, except $\beta/U_1 = 0.9$.

misleading. For $|\beta/U_1| < 1$, $\beta \neq 0$ (Figs. 2 and 4), there is another pair of stable branches at wavenumbers below the classical instability range. For $|\beta/U_1| > 1$, (Figs. 1 and 5), these branches are continuous with the high frequency branches. In either event, towards low wavenumber (2.12) can be approximated by

$$\frac{\omega}{k_y} = 1/2 U_1 - \frac{\beta}{k^2 + 2}, \quad 1/2 U_1 - \frac{\beta}{k^2}$$

These correspond to the baroclinic and barotropic Rossby wave modes.

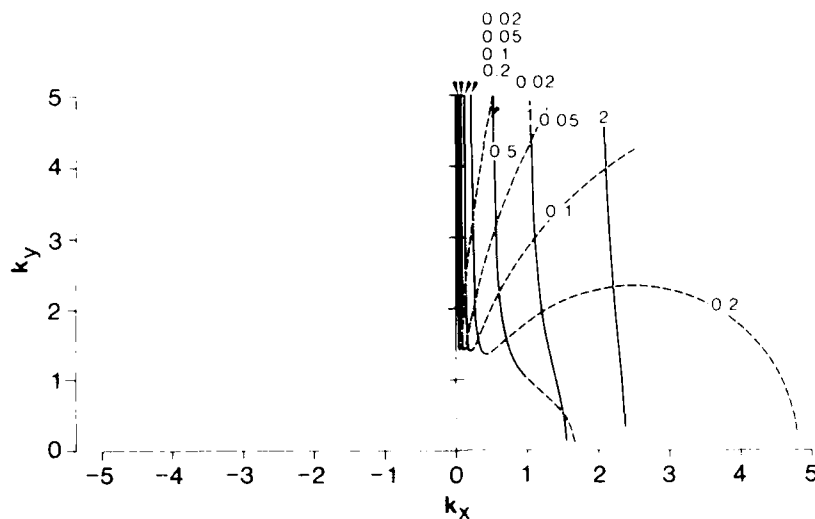


Fig. 3. Like Fig. 1, except $\beta/U_1 = 0$.

respectively, Doppler-shifted by the mean speed of the entire water column $1/2 U_1$. The respective amplitude ratios are -1 and $+1$.

2.2. The nonlinear solution

Suppose topography η_B contains components like

$$\eta_B \exp(i\mathbf{k}_p \cdot \mathbf{x}) + \text{c.c.} \quad (2.13)$$

where 'c.c.' denotes the complex conjugate of what precedes it. We seek an approximate solution to (2.7), including nonlinear and topographic effects, of the form

$$\psi_n = \sum_{p=1}^3 A_p(t) a_{np} \exp\{i\mathbf{k}_p \cdot \mathbf{x} - i\omega_p t\} + \text{c.c.} + \text{higher-order terms.} \quad (2.14)$$

We take the first two components of this form to be primary linear modes at the same basic frequency so that

$$\omega_1 = \omega_2 = k_{y1}c(k_1^2) = k_{y2}c(k_2^2) \quad (2.15)$$

(subscripts on the frequency will hereafter be dropped), and

$$a_{2p} = 1, \quad a_{1p} = \mu_p = \mu(k_{2p}) \quad \text{for } p = 1, 2 \quad (2.16)$$

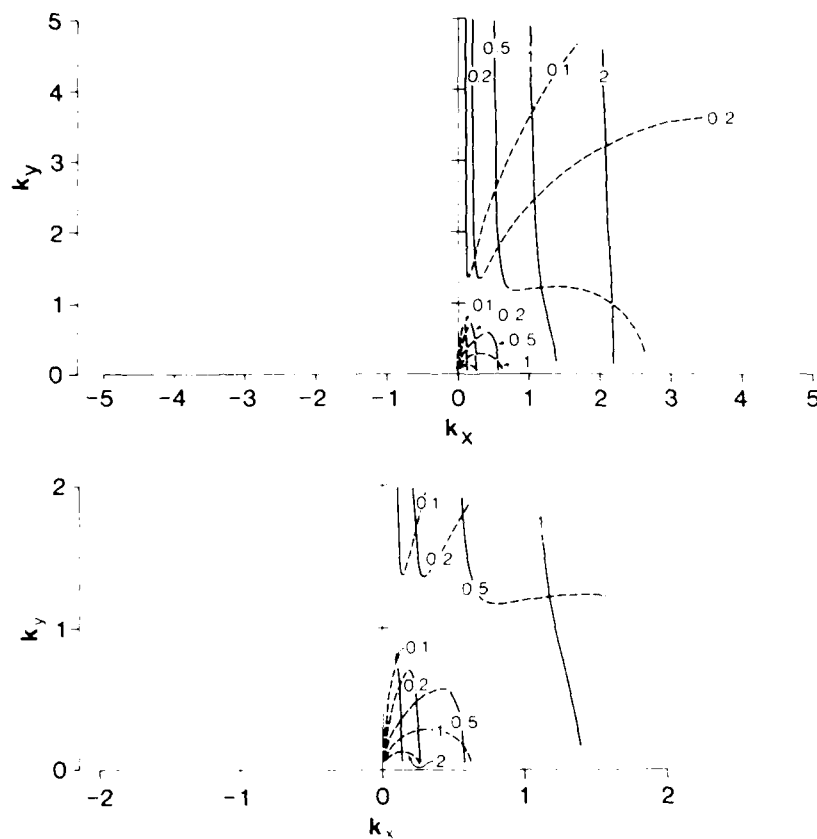


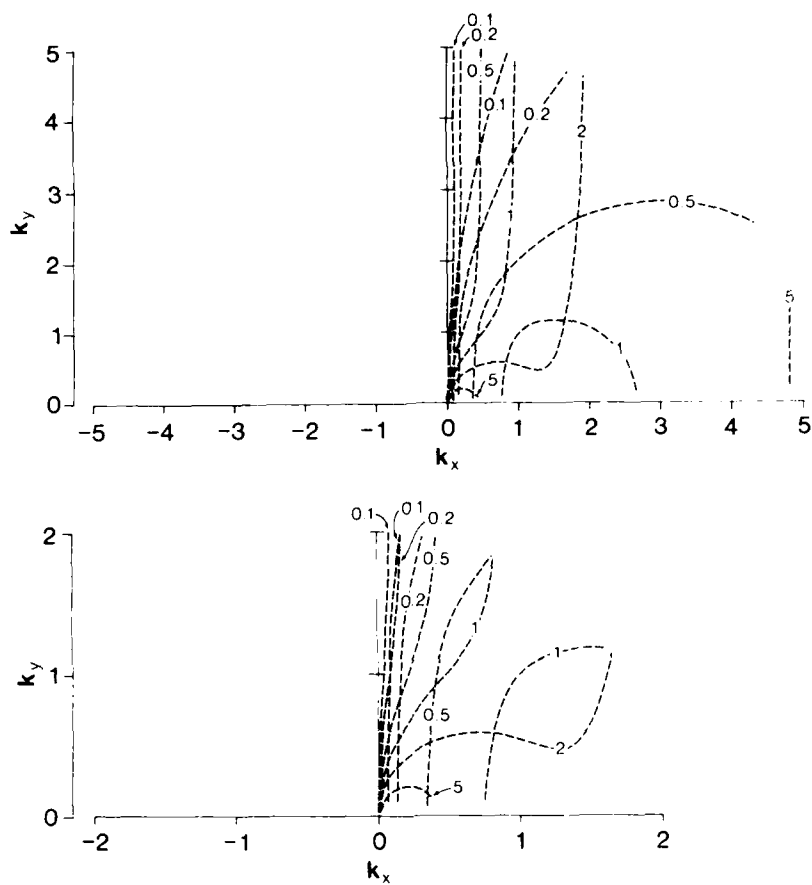
Fig. 4 Like Fig. 1, except $B/U = 0.5$.

The time-dependence of the amplitudes $A_j(t)$ is implicitly assumed to be slow compared to the primary frequency ω . The third mode we take to be an approximately steady correction ($\omega_3 = 0$) to the first two, generated by their nonlinear and topographic interaction at the difference wavenumber $k_3 = k_1 - k_2$. Its amplitude may be readily calculated by balancing coefficients of $\exp(ik_3 \cdot x)$ in (2.7). This gives

$$A_3(t) = -ik_*\omega^{-1}A_1(t)A_2^*(t) \quad (2.17)$$

with

$$a_{-1} = 1, \quad a_{11} = -\omega/\Omega \quad (2.18)$$

Fig. 5. Like Fig. 1, except $\beta/U_1 = 2$

where

$$\Omega^{-1} = \left[(k_1 - k_2)^2 - \frac{\beta}{U_1} \right]^{-1} \left[\frac{\omega \mu_1 \mu_2 (\beta/U_1 + 1)}{(\omega - k_{y1} U_1)(\omega - k_{y2} U_1)} - \frac{1}{\omega} \right] \quad (2.19)$$

$$\kappa_* = \hat{z} \cdot k_1 \times k_2 \quad (2.20)$$

The development in time of the primary mode amplitudes needs to be calculated. To see how this must be done, we observe that substitution of (2.14) into (2.7) leaves unbalanced terms of the form $C_{np} \exp\{ik_p \cdot \underline{y} - i\omega t\}$, $p = 1, 2$. Because they are eigenfunctions of the linear operator contained within (2.7), these terms would tend to generate secular resonant contribu-

tions among the higher-order terms. As this is unacceptable, the time development of the primary modes $A_1(t)$, $A_2(t)$ is allowed to adjust so that no higher-order resonances occur. This is done by making the unbalanced terms, put in a form compatible with the self-adjoint version of the linear operator in (2.7), orthogonal to the linear solutions (Kevorkian and Cole, 1981). This gives two solvability conditions, $\mu_p(\omega - k_{1p}U_1)^{-1}C_{1p} + \omega^{-1}C_{2p} = 0$, for $p = 1, 2$. Now the C_{np} contain three types of terms: (1) terms of the form $\dot{A}_p(t)$, from the slow development of the primary modes; (2) terms of the form $\eta_1 A_p$, from the interaction of the primary modes with topography; and (3) terms like $|A_q|^2 A_p$, from the nonlinear interaction. The coefficients in these terms can be readily, if laboriously, computed. The solvability conditions may be finally written

$$\lambda_1 \dot{A}_1 + i\kappa_*^2 \Lambda_1 |A_2|^2 A_1 + \epsilon \kappa_* \eta_1 A_2 = 0 \quad (2.21a)$$

$$\lambda_2 \dot{A}_2 + i\kappa_*^2 \Lambda_2 |A_1|^2 A_2 + \epsilon \kappa_* \eta_1 A_1 = 0 \quad (2.21b)$$

The coefficients are

$$\Lambda_q = \frac{-\omega \mu_1 \mu_2}{(\omega - k_{1q}U_1)} \left[\frac{1 + (k_1 - k_2)^2}{\Omega} + \frac{1}{\omega} \right] + \frac{1 + (k_1 - k_2)^2}{\omega} + \frac{1}{\Omega} \\ + \left[\frac{-\mu_1 \mu_2 (\beta + U_1)}{(\omega - k_{1q}U_1)(\omega - k_{2q}U_1)} \frac{\omega}{\Omega} + \frac{\beta - U_1}{\omega^2} \right] k_{1,2} k_{2,q} \quad (2.22)$$

and

$$\lambda_q = \lambda(k_q^2) = \omega k_{1q} \sum_{n=1,2} \frac{dQ_n/dy}{(\omega - k_{1q}U_n)} \frac{1}{\omega^2} |a_{nq}/a_{2q}|^2 \\ = \omega k_{1q} \left[\frac{(\beta + U_1)\mu_q^2}{(\omega - k_{1q}U_1)^2} + \frac{\beta - U_1}{\omega^2} \right] \quad (2.23)$$

where $dQ_n/dy = \beta + (-1)^n U_1$ is the background potential vorticity gradient in each layer.

Equations (2.21), with their initial conditions, describe the nonlinear development of the mode amplitudes A_q interacting with topography at the bridging wavenumber $k_3 = k_1 - k_2$. Neglecting topography ($\eta_1 = 0$) and nonlinear terms, we must have either $\lambda_n = 0$ or $A_n(t) = 0$ for each mode. The former is the well-known Charney–Stern criterion for baroclinic instability.

By neglecting the nonlinear terms in (2.21), we obtain equations whose solutions can be easily written down

$$A_q(t) = A_q(0) e^{\sigma t} \quad (2.24a)$$

where

$$A_1/A_2 = -\epsilon \kappa_* \eta_3 / \lambda_1 \sigma \quad (2.24b)$$

$$\sigma^2 = -\kappa_*^2 |\epsilon \eta_3|^2 / \lambda_1 \lambda_2 \quad (2.24c)$$

The amplitudes grow if

$$\lambda_1 \lambda_2 < 0 \quad (2.25)$$

This result should be compared with de Szoeke's (1983), who established the condition $\lambda_1 \lambda_2 < 0$, for the Eady model over topography. (Note that with $\beta = 0$, as in the Eady model, k_{y1} , k_{y2} must have the same sign.) The sign of function $\lambda(k^2)$ is shown in Figs. 1–5 for the various values of β/U_1 by drawing constant-frequency curves corresponding to positive λ solid, and those with negative λ dashed. Modes with wavenumbers k_1 , k_2 , at the same frequency ω , can be selected from inspection of diagrams like Figs. 1–5 for the appropriate value of β/U_1 . For 'instability' one of the modes must correspond to a solid curve, the other to a dashed curve, and topography with some amplitude η_3 at the bridging wavenumber $k_2 - k_1$ must be present. For example, for $\beta = 0$ (Fig. 3) one of the modes must belong to the upper (solid) branch of the dispersion relation, the other to the lower (dashed) branch. In general, two branches which meet at a marginally neutral wavenumber have λ of opposite sign, and eastward ($\omega/k_x > 0$) and westward ($\omega/k_x < 0$) propagating modes on any branch change sign of λ as ω/k_x changes sign (e.g., Figs. 1 and 2). Note, however, that $\lambda \rightarrow 0$ as a marginally neutral wavenumber is approached, while λ approaches $+\infty$ or $-\infty$ as a point at which $\omega/k_x = 0$ is neared. For $\beta/U_1 < 0$, no westward propagating modes are permitted. For $\beta/U_1 < -1$, no classical baroclinic instability is possible, hence λ cannot change sign (e.g., Fig. 5), so topographic instability is also impossible. For $\beta/U_1 > 1$, despite the impossibility of classical instability, because both westward and eastward modes are possible (Fig. 1), topographic instability is possible.

Further nonlinear and topographic interaction will produce higher harmonics and hybrids of the primary modes. As long as these harmonics are not near resonance, they will produce quite ordinary higher-order corrections in (2.14). Although these corrections will be successively smaller if it is assumed that amplitudes or topography (measured by the parameter ϵ) are small, it is not necessary to make such an assumption. In general, a finite radius of convergence for ϵ or amplitude may be expected. Indeed, we shall see below that for realistic parameters in nature ϵ is of order one.

3. EXACT SOLUTIONS

We now attempt to solve eqs. 2.21, which, because A_1 , A_2 are complex, constitute a set of fourth-order coupled nonlinear differential equations.

Because we are able to derive two exact integrals of the motion, this order can be reduced by two. Of the resulting two first-order equations, one decouples from the other and its solutions are elliptic integrals.

Without loss of generality, take η_3 to be real. If it is not, i.e., $\eta_3 = |\eta_3|e^{i\theta}$, then simply replace A_1, A_2 in (2.21) by

$$\tilde{A}_1 = A_1 e^{-i\theta/2}, \quad \tilde{A}_2 = A_2 e^{i\theta/2}$$

It is convenient to rescale time and the amplitudes by

$$t = \frac{(-\lambda_1 \lambda_2)^{1/2}}{\epsilon \kappa_* \eta_3} t', \quad (3.1a)$$

$$A_1 = \left[\frac{\eta_3}{\kappa_* \Lambda_1} \right]^{1/2} \left[-\frac{\lambda_2}{\lambda_1} \right]^{1/4} A'_1 \quad (3.1b)$$

$$A_2 = \left[\frac{\eta_3}{\kappa_* \Lambda_1} \right]^{1/2} \left[-\frac{\lambda_2}{\lambda_1} \right]^{1/4} A'_2 \quad (3.1c)$$

Suppose, without loss of generality, that the signs of λ_1 and λ_2 are, respectively, positive and negative. Then eqs. 2.21 become (dropping primes)

$$\partial_t A_1 + A_2 + i |A_2|^2 A_1 = 0 \quad (3.2a)$$

$$\partial_t A_2 + A_1 - id |A_1|^2 A_2 = 0 \quad (3.2b)$$

where $d = \Lambda_2/\Lambda_1$. Multiplying (3.2a) by A_1^* , its complex conjugate by A_1 , and adding, we get

$$\partial_t |A_1|^2 + A_1^* A_2 + A_1 A_2^* = 0 \quad (3.3a)$$

A similar process applied to (3.2b) gives

$$\partial_t |A_2|^2 + A_1 A_2^* + A_1^* A_2 = 0 \quad (3.3b)$$

Hence, subtracting and integrating,

$$|A_1|^2 - |A_2|^2 = e_0 \quad (3.4)$$

where e_0 is a constant. This is the first integral of the motion. Topography does not explicitly appear in this constraint. Indeed the terms $A_1 A_2^* + A_1^* A_2$ in (3.3a,b), which descend from the topography terms in (2.21) or (3.2), cancel upon subtraction. Without topography these terms are identically zero in (3.3a,b) before the re-scaling (3.1). This appears to lead to the uninteresting result $\partial_t |A_1|^2 = 0$, but the other possibility is that the coefficient $\lambda_1 = 0$; this is in fact the Charney-Stern criterion. Hence (3.4) should be thought of as a generalization of this criterion.

Next, observe that

$$\partial_t (A_1^* A_2 - A_1 A_2^*) = i(|A_2|^2 + d|A_1|^2)(A_1^* A_2 + A_1 A_2^*) \quad (3.5)$$

by using (3.2). Substituting for $(A_1^* A_2 + A_1 A_2^*)$ from (3.3a,b), eq. 3.5 can be integrated

$$i(A_1^* A_2 - A_1 A_2^*) - 1/2 |A_2|^4 - 1/2 d |A_1|^4 = 2f_0 \quad (3.6)$$

where f_0 is a constant. This is the second integral of the motion. While (3.4) is a fundamental result for baroclinic systems, with links to related physical systems, (3.6) is not so general a result, and appears to be a consequence of the truncation of the two-component physical system under consideration. Hence, the simplifications that follow in its train can probably not be achieved in more complicated systems, and must be treated with caution.

Setting

$$A_1 = R e^{i\alpha_1}, \quad A_2 = (R^2 - e_0)^{1/2} e^{i\alpha_2} \quad (3.7)$$

(3.6) becomes

$$R(R^2 - e_0)^{1/2} \sin(\alpha_1 - \alpha_2) - 1/4(R^2 - e_0)^2 - 1/4 d R^4 = f_0 \quad (3.8)$$

Using this to eliminate $(\alpha_1 - \alpha_2)$ from (3.3a), we obtain

$$\partial_t R^2 = \pm \{f_4(R^2)\}^{1/2} \quad (3.9)$$

where

$$f_4(R^2) = 4R^2(R^2 - e_0) - \{2f_0 + 1/2(R^2 - e_0)^2 + 1/2 d R^4\}^2 \quad (3.10)$$

is a quartic polynomial in R^2 .

The general solution of (3.9) can be written in terms of elliptic integrals (Abramowitz and Stegun, 1964). Since the coefficient of R^8 in $f_4(R^2)$ is certainly negative, the quartic must behave as shown schematically in Fig. 6. Note that the negative side of the abscissa is forbidden. The zeros of the polynomial are at a_1, a_2, a_3, a_4 (not necessarily all real). The solution of (3.9) must be a limit cycle as shown on the phase diagram in Fig. 7, oscillating within a positive range of $f_4(R^2)$. The phase diagram is symmetric to reflection in the R^2 -axis: this is the significance of the sign ambiguity in (3.9). Any limit cycle on the negative side of the R^2 -axis is clearly forbidden. A little thought establishes that the initial amplitude-squared R_0^2 must lie between two zeros of $f_4(R^2)$ in such a way that $f_4(R_0^2) > 0$.

With the amplitude R determined, the phase difference $(\alpha_1 - \alpha_2)$ between the modes can then be obtained from the second motion integral (3.7). It remains to determine the absolute phases. This is done by substituting (3.7)

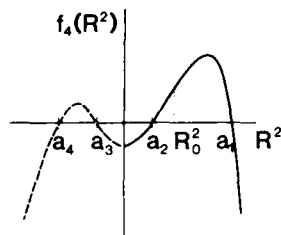


Fig. 6. Schematic of the polynomial $f_4(R^2)$ showing zeros at a_1 , a_2 , a_3 , a_4 .

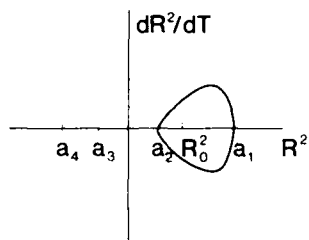


Fig. 7. Schematic of the phase diagram of eq. 3.9 showing a limit cycle between two zeros of $f_4(R^2)$.

into (3.2a,b), dividing by R_1 , R_2 , respectively, and adding the resulting equations

$$\partial_t(\alpha_1 + \alpha_2) + \frac{e_0 \sin(\alpha_1 - \alpha_2)}{R(R^2 - e_0)^{1/2}} + R^2(1 - d) - e_0 = 0 \quad (3.11)$$

Equation (3.8) may be used to eliminate $\sin(\alpha_1 - \alpha_2)$ in favor of R^2 . Hence, once $R^2(t)$ is known from the solution of (3.9), this equation can be solved by standard methods of quadrature.

4. SOME APPROXIMATE SOLUTIONS

Although the solution of (3.9) can be formally rendered in terms of elliptic integrals, various approximations can be exploited to give useful insight.

4.1. Small initial amplitudes

Suppose that the initial amplitudes of a disturbance are small

$$|A_1(0)|^2, \quad |A_2(0)|^2 \ll 1$$

then, from the motion integrals (3.4), (3.6), it follows that e_0, f_0 are small. From (3.10), the polynomial $f_4(R^2)$ has two positive zeros. These are approximately $R_2^2 = 4/(1+d)$ and $R_1^2 = 1/2 e_0 + (1.4 e_0^2 + f_0^2)^{1/2}$, the former being order-unity, the latter small. By approximating $f_4(R^2)$ appropriately in the vicinity of either of these zeros, (3.9) can be solved approximately. This gives

$$R^2 \approx 1/2 e_0 + (R_1^2 - 1/2 e_0) \cosh 2(t - t_1) \quad (4.1)$$

where t_1 is a time when $R^2 \approx R_1^2$; while

$$R^2 \approx R_2^2 \operatorname{sech} 2(t - t_2) \quad (4.2)$$

where t_2 is a time when $R^2 \approx R_2^2$.

Each of these is symmetric about $t = t_1$ or t_2 , respectively. By choosing $t_2 - t_1$ appropriately, the two forms can be made to overlap, and a uniformly valid solution may be constructed. This matching procedure gives

$$P = 2(t_2 - t_1) = \ln \{ 4R_2^2 / (R_1^2 - 1/2 e_0) \} \quad (4.3)$$

for the period of a complete vacillation cycle of the amplitude envelope $R(t)$. Since the argument of the logarithm in (4.3) is large, this period is large (though only weakly!). The solutions (4.1), (4.2) recur indefinitely with this period.

The repetition period P of the amplitude envelope depends on the initial amplitude. Figure 8 shows the shape of amplitude-squared R^2 for a few choices of P , namely $P = 4, 8, 16$. The maximum amplitudes have been normalized to be the same. The figure shows two cycles of vacillation; the time-axis is scaled by P so that the length of a cycle is the same in all cases. For larger P , the response becomes more peaked.

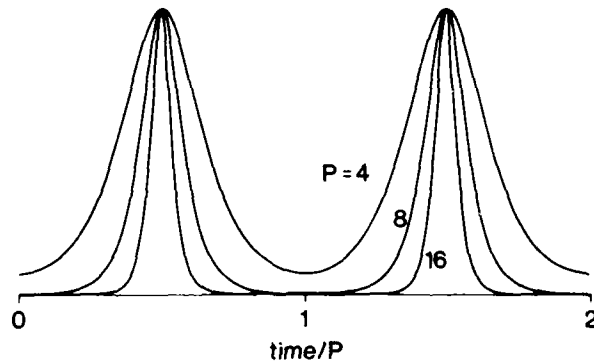


Fig. 8. Amplitude-squared R^2 as a function of time: $P = 4, 8, 16$.

Both (4.1) and (4.2) show R behaving like $e^{\pm t}$ in various ranges, with smooth transitions in between. This behavior reflects the simple growth and decay solutions that are the results of neglecting the nonlinear terms in (3.2). It is remarkable that the linearized growth and decay phases can be used to construct approximations to the nonlinear solution for all times except a brief transition interval around the maximum amplitude R_2 .

It is not necessary to posit, for the validity of this solution, that initial amplitudes-squared are small. The essential condition is that the motion integrals e_0, f_0 be small. This means that the initial amplitudes-squared may be order-unity, as long as they are less than $4/(1+d)$, and their difference is small, and their initial phase difference $(\alpha_1 - \alpha_2)$ must be nearly $\arcsin R(0)^2/R_2^2$, by (3.8).

4.2. An approximate solution for arbitrary initial amplitudes

Suppose that the zeros of the polynomial f_4 can be written a_1, a_2, a_3, a_4 . The nonlinear limit cycle must oscillate between some adjacent pair of these where the polynomial is positive: say

$$0 < a_2 < R^2 < a_1$$

By setting

$$R^2 = 1/2(a_1 + a_2) + 1/2(a_1 - a_2) \sin \theta \quad (4.3)$$

and approximating f_4 in (3.9), this equation may be written

$$\frac{d}{dt} \sin \theta = \beta \cos \theta (1 + b \sin \theta) \quad (4.4)$$

where

$$\beta = 1/2(1+d) \{1/2(a_1 + a_2) - a_3\}^{1/2} \{1/2(a_1 + a_2) - a_4\}^{1/2} \quad (4.5)$$

and

$$b = 1/4(a_1 - a_2) \left[\{1/2(a_1 + a_2) - a_3\}^{-1/2} + \{1/2(a_1 + a_2) - a_4\}^{-1/2} \right] \quad (4.6)$$

The formal condition for this approximation only requires that $|b| < 1$. The solution of (4.4) may be written

$$\frac{R^2 - 1/2(a_1 + a_2)}{1/2(a_1 - a_2)} = \sin \theta = \frac{2\sigma}{1 + \sigma^2} \quad (4.7)$$

where

$$\sigma = (1 - b^2)^{1/2} \tan \left\{ 1/2(1 - b^2)^{1/2} \beta(t - t_0) \right\} + b \quad (4.8)$$

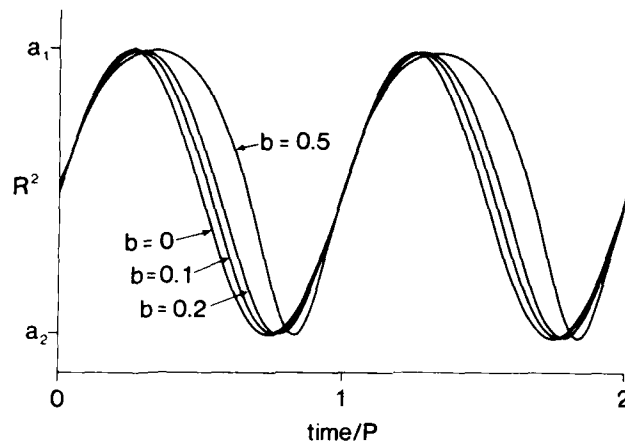


Fig. 9. Amplitude-squared R^2 as a function of time, $b = 0, 0.1, 0.2, 0.5$.

The periodicity exhibited by this solution is $P = 2\pi/\beta(1 - b^2)^{1/2}$, which is approximately $2\pi/\beta$ if b is small. Figure 9 shows this solution for several values of b : $b = 0, 0.1, 0.2, 0.5$. Two complete vacillation cycles for each value are shown; the time-axis has been scaled so that the periods of the cycles appear the same. The maximum value shown corresponds to a_1 ; the minimum to a_2 . For $b = 0$, the cycle is precisely sinusoidal.

5. DISCUSSION: SOME TYPICAL SCALES

It is instructive to compute typical dimensional maximum amplitudes for disturbances in the ocean and atmosphere by choosing appropriate values for parameters. For the ocean, take topography-to-depth ratio to be $\Delta h/H_1 = 0.1$, mean upper layer current $U_{1*} = 0.1 \text{ m s}^{-1}$, baroclinic Rossby deformation radius $r_0 = 50 \text{ km}$, and Coriolis parameter $f_0 = 10^{-4} \text{ s}^{-1}$ as representative values. For the atmosphere, on the other hand, again take $\Delta h/H_1 = 0.1$, $f_0 = 10^{-4} \text{ s}^{-1}$, but with $U_{1*} = 10 \text{ m s}^{-1}$, $r_0 = 1000 \text{ km}$. These give, for the parameter defined by (2.9), $\epsilon \approx 5$ (ocean), and $\epsilon = 1$ (atmosphere). These settings are not particularly small and indicate that more terms must be computed from the iterative method of solution used in section 2 before numerical accuracy can be assured. However, the method appears to be nonsingular so that only quantitative, not qualitative modifications may be expected. Of course, we can always imagine sufficiently small topography for which ϵ will be satisfactorily small and the perturbation theory of section 2 readily applicable. The largeness of ϵ even for moderate topography

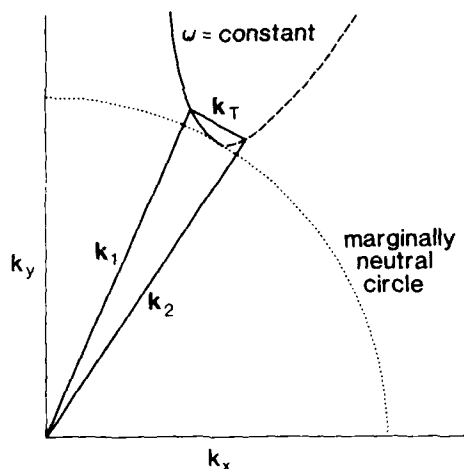


Fig. 10. Schematic of topographic instability near the marginally neutral circle between wavenumber modes \underline{k}_1 , \underline{k}_2 bridged by topography \underline{k}_T , where $k_T \ll k_1 \approx k_2$.

strongly suggests that the influence on baroclinic eddy dynamics may be very important. The theory presented above represents a first attack on the problem.

Despite moderately large ϵ , there may be situations where the present first-order theory gives accurate results. This occurs where the horizontal scale L_T of the topography is much longer than the wavelengths of the modes, of order Rossby radius r_0 . Then the term involving the Jacobian of topography and streamfunction in eqs. 2.7 is of order $\epsilon r_0/L_T$. This parameter, rather than ϵ , then becomes the effective perturbation parameter of section 2. To satisfy the resonance condition,

$$\underline{k}_1 - \underline{k}_2 = \underline{k}_T$$

where $|\underline{k}_T| \approx r_0/L_T \ll |\underline{k}_1|$, $|\underline{k}_2|$, and to achieve λ_1 , λ_2 of opposite signs, we must ensure that the wavenumbers \underline{k}_1 , \underline{k}_2 straddle a marginally neutral wavenumber on the marginal circles of Figs. 1-5. This is represented schematically in Fig. 10. The nonlinear solution of section 4 then looks like a disturbance of wavenumber \underline{k}_1 ($\approx \underline{k}_2$), propagating along the crests of topography, with a modulated spatial envelope across the topography at the wavenumber \underline{k}_T . The envelope waxes and wanes on a longer time scale as in Fig. 8. The modulation period P [eq. 4.3] of the envelope depends on the initial values of the amplitudes of the participating modes. The maximum nondimensional envelope amplitude of the amplitude envelope is $R_2 = 2(1 + d)^{-1/2} \approx 2^{1/2}$, from eq. 4.2, where $d = \Lambda_2/\Lambda_1 \approx 1$, for $\underline{k}_1 \approx \underline{k}_2$ [eq. 2.22].

The scale for the dimensional envelope amplitude can be traced from the scalings of (2.6) and (3.1); it is

$$r_0 U_1 \epsilon^{1/2} \left[\frac{\eta_3}{\kappa_* \Lambda_1} \right]^{1/2} \left[-\frac{\lambda_2}{\lambda_1} \right]^{1/4}$$

where ϵ is given by (2.9). This is a scale for the disturbance stream function. The precise values of λ_1 , λ_2 are sensitive functions of the distance of k_1 , k_2 from the marginally neutral circle. Take $-\lambda_2/\lambda_1 \approx 0(1)$. Also, take $\Lambda_1 \approx 0(1)$. Without loss of generality, the superfluous topography parameter η_3 can be set to 1. Now

$$\kappa_* = \bar{z} \cdot k_1 \times k_2 \approx k_1 k_T$$

where k_1 , k_2 , k_T are nondimensional wavenumbers scaled by r_0 . Take $k_1 \approx 0(1)$, but $k_T = r_0/L_T \ll 1$. The disturbance velocity scale that corresponds to the above is then roughly

$$(U_1 f_0 L_T \Delta h / H_1)^{1/2}$$

For the ocean, take $\Delta h/H_1 = 0.1$, $U_1 = 0.1 \text{ m s}^{-1}$, $f_0 = 10^{-4} \text{ s}^{-1}$, $L_T = 500 \text{ km}$. This velocity scale is 0.7 m s^{-1} , which is quite considerable. Although it is larger than the mean flow scale U_1 , it is not inconsistent with the requirements for validity of the perturbation expansion. For the atmosphere take $U_1 = 10 \text{ m s}^{-1}$, $L_T = 1000 \text{ km}$, other parameters being comparable to the ocean; then the disturbance velocity scale is 10 m s^{-1} . Although these estimates are quite crude—a given situation requires a more precise calculation of λ_1 , λ_2 , Λ_1 , etc.—they serve to show that substantial disturbance velocities can be achieved.

In summary, we have shown how the amplitudes of hybrid modes of baroclinic instability generated by interaction with topography execute finite amplitude limit-cycles of growth and decay. It must be stressed that the solutions were calculated by perturbing the nonlinear, nontopographic, normal modes, so that the effects of nonlinearity and topography must be considered 'weak'. However, Hopf bifurcation theory (Iooss and Joseph, 1980) guarantees a finite radius of convergence for such a perturbation theory, so that quantitatively accurate finite-amplitude approximations are in principle accessible by repeated iterations. We claim only a qualitative approximation to these accurate solutions with our first-order theory.

ACKNOWLEDGMENTS

This work has been supported by the National Science foundation under grants OCE-8117700, 8316930, and by the Office of Naval Research under contract number N00014-84-C-0218.

REFERENCES

- Abramowitz, M. and Stegun, I.A., 1964. Handbook of Mathematical Functions. Dover, 1046 pp.
- Blumsack, S.L. and Gierasch, P.J., 1972. Mars: the effect of topography on baroclinic instability. *J. Atmos. Sci.*, 29: 1081-1089.
- Charney, J.G., 1947. The dynamics of long waves in a baroclinic westerly current. *J. Meteorol.*, 4: 135-163.
- Charney, J.G. and Devore, J.G., 1979. Multiple flow equilibria in the atmosphere and blocking. *J. Atmos. Sci.*, 36: 1205-1216.
- Charney, J.G. and Straus, D.M., 1980. Form-drag instability, multiple equilibria and propagating planetary waves in baroclinic, orographically forced, planetary wave systems. *J. Atmos. Sci.*, 37: 1157-1176.
- De Szoeke, R.A., 1975. Some effects of bottom topography on baroclinic stability. *J. Mar. Res.*, 33: 93-122.
- De Szoeke, R.A., 1983. Baroclinic instability over wavy topography. *J. Fluid Mech.*, 130: 279-298.
- Drazin, P.G., 1970. Nonlinear baroclinic instability of a continuous zonal flow. *Q.J.R. Meteorol. Soc.*, 96: 667-676.
- Eady, E.T., 1949. Long waves and cyclone waves. *Tellus*, 1: 33-52.
- Hart, J.E., 1979. Barotropic quasi-geostrophic flow over anisotropic mountains. *J. Atmos. Sci.*, 36: 1736-1746.
- Hide, R. and Mason, P.J., 1975. Sloping convection in a rotating fluid. *Adv. Phys.*, 24: 47-100.
- Iooss, G. and Joseph, D.D., 1980. Elementary Stability and Bifurcation Theory. Springer-Verlag, New York, 285 pp.
- Kevorkian, J. and Cole, J.D., 1981. Perturbation Methods in Applied Mathematics. Springer-Verlag, New York, 558 pp.
- Lorenz, E.N., 1963. The mechanics of vacillation. *J. Atmos. Sci.*, 20: 448-464.
- Pedlosky, J., 1970. Finite amplitude baroclinic waves. *J. Atmos. Sci.*, 27: 15-30.
- Pedlosky, J., 1979. Geophysical Fluid Dynamics. Springer-Verlag, New York, 624 pp.
- Taylor, G.I., 1923. Experiments on the motion of solid bodies in rotating fluids. *Proc. R. Soc. A104*, 213-218.

Observations of Internal Gravity Waves Under the Arctic Pack Ice

MURRAY D. LEVINE AND CLAYTON A. PAULSON

College of Oceanography, Oregon State University, Corvallis

JAMES H. MORISON

Polar Science Center, University of Washington, Seattle

Internal gravity waves measured under the Arctic pack ice were strikingly different from measurements at lower latitudes. The total wave energy, integrated over the internal wave frequency band, was lower by a factor of 0.03-0.07, and the spectral slope at high frequency was nearly -1 in contrast to the -2 observed at lower latitudes. This result has implications for theoretical investigations of the generation, evolution, and destruction of internal waves and is also important for other processes, such as the propagation of sound, and the wave-induced turbulent diffusion of heat, plankton, and chemical tracers.

INTRODUCTION

Internal gravity waves are responsible for much of the variability in the ocean at short time scales, from the inertial to buoyancy periods, and at small space scales, from 0.1 to 10 km [Olbers, 1983]. These waves transport energy vertically and horizontally and may transform large-scale geostrophic circulations to small-scale turbulent motions. Away from topographic features the internal wave spectrum has been observed to be remarkably steady in time and uniform throughout most of the world's oceans. However, beneath the Arctic pack ice the wave field differs markedly from lower-latitude observations. Results from the Arctic Internal Wave Experiment (AIWEX) indicate that the internal waves are substantially less energetic with a significantly different spectral composition compared with lower-latitude observations. We believe that the measurements made during AIWEX represent one of the best sets of observations of an oceanic internal wave field in which the spectral level and shape are significantly different from the universal Garrett-Munk model [Garrett and Munk, 1972, 1975] (hereinafter referred to as GM).

Oceanic measurements over the past two decades reveal that the internal wave field is composed of a wide spectrum of frequencies and wave numbers with statistics that are nearly stationary in time and space. This conclusion allowed GM to derive a universal spectral representation of the wave field that is consistent with observations and linear wave theory. Although the GM model is a simplified view of internal waves, experience has demonstrated that new observations tend to follow the main features of the model.

While the spectral description of the internal wave field has continued to improve, we do not yet understand the physical processes that generate and dissipate internal waves. Theoretical studies have suggested a variety of plausible mechanisms, but verification is difficult. One approach has been to search for deviations from the universal GM description and to attempt to correlate these deviations with fluctuations in external forcing [Wunsch, 1975]. Some success has been achieved in correlating wind forcing with the generation of internal waves at near-inertial frequencies [e.g., Pollard, 1970; Fu,

1981; D'Asaro, 1985]. However, establishing a cause and effect relationship between a forcing mechanism and the remainder of the internal wave spectrum has not been as successful. The possibility of topographic forcing is suggested from measurements of enhanced levels of wave energy near significant topographic features such as seamounts [e.g., Wunsch and Webb, 1979] and canyons [e.g., Hotchkiss and Wunsch, 1982]. Atmospheric forcing appears to produce a seasonal variation in energy from 1.2-1.3 to 2-3 times the mean level in observations made during the Long-Term Upper Ocean Study [Briscoe and Weller, 1984]. Further evidence connecting specific forcing mechanisms with variations in the internal wave field will aid in determining the identity of the important sources of internal waves.

It was in the spirit of searching for an anomalous internal wave field that AIWEX was organized. Scant evidence indicated that internal wave energy levels might be low in the Arctic Ocean [Levine et al., 1985]. AIWEX was designed to test this hypothesis by making intensive observations of the internal wave field beneath the polar ice cap. In this paper we present measurements of the internal wave spectra measured during AIWEX and compare these observations with the GM model.

OBSERVATIONS

The experiment took place at an ice camp established about 350 km north of Prudhoe Bay, Alaska, in the Beaufort Sea, with researchers from Oregon State University, the University of Washington, Scripps Institution of Oceanography, and private industry. During nearly 2 months of occupancy from March to May 1985 the camp drifted about 120 km to the west from its origin at 74°N, 143°W. An extensive set of temperature, conductivity, and velocity data were gathered from a variety of instruments. Access to the water was obtained through holes in the 3-m-thick ice. The measurements reported here were made from both fixed and vertically profiling instruments.

To determine the density field through which the internal waves propagate, vertical profiles of temperature and salinity were measured with the Arctic profiling system [Morison, 1980]. The buoyancy frequency N was then estimated from the vertical gradient of density. There are significant variations in N in the upper 250 m reflecting the different water masses that compose the upper Arctic Ocean [Aagaard et al., 1985] (Figure 1). Values range from 4 cph to peaks near 12 cph.

Copyright 1987 by the American Geophysical Union.

Paper number 6C0595.
0148-0227/87/006C-0595\$05.00

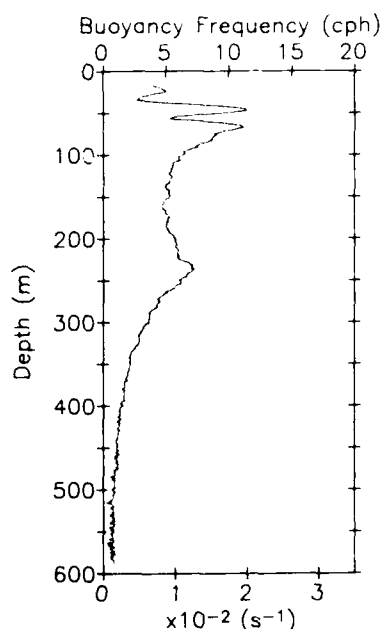


Fig. 1. Vertical profile of buoyancy frequency.

Below 250 m, N decreases nearly exponentially to the bottom at 3700 m.

Time series of temperature were measured by a vertical and horizontal array of temperature sensors (Sea-Bird Electronics, sensor SBE-3). Seven of the sensors were located at 250 m, where the fluctuations in temperature are due primarily to the vertical displacement of the internal waves. The vertical displacement is inferred by dividing the temperature time series by the average vertical temperature gradient. An observed spectrum of vertical displacement from the period March 20 to April 5 is shown in Figure 2. The spectrum decreases as ω^{-1} up to 6 cph, the local value of the buoyancy frequency. Above N there is a sharp break in slope and a steep falloff in energy.

Over the same period a time series of horizontal velocity at 100 m was measured with an electromagnetic current meter (InterOcean S4). Because the ice pack drifts, the observed velocity is the sum of the ice and water motion. The ice motion was removed from the velocity time series using the time history of the camp position determined from a fit to satellite navigation. The method used is due to McPhee [1986]. Positions were obtained approximately 40 times per day. The frequency spectra of the two rotary components of horizontal velocity are shown in Figure 2. There is a peak in the clockwise component at the inertial frequency as expected in the northern hemisphere. Above f the clockwise component is higher than the counterclockwise; at high frequency the components are nearly the same and follow ω^{-1} . The falloff above N is not observed because the sampling rate was too low.

DISCUSSION AND CONCLUSIONS

To compare these observations with those from other oceans, the GM spectrum was calculated; it is a good representation of the internal wave field at lower latitudes away from topography. The GM spectra of vertical displacement S_z and of clockwise and counterclockwise rotary velocity S_{\pm} and

S_{\pm} are given by

$$S_z(\omega) = \frac{2}{\pi} E b^2 N_0 \frac{f}{N(z)} \frac{(\omega^2 - f^2)^{1/2}}{\omega^3}$$

$$S_{\pm}(\omega) = 4\pi E b^2 N_0 f N(z) \frac{(\omega \mp f)^2}{\omega^3 (\omega^2 - f^2)^{1/2}}$$

where we use the same values of the parameters as GM: $E = 6.3 \times 10^{-5}$ (nondimensional energy level), $b = 1300$ m (vertical depth scale of N), and $N_0 = 3$ cph (buoyancy frequency scale). The units of S_z and S_{\pm} are $\text{m}^2 (\text{cph})^{-1}$ and $\text{m h}^{-1} (\text{cph})^{-1}$ respectively, for frequency specified in units of cycles per hour. The GM description is confined to freely propagating, linear internal waves which are restricted to frequencies between the inertial frequency f and N . The GM spectra are plotted with the observations in Figures 2 and 3. The local value of N is used to scale the level of the spectra. The values of N at 100 and 250 m were taken from Figure 1 and found to be near 6 cph at both depths. At high frequency, $\omega \gg f$, the frequency dependence of the GM spectra of velocity and vertical displacement is ω^{-2} .

The Arctic spectra are strikingly different from lower-latitude observations: The total internal wave energy is significantly lower by a factor of 0.03–0.07, and the spectral slope is substantially less steep, with a frequency dependence near ω^{-1} at high frequency. The total internal wave energy is estimated from the total variance of the velocity or vertical displacement over the internal wave frequency band from f to N . The total energy is lower than GM by a factor of 0.03 based on vertical displacement and a factor of 0.07 based on velocity. However, the spectral density ranges below GM by a factor of 0.6 near N to a factor of 0.01 near f (Figures 2 and 3).

These observations have a potential impact on a variety of

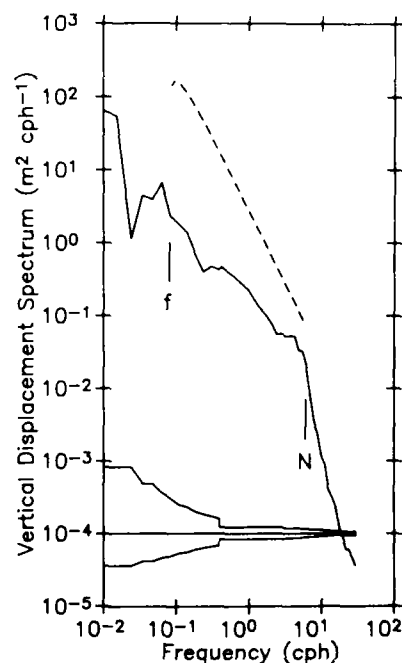


Fig. 2. Spectrum of vertical displacement from 250-m depth (solid line). Vertical displacement was inferred from temperature by dividing by the average vertical temperature gradient of $0.02 \text{ } ^\circ\text{C m}^{-1}$. The Garrett-Munk spectrum is shown for comparison (dashed line). The 95% confidence limits are indicated below.

active research areas. Recent theoretical studies have sought to explain the observed spectral composition of the wave field by nonlinear interactions (see Müller *et al.* [1986], for a recent review of the topic). Researchers have typically used a spectrum similar to GM to characterize the oceanic internal wave field. The theories can now be tested with a wave field having a different spectral composition. A successful theory will need to explain both the low-latitude and Arctic measurements. Studies of acoustic propagation have been able to relate amplitude and travel time fluctuations of sound pulses to the fluctuations due to internal waves [e.g., Flatté, 1983; Ewart and Reynolds, 1984]. The Arctic Ocean, with its unique internal wave environment, provides a valuable laboratory for testing new theoretical ideas in acoustic propagation. The role of internal waves in vertical and horizontal mixing [e.g., Young *et al.*, 1982; Desaubies and Smith, 1982] may be elucidated by comparing observations from lower latitude with the Arctic. Differences in mixing could affect the large-scale circulation as well as the diffusion of plankton and chemical tracers.

Why are Arctic internal waves so different from those at lower latitudes? The search for answers to this question is a topic of active research. We can, however, suggest some hypotheses.

It is instructive to examine the physical processes that are unique to the Arctic Ocean. The ice cover acts as a rigid lid to the internal waves. The formation of a turbulent boundary layer below the ice causes increased internal wave dissipation compared to ice free oceans [Morison *et al.*, 1985]. The nature of surface forcing is also quite different in the Arctic. The wind stress usually must be transferred through the ice to reach the water below. This forcing is generally weaker than other oceans because the winds themselves are weaker [Paulson, 1980], and some momentum is transmitted through the ice to the coast. Ice keels, which add topographic relief to the underside of the ice, may generate internal waves when the ice

moves [Ripty, 1976]. Large surface buoyancy fluxes, which occur within leads, may generate internal waves by perturbing the pycnocline at the base of the surface-mixed layer [Morison, 1980, 1986]. It is theoretically possible to transfer momentum to internal waves from surface gravity waves [Olbers, 1983; Phillips, 1977]; this mechanism is not possible in an ice-covered ocean. Another source of energy for the internal wave field may be provided by the spectral transfer of internal tide energy through nonlinear wave-wave interactions [Bell, 1975]. The internal tide is an internal wave at tidal frequencies that is generated by the interaction of the barotropic tide with topography, such as continental shelves (see Hendershott [1981], for a review of internal tides). In the Arctic Ocean the internal tide is weak due to a small barotropic tide over much of the Arctic Ocean [Kowalik and Untersteiner, 1978] coupled with the fact that free internal waves cannot exist at latitudes higher than 75° at the lunar semidiurnal frequency (M_2 tide). Internal waves may also gain energy from low-frequency motions, such as mesoscale eddies and mean geostrophic circulations [Olbers, 1983]. The mean circulation in the Beaufort Sea is relatively weak compared to most oceans [Coachman and Aagaard, 1974]; however, the basin is populated with intense, long-lived small-scale eddies (10–20 km) [Manley and Hunkins, 1985]. Identification of which of the foregoing or other processes are most important in generating, modifying, and dissipating internal waves awaits further investigation.

Acknowledgments. We thank Andy Heiberg, Allen Hielscher, and Imants Virsnieks of the Polar Science Center, University of Washington, for the efficient logistic support. Special thanks are extended to Rick Baumann, Jay Simpkins, Roger Andersen, and Steve Gard for their efforts on and off the ice. We gratefully acknowledge the support of the Office of Naval Research through contracts N00014-84-C-0218 (M.D.L. and C.A.P.) and N00014-85-G-0052 N00014-84-0111 (J.H.M.).

REFERENCES

- Aagaard, K., J. H. Swift, and E. C. Carmack, Thermohaline circulation in the Arctic mediterranean seas, *J. Geophys. Res.*, **90**, 4833–4846, 1985.
- Bell, T. H., Jr., Topographically generated internal waves in the open ocean, *J. Geophys. Res.*, **80**, 320–327, 1975.
- Briscoe, M. G., and R. A. Weller, Preliminary results from the long-term upper ocean study (LOTUS), *Dyn. Atmos. Oceans*, **8**, 243–265, 1984.
- Coachman, L. K., and K. Aagaard, Physical oceanography of Arctic and subarctic seas, in *Marine Geology and Oceanography of the Arctic Seas*, edited by Y. Herman, pp. 1–72, Springer-Verlag, New York, 1974.
- D'Asaro, E. A., Upper ocean temperature structure, inertial currents, and Richardson numbers observed during strong meteorological forcing, *J. Phys. Oceanogr.*, **15**, 943–962, 1985.
- Desaubies, Y., and W. K. Smith, Statistics of Richardson number and instability in oceanic internal waves, *J. Phys. Oceanogr.*, **12**, 1245–1259, 1982.
- Ewart, T. F., and S. A. Reynolds, The mid-ocean acoustic transmission experiment, MATE, *J. Acoust. Soc. Am.*, **75**, 785–802, 1984.
- Flatté, S. M., Wave propagation through random media: Contributions from ocean acoustics, *Proc. IEEE*, **71**, 1267–1294, 1983.
- Fu, L.-L., Observations and models of inertial waves in the deep ocean, *Rev. Geophys.*, **19**, 141–170, 1981.
- Garrett, C. J. R., and W. H. Munk, Space-time scales of internal waves, *Geophys. Astrophys. Fluid Dyn.*, **2**, 255–264, 1972.
- Garrett, C. J. R., and W. H. Munk, Space-time scales of internal waves: A progress report, *J. Geophys. Res.*, **80**, 291–297, 1975.
- Hendershott, M. C., Long waves and ocean tides in *Evolution of Physical Oceanography*, edited by B. A. Warren and C. Wunsch, pp. 292–341, MIT Press, Cambridge, Mass., 1981.
- Hotchkiss, E. S., and C. Wunsch, Internal waves in Hudson Canyon with possible geological implications, *Deep Sea Res.*, **29**, 415–442, 1982.

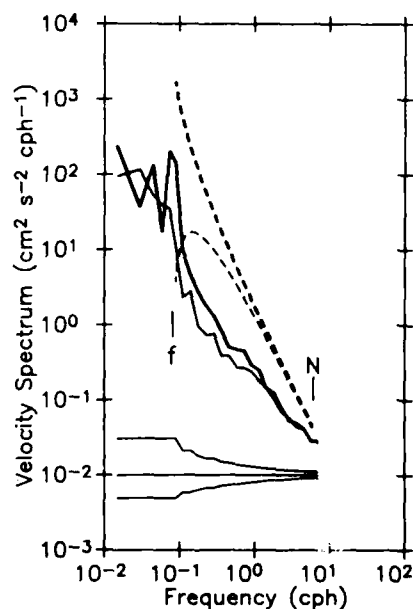


Fig. 3. Spectrum of the clockwise (bold solid line) and counter-clockwise (light solid line) components of horizontal velocity at 100-m depth. The Garrett-Munk spectrum is shown for comparison (dashed line). The 95% confidence limits are indicated below.

- Kowalik, Z., and N. Untersteiner, A study of the M_2 tide in the Arctic Ocean, *Dtsch. Hydrogr. Z.*, 31, 216-229, 1978.
- Levine, M. D., C. A. Paulson, and J. H. Morison, Internal waves in the Arctic Ocean: Comparison with lower-latitude observations, *J. Phys. Oceanogr.*, 15, 800-809, 1985.
- Manley, T. O., and K. Hunkins, Mesoscale eddies in the Arctic Ocean, *J. Geophys. Res.*, 90, 4911-4930, 1985.
- McPhee, M. G., Analysis and prediction of short-term ice drift, in *Proceedings of the Fifth International Offshore Mechanics and Arctic Engineering Symposium*, vol. 4, pp. 385-393, American Society of Mechanical Engineers, New York, 1986.
- Morison, J. H., Forced internal waves in the Arctic Ocean, *Tech. Rep. Ref. M80-10*, 289 pp., Univ. of Wash., Seattle, 1980.
- Morison, J. H., Internal waves in the Arctic Ocean: A review, in *Geophysics of Sea Ice*, edited by N. Untersteiner, Plenum, New York, in press, 1986.
- Morison, J. H., C. E. Long, and M. D. Levine, Internal wave dissipation under sea ice, *J. Geophys. Res.*, 90, 11,959-11,966, 1985.
- Müller, P., G. Holloway, F. Henyey, and N. Pomphrey, Nonlinear interactions among internal gravity waves, *Rev. Geophys.*, 24, 493-536, 1986.
- Olbers, D. J., Models of the oceanic internal wave field, *Rev. Geophys.*, 21, 1567-1606, 1983.
- Paulson, C. A., A review of the AIDJEX atmospheric program, in *Sea Ice Processes and Models*, edited by R. S. Pritchard, pp. 28-33, University of Washington Press, Seattle, 1980.
- Phillips, O. M., *The Dynamics of the Upper Ocean*, pp. 253-254, Cambridge University Press, New York, 1977.
- Pollard, R. T., On the generation by winds of inertial waves in the ocean, *Deep Sea Res.*, 17, 795-812, 1970.
- Rigby, F. A., Pressure ridge generated internal wave wakes at the base of the mixed layer in the Arctic Ocean, M.S. thesis, Univ. of Wash., Seattle, 1976.
- Wunsch, C., Deep ocean internal waves: What do we really know?, *J. Geophys. Res.*, 80, 339-343, 1975.
- Wunsch, C., and S. Webb, The climatology of deep ocean internal waves, *J. Phys. Oceanogr.*, 9, 235-243, 1979.
- Young, W. R., P. B. Rhines, and C. J. R. Garrett, Shear-flow dispersion, internal waves and horizontal mixing in the ocean, *J. Phys. Oceanogr.*, 12, 515-527, 1982.
- M. D. Levine and C. A. Paulson, College of Oceanography, Oregon State University, Corvallis, OR 97331.
- J. H. Morison, Polar Science Center HN-10, University of Washington, Seattle, WA 98195.

(Received September 24, 1986;
accepted September 24, 1986.)

Simultaneous Spatial and Temporal Measurements of the Internal Wave Field During MATE

MURRAY D. LEVINE

College of Oceanography, Oregon State University, Corvallis

JAMES D. IRISH

University of New Hampshire, Durham

TERRY E. EWART AND STEPHEN A. REYNOLDS

Applied Physics Laboratory, University of Washington, Seattle

A statistical description of the deep ocean internal wave field is presented using measurements from the Midocean Acoustic Transmission Experiment, conducted near Cobb Seamount in the NE Pacific (46°46'N, 130°47'W) during June-July 1977. The unique feature of this experiment is the variety of data obtained simultaneously from the same location: time series of temperature and velocity, and vertical and horizontal profiles of temperature. A generalized form of the Garrett-Munk (GM) internal wave spectrum is developed and used to interpret the data. This spectral model is specified by three parameters, \bar{E} , t , and p (energy level, wave number bandwidth, and frequency spectral slope, respectively). The variety of measurement types permit these three model parameters to be estimated from more than one measurement. The overall best fit values to the MATE data were $p = 2.7$ (GM use $p = 3$), $t = 3.1 \text{ m}^{-1} \text{ s}$ (equivalent to $j_* = 6$, twice the GM value), and $\bar{E} = 8 \times 10^{-4} \text{ J kg}^{-1}$ (within 20% of the GM level). Although significant differences were found in the values of the bandwidth (t) and spectral slope (p) from those specified by Garrett-Munk, the deviations are consistent with the behavior expected in a random internal wave field.

1. INTRODUCTION

Our knowledge of internal gravity waves in the ocean has increased dramatically in the past few decades. While internal waves have been observed since the beginning of the century, the pervasiveness of the phenomena has only been realized with the advent of instruments capable of measuring time series of velocity and temperature. However, internal waves are sufficiently complicated that relating observations to theoretical ideas is difficult. In order to resolve the internal wave field, in even a rudimentary way, simultaneous measurements of the vertical, horizontal, and temporal variability of the ocean are necessary. For more background, see recent reviews by Munk [1981], Levine [1983], and Olbers [1983].

The extensive set of environmental and acoustic data gathered during the Midocean Acoustic Transmission Experiment (MATE) provides an opportunity to study simultaneous observations from several different types of measurements. The experiment was conducted near Cobb Seamount in the NE Pacific about 450 km from the coast of Washington (46°46'N, 130°47'W) during June-July 1977 [Ewart *et al.*, 1977]. To accommodate the requirements of the acoustic experiment, the internal wave measurements were made between Cobb Seamount and a second smaller seamount to the southwest in a water depth of 2200 m (Figure 1). Cobb Seamount is an imposing topographic feature rising to within 30 m of the surface; the top of the smaller seamount (labeled "Corn" in Figure 1) is nearly 1000 m below the surface. While the proximity of these two features (about 9 km away) may affect the

internal wave field, other studies suggest that the perturbation of the internal wave field is limited to regions very near the seamounts [Wunsch, 1976; Wunsch and Webb, 1979; Eriksen, 1982]. The seamounts, however, could be a significant source of internal tide [e.g., Baines, 1982].

The purpose of this paper is to present the variety of temperature and velocity data gathered during MATE and to describe statistically the internal wave field suggested by these observations. The empirical model of Garrett and Munk [1972, 1975; hereafter referred to as GM] is used as a framework for comparing the various statistical quantities that could be estimated from the measurements. Guided by the observations, the form of the GM internal wave spectrum is generalized to accommodate an arbitrary frequency spectral slope; this formalism may also be useful in interpreting other observations where the frequency spectral slope differs from the GM model. The unique feature of the MATE observations is that the different types of measurements were made nearly simultaneously in the same part of the ocean. This invites a close comparison with theory, since model parameterizations can be checked for consistency with the same parameters estimated from more than one measurement.

This paper serves as an overview of the data gathered during MATE; the association with internal waves is made by using the GM model as the standardized "yardstick." More detailed analyses and modeling of specific aspects of the data set, such as fine structure [Levine and Irish, 1981] and the internal tide, are deferred to other studies.

The observed temperature and velocity measurements and associated spectral quantities are presented in section 2. The observations are compared with internal wave consistency relations in section 3. A generalized form of the GM spectral model is presented in section 3, and the parameters of the model are determined in section 4. A comparison with histori-

Copyright 1986 by the American Geophysical Union.

Paper number 6C0272
0148-0227/86/006C-0272\$05.00

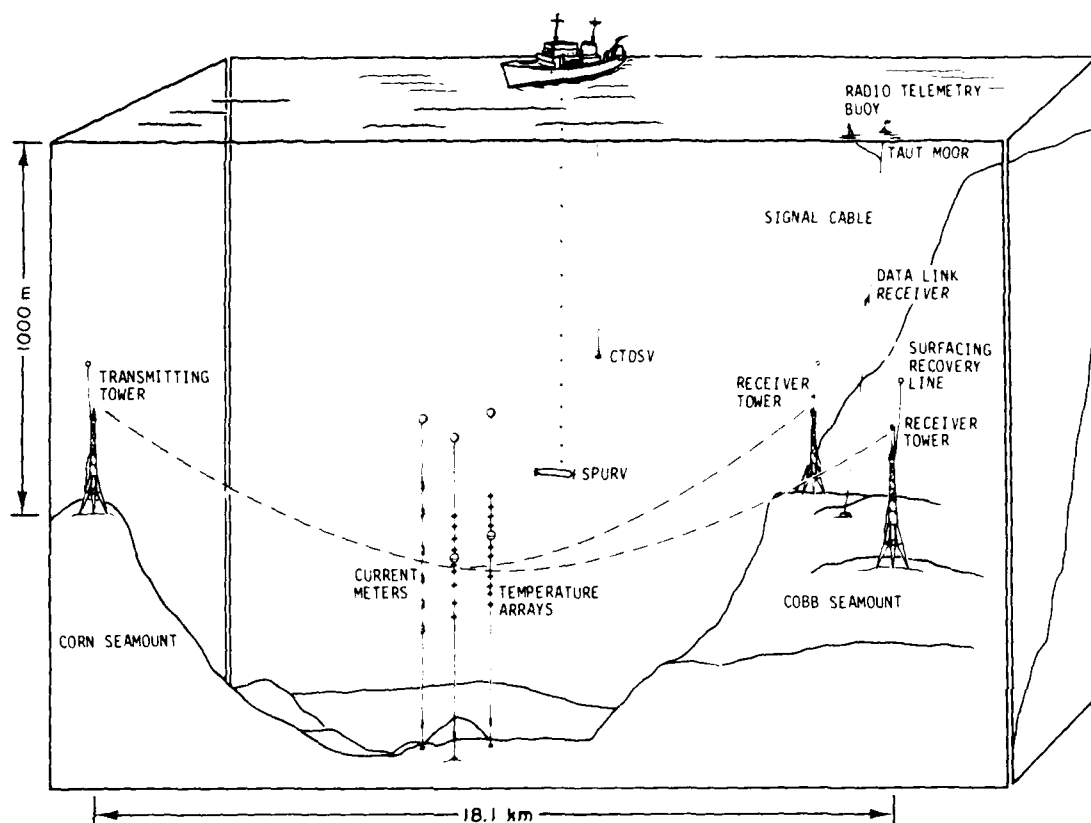


Fig. 1. A schematic overview of MATE showing the three moored arrays, SPURV, CTDSV, and the relationship to the acoustic experiment.

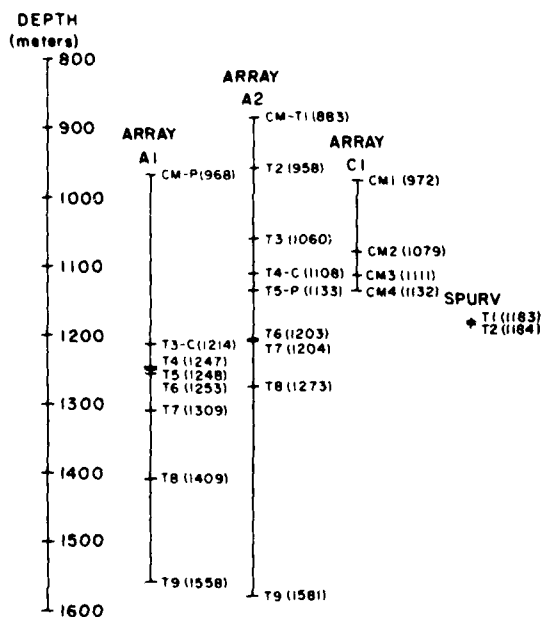


Fig. 2. Depths of the current meters (C/M), temperature (T), conductivity (C), and pressure (P) sensors located on arrays A1, A2, and C1 and SPURV.

cal data is made in section 5, and a summary and conclusions are given in section 6.

Throughout the paper units of radians per second (s^{-1}) and radians per meter (m^{-1}) are used exclusively in equations. Units of cycles per hour (cph) and cycles per meter (cpm) are also used in discussions and in presentation of the data.

2. OBSERVATIONS

A schematic overview of the components of MATE is shown in Figure 1. The vertical structure was sampled repeatedly using a conductivity, temperature, depth, sound velocity measuring instrument (CTDSV). Temporal variability at fixed points was monitored with three moored arrays. Two moored temperature arrays (referred to as A1 and A2) and one current meter array (C1) were deployed midway between the two seamounts in 2.2 km of water. Horizontal temperature profiles were obtained with the free-swimming self-propelled underwater research vehicle (SPURV) [Widditsch, 1973]. The depths of the moored sensors and SPURV observations are shown in Figure 2.

CTDSV Profiles

A total of 38 CTDSV profiles from the surface to 1500 m were taken at three stations with a Bissett-Berman 9040-5 CTDSV. The primary station was midway between the sea-

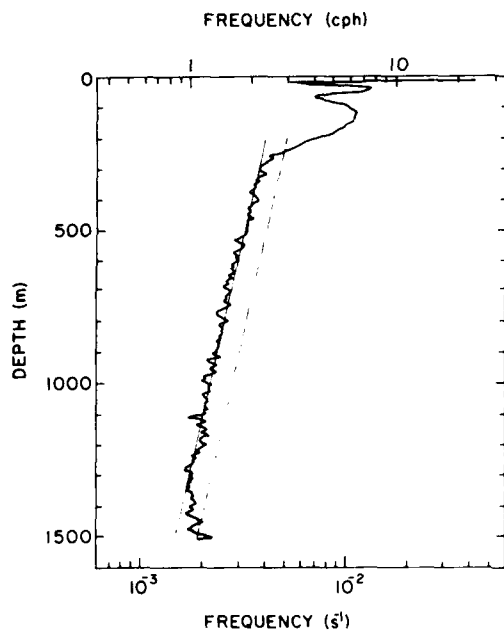


Fig. 3. The average buoyancy frequency profile $N(z)$. The data are fit with an exponential $N(z) = N_0 \exp[-(z - 200)/1300]$ with $N_0 = 4.0 \times 10^{-3} \text{ s}^{-1}$ (solid line). The average oceanic profile used by Garrett and Munk [1972] with $N_0 = 5.2 \times 10^{-3} \text{ s}^{-1}$ is shown for comparison (dashed line).

mounts near the moored arrays. The other two stations were midway between this central site and each seamount. In addition, at the primary site a 25-hour series of CTDSV profiles was recorded, consisting of a profile from 1000 to 1300 m every 20 min. As the vertical sampling was nonuniform, the profiles were filtered to 1-m intervals with a 2-m triangular filter centered around each 1-m interval. The 38 deep profiles

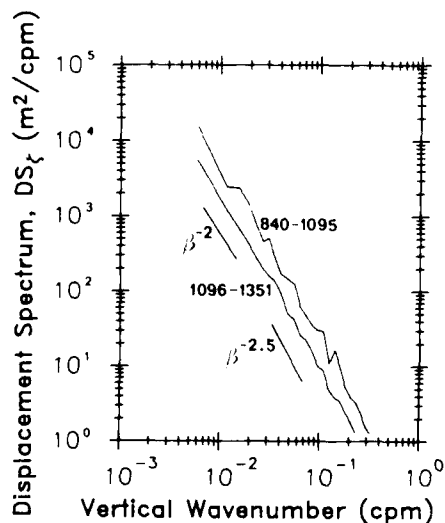


Fig. 4. Vertical wave number spectra of vertical displacement DS_z calculated from temperature profiles measured with the CTDSV over depth ranges of 840–1095 and 1096–1351 m. The vertical displacement is inferred from temperature by assuming a constant vertical adiabatic temperature gradient of $1.9 \times 10^{-3} \text{ C m}^{-1}$.

were ensemble averaged to produce profiles representative of the average conditions during the experiment. Since the profiles were taken at somewhat random times, it was assumed that the variations due to tides, internal waves, and non-persistent structure were nearly averaged out.

The average profiles of temperature, salinity, density, and sound velocity are nearly linear over the depth range of the moored sensors [Ewart *et al.*, 1977]. The buoyancy frequency was calculated from the average profile (Figure 3). Below 200 m the profile is fit to an exponential, as suggested by Garrett and Munk [1972], producing a representative profile for determining the local buoyancy frequency, $N(z)$. This profile is consistent with earlier measurements at Cobb Seamount [Ewart, 1976].

Vertical wave number temperature spectra were calculated from perturbation profiles formed by subtracting the average temperature profile from each of the 32 profiles made concurrently with the A2 measurements. Each profile was divided into nine depth ranges and Fourier transformed; spectra were estimated by a combination of ensemble and band averaging. Corrections were also made for sensor response. If the temperature fluctuations were caused primarily by the vertical advection of a linear temperature gradient, then the vertical displacement spectra (dropped spectra, DS_z), shown in Figure 4, can be formed by dividing each temperature spectrum by the square of the local mean adiabatic temperature gradient. This assumption is better at lower wave numbers and more suspect at higher wave numbers, which may be contaminated by the effects of fine structure. A comprehensive analysis of the effects of temperature fine structure in these measurements is given by Levine and Irish [1981]. The most energetic spectrum is the shallowest, with energy decreasing with increasing depth. The

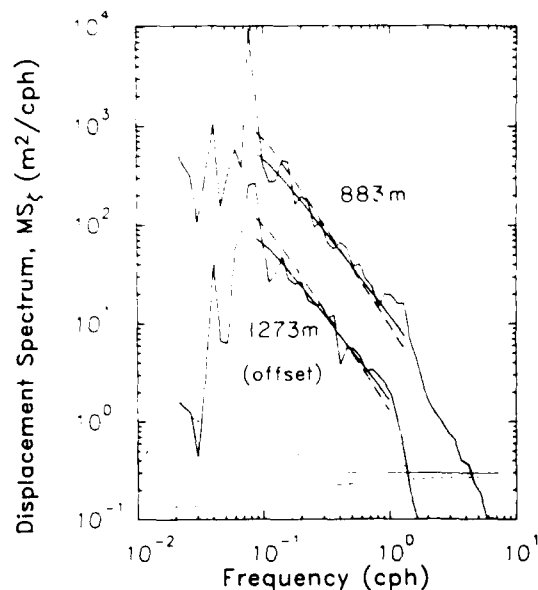


Fig. 5. Frequency spectra of vertical displacement MS_z observed from temperature sensors on A2 at 883 m (no offset) and 1273 m (offset by a factor of 0.11). The vertical displacement is inferred from temperature by assuming a constant vertical adiabatic temperature gradient of $2.00 \times 10^{-3} \text{ C m}^{-1}$ at 883 m and $1.62 \times 10^{-3} \text{ C m}^{-1}$ at 1273 m. The data are compared with the MATE model (solid line) and the GM model (dashed line). The 95% confidence limits are also indicated.

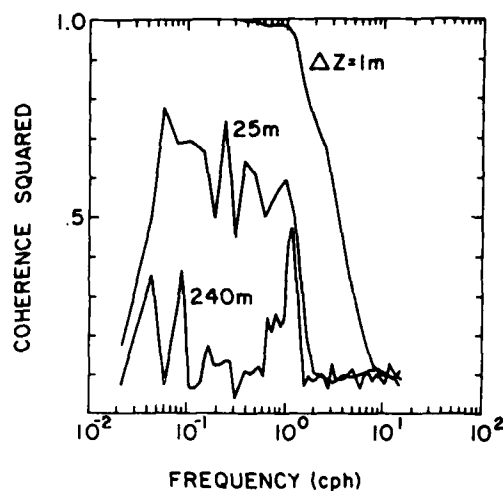


Fig. 6a

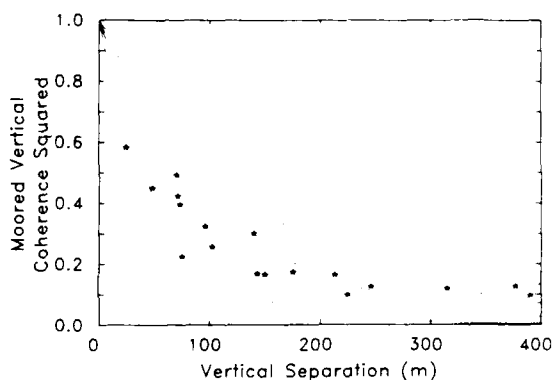


Fig. 6b

Fig. 6. The vertical coherence of vertical displacement MVC_z observed by temperature sensors on A2. (a) MVC_z as a function of frequency for vertical separation of 1, 25, and 240 m. (b) The average level of the MVC_z in the internal wave band (0.2–0.7 cph) as a function of vertical separation. The data are compared (stars) with the MATE model for the range of $t = 2.5$ to $3.6 \text{ m}^2 \text{ s}^{-1}$ for $N = 1.0$ to 1.35 cph (between solid lines) and the GM model with $t = 1.4 \text{ m}^2 \text{ s}^{-1}$ for $N = 1.0$ to 1.35 cph (between dashed lines).

spectra drop at $\beta^{-2.1}$ from $6 \times 10^{-3} \text{ cpm}$ to about $6 \times 10^{-2} \text{ cpm}$, then fall faster at about $\beta^{-2.6}$.

Moored Temperature Arrays

The two temperature arrays were designed as taut moorings with all buoyancy at 400 m, below the influence of the wind wave field. The top sensor on each array was an Aanderaa current meter measuring horizontal velocity and temperature; the other sensors, 18 temperature (Sea-Bird Electronics), two conductivity (Sea-Bird Electronics), and two pressure (Vibron), were divided equally between the arrays (Figure 2). Acoustic transponders on the arrays allowed shipboard tracking; A1 was positioned 332 m southeast of A2.

The pressure records show the mean depth, tidal fluctuations, and array motion. The amplitude of the pressure fluctuations recorded on A2 agrees to within 1/4 m of the barotropic tide predicted from previous measurements on Cobb Sea-

mount [Larsen and Irish, 1975]. Therefore the vertical excursion of the sensors is neglected. However, the vertical motion of A1 having 1/3 the buoyancy of A2 may not be negligible. Hence most results will be based on data from A2.

Frequency spectra were calculated from all the moored temperature records. A linear trend was removed from each series and a cosine taper applied to the first and last 10% of the series to correct for end-effects, as suggested by Bingham et al. [1967]. The temperature spectra were converted to vertical displacement spectra by dividing by the square of the local average adiabatic temperature gradient. Examples of moored vertical displacement spectra (MS_z) corrected for sensor response are shown in Figure 5.

The energy below the inertial frequency ($f = 1.06 \times 10^{-4} \text{ s}^{-1}$) is attributed to the advection of temperature structure by low-frequency currents as well as the internal wave field itself [Levine and Irish, 1981]. The dominant energy is tidal; significant peaks are present at both the diurnal and semidiurnal frequencies. As typically observed in internal wave spectra, there is a sharp rise at f followed by a smooth spectral roll-off. Near N there is a sharp break in slope with an $\omega^{-2.5}$ dependence above N .

Estimates of the coherence in frequency space between vertically separated sensors (moored vertical coherence, MVC_z) are shown in Figure 6. Each temperature record was divided into 50% overlapping blocks as suggested by Carter et al. [1973]. A linear trend was removed and a cosine taper applied to the first and last 10% of each block. Cross-spectral estimates were formed by ensemble averaging the blocks, and coherences were estimated by normalizing by the appropriate autospectra. For the three vertical separations shown in Figure 6a, the coherence in the internal wave band decreases with increasing separation. There are peaks at the tidal and buoyancy frequencies for separations of 25 and 240 m. Above the local buoyancy frequency, the coherence drops to a bias level that is statistically indistinguishable from zero. Since there is significant variation of coherence with frequency, the average coherence in the band between 0.2 to 0.7 cph was

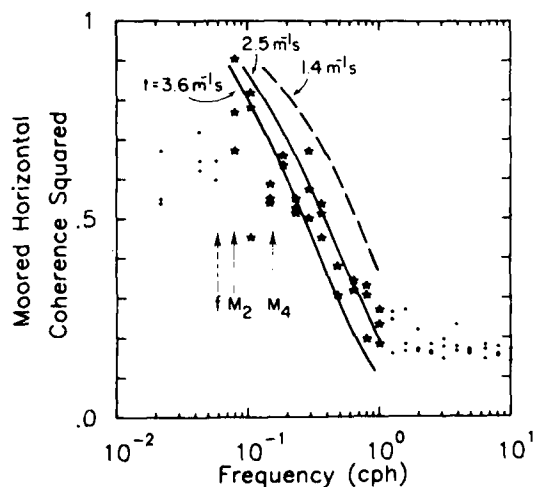


Fig. 7. The horizontal coherence of vertical displacement MHC_z between three pairs of temperature sensors on A1 and A2 separated horizontally by 332 m at nearly the same depth. Values in the internal wave frequency band (stars) are compared with the MATE model (solid lines) and the GM model (dashed line).

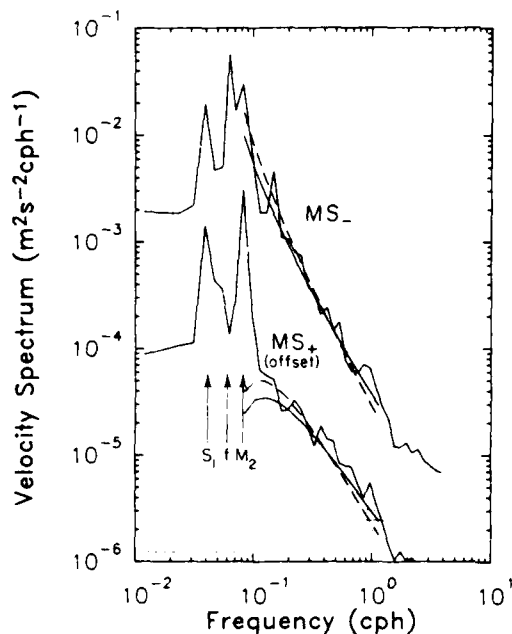


Fig. 8. Frequency spectra of the clockwise MS_+ and the counterclockwise MS_- (offset by a factor of 0.1) components of horizontal velocity observed from C1 at 1079 m. The data are compared with the MATE model (solid line) and the GM model (dashed line). The 95% confidence limits are also indicated.

calculated and plotted as a function of vertical separation in Figure 6b.

The coherence in frequency space between sensors horizontally separated on A1 and A2 (moored horizontal coherence, MHC_f) was calculated in a manner similar to the MVC_f . The coherence was estimated between pairs of sensors moored at nearly the same depth at the horizontal separation of 332 m (Figure 7). There is significant coherence above f to nearly 1 cph, where the coherence falls to the bias level.

Moored Current Meter Array

The current meter array consisted of four Aanderaa current meters. The array was less buoyant than either of the temperature arrays, and hence larger array motion was expected. Because there was no pressure sensor on this array, the magnitude of the vertical motion is unknown. The location of the array, which had no tracking transponder, was estimated to be about 500 m west of A2.

Spectra were calculated using the rotary representation of the velocity vector. Representative rotary spectra from 1079 m (MS_+ and MS_- for the counterclockwise and clockwise components, respectively) are shown in Figure 8. There is a sharp peak at the inertial frequency as well as at the diurnal and semidiurnal tidal frequencies. The inertial peak is the largest and is almost entirely in the clockwise component as expected. An additional peak is seen at 0.14 cph, at about twice the inertial frequency. This peak is not an exact harmonic of either the inertial peak (which is observed at a slightly higher frequency than f) or the semidiurnal tidal frequency, and its origin is unknown. Above f , the spectra fall off smoothly toward N , where there is a slight but significant break in slope. Approaching N , the MS_+ and MS_- are nearly the

same. Above the fall-off at N , the velocity spectra become whiter due to the effects of spectral aliasing, current fine structure, and/or array motion.

SPURV

Horizontal temperature profiles were measured by running SPURV along an isobaric trajectory (1184 dbars). In the region midway between the two seamounts, two 11-km legs were made at right angles (west-to-east followed by north-to-south) to test horizontal isotropy. The horizontal wave number spectra (towed spectra, TS_f) for the two legs are shown in Figure 9 using an equivalent vertical displacement scale based on the mean vertical adiabatic temperature gradient. The spectra were truncated at a wave number where sensor response and digitizing effects become dominant. At low wave number the spectra exhibit an ω^{-2} dependence. At 0.03 cpm there is a break in slope followed by an $\omega^{-1.6}$ dependence at higher wave number. The lack of any significant difference between the spectra is consistent with a horizontally isotropic wave field.

Two temperature sensors attached to SPURV and separated vertically by 0.94 m measured the coherence in horizontal wave number space (towed vertical coherence, TVC_f). The TVC_f was calculated for the two legs, using the same method described for the MVC_f , and plotted in Figure 10. The results from the north-south and east-west legs are statistically identical. The TVC_f is near 1 at low wave numbers and drops to near zero above 0.01 cpm.

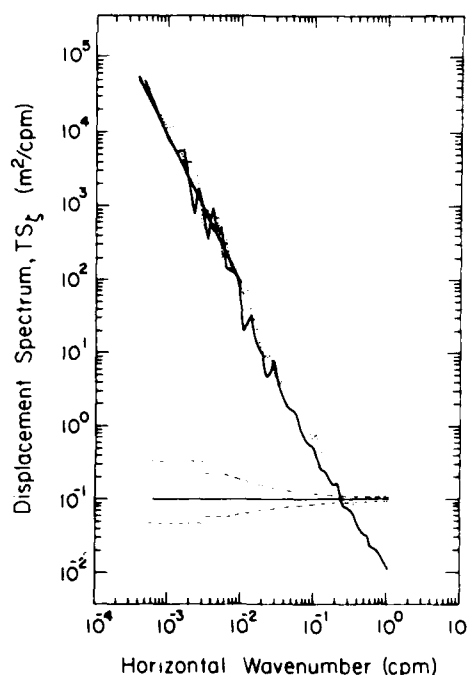


Fig. 9. Horizontal wave number spectra of vertical displacement TS_f observed by SPURV during horizontal runs oriented north to south (solid line) and west to east (dotted line) at 1184 dbar. The vertical displacement is inferred from temperature by assuming a constant vertical adiabatic temperature gradient of $1.64 \times 10^{-3} \text{ } ^\circ\text{C m}^{-1}$. The best fit to ω^{-2} over the wave number band 4.7×10^{-4} to 9.0×10^{-3} cpm is shown by a straight solid line. The 95% confidence limits are also shown.

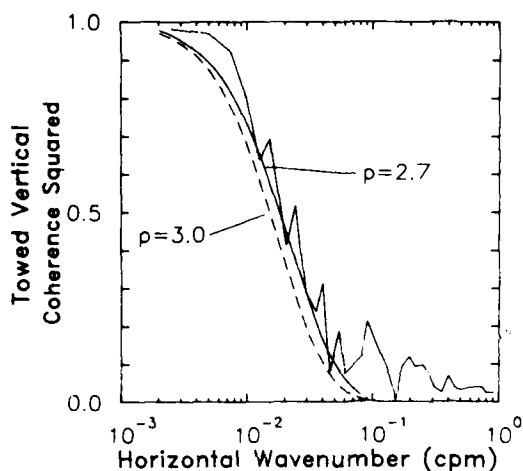


Fig. 10. The horizontal wave number coherence of vertical displacement TVC, between a pair of temperature sensors separated vertically by 0.94 m on SPLRV. The data are compared with the MATE model (section 5) with $p = 2.7$ (solid line) and the GM model with $p = 3.0$ (dashed line).

3. CONSISTENCY RELATIONS

Internal wave consistency relationships express constraints between the horizontal velocity and vertical displacement fields at a single point. Although there are only a few general relations, they are worth examining because they are independent of the specific spectral composition of the wave field. Two independent consistency relationships are applied to the MATE data set. These expressions are valid for a sum of any number of waves of different wave numbers; the wave field is not restricted to be horizontally or vertically isotropic. The derivations hinge on the assumptions that the wave field is linear and each wave component is independent.

The first, originally presented by Fofonoff [1969], relates the potential energy to horizontal kinetic energy:

$$\frac{N^2 MS_v(\omega)}{MS_u(\omega) + MS_v(\omega)} = \frac{N^2}{N^2 - \omega^2} \frac{\omega^2 - f^2}{\omega^2 + f^2} \quad (1)$$

As $\omega \rightarrow f$, the vertical displacement goes to zero, and as $\omega \rightarrow N$, the horizontal velocity becomes negligible. To compare with measurements made at various values of $N(z)$, the equation is rewritten

$$\frac{N^2 MS_v(\omega)}{MS_u(\omega) + MS_v(\omega)} \frac{N^2 - \omega^2}{N^2} = \frac{\omega^2 - f^2}{\omega^2 + f^2} \quad (2)$$

The left-hand side can then be estimated from data and compared with the right-hand side.

The other expression relates the ratio of the counterclockwise to clockwise components of the rotary spectrum

$$\frac{MS_+}{MS_-} = \frac{(\omega - f)^2}{(\omega + f)^2} \quad (3)$$

This relation is a variation of the "rotary coefficient" originally derived by Gonella [1972].

These relationships are compared with data from the four current meters on C1 and the one on top of A2. The observed ratio of potential to kinetic energy is plotted with the theoretical relation (2) in Figure 11a. The amount of scatter of the data is reasonable when compared with the confidence limits.

The observed ratio of the rotary spectra MS_+/MS_- is plotted with the theoretical result in Figure 11b. At high frequency the agreement is good; however, this is not a very sensitive test for internal waves, since the ratio for random noise is also 1. Below about 0.16 cph there are significant deviations from the theory. One explanation is that the many waves of different horizontal wavelengths (modes) at tidal frequency are not statistically independent. If the nearby seamounts are a source of internal tide, then it is reasonable to expect the various wave numbers of the internal tide to be correlated, thereby violating one of the assumptions used in deriving (3).

4. SPECTRAL MODEL

We introduce a modified form of the Garrett-Munk internal wave model as a framework for comparing the variety of spatial and temporal measurements made during MATE. The primary alteration of the GM model is a generalization of the frequency dependence of the spectrum by adding a parameter p , which specifies the frequency spectral slope. This modification permits a closer comparison of the observations with the model. Some of the GM parameters are redefined to identify explicitly the total energy, frequency dependence, and depth scaling in the analytical expressions of the spectral quantities.

The moored spectra of both vertical displacement MS_v and

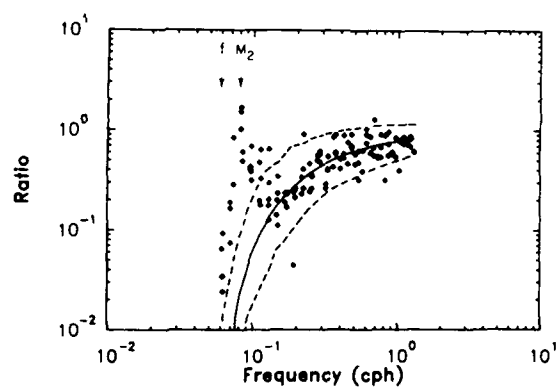


Fig. 11a

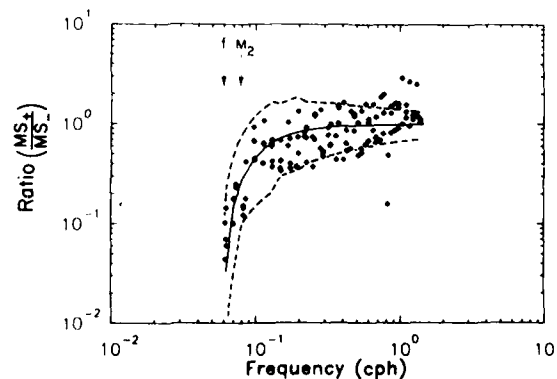


Fig. 11b

Fig. 11. (a) The ratio of potential to horizontal kinetic energy and (b) the ratio of counterclockwise to clockwise components of horizontal velocity are compared with the theoretical relationships (solid line). The data are from the four current meters on C1 and the one on top of A2. The 95% confidence limits (dashed lines) are also shown.

horizontal velocity MS_u are written in the following form:

$$MS_u(\omega) = MS_v(\omega) = \frac{\tilde{E}}{2} \left(\frac{N(z)}{\tilde{N}} \right) \left(\frac{(\Omega^2 + 1)(\Omega^2 - 1)^{-1/2} \Omega^{-p}}{Jf} \right) \quad (4)$$

$$MS_z(\omega) = \tilde{E} \left(\frac{1}{N(z)\tilde{N}} \right) \left(\frac{(\Omega^2 - 1)^{1/2} \Omega^{-p}}{Jf} \right) \quad (5)$$

where $\Omega = \omega/f$. These expressions can easily be derived from the GM formulation [e.g., Munk, 1981]. The first bracketed factor on the right-hand side of (4) and (5) represents the depth scaling referenced to frequency \tilde{N} (modified WKB approximation used by GM). The quantity \tilde{E} is the total internal wave energy per unit mass scaled to the reference frequency \tilde{N} ; quantities marked by tildes are referenced to a depth where $N(z) = \tilde{N}$. We choose \tilde{N} to be $1.74 \times 10^{-3} \text{ s}^{-1}$ (1 cph), a reasonable scale in the deep ocean. The choice of \tilde{N} is not critical, as it just serves as a common reference to compare measurements made at different buoyancy frequencies. The second bracketed term contains the frequency dependence as given by GM with the addition of the parameter p (in the GM model $p = 3$). At frequencies much greater than f , both MS_u and MS_z have ω^{-p+1} frequency dependence. The nondimensional normalization factor J is defined so that the total internal wave energy per unit mass (J kg) over all frequencies at a local buoyancy frequency of $N(z)$ is given by

$$\tilde{E}[N(z), \tilde{N}] = \frac{1}{2} \int_f^\infty [MS_u + MS_v + N^2 MS_z] d\omega \quad (6)$$

explicitly,

$$J = \int_1^\infty \Omega^2 (N^2 - 1)^{-1/2} d\Omega \quad (7)$$

Note that the contribution to the kinetic energy from the vertical velocity has been neglected in accordance with the approximation $(N^2 - \omega^2) \sim N^2$ assumed by GM (for a discussion of the model for $\omega \sim N(z)$, see Desaubies [1975]).

The energy \tilde{E} is related to the parameters of the GM model by equating total energy per unit mass [Munk, 1981],

$$[\tilde{E} \tilde{N}] N(z) = [Eb^2 N_0] N(z) \quad (8)$$

$$\tilde{E} = Eb^2 N_0 \tilde{N} \quad (9)$$

where the GM parameter E is the dimensionless energy level, b is the depth scale of $N(z)$, and N_0 is the buoyancy frequency scale. (Note that in the notation of Desaubies [1976], $r \equiv Eb^2 N_0$; hence $r = \tilde{E} \tilde{N}$.) Using the GM values of $E = 6.3 \times 10^{-5}$, $b = 1300 \text{ m}$, and $N_0 = 5.23 \times 10^{-3} \text{ s}^{-1}$ (3 cph) yields a value of $\tilde{E} = 9.7 \times 10^{-4} \text{ J kg}$.

To describe the partition of energy in wave number space, we choose the analytically convenient functional form of the GM model given by Desaubies [1976]. The GM parameter j_* , specifying the equivalent number of vertical modes, always appears in conjunction with other parameters. This combination of parameters has been defined by Desaubies [1976]

$$t = \pi j_* N_0 b = \text{m}^{-1} \text{ s} \quad (10)$$

For the GM value of $j_* = 3$, the quantity $t = 1.39 \text{ m}^{-1} \text{ s}$.

The vertical and horizontal wave number spectra of displacement can then be written as

$$DS_z(\beta) = \int_f^\infty d\omega MS_z(\omega) [(2/\pi) \beta_* (\beta_*^2 + \beta^2)^{-1}] \quad (11)$$

$$TS_z(x) = \int_f^\infty d\omega MS_z(\omega) \left[(4x_* - \pi^2) \int_0^1 \frac{d\eta}{(x_*^2 + \eta^2)(\eta^2 - x^2)^{1/2}} \right] \quad (12)$$

where x_* and β_* are the horizontal and vertical wave number scales given by $t(\omega^2 - f^2)^{1/2}$ and $t(N^2 - \omega^2)^{1/2}$, respectively [Desaubies, 1976]. The factors $[\]$ are the distribution of the energy density in wave number space at frequency ω and are normalized such that the integrals $\int [\] d\beta = 1$ and $\int [\] dx = 1$. In the TS_z , the factor $[\]$ is the sum of the energy contribution to the one-dimensional wave number x from all wave numbers greater than x in a horizontally isotropic wave field. At high wave number, $\beta \gg \beta_*$ and $x \gg x_*$, both spectra are proportional to t for any value of p :

$$DS_z(\beta) = B t \beta^{-2} \quad (13)$$

$$TS_z(x) = C t x^{-2} \quad (14)$$

where

$$B = \frac{2}{\pi} \int_f^\infty (N^2 - \omega^2)^{1/2} MS_z(\omega) d\omega \quad (15)$$

$$C = (4/\pi^2) \int_f^\infty (\omega^2 - f^2)^{1/2} MS_z(\omega) d\omega \quad (16)$$

Analytical expressions for the GM frequency dependence of $p = 3$ are

$$B = (\tilde{E}/\pi \tilde{N}) (1 - v)^2 \quad (17)$$

$$C = (8\tilde{E}/\pi^3 \tilde{N}) v [\frac{1}{2}(v^2 - 1) - \ln v] \quad (18)$$

where $v \equiv f/\tilde{N}$. For arbitrary p , values of C were evaluated analytically, while the integrals needed to calculate B required numerical integration.

The moored vertical and horizontal coherences (MVC_z and MHC_z) are independent of \tilde{E} and p . These quantities depend only on the parameter t and can be written [Desaubies, 1976]

$$\text{MVC}_z(\omega) = \exp [-(N^2 - \omega^2)^{1/2} t \Delta z] \quad (19)$$

$$\text{MHC}_z(\omega) = I_0(H) - L_0(H) \quad (20)$$

where $H = t f (\Omega^2 - 1)^{1/2} \Delta x$, Δx (Δz) is the horizontal (vertical) separation, I_0 is the modified Bessel function, and L_0 is the Struve function.

The towed vertical coherence (TVC_z) is not a function of \tilde{E} or t but in this parameterization depends only upon the vertical separation Δz and the parameter p . Modifying the expression given by Desaubies [1976] to include the parameter p , the TVC_z can be written

$$\text{TVC}_z(x; \Delta z) = \frac{1}{TS_z} \int_f^\infty d\omega MS_z(\omega) \cdot \left[(4x_* - \pi^2) \int_0^1 \frac{\cos(\theta \eta) d\eta}{(x_*^2 + \eta^2)(\eta^2 - x^2)^{1/2}} \right] \quad (21)$$

where

$$\theta = \Delta z \left(\frac{v^{-2} - \Omega^2}{\Omega^2 - 1} \right)^{1/2}$$

To evaluation for arbitrary p , numerical integration of the double integral was required.

A summary of the dependences of the statistical quantities on the parameters \tilde{E} , t , and p is presented in Table 1.

TABLE 1. Dependences of Statistical Quantities on Model Parameters

	Model Parameter			
	\bar{E}	t	$\bar{E}t$	p
MS_u	X			X
MS_v	X			X
TS_v			X	X
DS_v			X	X
MVC_v		X		
MHC_v		X		
TVC_v				X

An X indicates that the quantity is a function of that model parameter.

5. COMPARISON OF DATA WITH SPECTRAL MODEL

In this section the data presented in section 2 are compared with the theoretical formulation presented in section 4. There are three independent parameters, \bar{E} , t , and p , that must be chosen to completely specify the spectral behavior of the model. These parameters are selected to fit in an optimum way the many statistical quantities measured simultaneously during MATE. Because of the variety of measurements, several independent determinations of each parameter are possible. Both MS_v and MS_u provide estimates of \bar{E} , the moored vertical and horizontal coherences (MVC_v and MHC_v) allow estimation of t , and the DS_v and TS_v yield values of the product $\bar{E}t$ (Table 1). These quantities are all dependent upon p . The value of p can be determined directly from the slope of the frequency spectra of velocity and displacement; the TVC_v is also a function of p independent of \bar{E} and t . Consistency among estimates of \bar{E} , t , and p is then used to verify the behavior of the model.

Estimates of \bar{E} from moored spectra are found by minimizing the squared difference χ^2 between the logarithm of the observed spectrum and the logarithm of the model spectrum. Specifically,

$$\chi^2 = \frac{1}{MK} \sum_{k=1}^K \sum_{m=1}^M \left(\frac{\log S_{obs}(z_k, \omega_m) - \log S_{model}(z_k, \omega_m)}{\log [L(\omega_m)]} \right)^2 \quad (22)$$

where $S_{obs}(z_k, \omega_m)$ and $S_{model}(z_k, \omega_m)$ are the observed and model spectra, respectively, at depth z_k over a frequency band centered at ω_m . The function S_{model} for vertical displacement is MS_v (5) and for total horizontal velocity is $MS_u + MS_v$ (4). The quantity χ^2 is the average squared error over M frequency bands and K depths. The function $L(\omega_m)$ is the length of the 95% confidence band of S_{obs} ; its purpose is to give more weight to spectral estimates of higher statistical confidence [Levine et al., 1983].

The best fit values of \bar{E} as a function of p are shown in Figure 12a. These results are based on data from seven depths for displacement and five depths for velocity (883–1273 m). The fit is made over the internal wave frequency band from 0.2 to 0.7 cph; this is the center of the continuum away from the buoyancy frequency and the internal tide. The minimum squared error χ^2 occurs at $p = 2.5$ –2.7 for displacement and $p = 2.65$ –2.85 for velocity, although the precise locations of the minima are somewhat vague (Figure 12a). As a compromise, the value of $p = 2.7$ is chosen for overall best fit, and the spectral models of both displacement and velocity for this

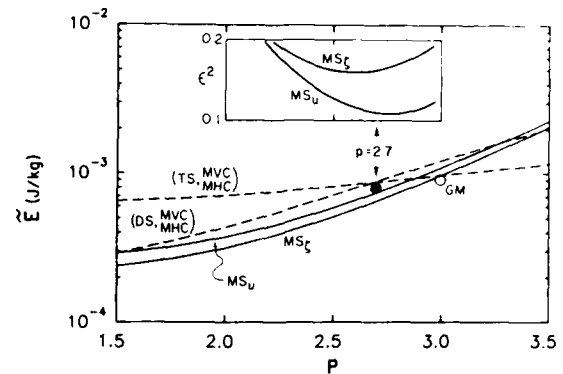


Fig. 12a

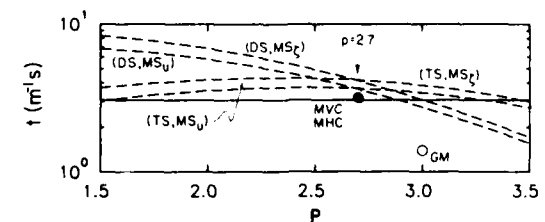


Fig. 12b

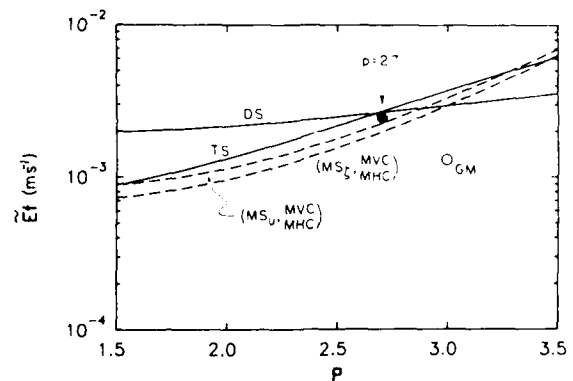


Fig. 12c

value are plotted with the observed spectra in Figures 5 and 8. It is clear from the figures that the spectral slope of $p = 2.7$ is a better fit than the $p = 3$ of the GM model. The TVC_v also provides an estimate of p independent of \bar{E} and t . The coher-

value are plotted with the observed spectra in Figures 5 and 8. It is clear from the figures that the spectral slope of $p = 2.7$ is a better fit than the $p = 3$ of the GM model. The TVC_v also provides an estimate of p independent of \bar{E} and t . The coher-

ence data compare more favorably with the value of $p = 2.7$ than the GM model value (Figure 10).

The MVC_z and MHC_z are used to determine the best value of t , since they are both independent of p and \bar{E} . The model MVC_z is also independent of frequency. Even though the observed MVC_z show significant fluctuations in frequency (Figure 6a), average values for the band 0.2–0.7 cph were calculated to compare with the model for all possible vertical separations (Figure 6b). At large vertical separations the coherence squared approaches the bias level; estimates near 0.1 are not significantly different from zero. The model results (19) are also plotted in Figure 6b for a range of values of $t = 2.5$ – $3.6 \text{ m}^{-1} \text{ s}$ and $N = 1.74$ – $2.35 \times 10^{-3} \text{ s}^{-1}$ (1.0–1.35 cph); the GM value of $t = 1.39 \text{ m}^{-1} \text{ s}$ ($j_* = 3$) is also shown. While there is large scatter in the data, it is clear that $t = 2.5$ – $3.6 \text{ m}^{-1} \text{ s}$ fits better than the GM values. The model MHC_z (20) is compared with the observations at the only horizontal separation of 332 m in Figure 7. The data are less coherent at a given frequency than predicted by the GM model. The observed horizontal coherences are remarkably consistent with the same range of t of 2.5–3.6 $\text{m}^{-1} \text{ s}$ that fits the vertical coherences. Although it is difficult to estimate a precise value of t from these coherences, the average value of $3.1 \text{ m}^{-1} \text{ s}$ is plotted in Figure 12b along with the GM result.

The product $\bar{E}t$ is estimated independently from the level of the TS_z from horizontal profiles made by SPURV, and the DS_z from vertical profiles made with the CTDSV. To fit the TS_z, the model spectral shape ω^{-2} (14) was fit to the observations, minimizing a squared error defined in an analogous manner to (20) over the wave numbers 4.7×10^{-4} to $9.0 \times 10^{-3} \text{ cpm}$ (Figure 9). The fit was not extended beyond 10^{-2} cpm because the wave number dependence of the spectrum changes, and these wavelengths are probably too small to be modeled reasonably by a linear model. The estimates of $\bar{E}t$ are plotted as a function of p in Figure 12c. A similar approach could be used to obtain $\bar{E}t$ from the DS_z; however, instead we use the results from the detailed analysis of Levine and Irish [1981]. They used the same data set and included the effects of temperature fine structure in the presence of the internal wave field. It was found that approximately 1/2 of the DS from wave numbers 0.004 to 0.05 cpm at 1013-m depth was caused by internal waves, while the remainder was temperature fine structure. Estimates of $\bar{E}t$ were obtained using their value for the level of the uncontaminated DS_z and are also plotted in Figure 12c.

The consistency among the independent estimates of \bar{E} , t , and the product $\bar{E}t$ can be checked, since any two quantities can be used to calculate the third. Direct estimates of $\bar{E}t$ from TS_z and DS_z (Figure 12c) and $t = 3.1 \text{ m}^{-1} \text{ s}$ from the MVC_z and MHC_z (Figure 12b) yield indirect estimates of \bar{E} , plotted as a dashed line in Figure 12a. Similarly, the indirect estimates of $\bar{E}t$, from direct estimates of \bar{E} and t , are displayed in Figure 12c, and indirect estimates of t , from direct estimates of $\bar{E}t$ and \bar{E} , are shown in Figure 12b. The agreement is remarkably good among all the measurements for $p = 2.7$ —better than a factor of 2.

6. DISCUSSION

To put the observations made during MATE into perspective, we briefly survey the historical set of internal wave observations. The major features of the wave field as observed in most internal wave studies can be reasonably described by the GM spectrum. The GM model serves as a benchmark that

can easily be related to other observations. Systematic discussions of the historical data are presented by Wunsch [1976], Wunsch and Webb [1979], Roth et al. [1981], and Levine et al. [1985].

In terms of total energy per unit volume, the internal wave field during MATE agrees with the GM level and falls in the middle among historical values [Levine et al., 1985]. Near steep topographic features such as Muir Seamounts, Hydrographer Canyon [Wunsch, 1976], and Hudson Canyon [Hotchkiss and Wunsch, 1982] the energy in the wave fields is significantly higher by a factor of 2–50 than the GM level. At MATE the effect of the nearby seamounts (9 km away) on the background energy is apparently not significant.

The frequency spectral slope ω^{-p-1} in the internal wave band at $\omega > f$ was found to be consistent with $p = 2.7$. This is slightly less steep than the canonical GM value of $p = 3$. However, other studies have noted that a dependence less steep than ω^{-2} generally fits moored spectral data better [e.g., Wunsch, 1976; Levine et al., 1983]. The modified GM model allows the variation of the parameter p to be tested by all relevant statistical quantities, not just the slope of the frequency spectrum itself; there is significant improvement between data and theory at MATE with $p = 2.7$.

The parameter t , which is directly related to the equivalent number of modes j_* , sets the wave number bandwidth in the GM model. At MATE the best fit value of $t = 3.1 \text{ m}^{-1} \text{ s}$ ($j_* = 6$) is a factor of 2 higher than the canonical GM value. There are not many accurate determinations of t , so the number of good comparisons are limited. The best comparison is with the results from the extensive measurements made during the Internal Wave Experiment (IWEX) [Briscoe, 1975; Müller et al., 1978]. The IWEX model allows t to be a function of frequency. To examine results from models with slightly different parameterizations, it is most useful to use "equivalent bandwidth" when comparing results [see Müller et al., 1978, p. 492]. The IWEX results, when converted to units of t , show a decrease from $t = 3.3 \text{ m}^{-1} \text{ s}$ ($j_* = 6.4$) at low frequency to $t = 1.7 \text{ m}^{-1} \text{ s}$ ($j_* = 3.2$) near N . In the frequency band where the MATE data were fit, above the tide and below N , the IWEX value of $t = 2.4 \text{ m}^{-1} \text{ s}$ ($j_* = 4.7$) falls between the MATE and GM value. If a value of t had been estimated at high-frequency near N for MATE, a lower value of t would result due to the high coherence near N (Figure 6). This feature is consistent with the decrease in t at high frequency in the IWEX model.

The modified GM model presented here is still admittedly crude—only three parameters to define the statistics of the internal wave field. However, it does permit a more accurate representation of the internal wave field at MATE than the GM model. The formalism can also be applied to other observations where the frequency spectral slope differs from ω^{-2} .

The spectral description of the internal waves at MATE may provide useful information to theoreticians seeking the best kinematic formulation of the wave field to test theories of internal wave dynamics. During the last 10 years there has been considerable effort in trying to understand the dynamics of a random sea of internal gravity waves. A variety of theoretical techniques have been used to study nonlinear interactions among internal waves (see West [1981] and Müller et al. [1986] for reviews of the topic). To relate their results to the ocean, some form of the GM model is usually used as the base state of the oceanic internal wave field. Transfers among wave components in frequency wave number space by nonlinear interaction are then estimated. If a different base state of the

internal wave field were chosen, such as that found during MATE, then some of the theoretical results may be modified. However, due to the complexity of these theories, further investigation is necessary to determine if the modifications would be significant.

Little has been mentioned about the effect of noninternal wave fine structure on the results of this analysis. From the detailed study of temperature fine structure by Levine and Irish [1981], we conclude that the moored vertical displacement spectrum MS_v is essentially uncontaminated by fine structure. The internal wave signal was found to be a factor of 10 higher than the fine structure contamination in the internal wave frequency band; this agrees quantitatively with the results from IWEX [Müller *et al.*, 1978]. The moored vertical coherences MVC_v also were found to be unaffected by fine structure at vertical separations greater than 10 m. However, the effects of fine structure are significant at high wave numbers in estimates of dropped spectra DS_v inferred from temperature measurements, and this effect has been taken into account. No estimate of the importance of current fine structure in the velocity observations has been made. However, if we apply the results from IWEX to the MATE data, then the contamination in the moored velocity spectrum MS_u is a factor of 2–3 below the internal wave signal over most of the internal wave frequency band. Near N , however, the fine structure effects may actually dominate. If one uses this estimate of current fine structure and removes it from our spectral estimates, the effect on the overall fit would be relatively small and would not significantly affect our conclusions.

7. SUMMARY AND CONCLUSION

The unique feature of the MATE internal wave study was the acquisition of towed and dropped measurements simultaneously with moored observations. This permits careful examination of internal wave statistics in frequency and vertical and horizontal wave number. A generalized formulation of the Garrett-Munk spectral model was used as a framework for comparing these diverse observations. In this modified version of the GM model, three parameters, p , \bar{E} , and t , are needed to specify the entire spectral behavior. The parameter p sets the frequency dependence; the spectral behavior for both horizontal velocity and vertical displacement is ω^{-p-1} at $\omega > f$. The quantity \bar{E} is the total energy of the internal wave field per unit mass at the reference buoyancy frequency N ; it appears as a factor in the expression for all spectral quantities ((4), (5), (11), (12)). We choose the value of $N = 1.74 \times 10^{-3} \text{ s}^{-1}$ (1 cph) as a reasonable scale. The parameter t sets the wave number bandwidth of the wave field, thereby controlling the spatial coherence scales and the vertical and horizontal wave number spectra. Expressed in terms of the GM parameters E , h , and j_* ,

$$\bar{E} N = E h^2 N_0$$

$$t = \pi j_* N_0 h$$

This model would be useful to apply to other observations where the value of p differs from the GM value.

Independent observations made during MATE were used to determine \bar{E} , t , and the product $\bar{E}t$, directly. The best fit of the data to the spectral model is summarized in Figure 12 as a function of p . The directly determined value of \bar{E} , from moored spectra of displacement and velocity, had the least error ± 2 for a value of $p = 2.7$, significantly less than the GM value of $p = 3$ (Figure 12a). However, the value of $\bar{E} = 8$

$\times 10^{-4} \text{ J kg}^{-1}$ at $p = 2.7$ is in good agreement with the GM model (about 10% lower). Indirectly inferred values of \bar{E} from estimates of t and $\bar{E}t$ from coherences and wave number spectra are consistent with the directly measured \bar{E} (Figure 12a).

The directly determined value of t from the moored coherences is independent of p and estimated to be $3.1 \text{ m}^{-1} \text{ s}$ (Figure 12b). This is about a factor of 2 larger than the GM value (equivalent to a $j_* = 6$ in the GM model). Indirectly inferred values of t from directly determined $\bar{E}t$ and \bar{E} are consistent and distinctly higher than the GM level.

Direct measurements of $\bar{E}t$ from both vertical and horizontal wave number spectra are nearly equal at $p = 2.7$ (Figure 12c). Indirect estimates are consistent and about twice the GM value.

An independent verification of the parameterization of the internal wave field is provided by the acoustic experiment. MATE was a unique experiment, designed to test our ability to relate observed internal wave fluctuations to simultaneously measured acoustic variability. The acoustic experiment consisted of observations of pulses at 2, 4, 8, and 13 kHz, transmitted over a fixed 18.1-km path between towers anchored on the two seamounts. The data were reduced to time series of pulse amplitude and travel time. The temporal fluctuations of the acoustic signals were due primarily to the oscillations of the sound speed field caused by tides, internal waves, and fine structure. The statistical description of the internal wave field presented here is used as input to acoustic theories, which can then be verified using the observed amplitude and travel time statistics. The observed travel time fluctuations agree well with the predictions using the description of the internal waves provided by the MATE model [Ewart and Reynolds, 1984]. There is significant improvement using the spectral slope $p = 2.7$ and bandwidth $t = 3.1 \text{ m}^{-1} \text{ s}$ ($j_* = 6$) compared with the canonical GM values. This independent sampling of the wave field increases confidence in the validity of the MATE model.

There are perhaps two perspectives with which to view these results. The internal wave specialist would stress the deviations from the GM model: (1) frequency spectral slope $\omega^{-1.7}$ ($p = 2.7$) at high frequency rather than ω^{-2} ($p = 3$) and (2) value of t about twice the GM value ($j_* = 6$). Certainly deviations from the GM model, of this magnitude and larger, have been reported previously [e.g., Wunsch and Webb, 1979]. But often only one or two types of measurements are available, and usually it cannot be determined if the deviations are consistent with internal waves or due to some other processes. Because of the variety of towed, dropped, and moored observations at MATE, the parameters were evaluated from independent measurements and found to be consistent with the kinematics of internal waves.

The generalist would note that the observations are still remarkably similar to the GM "universal" spectrum that was originally derived from fits to data taken at vastly different times and places. From this viewpoint the experiment can be seen as contributing another piece of evidence to better define the internal wave climatology. It is perhaps surprising that the deviations are so small given that MATE was a single experiment lasting less than 1 month in a unique topographic setting.

Acknowledgments. We profited from the advice and help of our colleague Yves Desaubies. The technical assistance of Le Olson and Art Pederson made the experiment a success. Thanks are also due to all the other MATE participants from the Applied Physics Labora-

tory, University of Washington, and the officers and crew of the USNS *DeSteiguer*. MATE was funded by the Office of Naval Research (contract N00017-74-C-1208) and the Naval Sea Systems Command (contract N00017-71-C-1305). Support for M. Levine for manuscript preparation was supplied by the Office of Naval Research under contracts N00014-79-C-0004 and N00014-84-C-0218.

REFERENCES

- Baines, P. G., On internal tide generation models, *Deep Sea Res.*, 29, 307-338, 1982.
- Bingham, C., M. D. Godfrey, and J. W. Tukey, Modern techniques of power spectrum estimation, *IEEE Trans. Audio Electroacoust.*, 2, 56-66, 1967.
- Briscoe, M. G., Preliminary results from the tri-moored Internal Wave Experiment (IWEX), *J. Geophys. Res.*, 80, 3872-3884, 1975.
- Carter, G. C., C. H. Knapp, and A. H. Nuttall, Estimation of the magnitude-squared-coherence function via overlapped fast Fourier transform processing, *IEEE Trans. Audio Electroacoust.*, AU-21, 337-344, 1973.
- Desaubies, Y. J. F., A linear theory of internal wave spectra and coherences near the Vaisala frequency, *J. Geophys. Res.*, 80, 895-899, 1975.
- Desaubies, Y. J. F., Analytical representation of internal wave spectra, *J. Phys. Oceanogr.*, 6, 976-981, 1976.
- Eriksen, C. C., Observations of internal wave reflection off sloping bottoms, *J. Geophys. Res.*, 87, 525-538, 1982.
- Ewart, T. E., Acoustic fluctuations in the open ocean: A measurement using a fixed refracted path, *J. Acoust. Soc. Am.*, 60, 46-59, 1976.
- Ewart, T. E., and S. A. Reynolds, The mid-ocean acoustic transmission experiment, MATE, *J. Acoust. Soc. Am.*, 75, 785-802, 1984.
- Ewart, T. E., J. D. Irish, and L. O. Olson, The MATE experiment: A preliminary report, *APL-UW Tech. Note 7-77*, Appl. Phys. Lab., Univ. of Wash., Seattle, 1977.
- Fofonoff, N., Spectral characteristics of internal waves in the ocean, *Deep Sea Res.*, 16, 58-71, 1969.
- Garrett, C. J. R., and W. H. Munk, Space-time scales of internal waves, *Geophys. Fluid Dyn.*, 2, 225-264, 1972.
- Garrett, C. J. R., and W. H. Munk, Space-time scales of internal waves: A progress report, *J. Geophys. Res.*, 80, 293-297, 1975.
- Gonella, J., A rotary-component method for analyzing meteorological and oceanographic vector time series, *Deep Sea Res.*, 19, 833-846, 1972.
- Hotchkiss, F. S., and C. Wunsch, Internal waves in Hudson Canyon with possible geological implications, *Deep Sea Res.*, 29, 415-442, 1982.
- Larsen, L. H., and J. D. Irish, Tides at Cobb Seamount, *J. Geophys. Res.*, 80, 1691-1695, 1975.
- Levine, M. D., Internal waves in the ocean: A review, *Rev. Geophys. Space Phys.*, 21, 1206-1216, 1983.
- Levine, M. D., and J. D. Irish, A statistical description of temperature fine structure in the presence of internal waves, *J. Phys. Oceanogr.*, 11, 676-691, 1981.
- Levine, M. D., R. A. de Szoeke, and P. P. Siler, Internal waves in the upper ocean during MILE, *J. Phys. Oceanogr.*, 13, 240-257, 1983.
- Levine, M. D., C. A. Paulson, and J. H. Morrison, Internal waves in the Arctic Ocean: Comparison with lower latitude observations, *J. Phys. Oceanogr.*, 15, 800-809, 1985.
- Müller, P., D. J. Olbers, and J. Willebrand, The IWEX spectrum, *J. Geophys. Res.*, 83, 479-500, 1978.
- Müller, P., G. Holloway, E. Henyey, and N. Pomphrey, Nonlinear interactions among internal gravity waves, *Rev. Geophys.*, 24, in press, 1986.
- Munk, W. H., Internal waves and small-scale processes, in *Evolution of Physical Oceanography*, edited by B. A. Warren and C. Wunsch, pp. 264-290, MIT Press, Cambridge, Mass., 1981.
- Olbers, D. J., Models of the oceanic internal wave field, *Rev. Geophys. Space Phys.*, 21, 1567-1606, 1983.
- Roth, M. W., M. G. Briscoe, and C. H. McComas III, Internal waves in the upper ocean, *J. Phys. Oceanogr.*, 11, 1234-1247, 1981.
- West, B. J. (Ed.), *Nonlinear Properties of Internal Waves*, 351 pp., American Institute of Physics, New York, 1981.
- Widditsch, H. R., SPURV, The first decade, *APL-UW Rep. 7215*, Appl. Phys. Lab., Univ. of Wash., Seattle, 1973.
- Wunsch, C., Geographical variability of the internal wave field: A search for sources and sinks, *J. Phys. Oceanogr.*, 6, 471-485, 1976.
- Wunsch, C., and S. Webb, The climatology of deep ocean internal waves, *J. Phys. Oceanogr.*, 9, 235-243, 1979.

T. E. Ewart and S. A. Reynolds, Applied Physics Laboratory, University of Washington, Seattle, WA 98105.

J. D. Irish, University of New Hampshire, Durham, NH 03824.

M. D. Levine, College of Oceanography, Oregon State University, Corvallis, OR 97331.

(Received November 30, 1985;
accepted February 3, 1986.)

Coastal-Trapped Waves on the East Australian Continental Shelf Part I: Propagation of Modes

JOHN A. CHURCH, HOWARD J. FREELAND* AND ROBERT L. SMITH**

Division of Oceanography, CSIRO Marine Laboratories, Hobart, Tasmania 7001 Australia

(Manuscript received 22 November 1985, in final form 16 May 1986)

ABSTRACT

The currents observed over the shelf and slope during the Australian Coastal Experiment (ACE) are used to determine the amplitudes (as functions of time) of the first three coastal-trapped wave (CTW) modes at three locations along the southeast coast of Australia. A statistical "eddy" mode is included to minimize contamination of the coastal-trapped wave currents from East Australian Current eddies. The first three CTW modes account for about 65% of the observed variance in the alongshelf currents on the shelf and slope at Cape Howe, about 40% at Stanwell Park, but only about 24% at Newcastle. Currents associated with the East Australian Current dominate the observations offshore from Newcastle. CTWs account for all but 10%, 37% and 27% of the currents observed at the most nearshore locations on the shelf at Cape Howe, Stanwell Park and Newcastle. The first two coastal-trapped wave modes propagate at close to the appropriate theoretical phase speeds, but the third coastal-trapped wave mode and the eddy mode are not coherent between the three current meter sections along the coast. Surprisingly, mode 2 carries a greater fraction of the coastal-trapped wave energy than does mode 1 at two of the sections. Modes 1 and 2 are coherent with each other at the 95% significance level. The major energy source for the CTWs is upstream (in the CTW sense) of the first line of current meters.

1. Introduction

Since the early observational work of Hamon (1962) and the explanation of these observations as continental shelf waves (Robinson, 1964), there have been extensive theoretical developments and numerous observations of alongshore propagation of sea level and current perturbations (see Mysak's, 1980, review). However, until the Australian Coastal Experiment (ACE) of 1983/84, no specific search was made for the alongshelf propagation of coastal-trapped wave (CTW) modes. All earlier studies of CTWs assumed that the first mode was dominant. The only attempt to fit the dynamic modes to data was made by Hsieh (1982a,b). In fitting barotropic dynamic modes to the data off Oregon, Hsieh (1982a) found the second mode to be dominant. However, this result is disputed by Denbo and Allen (1984). Yao et al. (1984) attempted to fit baroclinic modes to data off Vancouver Island, but the modes could not be unambiguously identified because the database was inadequate.

The Australian Coastal Experiment, described in Freeland et al. (1986), was specifically designed to search for CTWs. Freeland et al. (1986) use the ACE

data to identify, in the frequency domain, the first three CTW modes at each of three locations along the southeastern coast of Australia. They use the phase difference between the eigenfunction amplitudes at different locations to construct a dispersion diagram for the first three CTW modes. Although these dispersion curves are somewhat steeper than the theoretical curves, they are convincing evidence for the presence of the first three CTW modes. In contrast to the local wind-driven CTWs described by Clarke and Thompson (1984), Freeland et al. (1986) found the ACE region to be dominated by free waves originating further back along the wave guide but modified by the local winds. For the Freeland et al. analysis to work, the response must be dominated by free waves as any local wind forcing will introduce a bias into their results.

In this paper, we use the ACE dataset to determine the amplitude of CTW modes at three locations off southeastern Australia and to look for alongshelf propagation of these modes. The theory used in this paper and in Part II (Church et al., 1986, hereafter referred to as Part II) is summarized in the Appendix, and the data is briefly described in section 2. The observed alongshelf currents are expanded in terms of the first three CTW eigenfunctions and a statistical "eddy mode" for each of three current meter sections, and for each half day of the six-month record (section 3). Note that, unlike Freeland et al. (1986), we determine the amplitude of the first three CTW modes in the time

* Permanent affiliation: Institute of Ocean Sciences, Sidney, British Columbia V8L 4B2, Canada.

** Permanent affiliation: College of Oceanography, Oregon State University, Corvallis, OR 97331.

domain rather than the frequency domain. Our different method of analysis, which gives results slightly different from those of Freeland et al., allows us to examine the relationships between the various CTW amplitudes and their relationships with the observed alongshelf wind stress. Two other reasons for completing this analysis in the time (rather than the frequency) domain is that the model amplitudes are needed for boundary conditions for a time domain model (Part II) and because we feel this method is less biased by local wind forcing than are the results of Freeland et al. In section 4, cross spectra between the modal amplitude time series are used to derive the dispersion curves for the first two CTW eigenfunctions and to show that the eddy mode does not propagate along the shelf. The fact that the resultant dispersion curves are not significantly different from the theoretically expected curves is a valuable confirmation of CTW theory and indicates that the modal decomposition does provide meaningful results. In Part II, we use these amplitudes as boundary conditions for a CTW model and show that this CTW model does have predictive skill on the shelf.

2. The observed current, pressure and wind stress field

The main ACE array consisted of three sections of current meters (each with five moorings and each having a total of 15 current meters) offshore from Cape Howe, Stanwell Park and Newcastle (Fig. 1a). The designed placement of the current meters on each section is shown in Fig. 1b. The actual depths of the moorings were within 15% of these nominal depths with most moorings being closer than this. We shall refer to the three sections of current meters as line 1 (Cape Howe), line 2 (Stanwell Park) and line 3 (Newcastle). The current meters are coded as in this example: f23/1000 (f refers to lowpass filtered data) is a meter at a depth of 1000 m on the third mooring from the coast on line 2. The current meter sections are nominally identical, and the current meters were distributed so that the first three CTW modes could be separated. The meters are not, therefore, clustered close to the coast but are closer to the shelf edge and slope where the CTW modes exhibit sign changes. By having three current meter sections, we hoped to see CTW modes propagating along the coast and check these propagation speeds against theoretical predictions.

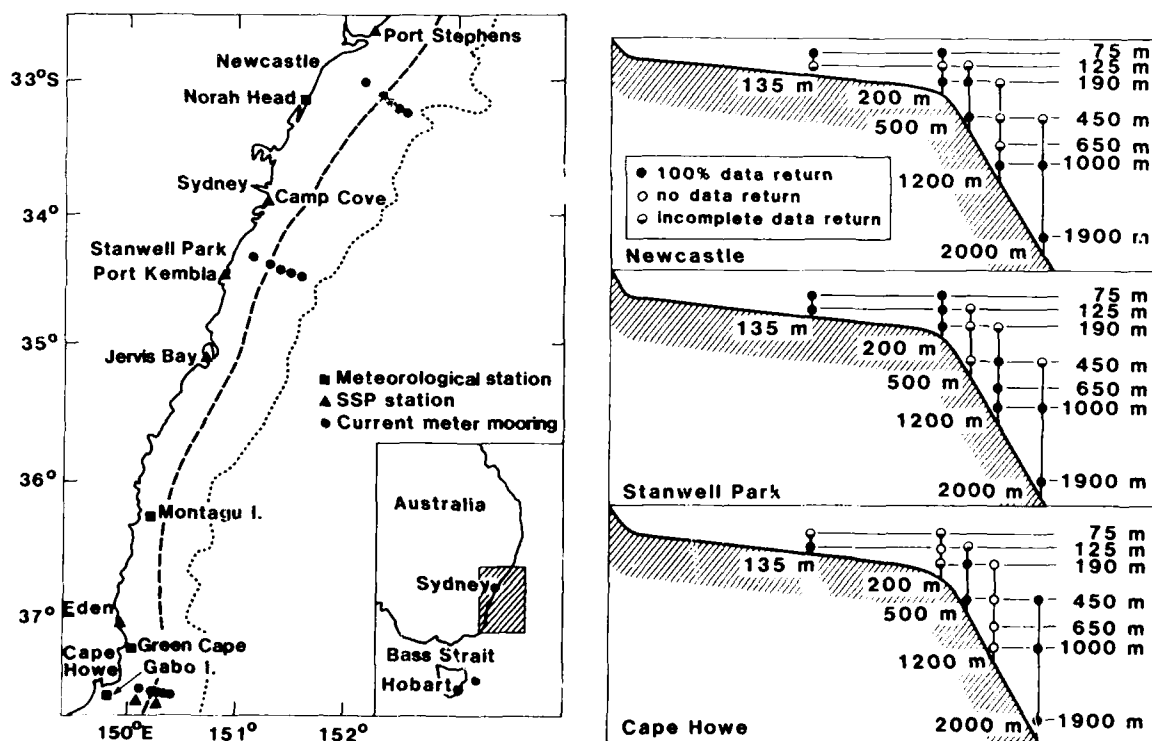


FIG. 1. Location diagram for the Australian Coastal Experiment. (a) The locations of the current meter moorings, SSP records and stations where meteorological data were collected. The sole mooring at 42°40'S on the east coast of Tasmania is shown on the inset. The dashed line is the 200 m isobath and the dotted line is the 4000 m isobath. (b) Schematic (not to scale) diagram of the locations of current meter sections at the sections of Cape Howe, Stanwell Park and Newcastle. A solid circle indicates 100% data return, an open circle zero data return, and a half shaded circle indicates an incomplete record. Accurate bottom profiles are given in Fig. 3.

Some data was lost due to trawlers moving moorings, extreme currents causing large tilt in some of the mooring lines, and the total loss of one mooring. How the raw data was processed, together with notes on the data collected, is given in Freeland et al. (1985). The data used here have been lowpass filtered (half-power point at about 40 h) and decimated to one value every 12 h. The principal axis of variance for all of the current meter records was almost parallel to the alongshelf direction, and we have used only the alongshelf component of the current throughout the analysis that follows.

Coastal sea level data was collected for ACE from six locations along the coast. The analogue sea level charts were digitized to hourly values, lowpassed, decimated to noon and midnight values, and corrected for atmospheric pressure variations to give subsurface pressure (SSP). Data are also available from two subsurface pressure gauges offshore from Cape Howe. These gauges, which were near the first and third moorings, will be referred to as fp11 and fp13. The details of the routine data processing and of the data available are given in Forbes (1985a).

Meteorological data from 16 stations were obtained from the Australian Bureau of Meteorology. For 12 of these stations, data were recorded twice daily at 0900 and 1500 LST, and for four stations, the data were recorded at 3-h intervals. All of the data were interpolated, filtered and decimated to noon and midnight values, and the principal components of variance of the wind stress determined. The wind stresses were calculated using the neutral steady-state drag coefficient of Large and Pond (1981). Meteorological data from three buoys moored at midshelf are also available. While these data were not continuous over the ACE period, they did indicate that the alongshelf wind stress did not vary significantly across the shelf (Forbes, 1986). We selected three stations that provided continuous data during ACE and that we thought to be representative of the wind stress field. The three stations—Green Cape, Montagu Island and Norah Head (Fig. 1)—are used in the application of the CTW theory (Part II). Details of the data and the wind field over the ACE region are discussed by Forbes (1985b, 1986).

The twice daily alongshelf current and sea level data were highpassed to decrease the amplitude of signals with periods greater than about 20 days. To achieve this, the individual series were Fourier transformed, the amplitude of the Fourier coefficients with periods greater than 20 days were set to zero, and the new highpassed series in the time domain were generated. Spectral results (using a different bandwidth) indicate that this filter passes a small amount of energy at periods of 24 days and has no effect at higher frequencies. Unless otherwise stated, all series (except the surface wind stress) were subjected to this highpassing before further analysis.

3. Eigenfunction representation of the observed currents

The currents at Cape Howe (and also the other sections) are due not only to CTWs but also to a number of other phenomena. The most important of these is eddies formed from the East Australian Current, and there were periods at all three current meter sections when offshore eddies had a strong effect on the shelf and slope currents. (A paper on these eddies is in preparation.) To determine the amplitude of the CTWs, we decomposed the observed currents in terms of the first three CTW eigenfunctions (section 3a) as well as a statistically defined eddy mode (section 3b).

The decomposition of the observed currents into the CTW eigenfunctions and the eddy mode was done in the time domain and used separate CTW modes and eddy modes at each of the current meter sections. This differs from the analysis of Freeland et al. (1986) in which the decomposition was done in the frequency domain, using a single set of eigenfunctions for all of the sections.

a. Density field and eigenfunction calculations

The density data during ACE were collected with a Neil Brown Mark 3 CTD along several sections perpendicular to the coast and along sections through offshore eddies [602 stations were completed during ACE (White and Church, 1986)]. The three current meter sections were the most often repeated: Cape Howe (6 times), Stanwell Park (14) and Newcastle (7). To allow the CTW eigenfunctions F_j (for the pressure field), the phase speeds c_j , the associated wind b_j , and frictional coupling coefficients (a_j) to change as the bathymetry and Brunt-Väisälä frequencies change with alongshelf distance, we calculated the eigenfunctions (and associated phase speeds and coupling coefficients) at these three sections.

The processing of the raw CTD data to 2-db averaged data is discussed by White and Church (1986). These 2 db data were averaged to determine 10 db data, and an average density section (over the ACE period) was calculated for the three locations. As the Brunt-Väisälä frequency profile varied slightly in the cross-shelf direction, an artificial profile was constructed for each section. This profile consisted of the profile at a midshelf location (depth 135 m), joined to a profile at the outer end of the section. Below the depth of the CTD data (1500 db), the Brunt-Väisälä frequency was assumed to decrease exponentially with a depth scale of 1.5 km. The profile at each of the sections (Fig. 2) agreed with the historical data presented by Levitus (1982). The profiles in the upper 1500 m are quite similar at Newcastle and Stanwell Park, but at Cape Howe the large peak in the near surface layers is absent.

The bottom profiles at the three locations, deter-

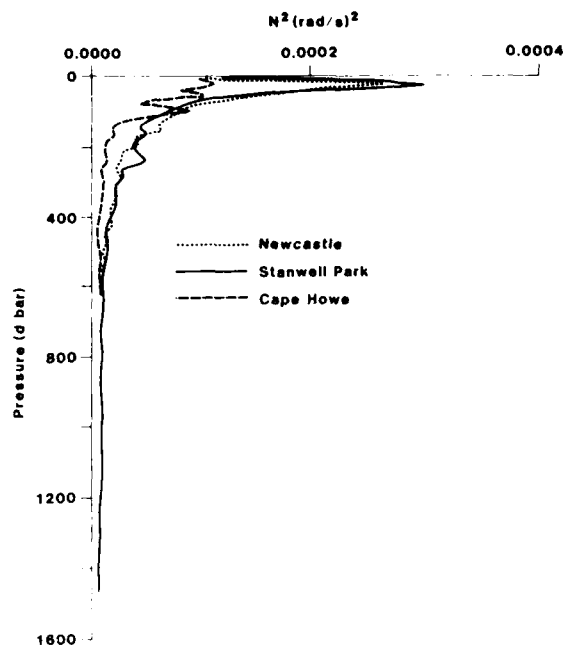


FIG. 2. The N^2 profile used in determining the CTW eigenfunctions at Cape Howe, Stanwell Park and Newcastle. Below 600 db all curves are very similar and to avoid confusion only one is drawn.

mined from charts and depth data recorded on each of the cruises during ACE, are shown in Fig. 3. Although the three profiles have a similar shape, there are considerable differences in the width of the shelf.

The CTW eigenfunctions $F_j(x, z)$ and the eigenvalues c_j were found by solving Eqs. (A5) using a numerical technique. (The program was generously supplied by Dr. K. Brink; the basis of the technique is outlined in

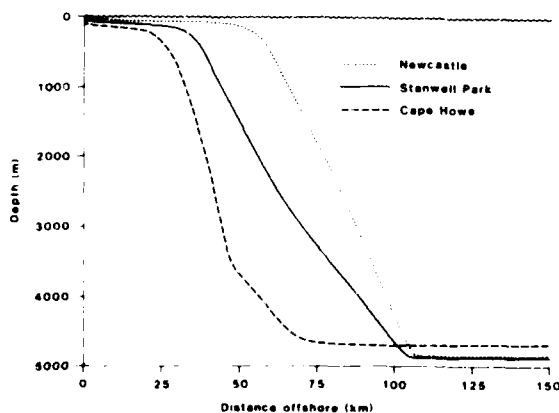


FIG. 3. The depth profile used in determining the CTW eigenfunctions at Cape Howe, Stanwell Park and Newcastle.

Brink and Chapman, 1985.) The numerical technique replaces the $x = \infty$ boundary condition with the condition that, at a large distance L from the coast, the x -derivative of the velocity normal to the coast is zero. This is a good approximation if the outer boundary is at least one deep-water Rossby radius beyond the bottom of the continental slope. We chose a value of $L = 150$ km to satisfy this condition. The grid is regular in the x -direction and stretched in the z -direction. We used a grid with 63 points in the x -direction and 23 points [between $z = 0$ and $z = -h(x)$] in the z -direction. The linear drag coefficient r was evaluated from $r = C_D |U_s|$ when C_D is a quadratic drag coefficient (of value 2.5×10^{-3}) and $|U_s|$ is a scale velocity (of value 0.2 m s^{-1}). The eigenfunctions were normalized such that for unit amplitude the energy flux was 1 erg s^{-1} .

The theoretical dispersion curves for the first three CTW modes at the three sections are shown in Fig. 4. For the purpose of comparing the theoretical curves with the observations, we shall ignore their very slight curvature and use the low wavenumber, low frequency limit. The first mode phase velocities increase from 3.2 m s^{-1} at Cape Howe to 4.0 m s^{-1} at Stanwell Park and 5.2 m s^{-1} at Newcastle. The corresponding phase velocities for mode 2 (and 3) are 1.77 (0.97), 2.15 (1.27) and 2.43 m s^{-1} (1.24 m s^{-1}), respectively, and are given with their respective eigenfunctions in Fig. 5. The increase in the phase speeds is due to the increased stratification in the north and also to the increased shelf width.

The calculated CTW eigenfunctions for the along-shelf current [$G_j(x, z)$] for the first three modes at the three current meter sections are shown in Fig. 5. We completed a number of sensitivity tests for variations

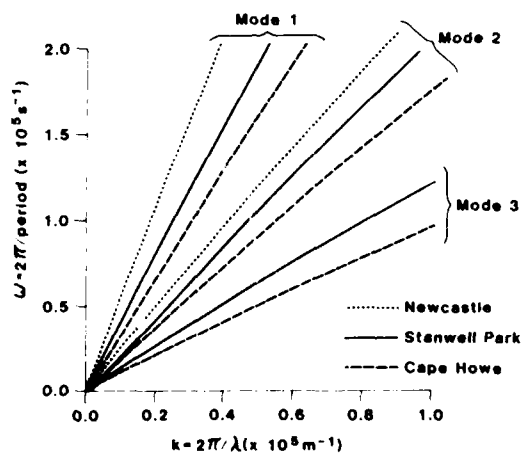


FIG. 4. Theoretical dispersion curves. The theoretical dispersion curves for CTW modes 1, 2 and 3 are given for the three current meter sections. For mode 3, the dispersion curves at Stanwell Park and Newcastle are almost identical.

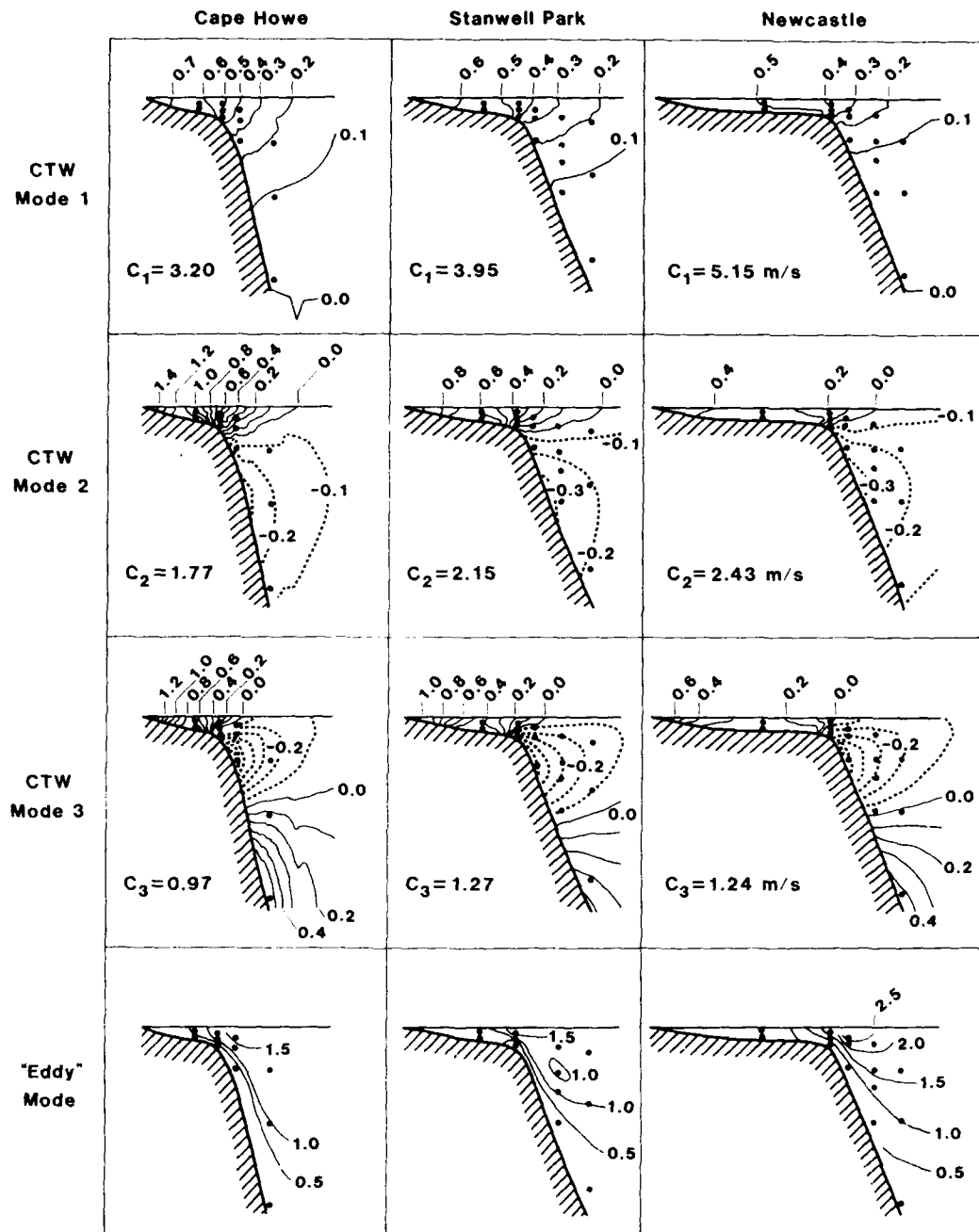


FIG. 5. The eigenfunctions. The first three theoretically determined CTW eigenfunctions and the statistically determined "eddy" mode for the current meter sections at Cape Howe, Stanwell Park and Newcastle are shown. The contouring is in arbitrary units.

in the depth profile $h(x)$ and the stratification $N^2(z)$. The results indicated that the eigenfunctions and the phase velocities were not sensitive to small changes in

the depth or stratification profiles (such as might be produced by inaccuracies in the data or local variations in the shelf conditions).

b. The statistical eddy mode

To define the eddy mode, we follow the technique of Freeland et al. (1986) and initially assume that currents $V_e(t)$ measured at 1000 m depth at the furthest offshore mooring at each of the sections (i.e., current meter n5/1000) are due primarily to eddies. This is a reasonable approach, as CTWs are trapped near the shelf and, relative to eddies, are not large far offshore and at depth. In contrast, eddies strongly affect the offshore region, and the density perturbation associated with eddies reaches to depths well in excess of 1000 m (Nilsson and Cresswell, 1981). Given this assumption, currents at any location on this section that are correlated with $V_e(t)$ are then assumed to be associated with eddies and not CTWs. The values $a(x, z)$ that minimize the mean square error

$$E = [V(x, z, t) - a(x, z)V_e(t)]^2 \quad (3.1)$$

define the distribution of eddy signal, which we interpret as a statistical eddy eigenfunction. The eddy eigenfunctions (Fig. 5) have their maximum amplitude offshore and near the surface. Their amplitudes decay towards the coast and with increasing depth. The eddy eigenfunctions at the three sections (Fig. 5) are quite similar to each other but are very different from the dynamical CTW eigenfunctions that have their maxima on the shelf and near the bottom. We believe that our results are not sensitive to the exact values chosen for the eddy eigenfunctions. The tendency for the eddy modes to increase in amplitude offshore ensures that they are badly matched to any CTW activity and so they should readily absorb energy associated with the eddy field. Rather than using the whole record to determine the eddy eigenfunctions, an alternative approach is to look at the current distributions across a section when a large eddy is present. We have done this for the Stanwell Park section, with results very similar to those we obtained using the above procedure.

c. Determination of the amplitude of the eigenfunctions

Having now defined a statistical eddy mode, we shall relax the assumption that the currents measured at locations n5/1000 are due solely to eddies and determine the amplitudes of the eigenfunctions in a least-squares sense.

The theoretical solution for the alongshelf currents of CTWs [see Eq. (A7)] is a sum over an infinity of modes. In practice, this sum has to be truncated at a finite number M , i.e.,

$$v(x, y, z, t) = \sum_{j=1}^M G_j(\cdot, z)\phi_j(y, t). \quad (3.2)$$

Even though the ACE dataset is large, the determination of the amplitude of the CTW modes is not trivial.

From the limited data available at any of the sections, we initially decided that we could, at best, determine the amplitude of only three CTW eigenfunctions and one statistical eddy eigenfunction, so $M = 4$. The amplitudes of the eigenfunctions are the solutions ϕ of

$$\mathbf{G}\phi = \mathbf{v}, \quad (3.3)$$

where the nj th element of the matrix \mathbf{G} is the value of the alongshelf current component of the j th eigenfunction ($j = 1$ to 4) at the n th ($n \leq 15$) current meter location on each section. The ϕ that satisfies this equation such that the residual is minimized (in the least-squares sense) is the Moore-Penrose solution:

$$\phi = (\mathbf{G}^t\mathbf{G})^{-1}\mathbf{G}^t\mathbf{v}. \quad (3.4)$$

A more stable solution is found by using a singular value decomposition i.e.,

$$\phi = \sum_{i=1}^R \frac{(\mathbf{G}^t\mathbf{v}) \cdot \mathbf{q}_i}{\lambda_i} \mathbf{q}_i, \quad (3.5)$$

where \mathbf{q}_i and λ_i are the eigenvectors and eigenvalues of the matrix $\mathbf{G}^t\mathbf{G}$ and R is the effective rank of the matrix ($R \leq 4$). $R = 4$ corresponds to the unstable Moore-Penrose solution. Equation (3.3) is badly conditioned, and even with the large amount of data available from the ACE array, the Moore-Penrose solution is unstable. The fact that the eigenvalues appear in the denominator of Eq. (3.5) is the reason why the Moore-Penrose solution is unstable. The eigenvectors and eigenvalues are slightly different for each line and also vary as gaps appear and disappear in the data. There are, in general, eigenvalues near 2%, 10%, 35% and 55% of the value of the trace of the matrix. The value of 2% is close to the accuracy of individual current meters, and the total experimental inaccuracy is certainly much greater than 2%. (See the residual variances at the end of the next paragraph.)

To choose the appropriate value of R , we carried out a series of tests using the data from the Cape Howe section. For the complete time series, we evaluated the residual variance and the variance of the solution for different values of R . At Cape Howe, as R was decreased from 4 to 3, the residual variance increased from about 10% to 13% of the observed currents, but the variance of the solution decreased by a factor of 3 (and a factor of 7 for mode 1). Further decreases in the value of R caused larger increases in the residual variance but less rapid change in the variance of the solution. Also, for each regression (at half day intervals), we applied F tests to see whether or not inclusion of a particular eigenvector significantly reduced the residual variance. The tests indicate that the smallest eigenvector is only significant (at the 95% level) in about 10% of the regressions, the second smallest eigenvector is significant in about 14% of the regressions, the third eigenvector is significant in about 30% of the regressions.

and the largest eigenvector is significant in about 43% of the regressions. The times at which no eigenvectors are significant correspond to times of small currents. On the basis of these tests, we omitted the smallest eigenvector from the solution and set $R = 3$. Note that omitting an eigenvector does not mean a particular mode is omitted, but rather a particular linear combination of modes is not allowed. The second smallest eigenvector is probably only marginally significant to the total solution. For $R = 3$, the residual variance, averaged over the total time series, is about 13% of the observed variance at Cape Howe, about 20% of Stanwell Park and about 23% at Newcastle; i.e., the least-squares fit to the observed currents accounts for at least 77% of the observed variance at each of the three sections.

The observed alongshelf currents are compared to the sum of the fitted modes for Cape Howe in Fig. 6. On the shelf, the sum of the fitted modes is a good approximation to the observations, but the fit offshore is poorer, and it is apparent that CTWs and a single "eddy" mode cannot account for the observations. The modal amplitude time series for the first two CTW modes at the three sections is shown in Fig. 7.

It is difficult to determine the amplitude of the CTW modes from the data. For our finite array (which is larger than most previous arrays used to study CTWs), the modes (the CTW modes and the eddy modes) are not orthogonal. Given noise in the experiment (due to inaccurate current meters, vertical movement of meters, changes in stratification, etc.), it is only possible to determine the amplitudes of some linear combina-

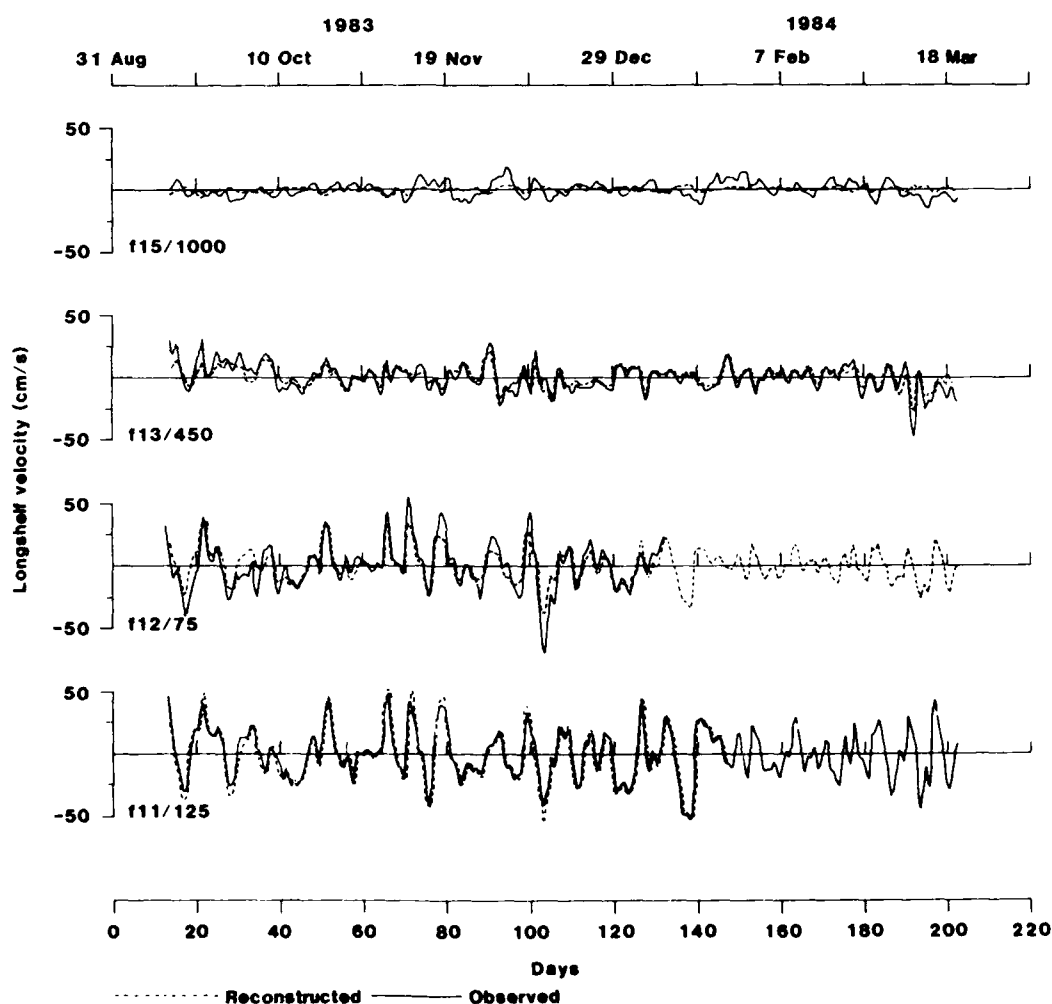


FIG. 6. Comparison of the observed alongshelf currents and the alongshelf currents calculated from the sum of the fitted CTW modes and the eddy mode.

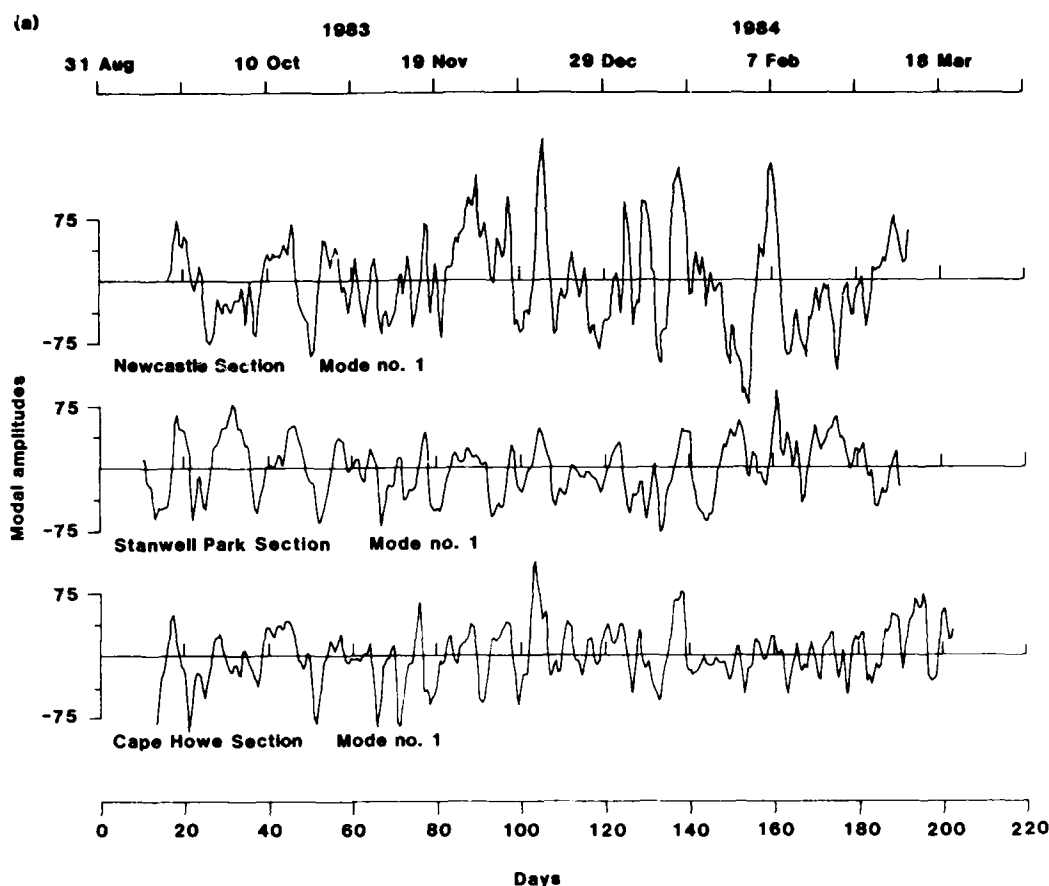


FIG. 7. Modal amplitudes (arbitrary units). The amplitudes of (a) CTW mode 1 and (b) mode 2, determined from the observed alongshelf currents, are shown for the three current meter sections. (The sign of the eigenfunctions is arbitrary and for comparison with the observed currents and winds these modal amplitudes need to be multiplied by -1 .)

tions of the modes (in our case, the first three eigenfunctions) rather than of the modes themselves. However, we have no choice but to proceed with the available database.

In determining the amplitudes of the modes, we could multiply the alongshore velocities by depth intervals to get transports and then minimize (in the least-squares sense) the residual transports rather than minimizing the residual velocities. However, this procedure places most weight on the offshore transports where the CTW response is small and produces unrealistic results. Minimizing the residual velocities places about equal weight on all except the deepest offshore meter.

4. Properties of the eigenfunction amplitudes

The first three CTW eigenfunctions account for about 65% of the variance at Cape Howe, about 40% of the variance at Stanwell Park, but only about 24%

of the variance at Newcastle. This suggests that CTWs are the dominant cause of variance at Cape Howe, whereas offshore eddies and the East Australian Current are the dominant source of variance at Newcastle. The determination of the amplitudes of the CTWs at Newcastle is far less reliable than at either of the other sections.

Spectra (Fig. 8) of the eigenfunction amplitudes (in energy conserving form) indicate that most of the energy at Cape Howe and Stanwell Park is in the band with periods ranging from 4 to 12 days. This is consistent with spectra of the alongshore component of the wind stress (Fig. 9). Note that these spectra were from eigenfunction amplitudes obtained without first highpassing the alongshelf component of currents. The calculated energy flux at Cape Howe [Eq. (A8)] due to the first three CTW modes is 2.9×10^8 W if the alongshelf currents are not highpass filtered (its distribution with frequency is shown in Fig. 8), and 1.9×10^8 W

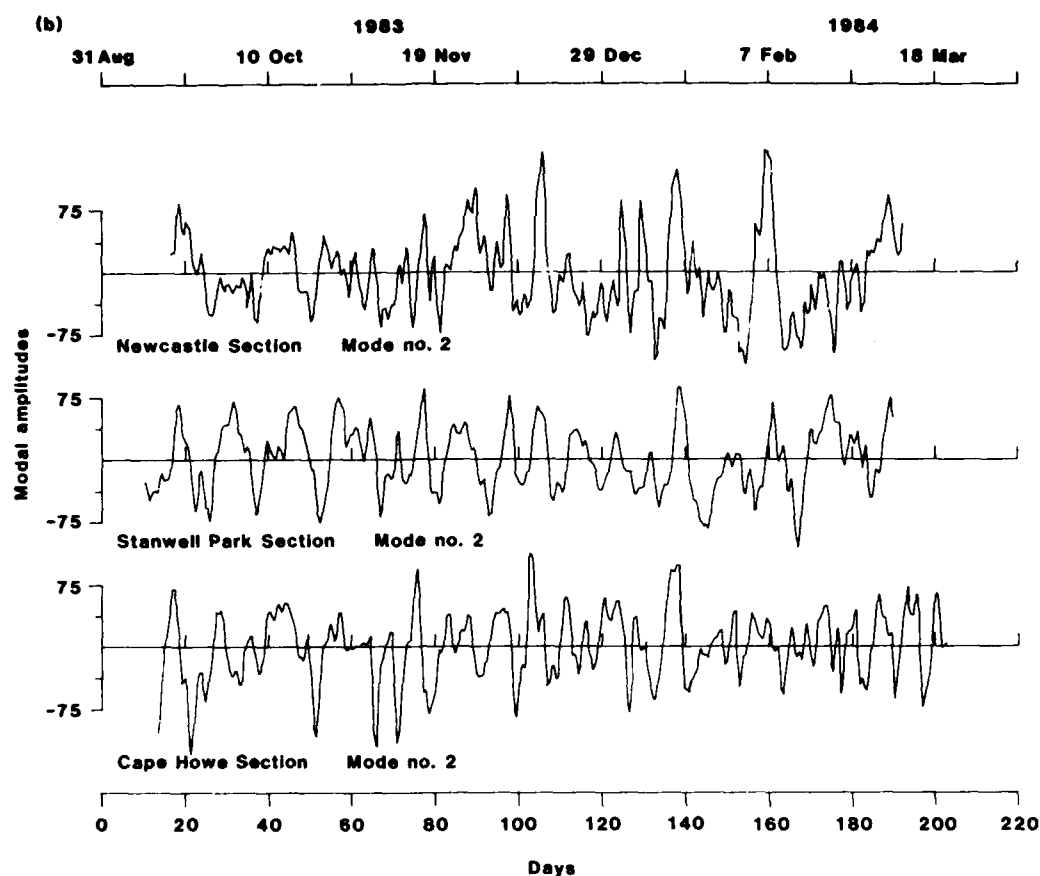


FIG. 7. (Continued)

if they are. Of this latter value, about 31% is carried by mode 1, about 49% by mode 2, and the remainder by mode 3. The relatively large energy flux carried by mode 2 at both Cape Howe and Stanwell Park (see Fig. 8) is rather surprising. (The eddy mode is more orthogonal to the second mode CTW than to the first, and it may be that *some* of the first mode CTW is appearing in the eddy mode. Even if this is the case, the energy flux of the second mode is at least as large as the energy flux of the first mode.) Cross spectra (not shown) were computed between the eigenfunction amplitudes. These show that eigenfunctions 1 and 2 are highly coherent with each other right across the wave band; no other pair of modes is as consistently coherent across the wave band at the 95% significance level. The phase lag between modes 1 and 2 is 5° – 10° at Cape Howe and close to zero at Stanwell Park. The eigenfunction amplitudes for modes 1 and 2 at Cape Howe are coherent with the wind at the 95% (and higher) significance level and lead the wind at Gabo Island by about 20° at a period of 24 days, but lag the wind

between 0° and 30° across the remainder of the wave band. These phase estimates have error bounds of about 30° .

The eddy eigenfunction also shows a peak in the wave band at a period of 12 to 8 days (Fig. 8). This may be due to higher order CTW eigenfunctions that were not explicitly included in the analysis or may indicate some influence of the CTWs, or the wind field, on the cross-shelf position of the East Australian Current.

At Newcastle, the energy levels of all of the modes are higher, and most of the energy is in the lowest frequencies. Also, a much smaller percentage of the variance is accounted for by CTWs. The explanations for these two observations are not clear; they are likely to be associated with the proximity to the East Australian Current and increased eddy activity levels offshore from Newcastle. The East Australian Current may be generating CTWs, or possibly the eigenfunction decomposition cannot resolve the CTWs adequately in the presence of such a large amount of noise. As for the

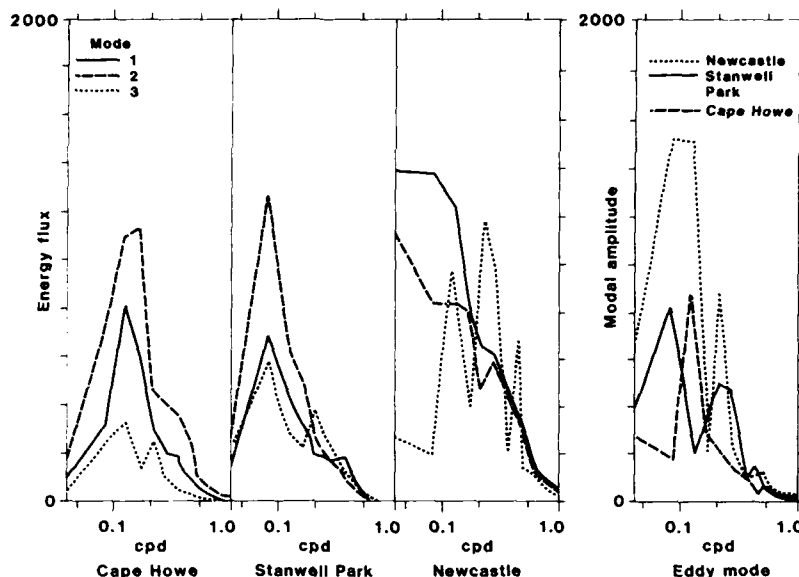


FIG. 8. Spectra of the amplitude of the first three CTW modes at Cape Howe, Stanwell Park and Newcastle. These spectra are normalized such that the area under the curve is proportional to $2f/\rho_0$ times the energy flux. The spectra of the eddy mode at Cape Howe, Stanwell Park and Newcastle are also shown. Note that the currents were not high-passed filtered before obtaining these spectra.

other two lines, amplitudes of modes 1 and 2 are highly coherent across the wave band and there is a near zero lag. Eigenfunction 1 is coherent with the eddy eigenfunction for periods of six and fewer days. If R in Eq. (3.5) is decreased to 2, the energy level in the CTWs at Newcastle is decreased by about 50%, but the energy

in the eddy eigenfunction is increased by only 17%. The general shapes of the spectra remain unchanged.

Cross spectra between corresponding eigenfunction amplitude time series at different locations have been computed for the three CTW eigenfunctions and for the eddy eigenfunction. The most significant coherences occur for CTW eigenfunctions 1 and 2 between Cape Howe and Stanwell Park (Fig. 10). In the band 6–24 days, modes 1 and 2 are coherent at the 95% significance levels and the Stanwell Park series lags the Cape Howe series. The transfer functions between Cape Howe and Stanwell Park show a peak of about 1.4 for mode 1 and 1.2 for mode 2 at the period of 12 days, but are less than unity for the rest of the wave band. This peak in the transfer function occurs at about the same frequency as the peak in the spectra for alongshelf wind stress (Fig. 9).

The third CTW eigenfunction amplitudes are not coherent at the 95% significance level for any pair of alongshelf locations. This contrasts with the results of Freeland et al. (1986), who derived a credible dispersion curve for the third CTW eigenfunction. The lack of significant coherence (at the 95% significance level) for mode 3 may result from the fact that the present technique of calculating the eigenfunctions in the time domain is more subject to contamination by noise than is the method of Freeland et al., where the Fourier analysis removes some of the system noise prior to

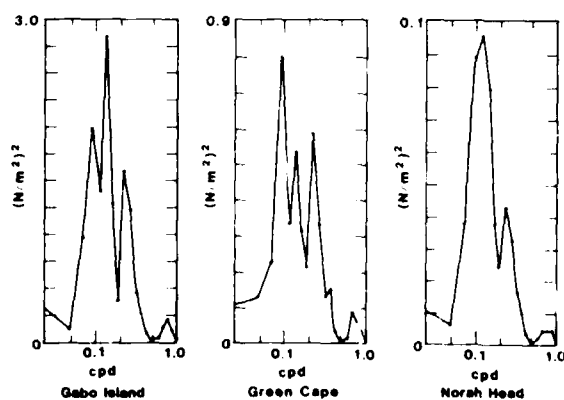


FIG. 9. Spectra of the alongshelf component of the wind stress at Cape Howe, Green Cape and Norah Head. The spectra are plotted in a form such that the area under the curve is proportional to the variance of the alongshelf component of the wind stress. Note that there are different scales on each plot.

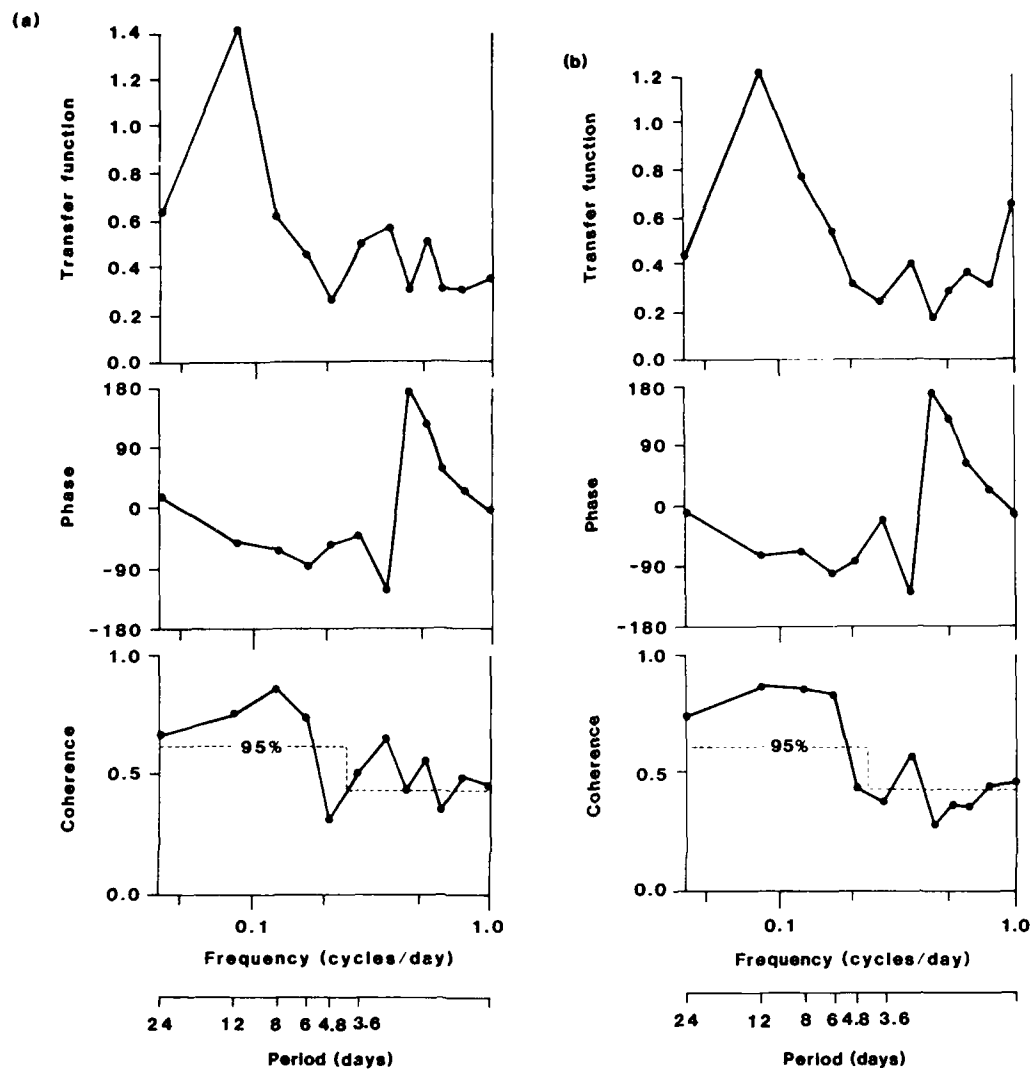


FIG. 10. Cross spectra (transfer function, phase and coherence) for (a) CTW mode 1 and (b) mode 2 between Cape Howe and Stanwell Park. The 95% significance level for the coherence is indicated by the dashed lines, and a negative phase implies that Stanwell Park lags Cape Howe.

modal fitting. However, in agreement with the results of Freeland et al., the eddy eigenfunction time series are not coherent with each other. The results for cross spectra between Cape Howe and Newcastle and between Stanwell Park and Newcastle were similar, except that the coherences were less significant than for Cape Howe to Stanwell Park.

For periods ranging from 3.6 to 24 days (i.e., the frequency band in which most of the CTW energy is located) and for modes 1 and 2, we completed a linear regression (with zero intercept) of the observed phase lag versus the distance between sections. The zero in-

tercept regression model is used because each eigenfunction amplitude time series is identically correlated at zero lag with itself. Also, choosing either a positive or negative frequency changes the sign of the phase lag and implies the regression must pass through the origin. The slopes of these regression lines are estimates of the wavenumbers of the first and second mode CTWs at each frequency. The resulting wavenumbers were then plotted against frequency and linear regressions, with zero intercept computed. (Note that the frequencies are the independent variables and the wavenumbers are the dependent variables, so we must regress k on

ω and not vice versa as shown in Fig. 11.) The inverse of the slopes of the regression lines is an estimate of the phase speed of the first and second CTW modes. The estimated phase speed for modes 1 and 2 are 3.0 and 1.76 m s⁻¹, respectively. Student's *t*-tests (Draper and Smith, 1966) indicate that the observed phase speeds are significantly different from zero and from each other (at greater than the 95% significance levels).

The theoretical phase speeds averaged over the ACE array are defined by

$$c_i^{-1} = \frac{1}{L} \int_0^L c_i^{-1} dy, \quad (4.1)$$

where L is the alongshore distance over which the average is taken and c_i is the phase speed of the i th mode. If 520 km (the distance between Cape Howe and New-

castle) is chosen as the value for L , then the theoretical averages for modes 1 and 2 are 3.8 and 2.0 m s⁻¹, respectively. The 95% confidence limits for the observed phase speeds include these theoretical values (Fig. 11). If the value chosen for L is 360 km (Cape Howe to Stanwell Park—the region with the largest coherences, which produced results that dominate in the regression), then the theoretical average for modes 1 and 2 are 3.5 and 1.9 m s⁻¹, respectively (somewhat closer to the observed phase speeds).

5. Discussion

Although coastal-trapped waves have been thought to exist in the ACE region and on most other shelves around the world (Mysak 1980), the only identification of the theoretical cross-shelf structure prior to ACE was that of Hsieh (1982a,b). Hsieh analyzed only one location, and thus alongshore propagation was not observable. Furthermore, Hsieh assumed barotropic rather than baroclinic theory. The results presented here (and in the paper of Freeland et al., 1986) are the first to indicate alongshelf propagation of theoretical coastal-trapped wave eigenfunctions at phase speeds not significantly different from the theoretical free wave phase speeds. The computed and observed phase speeds of the first CTW mode are in agreement with Hamon's (1976) result that a phase speed of 3.5 m s⁻¹ works better, in a CTW model used to hindcast coastal sea levels on the east Australian coast, than does a phase speed of 4.0 m s⁻¹ (as determined from coastal sea level observations by Hamon, 1966).

The phase speeds computed here are slower than those computed by Freeland et al. (1986) and are closer to the theoretical values. Freeland et al. used an analogous technique to that used here, except that the modal decomposition was done in the frequency domain rather than the time domain. The difference between the computed phase speeds occurs partly because the two data analysis techniques answer slightly different questions. Freeland et al. determined the apparent phase difference between the eigenfunction amplitudes at different locations. This method is subject to contamination from direct wind forcing. In contrast, the technique used here determines the phase difference between the coherent part of the eigenfunction amplitudes and is therefore less subject to contamination by direct wind forcing in the ACE region. Some component of the coherent signal that is due to the large-scale wind forcing in the ACE region will remain, however. Both techniques work reasonably well because the ACE region is dominated by free waves that originate further back along the wave guide, and direct wind forcing in the ACE region is of secondary importance.

The results from the modal decomposition indicate that CTWs account for a significant percentage of the variance of alongshelf currents over the shelf and slope.

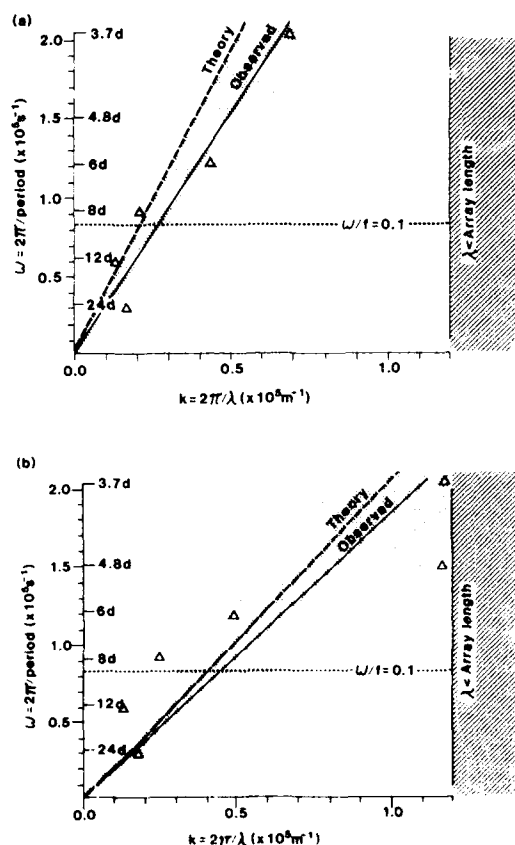


FIG. 11. Dispersion curves for the (a) first and (b) second coastal-trapped wave modes. The triangles indicate the estimated wavenumber for the various frequencies, and the solid line is the linear regression fit (with zero intercept) to these points. The stippled regions are the 95% confidence limits to this dispersion curve; the dashed line is the theoretical dispersion curve for the ACE region.

At Cape Howe, CTWs accounted for 65% of the variance. At the three current meter sections, the percentage of variance accounted for by the CTWs increases for the meters nearest the shore. In fact, for the meters f11/125, f21/125 and f31/75, CTWs account for all but 10%, 37% and 27% of the variance, respectively. We would expect that for locations closer to the shore than these moorings the percentage variance accounted for by CTWs would be even higher.

The CTW amplitudes at Cape Howe were significantly coherent with the wind at Gabo Island and modes 1 and 2 were significantly coherent with each other. Presumably, then, CTW modes 1 and 2 are generated simultaneously by the wind further back along the wave guide. A surprising result was that mode 2 carried more energy than mode 1 at Cape Howe. This was also true at Stanwell Park (Fig. 8). Three questions raised by the results presented are: What is the energy source for the observed CTWs? Why does mode 2 carry more energy than mode 1? Are modes 1 and 2 highly coherent because there is a small generation region or is there an alternative explanation? We hope to pursue these questions in future papers.

Acknowledgments. ACE was initiated and encouraged by Rory Thompson. We also thank him for critical comments on drafts of this manuscript. The participation of Oregon State University in ACE was supported by the U.S. Office of Naval Research. The participants from North America, Howard J. Freeland and Robert L. Smith, would like to thank CSIRO for its hospitality during the data analysis phase of the experiment. Finally, we would like to thank Bernadette Baker and Nikki Pullen for their patience in typing the many drafts of this paper.

APPENDIX A

Theory

Consider a stratified Boussinesq ocean initially at rest. In a right-handed, Cartesian coordinate system, perturbations from the mean state satisfy the equations

$$u_t - fv = -p_x + X_z \quad (\text{A1a})$$

$$v_t + fu = -p_y + Y_z \quad (\text{A1b})$$

$$p_z = -\frac{g\rho'}{\rho_0} \quad (\text{A1c})$$

$$u_x + v_y + w_z = 0 \quad (\text{A1d})$$

$$\rho'_t = \frac{\rho_0 N^2 w}{g} \quad (\text{A1e})$$

where t is time; u , v and w are velocities in the x , y and z directions, respectively; g is the acceleration due to gravity; ρ' the perturbation density; ρ_0 the mean water density; p the perturbation pressure divided by ρ_0 ; X

and Y are the turbulent stresses in the x and y directions divided by ρ_0 ; f is the Coriolis parameter; and N the Brunt-Väisälä frequency. The origin of the coordinate system is at the coast with x the offshore direction, y the alongshelf direction, and z vertically upward. For CTWs, the boundary conditions are that the motion is negligible for large x , there is no flow through the surface or bottom, and the depth-integrated velocity perpendicular to the coast is zero at $x = b$. As in Clarke and Van Gorder (1986), b is chosen such that the depth $h(b)$ is three times the Ekman layer e -folding scale. This coincides approximately with the depth contour $h = 20$ m. At the surface, an alongshelf wind stress $\tau^y(y, t)$ is specified. In contrast to Clarke and Thompson (1984), linear bottom friction is included.

Clarke and Brink (1985) and Clarke and Van Gorder (1986) consider the low frequency, low wavenumber limit of these equations. Under these conditions, the solution is

$$p(x, y, z, t) = \sum_{j=1}^{\infty} F_j(x, z) \phi_j(y, t), \quad (\text{A2})$$

where ϕ_j (the amplitude of the j th CTW mode) satisfies the first-order wave equation

$$-\frac{1}{c_j} \frac{\partial \phi_j}{\partial t} + \frac{\partial \phi_j}{\partial y} + \sum_{i=1}^j a_{ij} \phi_i = h_j \tau^y(y, t), \quad (\text{A3})$$

where

$$h_j = \frac{1}{h(b)} \int_{h(b)}^{z=0} F_j(h, z) dz / \gamma_j, \quad (\text{A4a})$$

$$a_{ij} = \gamma_i^{-1} \left[\int_{x=b}^{\infty} F_i(x, -h) \frac{d}{dx} [r F_{ij}(x, -h)] / f dx + \int_{z=h(b)}^{z=0} F_j r F_i f^{-1} h^{-1} dz \right] \quad (\text{A4b})$$

with

$$\gamma_j = \int_{z=h(b)}^{z=0} (F_j)^2 dz + \int_{x=b}^{\infty} (F_j)^2 h dx. \quad (\text{A4c})$$

Here r is a linear bottom friction coefficient and $\tau^y(y, t)$ is the surface wind stress in the y -direction (parallel to the shore) and is assumed independent of x . The h_j are the wind-coupling coefficients and the a_{ij} are the frictional-coupling coefficients that lead to decay of the modes and energy exchange between the modes. The $F_j(x, z)$ are the eigenvectors of the eigenvalue problem

$$\frac{F_{xx}}{f^2} + \left[\left(\frac{F_z}{N^2} \right) \right]_z = 0, \quad (\text{A5a})$$

with boundary conditions

$$\frac{c}{f} F_x + F = 0 \quad \text{at} \quad x = b \quad (\text{A5b})$$

$$F_z = 0 \quad \text{on} \quad z = 0 \quad (\text{A5c})$$

$$c \left(h_x F_x + \frac{f^2}{N^2} F_z \right) + f h_x F = 0 \quad \text{at} \quad z = -h(x) \quad (\text{A5d})$$

$$F = 0 \quad \text{at} \quad x = \infty. \quad (\text{A5e})$$

The eigenvalue c_j is the alongshelf phase speed of the j th CTW mode. The depth $h(x)$ increases from the coast to the abyssal depth of the ocean.

The eigenvectors have the following orthogonality property (Clarke, 1977):

$$\int_0^x F_j(x, z) F_l(x, z) \frac{\partial h}{\partial x} \Big|_{z=-h(x)} dx + \int_{h(x)}^0 F_j(b, z) F_l(b, z) dz = A_j \delta_{jl}, \quad (\text{A6})$$

where A_j is an arbitrary constant.

For conditions when wind forcing is of secondary importance and friction is small, Eq. (A3) states that the CTW modes F will propagate alongshelf at the free wave speed c_j .

Once the solution (A2) is obtained, the alongshelf velocity (in the small wavenumber, low-frequency limit) is found from

$$v(x, y, z, t) = \frac{1}{f \rho_0} \frac{\partial p}{\partial x} = \frac{1}{f} \sum_{j=1}^J \frac{\partial F_j(x, z)}{\partial x} \phi_j(y, t) = \sum_{j=1}^J G_j(x, z) \phi_j(y, t), \quad (\text{A7})$$

The energy flux Γ through a section perpendicular to the coast is (following Clarke and Battisti, 1983, but allowing for a coastal wall)

$$\Gamma = \frac{\rho_0}{2f} \left[\int_{y=0}^y \overline{[p^2]}_z = h(x) \frac{\partial h}{\partial x} dx + \int_{z=h(x)}^0 \overline{[p^2]}_x dz \right] \quad (\text{A8})$$

where the bar indicates a time average. Substituting (A2) and (A7) and using the orthogonality condition (A6), the time-averaged energy flux is

$$\Gamma = \frac{\rho_0}{2f} \sum_{j=1}^J \overline{\phi_j^2} A_j. \quad (\text{A9})$$

If the shelf topography or stratification changes with x , then the eigenfunctions $F_j(x, y)$ will also change but the amplitudes ϕ_j for a unit energy flux in the j th mode will remain constant.

Following Clarke and Van Gorder (1986) Eq. (A3) is solved by integrating along the characteristics $t = t_j(y)$ defined by

$$\frac{dt_j}{dy} = \frac{1}{c_j(y)}. \quad (\text{A10})$$

In this method, the number of modes included is truncated to a finite number M and boundary conditions for the modal amplitudes specified at some starting location (say $y = 0$), i.e.,

$$\phi_j(0, t) = \text{known function}. \quad (\text{A11})$$

Equation (A3) may be written as

$$\frac{d}{dy} [\phi_j(y, t) E(y)] = D[y, t(y)] E(y), \quad (\text{A12})$$

where

$$D[y, t_j(y)] = b_j(y) \tau'(y, t) + \sum_{l=1}^M a_{jl}(y) \phi_l(y, t) \quad (\text{A13})$$

$$E(y) = \exp \left[\int_0^y a_{jj}(y') dy' \right]. \quad (\text{A14})$$

Equation (A12) can be integrated from y to $y + \delta y$ using the trapezoidal rule. However, this integration requires knowledge of $D[y + \delta y, t(y + \delta y)]$. In the early version of the Clarke and Van Gorder (1986) method used here, $\phi[y, t(y)]$ is used as an initial approximation for $\phi[y + \delta y, t(y + \delta y)]$ and then the solution is iterated until it converges. Operationally, the iterative solution converges very rapidly (typically in two or three iterations for a tolerance of 1%). Clarke and Van Gorder (1986) have recently changed the iterative technique to a matrix inversion technique.

REFERENCES

- Brink, K. H., and D. C. Chapman, 1985. Programs for computing properties of coastal-trapped waves and wind-driven motions over the continental shelf and slope. Woods Hole Oceanographic Institute Tech. Rep. WHOI 85-17, 99 pp.
- Church, J. A., N. J. White, A. J. Clarke, H. J. Freeland, and R. J. Smith, 1986. Coastal trapped waves on the east Australian continental shelf. Part II: Model verification. *J. Phys. Oceanogr.*, **16**, 1945-1958.
- Clarke, A. J., 1977. Observations and numerical evidence for wind forced coastal trapped long waves. *J. Phys. Oceanogr.*, **7**, 231-247.
- , and D. S. Battisti, 1983. Identification of the fortnightly wave observed off the northern coast of the Gulf of Guinea. *J. Phys. Oceanogr.*, **13**, 2192-2200.
- , and R. O. R. Y. Thompson, 1984. Large-scale wind-driven ocean response in the Australian Coastal Experiment region. *J. Phys. Oceanogr.*, **14**, 338-352.
- , and K. H. Brink, 1985. The response of stratified, frictional shelf and slope waters to fluctuating large-scale low frequency wind forcing. *J. Phys. Oceanogr.*, **15**, 439-453.
- , and S. Van Gorder, 1986. A method for estimating wind-driven frictional, time-dependent, stratified shelf and slope water flow. *J. Phys. Oceanogr.*, **16**, 1013-1038.
- Denbo, D. W., and J. S. Allen, 1984. Rotary empirical orthogonal function analysis of currents near the Oregon coast. *J. Phys. Oceanogr.*, **14**, 25-46.
- Draper, N. R., and H. Smith, 1966. *Applied Regression Analysis*. Wiley and Sons, 407 pp.
- Forbes, A. M. G., 1985a. Sea level data from the Australian Coastal

- Experiment—a data report. CSIRO Mar. Lab. Rep. No. 171, 16 pp.
- , 1985b: Meteorological data from the Australian Coastal Experiment—a data report. CSIRO Mar. Lab. Rep. No. 170, 26 pp.
- , 1987: Wind stress in the Australian Coastal Experiment region. Submitted to *Aust. J. Mar. Freshwater Res.*
- Freeland, H. J., J. A. Church, R. L. Smith and F. M. Boland, 1985: Current meter data from the Australian Coastal Experiment—a data report. CSIRO Mar. Lab. Report No. 169, 51 pp.
- , F. M. Boland, J. A. Church, A. J. Clarke, A. M. G. Forbes, A. Huter, R. L. Smith, R. O. R. Y. Thompson and N. J. White, 1986: The Australian Coastal Experiment. A search for coastal trapped waves. *J. Phys. Oceanogr.*, **16**, 1230–1249.
- Hamon, B. V., 1962: The spectrums of mean sea level at Sydney, Coll's Harbour, and Lord Howe Island. *J. Geophys. Res.*, **67**, 5147–5155. [Correction, *J. Geophys. Res.*, **68**, p. 4635]
- , 1966: Continental shelf waves and the effects of atmospheric pressure and wind stress on sea level. *J. Geophys. Res.*, **71**, 2883–2893.
- , 1976: Generation of shelf waves on the east Australian coast by wind stress. *Mem. Soc. R. Sci. Liege Ser. 6*, **X**, 357–359.
- Hsieh, W. W., 1982a: On the detection of continental shelf waves. *J. Phys. Oceanogr.*, **12**, 414–427.
- , 1982b: Observations of continental shelf waves. *J. Phys. Oceanogr.*, **12**, 887–896.
- Large, W. S., and S. Pond, 1981: Open ocean momentum flux measurements in moderate to strong winds. *J. Phys. Oceanogr.*, **11**, 324–336.
- Levitus, S., 1982: *Climatological Atlas of the World Ocean*. NOAA Prof. Pap. **13**, 173 pp.
- Mysak, L. A., 1980: Recent advances in shelf wave dynamics. *Rev. Geophys. Space Phys.*, **18**, 211–241.
- Nilsson, C. S., and G. R. Cresswell, 1981: The formation and evolution of East Australia Current warm-core eddies. *Progress in Oceanography*, Vol. 9, Pergamon, 133–183.
- Robinson, A. R., 1964: Continental shelf waves and the response of the sea level to weather systems. *J. Geophys. Res.*, **69**, 367–368.
- White, N. J., and J. A. Church, 1986: CTD data from the Australian Coastal Experiment: a data report. CSIRO Mar. Lab. Rep. In preparation.
- Yao, L., H. J. Freeland and L. A. Mysak, 1984: A comparison of low-frequency current observations off British Columbia with coastal-trapped wave theory. *J. Phys. Oceanogr.*, **14**, 22–34.

AD-A191 689

COMPILATION OF REPRINTS NUMBER 64(U) OREGON STATE UNIV
CONFIDENTIAL COLL OF OCEANOGRAPHY NOV 87 REF-88-23
N88014-76-C-8867

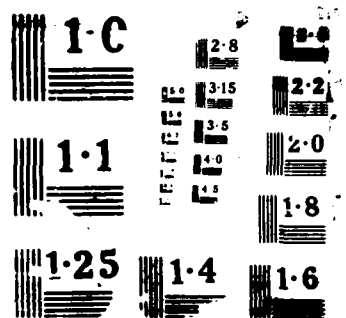
3/3

UNCLASSIFIED

F/G 8/3

HL

END
DATE
FILMED
88



Measurements of Near-Surface Shear in the Ocean

J. G. RICHMAN AND R. A. DE SZOEKE

College of Oceanography, Oregon State University, Corvallis

R. E. DAVIS

Scripps Institution of Oceanography, La Jolla, California

In an effort to measure current shear very near the sea surface a string of vector-measuring current meters suspended beneath a surface float was deployed 180 km off southern California at 34°N 121°30'W on November 26, 1981 and allowed to drift freely for over 6 days. This arrangement, which we call the current meter drifter (CMD), gave measurements at depths of 2.5, 5.5, 8.5, 11.5, 14.5, 25, and 63 m. During the first two days, when the winds were light (≈ 8 m/s) and variable in direction, a nearly uniform current shear was observed in the upper 15 m with a low-frequency velocity difference of 5 cm/s between the instruments at 2.5 and 14.5 m. During the last four days, when the winds were brisk (> 12 m/s) and steady in direction from the NNW, a strong downwind shear of order 10^{-2} s $^{-1}$ was observed in the upper 10 m with a velocity difference of ~ 7 cm/s between the instruments at 2.5 and 8.5 m. During this same period the shear below 10 m was much smaller. The average currents during the CMD drift veer to the right of the wind stress with angular displacement increasing with depth. Time series of the velocity difference between 2.5 and 5.5 m compare very well with $\theta(t)u_*\kappa^{-1} \ln(5.5/2.5)$, where $\theta(t)$ is the wind direction vector (of unit magnitude), $u_* = (\text{wind stress } \rho)^{1/2}$ is the friction velocity in water, and $\kappa = 0.4$ is von Karman's constant. On the other hand, a similar comparison of the velocity difference between 5.5 and 8.5 m to $\theta(t)u_*\kappa^{-1} \ln(8.5/5.5)$ is much poorer with observed velocity difference being much larger, possibly due to stable stratification effects. Possible errors in the measurements have been considered and estimated as less than the observed velocity differences. Near-surface shears as large as the observed are very important in closing the momentum budget for the oceanic boundary layer.

1. INTRODUCTION

The vertical structure of currents near the sea surface have long been a subject of profound study among oceanographers. Ekman [1905] showed, using a constant viscosity model of turbulent friction, that currents should turn steadily to the right of the wind with increasing depth (in the northern hemisphere). Sverdrup *et al.* [1942] cite evidence in favor of rightward turning, if not precisely of the form suggested by the constant viscosity model. Regardless of turbulent parameterization it is a robust theoretical result that the wind-driven mass transport of the sea surface frictional layer is the wind stress divided by Coriolis parameter, directed 90° to the right of the wind [Pedlosky, 1979]. Much evidence can be cited in favor of this [Davis *et al.*, 1981b; Weller, 1982]. The precise form of the current structure near the surface remains uncertain. Frictional boundary layers along rigid walls have been studied theoretically and experimentally since Prandtl [1925] and von Karman [1930]. The simple result is that velocity has a logarithmic profile receding from the wall. The subject is thoroughly reviewed by Monin and Yaglom [1975]. The theory has been applied with great success to air flow across land and sea, appropriate modifications having been made to the theory for the effects of stratification and earth's rotation [Csanady, 1967; Caldwell *et al.*, 1972] to describe the vertical structure of the atmospheric boundary layer [Busch, 1973]. Application of the theory to the ocean surface layer has lagged, probably due to the paucity of detailed near-surface current observations, itself a result of the difficulty of making the necessary measurements. Still, Jones and Kenney [1977] have proposed a logarithmic surface current profile and inter-

preted near-surface velocity spectra using a scaling argument based upon this profile and constant stress boundary layer. Wu [1975] found a logarithmic profile obeying law-of-the-wall scaling in the water in a laboratory wind-wave tank. Churchill and Csanady [1983] reported observations of logarithmic velocity profiles from drifters and drogues in Lake Huron and Cape Cod Bay. Dillon *et al.* [1981] observed the vertical dependence of turbulent kinetic energy dissipation in a mountain lake by measuring temperature microstructure and found a vertical decay from 50 cm to 5 m that resembled $u_*^3(\kappa z)^{-1}$, where u_* is friction velocity ((wind stress water density) $^{1/2}$) and κ is von Karman's constant. The role of surface gravity waves, so tremendously vigorous, in the transfer of low-frequency momentum across the air-sea boundary and then to greater depths is imperfectly understood. Kitaigorodskii and Lumley [1983] and Kitaigorodskii *et al.* [1983] attempt a computation of air-sea momentum and energy flux from high-frequency measurements of wave motion and turbulence. In their model, large increases in the kinetic energy dissipation occur very near the surface, although the turbulent transfer of momentum is nearly constant near the surface.

Davis *et al.* [1981b] measured shear in the upper ocean, from 10 m depth down. Though they report currents generally to the right of the wind, a quantitative attempt to balance Coriolis force, integrated vertically through the mixed layer, against surface wind stress fell short by as much as 40% [Davis *et al.*, 1981a]. Order of magnitude estimates suggest that the momentum budget could be reconciled if the shear above 10 m were of order $u_*(\kappa z)^{-1}$.

In this study we report the results of an experiment to measure current shear very near the surface, from 2.5 m depth downward. In section 2 we describe the experiment. In section 3 we present the results, while in section 4 we include an analysis of the expected performance of the instruments in the

Copyright 1987 by the American Geophysical Union

Paper number 6C0742
0148-0227/87/006C-0742\$05.00

CURRENT METER DRIFTER
ML-81 26 NOV - 3 DEC, 1981

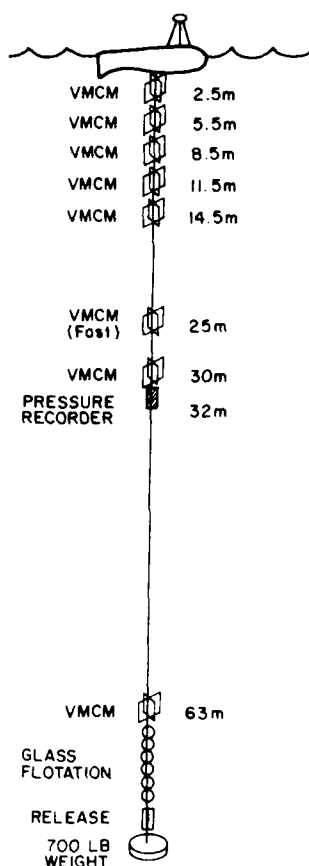


Fig. 1. Instrumentation on the current meter drifter.

surface waves encountered during the experiment. We find comparatively strong shears in the upper 8 m, of the order of 10^{-2} s^{-1} , comparable to $u_* (\kappa z)^{-1}$ shear magnitudes based on the applied wind stress, and weaker shear or none at all, within experimental accuracy, between 8 and 15 m. Currents averaged over the length of the experiment deployment (about 7 days) show a consistent turning to the right with depth, in agreement with Ekman theory.

2. EXPERIMENT

In November 1981 we deployed a vertical string of vector measuring current meters (VMCMs) [Weller and Davis, 1980], shown in Figure 1, for 6.8 days, in an area southwest of Point Conception off California (Figure 2). The string was suspended from a roughly cylindrical surface buoy, 6 m long, 1 m diameter; it was terminated by back up buoyancy and an acoustic release at 70 m, followed by a 350-kg anchor. The whole arrangement, dubbed the "current meter drifter" (CMD), was free to drift in the surface currents. Five VMCMs were placed every 3 m between 2.5 and 14.5 m below the waterline of the surface buoy with additional VMCMs placed at 25, 30, and 63 m. All current meters measured and averaged current at 60-s intervals for 6.8 days, except the meter at 25 m, which was set to record at 3.75-s intervals and ran for 3.8 days and the meter at 30 m which failed after 13.5 hours. A Sea-

Data model 635-11 wave pressure recorder at 32.5 m sampled and recorded every 0.5 s. The position of the CMD was determined at least 8 times a day by visual sighting or by triangulating on HF radio beacons on the surface buoy from the R V *New Horizon*. During part of the observational period, current-following drifters drogued to 1, 2, 4, and 8 m depths were also tracked by triangulation from the ship. Ship's position was determined by Loran-C. A Datawell wave rider spherical buoy was deployed twice a day from the ship to obtain surface wave characteristics and spectra. Frequent high-resolution temperature profiles were taken from the ship. No useful temperature data were recorded on the current meters.

3. RESULTS

The drift of the CMD is shown in Figure 2. It drifted 180 km over 6.8 days toward 160 T, generally downwind. The wind speed and direction are shown in Figure 3a. During the first two days of the CMD deployment the wind speed was variable and rotated gradually from the west to almost out of the north. Thereafter, it blew at 10–15 m s⁻¹ fairly steadily from 340 T. The 6.8-day average wind was 7.8 m s⁻¹ from 330 T, while the average for the last 4 days of the experiment was 10.6 m s⁻¹ from 338 T. The components of current at near-surface depths with respect to 14.5 m are shown, low-pass filtered with a cutoff at 0.25 cph, in Figure 4. Differences of velocity between adjacent current meters are generally small ($\sim 1 \text{ cm s}^{-1}$) and variable for the first 2 days, then moderately large ($> 2 \text{ cm s}^{-1}$) between the upper two pairs of instruments, and downwind. The 2.5-m current meter registered some 7 cm s⁻¹ more southward velocity than the 14.5-m current meter. Velocity differences between pairs of current meters below 8.5 m were slight.

Model

The simplest model of velocity profile at a boundary with an applied stress is that the velocity behave like

$$u(z) = u_* \kappa^{-1} \ln z + \text{const} \quad (1)$$

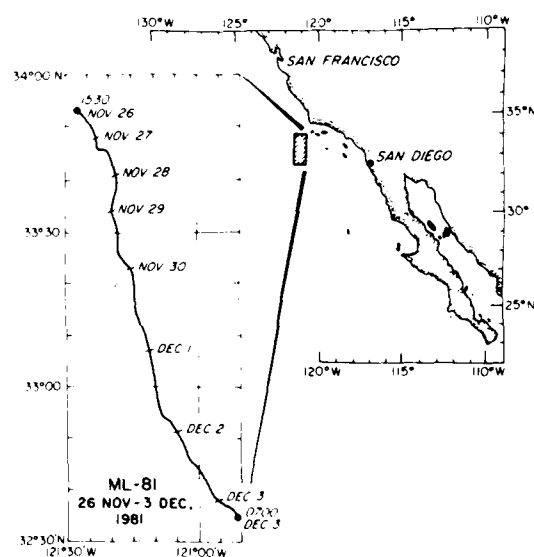


Fig. 2. Location and drift of the current meter drifter during the November-December 1981 experiment.

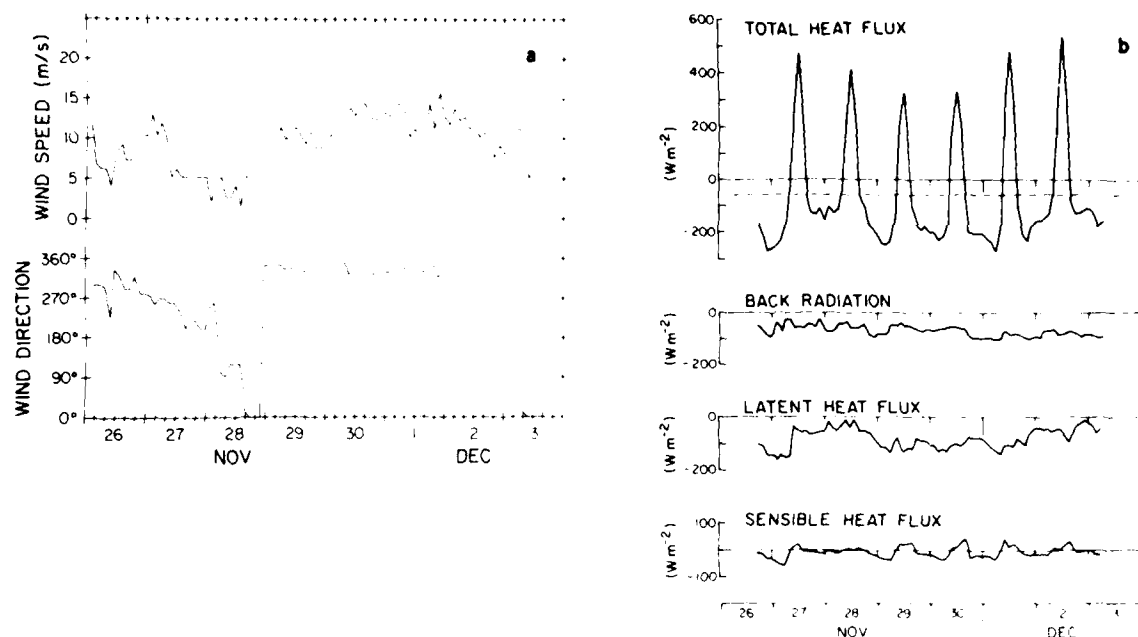


Fig. 3. (a) Wind speed and direction and (b) surface heat flux during the current meter drifter experiment

where u_* is (wind stress/water density)^{1/2} and κ is von Karman's constant. This classical model assumes constant stress in the boundary layer, little influence of stratification, and distances from the surface small compared to the planetary boundary layer scale $u_* f^{-1}$.

Comparison With Data

In Figure 5 we show time series of components of velocity difference between 2.5 and 5.5 m. These we compare to the wind, plotted as the predicted shear $(u_* \kappa) \ln(5.5/2.5)$, resolved into components parallel to wind direction. The coincidence of the observed and predicted shear is remarkable, especially for the last 4 days of record, corresponding to the steady wind period. In Figure 6 we show similar time series of velocity shear between 5.5 and 8.5 m, compared to the predicted shear $(u_* \kappa) \ln(8.5/5.5)$. The correlation between observed and predicted shear is again quite high, though the former is considerably larger than the latter.

A hodograph of current relative to 63 m, averaged over 6.8 days, is shown in Figure 7, together with the average wind stress for the whole 6.8 days. Ekman [1905] theory suggests that the relative current should rotate with depth to the right of the wind. This does indeed seem to be the case. Even on this figure, we see that average current shear between 2.5 and 5.5 m is approximately downwind, less so between 5.5 and 8.5 m. The integrated current transport between 1 and 16 m depth, taking the measurement at each level as representative of an average over a 3-m interval, is $1.2 \text{ m}^2 \text{ s}^{-1}$, directed toward 228 T. This is to be compared to the theoretical Ekman transport, $\varepsilon \tau / \rho f$, which is $1.8 \text{ m}^2 \text{ s}^{-1}$, directed toward 241 T. The 1- to 16-m transport is two thirds of the theoretical Ekman transport, which is directed some 13° of arc further to the right. This agreement is not unreasonable given that all of the mixed layer is not resolved. Similar hodographs have recently been observed by Weller et al. [1985] and Stacey et al. [1986].

4. INSTRUMENTAL PERFORMANCE

Are the velocity differences measured indications of actual velocities, or are they artifacts of sampling or high-frequency aliasing difficulties associated with the type of instrument or the motion of the vehicle in response to the forcing in the agitated environment of the upper ocean? We shall consider this question in two parts. First, we examine the motions of the CMD vehicle induced by wave motion, including any low-frequency rectifications induced by such forcing. Next, we consider the implications of Weller and Davis' [1980] careful laboratory calibrations of the VMCM sensor's response characteristics to combinations of steady and high-frequency reciprocating motions. Our conclusions are that current differences greater than 1 cm s^{-1} cannot be attributed to instrumental errors or errors due to carriage motion rectification. The velocity differences observed, even between adjacent pairs of instruments separated only by 2.5 m, are generally considerably larger than this threshold.

Surface Waves

It is important to our interpretation of the current meter time series to argue that the sensors' response to the low-frequency band (periods longer than $\sim 100 \text{ s}$) is not infected by rectification from the high-frequency gravity wave band. The evidence for this assertion is as follows. A Datawell wave rider buoy was deployed for 30 min twice a day during the experiment. The VMCM at 25 m was set to sample every 3.75 s, extending the current sampling into the surface gravity wave band. A pressure sensor at 32.5 m sampled every 0.5 s. Some typical results are shown in Figures 8 and 9. Figure 8 shows the wave rider buoy surface displacement spectrum for two 30-min periods during the experiment, beginning at 2200 UT November 27, 1981 and 1650 UT November 29, 1981. The earlier period coincides with 30-min average winds of 6 m s^{-1} from 250 T, the later to winds of 10 m s^{-1} from 340 T. The difference in the distribution of spectral variance between the

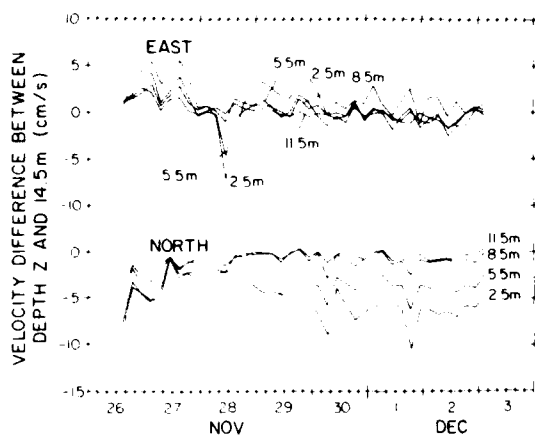


Fig. 4. Currents relative to 14.5 m observed at the current meter drifter.

two spectra is striking. In the relatively high-wind period the high-frequency part of the spectrum is higher than in the low-wind period. In contrast, the low-frequency band, beginning at 0.16 Hz and extending to 0.05 Hz, is more vigorous on November 27 than November 29. These spectra typify the fact that surface waves were dominated by low-frequency swell early in the experiment and by locally generated duration-limited wind waves later. Figure 9 shows a comparison of the VMCM velocity spectrum at 25 m and a velocity spectrum computed using standard surface gravity wave theory [Phillips, 1966] from the wave rider buoy displacement spectrum. The VMCM spectrum only barely extends into the surface wave band, but on both days an increase in energy in the surface wave band is observed. On November 27, when a long swell dominates the wave height spectrum, a rapid increase in kinetic energy at a 20-s period is observed corresponding to the increase in kinetic energy inferred from the swell spectrum. On November 29, shortly after the wind speed increases to 10 m s⁻¹, the wave height spectrum is dominated by short wind waves with approximately 10-s period. Again, an increase in

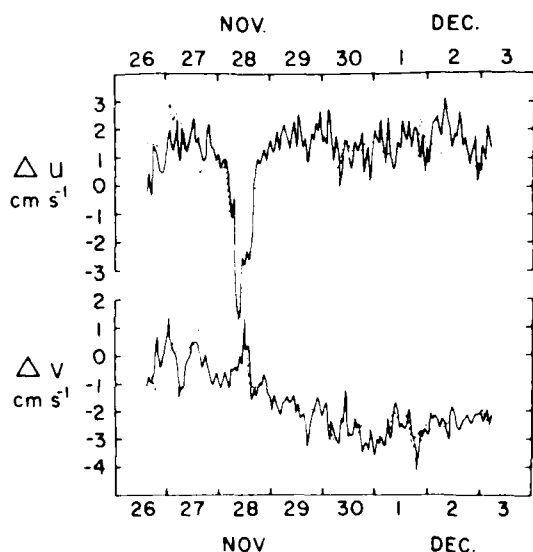


Fig. 5. Velocity differences between 2.5 and 5.5 m (solid line) compared to $u_{*k}^{-1} \ln(5.5/2.5)$ model (dashed line).

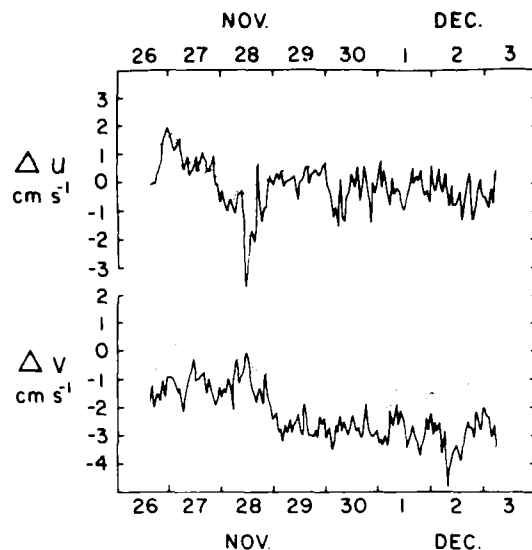


Fig. 6. Velocity differences between 5.5 and 8.5 m (solid line) compared to $u_{*k}^{-1} \ln(8.5/5.5)$ model (dashed line).

kinetic energy is observed in the VMCM spectrum near 10-s period. In general, the VMCM kinetic energy spectra are lower in energy than the theoretical surface gravity wave spectra calculated from the wave height spectra. The underspeeding at high frequencies may be instrumental, resulting from the VMCM propellers spending time in their own wakes, or it may be a result of instrument motion which reduces the relative flow. Nevertheless, the high-frequency VMCM spectra indicate that the current meters can respond to gravity wave motions. All of the spectra show a spectral gap at frequencies below the surface wave band. The VMCM spectrum rises most steeply for lower frequencies still, reflecting its more sensitive response in this band. The occurrence of the spectral gap in the VMCM spectrum indicates that this instrument, and, by inference, the others like it set to average and sample over longer 60-s intervals, were effectively rejecting the high-

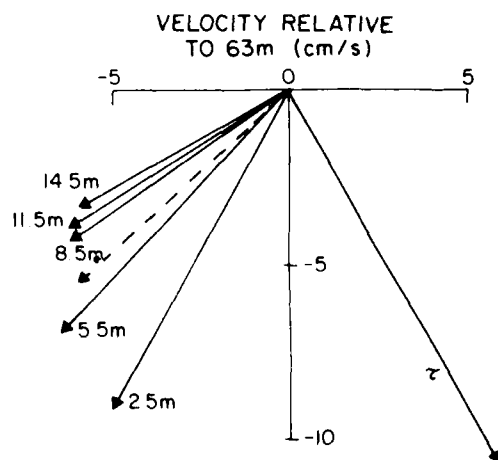


Fig. 7. Hodograph of the mean flow relative to 63 m. Mean wind stress vector is shown; its magnitude is 0.145 Pa. Note the turning to the right with depth relative to the wind stress and the predominantly downward shear at the top three instruments. Depth-averaged current is shown dashed.

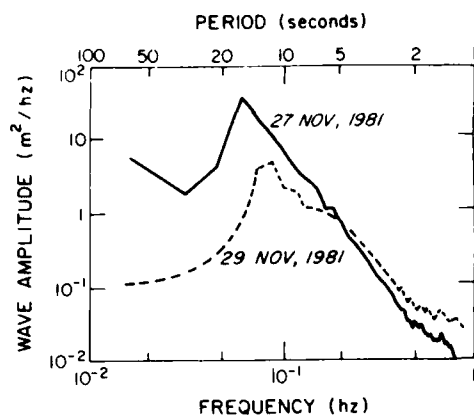


Fig. 8. Spectra of surface wave height for 30-min periods on November 27 (solid line) and November 29 (dashed line).

frequency surface wave variance and resolving low-frequency variance not infected by rectification of surface waves.

To determine the effect of surface waves on the motion of the CMD, we constructed models of the motion of the device. The model must give the motion of the CMD and the instruments affixed to it in response to a specified wave motion. Then the relative motion of water particles with respect to a particular instrument can be predicted. The mean relative motion so computed is not zero in general. The simplest (and least realistic) model is to suppose each instrument fixed in space. Then the mean relative motion would be the well-known Stokes drift [Phillips, 1966],

$$u_{\text{Stokes}} = A^2 s k e^{2kz} \quad s = (gk)^{1/2} \quad (2)$$

for a surface displacement of $A \cos(kx - st)$.

A more complicated, but rather more realistic model is to suppose that the surface buoy follows the motion of a surface wave perfectly and an instrument rigidly attached to it by a vertical line of length z_0 does the same, so that the two-dimensional time history of the instrument position would be

$$x_i = (a, z_0) + \int_0^t u_{Li}(a, z_0, t') dt' \quad (3)$$

where $u_{Li}(a, z, t)$ is the lagrangian velocity of a water particle initially at (a, z) with the subscript $i = (1, 3)$ corresponding to horizontal and vertical directions. The instantaneous relative

motion measured by the instrument of the water past it would be

$$u_{Mj}(a, z_0, t) = u_j(x_i, t) - u_j(a, 0, t) \quad (4)$$

where $u_j(x_i, t)$ is the velocity at the point x_i given by (3). The right side of (4) may be written approximately as

$$u_{Mj} = \int_0^t u_p(a, 0, t') dt' \partial_p [u_j(a, z_0, t) - u_j(a, 0, t)] \quad (5)$$

For a deep-water wave whose surface displacement is given by $A \cos(kx - st)$ the mean value of this is

$$u_{M1}(z_0) = A^2 s k (e^{kz_0} - 1) \quad u_{M3}(z_0) = 0 \quad (6)$$

not zero in general, nor identical to the Stokes drift, though obtained in an analogous way. Differences in velocity between adjacent instruments at levels z_1, z_2 would be

$$\Delta u_{M1} = A^2 s k (e^{kz_1} - e^{kz_2}) = A^2 s k^2 e^{kz} \Delta z = u_{\text{Stokes}}(k \Delta z)$$

approximately, where $\Delta z = z_1 - z_2$. For $A = 1$ m, $s = 2\pi$ (10 s), $1/k = 25$ m, and $u_{\text{Stokes}} = 3$ cm/s. But $k \Delta z = (3 \text{ m}) / (25 \text{ m}) = 1/8$, so $\Delta u_{M1} = 0.4$ cm/s, approximately, which is a great deal smaller than the Stokes drift.

Our most complicated model consists of representing the CMD as a taut compound pendulum made up of its various elements, the surface buoy and the instruments suspended from it, subject to the buoyancy and drag forces acting in a reciprocating motion equivalent to a surface wave field. Similar models have been used by Chhabra [1977, 1985]. We subjected the model CMD to surface wave motion in two dimensions made up of a small number of discrete spectral components, chosen to represent the wave field during the two time segments corresponding to Figure 8. The frequencies and amplitudes of these components are shown in Table 1. A given instrument in the CMD string executes a complicated path, which roughly follows the surface buoy, as in the previous example, but is in any case predicted by the detailed calculation of the model. With this model, we are able to perform a careful calculation taking the mooring motion point by point along the vertical line into account. Excerpts from the results are shown in Figures 10 and 11 for the two time periods of Table 1 and Figures 8 and 9. In Figure 10 we compare the predicted pressure spectrum at 32.5 m on the CMD, using the model response function for a random sea, with the observed wave height spectrum with remarkable success. Figure 11 shows the rectified current that a perfect instrument-

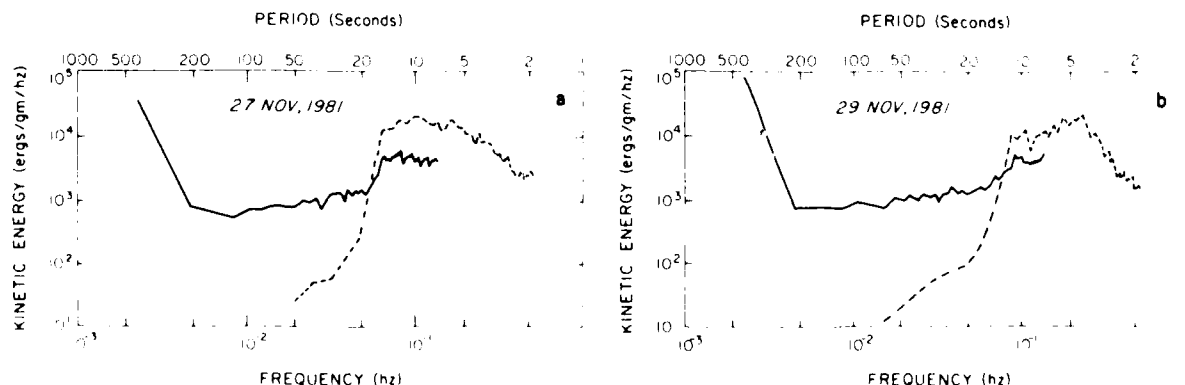


Fig. 9. High-frequency velocity spectrum at 25 m (solid line) compared to the predicted velocity spectrum from the wave height spectrum (dashed line) using linear gravity wave theory for (a) November 27 and (b) November 29.

TABLE 1. Surface Wave Characteristics for 2 Days During the Experiment: November 27 With Swell-Dominated Conditions and November 29 With Duration-Limited Seas.

Period, s	Amplitude	
	November 27	November 29
4	10 cm	25 cm
10	57 cm	44 cm
20	75 cm	33 cm
Significant wave height (crest-to-trough)	3.5 m	1.5 m

*Swell may be underestimated due to wave rider characteristics

measuring current in a plane normal to the instantaneous line orientation at a given depth would see. (The tilting of the line has been taken into explicit account in the model calculation.) Note that Figures 5 and 6 above refer to current differences over 3-m separations, so that it is fair to take differences between mean levels from Figure 11. Even so, the maximum surface wave rectified absolute currents are of order 1.5 cm s⁻¹, largest below the surface in the zone of most intense motion associated with the waves; 3-m differences are smaller, about 0.5 cm s⁻¹.

VMCM Rotor Underspeeding

A potential source of error is the imperfections of the response of the VMCM current sensor. *Weller and Davis* [1980] considered this question very carefully. They showed that the VMCM sensor has a response threshold of 1 cm s⁻¹, that its rotation rate is a linear function of current above 2 cm s⁻¹, that it responds quickly to sudden changes in speed, and that it responds to the component of current directed along the axle of the sensor. When the sensors were subjected to combinations of mean and fluctuating flows, it was found, the measured mean current tends to be lower than the true mean, apparently because of the sensor encountering its own wake in the downstream swing of the cycle. This "underspeeding" was largest, given the ratio of fluctuation to mean current, for aligned mean current, fluctuation, and sensor axle directions. *Weller and Davis* [1980] calibrated the sensors for this effect in tow tank experiments with various orientations of mean, fluctuation, and sensor axle and for a wide range of fluctu-

ation mean ratios. We have made use of these calibration experiments to assess the effect of underspeeding on our measurements. We supposed that the surface buoy is a perfect surface follower and that the near-surface current meters above 15 m are rigidly attached to it. Then the surface wave motions encountered at a depth z are attenuated by a factor $(1 - \exp(kz))$. For waves in the swell band, k^{-1} is far larger than 15 m, so that this factor is quite small. For example, for waves of period $T = 20$ s, $k^{-1} = 99$ m, peak-to-trough amplitude of 1.5 m (corresponding to the vigorous period on November 27; see Table 1), the underspeeding is negligible for mean speeds up to 20 cm s⁻¹. For $T = 10$ s, $k^{-1} = 248$ m, peak-to-trough amplitude of 1.14 m (November 27, Table 1), estimates of the amount of underspeeding U_p for various mean speeds U and observation depths z corresponding to current meter depths are shown in Table 2.

To estimate instrumental underspeeding, we used *Weller and Davis*' [1980] results for unsteady flow with mean flow and oscillation parallel and sensor axle 45° off the mean flow and oscillation direction. This was a situation found to give moderately large underspeeding biases. Though we cannot reconstruct the orientation history of the sensors in our experiment, this seems a modestly pessimistic choice. When mean flow and the oscillations are not colinear, underspeeding is reduced because the instrument encounters its wake less frequently. The underspeeding bias is moderate, ~ 1.5 cm s⁻¹, for observation depths 11.5 and 14.5 m, and for mean flows of 5 and 10 cm s⁻¹. For higher-frequency waves, for example, $T = 4$ s, $k^{-1} = 40$ m, peak-to-trough amplitude of 0.50 m (November 29, Table 1), results are shown in Table 2. Underspeeding biases of large magnitude, ~ 4 cm s⁻¹, are found. Table 2 can be used qualitatively in the following way. Suppose the CMD were drifting downwind at ~ 20 cm s⁻¹ and that the 2.5 and 8.8 m true mean currents were ~ 15 and ~ 10 cm s⁻¹. The current meters at these depths encounter mean relative currents of ~ 5 and ~ 10 cm s⁻¹, respectively. From Table 2 we deduce an underspeeding bias at 2.5 m of ~ 1.1 cm s⁻¹ for an observed relative mean flow of $5.0 - 1.1 = 3.9$ cm s⁻¹ and at 8.8 m a bias of ~ 2.5 cm s⁻¹ for an observed mean flow of $10.0 - 2.5 = 7.5$ cm s⁻¹. The observed current shear of ~ 3.6 cm s⁻¹ is actually smaller than the true shear ~ 5 cm s⁻¹. We do not advocate the use of these tables to correct the observed low frequency flows for underspeeding because of uncertainties about the actual behavior of the CMD in the wave motion; the orientation of

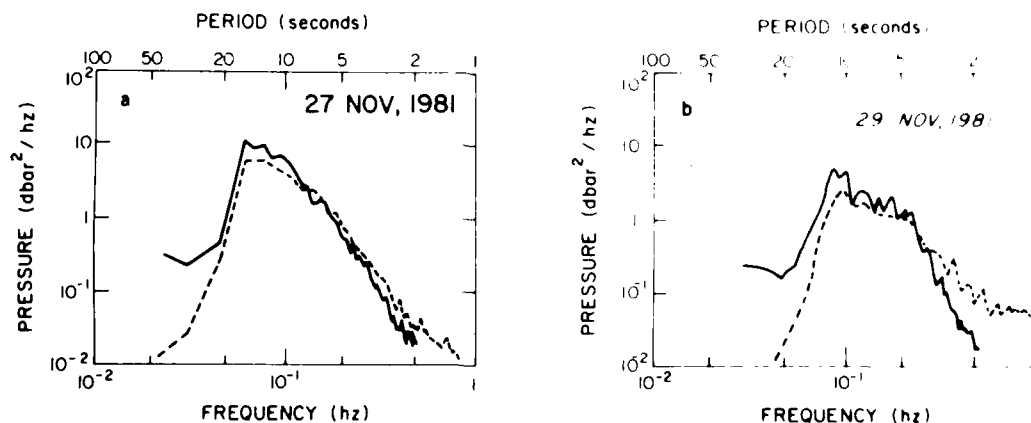


Fig. 10. High-frequency pressure spectrum at 32.5 m (solid line) compared to the predicted pressure spectrum (dashed line) using the drifter motion model response function for (a) November 27 and (b) November 29.

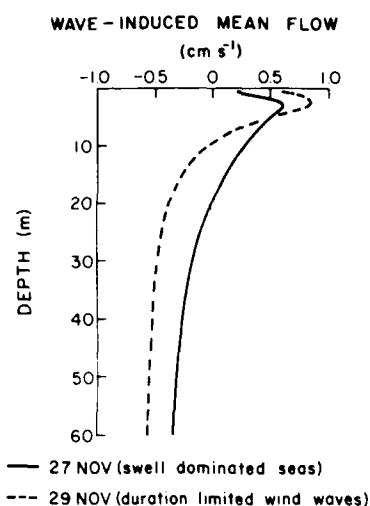


Fig. 11. Surface wave-induced mean flow observed by ideal cosine response current meters predicted from the drifter motion model forced by random seas using the wave height spectra of November 27 (solid line) and November 29 (dashed line).

mean flow, waves, and sensor axes, and the far greater complexity of a random wave field than the simple reciprocating motions that Weller and Davis [1980] studied in the laboratory tow tank. However, they show that, if anything, the current shears between adjacent current meters as in Figures 5 and 6 are underestimates, and that the error is of order 1 cm s⁻¹. We conclude that the current differences of Figures 5 and 6 are true indications of moderately high shears in the near-surface layer.

Near-Surface Drifters

In the latter portion of the CMD deployment, during the period of persistent brisk northwest winds, some small radio-tracked drifters [Davis *et al.*, 1982] drogued at 1, 2, 4, and 8 m depth were deployed. Two deployments were made at midday on November 28 and November 30, and positions were obtained at 6-hour intervals between midday of November 28 and early in December 2; during this period the average distance between the CMD and the current followers was 5 km. The drifter velocities exhibited substantially smaller shears than found by the current meters with drifters at all levels agreeing closely with the 5.5-m VMCM. Mean shears between drifters and between current meters for the 3.2-day period including November 29 and early December 2 are shown in Table 3. During this period the root mean square wind speed

TABLE 2a. Velocity Underspeeding U_1 as a Function of Depth and Mean Flow Speed Induced by a Surface Wave With 10-s Period and 57-cm Amplitude

Depth, m	Mean Flow Speeds, cm s ⁻¹			
	20	15	10	5
2.5	<0	<0	<0	<0
5.5	<0	<0	0.1	0.4
8.5	<0	<0	0.5	1.0
11.5	0.5	0.9	1.5	1.4
14.5	0.5	0.9	1.5	1.5

Velocities are in centimeters per second

TABLE 2b. Velocity Underspeeding U_1 as a Function of Depth and Mean Flow Speed Induced by a Surface Wave With 4-s Period and 25-cm Amplitude

Depth, m	Mean Flow Speeds, cm s ⁻¹			
	20	15	10	5
2.5	0.5	0.9	1.4	1.1
5.5	-2.3	3.0	2.5	1.8
8.5	3.4	3.5	3.0	2.1
11.5	-4.0	-3.8	-3.2	-2.3
14.5	4.3	3.9	3.3	2.3

Velocities are in centimeters per second

was 12 m s⁻¹ with small excursions around the mean direction of 330°.

Below 2 m depth the drifter shears are only 60% of the VMCM shears, and they are more nearly aligned with the wind direction. Remarkably, the 1-m versus 2-m drifter shear is unmeasurably small. This is surprising, since one would expect drifter shears to exceed current meter shears by the Stokes drift contribution. The differences in shear correspond to approximately 1 cm s⁻¹ over 3 m depth difference. Laboratory and field tests [Davis *et al.*, 1982] show the current-following errors of the drifters to be no larger than this but are insufficiently precise to demonstrate that the errors are smaller. Nevertheless, we believe that the differences between current meters and drifters are not the result of drifter performance in a seaway because relative errors between drifters will be significantly smaller than the absolute errors, which themselves are 1 cm s⁻¹. Thus we believe the differences are associated with the fact that drifters seek out regions of horizontal convergence. Weller *et al.* [1985] have shown that Langmuir cell circulation, often present in conditions like those observed here, are associated with strong three-dimensional flow. Further analysis (R. A. Weller, personal communication, 1986) indicates that in regions of downwelling, where drifters are most apt to be found, the maximum downwind velocity is found below the surface and the near-surface shear is upwind. We suspect that the preferential sampling of such regions by drifters is the cause of the lower downwind shear observed by drifters as compared to current meters.

5. DISCUSSION

The magnitudes of the current shears in Figures 5 and 6 and their obvious association with wind speed and direction are very suggestive. The coincidence of shear with $u_* (\kappa z)^{-1}$ between 2.5 and 5.5 m is striking and tends to support observations in lakes by Dillon *et al.* [1981] of near-surface dissipation varying like $u_*^3 (\kappa z)^{-1}$.

TABLE 3. Shear $\times 1000$ in Inverse Seconds Between Drifters and Between Current Meters

		Drifter		VMCM			
z_1	z_2	$\Delta u / \Delta z$	$\Delta t / \Delta z$	$\Delta u / \Delta z$	$\Delta t / \Delta z$	z_1	z_2
1 m	1 m	0	0.6				
2 m	4 m	2.8	3.3	3.6	6.5	2.5 m	5.5 m
4 m	8 m	3.2	3.0	0.3	7.1	5.5 m	8.5 m

Data is averaged over the 3.2 days beginning at the start of November 29

The depth of penetration of the $u_* (\kappa z)^{-1}$ layer, about 5 m, is quite thick and may be important in the momentum budget of the surface layer. It ought to be stressed that such a layer is not inconsistent with classical ideas about Ekman turning of currents. In this context, it is a useful exercise to write down and solve the Ekman layer equations with eddy viscosity given by $\kappa u_* |z|$. (The velocity profile is then given by Hankel functions.) Near the surface the velocity profile is approximately the classical $\kappa^{-1} u_*$. In z , and stress is consistent with depth. With increasing depth, the velocity turns to the right. Despite the linearly growing eddy viscosity the velocity profile is restricted to a boundary layer of thickness or order $u_* f$, in which the classical result holds that total transport is to the right of the wind stress and of magnitude $u_*^2 f$. The transition from logarithmic downwind profile to a rightward turning profile occurs at a depth which scales with $u_* f$. Of course, such a theory takes no account of stratification and is of limited practical use, but it shows how the classical constant stress logarithmic layer can be embedded in the Ekman layer.

Shear between 5.5 and 8.5 m is considerably larger than $u_* (\kappa z)^{-1}$. This may be accounted for by stratification: Temperature differences of only a few hundredths of a degree over 3 m would be sufficient, coupled with the shears observed, to produce gradient Richardson numbers as small as 0.2. Unfortunately, temperature differences so small could not be discerned with the temperature sensors on the VMCMs, so that a Richardson number time series cannot be constructed. Still, microstructure temperature profiles taken during the experiment from a ship operating near the CMD show that such small stable temperature gradients occur commonly in the near-surface layer. This is curious in light of pervasive unstable (downward) buoyancy fluxes throughout the course of the experiment (Figure 3b). Nor does there appear to be much diurnal modulation of the shear due to this buoyancy flux.

Acknowledgments. We thank Lloyd Regier and Jim Parks for preparing the current meters and deploying the Current Meter Drifter from the R/V *Horizon*. The support of this research by the Office of Naval Research through contracts N00014-79-C-0004 and N00014-84-C-0214 under project NR 083-102 to Oregon State University and contract N00014-85-C-0104 to Scripps Institution of Oceanography is gratefully acknowledged.

REFERENCES

- Busch, N. F., The surface boundary layer, *Boundary Layer Meteorol.*, **4**, 214-240, 1973.
- Caldwell, D. R., C. W. Van Atta, and K. N. Helland, A laboratory study of the turbulent Ekman layer, *Geophys. Astrophys. Fluid Dyn.*, **3**, 125-160, 1977.
- Chhabra, N. K., Correction of vector-averaging current-meter records from MODF-1 central mooring for effects of low-frequency mooring line motion, *Deep Sea Res.*, **24**, 279-287, 1977.
- Chhabra, N. K., Computation of errors in current meters attached to near-surface moorings, *J. Geophys. Res.*, **90**, 4995-4999, 1985.
- Churchill, J. H., and G. T. Csanady, Near-surface measurements of quasilagrangian velocities in open water, *J. Phys. Oceanogr.*, **13**, 1669-1680, 1983.
- Csanady, G. T., On the resistance law of a turbulent Ekman layer, *J. Atmos. Sci.*, **24**, 467-471, 1967.
- Davis, R. E., R. de Szoeke, D. Halpern, and P. Niler, Variability in the upper ocean during MILE, 1. The heat and momentum balances, *Deep Sea Res.*, **28A**, 1427-1451, 1981a.
- Davis, R. E., R. de Szoeke, and P. Niler, Variability in the upper ocean during MILE, 2. Modeling the mixed layer response, *Deep Sea Res.*, **28A**, 1453-1575, 1981b.
- Davis, R. E., J. E. Dufour, G. J. Parks, and M. R. Perkins, Two inexpensive current-following drifters, *Scripps Inst. of Oceanogr. Ref. Ser.*, 82-28, La Jolla, Calif., 1982.
- Dillon, T. M., J. G. Richman, C. G. Hanson, and M. D. Pearson, Near-surface turbulence measurements in a lake, *Nature*, **290**, 390-392, 1981.
- Ekman, V. W., On the influence of the earth's rotation on ocean currents, *Ark. Mat. Astron. Fys.*, **2**, 52 pp., 1905.
- Jones, I. S., and B. C. Kenney, The scaling of velocity fluctuations in the surface-mixed layer, *J. Geophys. Res.*, **82**, 1392-1396, 1977.
- Kitaigorodskii, S. A., and J. L. Lumley, Wave-turbulence interactions in the upper ocean, I. The energy balance of the interacting fields of surface wind waves and wind-induced three-dimensional turbulence, *J. Phys. Oceanogr.*, **13**, 1977-1987, 1983.
- Kitaigorodskii, S. A., M. A. Donelan, J. L. Lumley, and F. A. Terray, Wave-turbulence interactions in the upper ocean, II. Statistical characteristics of wave and turbulent components of the random velocity field in the marine surface layer, *J. Phys. Oceanogr.*, **13**, 1988-1999, 1983.
- Monin, A. S., and A. M. Yaglom, *Statistical Fluid Mechanics: Mechanics of Turbulence*, vol. 2, 874 pp., MIT Press, Cambridge, Mass., 1975.
- Pedlosky, J., *Geophysical Fluid Dynamics*, 624 pp., Springer-Verlag, New York, 1979.
- Phillips, O. M., *The Dynamics of the Upper Ocean*, 261 pp., Cambridge University Press, New York, 1966.
- Prandtl, L., Bericht über Untersuchungen zur ausgebildeten Turbulenz, *Z. Angew. Math. Mech.*, **5**, 136-139, 1925.
- Stacey, M. W., S. Pond, and P. H. LeBlond, A wind-forced Ekman spiral as a good statistical fit to low-frequency currents in a coastal strait, *Science*, **233**, 470-472, 1986.
- Sverdrup, H. U., M. W. Johnson, and R. H. Fleming, *The Oceans, Their Physics, Chemistry, and General Biology*, 1087 pp., Prentice-Hall, Englewood Cliffs, N. J., 1942.
- von Karman, T., Mechanische Ähnlichkeit und Turbulenz, *Nachr. Ges. Wiss. Göttingen Math. Phys. Kl. Fachgruppe I*, 58-76, 1930.
- Weller, R. A., The relation of near-inertial motions observed in the mixed layer during JASIN (1978) experiment to the local wind stress and to the quasigeostrophic flow field, *J. Phys. Oceanogr.*, **12**, 1122-1136, 1982.
- Weller, R. A., and R. E. Davis, A vector measuring current meter, *Deep Sea Res.*, **27**, 565-581, 1980.
- Weller, R. A., J. P. Dean, J. Marra, J. E. Price, E. A. Francis, and D. C. Boardman, Three dimensional flow in the upper ocean, *Science*, **227**, 1552-1556, 1985.
- Wu, J., Wind-induced drift currents, *J. Fluid Mech.*, **68**, 49-70, 1975.
- R. E. Davis, Scripps Institution of Oceanography, La Jolla, CA 92093.
- R. A. de Szoeke and J. G. Richman, College of Oceanography, Oregon State University, Corvallis, OR 97331.

(Received December 9, 1985;
accepted February 3, 1986.)

The Available Potential Energy of Overturns as an Indicator of Mixing in the Seasonal Thermocline

T. M. DILLON AND M. M. PARK

College of Oceanography, Oregon State University, Corvallis

Using empirical observations, it is shown that the available potential energy of fluctuations (the APEF) is proportional to the product of the Cox number C_x , the local buoyancy frequency N , and the molecular diffusivity of temperature D . The nondimensional number $C_x - \text{APEF} (ND)$ is shown to be a good predictor of the Cox number and can be used as an indicator of mixing in stratified fluids. Analysis of the APEF at ocean station P shows that turbulence in the seasonal thermocline responds to strong surface forcing.

1. INTRODUCTION

Most observations of three-dimensional turbulence in the sea involve measurements of gradients of velocity, temperature, or other scalars and therefore require the use of sensors able to resolve small length scale, large wave number fluctuations. A direct measurement of the kinetic energy dissipation rate requires the velocity to be resolved on length scales $O(0.01 \text{ m})$ [cf. Osborn, 1980; Oakey, 1982], and measurement of the Cox number [Osborn and Cox, 1972] demands a resolution of the temperature on even smaller scales [Dillon and Caldwell, 1980]. However, oceanic turbulence exists on a variety of length scales. For example, the length scale of turbulent overturns in stratified parts of the ocean is usually larger than a few tens of centimeters and often extends to a few meters [Dillon, 1982]. It may sometimes (though certainly not always) be more convenient to measure large length scale variables than microscale variables.

The notion that small-scale quantities may depend on large-scale fluctuations is consistent with turbulence being created at large length scales (often called the production or energy-containing range) and dissipated at smaller scales (called the dissipation range [e.g., Tennekes and Lumley, 1982]). A first-order hypothesis is that energy produced at large scale is transferred to smaller scale by nonlinear interactions and, if the time scale for changes in dissipation range variables is faster than the rate at which production range fluctuations change, an approximate equilibrium between large-scale and small-scale quantities may result. In those cases where there is not a large separation of scales, dissipation-scale fluctuations must depend strongly on production range scales.

Links have recently been established between the large length scales of overturns and dissipation-scale fluctuations. The kinetic energy dissipation rate ϵ and the buoyancy frequency N may be used to form the Ozmidov length, $L_o = (\epsilon/N^3)^{1/2}$ [Dougherty, 1961; Ozmidov, 1965]. L_o depends on ϵ , and ϵ is a dissipation range quantity; in this sense, L_o is a large-scale representation of microscale information. The Thorpe scale L_T [Thorpe, 1977; Dillon, 1982] has a size characteristic (perhaps within a factor of 2) of overturning structures and is a "production-range" variable, only in-

directly dependent on dissipation range turbulence. In most cases where L_T and L_o have been simultaneously measured, the Thorpe scale has been found nearly equal to the Ozmidov length [Dillon, 1982; Crawford, 1986; Gregg et al., 1986; Itsweire, 1984], though some important exceptions to this rule have been found [Dillon, 1982].

Gargett et al. [1981] have shown that in the stratified interior of the ocean, the vertical shear spectrum falls off with wave number k as k^{-1} in the approximate range 0.1–1 cpm and begins a gentle rise (perhaps proportional to $k^{1/3}$) near the wave number $k_b = L_o^{-1}$. The Thorpe scale, nearly equal to the Ozmidov scale, has a physical meaning in terms of the spectrum of stratified turbulence: L_T^{-1} is the wave number at which turbulence is constrained by buoyancy forces.

The available potential energy of unstable density fluctuations (the APEF [Dillon, 1984]) is another variable that can be found by ordering density profiles. Like the Thorpe scale, the APEF is a "large-scale" variable that indirectly depends on dissipation range fluctuations. The APEF is useful because it is a measure of the maximum potential energy that can be released by a turbulent overturn. The APEF is a unique quantity, while Thorpe displacements are not necessarily unique (e.g., the calculated Thorpe displacements will depend on the ordering algorithm if the profile has more than one sample with the same density). It is not our intention to suggest that the APEF is preferable to the Thorpe scale but rather to point out that Thorpe variables other than L_T also have physical significance.

The goals of this report are (1) to show that the APEF is proportional to the rate of potential energy dissipation and that an estimate of the Cox number can sometimes be made from fine scale rather than microscale measurements and (2) to demonstrate that the APEF is a useful indicator of mixing in the seasonal thermocline. Details of the methods of calculating the APEF are described in section 2. Section 3 discusses the significance of the APEF to the dynamics of turbulence. Section 4 applies the preceding results and uses the APEF to describe mixing in the seasonal thermocline at ocean station P. Section 4 contains a summary of the results and a discussion of their consequences.

2. CALCULATING THE APEF

The Thorpe profile is found by rearranging or ordering discrete density samples to form a monotonic, gravitationally stable profile. The Thorpe profile is a one-dimensional repre-

Copyright 1987 by the American Geophysical Union.

Paper number 6C0285.

0148-0227/87/006C-0285\$05.00

TABLE 1. Calculation of the APEF for a Hypothetical Vertical Density Profile and the Associated Thorpe Statistics Calculated for Three Depth Intervals

Z	ρ_0	ρ	d'	ρ'
10	1.12	1.12	0	0.00
9	1.32	1.15	5	0.17
8	1.57	1.17	7	0.40
7	1.38	1.20	4	0.18
6	1.15	1.24	3	0.09
5	1.46	1.27	3	0.19
4	1.24	1.32	2	0.08
3	1.20	1.38	-4	-0.18
2	1.27	1.46	3	0.19
1	1.17	1.57	7	-0.40
0	1.80	1.80	0	0.00

Depth Interval			
	1-9	1-4	5-9
APEF $\equiv \langle Z\rho' \rangle$	0.529	1.280	0.410
$\langle d'^2 \rangle^{1/2}$	4.47	4.65	4.65
$\langle \rho'^2 \rangle^{1/2}$	0.236	0.230	0.242
$\langle \rho' \bar{c} z \rangle$	0.053	0.083	0.030
$\frac{1}{2} \langle \rho' d' \rangle$	0.529	0.531	0.521
$\frac{1}{2} L_T^{-1} \langle \rho' \bar{c} z \rangle$	0.524	0.814	0.324
$\frac{1}{2} \langle \rho'^2 \bar{c}(\bar{c} z)^{-1} \rangle$	0.530	0.317	0.976

Depth intervals include the entire overturn (samples 1-9), the lower subregion (samples 1-4), and the upper subregion (samples 5-9). By definition (1), the APEF $\equiv \langle Z\rho' \rangle$ (in units where the acceleration of gravity and mean density are 1; angle brackets imply a vertical average). Definition (1) implicitly assumes that the region of calculation is at least one complete overturn; (1) gives misleading results in either the upper or lower subregion alone. However, when the approximation (2) (i.e., APEF $\equiv \langle \rho' d' \rangle / 2$) is used, the result for each subregion is representative of the overturn as a whole. The linear gradient approximations (3) and (4) are poor predictors of the APEF in both top and bottom subregions.

sensation of a minimum potential energy state. No profile composed of the same density samples can have a lower potential energy, because if the ordered profile is perturbed to any nonmonotonic profile, the potential energy of the perturbed profile will be greater than that of the ordered profile [Dillon, 1984]. The potential energy difference between a measured density profile and the corresponding Thorpe profile can be termed the available potential energy of the fluctuations because the energy could, in principle, be used for irreversible thermodynamic processes, such as mixing the fluid and changing the mean potential energy of the fluid, or for changing the kinetic energy.

Density samples are seldom used to calculate Thorpe profiles because density often cannot be calculated in salt water with sufficient precision on length scales as small as 0.01-0.02 m. Instead, it is usually assumed that the density is uniquely determined by the temperature, and the temperature profile itself is then ordered (of course, if salinity instead of temperature controls the density, basing the APEF on temperature fluctuations alone will be dynamically meaningless). An expansion coefficient α can be used to define the APEF by

$$\text{APEF} = (1/M) \sum_{n=1}^M \alpha g z_n \theta'_n \quad (1)$$

where the temperature samples occur at depth z_n , g is the acceleration of gravity, $\theta'_n = T(z_n) - T_0(z_n)$ is the Thorpe fluctuation, $T(z_n)$ is the measured temperature profile, $T_0(z_n)$ is the Thorpe profile, and $\alpha(S, T) = -\rho^{-1}(\partial \rho / \partial T)$.

It is inadvisable to use (1) when it is necessary to estimate the APEF over a fixed interval defined by specific depths or isotherms, because there is no guarantee that the interval encloses a complete overturn (a "complete overturn" is the smallest interval containing density inversions such that no densities between the minimum and maximum densities within the interval can be found outside of the interval). Table 1 illustrates a hypothetical case (using arbitrary depth and density units, and assuming for simplicity that the acceleration of gravity is unity) where the complete overturn extends from 1 to 9 depth units. Estimating the APEF in the range 1-4 depth units with (1) would give a misleading result: the APEF would be negative because only the lower half of the overturn, where the density fluctuations are all negative, would be included in the calculation. Similarly, the APEF characteristic of the entire overturn would be overestimated if only the upper half of the overturn were included. Another way to estimate the APEF is from the approximation

$$\text{APEF} \approx (1/2M) \sum_{n=1}^M \alpha g d'_n \theta'_n \quad (2)$$

where d'_n is a Thorpe displacement. While each displacement is uniquely associated with a single density sample, two depths can be associated with each displacement: one the depth of the density sample in the original profile, the other the depth of the same sample in the ordered profile. We define $d'(z)$ as the displacement of a density sample at the depth of the sample $\rho(z)$ in the original profile.

The approximation (2) is based on the observation that if any two density samples separated by a depth d' are exchanged, a potential energy change $g d'[\rho(z+d') - \rho(z)]$ must take place. The factor of 1/2 in (2) arises because each sample exchange is counted twice in the sum. If $\rho_0(z)$ can be constructed from $\rho(z)$ by any number of two-sample exchanges, with no sample exchanged more than once, then (2) is exact. For our data, the difference between (1) and (2) is less than 2% when both formulations are applied to entire profiles. When both (1) and (2) are applied to individual complete overturns (as opposed to entire profiles), the root-mean-square percentage difference between them is 14%.

If the temperature profile is linear, $\theta'_n = d'_n \bar{c} T' \bar{c} z$, and

$$\text{APEF} \approx (1/2M) \sum_{n=1}^M \alpha g (\bar{c} T' \bar{c} z) d_n'^2 = \frac{1}{2} N^2 L_T^{-2} \quad (3)$$

In terms of the root-mean-square temperature fluctuation, a linear temperature profile requires

$$\text{APEF} \approx (1/2M) \sum_{n=1}^M \alpha g (\bar{c} T' \bar{c} z)^{-1} \theta_n'^2 = \frac{1}{2} N^2 (\bar{c} T' \bar{c} z)^{-2} \langle \theta'^2 \rangle \quad (4)$$

The linear estimates (3) or (4) can differ from (2) by factors of 2 or 3 (Crawford [1987]; see also Table 1) because a linear density profile is often a poor approximation. It is preferable to use (1) for calculating the APEF, or if averaging must be done over fixed intervals, it is preferable to use (2) rather than (3) or (4). However, (3) and (4) are often useful in scaling arguments and order of magnitude estimates.

Thorpe variables can be adequately measured with less resolution than is necessary to resolve the entire temperature gradient spectrum. When the fluid is turbulent, the temper-

ature gradient spectrum has a high wave number peak containing most of the temperature gradient variance [Dillon and Caldwell, 1980]. The spectrum of Thorpe displacements, however, typically has a low wave number peak (Figure 1). The spectral slope at wave numbers higher than the peak is approximately $k^{-5/3}$, although the significance of this observation is not clear.

Instruments having slower frequency response than the one used for this report could be used to measure Thorpe statistics. A zeroth-order model for the displacement spectrum can summarize Figure 1:

$$\begin{aligned} S_d(k) &= (2/3)L_T^{-4/3}k^{-5/3} & k \geq L_T^{-1} \\ S_d(k) &= 0 & k < L_T^{-1} \end{aligned} \quad (5)$$

which satisfies

$$L_T^{-2} = \int_0^\infty S_d(k) dk \quad (6)$$

A lowered wave number response implies that the measured L_T would be smaller than the actual Thorpe scale. It can be shown using (5) that 90% of L_T is measured if a wave number $k > 30/L_T$ (wavelength $< L_T/5$) is resolved (cf. a 0.1-m resolution is adequate for estimating the APEF in a patch where the L_T is 0.5 m).

The smallest detectable APEF can be estimated using the root-mean-square temperature noise in place of T'' in (4). For the data presented here, temperature noise was less than 0.002 (one least count), and the smallest significant APEF is $8 \times 10^{-12} \text{ m}^2 \text{ s}^{-4} \text{ N}^{-2}$ (e.g., $2.6 \times 10^{-8} \text{ m}^2 \text{ s}^{-2}$ for $N = 0.0175 \text{ s}^{-1} = 10 \text{ cph}$).

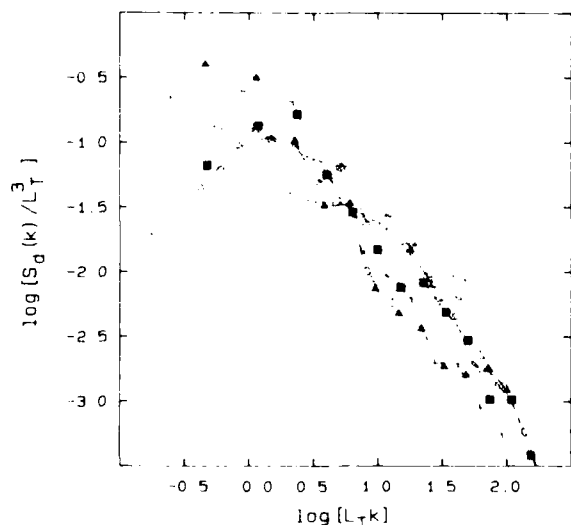


Fig. 1. Six representative nondimensional Thorpe displacement spectra. The nondimensional wave number is $L_T k$, where k is radian wave number and L_T is the Thorpe scale, $\int_0^\infty S_d(k) dk = L_T^{-2}$. The slope of the spectrum is greater than k^{-1} and less than $k^{-7/2}$, with $k^{-5/3}$ being a reasonable compromise. The spectra come from the following locations: cross and open triangle are from station P mixing layer, 10- to 30-m depth during second MHE storm; solid triangle and open square are from mixing layer of Green Peter Reservoir, 0- to 6-m depth during 8-m/s winds; solid square and open hexagon are from mixing layer of Puget Sound, 0- to 14-m depth, during 10-m/s winds.

3. APEF AS A MEASURE OF TURBULENCE

The rate at which potential energy fluctuations are dissipated is $N^2 DC$ [Dillon, 1984], where D is the molecular diffusivity and C is the Cox number [Osborn and Cox, 1972],

$$C = \sum_{i=1}^3 \langle (\tilde{c}T'' \tilde{c}\chi_i)^2 \rangle / \langle \tilde{c}T'' \tilde{c}Z \rangle^2 \quad (7a)$$

The summation in (7a) is over all three spatial directions, and T'' is a fluctuation from the mean. The Cox number is obtained from an isotropy assumption because it is impossible to measure the full three-dimensional temperature gradient spectrum. A one-dimensional vertical Cox number C_v can be defined as

$$C_v = \langle (\tilde{c}T'' \tilde{c}z)^2 \rangle / \langle \tilde{c}T'' \tilde{c}Z \rangle^2 \quad (7b)$$

If the turbulence is isotropic, $C = 3C_v$. Assuming that a potential energy production-dissipation balance holds, and the horizontal heat flux is on average small compared with the vertical heat flux, the vertical eddy diffusivity is $3DC_v$ [Osborn and Cox, 1972], and the buoyancy flux is

$$\alpha q_w w T'' = N^2 DC_v = 3N^2 DC_v \quad (8a)$$

Uncritical acceptance of (8a) is difficult because $\alpha w T''$ has never been measured in the ocean and the assumptions leading to (8) have not all been tested. Although the local production-dissipation balance assumption is often made, it may not be a good approximation. A counterassumption to (8a) is

$$N^2 DC_v \geq \alpha q_w w T'' \quad (8b)$$

that is, $3DC_v$ is an upper bound on the vertical diffusivity.

A nondimensional potential energy can be defined from the APEF, the buoyancy frequency, and the molecular diffusivity of temperature as $C_{pe} = \text{APEF}/(DN)$. The motivation for this choice is to be able to relate the available potential energy to

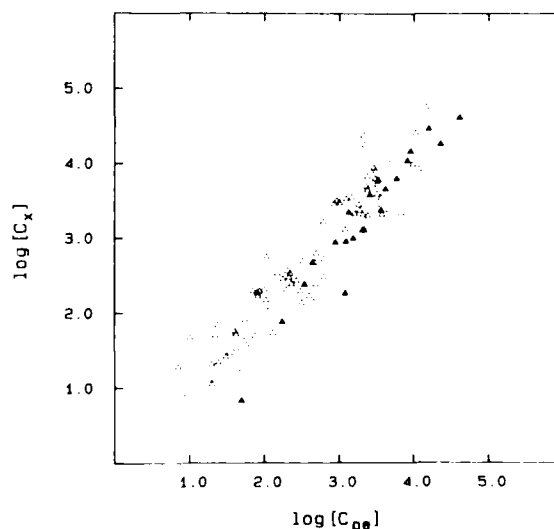


Fig. 2. The one-dimensional Cox number C_v plotted versus the nondimensional available potential energy, $C_{pe} = \text{APEF}/(DN)$, where N is buoyancy frequency and D is the diffusivity of temperature. Solid triangles are those samples where $4\text{APEF}/N > 1$, a criterion used by Dillon [1984] to distinguish those cases where gravitational collapse may be an important process.

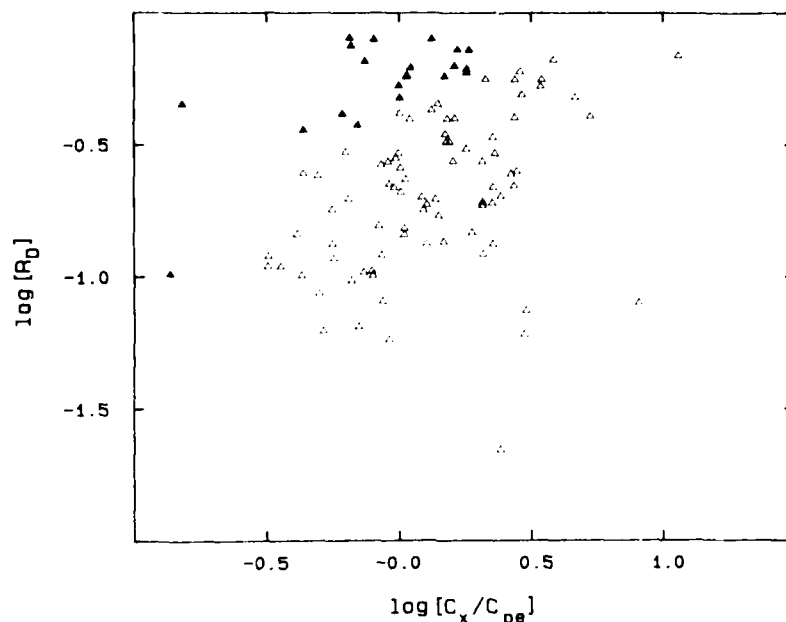


Fig. 3. The dissipation Richardson number $R_D = N^2 DC(u + N^2 DC)$ versus the ratio $C_x/C_{pe} = C_x/C_{pe}$ shows no systematic dependence on R_D . Solid triangles as in Figure 2.

the product of a basic time scale of the system (say, $1/N$) and the rate of potential energy dissipation, $N^2 DC$. The utility of this definition can be tested by comparing C_{pe} to the one-dimensional Cox number C_x . We find that they are nearly equal over four decades (Figure 2, using Dillon's [1982, 1984] data base, which is composed of measurements in actively mixing surface layers and the seasonal thermoclines of Green Peter Reservoir and ocean station P). There are no systematic departures from a constant proportionality between C_{pe} and C_x , and Figure 2 can be summarized as

$$C_x = (1.6 \pm 0.3)C_{pe} \quad (9)$$

The factor of 1.6 is the mean of C_x/C_{pe} for the 102 measured examples; the random uncertainty of the mean is 0.3, with a 90% confidence interval (determined from a bootstrap test consisting of 1000 separate averages of 102 components randomly chosen from the measured parent population of C_x/C_{pe}). In addition, there is a 30% systematic uncertainty in the value of C_x [Dillon, 1982]. The freshwater lake observations, where the density is completely determined by temperature, are not different from the oceanic observations, where a one-to-one relation between temperature and density is assumed.

C_x is used in Figure 2 rather than C to make clear that the relation is empirical and does not depend on an isotropy assumption. However, if the turbulence is isotropic, Figure 2 implies that the rate of dissipation of potential energy is proportional to the available potential energy. The proportionality constant is about $(3 \times 1.6)N = 4.8N$, i.e., the e -folding time for dissipation of the APEE is about $0.2/N$, 3% of a buoyancy period.

The APEE-Cox number relation is not equivalent to the Ozmidov scale-Thorpe scale relation [Dillon, 1982]. While the APEE is related to the square of the Thorpe scale through (3), the Cox number is related to the kinetic energy dissipation

rate, and therefore the Ozmidov scale, through the dissipation Richardson number R_D [Dillon, 1984]:

$$R_D = N^2 DC(u + N^2 DC)^{-1} \quad (10)$$

C_x/C_{pe} is not systematically dependent on R_D (Figure 3), but there is a systematic trend relating L_o/L_T to R_D (Figure 4). This suggests that the fundamental relationship is (9), with

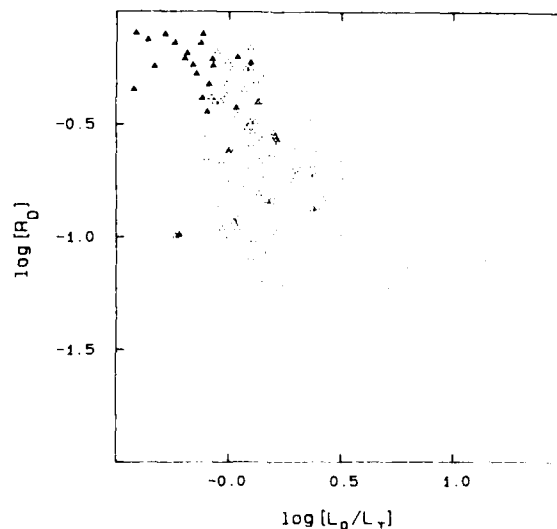


Fig. 4. The dissipation Richardson number $R_D = N^2 DC(u + N^2 DC)^{-1}$ versus the ratio $L_o/L_T = L_o/L_T$ does depend systematically on R_D , though for large R_D the approximation $L_o \approx L_T$ holds. Solid triangles as in Figure 2.

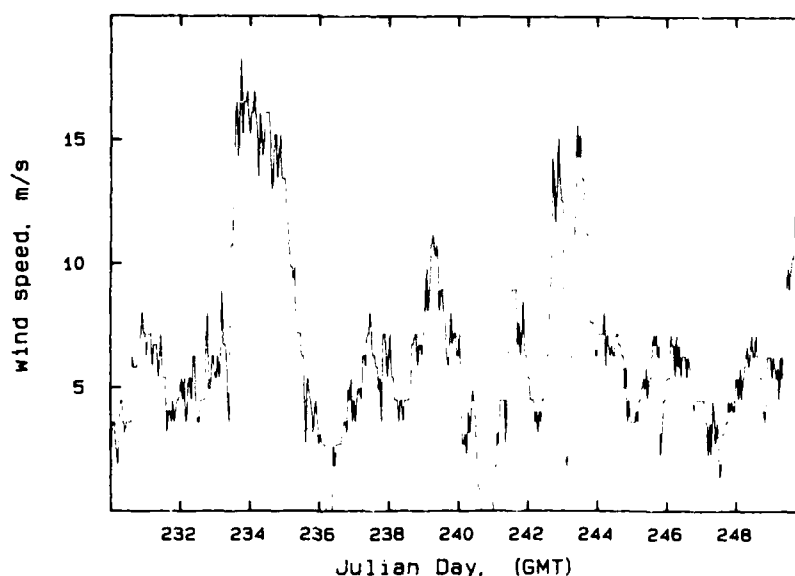


Fig. 5. Wind speeds measured from R/V *Oceanographer* during the MILE experiment. There are two major storms evident in the wind record, the strongest on days 234–235, the other on day 243.

$L_0 \approx L_T$ in some specific setting being contingent on having no large variation in R_p .

4. EXAMPLE: THE APEF AT STATION P

The utility of the APEF can be demonstrated by examining profiles of temperature microstructure in the seasonal thermocline. A large number of microstructure casts through the surface layer and seasonal thermocline were made at ocean station P in 1977 during the Mixed Layer Experiment (MILE). The instrument was a free-fall vehicle with high-frequency thermistors and a pressure sensor; occasionally, a Neal-Brown conductivity cell was also used [Dillon and Caldwell, 1980; Caldwell *et al.*, 1980; Dillon, 1982, 1984]. The vertical temperature gradient spectrum was entirely resolved much of the time, but in some casts, either the turbulence was too energetic or the high-frequency temperature gradient signal was too small to completely resolve the spectrum at all depths. Occasionally, the drop speed was too large to enable full spectral resolution. However, the temperature was resolved on 0.01- to 0.02-m vertical length scales in all cases and is adequate for calculating the APEF.

Caution is necessary when calculating Thorpe statistics in salt water because temperature inversions are not always associated with density inversions. Even when conductivity is measured, it is unlikely that density will be resolved on a small enough vertical scale to provide meaningful Thorpe statistics. We distinguish nonturbulent, salinity-stabilized intrusions from turbulent overturns by noting that in a nonmixing intrusion, there is no high-frequency temperature gradient signal. The few intervals found to contain nonturbulent inversions were discarded.

The profiles were analyzed in three segments, the "mixed layer," the "upper thermocline," and the "lower thermocline." All data above 10 m were rejected because the profiler was launched from the surface and depths shallower than 10 m might have been contaminated by the ship's wake. The mixed layer was operationally defined as the interval between 10-m depth and the depth where the temperature began to change rapidly (note that using this definition, the mixed layer is dis-

tinct from the mixing layer, and the mixed layer in this context may or may not be turbulent). The lower limit of the mixed layer was chosen such that at least a small interval of quiescent, nonoverturning fluid separated the mixed layer and upper thermocline regions. The change in temperature across the mixed layer was 0.4–0.5°C.

The upper thermocline region was defined as the interval between the mixed layer base and the 9°C isotherm. The lower boundary of the upper thermocline was defined in terms of fixed isotherms rather than fixed depths to minimize the influence of internal waves and tides. The approximate depth range of the upper thermocline was 30–35 m, although there was great variability in depth because of internal waves and tides. The mean buoyancy frequency in the upper thermocline was 20 cph, with a standard deviation of 6 cph. The lower thermocline region began at the 9°C isotherm (approximately 35-m depth) and extended to 50-m depth. The mean buoyancy frequency in the lower thermocline was 11 cph, with a standard deviation of 2 cph.

Casts were made on 18 days from Julian day 230 to 250, 1977. Winds used for this analysis were observations from the ship R/V *Oceanographer*, which was also the platform for the microstructure experiment. Two major storms were encountered, the first on days 233–235, with wind speeds to 20 m/s, and the second on days 242–243, with winds to 17 m/s. The latter storm was characterized by strong winds for an 8- to 10-hour period, a lull for 3–4 hours, followed by strong winds for 8–10 hours (Figure 5).

The APEF was averaged over all casts on each day except the day of the second storm, when data from the lull and strong wind periods were separately averaged. The mixed layer APEF is not very useful because sampling began at 10-m depth, and the upper mixed layer was never sampled.

Large peaks in the upper thermocline APEF are associated with the two major storms on days 234 and 243 (Figure 6a). The upper thermocline C_p is approximately 2000 on day 234, and 500 during the latter half of day 243 (Figure 6b). Apparently, surface stress can cause mixing in the upper thermocline. The rate of energy transfer from the wind stress to the upper

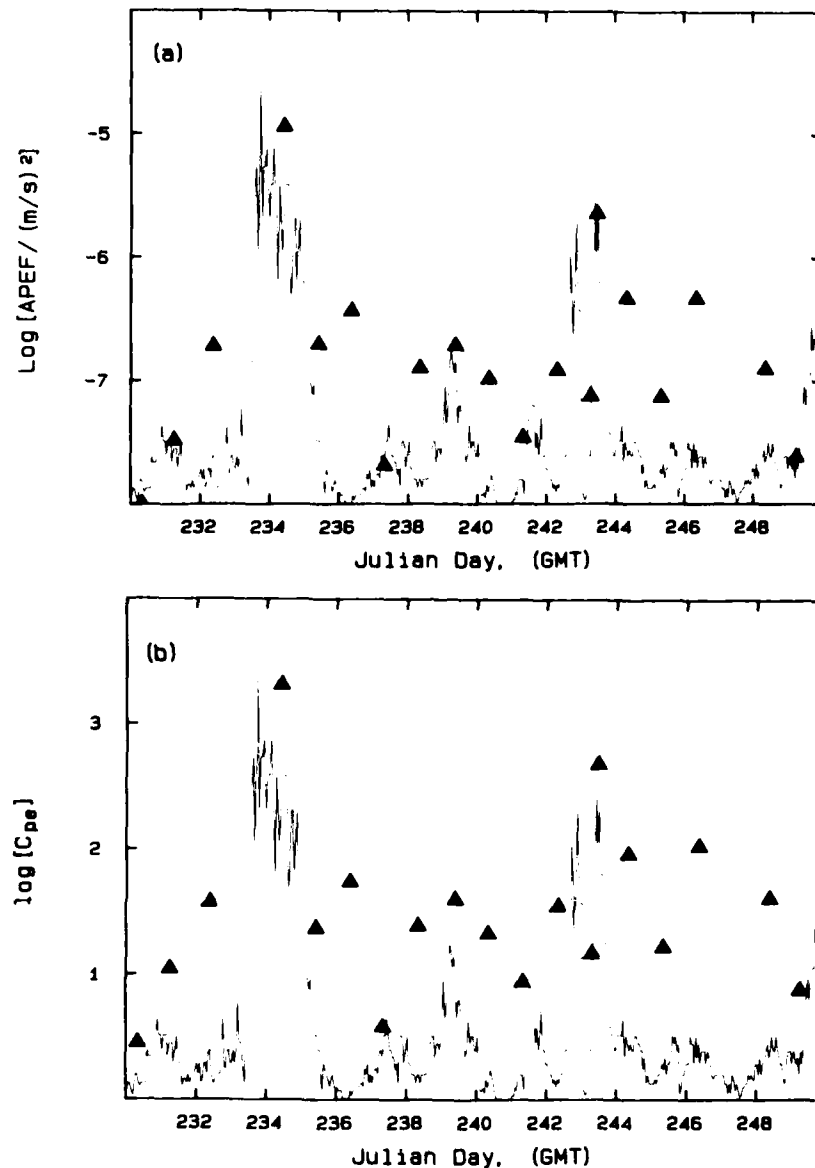


Fig. 6. Solid triangles are the (a) APEF and (b) C_{pe} for the upper seasonal thermocline during the MILE experiment. The continuous trace is proportional to the surface stress and is plotted on a linear scale. The APEF is large during both storms, when the surface stress was large.

thermocline must have been rapid, because during the second storm (day 243), the APEF is no larger than normal during the lull but is approximately 30 times larger than normal when the wind increases 2–3 hours later. The same fast response for thermocline kinetic energy dissipation rates has previously been noted [Dillon and Caldwell, 1980].

In the lower thermocline region, the APEF is largest ($1 \times 10^{-6} \text{ m}^2 \text{ s}^{-2}$) during the first storm (Figure 7a), but no response can be seen during the second storm. Occasionally, the lower thermocline APEF is large while the wind speed is small ($5 \times 10^{-7} \text{ m}^2 \text{ s}^{-2}$ on day 230 and $3.5 \times 10^{-7} \text{ m}^2 \text{ s}^{-2}$ on day 240). Apparently, significant mixing unrelated to wind stress can occur in the lower thermocline region.

The diffusivity can be estimated from (8) and (9) as of order SDC_{pe} (note that this may be an upper limit). During the first

storm, SDC_{pe} is $14 \times 10^{-4} \text{ m}^2 \text{ s}^{-1}$ in the upper thermocline, and $2.6 \times 10^{-4} \text{ m}^2 \text{ s}^{-1}$ in the lower thermocline.

Intermittent mixing events, presumably caused by internal waves, can be seen throughout the thermocline region even when the surface forcing is weak. This "background" mixing was analyzed by excluding the two storm events. The mean background APEF in the upper thermocline is $(16 \pm 5) \times 10^{-4} \text{ m}^2 \text{ s}^{-2}$ and is $(14 \pm 4) \times 10^{-4} \text{ m}^2 \text{ s}^{-2}$ in the lower thermocline. (The uncertainties reflect a 90% confidence interval and were determined from a bootstrap test. Sixteen random samples were chosen from the measured population of the APEF for a given region, and mean values were found. The test was repeated 100 times, and a histogram of the 100 means was prepared; 90% of the means were above the lower limit, and 90% of the means were smaller than the upper

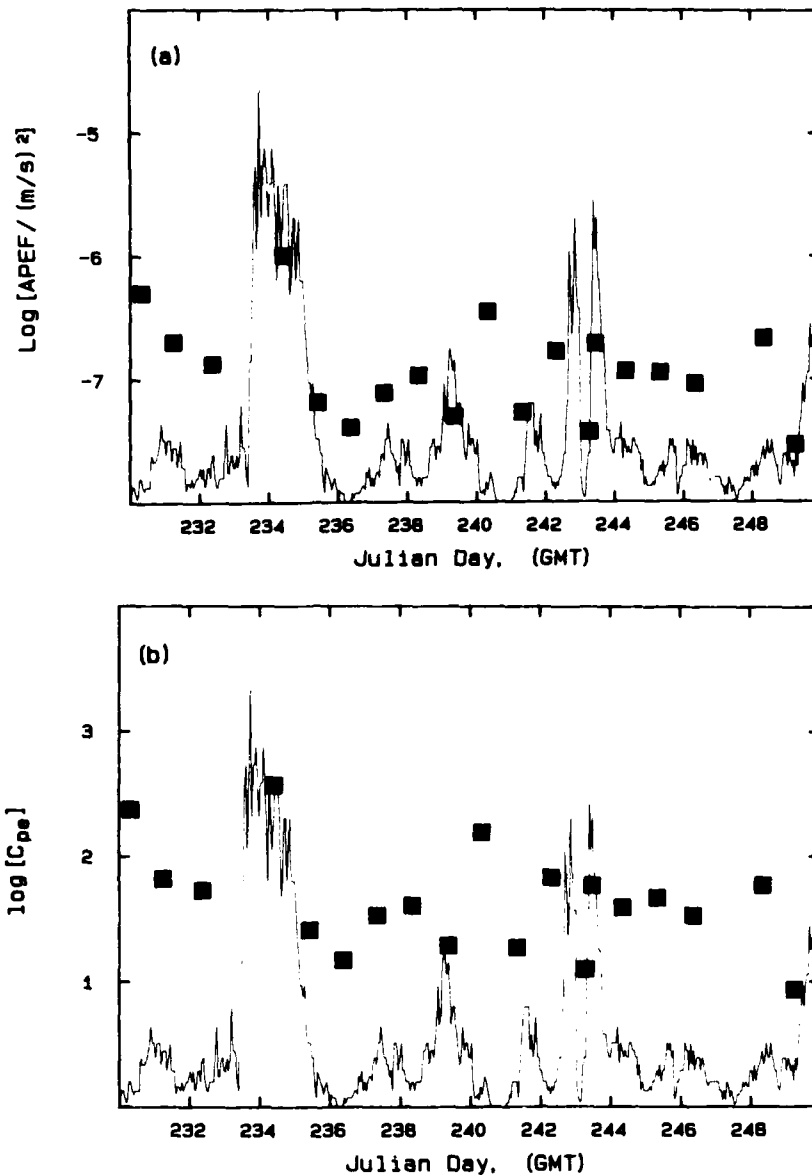


Fig. 7. Solid squares are the (a) APEF and (b) C_{pe} for the lower seasonal thermocline during the MILE experiment. The continuous trace is proportional to the surface stress and is on a linear scale. The APEF and C_{pe} are both large during the strong first storm. No significant response in the APEF or C_{pe} can be seen in the lower thermocline during the weaker second storm.

limit.) The upper thermocline APEF is not significantly different from the lower thermocline APEF at a 30% confidence level. There appears to be no systematic dependence of the background APEF on N ; both upper and lower thermocline APEF distributions could have come from the same populations (Figure 8).

The mean background C_{pe} is 33 ± 8 for the upper thermocline and 58 ± 16 for the lower thermocline (a bootstrap test similar to that described above was used to determine the 90% confidence limit uncertainties). The upper and lower thermocline C_{pe} difference is significant at the 98% confidence level. The "standing crop" of potential energy (i.e., the APEF) is statistically similar in the upper and lower thermocline, but C_{pe} is larger in the lower thermocline because the buoyancy frequency is smaller there. The background diffusivity estimate

$5DC_{pe}$ is $0.23 \times 10^{-4} \text{ m}^2 \text{ s}^{-1}$ in the upper thermocline and $0.41 \times 10^{-4} \text{ m}^2 \text{ s}^{-1}$ in the lower thermocline.

5. SUMMARY AND DISCUSSION

It is not necessary to measure the entire displacement spectrum in order to measure the available potential energy in overturns, and temperature probes with less than perfect vertical resolution can be used to find the APEF, as long as a one-to-one relation exists between temperature and density in the region of interest. If a wavelength of $1/5$ the Thorpe scale can be resolved, approximately 90% of the variance in the displacement spectrum can be resolved. The APEF provides a measure of mixing in thermoclines, and the Cox number can be estimated from the APEF and the buoyancy frequency.

During the MILE experiment, the seasonal thermocline ex-

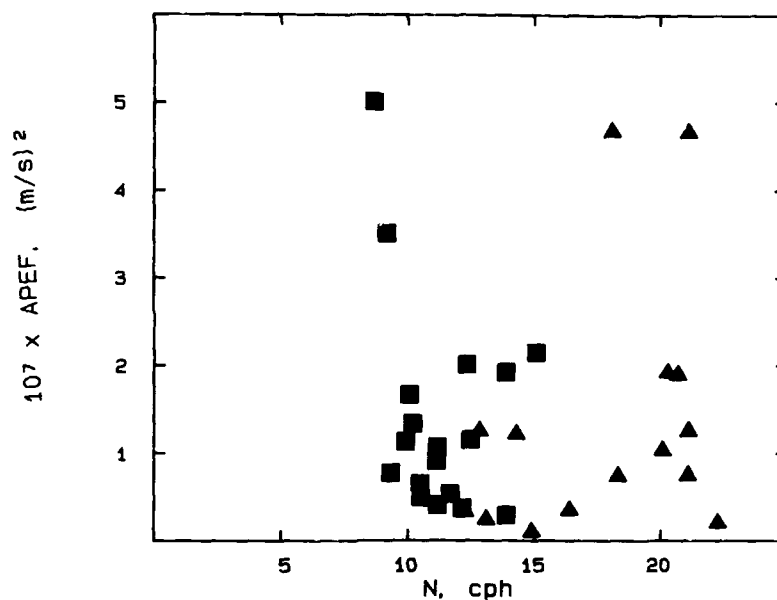


Fig. 8. The "background" APEF plotted against buoyancy frequency. The two stormy days (234 and 243) are excluded. Solid triangles are from the upper thermocline region, and solid squares are from the lower thermocline region. The mean APEF in the lower region is not significantly different from the upper thermocline APEF, and the distributions in each region have similar appearances.

hibited increased mixing when the surface was forced by strong winds. The response was rapid. The depth at which increased mixing was found depended on the strength of the forcing: during the strongest storm, the APEF was large in both the upper and lower thermocline, but during a weaker storm, the APEF was large only in the upper thermocline. On two days out of the 16 days examined, the lower thermocline APEF was between 1.3 and 1.2 as large as the APEF was during the strongest storm. These days are probably significant to any long-term average of heat and momentum transport, yet the enhanced mixing on these days was not related to the local wind. The upper thermocline APEF was not significantly different from the lower thermocline APEF when the surface was not strongly forced.

Other suggestions of a more speculative nature can be made. It is reasonable to assume that the background APEF is caused by the internal wave field and that the internal wave field at station P is reasonably well described by a universal internal wave spectrum. Gargett and Holloway [1984] (hereafter GH) suggest that the kinetic energy dissipation rate is proportional to N^q , within a factor of 2. GH examined two universal internal wave models, one yielding $q = 1$, the other $q = 1.5$, and gave some preference to the $q = 1$ model. If $q = 1$, there is a "universal" constant $\mu \approx 4 \times 10^{-7} \text{ m}^2 \text{ s}^{-2}$ (the numerical value taken from GH's figure), with $\epsilon \approx \mu N$. This is consistent with a model where the APEF is independent of depth and buoyancy frequency and so is constant wherever the internal wave field is universal. The "constant" value we would choose for the APEF would be $15 \times 10^{-8} \text{ m}^2 \text{ s}^{-2}$ (within a factor of 2, in the spirit of GH). This average APEF for both upper and lower thermocline is close to $\mu/3$.

If the APEF is constant (and we reiterate here that this is a speculation based on limited observations and not a proven conclusion), the scaling of some important quantities in the deep ocean can be predicted: C_{μ} , and hence the Cox number,

should be proportional to N^{-1} . Because of (3), the Thorpe scale should be proportional to N^{-1} , and because of (8), the turbulent heat flux should be proportional to N . Extensive measurements in the deep ocean must be made to test the truth of GH's model and these suggestions.

Acknowledgments. This work was supported by the National Science Foundation, contract OCE-8219921, and the Office of Naval Research, contract N00014-84-C-0218. W. Crawford, J. Imberger, and S. Thorpe read early versions of this report and offered useful suggestions.

REFERENCES

- Caldwell, D. R., T. M. Dillon, J. M. Brubaker, P. A. Newberger, and C. A. Paulson, The scaling of vertical temperature gradient spectra, *J. Geophys. Res.*, **85**, 1917-1924, 1980.
- Crawford, W. R., A comparison of length scales and decay times of turbulence in stably stratified flows, *J. Phys. Oceanogr.*, **16**, 1847-1854, 1986.
- Dillon, T. M., Vertical overturns: A comparison of Thorpe and Ozmidov length scales, *J. Geophys. Res.*, **87**, 9601-9613, 1982.
- Dillon, T. M., The energetics of overturning structures: Implications for the theory of fossil turbulence, *J. Phys. Oceanogr.*, **14**, 541-549, 1984.
- Dillon, T. M., and D. R. Caldwell, The Batchelor spectrum and dissipation in the upper ocean, *J. Geophys. Res.*, **85**, 1910-1916, 1980.
- Dougherty, J. P., The anisotropy of turbulence of the meteor level, *J. Atmos. Terr. Phys.*, **21**, 210-213, 1961.
- Gargett, A. E., and G. Holloway, Dissipation and diffusion by internal wave breaking, *J. Mar. Res.*, **42**, 15-27, 1984.
- Gargett, A. E., P. J. Hendricks, T. B. Sanford, T. R. Osborn, and A. J. Williams III, A composite spectrum of vertical shear in the upper ocean, *J. Phys. Oceanogr.*, **11**, 1258-1271, 1981.
- Gregg, M. C., H. Peters, J. C. Wesson, N. S. Oakey, and T. J. Shay, Intensive measurements of turbulence and shear in the equatorial undercurrent, *Nature*, **318**, 140-144, 1986.
- Itswire, E. C., Measurements of vertical overturns in a stably stratified turbulent flow, *Phys. Fluids*, **27**, 764-766, 1984.
- Oakey, N. S., Determination of the rate of dissipation of turbulent energy from simultaneous temperature and velocity shear microstructure measurements, *J. Phys. Oceanogr.*, **12**, 256-271, 1982.

- Osborn, T. R., Estimates of the local rate of vertical diffusion from dissipation measurements, *J. Phys. Oceanogr.*, 10, 83-89, 1980.
- Osborn, T. R., and C. S. Cox, Oceanic finestructure, *Geophys. Fluid Dyn.*, 3, 321-345, 1972.
- Ozmidov, R. V., On the turbulent exchange in a stably stratified ocean, *Izv. Acad. Sci. USSR Atmos. Ocean Phys.*, 1, 861-871, 1965.
- Tennekes, H., and J. L. Lumley, *A First Course in Turbulence*, 300 pp., MIT Press, Cambridge, Mass., 1972.
- Thorpe, S. A., Turbulence and mixing in a Scottish Loch, *Philos. Trans. R. Soc. London, Ser. A*, 286, 125-181, 1977.
- T. M. Dillon and M. M. Park, College of Oceanography, Oregon State University, Corvallis, OR 97331.

(Received December 6, 1985;
accepted May 20, 1986.)

On the Wind-Driven Circulation of the South Pacific Ocean

R. A. DE SZOEKE

College of Oceanography, Oregon State University, Corvallis, OR 97331

(Manuscript received 9 June 1986, in final form 6 November 1986)

ABSTRACT

A layered model of the steady circulation in the South Pacific Ocean is constructed along the lines of Luyten, Pedlosky and Stommel, and driven by the mean annual wind stress distributions computed by Hellerman and Rosenstein. The results of the model agree quite well with published maps of topography of density surfaces and circulation. Best agreement is found in the deeper layers. The deepest modeled layer, of density range $26.90 < \sigma_\theta < 27.30$, which contains the core layer of the Antarctic Intermediate Water, transports northwards some 14 Sv ($1 \text{ Sv} = 10^6 \text{ m}^3 \text{ s}^{-1}$) between New Zealand and South America. Of this, about three quarters comes from the west in an intense zonal jet that rounds the southern tip of New Zealand and quickly fans out from the boundary current along those islands into the anticyclonic gyre. Some 5 Sv returns southwards in the Australian boundary current. Much of the anticyclonic gyre in the western South Pacific is taken up by a shadow zone formed in the shelter of New Zealand, where the submerged layer loses direct contact with the wind driving, and where uniform potential vorticity is postulated. The modeled circulation in the shallowest layer in tropical regions is considerably weaker than the observed circulation.

Transport in the New Zealand western boundary current is determined by the necessity to achieve the same pressure in each layer at the northern end of the islands as at the southern. Similar considerations applied to the landmass of Australia and Papua-New Guinea, regarded as isolated from Southeast Asia, suggest a considerable net northward transport between Australia and South America, which can only escape through the Indonesian passages. The distribution of this transport among layers is set in the model by the input conditions at the southern boundary (where much of it must be in the deeper layers), after which it cannot change because of mass conservation within each layer (i.e., no cross-isopycnal flux is allowed). This modeling assumption is too strict and may be the reason for the prediction of shallow circulations much weaker than observed.

1. Introduction

In this paper we apply a simple model of wind-driven baroclinic circulation to the South Pacific Ocean. The model is identical (with slight modifications) to that developed by Luyten et al. (1983; hereafter LPS) and applied by them to the North Atlantic Ocean. Talley (1985) applied the same model to the North Pacific. The essential features of the model are the following. A vertical stack of homogeneous layers is driven at the surface by the wind stress. Water in layers at the surface becomes submerged under layers of lighter water as it flows equatorward. The densities of the layers and their subduction latitudes are choosable parameters of the model. The total (vertically integrated) mass transport is given by the curl of the wind stress (except in the western boundary currents), as proposed by Sverdrup (1947). Within each layer not directly in contact with the surface, potential vorticity is conserved by the motion. These principles serve to determine the partition of the Sverdrup transport among layers; that is, the circulation in each layer and the layer thicknesses.

Submerged layers are divided into ventilated and unventilated zones. In the ventilated zones, a streamline's potential vorticity is set at the point where it is first subducted and loses direct contact with the wind stress. Water in unventilated zones (shadow zones) is

never in direct contact with the wind, and an additional hypothesis about its potential vorticity distribution is necessary to determine its motion. The simplest assertion to make (unless the flow is stagnant) is that potential vorticity is constant throughout a shadow zone. This notion has some theoretical support (Rhines and Young, 1982), and reflects both numerical modeling experience (Holland et al., 1984) and oceanographic data (Keffer, 1985). The technical features of the model are reviewed in section 2. Some novelties are introduced into the circulation by the presence of New Zealand and the possibility of outflow of Pacific water into the Indian Ocean through the deep Indonesian Passages (Godfrey, 1987). Flows in the western boundary currents in each layer along New Zealand and Australia-Papua New Guinea (regarded as an isolated continent) are determined, not by the familiar requirement to balance the interior Sverdrup transport, as at the edge of a confined ocean basin, but by the necessity of achieving the same pressure at the northern end of the landmass as at the southern, so that there be no net geostrophic flow into the back side of the landmass. These considerations, discussed in sections 4 and 5, determine the transports and vertical structure of the boundary currents along eastern New Zealand and Australia-Papua-New Guinea.

The model, comprised of three moving layers, is

driven by the annual mean wind stress field, obtained from Hellerman and Rosenstein (1983). Results are shown in section 3. The topography of the deepest layer, in whose density range the salinity minimum core layer of the Antarctic Intermediate Water would fall, closely resembles the observed topography of a density surface representative of the core layer. The middle layer of the model, too, resembles the observed topography of density surfaces that would be contained in it, and exhibits circulation patterns similar to the observed. The shallowest layer, while showing some of the observed equatorward shift of the anticyclonic gyre with decreasing depth, and showing reasonable agreement with observed circulation in more temperate latitudes, gives only a poor representation of the observed shallow tropical circulation. Some reasons for this shortcoming are discussed.

The summary remark made by Warren (1970) that the South Pacific in the upper kilometer is described remarkably well by the Sverdrup (1947) theory of wind-driven transport is borne out. We may go further and say that the distribution of the Sverdrup transport among density layers in the vertical is fairly well described by considerations of potential vorticity conservation. This partition is basically determined at the southern boundary in the model. Thereafter it is immutable because of the assumption of continuity of net mass transport in each layer (i.e., no cross-isopycnal exchange between layers). This too strong insistence on layer-by-layer mass conservation may be the reason for the poor model agreement in the tropics, where the observed strong surface circulation may partially result from significant mass fluxes across the pycnocline.

2. The model

A brief description of the model is presented here. More details can be found in LPS and Talley (1985), whose notation we follow closely. The model consists of three layers with densities ρ_1 , ρ_2 , ρ_3 underlain by a fourth inert layer of density ρ_4 . The assumption of no motion in the fourth layer implies that the horizontally variable part of pressure in the lighter layers is given by

$$p_n/\bar{\rho} = \sum_{i=n}^3 \gamma_i H_i, \quad n = 1, 2, 3, \quad (2.1)$$

where $\gamma_i = g(\rho_{i+1} - \rho_i)/\bar{\rho}$ is reduced gravity between the i th and $(i+1)$ th layer, and H_i is the depth of the bottom of the i th layer (Fig. 1). The thickness of the i th layer is $h_i = H_i - H_{i-1}$. The bottom of the n th layer surfaces at the constant latitude y_n , poleward of which $H_n = 0$.

a. The Sverdrup relation

The vertically integrated meridional geostrophic transport is

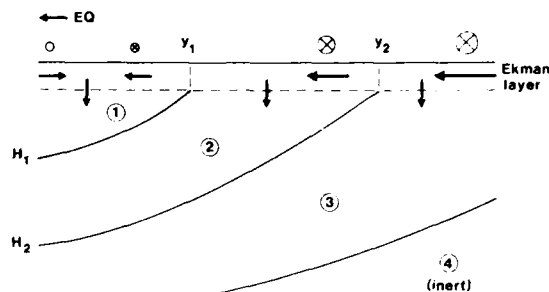


FIG. 1. A schematic meridional cross section of the layer structure of the model. The base of the n th layer outcrops at y_n .

$$-f^{-1}P \equiv -\frac{1}{2}f^{-1} \sum_{n=1}^3 \gamma_n H_n^2 = -\frac{1}{2}f^{-1} \gamma_3 (D_0^2 + H_{30}^2) \quad (2.2)$$

(Sverdrup, 1947), where

$$D_0^2(x, y) = -(\beta \gamma_3)^{-1} 2f^2 \int_0^y \hat{z} \cdot \nabla \times (\tau/\bar{\rho}f) dx', \quad (2.3)$$

and $P(x, y)$ is called the integrated steric height. At the eastern boundary $x_E(y)$, we take $H_1 = H_2 = 0$, and $H_3 = H_{30}$, a constant, taken to be 800 m for the South Pacific Ocean. (LPS omit the subscript 3 on H_3 and H_{30} .)

b. Potential vorticity conservation

From the assumptions of geostrophy and mass conservation in each layer, follows the conservation of potential vorticity in layers which are not directly forced by the wind, namely,

$$f/h_n = G_n(p_n). \quad (2.4)$$

The functions G_n are determined by the methods described by LPS and Talley (1985). For the present model only G_3 and G_2 are required. Table 1 specifies the possibilities for G_3 across the top row, and for G_2 down the left-hand column. The G_3 possibilities are distinguished by the symbols W, V, E for western shadow zone, ventilated zone, eastern shadow zone. The corresponding regions between y_1 and y_2 are marked on Fig. 2. In V, the potential vorticity of layer 3 is determined as the layer flows under the protective blanket of layer 2 at y_2 . Region E denotes the stagnant region along the eastern boundary in which $H_3 = H_{30}$ everywhere, and potential vorticity considerations are irrelevant. Region W is bounded in the east by $H_3 = H_{3W}$, the value of H_{3W} given by the theory for region V at the southern tip of New Zealand. Inside this unventilated region, potential vorticity is set equal to a constant, f_2/H_{3W} . As layer 2 slips under the protective blanket of layer 1 at y_1 , its potential vorticity G_2 is

TABLE 1. The G_2 and G_3 functions, and the regions of their definition.

G_2	G_3		
	$W: f_2/H_{3W}^*$	$V: f_2/H_3$	$E: H_{3E}^*$
$W: \frac{(1 + \gamma_2/\gamma_3)f_1}{\gamma_3^{-1}p_2 - f_1/f_2 - H_{3W}}$	WW [D]	VW [E]	EW
$V: \frac{(1 - f_1/f_2)^{-1} + \gamma_2/\gamma_3 f_1}{\gamma_3^{-1}p_2}$		VV [L]	EV [M]
$E: \frac{\gamma_2\gamma_3^{-1}f_1}{\gamma_3^{-1}p_2 - H_{3E}}$			EE [R]

* Constant

† Denotes that $H_3 = H_{30}$.

determined according to whether it overlies water in layer 3 belonging to region E, V or W. Hence, the G_2 possibilities are similarly designated E, V, W. The area equatorward of y_1 in Fig. 2 is split into a number of regions by the layer 2 and 3 streamlines (denoted in Fig. 2 by the labels "2" or "3") issuing from x_1^* and x_2^* , the longitudes defining the ventilated band V of layer 3 along y_1 . These regions are designated by a two-letter code on Fig. 2. The first letter identifies the G_3 function for the region, and the second letter the appropriate G_2 function. The two-letter codes are entered also in Table 1. Looking up region VW in Table 1, for example, we see that in this region in Fig. 2, $G_3 = f_2/H_3$, and $G_2 = (1 + \gamma_2/\gamma_3)f_1/(\gamma_3^{-1}p_2 - f_1/f_2 - H_{3W})$. The entries in braces in Table 1 indicate the regions denoted L, M, R by LPS and D, E by Talley (1985).

The mathematical problem in terms of H_1 , H_2 , H_3 is uniquely determined by (2.4) for $n = 2, 3$ (given the appropriate choice of G_3 , G_2 from Table 1 in a given region of interest), and by the Sverdrup transport constraint (2.2). [Poleward of y_1 , set $H_1 = 0$ and discard (2.4) for $n = 2$; poleward of y_2 , set $H_2 = 0$ also, and discard (2.4) altogether.]

TABLE 2. The density layer parameters used in the model.

Layer (n)	Density interval	Midlayer density, ρ_n	Reduced gravity ($10^3 \gamma_n/g$)	Outcrop latitude ($^\circ$)
1	26.05–26.25	26.15	0.425	39°S
2	26.25–26.90	26.575	0.525	51°S
3	26.90–27.30	27.10	0.30	—
4	27.30–27.50	27.40	—	—

c. Layer densities

The values of the layer densities used in the model are listed in Table 2. These layers are adapted from those defined by Keffer (1985), shown for comparison in Table 3, in his study of the potential vorticity distribution in the world's oceans. From Keffer's maps, a crude winter outcrop band can be estimated (the outcrop band is by no means zonally uniform) for each layer. A value near the equatorward extreme of this band is chosen for the outcrop latitude of the bottom of layers 1 and 2 in Table 2. Figure 3 shows a θ -S diagram for the South Pacific, with the density intervals of Tables 2 and 3 indicated. Note that layer 3 (and Keffer's, 1985, layer C) brackets the range of densities which occur at the intermediate-depth salinity minimum, the core layer of the Antarctic Intermediate Water.

d. Wind stress

The annual mean wind stress field prepared from normal monthly estimates by Hellerman and Rosenstein (1983), is used to drive the model. A map of the wind stress is shown in Fig. 4.

Wind stress curl is generally anticyclonic throughout the model domain. There is, however, a small region of cyclonic wind stress curl between 5° and 25°S along the South American coast, which drives a small cell of cyclonic circulation. This cell is shown shaded in Fig. 2. The model tends to predict surfacing of the bases of

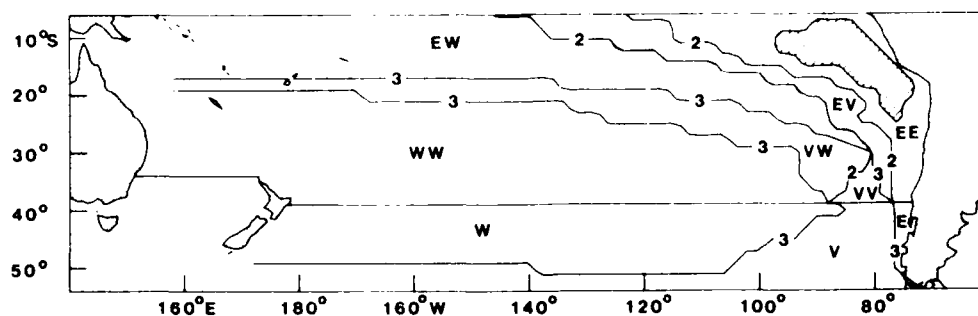


FIG. 2. The various regions of the model. Between y_1 and y_2 , W is the western shadow zone, V is ventilated zone, E is eastern shadow zone. Equatorward of y_1 , the two-letter codes denote appropriate choices for potential vorticity dependences G_3 , G_2 according to Table 1.

TABLE 3. Keffler's (1985) density layers in the South Pacific Ocean.

	Density interval	Midlayer density (σ_θ)	Outcrop band
A	26.05–26.25	26.15	
B	26.25–26.75	26.50	35°–50°S
C	27.00–27.30	27.15	50°–60°S
D	27.30–27.50	27.40	

layers 1 and 2 and upward doming of the base of layer 3 in this cell.

e. Model domain and resolution

The domain of the model is from the latitude of Cape Horn (57°S) almost to the equator, and from the South American continent to Australia and Papua-New Guinea. The model results are computed on a $2^\circ \times 2^\circ$ grid, to conform with the format in which the winds are supplied. Since all integrations have been explicitly carried out, there are no numerical difficulties associated with grid resolution.

Actual geographic land boundaries are used, except that shallow seas and straits are filled in. The southern tips of New Zealand and Tasmania are taken as $y_N = 50^\circ\text{S}$ and $y_{Tas} = 46^\circ\text{S}$, respectively, rather further south than the actual extremities of land, in order to represent the Campbell and Tasman plateaus. The northern tip of New Zealand is at $y_N = 32^\circ\text{S}$.

f. The transport streamfunction Ψ

Because the geostrophic transport is not horizontally nondivergent, it is convenient to augment it by adding the cumulative meridional Ekman transport from the eastern boundary, namely,

$$T_{EK}(x, y) = - \int_0^y \tau^{(p)} f^{-1} dx, \quad (2.5)$$

to both sides of (2.2). This total transport is nondivergent, so that a transport streamfunction

$$\Psi = f^{-1}P - T_{EK} - \frac{1}{2} f^{-1} \gamma_3 H_{30}^2 \quad (2.6)$$

can be defined ($\Psi = 0$ along the eastern boundary, while $\Psi < 0$ at a given point denotes northward transport between it and the eastern boundary).

3. Results

Though there are special considerations to be taken of the circulation around New Zealand in order to determine the flow in the Tasman Sea west of those islands, we shall postpone discussion of them to section 4, and present now solutions for the flow in the three

layers of the model, and discuss them in light of observations of the surface and intermediate circulation.

a. The Sverdrup circulation

Figure 5 shows the Sverdrup circulation in the South Pacific, computed from the winds in Fig. 4. This is part of a global map which has been presented and discussed by Godfrey (1987); it is included here for completeness, and comparison with the following figures. It shows the broad anticyclonic sweep of the South Pacific circulation. Western boundary currents are indicated as necessary to close the circulation.

The principle enunciated by Godfrey (1987) (see below, section 4) establishes that the northward transport, including the boundary current, between New Zealand and South America is 29 Sv ($1 \text{ Sv} \equiv 10^6 \text{ m}^3 \text{ s}^{-1}$); between Australia–New Guinea and South America, it is 17 Sv, which is held to escape unhindered into the Indian Ocean through the Indonesian passages. These estimates have been used in drawing the boundary current along Australia in Fig. 5. The 17-Sv stagnation streamline intersects the Australian coast at about 20°S , while Church's (1987) estimate, based on hydrographic and other data, for the latitude of bifurcation of the westward flow feeding the East Australian Current, is 18°S .

Lest the estimate for the Indonesian throughflow be considered too large, and a smaller figure, say 10 Sv, or zero, be preferred, then that transport streamline should be used as the stagnation streamline around Australia. Gordon (1986) reviewed estimates of the Pacific-to-Indian interocean exchange. The present es-

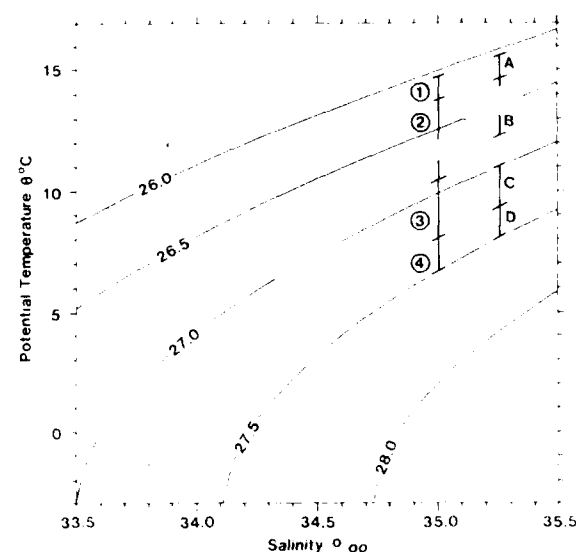


FIG. 3. A composite θ - S diagram for the South Pacific Ocean (adapted from Gordon et al., 1982). The density intervals 1, 2, 3, 4, of Table 2, and A, B, C, D of Table 3 (Keffler, 1985) are indicated.

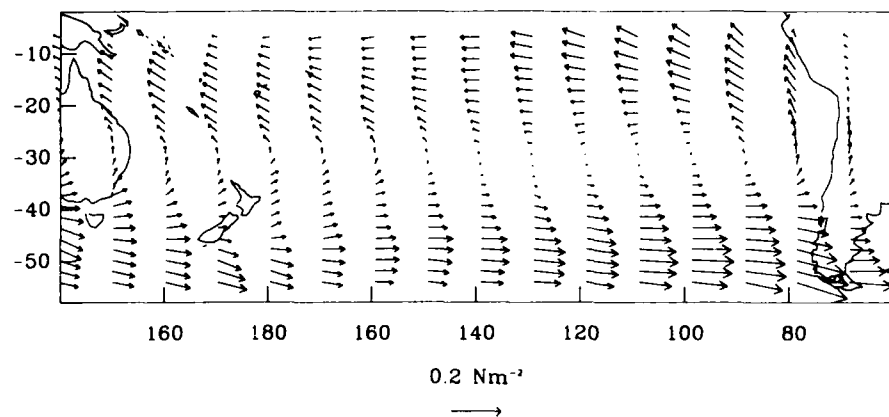


FIG. 4. Annual mean wind stress (Hellerman and Rosenstein, 1983).

timate of 17 Sv is certainly high compared to those, but not indefensible. Of course, a lower figure for the Indonesian throughflow implies a corresponding enhancement of the southward transport of the East Australian Current.

The boundary current required along eastern New Zealand is quite weak, the maximum transport of 14 Sv southwards being achieved only in a small cell along the southern part of New Zealand. A weak anticyclonic cell of magnitude 5 Sv is found in the Tasman Sea west of New Zealand. North of this, a stronger anticyclonic cell, of 17 Sv, is found.

The southern limit of this cell is quite intense, and should be compared to the estimates of 12–13 Sv eastward transport along the Tasman Front, by Stanton (1981), and 15 Sv in the separating limb of the Eastern Australian Current, made by Boland and Church (1981).

Figure 5 is remarkable also for the roughly C-shaped pattern of the ridge of anticyclonic circulation. The southward limb of the ridge appears weakly broken into two (note the $\Psi = -30$ Sv contour east of New

Zealand), and extends east along 40°S. The northward limb is centered on 30°S. The connection between the two limbs (the backbone of the C) is confused a little by the presence of New Zealand. Reid (1981) has noted such a feature in dynamic topography maps. It is remarkable that it should be evident in a diagram whose provenance is solely the wind field.

b. Errors in the Sverdrup transport

Hellerman and Rosenstein (1983) display calculations of Sverdrup transport based on monthly wind stress estimates. Apparently they neglect the presence of New Zealand and set the streamfunction to zero around Australia (i.e., zero Indonesian throughflow). They also provide monthly standard error estimates of the wind stress and propagate them through the circulation calculation to give error estimates for the Sverdrup transport. They show largest error estimates in the vicinity of New Zealand, of order 50 Sv, because of the paucity of data in the South Pacific. If the error is due to unresolved submonthly or synoptic scales in

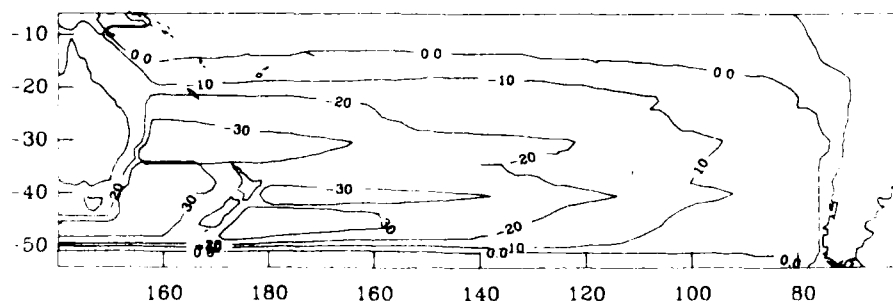


FIG. 5. Transport streamfunction Ψ , in sverdrups ($1 \text{ Sv} = 10^6 \text{ m}^3 \text{ s}^{-1}$). Identical to the Sverdrup streamfunction in the ocean interior (with some modifications west of New Zealand, see section 4). Note western boundary currents along New Zealand and Australia.

the wind observations, it seems fair to divide this monthly error by $(12)^{1/2}$ to give an error estimate for the annual mean of 15 Sv. This figure should be borne in mind in interpreting the details of the circulation cells east of New Zealand in Fig. 5. North of 30°S the monthly error estimates are much smaller: less than 20 Sv equatorward of 30°S. Dividing by $(12)^{1/2}$ reduces this to 6 Sv.

c. The baroclinic circulation: the model

The modeled circulation in the three layers will now be shown and discussed. Comparison with observations of the circulation will be given in the next subsection.

Figure 6 shows H_3 , the depth of the base of layer 3, calculated from the model. The diagram shows the broad sweep of the anticyclonic gyre in the intermediate depths of the South Pacific. The ventilated part of the gyre in layer 3, in the strict sense of LPS, is contained in the quite narrow corridor between the contours $H_{3w} = 958$ m and $H_{30} = 800$ m around the outside of the gyre. The shadow zone west of the H_{3w} contour is fed by a zonal jet passing to the south of New Zealand. This jet is supposed to feed the western boundary current along the east coast of the island, but much of it almost immediately peels off to feed the interior flow in the shadow zone. Calculations to be presented in section 4 show that the total northward transport of layer 3 water between New Zealand and South America is 14 Sv of which 74%, or about 10.4 Sv, is carried by the jet rounding southern New Zealand. It somewhat strains the intuitive notion of "ventilation" to not call the shadow zone ventilated, being fed as it is from west of New Zealand. The term here is used to mean water masses whose potential vorticity was determined by their history of contact with the wind when they were at the surface: in this sense, the shadow zone is not ventilated.

At the northern end of the islands, enough of the flow in the shadow zone has rejoined the boundary current to give a northward flow of 1.4 Sv, which rounds the island and feeds a weak eastward jet in layer 3 into the Tasman Sea.

Potential vorticity f_2/H_3 only changes by 20% across the ventilated corridor. It is constant in the shadow zone, by hypothesis. So it is roughly constant throughout the gyre, in good accord with Keffer's (1985) map of potential vorticity in what he designates as layer C.

The topography of the base of layer 3 is taken to be flat at a value of $H_3 = 1362$ m from New Zealand through the interior of the Tasman Sea up to the Australian continent where it is taken to shoal to a value of 1100 m at the southern tip of Tasmania (see section 5). This gives a southward transport of layer 3 water in the East Australian Current of 5 Sv.

On the eastern and northern edge of the gyre along South America and extending along the equator, a stagnant shadow zone is found with $H_3 = H_{30} = 800$ m, except for a weak cyclonic cell of circulation driven by positive wind stress curl, between 5° and 25°S along the South American coast extending west about fifteen degrees of longitude at the widest point. In this cell, H_3 shoals to 770 m, an effect which is not discernible in the contouring interval of Fig. 6. Because of considerable augmentation by southward Ekman transport in the trade winds, this cell extends much farther west in the streamfunction diagram of Fig. 5, with a maximum strength of about 10 Sv (southwards) at 6°S, declining to 5 Sv at 12°S, and 1 Sv at 20°S.

The effective pressure head driving geostrophic flow in layer 3 is $g^{-1}p_3/\bar{\rho} = g^{-1}\gamma_3 H_3$. The multiplicative factor is $g^{-1}\gamma_3 = 0.30 \times 10^{-3}$ (Table 2). This conversion can be readily done on the contours of Fig. 6. The unit is then equivalent to the "dynamic meter" of traditional geostrophic computations.

Next we show the depths H_2 , H_1 , of the bottom of layers 2 and 1 (Figs. 7, 9), and the pressure heads $p_2/g\bar{\rho}$, $p_1/g\bar{\rho}$ [Eq. (2.1)] driving the geostrophic flow in these layers (Figs. 8, 10). Layers 2 and 1 only exist equatorward of 51°S, 39°S, respectively. Both layers exhibit a broad anticyclonic circulation in the South Pacific. In the model, H_2 and H_1 are forced to zero along the South American coast, for the reasons LPS cite. Nature is not so tightly constrained, however, and depths of order 200–400 m and 100 m, respectively, are observed along South America for the isopycnals

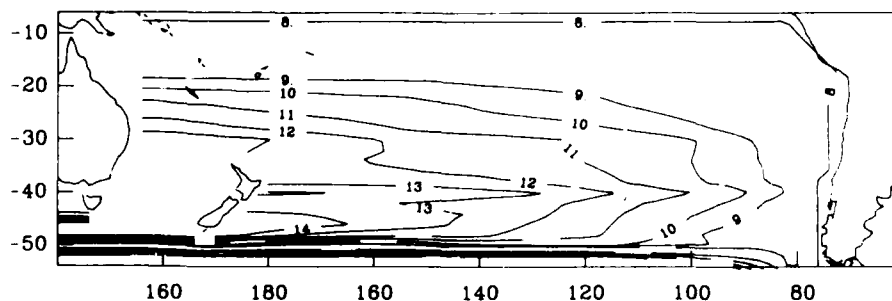


FIG. 6. Depth H_3 (in hectometers) of the base of the third layer calculated from the model. Multiplication by $\gamma_3 g^{-1} = 3 \times 10^{-4}$ (Table 1) gives pressure (dyn m) driving the flow in layer 3.

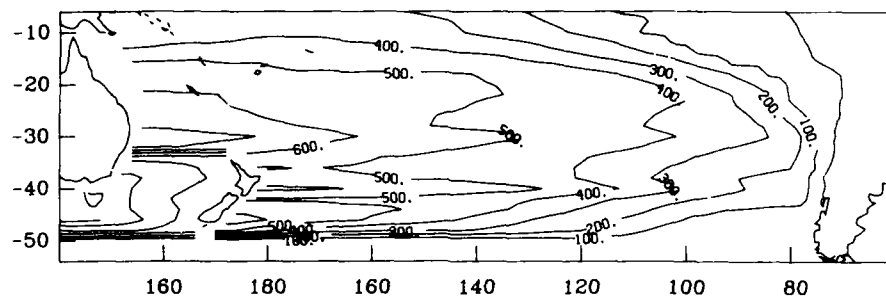


FIG. 7. Depth H_2 (meters) of the base of the second layer, calculated from the model.

corresponding to these interfaces (see below). This means that, in addition to modeled depths H_2 , H_1 being too shallow in the vicinity of the eastern boundary, gradients of H_2 , H_1 , and hence circulation, are stronger than observed. This bias in the model must be taken into account in making comparisons with observations.

d. The baroclinic circulation: comparison with observations

Let us compare the circulations computed from the model, and shown in Figs. 6–10, to observations of the circulation in the South Pacific Ocean. The material most readily at hand is the maps published by Reid (1965, 1973, 1986) of the depths of the density surfaces $\sigma_t = 27.28, 26.81, 26.23 \text{ kg m}^{-3}$ ($\delta_t = 80, 125, 180 \text{ cl/ton}$), as well as acceleration potential (dynamic height), salinity and oxygen on these surfaces. We shall reproduce here only one of these maps, namely, depth of $\sigma_t = 27.28 \text{ kg m}^{-3}$ (Fig. 11). Useful comparisons may be made also with the dynamic topography maps of Wyrtki (1974, 1975), the shallow density surface maps of Tsuchiya (1968) in the tropical Pacific Ocean, and Kefler's (1985) global maps of potential vorticity in density intervals.¹

The topography of H_1 ought to be compared to the topography of the $\sigma_t = 27.28 \text{ kg m}^{-3}$ density surface (Fig. 11). The correspondence of the broad features is quite remarkable, especially east of New Zealand. The strong zonal jet flowing around the south of New Zealand and feeding the anticyclonic gyre is apparent, though the oceanic situation south of New Zealand is apparently considerably complicated by the shoaling of the Campbell Plateau. The correspondence of the locations of, say, the 1200, 1000 and 800 m contours in the model and in nature is very close. There is a weak ridge of about 800 m depth along the South American coast. (This of course inspired the choice of

H_{30} .) More than that, the topography of the $\sigma_t = 27.28 \text{ kg m}^{-3}$ surface is indeed very flat behind (north and east of) the 800 m contour in Fig. 11. In the Tasman Sea north of New Zealand the modeled positions of the 1000 m, 1100 m contours are about right. The topography of the surface west of New Zealand is fairly flat and its depth, judged from the Scorpio section at 43°S (Stommel et al., 1973) is $1200 \pm 100 \text{ m}$, rather less than the $H_{30} = 1362 \pm 122 \text{ m}$ produced by the calculation to be described in section 4, though within the error bars.

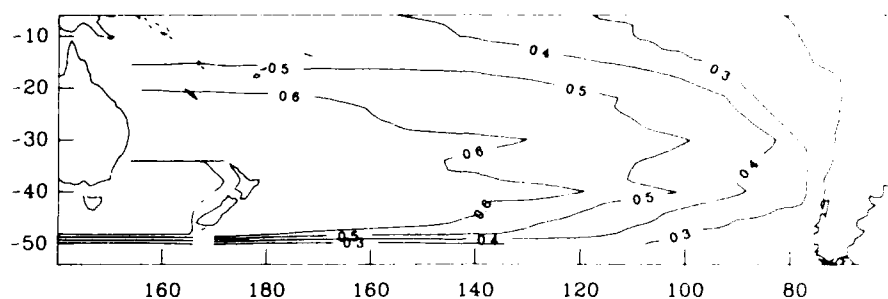
Reid (1965) also shows a map (his Fig. 23) of the dynamic topography (acceleration potential) of the $\sigma_t = 27.28$ surface, relative to 2000 dbar. The dynamic height contours correspond very closely to those of Fig. 11, as the theory requires.

Topography of density surfaces. The H_2 field may be compared to the topography of the $\sigma_t = 26.81 \text{ kg m}^{-3}$ density surface (Reid's (1965) Fig. 17). The choice of outcrop latitude, 51°S , is roughly borne out by this map. The model depths are considerably shallower in the vicinity of the eastern boundary where H_2 is forced to zero, while in nature the isopycnal is 200–400 m deep there. This shallow bias diminishes towards the west.

The model's 500 m contour describes a complicated region just east of New Zealand, while in nature the isopycnal is not found so deep in this region. North of 35°S , the model's 500 m contour extends eastward from the northern tip of New Zealand almost to 130°W , where it turns north and returns to Australia between 20° and 15°S . This accords fairly well with the position of the 500 m contour in nature, where it extends even farther east, to 120°W . Inside this contour, maximum depths of 700 m are found, in both model and nature, in the Tasman and Coral Seas.

Layer 1 depth, H_1 , ought to be compared to the topography of the $\sigma_t = 26.23 \text{ kg m}^{-3}$ density surface (Reid's (1973) Fig. 5). The outcrop latitude, 39°S , chosen for the model appears about right. The model depths are especially too shallow in the vicinity of the eastern boundary, where they are forced to zero, while depths of order 100 m are observed for this

¹ Kefler's (1985) maps show σ_θ surfaces; Reid's (1965, 1973, 1986) are σ_t surfaces. In the upper kilometer of the ocean, differences between the two are slight, and no distinction is made in making comparisons to the model.

FIG. 8. Pressure head $p_2/g\rho$ (meters) in the second layer.

isopycnal along the South American coast. Apart from this, the model isopleths of H_1 appear too shallow by about 50 m throughout the central and western South Pacific.

Keller (1985) shows a map of the depth of the $\sigma_{\theta} = 26.50$ surface, the median density of his layer B. This density surface falls in the range of our layer 2, $26.25 < \sigma_{\theta} < 26.90$. Accordingly, we have constructed a map of $\alpha H_1 + (1 - \alpha)H_2$, where $\alpha = (26.90 - 26.50)/(26.90$

$26.25) = 0.615$, to model the depth of this density surface, which is shown in Fig. 12, for comparison with Keller's map. Apart from the eastern boundary where H_1 and H_2 are forced to zero, agreement is quite good. The positions of the trough along 20°S , and of the 400 m, 300 m contours, accord well.

The mean depth of the $\sigma_{\theta} = 26.44$ density surface in the tropical band is shown by Tsuchiya (1968), and may be compared with H_1 , taken in the model to be the depth of the $\sigma_{\theta} = 26.575$ surface. The modeled H_1 is shallower than observed, right across the tropical band, not only in the east where it is forced to zero, though the trend from shallower to deep from northeast to southwest is reproduced. The depth contours of Tsuchiya's density surface are rather more zonal than those of Fig. 9.

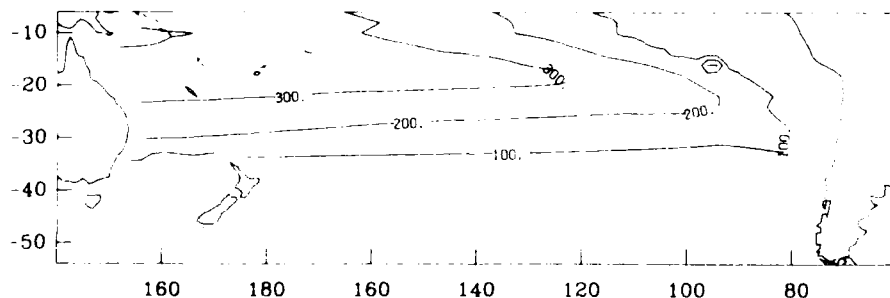
Acceleration potential. Comparison of the acceleration potential on the $\sigma_{\theta} = 26.80 \text{ kg m}^{-3}$ surface, with respect to 1000 db, which Reid (1965) shows, with $p_2/g\rho$, is rather problematical. The reference pressure,

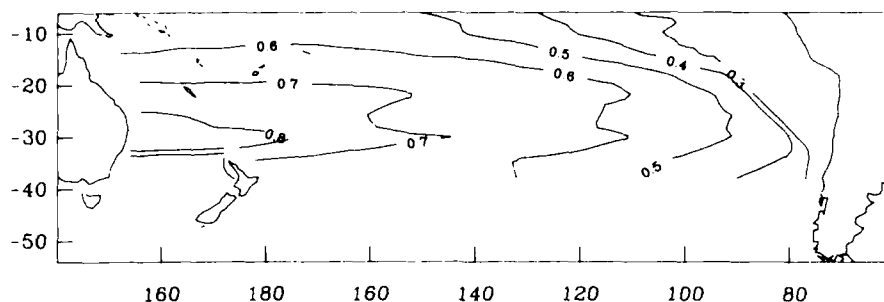
of 1000 dbar, for this isopycnal is rather shallow for a fair comparison with $p_2/g\rho$, and acceleration potential on this surface might better be compared with $\gamma_2 H_2 = (p_2 - p_3)/g\rho$. This comparison is quite good, in terms of both magnitude and pattern. On the other hand, comparing the acceleration potential of the $\sigma_{\theta} = 26.23 \text{ kg m}^{-3}$ surface, with respect to 1000 db (Reid, 1973), with modeled $(p_1 - p_3)/g\rho$, the magnitude of the modeled flow is at least twice as large as observed in nature, although a similar anticyclonic circulation pattern is seen.

Taking the three density surfaces together, a clear equatorward shift of the subtropical gyre with decreasing depth and density is seen in both the observations (as Reid (1981) remarks) and the model (Figs. 6-10).

In the western Pacific, between 15° and 34°S , where H_2 is greater than 500 m, it may be useful to compare p_2 with the mean dynamic topography of the 500 dbar surface relative to 1000 dbar, shown in Fig. 13, taken from Wyrtki (1974). The pattern is generally very similar, though the strength of the cell in Fig. 8 is about twice that of Fig. 13. Perhaps the choice of the 500 dbar surface is too deep for a fair comparison with Fig. 8, and a shallower surface corresponding more nearly to the center of the layer would show a stronger circulation.

Comparing Tsuchiya's (1968) map of acceleration potential of the $\sigma_{\theta} = 26.02 \text{ kg m}^{-3}$ surface relative to 500 db to Fig. 10 in the tropical band, and disregarding

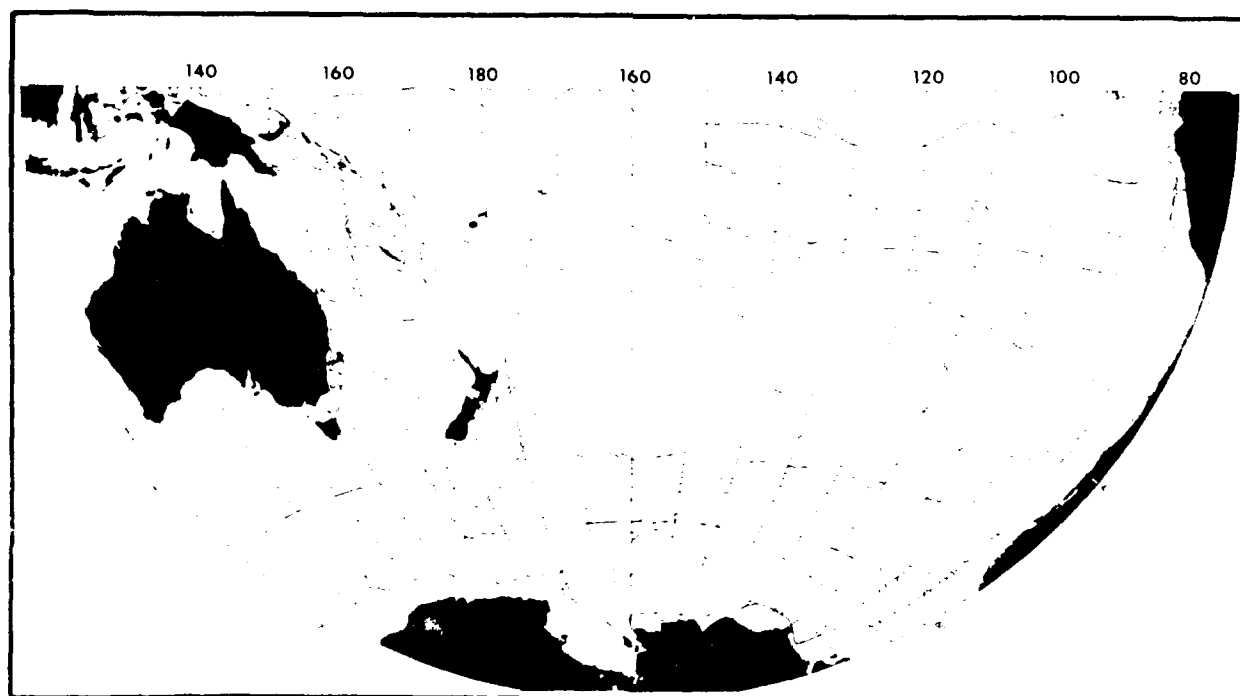
FIG. 9. Depth H_1 (meters) of the base of the first layer, calculated from the model.

FIG. 10. Pressure head $p_1/g\rho$ (meters) in the first layer.

the too large gradients in the model in the east (because of the unrealistic shoaling of H_1 that is required), the eastward flow with a 10–15 dyn cm pressure drop across it is reproduced quite well by the model.

On the other hand, comparing Fig. 10 to Wyrki's (1975) sea surface dynamic topography relative to 1000 db (Fig. 14), neither the strength nor the position of the shallow gyre is well reproduced. The strong ridge running from northwest near New Britain towards the southeast (Fig. 14) is apparently associated with the South Pacific Convergence Zone in the atmosphere (see Fig. 1.2 of Gill, 1982). As this suggests that the ridge

is a feature determined partly by advection of warm surface water out of the western equatorial zone, it is not surprising that a feature with such an origin is badly represented in this model. Layer 1 must represent all the water lighter than $\sigma_t = 26.25 \text{ kg m}^{-3}$. This density is found quite deep in the tropical thermocline, with water lighter by as much as 2 kg m^{-3} occurring at the surface. Significant geostrophic shear, which the model cannot represent, may occur over such a density range. So some allowance must be made in making these comparisons of the model to observations of nature, especially in the Tropics. Even so, as we shall argue in

FIG. 11. Depth in meters at the surface where $\sigma_t = 27.28 \text{ kg m}^{-3}$ (from Reid, 1965).

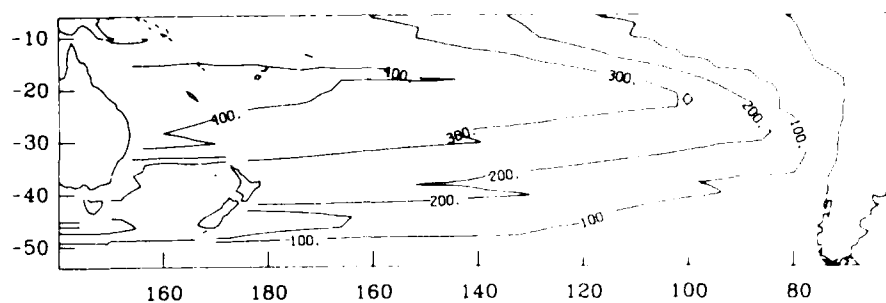


FIG. 12. Depth (meters) of $\sigma_t = 26.50 \text{ kg m}^{-3}$, given by $0.615H_1 + 0.385H_2$ (C. Keller (1985)).

section 6, the poor agreement in the Tropics may be due to a fundamental shortcoming in the potential vorticity conservation model.

Salinity and oxygen. Reid (1965, 1973, 1986) also shows the concentrations of salinity and oxygen on the three density surfaces named above. The sources of low salinity are generally in the high latitudes, high salinity in the Tropics. Regarding salinity as a tracer, all three surfaces show broad tongues of low salinity sweeping north in the eastern South Pacific with a narrower filament extending westwards in the tropics as far as the Coral Sea. Like the equatorward limb of the subtropical gyre, these zonal low-salinity filaments lie progressively farther northward with decreasing density: along about 20°–25°S for $\sigma_t = 27.28 \text{ kg m}^{-3}$, 15°–

20°S for $\sigma_t = 26.81 \text{ kg m}^{-3}$ and 15°S for $\sigma_t = 26.23 \text{ kg m}^{-3}$. The Tasman and Coral Seas contain the highest salinities on the respective surfaces, confirming the picture that this region is the stagnation zone of the circulation. The oxygen concentrations on these density surfaces seem less remarkable than the salinities, except that in the Tasman Sea on the $\sigma_t = 27.28 \text{ kg m}^{-3}$ surface a minimum in oxygen is found, rather confirming the hypothesis advanced in the model that flow is stagnant in this region at these depths.

4. Flow around New Zealand

In this section we compute the value of the transport streamfunction at New Zealand from the wind stress

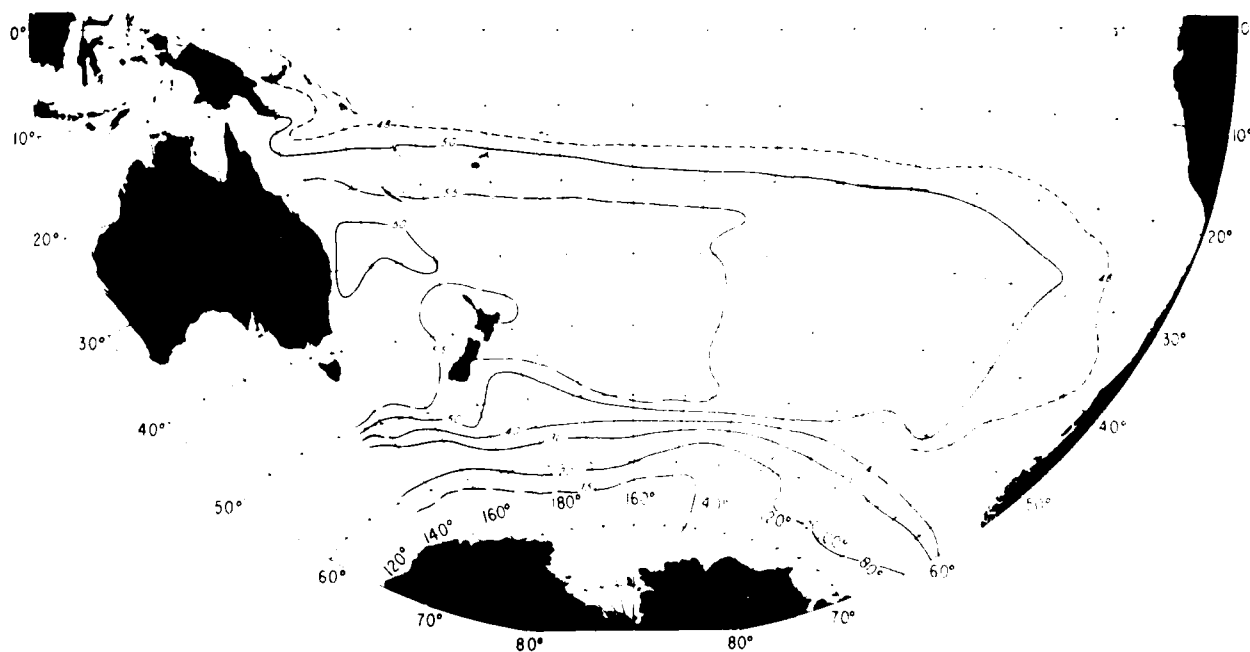


FIG. 13. Mean annual dynamic topography (dyn cm) of 500 db surface relative to 1000 db (Wyrki, 1974).

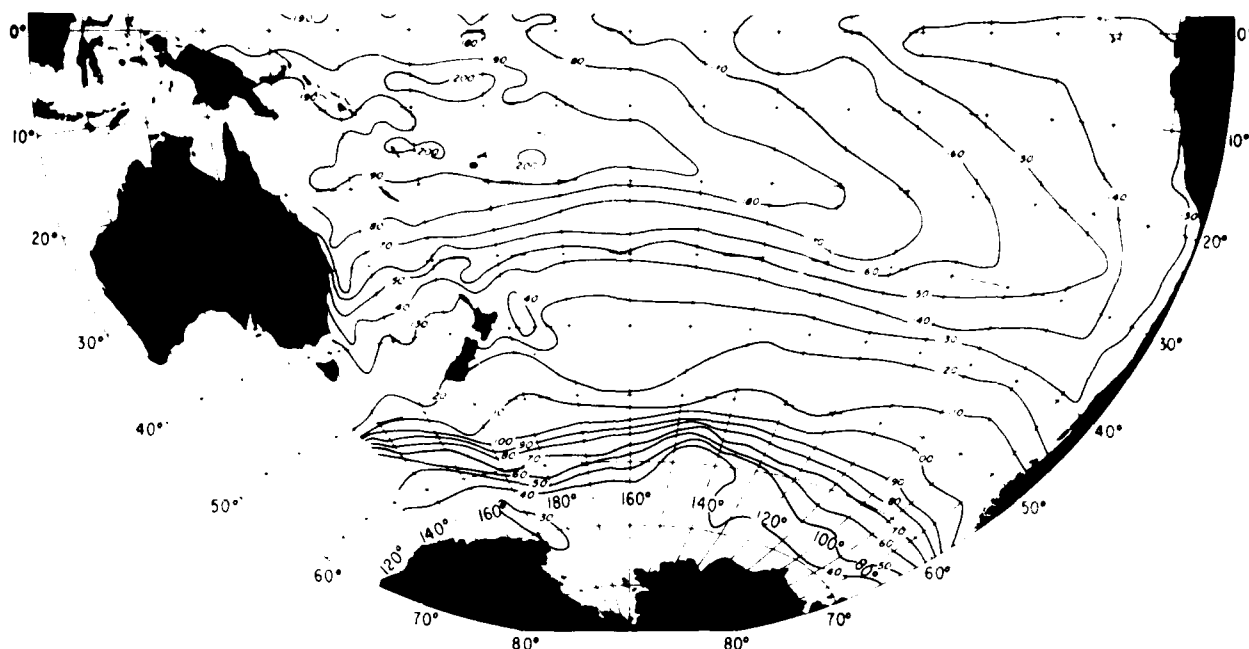


FIG. 14. Mean annual dynamic topography (dyn cm) sea surface relative to 1000 db (Wyrtki, 1975).

field and use that to determine the total flow in the boundary current on the eastern side of the islands. Flows in western boundary currents along islands are determined, not by the requirement of balancing the interior Sverdrup transport, but by the necessity of achieving the same pressure at the northern end of the island as at the southern, so that no pressure gradient (which would drive a normal geostrophic flow) occurs on the far side of the island. Similar considerations applied layer by layer determine H_1 and H_2 on the far side of the island. The values of H_1 and H_2 on the western side of New Zealand are necessary to determine the layered Sverdrup flow in the Tasman Sea in the latitude range of the islands. This fills a gap left in the theory presented in section 2.

We also compute estimated errors for the transport (and H_1 , H_2) from the standard errors quoted for the wind field.

a. The transport streamfunction at New Zealand

Consideration of the flow around an isolated island like New Zealand, shows that the constant value of the transport streamline that surrounds the island must be

$$\Psi_{NZ} = (f_S - f_N)^{-1} \bar{\rho}^{-1} \oint \tau \cdot d\mathbf{l}, \quad (4.1)$$

where the closed line integral is along a counterclockwise path enclosing New Zealand and the Pacific Ocean to the east of it up to the South American continent

(Fig. 15); f_S , f_N are the Coriolis parameters appropriate to the southern and northern ends of the islands. This result is due to Godfrey (1987), and comes about from a consideration of the integral of the vertically integrated momentum balance around the circuit described, along which no lateral or bottom friction acts. Computation of this value shows that $\Psi_{NZ} = 29$ Sv. This value must be used to restart the Sverdrup computation west of New Zealand.

b. Error estimation for Ψ_{NZ}

Inspection of Hellerman and Rosenstein's (1983) maps of the monthly standard error of zonal wind stress gives a figure of order 0.25 dyn cm^{-2} in the midlatitude South Pacific.

Multiplying this by $16 \times 10^3 \text{ km}$, the length of the circuit in the line integral of (4.1), and dividing by $f_S - f_N$ gives 12 Sv. Dividing by $(12)^{1/2}$ to obtain the annual standard error of (4.1) gives 3.5 Sv. This error should be used to interpret the estimate of Ψ_{NZ} given above. The error for Ψ_{NZ} is smaller than those for point estimates of Ψ , because the former is based on line integrals of wind stress, while the latter are integrals of wind stress curl, and hence more prone to error.

c. Transport constraints on H_1 and H_2

If we assume that longshore flow in western boundary layers is geostrophic, then $f^{-1}P$, defined by the first relation in (2.2), describes the geostrophic transport in

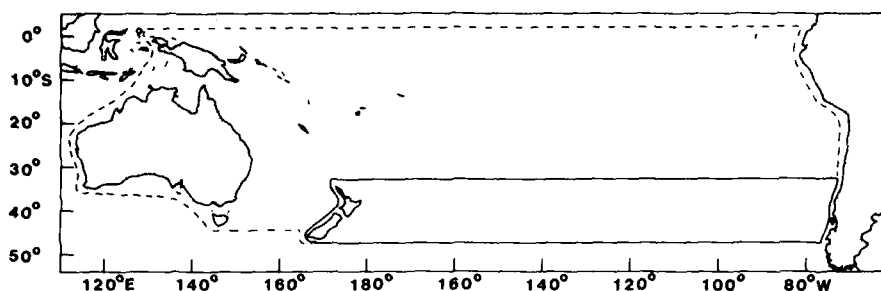


FIG. 15. Schematic integration path around New Zealand for Ψ_{NZ} (solid). Similarly for Ψ_{Aus} (dashed).

the boundary current [though the second equality of (2.2) fails]. Applying this in (2.6) at the southern tip of New Zealand, where only layers 2 and 3 exist and are in motion, we obtain

$$\frac{1}{2}(\gamma_3 H_{3,NZ}^2 + \gamma_2 H_{2,NZ}^2 - \gamma_3 H_{30}^2) = f_S(\Psi_{NZ} + T_{Ek,S}), \quad (4.2)$$

where $T_{Ek,S} = T_{Ek}(x_{NZ}, y_S) = +8.8$ Sv. Error analysis applied to (2.5) gives a standard error less than 1 Sv. Here $H_{3,NZ}$, $H_{2,NZ}$ are the constant depths of the bottoms of layers 3 and 2 along the western side of New Zealand. Along the eastern side, H_3 , H_2 may vary because the normal-to-shore momentum balance in the boundary current is not geostrophic, but they must return to the values $H_{3,NZ}$, $H_{2,NZ}$ at the northern and southern tips. Substitution of numerical values in (4.2) gives

$$\frac{H_{3,NZ}^2}{(1446 \pm 130 \text{ m})^2} + \frac{H_{2,NZ}^2}{(1093 \pm 100 \text{ m})^2} = 1. \quad (4.3)$$

The standard errors indicated in the denominators are based on an assumed error of 5 Sv in $\Psi_{NZ} + T_{Ek,S}$. (A reduced $|\Psi_{NZ} + T_{Ek,S}|$ leads to smaller values of the denominators.)

d The transport of layer 3

Another constraint is required to determine the distribution of the geostrophic transport in the boundary current between layers 2 and 3. This appears to be that the transport between New Zealand and South America in layer 3 be independent of latitude, in particular, that it be the same at the southern and northern ends of New Zealand. The layer 3 transport is

$$T_3(y) = \int_{NZ}^{SA} (H_3 - H_2) f^{-1} \gamma_3 (\partial H_3 / \partial x) dx, \quad (4.4)$$

At the southern tip of New Zealand, $y = y_S$, this is made up of contributions from the western boundary current and from the interior. For the latter $H_3 = H_{3W}$ just outside the boundary current, and from there to

South America $f/(H_3 - H_2) = f_2/H_3$ (see Table 1), so that the contribution to (4.4) from the interior is

$$\frac{1}{2} f_2^{-1} \gamma_3 (H_{30}^2 - H_{3W}^2).$$

The contribution from the western boundary current is

$$f_S^{-1} \gamma_3 \left[\frac{1}{2} (H_{3W}^2 - H_{3,NZ}^2) - \int_{WBC} H_2 dH_3 \right].$$

The Mean Value Theorem states that the second term is given by $\bar{H}_2(H_{3W} - H_{3,NZ})$, where $H_{2WS} < \bar{H}_2 < H_{2,NZ}$ (and $H_{2WS} = (1 - f_S f_2^{-1}) H_{3W}$). If H_2 were a linear function of H_3 , as could be the case if, for example, both variables had an exponential structure in the boundary current with the same relaxation scale, then $\bar{H}_2 = \frac{1}{2}(H_{2WS} + H_{2,NZ})$. We shall adopt this assumption. In total,

$$T_3(y_S) = \frac{1}{2} f_S^{-1} \gamma_3 [H_{3W} + H_{3,NZ} - H_{2WS} - H_{2,NZ}] \times (H_{3W} - H_{3,NZ}) + \frac{1}{2} f_2^{-1} \gamma_3 [H_{30}^2 - H_{3W}^2]. \quad (4.5)$$

At $y = y_N$, the northern end of New Zealand, the situation is a little different. The interior contribution splits into two parts: one comes from the shadow zone, where $f/(H_3 - H_2) = f_2/H_{3W}$, and H_3 ranges from H_{3WS} , just outside the western boundary current, to H_{3W} at the edge of the shadow zone, so that the value is

$$f_2^{-1} \gamma_3 H_{3W} (H_{3W} - H_{3WS});$$

the other is from the ventilated region, where $f/(H_3 - H_2) = f_2/H_3$, and H_3 ranges from H_{3W} to H_{30} , so that its value is

$$\frac{1}{2} f_2^{-1} \gamma_3 (H_{30}^2 - H_{3W}^2),$$

the same as the interior contribution at $y = y_S$. The western boundary current contribution is similar in form to that calculated at y_S . The total layer 3 transport is therefore

$$T_3(y_N) = \frac{1}{2} f_N^{-1} \gamma_3 [H_{3WN} + H_{3,NZ} - H_{2WN} - H_{2,NZ}] \\ \times (H_{3WN} - H_{3,NZ}) + f_2^{-1} \gamma_3 H_{3W} (H_{3W} - H_{3WN}) \\ + \frac{1}{2} f_2^{-1} \gamma_3 (H_{30}^2 - H_{3W}^2), \quad (4.6)$$

where $H_{2WN} = H_{3WN} - f_N f_2^{-1} H_{3W}$ is the value of H_2 just outside the western boundary current at $y = y_N$. Setting $T_3(y_S) = T_3(y_N)$, and manipulating, we obtain eventually

$$(H_{3,NZ} - \eta)(H_{3,NZ} - H_{2,NZ}) + C = 0, \quad (4.7)$$

where

$$\eta = (-f_N^{-1} + f_S^{-1})^{-1} (-f_N^{-1} H_{3WN} + f_S^{-1} H_{3W}),$$

$$C = (-f_N^{-1} + f_S^{-1})^{-1} f_2^{-1} H_{3W} (H_{3W} - H_{3WN}).$$

The numerical values for H_{3W} and H_{3WN} are, respectively, 958 and 1316 m, as computed from the theory of section 2. This gives $\eta = 2119$ m, and $C = +(871 \text{ m})^2$.

The solution of Eqs. (4.2) and (4.7) gives $H_{3,NZ}$, $H_{2,NZ}$. This is shown graphically on Fig. 16, as the intersection point of an ellipse given by (4.2) and a hyperbola given by (4.7). The solution is

$$H_{3,NZ} = 1362 \pm 122 \text{ m}, \quad H_{2,NZ} = 362 \pm 33 \text{ m}.$$

The standard errors given for these estimates are those due to the errors in the coefficients of (4.3). The transport of layer 3 between New Zealand and South America is then

$$T_3(y_S) = T_3(y_N) = 14 \pm 4 \text{ Sv}. \quad (4.8)$$

Of this, 74% is carried by the western boundary current as it swings around the southern tip of New Zealand; the remaining 26% by the interior. At the northern end, only 10% is carried by the boundary current, the remaining 64% having been shed to the interior in the shadow zone. This is shown in the schematic Fig. 17a.

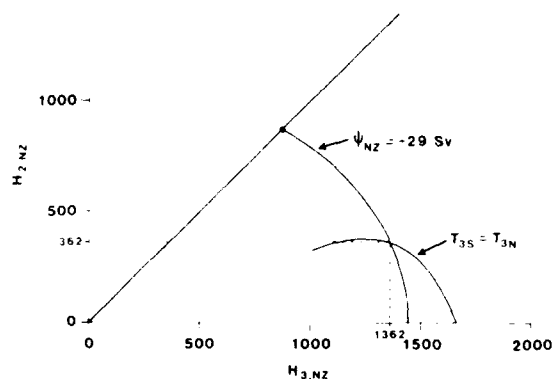


FIG. 16. The Sverdrup transport constraint (4.2), and the continuity of layer 3 transport (4.7). The intersection of the lines gives $H_{3,NZ}$, $H_{2,NZ}$.

which represents a section between New Zealand and South America along $y = y_S$. This section should be thought of as being along a latitude slightly south of New Zealand through the interior, until the island is reached, where it hooks north to cross the incoming current from the west. At this section the interior transport in the lighter layer, 9.5 Sv northwards, is almost entirely Ekman transport (8.8 Sv). A similar section at a slightly more equatorward latitude will show the depths H_2 , H_3 outside the boundary current considerably depressed as the stream sheds transport into the interior.

With these values for $H_{3,NZ}$, $H_{2,NZ}$ we can restart the integration west of New Zealand along the lines of the theory presented in section 2. A few remarks are first called for. There will be abrupt jumps between $H_{3,NZ}$, $H_{2,NZ}$ and the values of H_3 , H_2 given by the theory of section 2 at points just north and south of New Zealand. This suggests intense zonal jets emerging from, or impinging on, as required, the tips of New Zealand. Presumably, an account of the dynamics of these interior jets can be given, perhaps along the lines of the theory presented by Pedlosky (1968) for frictional boundary layers along a zonal boundary. We shall not attempt here to construct such a theory, a product of which would be a specification of the communication between the Tasman Sea and regions north and south of New Zealand, hence determining rigorous inflow and outflow conditions. Rather, we shall content ourselves with specifying ad hoc that layer 3 be stagnant in the Tasman Sea west of New Zealand, i.e.,

$$H_3 = H_{3,NZ} = 1362 \text{ m}, \quad (4.9)$$

and accept the resultant abrupt jumps in H_3 at latitudes y_S , y_N as eastward and westward jets, respectively, connected to and feeding or emerging from the boundary current on the eastern side of New Zealand. This is what was done in section 3 to obtain the solutions displayed in Figs. 6, 8. Against this hypothesis, we should note the tendency in Reid's (1985) dynamic topography maps for flow along the south of Australia and New Zealand to loop up into the Tasman Sea.

The topography of the $\sigma_t = 27.28$ surface in the southern Tasman Sea is observed to be fairly flat, perhaps 1200 ± 100 m, judged from the 43°S Scorpio section (Stommel et al., 1973). This puts it in the range of the estimate of $H_{3,NZ}$ given above. The $\sigma_t = 26.90$ surface is found at about 400 to 500 m around western New Zealand, in fairly good accord with the estimate of $H_{2,NZ}$. The somewhat larger estimate than observed of $H_{3,NZ}$ does suggest that Ψ_{NZ} may be too high by an amount of order 5 Sv, perhaps due to errors in the wind field. However, rather than tamper with Hellerman and Rosenstein's (1983) winds, we shall persist with them, while examining critically their implications for the ocean circulation.

The geostrophic transport west of New Zealand is given by

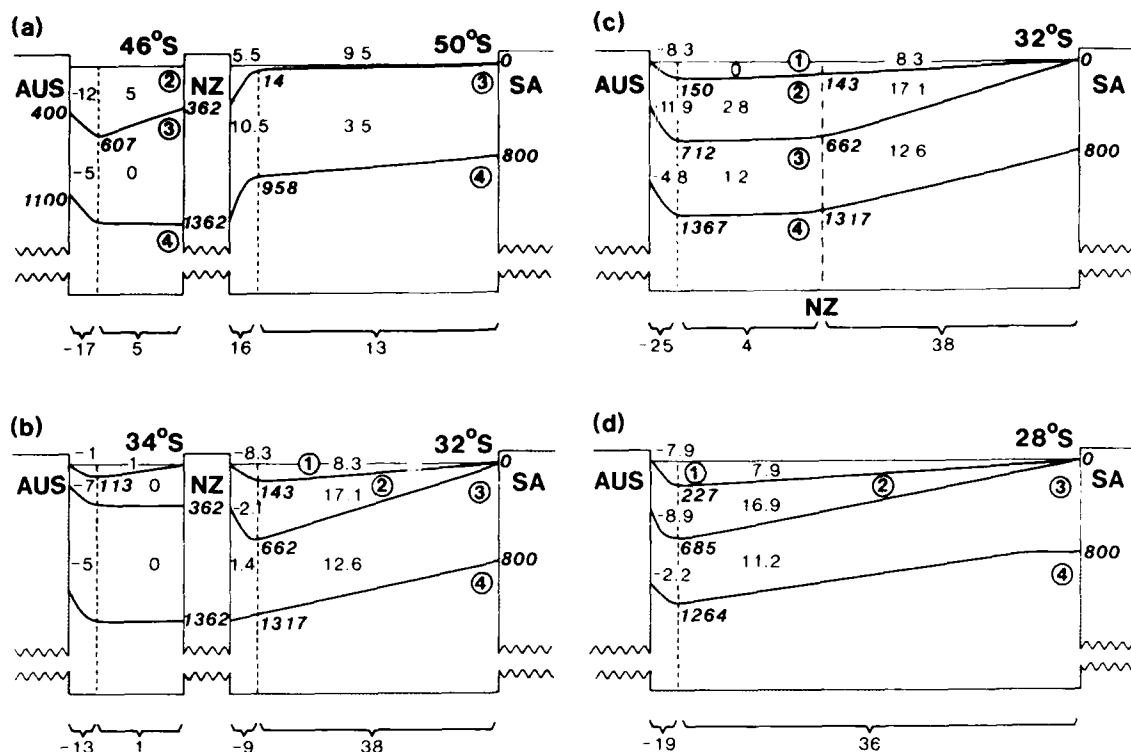


FIG. 17. Schematic sections across the South Pacific showing layer depths and transports (in Sv, positive northwards) of each layer, in the interior and in the boundary currents. (a) From Chile along 50°S, looping north at New Zealand; then along 46°S, looping north to Tasmania. (b) From Chile along 32°S, looping north to New Zealand; then along 34°S to Australia. (c) From Chile to Australia along 32°S. (d) From Chile to Australia along 28°S.

$$\frac{1}{2} f^{-1} (\gamma_2 H_2^2 + \gamma_1 H_1^2) = \frac{1}{2} f^{-1} (\gamma_3 D_1^2 + \gamma_2 H_2^2)_{NZ}, \quad (4.10)$$

where

$$D_1^2 = D_0^2(x, y) - D_0^2(x_{NZ}, y).$$

The same theory applies as in section 2, except that the role played formerly by layer 3 is here taken by layer 2, and that of layer 2 by layer 1. The boundary values of H_2 and H_1 on the west coast of New Zealand are

$$H_{2,NZ} = 362 \text{ m}, \quad H_{1,NZ} = 0. \quad (4.11)$$

The results of integrating this model in the Tasman Sea west of New Zealand have already been shown on Figs. 6–10. The level surface formed by $H_3 = 1362$ m and the variation of H_2 given by (4.10), with $H_1 = 0$, in the interior of the Tasman Sea along $y = y_{Tas}$ is shown schematically in Fig. 17a. The variation of the depth H_2 of the light layer might be compared qualitatively with the Scorpio section at 43°S, which shows a moderately deep (~400 m), warm, near-surface layer in the Tasman Sea shoaling gradually over the Chatham Rise, and then quite shallow over the remainder of the eastern Pacific.

5. The East Australian Current

Considerations parallel to those given in section 4 would determine the transport streamfunction at Australia–New Guinea, were the flow through the Indonesian passages unhindered by friction. In any event, such an estimate ought to give an upper bound on the Pacific–Indian flow through the archipelago. Given the Indonesian throughflow, the transport of the East Australian Current can be calculated. The distribution of this boundary current transport among the layers, in particular in the third layer, is discussed.

a. The transport streamfunction at Australia

A calculation similar to that in section 4, for Australia–New Guinea, regarded as an isolated, if large, island, shows that

$$\Psi_{Aus} = (f_{Tas} - f_{NG})^{-1} \left[\oint \bar{\rho}^{-1} \tau \cdot d\mathbf{l} - (f_S - f_{Tas}) \Psi_{NZ} \right], \quad (5.1)$$

where the line integral is taken along the path shown in Fig. 15. Computation yields

$$\Psi_{\text{Aus}} = -17 \text{ Sv},$$

which means that there must be an outflow of this magnitude from the Pacific to the Indian Oceans through the Indonesian passages (Godfrey, 1987). This figure, apart from any errors in the wind field used in the calculation, must be regarded as an upper bound on the magnitude of the outflow, for it depends on neglecting friction in the passages, which are quite narrow and convoluted. Friction in the passages would surely act to reduce this flow. (If the Indonesian passages were closed entirely, then plainly we would require that $\Psi_{\text{Aus}} = 0$.)

An error analysis applied to (5.1) gives an estimate of the standard error of Ψ_{Aus} of similar magnitude to the error of Ψ_{NZ} , namely, about 4 Sv. This error is solely that due to errors in wind stress, not systematic errors like the neglect of friction in the Indonesian passages.

b. Transport constraints on $H_{3,\text{Aus}}$ and $H_{2,\text{Aus}}$

The total geostrophic transport in layers 2 and 3 across the latitude y_{Tas} is

$$\frac{1}{2}(\gamma_3 H_{3,\text{Aus}}^2 + \gamma_2 H_{2,\text{Aus}}^2 - \gamma_3 H_{3,\text{NZ}}^2 - \gamma_2 H_{2,\text{NZ}}^2) = f_{\text{Tas}}(\Psi_{\text{Aus}} - \Psi_{\text{NZ}} + T_{\text{Ek,Tas}}), \quad (5.2)$$

where $T_{\text{Ek,Tas}} = +0.8 \text{ Sv}$ is the Ekman transport between Tasmania and New Zealand. Take $\Psi_{\text{NZ}} = -29 \text{ Sv}$, and $H_{3,\text{NZ}}, H_{2,\text{NZ}}$ as determined in the section 4. Then, for the stated values of Ψ_{Aus} , we get the corresponding constraints on $H_{3,\text{Aus}}, H_{2,\text{Aus}}$:

$\Psi_{\text{Aus}} = -17 \text{ Sv}$ (Indonesian passages unrestricted):

$$\frac{H_{3,\text{Aus}}^2}{(1120 \text{ m})^2} + \frac{H_{2,\text{Aus}}^2}{(847 \text{ m})^2} = 1; \quad (5.3a)$$

$\Psi_{\text{Aus}} = 0$ (Indonesian passages closed):

$$H_{3,\text{Aus}}^2 + \frac{\gamma_2}{\gamma_3} H_{2,\text{Aus}}^2 \approx 0; \quad (5.3b)$$

$\Psi_{\text{Aus}} = -10 \text{ Sv}$ (intermediate situation):

$$\frac{H_{3,\text{Aus}}^2}{(870 \text{ m})^2} + \frac{H_{2,\text{Aus}}^2}{(658 \text{ m})^2} = 1. \quad (5.3c)$$

Errors in the coefficients similar to those quoted for Eq. (4.3) ought to be anticipated.

The closing of the Indonesian passages requires $H_{3,\text{NZ}} \approx H_{2,\text{NZ}} \approx 0$; that is, the necessary southward return in the Tasman Sea of the northward 29 Sv in the South Pacific between New Zealand and South America, requires the isopycnals modeled by the H_3, H_2 interfaces practically to surface at the east Australian coast. This simply is not the case observed in nature.

The other two cited possibilities give maximum allowable depths for $H_{3,\text{Aus}}$ of 1120 and 870 m. The

former appears more in accord with observed depths of the $\sigma_t = 27.28$ surface at the Australian coast.

It may seem remarkable that considerations on the observed depths of isopycnals can suggest the Indonesian passage outflow. Yet this is merely a consequence of geostrophy. If (4.2) and (5.2) are added, one obtains, approximately,

$$\frac{1}{2}(\gamma_3 H_{3,\text{Aus}}^2 + \gamma_2 H_{2,\text{Aus}}^2 - \gamma_3 H_{30}^2) \approx f_S(\Psi_{\text{Aus}} + T_{\text{Ek,S}} + T_{\text{Ek,Tas}}), \quad (5.4)$$

because $f_{\text{Tas}} \approx f_S$. For $\Psi_{\text{Aus}} = 0$, and zero Ekman transport, this constraint could be satisfied, for example, by H_3, H_2 returning to their South American values at the Australian coast. It is the large Ekman transport, 9.6 Sv, which must be returned by a geostrophic flow, that requires the extreme shoaling of H_3, H_2 at the East Australian coast if $\Psi_{\text{Aus}} = 0$ is to be maintained.

It might be objected that an additional southward zonally averaged barotropic flow,

$$\bar{v}_4(y_S) = L^{-1} \int_{\text{Aus}}^{\text{SA}} v_4(x, y_S) dx < 0,$$

where L is the width of the South Pacific along latitude y_S , could redress the mass balance by adding (algebraically) the term $-f_S L D \bar{v}_4(y_S)$ to the left of (5.2), without requiring unrealistic shoaling of H_3 . However, evidence from the deep distributions of water properties suggests, if anything, that the reverse is the case, namely, northward flow of the water masses, including the Circumpolar Deep Water, and the Antarctic Bottom Water that are subsumed in our layer 4 (Warren, 1973).

c. Layer 3 transport

We now compute the transport in layer 3 in the Tasman Sea between Australia and New Zealand at $y = y_{\text{Tas}}$. Because the topography of H_3 is flat across the interior of the Tasman by assumption, the only contribution comes from the boundary current. Calculated by the methods given above, this is

$$T_3'(y_{\text{Tas}}) = \frac{1}{2} \int_{\text{Tas}}^{\text{Aus}} \gamma_3 [H_{3,\text{NZ}} + H_{3,\text{Aus}} - H_{2,\text{Aus}} - H_{2,\text{Aus}}](H_{3,\text{NZ}} - H_{3,\text{Aus}}), \quad (5.5)$$

where $H_{2,\text{Aus}} = H_2(x_{\text{Aus}}, y_{\text{Tas}}) = 607 \text{ m}$, from the solution of (4.10) in the Tasman Sea with $H_1 = 0$. It might be argued that, because the Indonesian passages likely do not admit much or any water as dense as layer 3, a consistent requirement on layer 3 is that it return the volume transport in that layer east of New Zealand, i.e., $T_3(y_{\text{Tas}}) = -T_3(y_S) = -14 \text{ Sv}$. This constraint turns out to be ludicrous when combined with (5.2), for any choice of Ψ_{Aus} : no positive mathematical solution is possible! The layer 3 interface must bank impossibly steeply to return 14 Sv in the East Australian Current.

On the other hand, we can select plausible values of $H_{3,Aus} = 1100$ m, $H_{2,Aus} = 400$ m, by inspection of the intersection of the $\sigma_0 = 27.30, 26.90$ density surfaces with the east Australian continental slope in the 43° S Scorpio section, for example (Stommel et al., 1973). These values, while not precisely satisfying (5.3a), fulfil it well enough (to within 20%), considering the large errors inherent in computing the coefficients of (5.3a). Inserting these values in (5.5), together with $H_{3,NZ} = 1362$ m, we obtain

$$T_3(V_{Tas}) = -5 \text{ Sv.}$$

This estimate is very sensitive to the difference ($H_{3,NZ} - H_{3,Aus}$), which is 262 m for the values cited, though with an expected error close to 100%! Nevertheless, this suggests, in terms of the model, in which no cross-isopycnal flux is envisaged, that a net transport of 9 Sv of layer 3 water must escape through the open northern boundary of the model near the equator. The natural ocean does permit cross-isopycnal flux, of course. In fact, a flux of about 3 m yr^{-1} distributed uniformly over the area of the Pacific Ocean north of 15° is required to balance a transport of 10 Sv. Such a magnitude is consonant with traditional estimates of vertical flux (Munk, 1966). [The condition on the continuity of layer 3 transport, Eqs. (4.4), (4.8), over the latitude range occupied by New Zealand, deserves to be reexamined in the light of such a putative cross-isopycnal flux. The area of the South Pacific between New Zealand and South America is about $8000 \text{ km} \times 2000 \text{ km}$. Multiplying by 3 m yr^{-1} gives about 1.6 Sv, not an insubstantial figure, but probably negligible compared to errors in the transport estimate (4.8).]

Finally, it is important to note that the discussion of this section is fairly robust in terms of modeling assumptions; the remarks made do not depend sensitively on the details of the model, but follow fairly directly from assumptions of geostrophy and the Sverdrup balance, applied to a zonal section passing the southern end of New Zealand.

6. Discussion

The simple baroclinic circulation theory of LPS, which distributes the wind-driven Sverdrup transport among a number of layers in a way consistent with conservation of potential vorticity, was applied to the South Pacific Ocean. The governing idea behind this model is that columns of water in a particular layer are imprinted with their potential vorticity by the wind stress curl in latitudes where they are in direct contact with the frictional surface layers, and that subsequently, as they flow equatorward beneath lighter water in anticyclonic gyres, they preserve whatever potential vorticity they had acquired. This idea has to be modified and augmented when it is discovered that there are certain regions in submerged layers that cannot be reached from high latitudes by paths that proceed di-

rectly through the geostrophic interior, but are instead linked to the forcing by paths passing through the western boundary currents. In the absence of a more detailed theory of how potential vorticity in such a region, called the "western shadow zone", is determined as flow leaves the western boundary current, I adopted, following LPS and Talley (1985), the hypothesis that potential vorticity is homogeneous throughout it. This shadow zone is enormous in the South Pacific, almost filling the basin (regions W, WW, VW, EW in Fig. 2). While the ad hoc nondeductive nature of the hypothesis must be stressed, the homogeneity of potential vorticity in layer 3 is borne out by comparison with Keffer's (1985) maps in the corresponding density layer.

The circulation produced by the model resembles quite well the actual circulation observed in the South Pacific, as judged by comparison of maps of modeled and actual isopycnal depths and dynamic topographies on various surfaces. Agreement is remarkable in the deepest modeled layer, which contains the density at the core of the Antarctic Intermediate Water, but poorer in the surface layers, especially in the tropical band, where stronger circulation is observed than the model allows. A reason for this deficiency is offered below.

There is a boundary current on the eastern side of New Zealand constrained, not by a requirement to balance the interior Sverdrup transport between New Zealand and South America, but by the necessity to achieve the same pressure in all layers at the northern end of the islands as at the southern. This must be so because, pressure being continuous from east to west around the northern and southern tips, it is not possible by any means to sustain a pressure gradient, which by geostrophy would require a normal flow, along the eastern boundary of an ocean basin. This constraint, together with a requirement of continuity of net mass transport between New Zealand and South America in each layer, is enough to determine boundary current transports in each layer, and layer depths. Cross-isopycnal flux, because it affects the layer-by-layer mass balance of the western boundary currents, alters the balances by which the depths of the layers on the western side of New Zealand, for example, are determined. I considered this effect crudely in order of magnitude in section 4 and concluded that its likely influence on determining the layer depths around New Zealand is negligible.

In principle, similar constraints should be allowed to determine the flow around Australia, considered as an island isolated by the deep passages through the Indonesian archipelago. However, I have used the constraints only to determine the depth-integrated transport in the East Australian Current and relied instead on empirically observed isopycnal depths at southeastern Australia to determine individual layer transports. The reason for this approach is that, unlike New Zealand, the neglect of cross-isopycnal flux is indefensible around Australia, as I shall make clear below.

We may summarize the results of considering the western boundary currents in a series of cartoons of vertical sections across the South Pacific at various latitudes. Figure 17a shows such a section crossing the model ocean at 50°S between South America and New Zealand, jogging north to cross the zonal jet feeding the western boundary current at New Zealand, thence crossing the Tasman Sea along 46°S, and jogging north across another zonal jet to reach Tasmania. The diagram shows the depths that the layer interfaces achieve both outside and inside the western boundary currents at the southern ends of New Zealand and Australia. It also shows the volume transports in the interior of the ocean and in the boundary current in each layer. The interior transports of layer 3 in the eastern South Pacific and Tasman Sea are, respectively, 3.5 Sv and zero. The corresponding estimates for layer 2 in the eastern South Pacific and Tasman Sea are 9.5 and 5 Sv; the former is composed of 8.8 Sv northward Ekman transport, and only 0.7 Sv geostrophic transport. These estimates are based solely on considerations of wind stress forcing and potential vorticity conservation in the interior. The boundary current transports at New Zealand are 10.5 and 5.5 Sv in layers 3 and 2; and at Australia, -5 Sv and -12 Sv. The Australian boundary current transports are determined by the selection of interface depths at the Australian continent from inspection of hydrographic data like the Scorpio sections (Stommel et al., 1973). If the New Zealand-South America section were taken only slightly further north, much of the large boundary current transports would already be distributed to the interior. This may be why the intermediate level isopycnals of the Scorpio section at 43°S, which was made considerably north of the southern end of the islands, do not show the pronounced boundary layer character of the base of layer 3. The model section shows the light water of layer 2, moderately deep (400–600 m) in the Tasman Sea and just to the east of New Zealand, but extremely shallow in the remainder of the eastern Pacific at this latitude. A similar feature, marked by light, warm ($>8^{\circ}\text{C}$), salty ($>34.6 \times 10^{-3}$) water can be discerned in the 43°S section in the Tasman Sea, and east of New Zealand, though it extends much farther eastward, to perhaps 165°W, than in the model section at 50°S.

The net transports of layers 3 and 2 in the South Pacific are 9 and 8 Sv (northwards). Mass continuity requires that the net transport be the same in each layer in any other Australia-South America section.

The next section shown is at the latitude of the northern end of New Zealand (Fig. 17b). It crosses the eastern Pacific along 32°S, jogs slightly south to reach New Zealand, and crosses the Tasman Sea along 34°S. A lighter layer of water (layer 1) has joined the vertical stack of layers. Each of layers 2 and 3 preserves the net volume transport it acquired at the southern section. The net transport of layer 1 must be zero in each of the two sub-basins because it cannot be supplied from further south. Layer 2 in the Tasman Sea is in a stag-

nant shadow zone formed to the west of New Zealand. The interior transport of layer 1 in the eastern Pacific is 8.3 Sv, composed of 2.0 Sv Ekman transport, and 6.3 Sv geostrophic transport. Note the reversal of the boundary current in all layers but the third, in which it is still weakly northward, at the northern end of New Zealand.

For contrast we show in Fig. 17c a slightly different section, crossing the entire Pacific along 32°S, passing the north tip of New Zealand without crossing the boundary current, and passing north of the zonal jet in the Tasman Sea that supplies the New Zealand boundary current. The eastern part of the section is identical with the corresponding part of Fig. 17b. Contrasting Figs. 17b, c shows the shallow layer transports in the boundary currents shifting from Australia to New Zealand.

Finally, we show a section north of New Zealand along 28°S (Fig. 17d). The southward transport in the deeper layers in the boundary current is weakened, most markedly in layer 3.

Many of the oceanographic features that have been remarked on in the investigations that have been done around New Zealand (see Heath, 1985, for a review) are apparent in the model. The turning of 10–15 Sv of the southward flow from the East Australian Current, to proceed along the Tasman Front to the northern tip of New Zealand (Stanton, 1981), and perhaps connect with the East Auckland or East Cape Current on the eastern New Zealand coast can be seen in the observations. A jet of this magnitude connecting the boundary current at Australia to the northern tip of New Zealand in the zonal band 32°–34°S is clearly reproduced in the model (Figs. 5, 17b, c). Similarly, an eastward jet can be discerned in the observations, penetrating to at least intermediate depths, and lying west of the southern cape of New Zealand. This jet turns around the islands in a complicated way, presumably because of the complexity of the topography of the Campbell Plateau and Chatham Rise, becomes associated with the Southland Current, and feeds the anticyclonic gyre east of New Zealand. Bottom topography is lacking in the model, so the observed complexity of flow cannot be adequately rendered, but the zonal jet west of New Zealand, and its feeding of the anticyclonic gyre to the east, are clearly seen in the model (Figs. 5, 17a). These zonal jets are required in the model for the following reasons: (i) the pressure must adjust to be constant in each layer along the west side of New Zealand; (ii) on the other hand, pressure in each layer just to the north and south of the islands is determined by the Sverdrup balance and the conservation of potential vorticity; (iii) the resulting imbalances in pressure draw geostrophically balanced jets from the west.

The continuity of net transport in each layer in the sections of Fig. 17 is a consequence of the assumption in the model that layer interfaces are material surfaces. Hence the 17 Sv total northward transport between

Australia and South America in the model ocean is made up at every latitude of zero (in layer 1), 8 Sv (layer 2), and 9 Sv (layer 3). In the natural ocean, such cold, dense watermass transports would allow themselves to be converted into warmer, lighter water masses before flowing out of the Pacific through the Indonesian passages. Hence it seemed vain to apply the theory of section 4 to flow around Australia and determine layer depths at the continental boundary. Permitting cross-isopycnal fluxes in the model, though essential to an eventual fuller understanding of the thermohaline circulation patterns, would vitiate its simplicity, for which reason the effect was omitted from the present model. Nonetheless, some qualitative effects of doing so can be anticipated. Suppose cross-isopycnal flux from a deeper to a shallower layer occurs. Then the effect on the shallower (deeper) layer is to compress (stretch) vortices and make the flow more (less) anticyclonic; in other words, to transfer the anticyclonic subtropical circulation from deeper to shallower layers. Among the deficiencies of the model we have noted the prediction of stronger circulations at mid-depth, and weaker circulations near the surface than observed, especially in the tropics. Proper allowance of cross-isopycnal flux may redress this deficiency.

7. Summary

In summary, Warren's (1970) assessment that the Sverdrup balance accounts for the circulation of the South Pacific Ocean appears well borne out. More than that, the principle that, after they have been imprinted by surface contact with the wind, water columns conserve potential vorticity in submerged layers along paths in the geostrophic interior, and the hypothesis that, where paths do not lead directly from the forcing regions but through the western boundary current, potential vorticity is uniform (western shadow zones) or flow is stagnant (eastern shadow zones), give a picture of baroclinic circulation in good accord with observations. Where agreement is poorer, for example, in the surface circulation in the Tropics, I have suggested that the proper inclusion of cross-isopycnal mixing into the model, as well as a system of layers giving finer near-surface resolution, might reconcile the model with the observations. Neglect of cross-isopycnal mixing also means that the meridional transport in zonal sections of watermasses in the model (where each layer might be regarded as a watermass) cannot change with latitude: a fatal deficiency in any attempt to give an account of the thermohaline circulation.

Acknowledgments. I am grateful to the CSIRO Division of Oceanography for its hospitality while conducting this work. I have enjoyed useful discussions with and assistance from Stuart Godfrey and Gary Meyers. Joseph L. Reid loaned the plate from which Fig. 11 was made. My research is partially supported also under National Science Foundation Grant OCE-

8541635, and Office of Naval Research Contract N00014-84-C-0218.

REFERENCES

- Boland, F. M., and J. A. Church, 1981: The East Australian Current 1978. *Deep-Sea Res.*, **28**, 937-957.
- Church, J. A., 1987: The East Australian Current adjacent to the Great Barrier Reef. *Aust. J. Mar. Freshwater Res.*, in press.
- Gill, A. E., 1982: *Atmosphere-Ocean Dynamics*. Academic Press, 662 pp.
- Godfrey, J. S., 1987: A Sverdrup model of the depth integrated flow for the world ocean allowing for island circulations. *Geophys. Astrophys. Fluid Dyn.*, submitted.
- Gordon, A. L., 1986: Inter-ocean exchange of thermocline water. *J. Geophys. Res.*, **91**(C4), 5077-5046.
- , E. J. Molinelli and T. N. Baker, 1982: *Southern Ocean Atlas*. Columbia University Press.
- Heath, R. A., 1985: A review of the physical oceanography of the seas around New Zealand—1982. *N. Z. J. Mar. Freshwater Res.*, **19**, 79-124.
- Hellerman, S., and M. Rosenstein, 1983: Normal monthly wind stress over the world ocean with error estimates. *J. Phys. Oceanogr.*, **13**, 1093-1104.
- Holland, W. R., T. Keffler and P. B. Rhines, 1984: Dynamics of the general circulation: the potential vorticity field. *Nature*, **308**, 698-705.
- Keffler, T., 1985: The ventilation of the world's oceans: maps of the potential vorticity field. *J. Phys. Oceanogr.*, **15**, 509-523.
- Luyten, J. R., J. Pedlosky and H. Stommel, 1983: The ventilated thermocline. *J. Phys. Oceanogr.*, **13**, 293-309.
- Munk, W. H., 1966: Abyssal recipes. *Deep-Sea Res.*, **13**, 707-730.
- Pedlosky, J., 1978: An overlooked aspect of the wind-driven oceanic circulation. *J. Fluid Mech.*, **32**, 809-821.
- Reid, J. L., 1965: Intermediate waters of the Pacific Ocean. *The Johns Hopkins Oceanographic Studies*, No. 2. The Johns Hopkins Press, Baltimore, 85 pp.
- , 1973: The shallow salinity minima of the Pacific Ocean. *Deep-Sea Res.*, **20**, 51-68.
- , 1981: On the mid-depth circulation of the world ocean. In: *Evolution of Physical Oceanography*, B. A. Warren and C. Wunsch, Eds., MIT Press, 70-111.
- , 1986: On the total geostrophic circulation of the South Pacific Ocean: flow patterns, tracers and transport. *Progress in Oceanography*, Vol. 16, Pergamon, 1-61.
- Rhines, P. B., and W. R. Young, 1982: A theory of the wind-driven circulation. I. Mid-ocean gyres. *J. Mar. Res.*, **40**(Suppl.), 559-596.
- Stanton, B. R., 1981: An oceanographic survey of the Tasman Front. *N. Z. J. Mar. Freshwater Res.*, **15**, 289-297.
- Stommel, H., E. D. Stroup, J. L. Reid and B. A. Warren, 1973: Trans-Pacific hydrographic sections at Lats 43°S and 28°S: the Scorpia Expedition—I. Preface. *Deep-Sea Res.*, **20**, 1-7 (Plates 1-6).
- Sverdrup, H. U., 1947: Wind-driven currents in a baroclinic ocean: with application to the equatorial currents in the eastern Pacific. *Proc. Natl. Acad. Sci. U.S.A.*, **33**, 318-326.
- Talley, L., 1985: Ventilation of the subtropical North Pacific: the shallow salinity minimum. *J. Phys. Oceanogr.*, **15**, 633-649.
- Tsuchiya, M., 1968: Upper waters of the intertropical Pacific Ocean. *The Johns Hopkins Oceanographic Studies*, No. 4. The Johns Hopkins Press, 50 pp.
- Warren, B. A., 1970: General circulation of the South Pacific. *Scientific Exploration of the South Pacific*, W. S. Wooster, Ed., Natl. Acad. Sci., pp. 33-49.
- , 1973: Trans-Pacific hydrographic sections at 43°S and 28°S: the Scorpia Expedition—II. Deep Water. *Deep-Sea Res.*, **20**, 9-38.
- Wyrtki, K., 1974: The dynamic topography of the Pacific Ocean and its fluctuations. *Hawaii Institute of Geophysics HIG-74-5*.
- , 1975: Fluctuations of the dynamic topography in the Pacific Ocean. *J. Phys. Oceanogr.*, **5**, 450-459.

Coastal-Trapped Waves on the East Australian Continental Shelf Part II: Model Verification

JOHN A. CHURCH, NEIL J. WHITE, ALLAN J. CLARKE,* HOWARD J. FREELAND,** AND ROBERT L. SMITH†

Division of Oceanography, CSIRO Marine Laboratories, Hobart Tasmania 7001 Australia

(Manuscript received 20 November 1985, in final form 4 August 1986)

ABSTRACT

The Australian Coastal Experiment (ACE) was designed to test coastal-trapped wave (CTW) theory and the generation of coastal-trapped waves by the wind. For the ACE dataset, we use CTW theory to attempt to hindcast the observed alongshelf currents and coastal sea levels at locations remote from the upstream (in the CTW sense) boundary of the ACE region. Local (in the ACE region) wind forcing is responsible for only about a quarter of the CTW energy flux at Stanwell Park (the center of the ACE region), and the remainder enters the ACE region from the south and propagates northward through the ACE region. Including the second-mode CTW improves the correlation between the hindcast and the observed near-bottom currents on the upper slope at Stanwell Park, but the use of the third-mode CTW cannot be justified. A linear bottom drag coefficient of $r = 2.5 \times 10^{-4} \text{ m s}^{-1}$ works better than a larger drag coefficient, and simplifying the CTW equations by assuming the modes are uncoupled does not detract from the quality of the hindcasts. The hindcast and observed coastal sea levels are correlated at greater than the 99% significance level. For the nearshore locations at Stanwell Park, the hindcast and observed alongshelf currents are correlated at greater than the 99% significance level, and the CTW model can account for about 40% of the observed variance. On the shelf at Stanwell Park, we find the hindcasts agree with the observations only if direct wind forcing within the ACE region and the correct (nonzero) upstream boundary conditions are included. However, even after attempting to remove the effects of the eddies and the East Australian Current, the CTW model is not useful for predicting the currents on the slope at Stanwell Park and on the shelf and slope at Newcastle (the northern boundary of the ACE region). The currents at these locations are dominated by the effect of the East Australian Current and its eddies.

1. Introduction

Since subinertial frequency coastal-trapped waves (CTWs) were first studied in the early 1960s (Hamon, 1962), there have been a number of attempts to use theory to hindcast various aspects of CTWs. The first attempt to use forced wave theory to hindcast continental shelf waves was made by Hamon (1976). He used the barotropic theory of Gill and Schumann (1974) to hindcast sea levels at Evans Head on the east coast of Australia. Hamon (1976) assumed an along-shore phase velocity of 4.0 m s^{-1} [determined from the observed alongshore propagation of sea levels (Hamon, 1966)], but concluded that better agreement between theory and observations would be obtained with a phase velocity of 3.5 to 3.0 m s^{-1} . He also concluded that there was only a small amount of frictional dissipation. The theoretical predictions were of somewhat smaller amplitude than observed, but the amplitude

agreement was within a factor of 3 or better. Clarke (1977) showed that the CTW theory could be used to explain, at least qualitatively (and quantitatively for Lake Ontario), a range of observational and numerical results.

Brink (1982) used the CTW theory, with realistic bottom topography and stratification, to predict along-shelf currents off the Peru coast. While the results indicated that the observed variance could only be accounted for if CTWs were present, the quantitative agreement between observed and hindcast currents was not significant over most of the CTW band. More recently, Battisti and Hickey (1984) hindcast sea levels and alongshelf currents for the west coast of the United States. For sea levels, the coherence between observed and hindcast results was significant at the 95% significance level. For alongshelf currents, the agreement was less satisfactory, but the theoretical predictions still accounted for a significant percentage of the variance.

All of these attempts to hindcast observations assumed that the first-mode CTW was dominant. Recently, Mitchum and Clarke (1986) have used up to seven CTW modes to hindcast currents and sea levels on the West Florida Shelf. In Part I of this paper (Church et al. 1986, hereafter referred to as Part I), the second-mode CTW was found to carry at least as much

* Permanent affiliation: Department of Oceanography, Florida State University, Tallahassee, FL 32306.

** Institute of Ocean Sciences, Sidney, British Columbia V8L 4B2, Canada.

† College of Oceanography, Oregon State University, Corvallis, OR 97331.

energy as the first-mode CTW in the dataset obtained for the Australian Coastal Experiment (ACE).

In this paper, we shall use the ACE dataset described in Freeland et al. (1986) to attempt some quantitative tests of the CTW theory. We are not attempting to explain all of the observed variance on the shelf and slope. On the slope, the observed variance is dominated by eddies and the East Australian Current and this makes verification of the theory more difficult. The theory as presented by Clarke and Brink (1985) and Clarke and Van Gorder (1986) is summarized in the Appendix of Part I. This theory includes arbitrary stratification, cross-shelf topography, and linear bottom friction; the waves are assumed to be driven by the alongshelf component of the wind stress or to originate upstream (in the CTW sense) of the ACE region. In section 2, the observations are briefly described and the method of application of the theory of the Appendix of Part I is presented. In section 3, the theory, together with the observed winds and the boundary conditions at the upstream end of the ACE wave guide, is used to hindcast coastal sea levels and alongshelf currents. Correlation and cross-spectral techniques indicate that the hindcasts are significantly coherent with the ob-

servations on the shelf and the upper slope. However, the near-surface currents above the slope are dominated by eddies and the East Australian Current, and the theory is unsuccessful at hindcasting these currents. Finally, the usefulness of the model is discussed in section 4.

2. Application of the theory to the ACE dataset

a. The observed currents and pressure and wind stress fields

The main ACE array consisted of three sections of current meters (each with five moorings and each having a total of 15 current meters) offshore from Cape Howe, Stanwell Park and Newcastle (Fig. 1a). The designed placement of the current meters on each section is shown in Fig. 1b. We shall refer to the three sections of current meters as line 1 (Cape Howe), line 2 (Stanwell Park) and line 3 (Newcastle). The current meters are coded as in this example: f23/1000 (f refers to low-pass filtered data) is a meter at a depth of 1000 m on the third mooring from the coast on line 2.

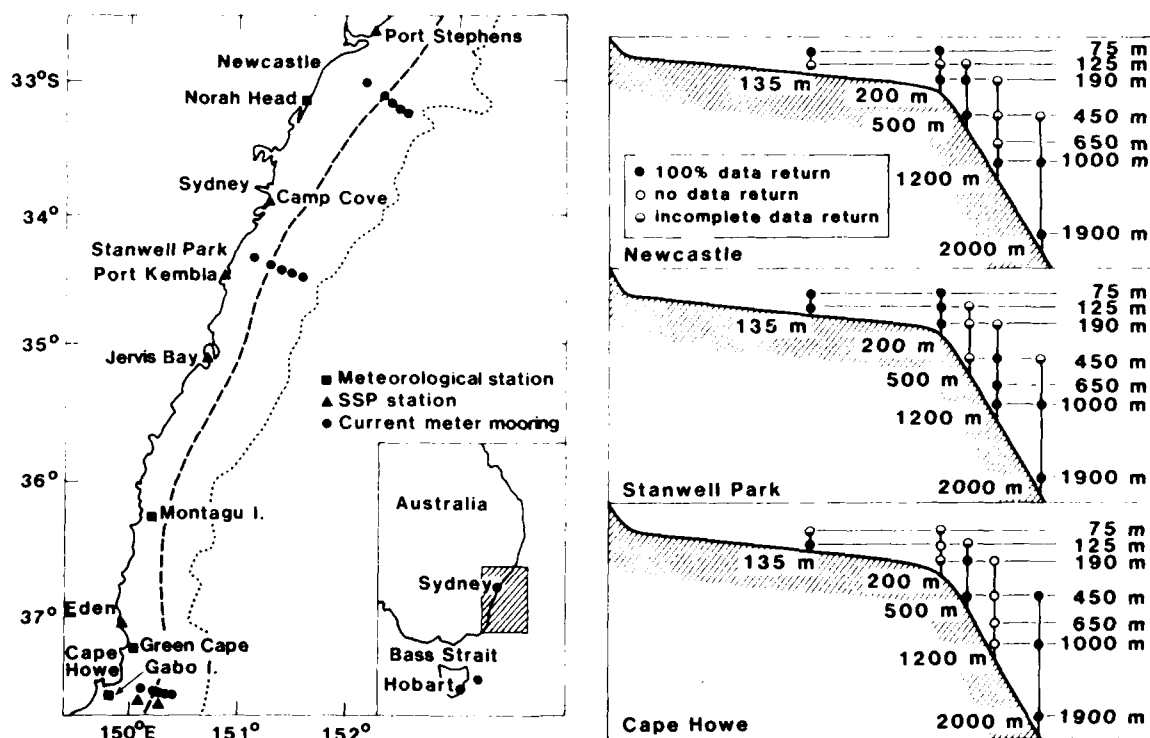


FIG. 1. Location diagram for the Australian Coastal Experiment. (a) The locations of the current meter moorings, SSP records and locations where meteorological data were collected. The sole mooring at 42°40'S on the east coast of Tasmania is shown on the inset. The dashed line is the 200 m isobath and the dotted line is the 4000 m isobath. (b) Schematic (not to scale) diagram of the locations of current meters on the sections at Cape Howe, Stanwell Park and Newcastle. A solid circle indicates 100% data return, an open circle zero data return, and a half shaded circle indicates an incomplete record.

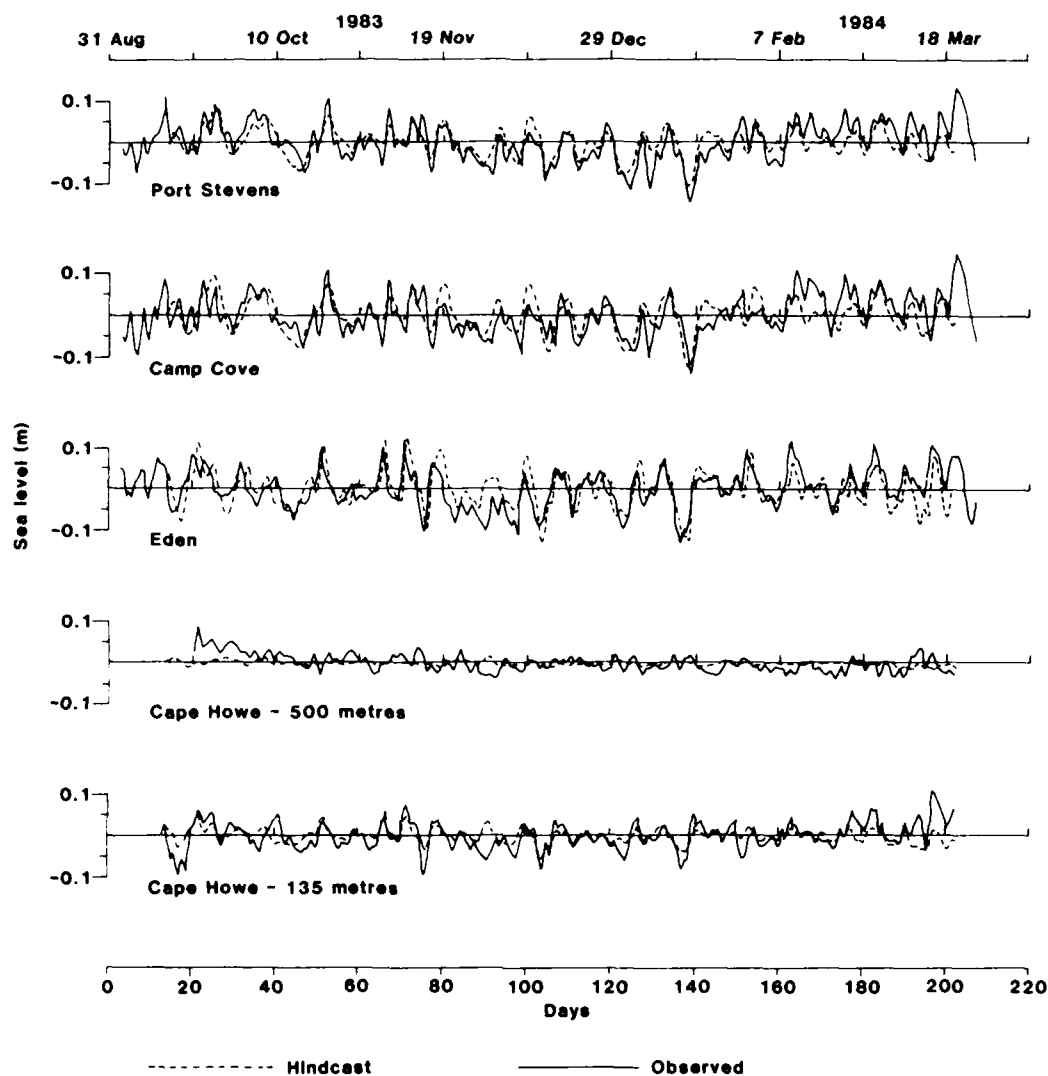


FIG. 2. Comparison of hindcast and observed sea levels.

The details of the preliminary data analysis are given in Part I and Freeland et al. (1985). Briefly, the data was bandpassed to remove periods greater than 24 days and less than 2 days, and only the alongshelf component of the current was used.

Coastal subsurface pressure (SSP) data are available at Eden, Jervis Bay, Port Kembla, Camp Cove and Port Stephens (Fig. 1). SSP data are also available at the bottom of the 135 and 500 m moorings at Cape Howe; they are referred to as fp11 and fp13, respectively. Details of the data and data processing are given in Forbes (1985a). As with the current meter data, the series were bandpassed.

Meteorological data were obtained for 16 Bureau of Meteorology stations and for three buoys moored at

midshelf. From this dataset, we selected three stations that provided continuous data during ACE and which we considered to be representative of the wind stress field. These stations, at Green Cape, Montagu Island and Norah Head (Fig. 1), were used in the application of the CTW theory. Full details of the data and the wind field over the ACE region are given in Forbes (1985b and personal communication, 1985).

b. Application of the theory

To hindcast the alongshelf currents and coastal sea levels, it is first necessary to know the amplitude ϕ of the CTW modes at the upstream end of the wave guide. In Part I, these amplitudes of the CTW modes were found by solving

TABLE 1. Observed and hindcast variance for the SSPs and the correlation coefficient between these two signals. The record is incomplete for the stations marked with an asterisk.

Location	Observed variance (cm^2)	Hindcast variance (cm^2)	Correlation coefficient
tp13	6.3	0.4	0.23
tp11	16.0	4.6	0.54
Eden	32.8	30.0	0.64
Jervis Bay*	25.4	30.4	0.66
Port Kembla*	43.9	26.6	0.60
Camp Cove	31.1	24.9	0.63
Port Stephens	30.9	17.6	0.75

$$\mathbf{G}\phi = \mathbf{v}, \quad (2.1)$$

where the n /th element of the matrix \mathbf{G} is the alongshelf current component of the j /th eigenfunction at the n th ($n \leq 15$) current meter location at Cape Howe. Because of the finite quantity of data and the presence of other phenomena besides CTWs (such as East Australian Current eddies), only the amplitude of the first three CTW modes was estimated. To minimize contami-

nation from the East Australian Current, a statistical "eddy" mode (see Part I) was defined and included in the analysis so that \mathbf{G} consisted of four column vectors. As this analysis was completed at all three sections, the modal amplitudes are known at Cape Howe, Stanwell Park and Newcastle.

The theory outlined in the Appendix of Part I was then used to step along the coast. In completing this hindcast, we allow the eigenfunctions F_j (for the pressure field) (and hence G_j for the velocity field), the phase speeds c_j , and the coupling coefficients b_j and a_j to vary with the alongshelf location. All of these parameters were evaluated for the Cape Howe, Stanwell Park and Newcastle sections and linearly interpolated for locations between the sections. The eigenfunctions and eigenvalues were computed for the estimated topography and Brunt-Väisälä frequency profiles (see Part I for details) using the methods of Brink and Chapman (1985). The first-mode phase velocities increase from 3.2 m s^{-1} at Cape Howe to 4.0 m s^{-1} at Stanwell Park and to 5.2 m s^{-1} at Newcastle. The increase is due to the increased stratification in the north and also to the increased shelf width. Sensitivity tests indicated that the eigenfunctions and the phase velocities were not

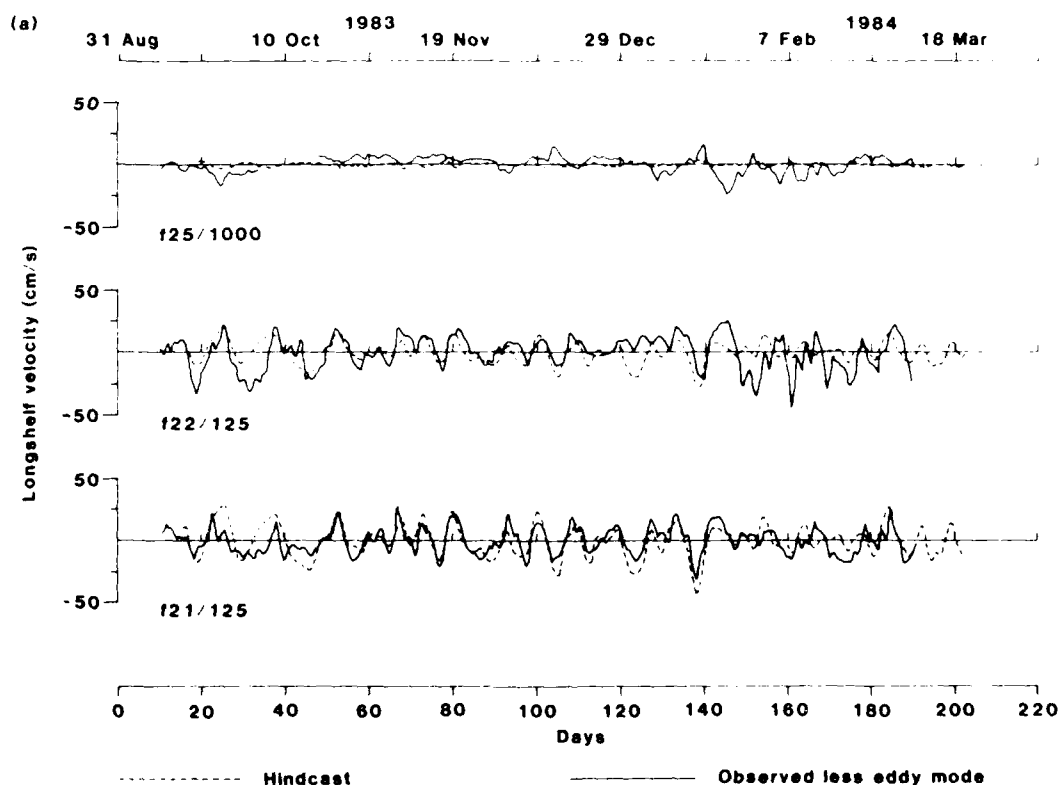


FIG. 3. Comparison of the hindcast alongshelf current with the de-eddyed observations for (a) Stanwell Park and (b) Newcastle. The predictions were completed with a model using three CTW modes. The observations have been band-passed and the effects of the eddy mode removed [Eq. (4.1)]. Only a representative selection of current meter records is presented.

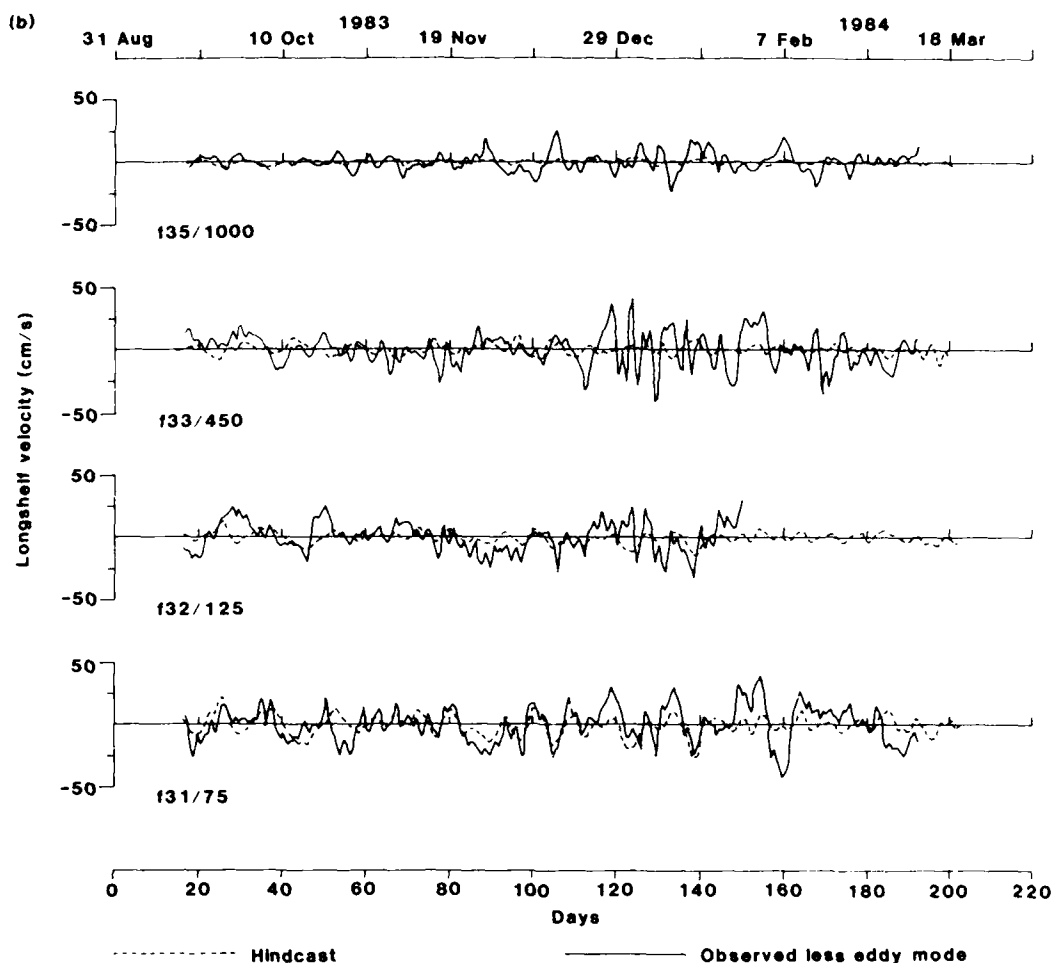


FIG. 3. (Continued)

sensitive to small changes in the depth or the stratification profiles (such as might be produced by inaccuracies in the data or local variations in the shelf conditions), but that for accurate quantitative results it is necessary to allow for gross changes in $h(x)$ and $N^2(z)$ that occur between current meter sections.

The frictional coupling coefficients were evaluated using linear bottom friction evaluated from $r = C_D U_b$. A value of 0.0025 was used for the bottom drag coefficient C_D , and a value of 0.2 m s^{-1} for the scale velocity U_b , which implies that $r = 5 \times 10^{-4} \text{ m s}^{-1}$. The value of r was taken to be independent of the cross-shelf coordinate.

Wind stress was calculated from the observed winds at Green Cape, Montagu Island and Norah Head (Fig. 1) using the neutral steady state drag coefficient of Large and Pond (1981).

The wave band we shall consider is that associated with synoptic weather events with periods ranging from a few days to a few weeks. In particular, the lowest

frequency motion we consider has a period of 24 days and the highest frequency has a period of 3.7 days.

3. Comparison of observed and modeled coastal-trapped waves

a. Sea levels

The SSPs and alongshelf velocities observed during ACE were hindcast using the theory outlined in the Appendix of Part I, the boundary conditions (at Cape Howe) determined in Part I, and the observed winds. The hindcast and observed SSPs are compared in Fig. 2 and Table 1. For the pressure record at the most southerly location on the coast (Eden), the hindcast and observed SSPs are of comparable magnitude and are significantly correlated at above the 99% significance level. We calculated the integral time scales following Davis (1976). If Eden and Camp Cove sea levels are used, the integral time scale is 5 days (as used by

TABLE 2. Correlation coefficients between the de-eddied observed alongshelf currents and the hindcast currents at Stanwell Park and Newcastle. The correlation coefficients are given for the total ACE period and, for Stanwell Park, are also given for the period when no eddies were present (days 50 to 140).

Location	Stanwell Park		Location	Correlation coefficient (complete record)
	Correlation coefficient (complete record)	Correlation coefficient (days 50–140)		
f21/75	0.43	0.76	f11/75	0.45
f21/125	0.65	0.79	f31/125	0.63
f22/75	0.29	0.52	f32/75	0.39
f22/125	0.40	0.60	f32/125	0.33
f22/190	0.49	0.62	f32/190	0.13
f23/125	0.57	No data	f33/25	0.22
f23/190	0.20	No data	f33/190	0.18
f23/450	0.07	No data	f33/450	0.17
f24/170	0.02	0.41	f34/190	0.02
f24/450	-0.04	0.28	f34/450	0.16
f24/650	-0.04	0.00	f34/650	0.06
f24/1000	0.36	0.36	f34/1000	0.35
f25/450	0.28	0.18	f35/450	0.03
f25/1000	0.22	0.18	f35/1000	0.21
f25/1900	0.15	0.17	f35/1900	0.10

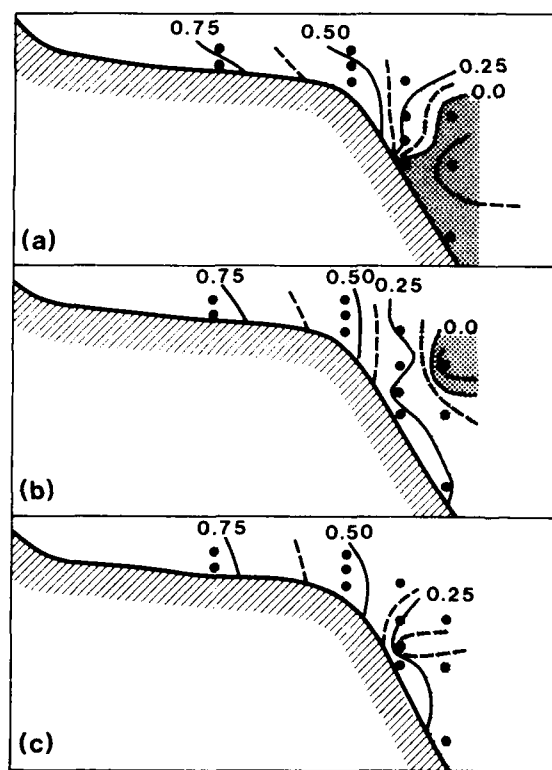


FIG. 4. Contour plot of the correlation between the hindcast alongshelf current and the de-eddied observations between days 50 and 140. Only one CTW mode is used in (a), two CTW modes are used in (b), and three CTW modes are used in (c). Regions of negative correlation are indicated by heavy stippling; light stippling indicates regions where the correlation coefficient is less than 0.25 but greater than zero.

Freeland et al., 1986). However, if the currents at f11/125 and f21/125 are used, the integral time scale is about 3 days. To estimate significance levels, we have used the more conservative time scale of 5 days, and thus for a record length of 180 days and an integral time scale of 5 days the 95% significance level is 0.325 and the 99% significance level is 0.418. In contrast, for the record at the 500 m isobath (fp13), both the observed and hindcast signals are small (as is expected for CTWs) and are not significantly correlated. At midshelf (the 135 m isobath—fp11), the observed and hindcast series are of intermediate magnitude (compared to Eden and fp13) and are significantly correlated. For the coastal SSP at Camp Cove and Port Stephens (the two other sites with complete records), the hindcast and observed series have similar variances and are significantly correlated at greater than the 99% significance level (Table 1).

Although we have used only the velocities at Cape Howe to determine the amplitudes of the CTW modes, the model can successfully hindcast the observed SSP at the northern limit of the ACE array. It is also apparent (Fig. 2) that the comparison is poorer at some times than others. This is at least partially due to the presence of offshore eddies that are affecting the coastal sea levels, which, as we shall see, have an even more marked effect on the alongshelf currents.

b. Currents

In comparing the hindcast alongshelf currents with the observations, it must be remembered that offshore events (eddies and the East Australian Current) strongly affect the currents on the shelf and that CTWs only

account for a fraction of the observed variance. In Part I, an attempt was made to minimize the contamination of the CTW mode amplitudes by including a statistical eddy mode in the least-squares fit. For an initial comparison of hindcast currents with the observations, we have attempted to remove that part of the current due to eddies by generating a "de-eddied" current v_n^{de} given by

$$v_n^{de} = v_n - G_{n3}\phi_3. \quad (3.1)$$

Note that v_n^{de} includes the contribution from the first three CTW modes and a residual noise factor ϵ , which could include contributions from higher-order CTW modes and from the East Australian Current.

This de-eddied current is compared with a representative range of hindcast currents at Stanwell Park and Newcastle in Fig. 3. The correlation coefficients (Table 2) are largest for the nearshore meters, where the hindcast and observed variances are of a similar magnitude, and the correlation coefficients gradually decrease with increasing distance from the coast. The variance in both the observed and hindcast series decreases with increasing distance beyond the shelf break, with the hindcast variance decreasing faster than the observed variance. This result is not surprising given that CTWs are trapped on the continental shelf and slope, and the presence of East Australian Current eddies in the offshore region. Also, the correlation coefficients are larger for Stanwell Park than for Newcastle. This is because of the small amount of variance accounted for by the first three CTW modes at Newcastle (See Part I). As for the sea levels, the correlation coefficients for the nearshore velocities are well above the 99% significance level of 0.418 (Table 2).

Offshore, the correlations are not significant at the 95% level. Due to the effects of eddies, there are periods when the hindcast is significantly worse than at other times; i.e., while we have reduced the effects of eddies on the currents by using a statistical eddy mode, we have not entirely removed their effects. In fact, there are periods (particularly from late January to February at Stanwell Park) when the eddies dominate the observed currents at all locations across the shelf. In contrast, for the period between days 50 and 140, other observations (CTD data, XBT data, satellite-tracked buoys and satellite infrared images) taken during ACE indicate that no large eddies were affecting the currents at Stanwell Park. The correlations for this period are considerably higher than they are for the complete ACE period (Table 2); in the offshore region all the correlations are positive and some are significant at the 95% level.

We have attempted to answer the question "How many CTW modes are necessary to hindcast the observed currents successfully?" For this test, we concentrated on the alongshelf currents at Stanwell Park for the period between days 50 and 140 when eddies were

absent from the Stanwell Park region. We repeated the fitting of CTW modes at Cape Howe and the subsequent hindcasting of alongshore velocities at Stanwell Park using two rather than three CTW modes, and one rather than three CTW modes, and compared the results with the de-eddied currents at Stanwell Park. For the locations on the shelf, including only two modes gives marginally higher correlations than including three modes, which in turn gives higher correlations than including only one mode. However, for locations 24/1000, 24/450, 25/1000 and 25/1900, using only one mode (Fig. 4) resulted in negative correlations; i.e., one mode cannot account for the observed reversal of sign of the longshore currents. In contrast, when two modes were used, the only negative correlation was at 25/450, and for three modes all correlations were positive.

In Part I, it was found that CTWs accounted for only a fraction of the observed variance and that even when an eddy mode was included some variance was still unaccounted for. We also found that removing the eddy mode from the observations did not remove all of the eddy signal from the data. To avoid this noise, we applied a more realistic test of CTW theory by comparing the predictions with currents we believe to be associated with CTWs. At Stanwell Park and Newcastle sections, we define reconstructed currents as

$$v_n' = \sum_{j=1}^3 G_{nj}(\lambda, y)\phi_j(y, t) \quad (3.2)$$

where ϕ_j is determined from the data (see Part I). Since Eq. (3.2) involves a summation limited to the first three CTW modes, the reconstructed currents are due to the dynamical modes with a relatively small amount of contamination from eddies or from other phenomena; i.e., the residual noise factor ϵ is not included in Eq. (3.2) whereas it is included in Eq. (3.1). A comparison of the reconstructed currents with the hindcast velocities is shown in Fig. 5 and Table 3. Compared to the correlations for the de-eddied currents, the correlation between the two signals is only marginally different near the coast but is significantly improved offshore.

The time series of the amplitudes of modes 1, 2 and 3 at Stanwell Park, as calculated from the observations and as hindcast from the above theory, are shown in Fig. 6. The correlation coefficients between the observed and hindcast time series are 0.47 and 0.51, respectively, for modes 1 and 2 at Stanwell Park; for mode 1 at Newcastle the correlation coefficient is 0.44. The correlation coefficients for mode 3 are not significant for either location, and for mode 2 the correlation coefficient is not significant for Newcastle. Cross spectra (Fig. 7) between observed and hindcast series at Stanwell Park indicate that for mode 1 the series are significantly correlated for all periods, except 4.8 days over the 24 to 3.7 day wave band, and there is a near zero phase difference for the entire wave band. The

transfer function is about 1.2 for periods of 8 and 6 days, but is about 0.7 for the rest of the wave band. These estimates of the transfer function are not significantly different from unity. For mode 2, the series are significantly correlated over the entire wave band and there is a near zero phase difference for periods from 24 to 4.8 days; however, at a period of 3.6 days this phase difference suddenly jumps to 180° . The transfer coefficient ranges from 0.4 for a period of 3.6 days to 0.7 at a period of 6 days; i.e., the hindcast series is too small by about 40%. For mode 3, the series are not significantly correlated in the wave band.

To estimate the sensitivity of the solution to variations in the friction coefficients, we arbitrarily halved and doubled the frictional coupling coefficients a_{ij} . When the coupling coefficients were doubled (increased friction), the coherences fell slightly and the phase lags increased by 10° to 20° . However, the transfer function decreased by between 10% and 50% for mode 1 and by between 20% and 50% for mode 2. When the coupling coefficients a_{ij} were halved, the transfer coefficients for mode 1 increased for periods greater than 6 days but were smaller for higher frequencies. For mode

2, the transfer function increased by about 20% to a range from 0.64 to 0.9 for periods greater than 3.6 days. The final sensitivity test was to set the off-diagonal terms of the matrix of frictional coupling coefficients (a_{ij}) equal to zero. This approach greatly simplifies Eq. (2.3) in that it decouples the modes, and one equation can be solved for each mode rather than a set of coupled equations. The cross spectra for this case are also shown in Fig. 7. The mode 2 transfer function is marginally closer to unity, but otherwise the results are not significantly different from the standard case.

4. Discussion

The theoretical frictional space (and time) decay scales used in the model for modes 1, 2 and 3 for the Stanwell Park section are 1800 km (5.2 days), 1200 km (6.5 days) and 1100 km (10 days), respectively. Mode 3 (and higher-order modes) have a shorter decay distance than mode 1, and in Part I it was shown that the observed modal amplitudes for mode 3 were not coherent between any pair of sections. Moreover, the hindcast and observed mode 3 amplitudes were not

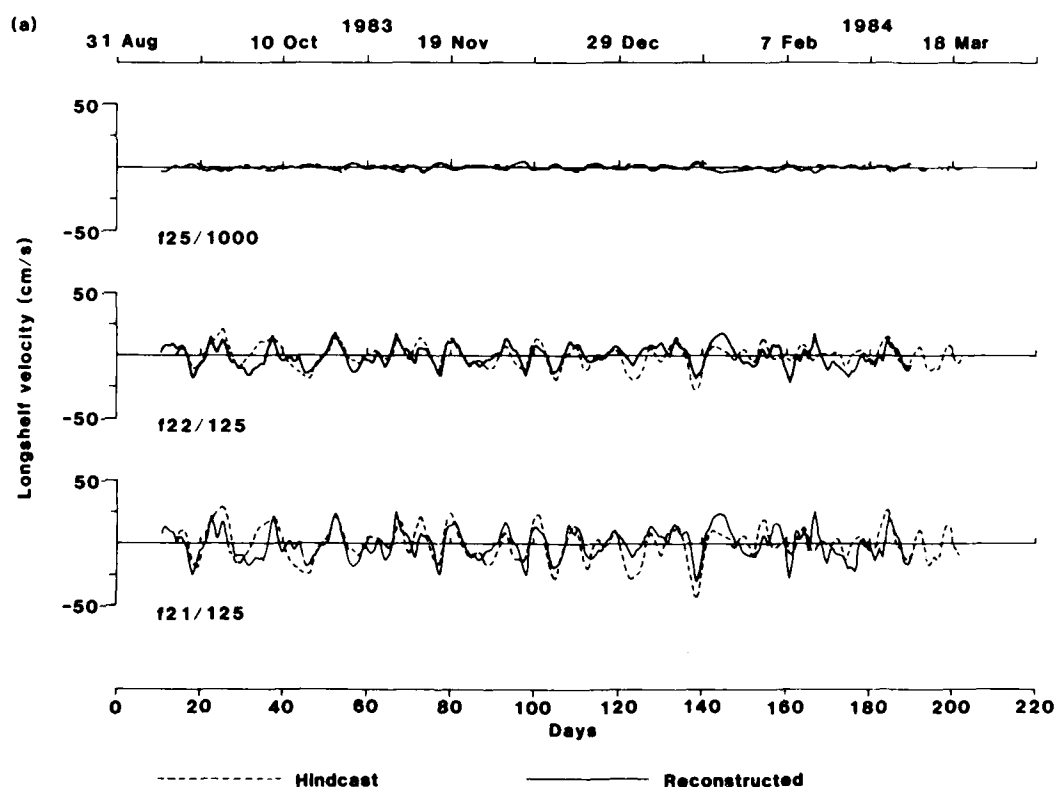


FIG. 5. Comparison of the hindcast alongshelf currents with the reconstructed currents at (a) Stanwell Park and (b) Newcastle. The predictions were completed using a model using three CTW modes, and Eq. (4.2) was used for the reconstructed velocities. Only a representative selection of current meter records are presented.

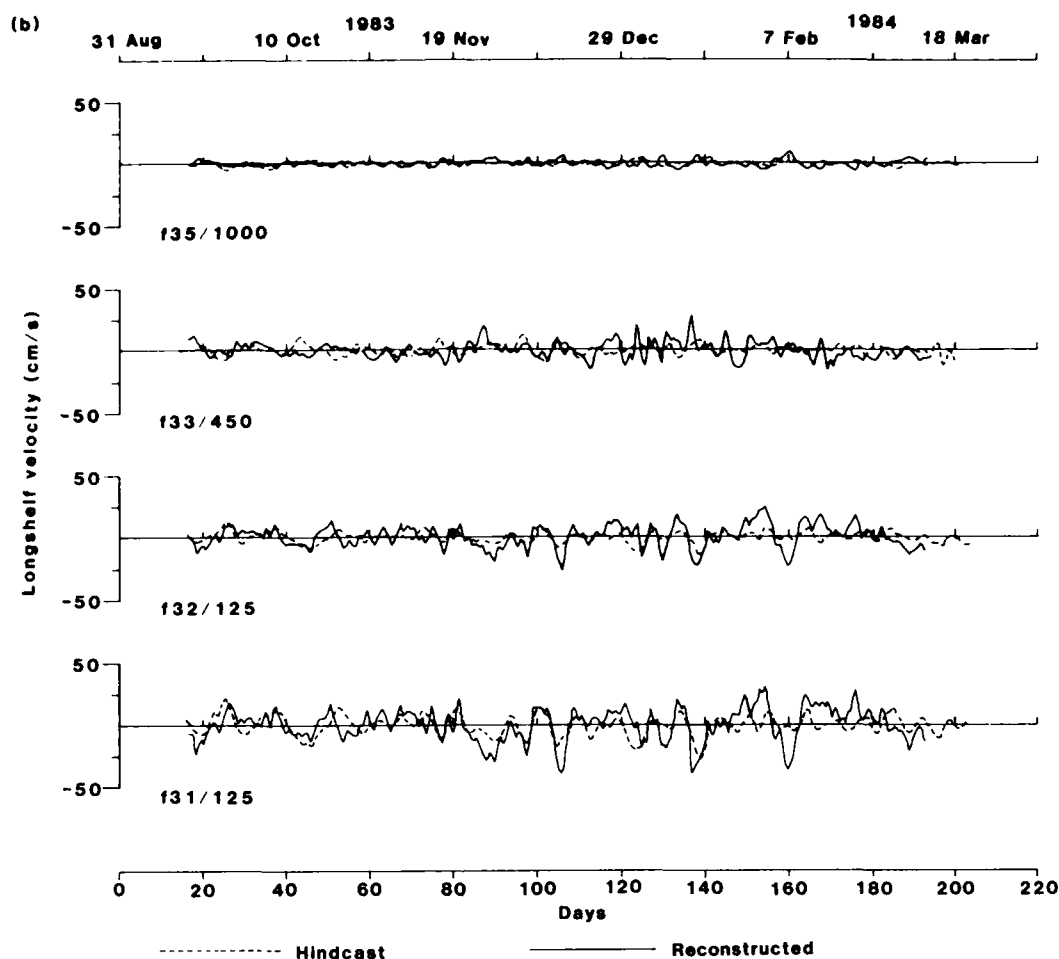


FIG. 5. (Continued)

coherent, and it is unlikely that higher order modes can be identified with most practical instrument arrays. For these reasons, mode 3 (and higher order modes) are not very useful in ACE for a hindcast of alongshelf currents. However, at least two modes are necessary to hindcast the currents on the upper slope at Stanwell Park. For nearshore locations where friction becomes relatively more important, the inclusion of higher order modes may be necessary.

The attempts to hindcast the observations using a CTW model indicated that halving the friction parameter to $r = 2.5 \times 10^{-4} \text{ m s}^{-1}$ gave a transfer function closer to the theoretically expected value of unity. This conclusion agrees with Battisti and Hickey (1984), who found that a decay time scale of 5 days or longer worked best. Also, Hamon (1976) found higher correlations between hindcast and observed sea levels on the east Australian coast when he used a relatively small friction

parameter. Note that even when the friction parameter is reduced by a factor of 2, the decay time scales for the CTW modes are on the order of the period of the waves, and they will decay substantially before they have propagated one wavelength; the CTWs are heavily damped. Despite this heavy damping, CTWs can carry energy substantial distances (perhaps 1000 or 2000 km). For a number of continental shelves, strong forcing is remote and upstream (in the CTW sense) from the region of interest; i.e., the CTWs are mainly freely propagating through the region of interest. The ACE region and the shelf off Peru (Brink, 1982) are two regions where remote forcing is important.

Assuming that the modes are uncoupled does not appear to detract from the quality of the hindcasts. Since this greatly simplifies the problem, it seems preferable to assume that the CTW modes are uncoupled. These conclusions could possibly change if different

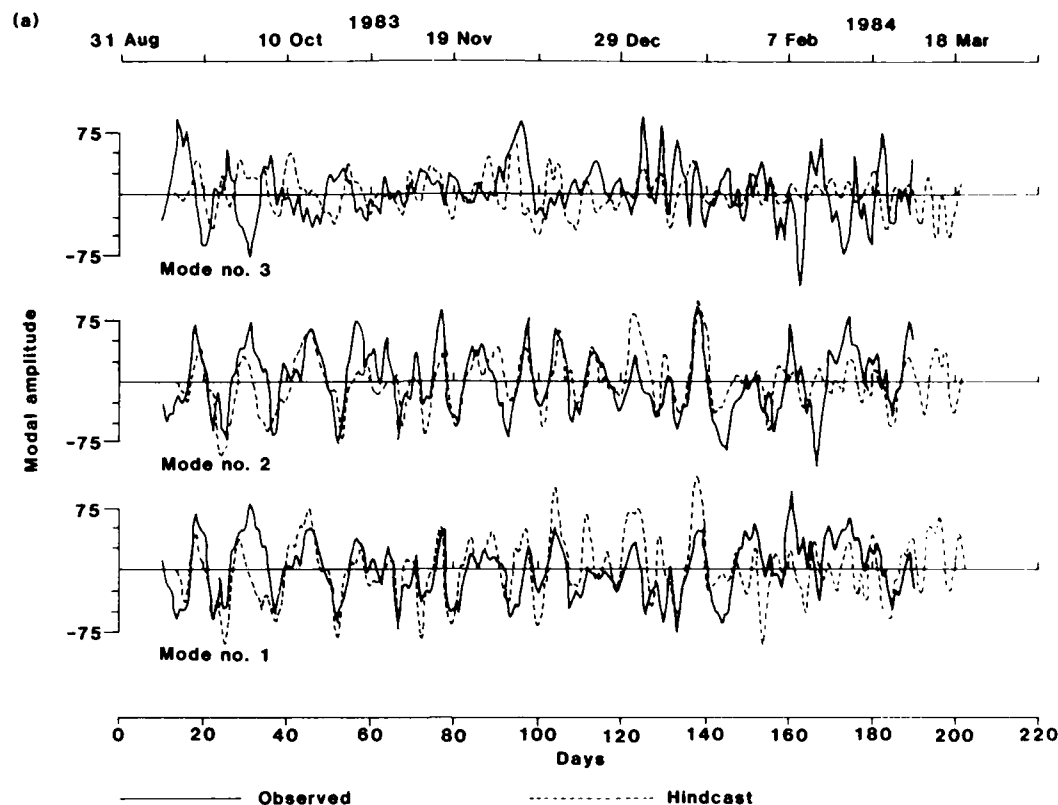


FIG. 6. Comparison of the first three CTW mode amplitudes as estimated from the observations and hindcast by the model at (a) Stanwell Park and (b) Newcastle

distributions of bottom friction, as might be induced by surface waves or other phenomena, were assumed.

Given that we found that the hindcast and observed

SSPs and alongshelf currents were highly coherent on the shelf at Stanwell Park, how well does the coastal-trapped wave theory work as a predictive tool? For the

TABLE 3. Correlation coefficients between the "reconstructed" alongshelf currents and the hindcast currents at Stanwell Park and Newcastle. The correlation coefficients are given for the total ACE period and, for Stanwell Park, are also given for the period when no eddies were present (days 50 to 140).

Location	Stanwell Park		Location	Newcastle
	Correlation coefficient (complete record)	Correlation coefficient (days 50-140)		Correlation coefficient (complete record)
f21/75	0.62	0.74	f31/75	0.50
f21/125	0.62	0.74	f31/125	0.50
f22/75	0.61	0.74	f32/75	0.49
f22/125	0.61	0.73	f32/125	0.47
f22/190	0.55	0.69	f32/190	0.17
f23/125	0.50	0.66	f33/125	0.36
f23/190	0.36	0.55	f33/190	0.20
f23/450	0.00	0.26	f33/450	0.19
f24/190	0.23	0.45	f34/190	0.18
f24/450	0.01	0.27	f34/450	0.23
f24/650	0.24	0.45	f34/650	0.32
f24/1000	0.51	0.57	f34/1000	0.22
f25/450	0.10	0.35	f35/450	0.25
f25/1000	0.42	0.50	f35/1000	0.15
f25/1900	0.07	0.18	f35/1900	0.08

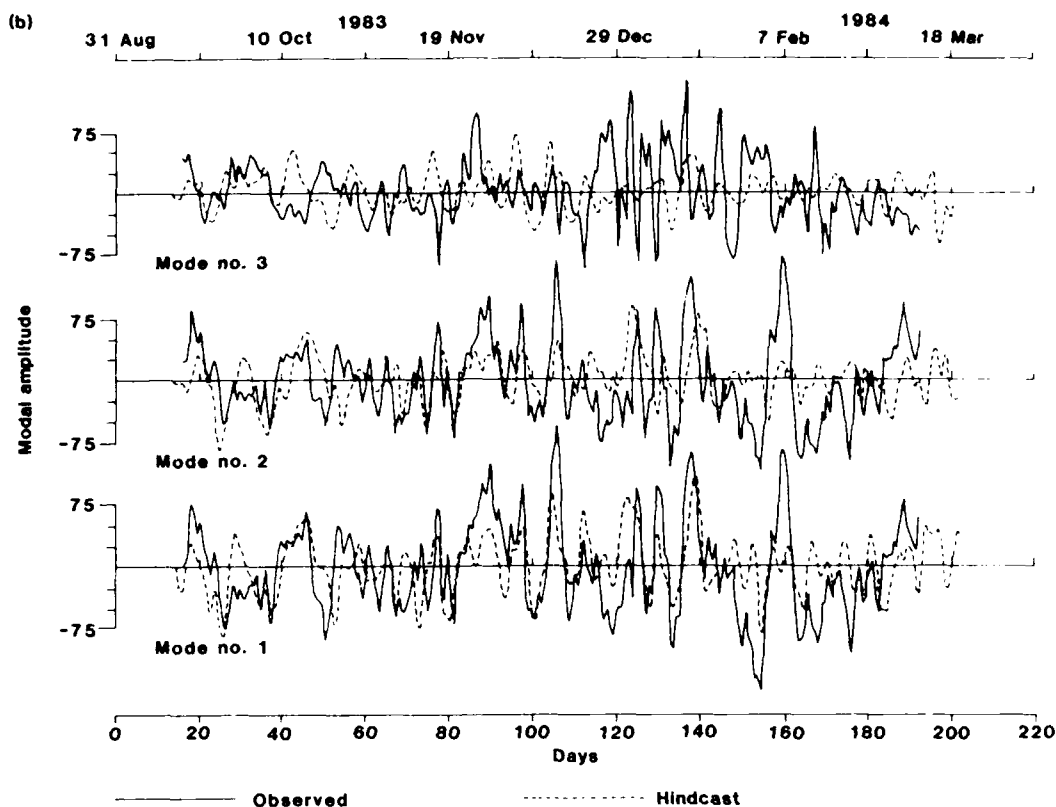


FIG. 6. (Continued)

nearshore current meters at Stanwell Park, we have calculated the residual variance (i.e., we subtracted the hindcast alongshelf currents from the observed alongshelf currents and calculated the variance of this residual). For the periods when eddies were not present, the observed variances for meters f21/75 and f21/125 are 114 and 131 $\text{cm}^2 \text{s}^{-2}$, respectively, while the residual variances are 69 and 72 $\text{cm}^2 \text{s}^{-2}$, respectively. These residual variances are 61% and 55% of the observed variances, so for these nearshore regions the CTW model is a practical tool for estimating the alongshelf currents. Further offshore and at Newcastle, the predictions are not useful because eddies and the East Australian Current dominate. Closer to shore, where the East Australian Current eddies have less effect, one would expect the CTW model to do somewhat better than further offshore. An alternative predictive model would be to assume that, because shelf currents generally have a large alongshelf scale, the currents at Cape Howe are identical to those at the corresponding location at Stanwell Park. However, examination of records f11/125 and f21/125 shows that at zero lag the correlation coefficient is only 0.29 (in contrast to 0.74; Table 3), and if f11/125 is used as a predictive tool for

f21/125 then the residual variance is larger than the variance of f21/125.

In contrast to the situation at Stanwell Park, the East Australian Current and its eddies dominate currents offshore from Newcastle, and for the observation locations the CTW model is not a useful predictive tool.

The dominant energy source for the observed coastal-trapped waves does not lie in the ACE region; i.e., it is not the "local" wind that is dominant in driving the currents on the shelf. If the amplitudes of the CTWs at Cape Howe are set to zero, then the energy fluxes predicted for Stanwell Park are too small by about a factor of 3 for mode 1 and about a factor of 7 for mode 2. Similarly, when the correct upstream boundary conditions were used but the winds within the main ACE region were set to zero, the energy flux at Stanwell Park was too small by about a factor of 2 for mode 1 and a factor of about 3 for mode 2. When both the correct boundary conditions and the winds were used, the energy flux at Stanwell Park was too large by about 20% for mode 1 and too small by about 35% for mode 2. It appears that about three-quarters of the CTW signal observed at Stanwell Park is the result of free propagation from Cape Howe and the remainder due to wind

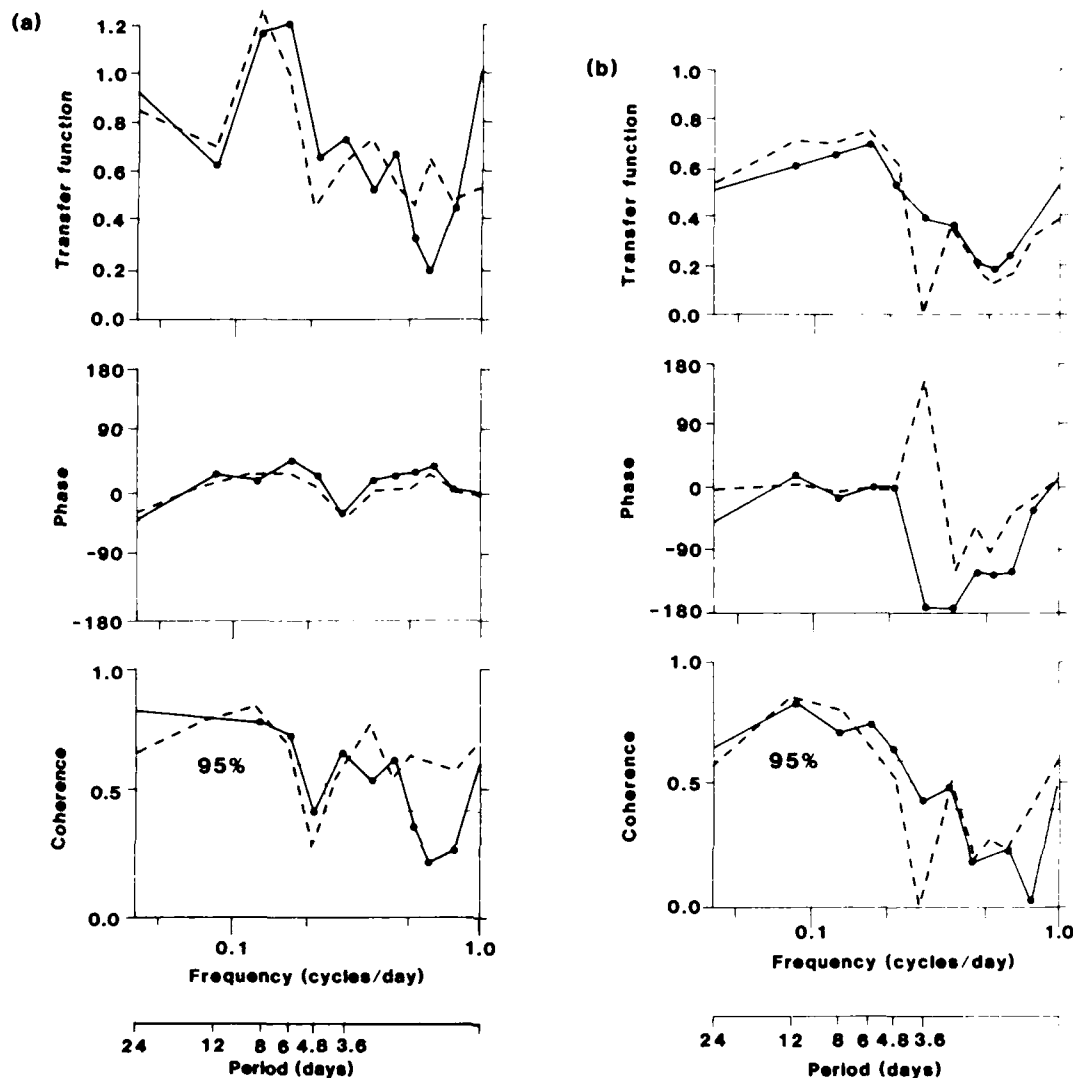


FIG. 7. Cross spectra between the amplitude of the CTW modes calculated from the observations at Stanwell Park and hindcast using the CTW model. Mode 1 is shown in (a) and mode 2 in (b). The solid line is the standard case and the dashed line is assuming the matrix (a_{ij}) is diagonal. The 95% significance level is indicated by the dotted line.

forcing north of Cape Howe. To successfully hindcast the observations, both the correct boundary conditions and the correct winds are necessary. The free wave assumption implicit in the analysis of Freeland et al. (1986), and in Part I, works well because the CTWs are dominated by free rather than forced waves, and as Clarke and Thompson (1984) showed, the response forced by a reasonable distribution of wind stress in the ACE region appears to propagate at speeds not greatly different from the phase speeds of the free waves.

While Hamon (1976) found high coherence between sea levels at Evans Head (29°S) and results from the Gill and Schumann (1974) model, the gain between

the model results and the observations was somewhat larger than the expected value of unity. It appears that the likely explanation for this result is that Hamon (1976) assumed (in contradiction to the present results) that there was no CTW energy propagating past Gabo Island and that the response at Evans Head was due to wind forcing between Gabo Island and Evans Head.

A substantial fraction of the energy for the observed CTWs must be input into the coastal-wave guide south and west of Cape Howe. One possibility is that the very strong winds at and just to the south and west of Cape Howe generated the observed signals. Forbes (personal communication, 1985) found that for Gabo Island the

wind-stress rms variance during the ACE period was 0.31 N m^{-2} . This hypothesis was tested by using the Gabo Island winds over the 150 km between Cape Howe and the eastern extremity of Bass Strait to drive the CTW model. For the nearshore locations, the coherences between observed and hindcast currents were up to 0.68 (compared with 99% significance level of 0.418). However, the energy flux at Cape Howe calculated in this model was about a factor of 4 too small for mode 1 and about a factor of 5 too small for mode 2. As pointed out by Freeland et al. (1986), not much CTW energy is propagated past the sole mooring off the eastern coast of Tasmania. However, another alternative discussed by Freeland et al. (1986) is that the CTW energy is generated in Bass Strait or on the east coast of Tasmania (north of the sole mooring at $42^{\circ}40'S$). If the winds measured at Gabo Island are representative of winds over the entire region, then this solution is certainly possible. A wind-generated east-west flow through Bass Strait would experience rapid topographic variations at the eastern end of Bass Strait, which might allow the generation of the second (and higher order) CTW modes as observed at Cape Howe. Theoretical work (e.g., Allen, 1976) does allow the possibility of the scattering of energy from a first-mode continental shelf wave to higher-order modes. Recent theoretical work (Buchwald and Kachoyan, personal communication, 1985) has shown that an eastward flow through Bass Strait does generate higher order CTWs on the east coast and that almost all of this energy travels to the north through the ACE region. Recent observational work (Church and Freeland, 1986) has shown that sea levels are highly correlated right across the south coast of Australia, through Bass Strait, and into the ACE region. These two pieces of work suggest that it is the strong wind on the south coast of Australia which is the predominant driving force for the CTWs on the south east Australian continental shelf.

Acknowledgments. ACE was initiated and encouraged by Rory Thompson. We also thank him for critical comments on drafts of this paper. The participation of Oregon State University in ACE was supported by the U.S. Office of Naval Research. Support for Allan J. Clarke was received from the U.S. National Science Foundation (Grant OCE-8300029). The participants from North America, Howard J. Freeland, Allan J. Clarke and Robert L. Smith, would like to thank the CSIRO for its hospitality during the data analysis phase of the experiment. Finally, we would like to thank Bernadette Baker and Nikki Pullen for their patience in typing the many drafts of this paper.

REFERENCES

- Allen, J. S., 1976: Continental shelf waves and alongshore variations in bottom topography and coastline. *J. Phys. Oceanogr.*, **6**, 864-878.
- Battisti, D. S., and B. M. Hickey, 1984: Application of remote wind-forced coastal trapped wave theory to the Oregon and Washington coasts. *J. Phys. Oceanogr.*, **14**, 887-903.
- Brink, K. H., 1982: A comparison of long coastal trapped wave theory with observations off Peru. *J. Phys. Oceanogr.*, **12**, 897-913.
- , and D. C. Chapman, 1985: Programs for computing properties of coastal-trapped waves and wind-driven motions over the continental shelf and slope. Woods Hole Oceanographic Institute Tech. Rep. WHOI-85-17, 99 pp.
- Church, J. A., and H. J. Freeland, 1986: The energy source for the coastal-trapped waves in the Australian Coastal Experiment region. *J. Phys. Oceanogr.*, in press.
- , and R. L. Smith, 1986: Coastal-trapped waves on the east Australian continental shelf. Part I: Propagation of modes. *J. Phys. Oceanogr.*, **16**, 1929-1943.
- Clarke, A. J., 1977: Observations and numerical evidence for wind-forced coastal-trapped long waves. *J. Phys. Oceanogr.*, **7**, 231-247.
- , and R. O. R. Y. Thompson, 1984: Large-scale wind-driven ocean response in the Australian Coastal Experiment region. *J. Phys. Oceanogr.*, **14**, 338-352.
- , and K. H. Brink, 1985: The response of stratified, frictional shelf and slope waters to fluctuating large-scale low-frequency wind forcing. *J. Phys. Oceanogr.*, **15**, 439-453.
- , and S. Van Gorder, 1986: A method for estimating wind-driven frictional, time-dependent, stratified shelf and slope water flow. *J. Phys. Oceanogr.*, **16**, 1013-1028.
- Davis, R. E., 1976: Predictability of sea surface temperature and sea level pressure anomalies over the North Pacific Ocean. *J. Phys. Oceanogr.*, **6**, 249-266.
- Forbes, A. M. G., 1985a: Sea-level data from the Australian Coastal Experiment—a data report. CSIRO Marine Lab. Rep. No. 171, 16 pp.
- , 1985b: Meteorological data from the Australian Coastal Experiment—a data report. CSIRO Marine Lab. Rep. No. 170, 26 pp.
- Freeland, H. J., J. A. Church, R. L. Smith and F. M. Boland, 1985: Current meter data from the Australian Coastal Experiment: a data report. CSIRO Marine Lab. Rep. No. 169, 51 pp.
- , F. M. Boland, J. A. Church, A. J. Clarke, A. M. G. Forbes, A. Huyer, R. L. Smith, R. O. R. Y. Thompson and N. J. White, 1986: The Australian Coastal Experiment: A search for coastal-trapped waves. *J. Phys. Oceanogr.*, **16**, 1230-1249.
- Gill, A. E., and E. H. Schumann, 1974: The generation of long shelf waves by the wind. *J. Phys. Oceanogr.*, **4**, 83-90.
- Hamon, B. V., 1962: The spectrums of mean sea level at Sydney, Coll's Harbour, and Lord Howe island. *J. Geophys. Res.*, **67**, 5147-5155. [Correction, *J. Geophys. Res.*, **68**, p. 4635.]
- , 1966: Continental shelf waves and the effects of atmospheric pressure and wind stress on sea level. *J. Geophys. Res.*, **71**, 2883-2893.
- , 1976: Generation of shelf waves on the East Australian coast by wind stress. *Mem. Soc. R. Sci. Liege, Ser. 6*, **X**, 359-367.
- Large, W. S., and S. Pond, 1981: Open ocean momentum flux measurements in moderate to strong winds. *J. Phys. Oceanogr.*, **11**, 324-336.
- Mitchum, G. T., and A. J. Clarke, 1986: Evaluation of frictional, wind forced long-wave theory on the West Florida Shelf. *J. Phys. Oceanogr.*, **16**, 1029-1037.

Vertical Heat Fluxes Through the Beaufort Sea Thermohaline Staircase

LAURIE PADMAN AND THOMAS M. DILLON

College of Oceanography, Oregon State University, Corvallis

Microstructure profiles of temperature, conductivity, and velocity shear during the Arctic Internal Wave Experiment (AIWEX) in March-April 1985 in the Beaufort Sea are used to investigate the thermodynamic processes in a diffusive thermohaline staircase. The staircase occurs between depths of about 320 and 430 m, above the core of the relatively warm, salty Atlantic water, where the mean temperature and salinity are increasing with depth. Individual isothermal layers can be tracked for at least several hours, suggesting a horizontal length scale of several hundred meters or more, assuming a typical relative velocity of 0.01 m s^{-1} at this time. Over the depth range 320-430 m the mean (average over several steps) density ratio $(R_\rho = \beta(S_p - x)/T_p)$ varies between 4 and 6, while the typical temperature difference between layers decreases from 0.012 to 0.004 °C. The mean thickness of the layers also varies, from 1 m at 320 m depth to 2 m at 430 m. The relationship proposed by Kelley (1984), relating layer height to $(N^2/\rho_0 R_\rho)$, and molecular properties of the fluid, overestimates the mean layer thickness by about a factor of 2. The variability of staircase characteristics suggests that oceanic staircases may rarely, if ever, be steady state, but in general be slowly evolving from previous perturbations. Heat fluxes estimated from laboratory-based flux laws, involving R_ρ and ΔT , are in the range $0.02 < F_H < 0.1 \text{ W m}^{-2}$, which is in agreement with the molecular heat fluxes through the maximum interfacial temperature gradients. There are no interfaces where the kinetic energy dissipation rate (averaged over 0.5 m) exceeds the lower limit for diapycnal mixing, 24.5 N^2 .

1. INTRODUCTION

In many regions of the world's oceans and lakes, fine-scale and microscale profiles of temperature (T) and salinity (S) contain "staircases," consisting of series of homogeneous layers separated by sheets, i.e., regions of relatively high temperature and salinity gradient. Where both gradients have the same sign, the staircase can be explained by double diffusion [Turner, 1973], a process which depends on the differing molecular diffusivities of heat and salt. Where T and S both decrease with depth, the "salt fingering" instability may occur, while when T and S both increase with depth, the "diffusive" instability is possible. This paper describes observations of a diffusive staircase in the Canada Basin of the Arctic Ocean beneath the ice pack during the Arctic Internal Wave Experiment (AIWEX), March-May 1985, and estimates the vertical heat fluxes which are associated with the diffusive instability.

Diffusive interfaces have often been studied in laboratories (see for example, Turner [1965, 1968], Huppert [1971], Marmorino and Caldwell [1976], Newell [1984], and Kelley [1986]). The usual experimental arrangement involves heating the base of a tank containing salinity-stratified water and observing the growth of layers which are homogeneous in both temperature and salinity. In these experiments the rate of heating is a known quantity, and assuming no heat losses through the sidewalls, scaling parameters for the staircase can then be based on this heat flux. In most geophysical fluids, however, it is rarely obvious what the heat flux should be at any particular depth. The lower boundary of a staircase may be continually replenished with heat through lateral advection, or it may vary as the vertical heat flux cools the deeper water. In general, the heat flux through the staircase is expected to be set by the staircase characteristics rather than vice versa.

Section 2 provides a brief description of the AIWEX experiment and the microstructure profiler. Section 3 gives an overview of the staircase characteristics, while section 4 discusses the vertical heat fluxes through the staircase.

2. EXPERIMENTAL DESCRIPTION

AIWEX was a multi-institute ice camp experiment designed primarily to measure the characteristics of the internal wave field of the Canada Basin in the Arctic Ocean, but it also incorporated subsidiary projects for nutrient sampling, measurements of small baroclinic eddies, and instrument trials. The drift track for the ice camp, determined from approximately two-hourly satellite fixes, is shown in Figure 1.

Seven hundred and twenty-three microstructure profiles were made between March 20 and April 26, 1985, the maximum profiled depth being 465 m. However, many casts covered only the limited depth ranges required to study specific features, such as 0-200 m, in which thermal anomalies indicative of thermohaline intrusions occurred, and 300-450 m, where the thermohaline staircase was most clearly defined. The small depth ranges for these specific studies allowed a reduced cycling time between profiles of about 10 min, compared with 20 min for extended profiles. Several slow drops were also made to study the response of the thermistor and to investigate the response of the shear probes to changes in temperature, as discussed by Osborn and Crawford [1980].

In this paper we shall concentrate upon a 20-hour series of 100 profiles through the staircase, collected on April 21-22, 1985, at the location shown in Figure 1. Most of these profiles extend from 300 m to 460 m. The average sampling frequency of 5 cph is well above the mean (average over several steps) buoyancy frequency of about 1 cph but is less than a typical buoyancy frequency of $O(10)$ cph for individual sheets. At the time this series was taken, the absolute velocity of the ice camp varied from almost stationary to about 0.08 m s^{-1} , with several reversals in direction. Assuming the current at the depth of the staircase to be negligible, the total horizontal extent of the survey is about 600 m. We shall show below that

Copyright 1987 by the American Geophysical Union.

Paper number 7C0526.

0148-0227/87/0007C-0526\$05.00

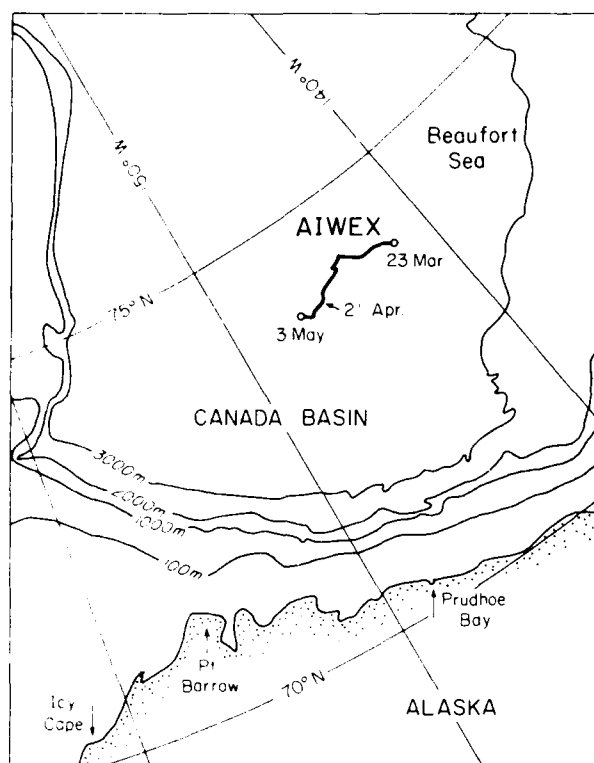


Fig. 1. Drift track of AIWEX ice camp from March 23 to May 3, 1985. Location of intensive series of profiles commencing April 21 is shown.

because of the very long time scales for double-diffusive processes, differences between profiles should be interpreted as being due to horizontal variability rather than due to temporal evolution of the staircase.

Microstructure data were obtained with the Rapid-Sampling Vertical Profiler (RSVP), described by Caldwell *et al.* [1985]. The RSVP is a tethered, free-fall profiler about 2 m long, which carries sensors for measuring pressure, microscale velocity shears u_z and v_z , temperature, and conductivity. The probe length is a compromise between ease of deployment and resolution of low-wave number velocity structure. The average fall rate is about 0.9 m s^{-1} , constrained by a drag element consisting of an annular brush near the rear of the probe. The raw data sampling rate is 130 Hz for temperature, conductivity, and pressure. Temperature is measured with a Thermometrics FP07 thermistor, which projects forward from the probe nose assembly. This thermistor has an approximately flat frequency response to 20 Hz, correctable to 40 Hz, with an rms noise level based on a 20-Hz bandwidth of about $4 \times 10^{-4} \text{ }^\circ\text{C}$.

Two versions of the RSVP were used during AIWEX, the principal difference being the way in which conductivity was measured. Two profilers used a Neil Brown Instrument Systems (NBIS) conductivity cell mounted on the side of the probe, 0.1 m above the probe tip. For salinity determination a second Thermometrics FP07 thermistor was mounted adjacent to the cell. The NBIS cell has a response length of about 0.1 m [Gregg *et al.*, 1982], so that at the nominal fall rate the time constant of the conductivity cell is 0.1 s. A further two profilers used a four-electrode microconductivity probe,

manufactured by Precision Measurement Engineering (PME) and described by Head [1983]. This probe has a response time set by the rate at which the boundary layer entrained by the probe tip is replenished. The estimated spatial resolution at the nominal fall speed is about 3 mm. The data are analog filtered at 40 Hz before digitization, giving an effective resolution of $O(0.02) \text{ m}$ at a drop speed of 0.9 m s^{-1} . The conductivity records from the PME sensor are occasionally contaminated both by rapidly occurring offsets and by low-frequency variations in the output voltage. The former problem may be due to contamination of the electrodes by organic matter and leads to spiking in the salinity record. The low-frequency variations prevent the accurate determination of average salinity for particular layers and hence affect the estimates of salinity differences across interfaces. The PME conductivity data will therefore be used only to investigate the thickness of individual sheets, and not for estimating mean layer salinities.

At typical temperatures and salinities ($0 \text{ }^\circ\text{C}$, 35 practical salinity units (psu)) the equation relating changes in salinity to changes in conductivity and temperature can be linearized to

$$\Delta S \approx 13.2\Delta C - 1.13\Delta T$$

or

$$\Delta C \approx 0.076\Delta S + 0.086\Delta T$$

Least significant bit resolutions of the raw (130 Hz) 12-bit records are about $1.3 \times 10^{-4} \text{ }^\circ\text{C}$ in temperature and $1.5 \times 10^{-5} \text{ S m}^{-1}$ in conductivity for the NBIS cell; however, typical rms noises are about $4 \times 10^{-4} \text{ }^\circ\text{C}$ and $1 \times 10^{-4} \text{ S m}^{-1}$, based on measurements in the quietest homogeneous layers. Layer-averaged salinities are estimated by locating each layer from the temperature profile and then determining the average temperature and conductivity of the layer. For a typical layer thickness of $O(1) \text{ m}$ this procedure reduces the noise levels in T and C to about $4 \times 10^{-5} \text{ }^\circ\text{C}$ and $1 \times 10^{-5} \text{ S m}^{-1}$, respectively. The corresponding noise in the salinity estimate is then about $2 \times 10^{-4} \text{ psu}$, although if a layer is sufficiently thin (fewer raw estimates), this noise level may be substantially higher. For sheets across which the salinity difference is small, the noise may be sufficient to indicate an apparent instability in the density profile where none actually exists. Because the heat flux is expected to be substantially higher through sheets which are only marginally stable than through those which are very stable, based on laboratory measurements, this noise in the estimate of the salinity difference limits the accuracy of our heat flux estimates.

Velocity microstructure was measured with two Undersea Technology airfoil shear sensors mounted orthogonally on the nose assembly. Estimates of the turbulent kinetic energy dissipation rate were made for approximately 0.5-m depth intervals by integrating the shear spectrum in the wave number range of 2–20 cpm .

3. OVERVIEW OF THE T - S STEPS

Typical profiles of T , S , and σ_t are shown in Figure 2a. An isothermal layer near the freezing point is present from the ice base to about 30 m. From 30 m to the local temperature minimum near 200 m, the water properties are attributable to both influx through the Bering Strait and shelf modification of existing subsurface Arctic water [Coachman and Aagaard, 1974]. The frequent occurrence of salinity-stabilized temperature inversions in this depth range reflects the variability of

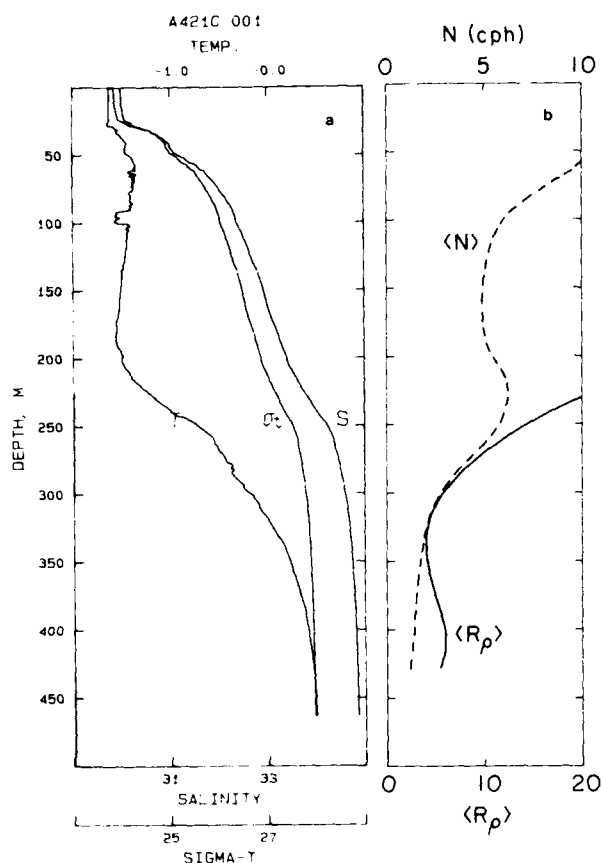


Fig. 2. (a) Representative profiles of temperature, salinity, and sigma- t taken on April 21, 1985. (b) Buoyancy frequency N and density ratio R_ρ averaged over 10 m, for the same profile.

these sources. Below 200 m, both T and S increase monotonically with depth, a necessary condition for the diffusive instability. Of particular interest in the present study is the region between 300 and 450 m, shown magnified in Figure 3, which is the approximate depth range for the diffusive staircase. The homogeneous layers are of $O(1)$ m vertical extent, while the high-gradient sheets are typically several centimeters thick. Above about 320 m the temperature profile becomes less regular over several layer heights, until no steppiness remains above about 280 m. Below 430 m, to the maximum profiled depth of 465 m, thicker sheets and less homogeneous layers are found.

The large-scale density profile is statically stable because the contribution of salinity to the change in density with increasing depth (decreasing z) exceeds that due to the destabilizing temperature gradient, i.e., $\rho_z = \rho_0(\alpha T_z - \beta S_z) > 0$, or equivalently, $R_\rho - \beta S_z / \alpha T_z > 1$, where R_ρ is called the density (or stability) ratio. At temperatures near 0°C and typical salinities the thermal expansion coefficient α ($= -\rho^{-1} \partial \rho / \partial T$) is approximately $6 \times 10^{-4} \text{ K}^{-1}$, while the contraction coefficient for salinity, β ($= \rho^{-1} \partial \rho / \partial S$), is about $7.8 \times 10^{-4} (\text{psu})^{-1}$. The large-scale density ratio $\langle R_\rho \rangle$ and buoyancy frequency $\langle N \rangle$, where angle brackets denote an average over 10 m, are shown for the entire profile depth in Figure 2b. With decreasing depth above the staircase, $\langle R_\rho \rangle$ increases rapidly to about 30 just below the subsurface temperature minimum near 200 m.

Initially, each profile was analyzed to locate isothermal layers, defined as regions with less than 0.001°C difference in temperature between averages over about 0.1 m (16 raw samples). It follows that an interface between layers is defined when a temperature gradient greater than 0.01 C m^{-1} is found in the finite-differenced gradient trace. Average depth D , temperature T , salinity S , and height H are determined for each layer. H is defined as the distance between the midpoints of the adjacent interfaces; however, salinity is determined from averages of temperature and conductivity in the isothermal region only. Layer averages then define the temperature and salinity differences ΔT and ΔS across the density interfaces and consequently the density ratio R_ρ for each interface.

Mean values of H , ΔT , ΔS , and R_ρ are listed in Table 1 for 10-m depth intervals from 300 to 430 m. The standard deviation for each variable is given in parentheses. Figure 4 shows the distribution of each parameter for the depth interval 360–370 m, in the middle of the staircase. Similar variability is found at all depths and in the observations of Neshyba *et al.* [1971].

The mean values from Table 1 are shown also in Figure 5 (the mean heat flux, discussed in section 4, is also shown). $\langle H \rangle$ increases from about 1 m to greater than 2 m with increasing depth, while $\langle \Delta T \rangle$ and $\langle \Delta S \rangle$ both decrease. A small variation only, from 3.9 to about 5.8, is apparent in $\langle R_\rho \rangle$; i.e., the large-scale temperature and salinity gradients are closely coupled. However, a joint probability distribution of ΔT against ΔS (Figure 6) shows that the density ratios for individual steps are more variable, ranging from near unity to about 10.

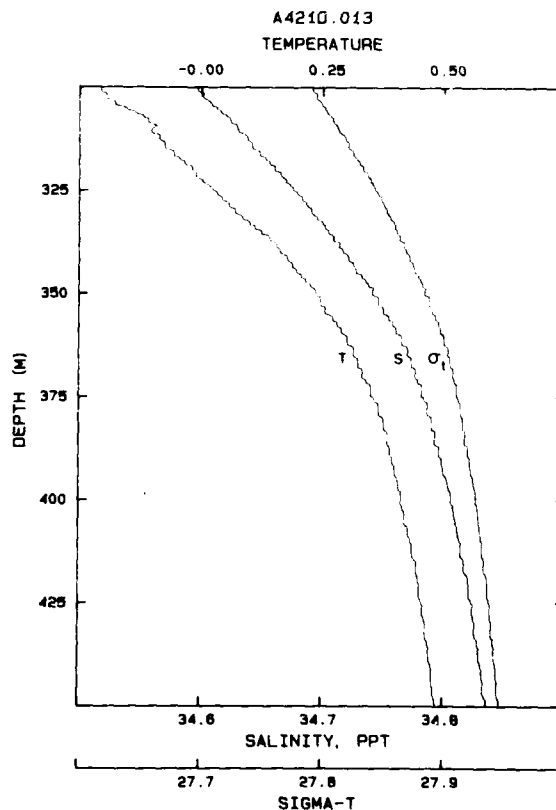


Fig. 3. Temperature, salinity, and sigma- t profiles for 300–450 m.

TABLE 1. Means, With Standard Deviations in Parentheses, of Temperature Difference ΔT , Salinity Difference ΔS , Density Ratio R_ρ , and Layer Height H , for 10-m Depth Intervals From 300 to 430 m in the Beaufort Sea Diffusive Staircase (AIWEX, April 21–22, 1985)

Depth Range, m	No. of Steps	ΔT , 10^{-3}°C	ΔS , 10^{-3} psu	R_ρ	H , m
300–310	788	13.1 (5.1)	4.9 (1.5)	6.0 (3.9)	1.2 (0.44)
310–320	656	12.8 (3.3)	4.8 (1.1)	5.1 (2.9)	1.5 (0.41)
320–330	753	11.4 (3.6)	3.5 (1.3)	4.1 (2.1)	1.3 (0.41)
330–340	692	11.3 (3.5)	3.4 (1.2)	3.8 (1.8)	1.4 (0.41)
340–350	638	9.2 (1.9)	3.0 (1.1)	3.9 (2.2)	1.5 (0.50)
350–360	432	9.8 (2.1)	3.6 (1.0)	4.2 (1.7)	2.0 (0.71)
360–370	429	9.7 (2.9)	3.4 (1.1)	4.1 (1.9)	2.0 (0.74)
370–380	451	7.8 (1.6)	2.7 (0.8)	3.9 (1.4)	2.1 (0.76)
380–390	306	8.3 (2.4)	2.8 (0.8)	4.1 (1.4)	3.0 (0.86)
390–400	427	4.6 (1.0)	2.1 (0.8)	5.2 (2.2)	2.2 (0.86)
400–410	353	4.8 (1.4)	1.8 (0.9)	4.6 (3.8)	2.4 (0.87)
410–420	368	4.1 (1.2)	1.6 (0.9)	4.3 (2.7)	2.2 (1.26)
420–430	329	3.5 (0.9)	1.6 (0.8)	5.6 (3.3)	2.3 (1.06)

In Table 2 the mean characteristics of the staircase are compared with those described by *Neshyba et al.* [1971]. Although the data were collected in regions with similar large-scale averages $\langle N \rangle$ and $\langle R_\rho \rangle$, the mean temperature difference $\langle \Delta T \rangle$ and layer height $\langle H \rangle$ are much smaller in the present experiment.

A given isothermal layer, identified by its temperature, can typically be tracked for several hours or more, provided the spacing between consecutive profiles is no greater than about 1 hour. During this time the temperature of the layer may vary slowly, typically less than $3 \times 10^{-3}^\circ\text{C h}^{-1}$. Assuming a mean flow relative to the ice of 0.01 m s^{-1} and no temporal variability, the horizontal extent L_h of layers varies from only one profile, i.e., less than 7 m for some very thin layers, up to the entire series, or at least 600 m. A typical aspect ratio L_h/H for a layer is therefore at least $O(10-100)$.

Root-mean-square vertical displacements for sheets are only $O(1)$ m. The average sampling interval of 12 min is smaller than the buoyancy period $2\pi/\langle N \rangle$, about 40 min; therefore we expect that most of the variance of isopycnal displacements has been captured. With so little internal wave energy, the likelihood of shear-induced instabilities on a large scale is small. This does not preclude the possibility that high frequency internal waves trapped within the interfacial sheets may at times be responsible for shear instabilities in, and subsequent enhanced buoyancy flux through, the sheets. A buoyancy period based on the density gradient within the sheets only is typically 5–10 min and will not be resolved in the present data set.

Measurements by airfoil probes of the microscale velocity shears u_z and v_z were used to determine the kinetic energy dissipation rate ϵ averaged over 0.5-m depth intervals. Across the diffusive interfaces, ϵ never exceeds the *Stillinger et al.* [1983] criterion for diapycnal mixing, $\epsilon_c = 24.5\nu N^2$, where ν is the kinematic viscosity (about $1.8 \times 10^{-6} \text{ m}^2 \text{ s}^{-1}$ in the Arctic) and is frequently at the noise floor of about 10^{-7} W m^{-3} ($10^{-10} \text{ m}^2 \text{ s}^{-3}$). Accurate determination of the absolute shear across each interface is precluded by the sensitivity of the airfoil probes to rapid changes in temperature.

4. THERMODYNAMICS OF DIFFUSIVE STAIRCASES

The diffusive instability is discussed by *Turner* [1973], and a summary of recent laboratory studies is given by *Newell*

[1984]. *Kelley* [1984, 1986] provides a precis of geophysical observations of diffusive staircases. A significant parameter is double diffusion is the density ratio $R_\rho = \beta \Delta S / \alpha \Delta T$, now defined in terms of the salinity and temperature differences at the interface, ΔS and ΔT , respectively. Again, static stability requires that $R_\rho > 1$. A second parameter which is valuable in understanding the laboratory observations is the buoyancy flux ratio $R_f = 10^3 c_p \beta F_s / \alpha F_H$, where F_s ($\text{kg m}^{-2} \text{ s}^{-1}$) and F_H (W m^{-2}) are the fluxes of salt and heat, respectively. At low values of R_ρ (< 2), where the change in salinity across a step just compensates for the unstable temperature difference, density changes associated with the fluxes of both salt and heat are comparable. At medium R_ρ ($2 < R_\rho < 7$), R_f is approximately constant for a fixed heat flux but decreases as the heat flux through the interface increases [*Marmorino and Caldwell*, 1976]. (The estimated flux through the AIWEX sheets, about 0.1 W m^{-2} ($2.4 \times 10^6 \text{ cal cm}^{-2} \text{ s}^{-1}$), is two orders of magnitude below the smallest heat flux used by *Marmorino and Caldwell*). At higher R_ρ , a regime first studied in detail by *Newell* [1984], R_f rises with increasing R_ρ .

An R_ρ -dependent model of the character of the diffusive interface has been developed to explain these observations and is given by *Newell* [1984]. At low R_ρ the interface is very thin as a result of the energetic turbulence of the adjacent layers, and direct interaction between these layers occurs. At intermediate R_ρ the bulk of the transport of heat and salt occurs by diffusion through a stable interface core. Because of the high diffusivity of heat relative to that of salt ($\tau^{-1} = \kappa_T / \kappa_S \approx 100$) the mean thermal interface thickness δ_T is greater than the salinity interface thickness δ_S [*Marmorino and Caldwell*, 1976].

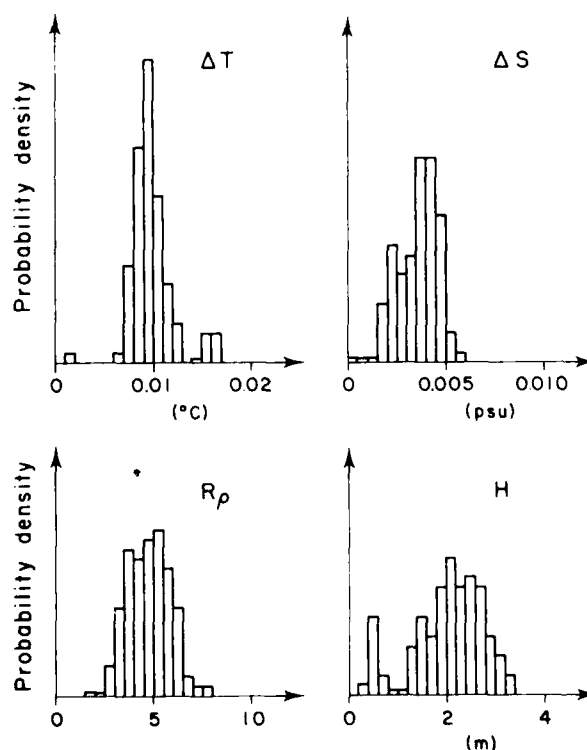


Fig. 4. Distributions of layer height H , temperature and salinity steps ΔT and ΔS , and density ratio $R_\rho = \beta \Delta S / \alpha \Delta T$ for the depth range 360–370 m in the AIWEX diffusive staircase.

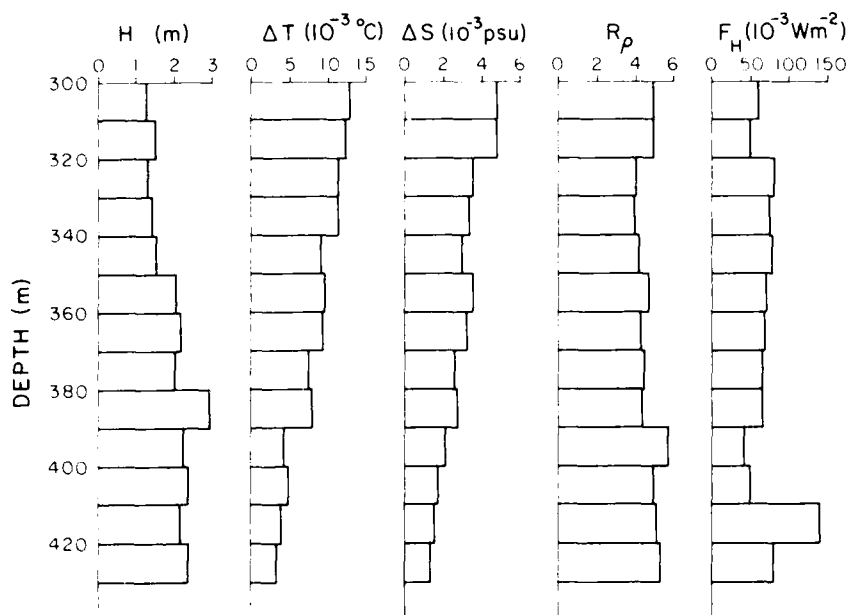


Fig. 5. Averages of layer height H , temperature and salinity differences ΔT and ΔS between adjacent layers, density ratio $R_\rho = \beta \Delta S / \alpha \Delta T$ of sheets, and mean vertical heat flux F_H averaged over 100 profiles for 10-m depth ranges.

although the ratio (δ_T / δ_S) may be less than expected from pure diffusion, $\tau^{-1/2}$. Because $\delta_T > \delta_S$, convective instabilities occur at the edges of the interface (Figure 7). The interface thickness is controlled either by entrainment of the unstable, or only weakly stratified, interfacial boundary layers by eddies in the adjacent layers, or by buoyancy-driven separation of the unstable boundary layers. The intermittency of this process is demonstrated by time series of temperature near a diffusive interface [Marmorino and Caldwell, 1976]. At high R_ρ , Newell [1984] showed that the interface becomes much thicker, further inhibiting the diffusive flux of both heat and salt. The ratio δ_T / δ_S approaches unity, which implies that R_ρ is proportional to R_ρ .

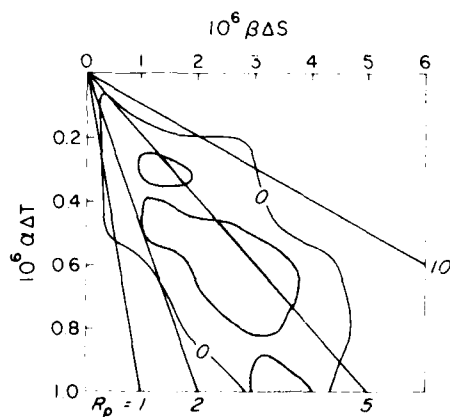


Fig. 6. Joint probability of occurrence of $\alpha \Delta T$ and $\beta \Delta S$, in counts per 1000 sheets, for bin widths of 5×10^{-4} and 5×10^{-3} respectively. Sheets bounded by at least one layer less than 0.2 m thick have been excluded. The shaded area indicates more than 10 counts per bin. Lines of constant density ratio R_ρ are shown.

To estimate the vertical heat flux through the AIWEX staircase, we assume that the laboratory-based relationships between heat flux F_H and R_ρ and ΔT for diffusive interfaces are valid in the ocean. Several relationships have been proposed (see Newell [1984] for a summary); however, over the range of R_ρ ($1 < R_\rho < 10$) observed in the present data, the function suggested by Marmorino and Caldwell [1976] appears to fit the laboratory data most accurately. Uncertainties in the density ratios arising from measurement limitations on ΔS limit the accuracy of this technique; however, the results are comparable to the fluxes which occur through the high-gradient sheets (see below), assuming no turbulent mixing occurs at these interfaces.

The nondimensional heat flux from Marmorino and Caldwell [1976] is

$$(F_H / F_{Hsp}) = 0.101 \exp \{4.6 \exp [-0.54(R_\rho - 1)]\} \quad (1)$$

$$1 < R_\rho < 10$$

where F_{Hsp} is the heat flux which would be measured if the diffusive interface were replaced by a solid, infinitely conducting, nondeformable plane surface through which only heat could pass, separating the same two homogeneous layers. F_{Hsp}

TABLE 2. Comparison of the Arctic Ocean Diffusive Staircase From the Present Study With That Found by Neshyba et al. [1971]

	Present Study	Neshyba et al. [1971]
Location	74° N, 145.5° W	84° N, 126° W
Date	April 21–22, 1985	November 1969
Staircase depth	300–450 m	200–500 m
Mean density ratio $\langle R_\rho \rangle$	4.9	6.5
Mean buoyancy frequency $\langle N \rangle$	0.0031 s ⁻¹	0.0047 s ⁻¹
Mean layer height $\langle H \rangle$	1.9 m	3.1 m
Mean temperature step $\langle \Delta T \rangle$	0.009 °C	0.022 °C

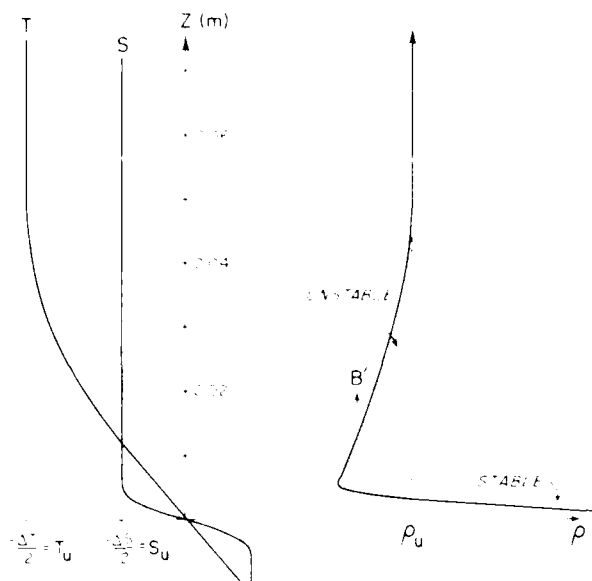


Fig. 7. Profiles of T , S , and ρ for a diffusive interface with thermal thickness much greater than salinity thickness. The upper layer temperature, salinity, and density are T_u , S_u , and ρ_u , respectively. The more rapid diffusion of heat relative to salt ($\kappa_T/\kappa_S \approx 100$) creates a convectively unstable boundary layer (shaded) which can separate when the net buoyancy B overcomes viscous forces, or be more easily entrained by the turbulence of the adjacent layer. The dashed line indicates the position within an interface of total temperature step ΔT and salinity step ΔS where the density profile first becomes unstable.

is given by

$$F_{HSP} \approx (\rho c_p \kappa_T / g \alpha \nu \kappa_S)^{1/3} \Delta T^m \quad (2)$$

The constant c is approximately 0.085 [Chandrasekhar, 1961], while m is usually taken as $\frac{1}{3}$ [Turner, 1973], based on dimensional arguments, although there is some observational evidence for a slightly smaller value in "salt-finger" interfaces [McDougal and Taylor, 1984], and a justification by Kelley [1986] for an exponent closer to $\frac{1}{2}$ for diffusive interfaces.

Using (1) and (2), the heat flux F_H was estimated for each step and then these estimates were averaged over the 100 profiles in 10-m depth intervals. The depth-dependent averaged heat flux F_H is shown in Figure 8 (profile a). The error bars account for uncertainty in R_ρ due to possible errors in ΔS across each sheet (arising from digitization, probe contamination, or electronic drift in the temperature and conductivity sensors). The maximum indicated heat flux is obtained by assuming that the true value of ΔS is always 2×10^{-4} psu smaller than the measured value, with the proviso that $R_\rho > 1$. The minimum flux is obtained by assuming that ΔS is always 2×10^{-4} psu greater than measured, i.e., that each sheet is more stable than measured. These errors are extremely conservative, since the sum of the errors in ΔS over more than one step is still only 2×10^{-4} psu. That is, if several steps are less stable (lower R_ρ) than measured, others must be more stable to preserve the small sum in ΔS . However, the errors do not simply average out in the heat flux estimates because of the nonlinearity of the $(F_H/F_{HSP}) = f(R_\rho)$ relationship at low R_ρ .

The heat flux based on the depth-time-averaged values $\langle R_\rho \rangle = \beta \langle \Delta S \rangle / \alpha \langle \Delta T \rangle$ and $\langle \Delta T \rangle$ is also shown in Figure 8 (profile b). This is the flux profile which would be obtained by treating the staircase as a series of uniform sheets and layers,

where R_ρ and $\langle \Delta T \rangle$ are slowly varying functions of z only. For comparison, the molecular heat flux through a fluid with the same temperature gradient as the large-scale gradient (averaged over 10 m) is also indicated (profile c). Heat fluxes estimated by the first method (profile a) exceed the fluxes determined by the second method (profile b) by about a factor of 2. The discrepancy between the two methods is most pronounced below 390 m, where the probability of sheets with low R_ρ and ΔT occurring is greater than at shallower depths. The effect on the heat flux of errors in the ΔS estimates is therefore larger at this depth, although, as the error bars on profile a indicate, it is still not possible to reconcile both estimates.

The effectiveness of the laboratory flux laws in this staircase can be judged by comparing the heat fluxes determined above with the molecular transport through the high-gradient sheets. If the core regions of the double-diffusive interfaces are always laminar, then the heat flux can be estimated from $F_H = \rho c_p \kappa_T T_z$. The method provides a lower limit only, since the thermometer can resolve only to about 0.04 m at the normal drop speed. Analysis of several slower drops, however, and also analysis of those drops where the PMF four-electrode microconductivity sensor was in use, suggests that the thickness of the interfaces is seldom less than 0.03 m and is typically 0.05–0.1 m. A potentially significant error in estimated heat flux arises if the assumption of laminar interface cores is

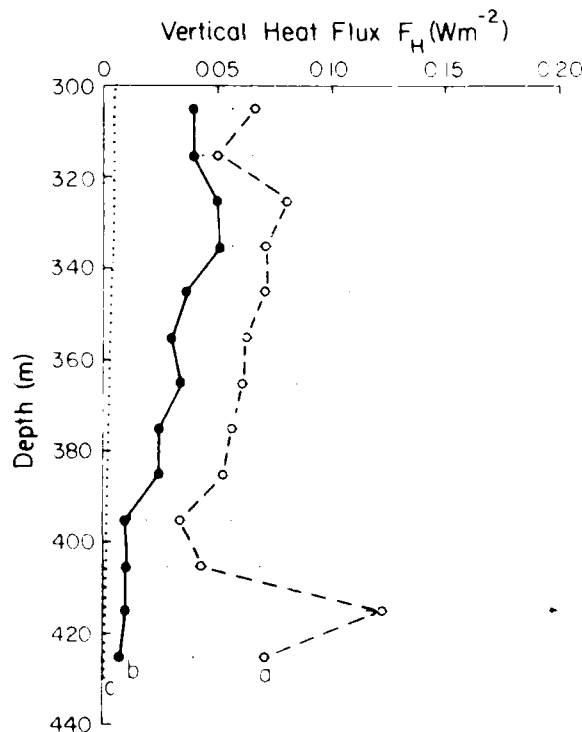


Fig. 8. Average vertical heat flux estimates from equations (1) and (2) applied to each sheet, i.e., $F_H = f(\Delta T, R_\rho)$ (profile a), equations (1) and (2) applied to the mean temperature step and density ratio, i.e., $F_H = f(\Delta T, \langle R_\rho \rangle)$ (profile b), and molecular flux through the large-scale (10 m averaged) temperature gradient (profile c). Angle brackets denote an average over 100 profiles and 10 m in depth. Source of errors in profile a are described in the text.

violated. Since this is the essence of interpretations of elevated heat fluxes at low density ratios [Turner, 1968; Huppert, 1971], it must be considered. However, using a typical step size of 0.01°C and sheet thicknesses of 0.03–0.1 m, the molecular heat flux through the sheets is approximately $0.05 < F_H < 0.2 \text{ W m}^{-2}$, in good agreement with the fluxes calculated from the Marmorino and Caldwell model.

5. DISCUSSION AND CONCLUSIONS

The present diffusive staircase data set can be compared to that which Kelley [1984] collated from diverse sources. Kelley's analysis suggested that a scaling length of $H_0 = (\kappa_T \langle N \rangle)^{1/2}$ collapses layer thicknesses as a function of the density ratio R_ρ , based on an empirical relationship between R_ρ and the layer Rayleigh number Ra . However, these data are unevenly distributed in R_ρ and can effectively be divided into just two subclasses, $1.3 < R_\rho < 2.5$ and $6.1 < R_\rho < 7.7$. Figure 9, adapted from Kelley [1984], shows the dependence of scaled layer height G^* on R_ρ . Note that G^* in Figure 9 is simply Kelley's $G (=H/H_0)$ divided by $Pr^{1/4} = (\nu \kappa_T)^{1/4}$ to remove the Prandtl number dependence suggested by his equation 9b (Pr varies only by a factor of 2 in Kelley's data set, and hence the impact of this change in scaling is negligible). The exact form of the relationship between layer height and R_ρ , however, may be much more complex. We have already seen (section 4) that the interface has different characteristics in different ranges of R_ρ . It is probable that the characteristics of the convective layers are also R_ρ -dependent, with a cellular structure [Kelley, 1986] only when the heat flux is sufficiently high, e.g., large ΔT or small R_ρ , while when the heat flux is low, convection may consist of essentially noninteracting buoyant plumes separating intermittently from the diffusive interface.

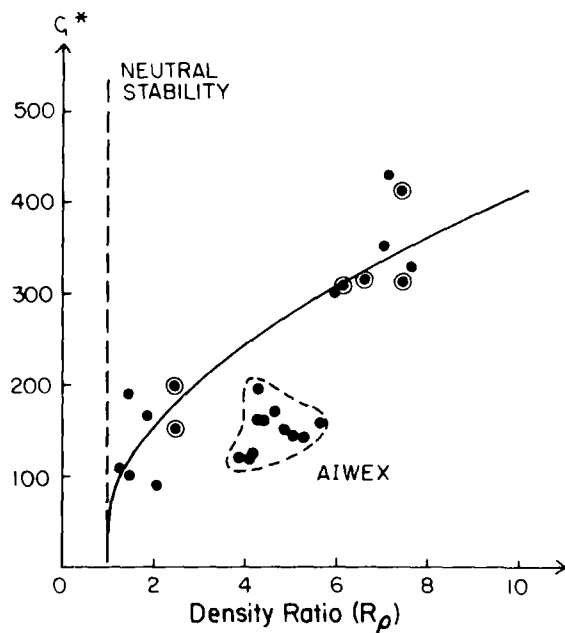


Fig. 9. Comparison of AIWEX step characteristics with previous observations and the function $G^* = f(R_\rho)$ proposed by Kelley [1984]. G^* is a scaled layer height $H/[(\kappa_T N)^{1/2} \sigma^{1/4}]$. Other Arctic data are circled.

The AIWEX data, with a depth-dependent mean density ratio $\langle R_\rho \rangle$ of 3.9–5.7, are also shown in Figure 9, using the mean layer height $\langle H \rangle$ and $\langle R_\rho \rangle$ averaged over 10-m depth intervals and 100 profiles. However, the observed step sizes are by no means uniform in any depth range (see Figure 4 and Table 1). We have shown in section 4 that the nonuniformity of step characteristics results in mean heat fluxes which are $O(2)$ times greater than would be obtained from the mean step parameters $\langle R_\rho \rangle$ and $\langle \Delta T \rangle$; hence an effective model of oceanic staircases must consider instead the distributions of R_ρ and ΔT .

Why is the observed staircase so irregular? Note that although the heat flux in the Canada Basin staircase is $O(10)$ times greater than the molecular flux in a uniformly stratified fluid with the same large-scale temperature gradient, it is still a very small value relative to other heat fluxes in the ocean, such as at the air-sea interface or where shear-induced mixing occurs. As a result, if the staircase is perturbed in any way, the time taken for double diffusion to erase that perturbation is extremely long. An evolution time scale for a staircase can be estimated from the ratio of the heat content difference between layers, $\Delta F_H \approx \rho c_p \langle \Delta T \rangle \langle H \rangle$, and the difference in heat flux between two consecutive sheets. Assuming a heat flux divergence ΔF_H across a typical layer of about 0.02 W m^{-2} , a time scale of $O(1)$ month is obtained. This suggests that perturbations (e.g., intrusions or shear instabilities) to the staircase at any time in the last several months could have contributed to the observed staircase characteristics. Following the same argument used by Schmitt [1981] to account for the constant R_ρ sections of oceanic T - S curves in the salt-fingering regime, we expect that in the absence of further perturbations the profile will slowly evolve to a more uniform form (reduced variability in the distributions of R_ρ , ΔT , and H) by local convergence/divergence of the heat and salt fluxes in the irregular staircase. It is possible, however, that in the Canada Basin, with low diffusive fluxes, the staircase is never able to attain equilibrium. We should therefore be surprised neither by the nonuniformity of the observed staircase nor by the lack of agreement between our observations and models in which only the diffusive instability contributes to the evolution of the temperature and salinity profiles.

At present, we can only speculate as to why thermohaline sheets and layers gradually disappear above and below the staircase. Marmorino and Caldwell [1976] and Newell [1984] found from laboratory experiments that thicker interfaces occurred at higher density ratios, presumably because the turbulent energy of the convecting layers is reduced relative to the static stability of the interface core at higher R_ρ (the former is dependent upon $\alpha \Delta T$, while the latter is dominated by $\beta \Delta S$). Broader steps are found intermittently in the present data set up to about 250 m, where the large-scale density ratio is about 15 (Figure 2b), and below 430 m, and also by Mellor et al. [1984]. Above 250 m, R_ρ increases further to a maximum of about 30 just below the subsurface temperature minimum near 200 m, and no steps are found in this depth range. If we assume that the steps are initially created by the vertical heat flux from below into an initially smooth stratification, it is possible that staircase growth has not continued for sufficiently long for steps to form in this region. If, on the other hand, steps result from the modification of vertically limited perturbations in the density profile by diffusive instabilities, then perhaps at sufficiently high R_ρ this mechanism is ineffec-

tive because of the dominance of static stability relative to the convectively driven velocity fluctuations.

The vertical heat flux calculated in section 4 is two orders of magnitude smaller than the basin-averaged estimate of heat loss from the Atlantic layer [Aagaard and Greisman, 1975] of 7 W m^{-2} . Within the constraints imposed by the large-scale values of buoyancy frequency $\langle N \rangle$ and density ratio $\langle R_\rho \rangle$ between the Atlantic layer and the subsurface Arctic water, it is implausible that diffusive interfaces could transport this heat flux (for $R_\rho = 5$ a step with $\Delta T = 0.6^\circ \text{C}$ would be required). Enhanced heat flux through the sheets by turbulent mixing is not observed in the profiles of turbulent kinetic energy dissipation. Direct contact with the air by upwelling, either at the coast or by surface layer divergences (Ekman pumping), is also unlikely because of the large density difference between the Arctic surface waters and the Atlantic water. The hypothesis of Melling *et al.* [1984], that the heat flux from the Atlantic layer is dominated by benthic stirring where the layer intersects the continental shelf and slope, appears to best explain the basin-averaged heat flux.

Acknowledgments. We thank M. Brown and R. Samelson, who spent many long, cold hours helping collect the data for this report, and H. Garrow, who helped in the analysis. E. Kunze, D. Kelley, and N. Larson contributed valuable comments on an earlier draft. This report would not have been possible without the dedication of Andy Heiberg, Allen Hielscher, and Imants Virsnieks, who provided logistics support in a difficult environment. The guidance and planning efforts of J. Morison are appreciated. This work was supported by the Office of Naval Research, contract N00014-84-C-0218.

REFERENCES

- Aagaard, K., and P. Greisman, Toward new mass and heat budgets for the Arctic Ocean, *J. Geophys. Res.*, **80**, 3821-3827, 1975.
- Caldwell, D. R., T. M. Dillon, and J. N. Moum, The rapid-sampling vertical profiler: An evaluation, *J. Atmos. Oceanic Technol.*, **2**, 615-625, 1985.
- Chandrasekhar, S., *Hydrodynamic and Hydromagnetic Stability*, Clarendon, Oxford, 1961.
- Coachman, L. K., and K. Aagaard, Physical oceanography of Arctic and subarctic seas, in *Marine Geology and Oceanography of the Arctic Seas*, pp. 1-72, Springer, New York, 1974.
- Gregg, M. C., J. C. Shedvin, W. C. Hess, and T. B. Meagher, Dynamic response calibration of the Neil Brown conductivity cell, *J. Phys. Oceanogr.*, **12**, 720-742, 1982.
- Head, M. J., The use of miniature four-electrode conductivity probes for high resolution measurement of turbulent density or temperature variations in salt-stratified water flows, Ph.D. thesis, 211 pp., Univ. of Calif., San Diego, 1983.
- Huppert, H. E., On the stability of a series of double-diffusive layers, *Deep Sea Res.*, **18**, 1005-1021, 1971.
- Kelley, D. E., Effective diffusivities within oceanic thermohaline staircases, *J. Geophys. Res.*, **89**, 10,484-10,488, 1984.
- Kelley, D. E., Oceanic thermohaline staircases, Ph.D. dissertation, Dalhousie Univ., Halifax, Nova Scotia, 1986.
- Marmorino, G. O., and D. R. Caldwell, Heat and salt transport through a diffusive thermohaline interface, *Deep Sea Res.*, **23**, 59-67, 1976.
- McDougall, T. J., and J. R. Taylor, Flux measurements across a finger interface at low values of the stability ratio, *J. Mar. Res.*, **42**, 1-14, 1984.
- Melling, H., R. A. Lake, D. R. Topham, and D. B. Fissel, Oceanic thermal structure in the western Canadian Arctic, *Continental Shelf Res.*, **3**, 233-258, 1984.
- Neshyba, S., V. T. Neal, and W. Denner, Temperature and conductivity measurements under ice-island T-3, *J. Geophys. Res.*, **76**, 8107-8120, 1971.
- Newell, T. A., Characteristics of a double-diffusive interface at high density stability ratios, *J. Fluid Mech.*, **149**, 385-401, 1984.
- Osborn, T. R., and W. R. Crawford, An airfoil probe for measuring turbulent velocity fluctuations in water, in *Air-Sea Interaction: Instruments and Methods*, 801 pp., Plenum, New York, 1980.
- Schmitt, R. W., Form of the temperature-salinity relationship in the central water: Evidence for double-diffusive mixing, *J. Phys. Oceanogr.*, **11**, 1015-1026, 1981.
- Stillinger, D. C., K. N. Helland, and C. W. Van Atta, Experiments on the transition of homogeneous turbulence to internal waves in a stratified fluid, *J. Fluid Mech.*, **131**, 91-122, 1983.
- Turner, J. S., The coupled turbulent transports of salt and heat across a sharp density interface, *Int. J. Heat Mass Transfer*, **8**, 759-767, 1965.
- Turner, J. S., The behavior of a stable salinity gradient heated from below, *J. Fluid Mech.*, **33**, 183-200, 1968.
- Turner, J. S., *Buoyancy Effects in Fluids*, Cambridge University Press, New York, 1973.
- T. M. Dillon and T. Padman, College of Oceanography, Oregon State University, Corvallis, OR 97331.

(Received March 21, 1987;
accepted April 16, 1987.)

FILMED
88